Université catholique de Louvain

Institute of Condensed Matter and Nanosciences

Molecular Chemistry, Materials and Catalysis (MOST) division

Photocatalysts heterogenization on silica nanoparticles for the photosensitization of oxygen and photoredox applications

Thèse présentée en vue de l'obtention

du grade de docteur en sciences par

Body Nathalie

Louvain-la-Neuve

Août 2023

Jury Members

Professor Yann Garcia (UCLouvain, President)

Professor Cécile Moucheron (ULB, Belgium)

Professor Emmanuelle Schulz (Université Paris-Saclay, France)

Professor Charles-André Fustin (UCLouvain)

Professor Raphaël Robiette (UCLouvain)

Professor Sophie Hermans (UCLouvain, Supervisor)

Professor Olivier Riant (UCLouvain, Supervisor)

Remerciements

Tout ce chemin parcouru ne peut se résumer en quelques pages. Si aujourd'hui, ce manuscrit est entre vos mains, c'est grâce à l'aide de nombreuses personnes que je tiens à remercier dans ces quelques lignes.

Il est impossible de débuter ces remerciements sans évoquer les Pr. Sophie Hermans et Olivier Riant. Je tiens à les remercier chaleureusement pour leur aide précieuse, leur disponibilité, leurs conseils, leur bienveillance et leur partage de connaissances. Grâce à vous, j'ai pu grandir, prendre confiance en moi et en mes capacités (ce qui n'était pas chose aisée, stressée que je suis !) et je vous en suis très reconnaissante. Ce fut un réel plaisir de vous pouvoir échanger avec vous lors de discussions scientifiques. Pour tout ça et bien plus encore, je vous remercie.

Merci également aux membres du jury (Pr. Y. Garcia, Pr. R. Robiette, Pr. C.-A. Fustin, Pr. Cécile Moucheron et Dr. Emmanuelle Schulz) d'avoir pris le temps de lire, d'évaluer et de corriger ce manuscrit.

Je voudrais également remercier Ludo pour toute son aide apportée et son énorme partage de connaissances. Ce fut un réel plaisir de pouvoir travailler avec toi et je te souhaite de tout cœur une bonne continuation ainsi que beaucoup de succès dans le domaine académique mais également personnel.

Merci à tous les membres des deux labos pour ces riches échanges scientifiques ainsi que les nombreuses activités réalisées ensemble (mémorables souper de Noël et laser game !). Je tiens à remercier tout particulièrement Michela pour avoir été mon binôme dans ce parcours à l'allure de montagnes russes. Ta présence et ton écoute m'ont été d'une aide précieuse et sans toi, cette thèse n'aurait pas été pareille. Merci aussi à Gilles de m'avoir épaulé et rassuré en début de thèse mais également pour son amitié et tous ces bons moments passés ensemble au labo. Ton départ du labo a laissé un grand vide et je te souhaite plein de réussite pour ces futures années (mais

je sais que c'est en bonne voie !). Merci aussi à Yonghua, Marine et François P. pour leur dynamisme. Je leur souhaite beaucoup de réussite pour la suite/fin de leur thèse. Merci aussi à mon encadrant Antonin. Je ne peux terminer ces remerciements particuliers sans mentionner les post-doctorants, Julien et Corentin, pour m'avoir aidée et guidée dans mes démarches scientifiques. Ce fut une chance de pouvoir travailler et apprendre avec vous et je suis fière du travail que l'on a pu publier ensemble.

Tout ce travail n'aurait pu être réalisé sans l'aide d'étudiantes déterminées. En effet, Sarah et Anne-Sophie ont réalisé un travail remarquable durant leur mémoire et m'ont grandement aidé dans ma recherche. Merci pour votre grande quantité de travail et je vous souhaite beaucoup de réussite et de plaisir dans vos doctorats respectifs.

Deux autres personnes des laboratoires mériteraient bien plus qu'un simple merci. Il s'agit de François B. et de Jean-François bien sûr ! C'est grâce à vous que nous pouvons travailler dans de bonnes conditions et avancer sereinement dans notre travail. Merci pour toutes les discussions personnelles et fous rires que nous avons pu avoir ainsi que pour l'amitié que nous avons tissé au fil de ces quatre années.

Encore merci à Audrey et Céline pour tout leur travail administratif (et oh combien difficile pour nous doctorants) réalisé au cours de ces quatre années. Merci aussi au personnel de l'UCLouvain pour toutes les analyses qui ont été réalisées hors labo et qui, comme vous le savez, sont très importantes. Un merci plus particulier à Pierre pour son aide précieuse dans les interprétations des spectres XPS.

Finalement, je tiens à remercier mes incroyables (belle)-familles. Merci à Maman et Jf de m'avoir toujours épaulée dans mes choix et de m'avoir soutenue, même lorsque j'étais invivable en période d'examens. Merci à ma mamie qui n'a absolument jamais oublié une seule date d'examens et a toujours dirigé ses pensées positives vers moi. Merci à mes beaux-parents

d’avoir toujours été là et pour leurs encouragements. J’ai beaucoup de chance d’avoir trouvé une belle-famille comme la vôtre. Une grosse pensée également à mes étoiles qui veillent sur moi de là-haut. Merci à tous mes amis, de Gaume ou de LLN, pour leur soutien. Finalement, merci à toi, Timo. Je ne peux livrer tous mes sentiments ici mais je ne saurai jamais assez te remercier pour tout ton soutien, ton amour, ta patience et pour tout le bonheur que tu m’apportes au quotidien. Du plus profond de mon cœur, merci !

Je vous laisse maintenant découvrir ce manuscrit avec autant de plaisir (je l’espère) que j’ai pu en avoir pour le réaliser durant ces quatre années de doctorat.

List of Abbreviations and Symbols

°C	Celsius degree
$\Delta G^{\neq}$	Free Energy of Activation
ΔG^{0}	Free Energy of Change
ϕ	Quantum yield
ε	Molar Absorption Coefficient
τ	Excited-state lifetime
ν	Frequency
λ	Wavelength
A/Abs	Absorbance
abpy	4-Formyl-4'-methyl-2,2'-bipyridine
AIBN	Azobisisobutyronitrile
AIM	Atom in Molecules
APTES	Aminopropyltriethoxysilane
APTMS	(3-Aminopropyl)trimethoxysilane
at.%	Atomic percentage
AVS	Anthracene-9,10-divinylsulfonate
BCP	Bond Critical Point
BET	Brunauer Emmett Teller
BJH	Barret-Joyner-Halenda
BODIPY	Boron-dipyrromethene
bpy	Bipyridine
CMC	Critical Micellization Concentration
CPB	Cetylpyridinium Bromide
CS	Core-Shell
CTAB	Hexadecyltrimethylammonium bromide
CTB	Cetyltrimethylammonium Bromide
CV	Cyclic Voltammetry
dap	2,9-Bis(*p*-anisyl)-1,10-phenanthroline
DAPTMS	(*N*,*N*-dimethylaminopropyl)trimethoxysilane
dbrbpy	5,5'-Dibromo-2,2'-bipyridine
DCA	9,10-Dicyanoanthracene
DCM	Dichloromethane
DFT	Density Functional Theory
DIC	N,N'-diisopropylcarbodiimide
DIPEA	N,N-diisopropylethylamine
DLS	Dynamic Light Scattering

DMF	Dimethylformamide
DMP	Dimethylphenanthroline
DMS	Dimethylsulfone
DMSO	Dimethylsulfoxide
DPBF	1,3-Diphenylisobenzofuran
DPEPhos	Bis[(2-diphenylphosphino)phenyl]ether
DPV	Differential Pulse Voltammetry
DRS	Diffuse Reflectance Spectroscopy
DSSC	Dye-sensitized Solar Cells
E	Energy
$E_{0,0}$	Excitation Energy
EDA-NOCV	Energy Decomposition Analysis based on Natural Orbital for Chemical Valence
EDDA	Ethylenediammonium diacetate
EnT	Energy Transfer
ESI	Electronspray Ionization
EtOH	Ethanol
eV	Electron-Volt
EY	Eosin Y
Fluo	Fluorescence
FT-ATR	Fourier Transformed – Attenuated Total Reflectance
GBP	Gradient-based Partition
GC	Gas Chromatography
GO	Graphene Oxide
HOMO	Highest Occupied Molecular Orbital
HRMS	High Resolution Mass Spectrometry
IBSI	Intrinsic Bond Strength Index
IBX	2-Iodoxybenzoic Acid
IC	Internal Conversion
ICP-OES	Inductively Coupled Plasma Optical Emission Spectroscopy
IR	Infrared
IRF	Instrument Response Factor
ISC	Intersystem Crossing
k_{nr}	Non radiative Deactivation Constant
k_q	Quenching Rate Constant
k_r	Radiative Deactivation Constant
LC	Ligand Centered
LED	Light-Emitting Diodes

LUMO	Lowest Unoccupied Molecular Orbital
MB	Methylene Blue
MCM	Mobil Composition of Matter
Mebib	Bis(*N*-methylbenzimidazolyl)pyridine
MeCN	Acetonitrile
MeOH	Methanol
mM	Millimolar
MOF	Metal Organic Framework
NBO	Natural Bond Orbital
NHE	Normal Hydrogen Electrode
NIphen	5-(1,8-Naphthalimide)-1,10-phenanthroline
nm	Nanometer
NMR	Nuclear Magnetic Resonance
NP	Nanoparticle
NRD	Non radiative Deactivation
NS	Nanospheres
NTA	Nanosecond Transient Absorption
NuH	Nucleophile
OLED	Organic Light-Emitting Diodes
OS	One-step methodology
Ox	Oxidative quenching cycle
PC	Photocatalyst
PC*	Excited Photocatalyst
Phospho	Phosphorescence
PJT	Pseudo Jahn-Teller
PL	Photoluminescence
PLI	Photoluminescence Intensity
POP	Bis[2-(diphenylphosphino)phenyl]ether
PP	Polypropylene
ppy	Phenylpyridine
PS	Photosensitizer
PS*	Excited Photosensitizer
PTFE	Polytetrafluoroethylene
PVDF	Polyvinylidene Fluoride
Q	Quencher
RB	Rose Bengal
Red	Reductive quenching cycle
rGO	Reduced Graphene Oxide
RISC	Reverse Intersystem Crossing

ROS	Reactive Oxygen Species
r.t.	Room Temperature
SAR	Structure-Activity Relationship
SBA	Santa Barbara Amorphous
SET	Single Electron Transfer
SI	Supporting information
SMD	Solvation model based on Density
SOC	Spin-orbit Coupling
SSL	Solid State Lighting
SSPL	Steady-State Photoluminescence
SV	Stern-Volmer
TA	Transient Absorption
TADF	Thermally Activated Delayed Fluorescence
TBA	Tertbutylammonium
TEA	Triethylamine
TEM	Transmission Electron Microscopy
TEMPO	(2,2,6,6-Tetramethylpiperidin-1-yl)oxidanyl
TEOS	Tetraethylorthosilicate
TFA	Trifluoroacetic Acid
TfOH	Triflic Acid
tfpb	Tetrakis(3,5-bis(trifluoromethyl)phenylborate
TGA	Thermogravimetric Analysis
THF	Tetrahydrofuran
TLC	Thin Layer Chromatography
ToF-SIMS	Time of Flight – Secondary Ion Mass Spectrometry
TON	Turn-over Number
TPP	Tetraphenylporphyrin
TPP^+	Triphenylpyrylium cation
TRPL	Time-resolved Photoluminescence
Ts	Tosyl
TS	Two-step Methodology
TTA	Triplet-Triplet Annihilation
U	Urchins
UV	Ultra-Violet
UV-vis	UV-visible
VR	Vibrational Relaxation
wt.%	Percentage by weight
XPS	X-ray Photoelectron Spectroscopy

Summary

Photocatalysis is an incredible tool to work with to synthesize organic compounds. The versatility of the available photocatalysts reinforces the power of photochemistry, in addition to its "green" nature and unique one-electron pathways. Ruthenium and iridium polypyridyl complexes dominate this field but their use is limited due to their price and scarcity. Organic dyes and copper complexes have been extensively investigated to replace them, but their low photostability, hard separation from the reaction products or expensive synthesis still hamper their implementation.

In this context, the main goal of this PhD thesis is to design robust heterogeneous systems based on immobilized organic dyes or copper complexes on the surface of silica nanoparticles in order to circumvent their main drawbacks or even increase their performances and allow their recyclability and reuse. For accomplishing this, we have investigated firstly the impact of the solid SiO_2 support morphology on the generation of singlet oxygen by Rose Bengal. We identified that the core-shell was the best structure to employ in terms of photophysical properties, activity and recycling of the surface-bound molecule. Next, we established a structure-activity relationship of benzophenazines which are simple dyes prone to functionalization in order to identify how to immobilize those photocatalysts without influencing their efficiency towards the generation of singlet oxygen. Finally, heteroleptic and homoleptic copper(I) complexes were anchored onto silica nanoparticles to increase their photostability by limiting the ligand exchange that they may undergo under specific conditions. Such strategy was not successful with heteroleptic complexes which formed the corresponding homoleptic complex at the solid surface. Nevertheless, we demonstrated that grafted homoleptic complexes were competent for excited-state electron transfer to 4-nitrobenzene diazonium tetrafluoroborate which generated the corresponding Cu(II) analogue that persisted on the millisecond timescale.

Résumé

La photocatalyse est un outil efficace pour la synthèse de composés organiques. Son utilisation est d'autant plus renforcée par la variété de photocatalyseurs disponibles, sa nature « verte » et les mécanismes impliquant des transferts monoélectroniques. Les complexes de ruthénium et d'iridium sont les plus communs d'utilisation mais leur prix et leur rareté impliquent le besoin d'alternatives. Parmi elles, les colorants et complexes de cuivre sont étudiés mais leur faible photostabilité, leur séparation difficile en fin de réaction et leur synthèse pouvant être onéreuse limite leur mise en place.

Dans ce contexte, le principal objectif de cette thèse est de mettre au point des systèmes hétérogènes robustes et performants à base de colorants ou de complexes de cuivre immobilisés sur nanoparticules de silice afin d'améliorer leurs performances et de les rendre recyclables et réutilisables. Pour atteindre cet objectif, nous avons tout d'abord investigué l'impact de la morphologie du support solide sur la génération d'oxygène singulet par le Rose Bengale. La structure *core-shell* a été identifiée comme la plus efficace, garantissant un photocatalyseur avec les meilleurs propriétés photophysiques, activité et recyclage. Ensuite, nous avons établi une relation structure-activité pour des colorants simples et faciles à fonctionnaliser que sont les benzophénazines, dans le but d'identifier la meilleure approche d'immobilisation n'influençant pas leur efficacité dans la production d'oxygène singulet. Finalement, des complexes de cuivre hétéroleptiques et homoleptiques ont été ancrés sur des nanoparticules de silice afin d'améliorer leur photostabilité en limitant l'échange de ligands qui peut se produire sous certaines conditions. Cette stratégie s'est révélée infructueuse avec les complexes hétéroleptiques. Cependant, nous avons démontré la capacité des complexes homoleptiques hétérogénéisés à réaliser un transfert monoélectronique avec un dérivé diazonium, formant ainsi l'analogue Cu(II) persistant pendant plusieurs millisecondes.

Table of contents

CHAPTER 1 1
INTRODUCTION 1
1. The light 1
1.1. Light as an energy source 1
1.2. Pathway to resurgence of photochemistry 4
2. Photocatalysis 7
2.1. Organic Photocatalysts 7
2.1.1. Organic dyes 8
2.1.2. Copper complexes 10
2.2. Fundamental concepts of photophysics 12
2.2.1. The Jablonski diagram 12
2.2.2. Intermolecular excited-state relaxation 17
2.3. Activation modes of organic molecules by photocatalysis 21
2.3.1. Single electron transfer (SET) – Photoredox 21
2.3.2. Energy transfer – Photosensitization 31
3. Supported homogeneous photocatalysis 39
3.1. Immobilization strategies 40
3.2. Applications of immobilized photosensitizers 42
3.2.1. Silica nanoparticles 42
3.2.2. Zeolites 45
3.2.3. Polymers 46
3.2.4. Graphene oxide (GO) 48
3.2.5. Natural supports 49
4. Silica Nanoparticles 50
4.1. Porosity and structures 51
4.2. Synthesis 52
4.2.1. Non-porous silica particles 52
4.2.2. Mesoporous materials 54
4.2.3. Particular case of KCC-1 55
4.3. Surface chemistry 56
4.3.1. Functionalization 57

CHAPTER 2 61
THESIS OBJECTIVES 61
1. Detailed methodologies 64
2. Characterization methods 67
3. Contents of the Manuscript 69

CHAPTER 3 71
IMPACT OF SILICA NANOPARTICLES ARCHITECTURES ON THE PHOTOSENSITIZATION OF O_2 BY IMMOBILIZED ROSE BENGAL 71
1. Abstract 73
2. Introduction 74
3. Results and discussion 76
4. Conclusion 95
5. Experimental section 97

5.1. Chemicals and materials 97
5.2. Characterization methods 97
5.3. Experimental protocols 100

CHAPTER 4 109
STRUCTURE-ACTIVITY RELATIONSHIP INVESTIGATION OF NEW BENZOPHENAZINE DERIVATIVES AS HOMOGENEOUS AND HETEROGENIZED PHOTOOXYGENATION CATALYST 109
1. Abstract 111
2. Introduction 112
3. Results and discussion 118
3.1. Cyclic ether case 118
3.2. Computational prediction of the absorption wavelengths and the triplet energy of benzophenazine derivatives 122
3.3. Experimental photophysical properties of benzophenazine derivatives 127
3.4. $^3O_2$ photosensitization 137
3.5. Photostability investigation 142
3.6. Benzophenazine heterogenization on silica nanoparticles 146
4. Conclusions 152
5. Experimental section 154
5.1. Chemicals 154
5.2. Characterization methods 155
5.3. Experimental protocols 158

CHAPTER 5 197
THE DIETHYLANILINE PHOTOCATALYST 197
1. Introduction 197
2. Results and discussion 198
2.1. Electrochemical properties 198
2.2. Excited-state and photoreactivity investigation 203
2.2.1. Characterization in dichloromethane 204
2.2.2. Excited-state photostability 206
2.2.3. Photoproduct identification 213
2.2.4. Comparison with another benzophenazine derivative 216
3. Conclusions and perspectives 218

CHAPTER 6 221
PHOTO-CATALYZED α-ARYLATION OF ENOL ACETATE USING RECYCLABLE SILICA-SUPPORTED HETEROLEPTIC AND HOMOLEPTIC COPPER(I) PHOTOSENSITIZERS 221
1. Abstract 223
2. Introduction 224
3. Results and discussion 228
3.1. Synthesis 228
3.2. Photophysical and electrochemical properties 238
3.3. Excited-state reactivity 243
3.4. Photocatalytic tests 247
4. Conclusions 253
5. Experimental section 254

5.1. Chemicals and materials 254
5.2. Characterization methods 254
5.3. Experimental protocols 260

CHAPTER 7 277
CONCLUSIONS AND PERSPECTIVES 277
1. General conclusions 277
2. Perspectives of this work 281

ANNEX A 287
SUPPORTING INFORMATION – CHAPTER 3 287

ANNEX B 307
SUPPORTING INFORMATION – CHAPTER 4 307

ANNEX C 411
SUPPORTING INFORMATION – CHAPTER 5 411

ANNEX D 421
SUPPORTING INFORMATION – CHAPTER 6 421

BIBLIOGRAPHY 452

PUBLICATIONS AND SCIENTIFIC COMMUNICATIONS 472

Chapter 1

Introduction

1. The light

Light is a powerful tool that is ubiquitous and vital for any life on the planet. In our daily life, products that are produced with the assistance of photochemistry or that exploit photochemistry or photophysics to perform their function surround us. This is the case for example of photosynthesis performed by green plants (or photosynthetic bacteria) that naturally convert water and carbon dioxide into oxygen and energy (sugars) using sunlight. Other processes requiring sunlight absorption are the synthesis of vitamin D and the *cis-trans* isomerization of retinal leading to vision in vertebrates. Light is also useful for bioluminescent organisms such as fireflies or dinoflagellates. Sustainable technologies (solar energy storage), environment (waste water cleaning, pollutant detectors,…), medicine (photodynamic therapy, biological markers) or atmospheric chemistry are numerous examples that highlight the importance of light also for man-made applications.[1–4]

1.1. Light as an energy source

Light can be defined as an electromagnetic radiation composed of oscillating electrical and magnetic fields. If we consider this wave model, electromagnetic radiation is characterized by a wavelength λ (the distance

between two peaks in the wave), a frequency ν (number of oscillations per second), and a velocity *c*. The speed of light *c* is constant (3.0×10^8 m s^{-1} in vacuum), whereas λ (and ν) may cover a wide range of values forming the electromagnetic spectrum (**Figure 1.1**). The latter encompasses a variety of radiation types from γ-rays to radiowaves distinguished by their wavelengths and frequencies, hence with very different energies.

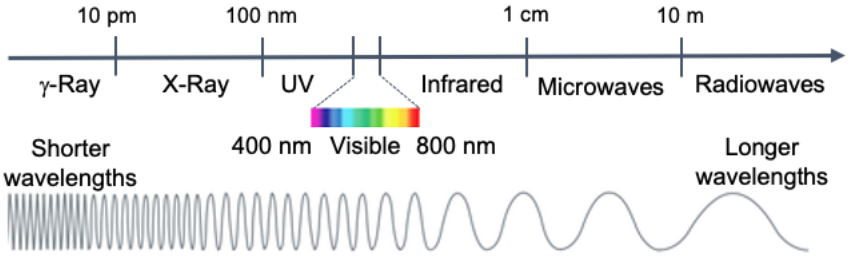


Figure 1.1. Electromagnetic spectrum.

In the quantum model, a light source is not considered as a wave anymore but is considered as a stream of photons which has a specific energy, *E*, related to the frequency ν (coming from the wave model), as stated by the Planck-Einstein relationship where *h* is Planck's constant (6.63×10^{-34} J.s):

$$E = h\nu = h\frac{c}{\lambda} \qquad (1.1)$$

This definition of light as made up of individual photons is essential to photochemistry and photophysics as the interaction of light with molecular systems is generally an interaction between one molecule and one photon at a time.[1] Indeed, a molecule can absorb one photon to reach its excited state and gain energy that can further be exploited in photochemistry. As a starting point, one can consider that this energy will depend on the gap existing between the highest occupied molecular orbital (HOMO) and the lowest unoccupied molecular orbital (LUMO). Such activation pathway is interesting as the reached excited state shows new properties and reactivities compared to the fundamental one and is considered as a new species. Nevertheless, photon energy needs to be controlled when carrying out photochemistry as it

can also induce damages to the molecules. From equation **1.1**, the energy of one mole of photons (an Einstein) can be determined and values for some relevant wavelengths are gathered in **Table 1.1**. It is interesting to compare the energy of a photon with the energy of a chemical bond. For example, the energy required to break a C–Br bond is 276 kJ mol^{-1} and is of similar magnitude than the energy of one Einstein at 433 nm which corresponds to the blue region of the visible light. For an O–H chemical bond (463 kJ mol^{-1}), the energy corresponds to an Einstein of photons at 260 nm.[5]

Table 1.1. Relationship between wavelength and energy.[5]

Type of light	Wavelength (nm)	Energy (kJ mol^{-1})
Near-UV	300–400	400–300
Blue	~ 450	266
Green	~ 500	240
Orange	~ 600	199
Red	~ 700	171

Solar energy which has attracted much attention these last decades as the supply of secure, clean, and sustainable energy and has been identified as one of the most important scientific and technical challenge facing humanity in the 21st century.[6] Solar energy is a promising candidate to replace fossil fuels and was already considered by Giacomo Ciamician more than one hundred years ago.[7] Solar energy is abundant. In less than an hour, the Earth receives an amount of energy equal to the entire world's annual energy consumption (176.4 TWh in 2021).[4,8] Moreover, solar energy is well-distributed and is considered inexhaustible on our time scale as it should shine for a few billion years more. Although solar energy presents incredible qualities, they are mitigated by two drawbacks: the intensity of solar energy that the Earth is receiving is low and intermittent due to weather conditions and day-and-night cycles. The power density of solar energy is on average approximately 170 W m^{-2} and its most intense irradiance is exhibited by the visible part, between

400 and 750 nm (**Figure 1.2**). This observation highlights the importance of this region of the electromagnetic spectrum to perform photochemistry as it combines a high irradiance with photons having sufficient energy to induce electronic transitions between the HOMO and the LUMO.[4]

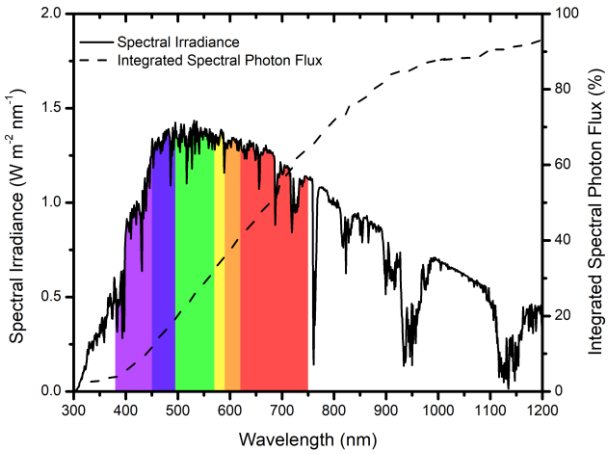


Figure 1.2. Solar irradiance spectrum (figure realized by S. De Kreijger and L. Troian-Gautier).[9]

1.2. Pathway to resurgence of photochemistry

Although photochemistry has been identified a long time ago as a powerful and sustainable tool to use, its development in organic synthesis has resurged only recently. Most organic compounds possess no or low number of insaturations which implies a huge HOMO-LUMO gap leading to the absorption of photons from the ultraviolet (UV) region which are not abundant in the solar radiation. Moreover, UV photons are quite high in energy, of the order of a C–C bond, and can cause considerable unproductive decomposition reactions to occur, particularly when relatively weak bonds are present or when the target compounds possess substantial structural complexity. This has limited the development of photochemistry.[10] Moreover, a restricted access to safe light sources hampered the practical development of early photochemistry.

In 1960s, the light amplification by stimulated emission of radiation (laser) was developed and was decisive for the growth of modern photochemistry as it delivers a powerful and monochromatic light that can be eventually pulsed (**Figure 1.3**).[3] In 1962, another breakthrough in light sources was made by N. Holonyak and S. F. Bevacqua with the development of the first operational light-emitting diodes (LEDs).[11] Based on the emerging concept of solid-state lighting (SSL), LEDs are a p-n junction semiconductor device emitting light in a narrow band. It is made of a thin layer of gallium arsenide (GaAs), gallium arsenide phosphide (GaAsP), gallium phosphide (GaP), or indium gallium nitride (InGaN).[12–14] By varying the composition of the semi-conductor and its thickness, scientists are able to make a LED emitting any desired color.[14] In 1994, S. Nakamura *et al.* presented the first blue LED[15] and rapidly after, white light-emitting LEDs were also developed by coating blue indium gallium nitride with a Ce:YAG ($Y_3Al_5O_{12}$) glass-ceramic phosphor.[14,16] Nowadays, LEDs are standard for screen backlighting, automotive applications, traffic signaling, urban lighting, advertising, decoration, and even photochemistry. Other advantages of using LEDs are their small size, available forms (bulb or chip), robustness, safety, easy setup, low costs of production and operation, and long-life span (more than 100.000 hours).[12,13,17]

Another technology emerging from SSL concept is organic light-emitting diodes (OLEDs) which was firstly built in 1987 by Tang and Van Slyke from Kodak.[18–20] The market of OLEDs has grown rapidly since then and these are now used in smartphones, tablets, computers, televisions, automobile, smart watches and so on. However, this technology has major drawbacks such as a low lifetime and a complex method of fabrication leading to a high production cost.[21]

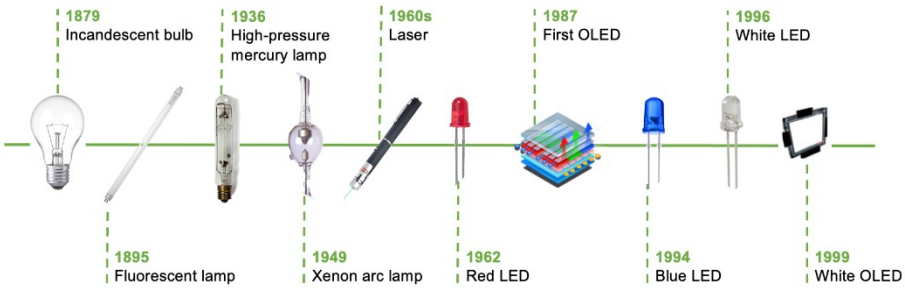


Figure 1.3. Development of light sources.

The developments of laser and LED technologies capable of emitting multiple wavelengths while being small, efficient, low-cost and easy to use was a strong step towards the use of photochemistry in organic synthesis. In the 1970s and 1980s, the first examples of photoredox catalysis applied to organic transformations were reported by Pac[22], Kellogg[23], Deronzier[24] and Kern and Sauvage.[25] They identified the potential of transition metal-based complexes such as $[Ru(bpy)_3]^{2+}$ (bpy = bipyridine) and $[Cu(dap)_2]^{+}$ (dap = 2,9-bis(*p*-anisyl)-1,10-phenanthroline) to participate in light-mediated electron transfer used in organic synthesis. However, these photocatalysts were involved in relatively simple reactions which hampered their further development. Photoredox catalysis for organic transformations came back in the foreground of research only in 2008 with the reports of Yoon[26] and MacMillan's groups[27] and by Stephenson rapidly after using $[Ru(bpy)_3]^{2+}$ as photocatalyst for the synthesis of complex and chiral organic molecules.[28] Ruthenium and iridium complexes were already known before in photochemistry but were dedicated to convert solar energy into electrical current, water splitting, oxygen sensing, or in OLEDs.[29–35] Since this discovery, photocatalysis has become an area of intense investigation. Light adds a new dimension to chemistry as, in many cases, photochemistry achieves what ground-state chemistry cannot. Moreover, photochemical synthesis on a gram scale is simple and requires only relatively inexpensive equipment.[2] With all these information in mind, we can be convinced that photochemistry is a new efficient way to perform outstanding chemistry.

2. Photocatalysis

Photochemistry is the branch of science that studies the chemical reactions that occur following light absorption and/or that emit light. When a photochemical process involves the use of a catalyst, the term *photocatalysis* is more appropriate. Photocatalysis describes chemical transformations that require light as an energy input to proceed and typically use catalytic amounts of light-absorbing photocatalysts (PC) for activation.[36] Heterogeneous photocatalysis based on semiconductor solids such as TiO_2[37–41], ZnO[42–44], bismuth oxides and oxyhalides[45–48], CdSe and CdS[49,50], or the more recently developed, carbon nitrides[51–55], is the most extensive use of photochemistry in commercial applications: autocleaning surfaces, water and air disinfection, anti-mist for glasses and mirrors, or skin protection. These PCs work on the principle of bands theory and the formation of electron/hole pairs upon irradiation, and as their behavior differs completely from the targeted PCs in this work, namely organic and soluble PCs, heterogeneous PCs will not be overviewed in details and the reader is referred to relevant literature.[56–60]

2.1. Organic Photocatalysts

Homogeneous (in the sense of soluble) photosensitizers (PS) are mainly dominated by the use of organometallic polypyridyl complexes of expensive iridium and ruthenium noble metals. *Via* their incredible photophysical properties such as a strong absorption in the visible region of the electromagnetic spectrum, a long excited-state lifetime, a great photostability and high excited-state redox properties, these organometallic complexes have been largely used in various applications since decades. Even though their efficiency is outstanding, their rather high cost, potential toxicity (due to their coordination to nucleic acids and proteins inducing cytotoxicity)[61] and scarcity of the corresponding metal salts are major drawbacks. Employing precious and rare-Earth metals is furthermore not ecological as mining, extraction and separation are highly energy and water consuming. All these

facts might hamper their use in the development of economical chemical processes or their scale-up at an industrial scale.[62–64] Alternatives are needed and trigger our attention, such as organic dyes and Earth-abundant complexes.

2.1.1. Organic dyes

Recently, research has begun to shift towards organic-based photocatalysts that can compare to or even outperform transition metal photocatalyst efficiencies. This has already been detailed in several reviews.[65–71] The main advantage of organic photocatalysts is the wide availability of chemical scaffolds that induces a broad range of photophysical properties, essential point for their use in various synthetic pathways. Their relatively low-cost and toxicity, high solubility in organic solvents along with no metal contamination of the products reinforce their potential for applications in photocatalysis.[70] To highlight such great potential, several examples of organic dyes are reported in **Figure 1.4** with their photophysical properties and mechanisms of action (which will be discussed in section 2.3).

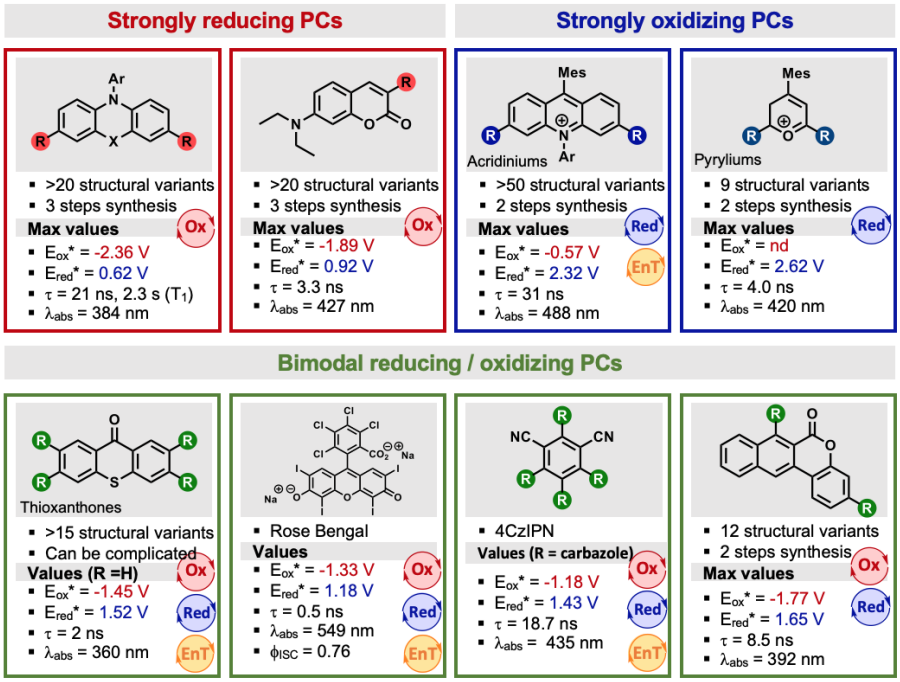
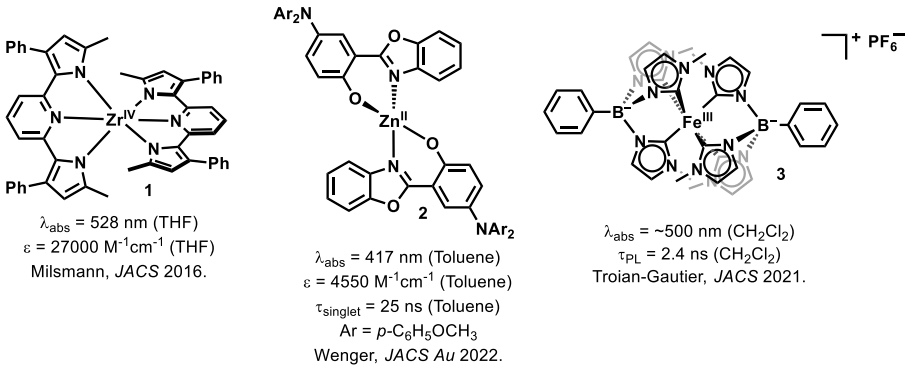


Figure 1.4. Structures of common organic photocatalysts classified in strongly or bimodal reducing/oxidizing photocatalysts depending on the redox partner involved in the considered photocatalytic process. The redox potentials were recorded *versus* saturated calomel electrode (SCE). The mechanisms of action are reported as follows: **Ox** = oxidative quenching, **Red** = reductive quenching and **EnT** = Energy Transfer.[65,68,72]

2.1.2. Copper complexes

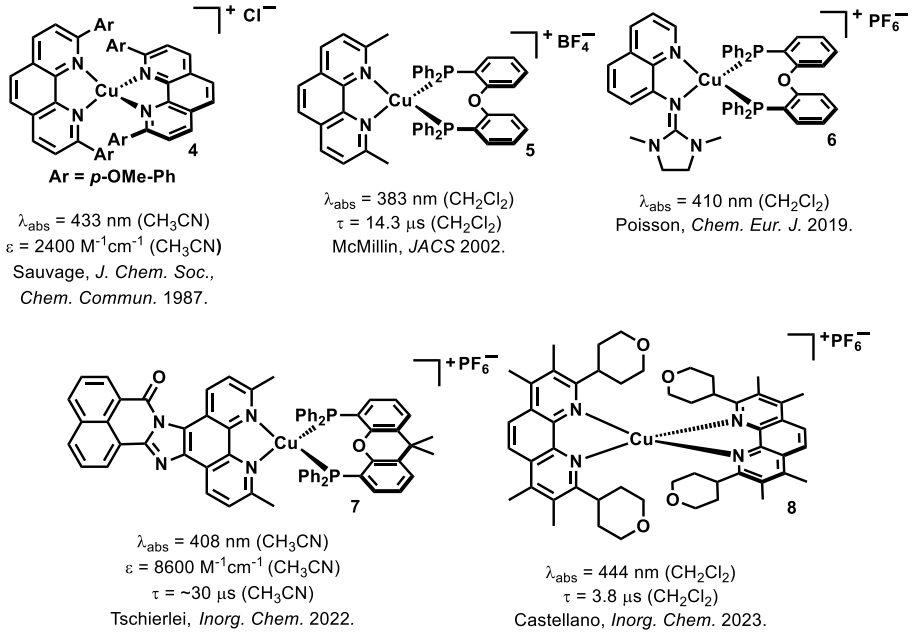
Alternatives based on Earth-abundant photoactive coordination complexes, such as those based on iron, zirconium, zinc or copper, have recently emerged (**Scheme 1.1**).[28,73–90]



Scheme 1.1. Earth-abundant complexes used in photocatalysis.

Among all non-noble metals, copper is especially interesting since copper(I) complexes (**Scheme 1.2**), thanks to their closed-shell d^{10} ground-state configuration, do not exhibit fast nonradiative deactivation of the excited state *via* low-lying metal-centered (MC) states as observed for other first row transition metal complexes such as $3d^6$ Fe(II) and other 3d metal complexes with a d^1-d^9 electron configuration.[83] From an historical point of view, homoleptic copper(I) complexes $[Cu(NN)_2]^+$, where NN is a bidentate diimine ligand, were the first copper(I) complexes to be developed in photocatalysis. In the late 1980s, Kern and Sauvage reported the synthesis of $[Cu(dap)_2]^+$ and its application in the homocoupling of *p*-nitrobenzyl bromide.[25] Drawbacks such as the low excited-state lifetime of homoleptic complexes limited their applications which led to their gradual disuse compared to Ru(II) and Ir(III) analogues.[83] $[Cu(NN)_2]^+$ have nonetheless experienced a recent upsurge due to their notable reducing properties and the development of new diimine ligands enhancing the photophysical properties of such copper complexes.[75,76,91–98] In an effort to enhance their photophysical properties, new derivatives of 1,10-phenanthroline ligands bearing bulky substituents

were indeed developed to prevent excited-state geometry changes *via* pseudo Jahn-Teller distortion.[99,100] In 2002, McMillin and coworkers drastically improved the field of copper photocatalysis by associating these sterically hindered diimine ligands with a diphosphine POP ligand (POP = bis[2-(diphenylphosphino)phenyl] ether). This led to the development of a new family of heteroleptic photocatalysts with excited-state lifetimes that could exceed those of ruthenium and iridium photocatalysts.[101] Since then, heteroleptic copper complexes have been tremendously developed and their potential was demonstrated in multiple organic synthesis applications.[83,86,102–106]



Scheme 1.2. Homoleptic and heteroleptic copper complexes investigated as PCs.

In order to understand how these alternatives can induce a photochemical process to occur, we need to review some fundamental concepts, regarding light-induced phenomena leading to photochemical applications.

2.2. Fundamental concepts of photophysics

2.2.1. The Jablonski diagram

The behavior of all photoactive compounds can be represented in a schematized energy diagram with the possible transitions that can occur between the different energy levels, named the Jablonski diagram (**Figure 1.5**).

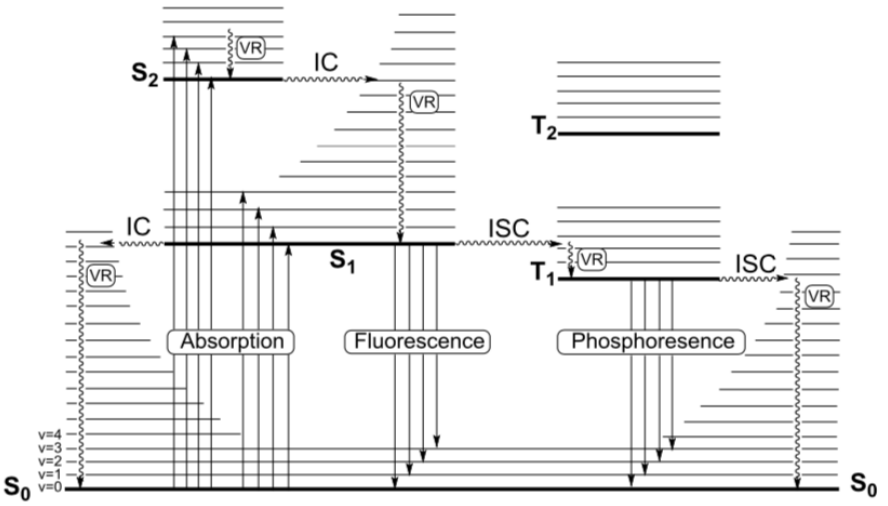


Figure 1.5. The Jablonski diagram showing the fundamental and excited states of a molecule with the possible deactivation pathways. S_0 = fundamental state, S = singlet excited state, T = triplet excited state, IC = internal conversion, VR = vibrational relaxation, ISC = intersystem crossing.[5]

Let us navigate through this scheme to understand the electronic transitions that may occur upon irradiation in a photoactive compound such as an organic dye or a copper complex.

2.2.1.1. Light absorption - Excitation

The simplest and usual interaction between molecules and light is that one molecule absorbs one photon[1] allowing an electronic transition if the photon has sufficient energy for the molecule to reach an allowed excited-state level. The energy difference between the ground and excited states must match exactly the energy of the incident photon. Furthermore, there must be a

specific interaction between the electric vector of the electromagnetic wave and the electric dipole of the molecule to allow an electronical transition.

Electronic transitions are governed by two selection rules that qualify a transition as forbidden or allowed and help to predict the intensity of electronic transitions. The **Laporte** selection rule states that the only allowed transitions are those with a change of parity for molecules doted of a symmetry center. As copper complexes adopt a tetrahedral geometry that does not exhibit a symmetry center, intense bands of absorption are observed for such complexes. The second rule, the **spin** one, states that a transition is allowed only if no change in spin multiplicity occurs during the transition. A vast majority of molecules have a singlet ground state and consequently their absorption spectra are mainly constituted by spin-allowed singlet → singlet transitions. Experimentally, forbidden transitions can nonetheless be observed and the key element here is that there are various mechanisms by which selection rules are bypassed so that these transitions can occur, but usually then with low intensities. For example, the spin selection rule can be bypassed with molecules containing heavy atoms ($Z > 40$) and thus exhibiting spin-orbit coupling, such as the Rose Bengal dye with the presence of iodide atoms. The spin-orbit coupling induces interactions between wave functions of different multiplicity allowing singlet → triplet transitions.[5,107]

The efficiency with which the reactive excited state is formed upon photon absorption is defined by its quantum yield ϕ of formation. A quantum yield of any given process induced by light absorption is defined as the ratio between the number of molecules undergoing the process per unit time and the number of photons absorbed per unit time. Thus, a perfect formation of the excited state will correspond to a quantum yield equals to 1.[1,108]

On the Jablonski diagram, electronic transitions are represented as vertical arrows according to the Franck-Condon principle stating that an electronic transition occurs on a short time scale compared to nuclear motion

and bonds vibrations, so that the transition probability can be calculated at fixed nuclear position from the lowest vibrational level of the ground state to the n^{th} vibrational level of the excited state, the lowest vibrational level of the ground state being the most populated at room temperature according to the Maxwell-Boltzmann distribution equation.[109,110] This is in agreement with the experimental observation that the absorption of a photon is taking place in 10^{-15}–10^{-16} s and nuclear vibrations are taking place in 10^{-13}–10^{-14} s.[111] Moreover, the Franck-Condon principle states that the electronic transition is more intense when favoring the overlap of wave vibrational functions.[109,110]

The energy difference that exists between the ground state and an excited state will determine the photon minimal energy to induce an electronic transition and thus, *via* the **equation 1.1**, the photon wavelength to bring one electron from the HOMO to the LUMO which is the lowest-energy transition. For organic molecules, the energy of the electronic transitions usually follows:

$$n \rightarrow \pi^* < \pi \rightarrow \pi^* < n \rightarrow \sigma^* < \sigma \rightarrow \pi^* < \sigma \rightarrow \sigma^*$$

with corresponding intensities, and thus molar extinction coefficients (ε), that will depend on the respect of selection rules.

For copper complexes, the electronic transitions are of two main types. The absorption bands located in the UV part of the spectrum correspond to intense π–π^* ligand centered (LC) transitions, while the bands located in the visible part of the spectrum are d–d metal to ligand charge transfer (MLCT) transitions, with the latter being the most important and useful bands for photochemistry. MLCT transitions are usually lower in intensity than LC transitions, as the electron is taken from an orbital partly localized on the metal to a higher lying empty orbital localized on a ligand. The orbital overlap is much smaller in this case.

2.2.1.2. Intramolecular deexcitation

Once a photocatalyst has reached its excited state thanks to light absorption, various intramolecular relaxation mechanisms can happen.[112]

After light absorption, a S_n excited state of the molecule is populated depending on the energy of the incident photon. Firstly, a non-radiative relaxation occurs, called vibrational relaxation (VR), to populate the fundamental vibrational state of the excited state. If excited states higher in energy than S_1 are populated, another non-radiative relaxation can occur, *i.e.* internal conversion (IC), followed by a VR to access the fundamental vibrational state of the S_1 excited state. IC can come from collisions between excited molecules or with the solvent. This loss in vibrational energy is highlighted by the Stokes shift observed on emission spectra.[113] Reaching the lowest excited state is governed by Kasha's rule which stipulates that excited singlet states higher in energy than S_1 relax rapidly in a non-radiative way and that radiative mechanisms occur in appreciable yield only from the lowest excited state of a given multiplicity.[114] One exception for Kasha's rule is the azulene molecule for which fluorescence starts from S_2. The difference in energy between states S_1 and S_2 is too important and slows down the IC which is, in other cases, rapid.[3]

The fundamental vibrational state of the lowest excited state being populated, three basic mechanisms can then occur:

1. S_1 excited state participates in IC and VR to return to its fundamental state in a non-radiative pathway. This mechanism leads to no photochemistry.
2. S_1 relaxes to its ground state by emitting light which is called **fluorescence**. This allowed relaxation ($S_1 \rightarrow S_0$) is fast, in the range of 10^{-10} to 10^{-7} s.
3. S_1 participates in an intersystem crossing (ISC) to reach T_1 excited state. This ISC is favored by the presence of heavy atoms and the rate of ISC

is relatively large if the radiationless transition involves a change of orbital type. A typical case is the transition from the lowest singlet state to the triplet manifold, e.g., $^1\pi,\pi^* \rightarrow {}^3n,\pi^*$ is faster than $^1\pi,\pi^* \rightarrow {}^3\pi,\pi^*$ and $^1n,\pi^* \rightarrow {}^3\pi,\pi^*$ is faster than $^1n,\pi^* \rightarrow {}^3n,\pi^*$. After reaching the fundamental vibrational state of the T_1 excited state by VR, T_1 relaxes to the ground state by emitting light according to a forbidden transition ($T_1 \rightarrow S_0$ implies a change in spin multiplicity) that induces a long lifetime of 10^{-6}-1 s. This light emission is defined as **phosphorescence**.[3]

A more complex deactivation pathway is also possible. Thermally activated delayed fluorescence (TADF) consists in an emission with a long lifetime and the characteristics of usual fluorescence by populating again the S_1 excited state from the T_1 excited state by an inverse intersystem crossing (RISC) (**Figure 1.6**). Two types of TADF exist. The first one is called E-type TADF and was observed with eosin B for the first time. Eosin possesses a high ISC quantum yield and the difference in energy between S_1 and T_1 is low (ΔE_{ST} = 18 kJ mol^{-1}). This low ΔE_{ST} is primordial as T_1 lies energetically below S_1. Thus, the gap can be easily filled by absorbing nearby thermal energy to undergo inverse ISC and reach again the S_1 excited state.[3] The E-type TADF is occurring also with the copper complexes in photocatalysis. The spin-orbit coupling induced by the heavy copper ion allows an ISC to happen from the ^{1}MLCT to a ^{3}MLCT excited state. However, this coupling is weaker in the flattened geometry (induced by a pseudo Jahn-Teller distortion), leading to both pathways ($^1\text{MLCT} \rightarrow {}^3\text{MLCT}$ and $^1\text{MLCT} \rightarrow {}^1\text{MLCT}_{flat}$) being in competition. Both ISC and the flattening distortion occur on a femtosecond to early picosecond time scale. After the ISC process, the populated ^{3}MLCT excited state relaxes to a flat $^3\text{MLCT}_{flat}$ state lying below the $^1\text{MLCT}_{flat}$. Once the excited complex is fully relaxed, it can deactivate either nonradiatively or radiatively. If the energy gap between the $^1\text{MLCT}_{flat}$ and the $^3\text{MLCT}_{flat}$ is small enough (ΔE_{ST} < 0.37 eV), the luminescence is mostly occurring from the

$^1MLCT_{flat}$ state through TADF. If the ΔE_{ST} is larger, then the observed luminescence mainly corresponds to phosphorescence.[83]

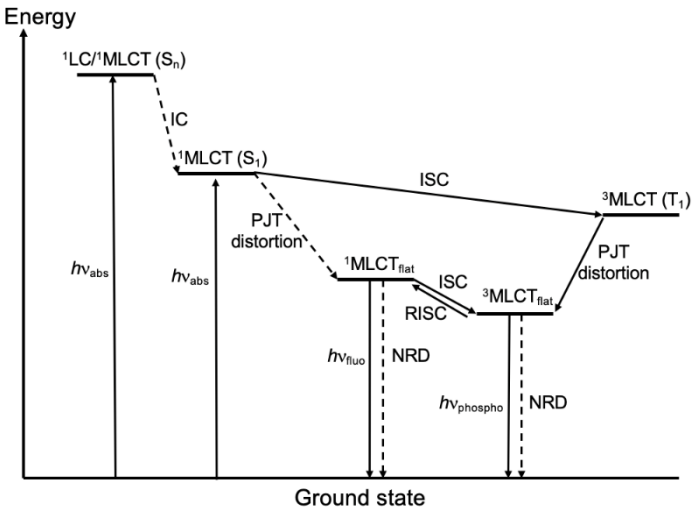


Figure 1.6. General photophysical scheme for tetracoordinated copper(I) complexes: internal conversion (IC), intersystem crossing (ISC), metal to ligand charge transfer (MLCT), ligand-centered transitions (LC), nonradiative deactivation (NRD), pseudo-Jahn-Teller distortion (PJT distortion), reverse intersystem crossing (RISC), absorption (abs), fluorescence (fluo), flattened geometry (flat), phosphorescence (phospho) The dashed arrows correspond to nonradiative deactivation and the solid ones correspond to radiative transitions. Adapted from [83].

The second one is P-type TADF consisting in an energy transfer mechanism between two molecules in their triplet states which leads to one molecule being excited in its singlet state while the other goes back to its ground state, *i.e.* triplet-triplet annihilation (TTA). This type of deactivation is an intermolecular process and this latter will be discussed in the next section.[115,116]

2.2.2. Intermolecular excited-state relaxation

So far, we have investigated mostly intramolecular deactivation of an excited state but intermolecular deactivation is also possible as seen with TTA. A "quencher" (Q) corresponds to any species that quenches the excited state as measured by a decrease in the steady-state photoluminescence intensity, PLI_0, and/or its lifetime τ_0. The excited-state lifetime of a compound is given

by the inverse of the kinetic constants of deactivation processes (radiative (k_r) and nonradiative (k_{nr})) such as:[117]

$$\tau_0 = \frac{1}{k_r + k_{nr}} \qquad (1.2)$$

When a quencher is added, it participates in the deactivation processes decreasing the excited-state lifetime. Various quenchers exist and one of the best-known collisional quenchers is molecular oxygen. Aromatic and aliphatic amines are also efficient quenchers along with heavy atoms such as iodide and bromide.[118] Several cases can be identified in which an intermolecular process involving the photosensitizer and Q is in competition with intrinsic relaxation of PS*:

- **Case A**: the photosensitizer and quencher encounter to form a nonfluorescent ground-state complex, before excitation occurs. When this complex absorbs light, it immediately returns to its ground state without emission of a photon. This type of quenching is called *static quenching*. Such quenching does not rely on diffusion or molecular collisions.
- **Case B**: Q and PS* cannot diffuse towards each other rapidly enough during the excited-state lifetime of the photosensitizer because its lifetime is too short or the solvent too viscous. Quenching can then occur only if the interaction is significant at distances longer than the collisional distance. This is the case for long-range non-radiative energy transfer that can happen between two molecules at distances up to ~80 Å.
- **Case C:** Q can encounter and interact with the excited PS* (after excitation) during the excited-state lifetime range. This bimolecular and collisional process is called *dynamic quenching*. Such process can be diffusion-controlled if the electron transfer kinetic constant is higher than the diffusion one for example.[111,118]

2.2.2.1. Dynamic quenching

In 1919, Otto Stern and Max Volmer introduced a model to quantify the quenching process where the excited-state concentration is fixed and the quencher concentration is systematically varied.[119] Plots of PLI_0/PLI or τ_0/τ *versus* the quencher concentration [Q] provide mechanistic insights. When such data is linear, the slope provides the Stern-Volmer constant, K_{SV}, and can confirm that a dynamic quenching mechanism that involves diffusion is operative if by increasing the temperature, the slope increases because the diffusion of species will be favored.[117] K_{SV} is also directly related to the bimolecular quenching rate constant (k_q) through the excited-state lifetime in the absence of quencher, τ_0 (**eq. 1.3**).[118]

$$\frac{(PLI_0)}{(PLI)} = \frac{\tau_0}{\tau} = 1 + K_{SV}[Q] = 1 + k_q\tau_0[Q] \qquad (1.3)$$

The constant k_q is important as it reflects the efficiency of quenching or the accessibility of the PS to the quencher. If the bimolecular quenching process is diffusion-controlled, k_q will typically range near 10^{10} M^{-1} s^{-1} value. Values of k_q smaller than the diffusion-controlled value can result from steric shielding of the fluorophore or a low quenching efficiency.[118] Other models were also introduced to quantify the dynamic quenching processes.[120–122]

2.2.2.2. Static quenching

As stated above, static quenching implies the formation of a nonfluorescent ground-state complex between the PS and the quencher, before excitation occurs, that absorbs light and deactivates immediately without emission of a photon (**Figure 1.7**).[111] A static quenching gives also linear data in lifetime measurements but the slope will decrease if the temperature is increased as it will favor the dissociation of the nonfluorescent ground-state complex.[118]

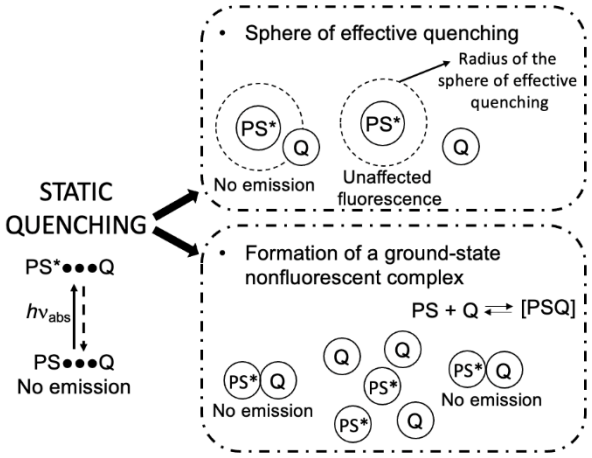


Figure 1.7. Illustration of static quenching.[111]

Static quenching is observed when the quencher decreases the photoluminescence intensity but not the excited-state lifetime. If we consider the formation of the nonfluorescent ground-state complex in a 1:1 association:

$$PS + Q \leftrightarrow [PSQ]$$

only the photosensitizers that are free in solution will exhibit a radiative deexcitation while the ones bound with the quencher will be inhibited. If the quenching is purely static, the lifetime of excited PS will not be affected but the photoluminescence intensity will be impacted by the concentration of free PS:

$$\frac{[PS_0]}{[PS]} = \frac{PLI_0}{PLI} = 1 + K_S[Q] \qquad (1.4)$$

with $[PS_0]$ and $[PS]$ being the concentration of free PS before and after the addition of the quencher, respectively and K_S being the equilibrium constant for the quencher-photosensitizer adduct.[118] The formation of the [PSQ] complex relies on the capacity of PS and Q to encounter in the ground state. When PS and Q cannot change their positions to form the nonfluorescent ground-state complex (*i.e.* viscous media or rigid matrices), a particular case of static quenching is observed, explained by the Perrin model (**Figure 1.7**).

The quenching of a PS is assumed to be complete if a quencher molecule is located inside a sphere called the sphere of effective quenching. If a quencher is outside that sphere, it will not impact the photophysics of the PS.[111]

2.2.2.3. Combined dynamic and static quenching

In many instances, the photosensitizer can be quenched both by collisions and by complex formation with the same quencher.[118] The consequence is that the PLI_0/PLI ratio is multiplied by the fraction of quenched photosensitizers free in solution. The characteristic feature of the Stern-Volmer plot is then an upward curvature (nonlinear anymore).[118] Specific experimental conditions can lead to both quenching mechanisms in such combinations, such as with ionic excited states and halogen species.[117]

The quenching mechanism (and its kinetics) is important to characterize an excited state and gives information about its reactivity with a specific quencher. The quenching of an excited photosensitizer by a given quencher is one of the key steps of a photocatalytic cycle and can initiate the production of radicals for example leading to a product of interest (*vide infra*). The nature of quenching mechanism can be different from one quencher to another.

2.3. Activation modes of organic molecules by photocatalysis

2.3.1. Single electron transfer (SET) – Photoredox

2.3.1.1. Concepts and theory

One mode of action in visible-light catalysis is to induce an electron transfer between an excited photosensitizer (PS*) and a substrate (which acts as a quencher) to generate radical anions or cations that can further initiate a chemical transformation. Such reactions are described as *photoredox catalysis*.[36]

Most steps in a photoredox catalytic cycle are bimolecular reactions and can be represented as shown in **Figure 1.8**:

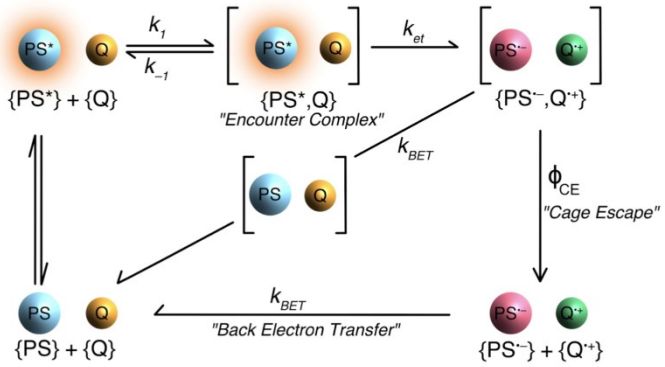


Figure 1.8. Schematic representation of the different steps occurring in a photoredox catalytic cycle.

The first step is the absorption of light to populate the excited state of the PS (PS*) which can either relaxes to its ground state radiatively or non-radiatively or encounter a quencher. The formation of the encounter complex relies on the diffusion constant of the species, k_1, and once it is formed, the two species can react by transferring an electron, for example, according to the constant of electron transfer, k_{et}. Thus, radical ions are formed and need to escape the solvent cage to trigger a desired photochemical transformation. A competitive pathway can also occur which is the back-electron transfer that tends to form the starting species without triggering any desired reactions.

During a single electron transfer (SET), two mechanisms are possible and depend on the redox properties of the photocatalyst used (**Figure 1.9**):

- **Oxidative** quenching cycle  :the excited PS* acts as a reducer, donating an electron to an acceptor (A) in solution. This generates the oxidized form of the photocatalyst, $PS^{\bullet+}$, and $A^{\bullet-}$, the reduced form of the acceptor (quencher). The latter can participate in a radical reaction while the PS is regenerated in its ground state by a sacrificial electron donor.
- **Reductive** quenching cycle  : the excited PS* acts as an oxidant promoting a SET oxidation of the electron donor D (quencher). This leads to the reduced photocatalyst, $PS^{\bullet-}$ and the oxidized donor, $D^{\bullet+}$. The PS is

regenerated by an electron acceptor. Copper complexes undergo rarely a reductive quenching due to their average oxidant power.

In each of these steps, the role of A and D is assumed by a redox-active agent, either the substrate to be transformed, a sacrificial electron donor/acceptor, or a reactive intermediate.[123]

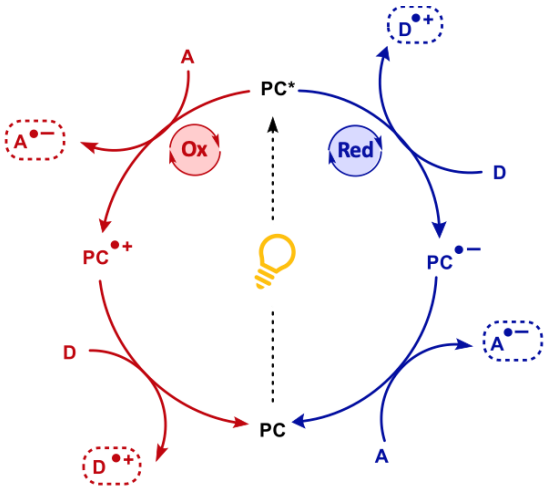


Figure 1.9. Oxidative and reducing single electron transfer mechanisms.

A photocatalyst in its excited state is an entirely new chemical species exhibiting different properties, such as redox potentials, than the starting compound. The great advantage of SET is that it produces greater oxidants and reducers than the ones in their ground states allowing photoredox chemistry that would not be possible in the ground state. As seen on **Figure 1.10**, the electron promoted into the LUMO after light absorption is localized further away from the nucleus than in the ground state and it is then easier to donate, making the excited photocatalyst a better reducer. On the other side, *via* the promotion of an electron into the LUMO, a hole is created in the HOMO. This hole at a lower energy than the ground state makes the photocatalyst also a better oxidant in the excited state.

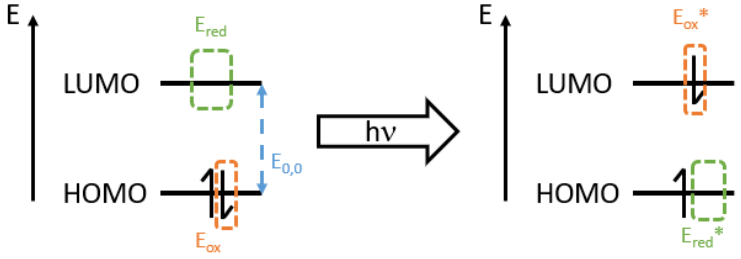


Figure 1.10. Schematic illustration explaining the enhanced redox properties of an excited state.

The two quenching cycles yield the same products but differ by the potentials involved. Thus, depending on the oxidant and the reducer present, one of the two cycles can be favored over the other or the two can be operative at the same time.[123]

The excited-state lifetime is a key parameter to extend to obtain an efficient PC for the diffusion and the electron transfer to have enough time to proceed. The kinetics for an electron transfer between two molecules in the ground state, or one in the excited state and one in the ground state can be described by the Marcus quadratic relationship (**eq. 1.5**), where $\Delta G^{\neq}$ is the free energy of activation, ΔG^0 is the free energy of change, and λ the nuclear reorganization energy that is the sum of two independent contributions corresponding to the reorganization of the inner sphere λ_i (bond lengths and angles within the two partners) and the outer sphere λ_0 (solvent molecules reorientation surrounding the pair), the latter being predominant.

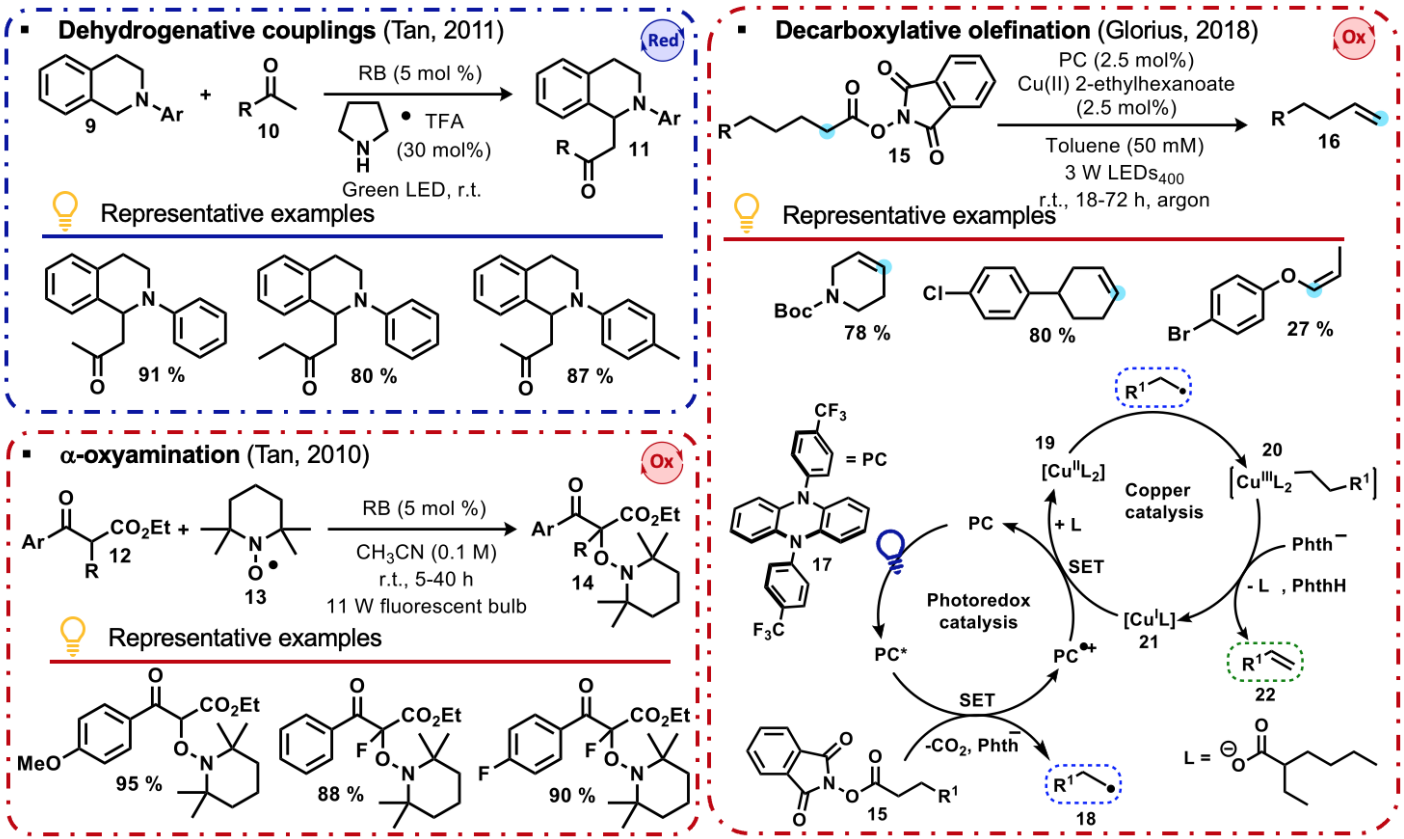
$$\Delta G^{\neq} = \frac{(\lambda + \Delta G^0)^2}{4\lambda} \qquad (1.5)$$

By the quadratic nature of the relationship, three kinetic regimes exist: the normal regime ($\lambda > -\Delta G^0$) where a more exergonic electron transfer will occur with an enhanced rate as the reaction is more favored, a maximum regime ($\lambda = -\Delta G^0$) where the transfer rate is the highest, and an inverse regime ($\lambda < -\Delta G^0$) where a more exergonic electron transfer will occur with a reduced rate. This inverse regime has not been observed for intermolecular electron

transfer because for that regime where $\Delta G^0 << 0$, k_{ET} is so large that the reaction is diffusion-limited and the Marcus theory becomes irrelevant.[1,3,111]

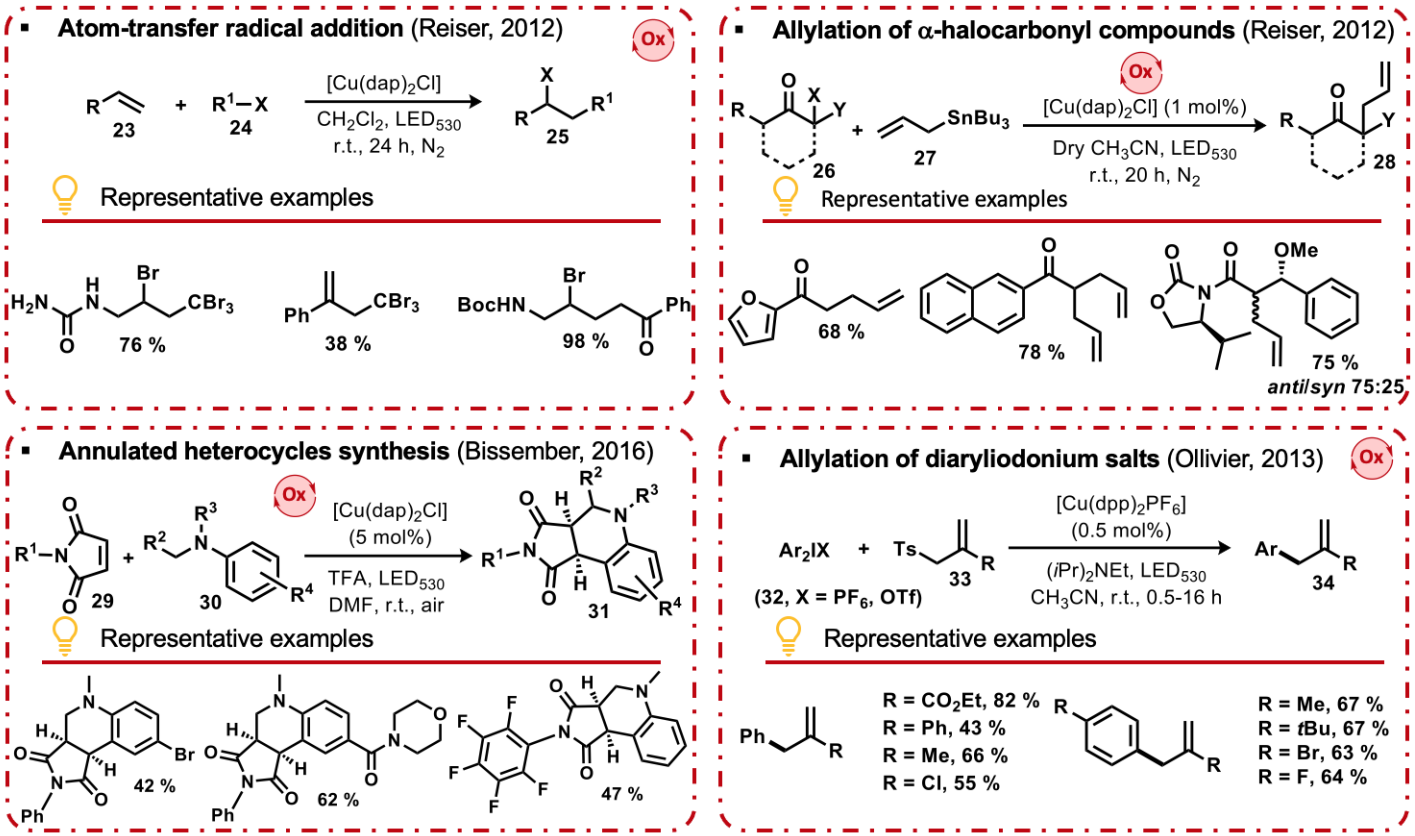
2.3.1.2. Applications of SET with organic dyes and copper complexes

Organic dyes and copper complexes are known to be used in photoredox catalysis according to either oxidative or reducing quenching cycles. For example, Rose Bengal (RB) has given applications in reactions relying on photoinduced electron transfer[124–127], even though its primary application is the generation of singlet oxygen (**Scheme 1.3**). Both oxidative and reducing quenching cycles are possible with this dye. One of the most extensively explored reaction types in organic photoredox catalysis in which RB is used is dehydrogenative couplings, an important methodology for C–C bond formation, which was demonstrated by Tan and co-workers.[128] They also highlighted the reduction capability of RB excited state involved in the α-oxyamination of aromatic β-ketoesters **12** in the presence of TEMPO **13** ((2,2,6,6-tetramethylpiperidin-1-yl)oxidanyl) to form a C–O bond. Compounds that are difficult to obtain such as quaternary fluorinated compounds were synthesized using this method.[129] The group of Glorius investigated another type of organophotocatalyst, a phenazine derivative **17**. The latter, combined with a Cu(II) complex as catalyst, were used to provide rapid access to a wide variety of olefins under mild light-mediated conditions.[130] This family of PCs found also an interest in photoinduced organocatalyzed atom transfer radical polymerization where dihydrophenazine based-photosensitizers are mostly used.[131–134]



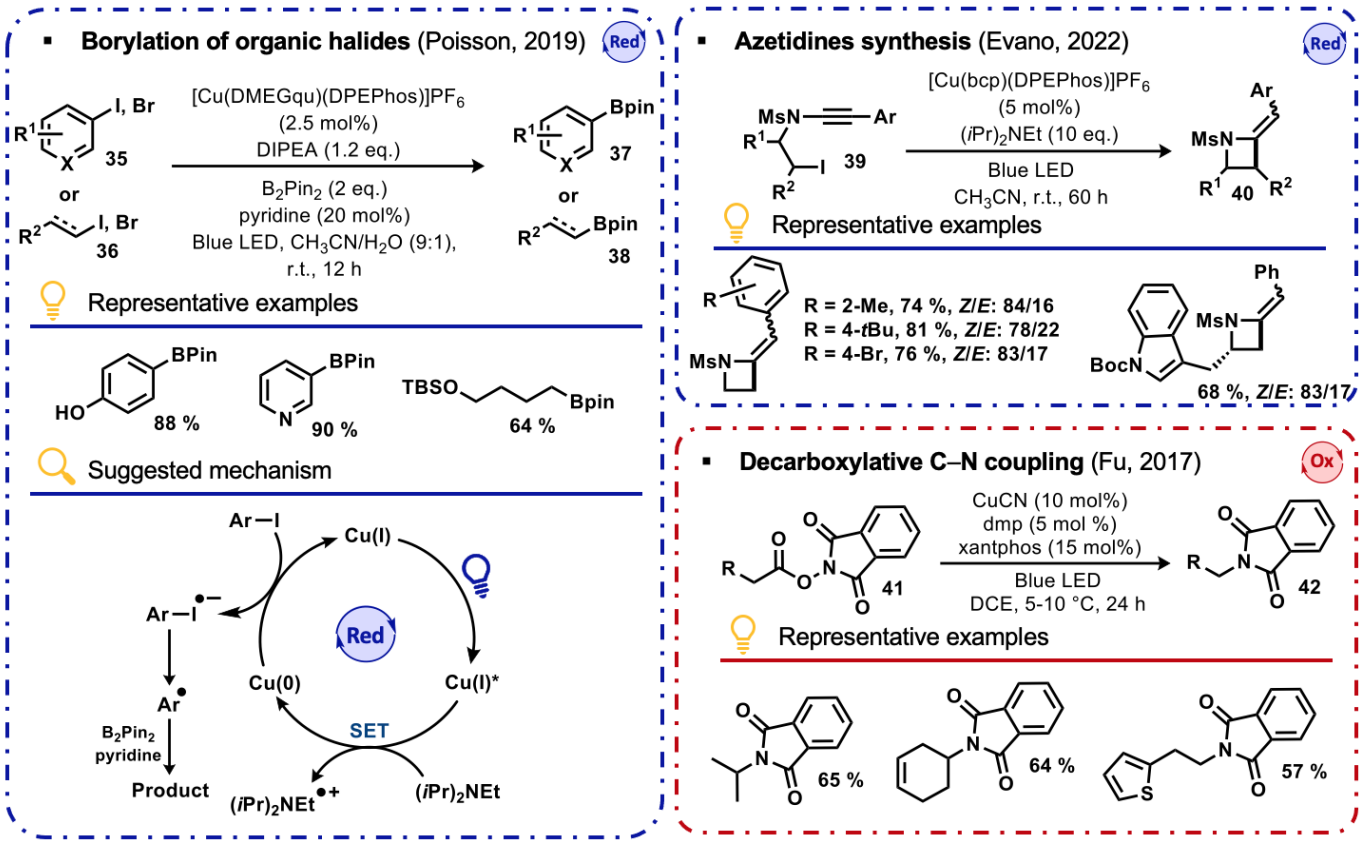
Scheme 1.3. Photoredox applications for organic synthesis using organophotocatalysts.

For copper complexes, since 2012, $[Cu(dap)_2]^+$ has found many applications in organic synthesis stimulated by the work of the Reiser's group who started to further investigate the potential of that PC for a wide variety of transformations (**Scheme 1.4**).[75,76,91,135] The Reiser group reported the atom-transfer radical addition (ATRA) of organic halides **24** to alkenes **23** that readily occurs at room temperature in good yields with low catalyst loadings. This same group also developed the radical allylation of organohalides **26** with allyltributyltin **27** using $[Cu(dap)_2]Cl$ under visible light. A Cu(I)/Cu(I)*/Cu(II) catalytic cycle was proposed but a radical-chain mechanism was not ruled out. This new protocol avoids the use of toxic azobisisobutyronitrile (AIBN) or energetic UV irradiation.[91] The group of Bissember reported in 2016 the first example of a direct α-amino C–H bond functionalization using also $[Cu(dap)_2]Cl$ as PC, in the presence of trifluoroacetic acid (TFA). Detailed mechanistic studies suggested that TFA used as an additive was a crucial mediator for the aerobic oxidation of the excited state copper(I) species to copper(II), thus favoring an oxidative quenching cycle.[136] Another homoleptic copper(I) complex, $[Cu(dpp)_2]PF_6$, demonstrated its efficiency in the photoredox activation of diaryliodonium salts **32** whose allylation with allylsulfones **33** was found to be actively promoted by the excited copper center.[137]



Scheme 1.4. Examples of oxidative quenching catalytic cycles catalyzed by homoleptic copper(I) complexes.

Heteroleptic copper(I) complexes, made of a diimine and diphosphine ligands, have also found a lot of applications in organic synthesis thanks to their excited-state lifetimes longer than their homoleptic counterparts (**Scheme 1.5**). With this kind of PCs, the rarest reductive quenching cycle is more observed. In 2019, Poisson's group reported the copper photocatalyzed borylation of aryl, heteroaryl, vinyl and alkyl halides (I and Br) performing a reductive quenching cycle with a new copper complex. The corresponding boronic acid esters were obtained in good to excellent yields and were also obtained *via* continuous flow conditions to allow an easy scale-up.[138] A reductive quenching cycle was also proposed by Evano's group for an anti-Baldwin radical 4-exo-dig cyclization from nitrogen-substituted alkynes **39**, such as ynamides, to produce corresponding azetidines **40**, useful building blocks in natural products synthesis.[86] In 2017, Peters and Fu developed a photoinduced, copper-catalyzed decarboxylative C–N coupling to generate protected amines **42** as an alternative to the Curtius rearrangement. The copper PC is generated *in-situ* and N-hydroxyphthalimide (NHP) esters **41** were employed as precursors to organic radicals. The phthalimide core was valorized by being the source of a protected amine. The C–N bond-forming process is compatible with a wide array of functional groups.[139] For examples of SET performed with heteroleptic copper complexes made of two different diimine ligands, relevant literature is furnished.[83,95,140]



Scheme 1.5. Examples of oxidative and reducing quenching cycles with heteroleptic copper(I) complexes as photocatalysts.

2.3.2. Energy transfer – Photosensitization

The second activation mode discussed in this work is the energy transfer induced in a photosensitization process. The energy transfer between a donor D and an acceptor A can either be radiative, *i.e.* D* emits a photon that is absorbed by A, or non-radiative (no photon emission) which requires an interaction between the two molecules and occurs only if the emission spectrum of D overlaps the absorption spectrum of A. These interactions may be Coulombic and/or due to intermolecular orbital overlap (**Figure 1.11**). The Coulombic interactions consist of short-range multi-polar or long-range dipole-dipole interactions that characterize the Förster's mechanism. The interactions due to intermolecular orbital overlap, which include electron transfer, characterize the Dexter's mechanism. Due to orbital overlap, this mechanism is performed at short-range distances and is limited by diffusion. Moreover, the Dexter's mechanism allows triplet-triplet energy transfer which is highly valuable in photochemistry as this allows the energy transfer from a triplet excited PS* to the triplet state of another molecule that exhibits a low or even null ISC quantum yield. This is explained by the fact that for allowed transitions, the Coulombic interaction is predominant, even at short distances. For forbidden transitions (e.g. in the case of transfer between triplet states (^{3}D* + ^{1}A→^{1}D + ^{3}A*), in which the transitions $T_1 \rightarrow S_0$ in D* and $S_0 \rightarrow T_1$ in A are forbidden), the Coulombic interaction is negligible and the electron exchange is found, but is operative only at short distances.[3,111]

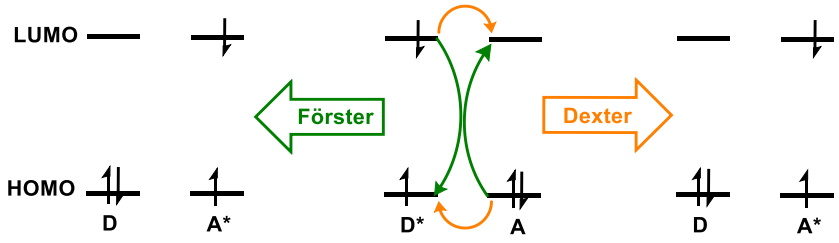


Figure 1.11. Schematic representation of Förster and Dexter energy transfer mechanisms.

The most famous example of Dexter energy transfer in photochemistry is the photoproduction of singlet oxygen. Oxygen is peculiar as it exhibits a triplet ground state and is considered as a diradical species while most compounds present a singlet ground state. Triplet oxygen is especially reactive in contact with other radicals while it is kinetically persistent (and thus weakly reactive) toward reactions with most other compounds that are in a non-radical singlet state. When oxygen is excited in its singlet state ($^1O_2$), it becomes a powerful oxidant. Singlet oxygen is electrophilic and is considered as a zwitterion species (non-radical) that reacts rapidly with most compounds which explains its relevance for use in applications such as photodynamic therapy or organic synthesis instead of its triplet homologue. Singlet oxygen is readily produced due to its easily accessible singlet state.[141] Indeed, molecular oxygen has two low-lying singlet excited states, $^1\Delta_g$ and $^1\Sigma_g^+$, 22.5 and 31.5 kcal mol^{-1} above the triplet state, respectively (**Figure 1.12**). The excited states are frequently named by their molecular term symbols used in spectroscopy with the general formula: $^{2S+1}\Lambda_{g/u}^{+/-}$ where *S* is the total spin quantum number, Λ is the projection of the orbital angular momentum along the internuclear axis, g/u indicates the symmetry with respect to a center of inversion and +/- is the reflection symmetry along an arbitrary plane containing the internuclear axis.[107]

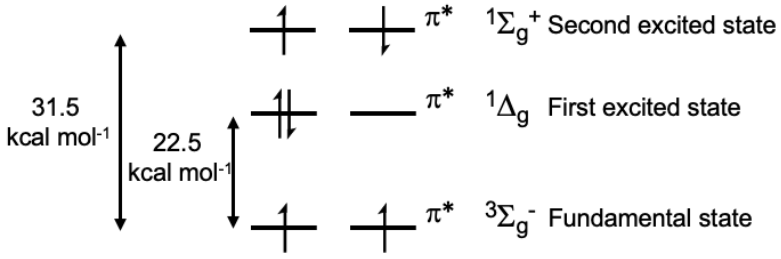


Figure 1.12. Schematic representation of fundamental and excited states of dioxygen.

$^1\Delta_g$ is a relatively long-lived species as the transition from $^1\Delta_g$ to $^3\Sigma_g^-$ is forbidden while the second excited state of oxygen, on the other hand, is short-

lived due to a spin-allowed transition to the $^1\Delta_g$ state. This difference in stability is confirmed by the excited-state lifetimes of $^1\Delta_g$ and $^1\Sigma_g^+$ which are 10^{-6}-10^{-3} s, and 10^{-11}-10^{-9} s in solution, respectively.[142] These excited-state lifetimes are also impacted by the solvent as seen in **Table 1.2** with the values for $^1\Delta_g$ excited state:

Table 1.2. Oxygen concentration and lifetime of $^1\Delta_g$ in different solvents.[1]

Solvent	**[O_2] (mM) (1.013 bar O_2)**	**τ ($^1\Delta_g$) (μs)**
Acetone	11.4	45
Acetonitrile	9.1	61
Dichloromethane	10.7	90
Methanol	10.3	9
Water	1.39	4
Carbon tetrachloride	12.4	900

Direct excitation of oxygen in a laboratory environment is difficult because of its low absorption in the visible or near-UV spectral regions. However, the lowest energy $^1\Delta_g$ excited state, known simply as **singlet oxygen**, can be easily populated through energy transfer from many excited photosensitizers having their lower excited state above 22.5 kcal mol^{-1}.[1] Indeed, having the energy of the donor higher than the one of the acceptor favors the kinetic constant of the energy transfer that can be diffusion-limited. The more important is the energy difference, the more favored will be the energy transfer.[3]

To study the generation or disappearance of singlet oxygen requires an appropriate method to detect $^1O_2$, ideally quantitatively. The most direct method for doing so is the monitoring of the characteristic $^1O_2$ emission band at 1270 nm. However, this necessitates specialized equipment and can be difficult due to extremely low quantum yield of the $^1O_2$ emission. Therefore, it is more common to use molecular singlet oxygen probes whose fluorescence or absorbance properties change upon reaction with $^1O_2$. Among such

fluorescence probes is found the widely used 1,3-diphenylisobenzofuran (DPBF) but this probe is not specific to $^1O_2$ and readily reacts with other reactive oxygen species (ROS), such as O_2^{-}, hydroxyl radical, or H_2O_2. This issue can be overcome by more recently developed anthracene-based fluorescence probes, such as anthracene-9,10-divinylsulfonate (AVS), that are specific to singlet oxygen.[143]

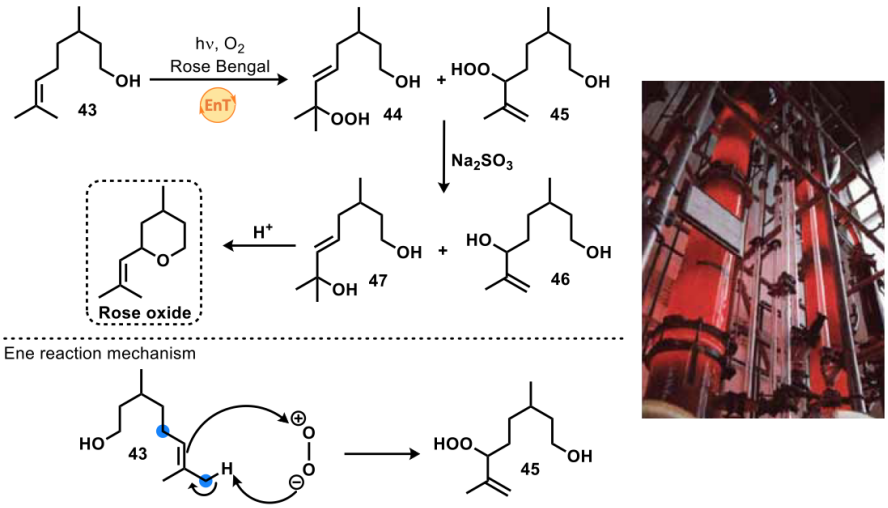
2.3.2.1. Applications of $^1O_2$ in organic synthesis

The use of singlet oxygen has been widely investigated in organic synthesis for transformations such as ene reactions, [2+2] and [4+2] cycloadditions, heteroatom oxidations, or heterocyclic photooxygenations.[144] The most common used photosensitizers are organic dyes due to their performant ISC quantum yield (**Table 1.3**). Recently, transition metal complexes have also emerged as potential producers for singlet oxygen.[145]

Table 1.3. Photophyscial properties of organic dyes. E_T = triplet energy, τ = triplet lifetime, ϕ_Δ = singlet oxygen production quantum yield, ϕ_{ISC} = intersystem crossing quantum yield, solvent is for ϕ_Δ, dmbiipo = 2,9-dimethyl 16*H*-benzo-[4',5']-isoquinolino-[2',1':1,2]-imidazo-[4,5-*f*]-[1,10]-phenanthrolin-16-one.[88,142,146]

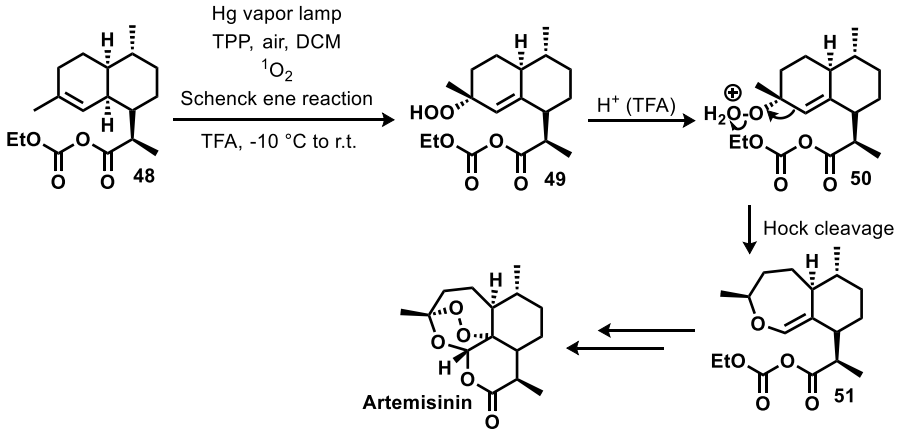
Photosensitizer	**E_T (kcal mol^{-1})**	**τ ($^1\Delta_g$) (μs)**	**ϕ_Δ**	**ϕ_{ISC}**	**Solvent**
Methylene Blue	32.0	450	0.51	0.52	MeOH
Tetraphenyl-porphyrin	35.9	1500	0.78	-	C_6H_6
Rose Bengal	42.0	130	0.76	0.77	H_2O
Triphenylpyrylium	56.6	10	-	0.42	-
4-Phenyl-benzophenone	65.0	40	0.75	-	EtOH
9,10-Anthraquinone	66.8	0.11	0.62	1.0	CH_3CN
$[Ru(bpy)_3]^{2+}$	50.5	0.72	0.73	-	MeOH
[Cu(dmbiipo)(XantPhos)]$^+$	-	29	0.68	-	THF

Photooxygenation is applied at industrial scale for the production of rose oxide which is highly sought after in cosmetic and fragrance industries. In Dragoco process developed by the Symrise company, the hydroperoxides **44** and **45** are synthesized *via* the addition of $^1O_2$ generated by energy transfer with Rose Bengal (**Scheme 1.6**). Thereafter, reduction in alcohols **46** and **47** and cyclization of isomer **47** at acidic pH afford rose oxide. Cylindrical reactors of a 3 meters height are used, irradiated by 5000 W mercury lamps. The production of rose oxide is higher than one ton per year.[147] Methylene blue is another PS that is also efficient in the citronellol photooxidation.[148]



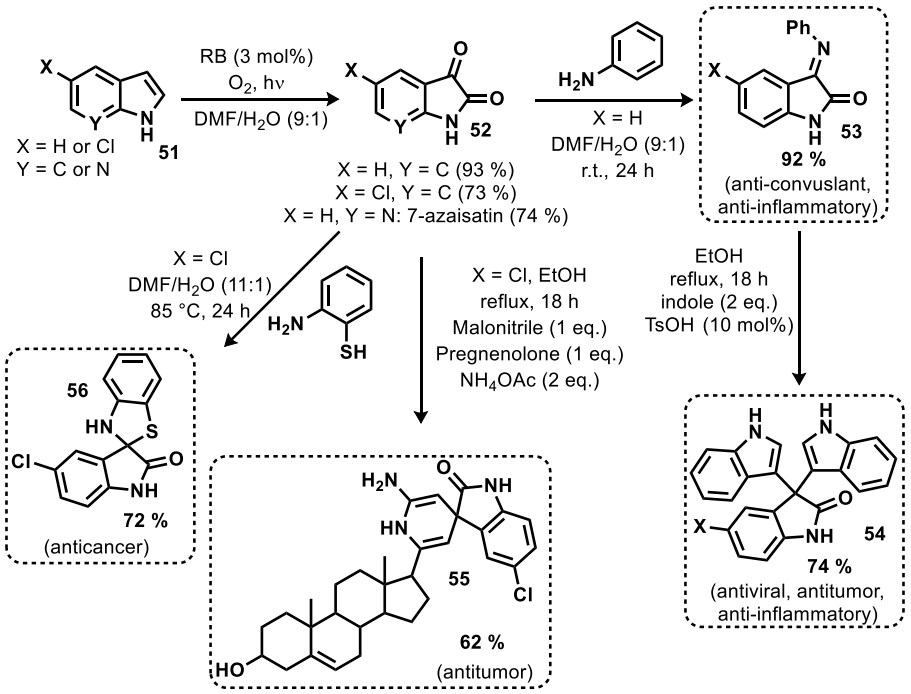
Scheme 1.6. Industrial synthesis of rose oxide in high cylindric reactors and the corresponding ene reaction mechanism involved in the first step of rose oxide synthesis. The carbons highlighted in blue correspond to the two positions where the H atom can be abstracted to form the two regioisomers.

Another industrial application is the photooxygenation of dihydroartemisinic acid in the synthesis of artemisinin commercialized by Sanofi. Mechanistically, it is assumed that a regioselective Schenck ene reaction between singlet oxygen and a double bond takes place, followed by a Hock cleavage and a subsequent oxygenation and cyclization (**Scheme 1.7**). In this case, the tetraphenylporphyrin (TPP) is used as photosensitizer.[149]



Scheme 1.7. Proposed photooxidation mechanism for the synthesis of artemisinin.[149]

At the laboratory scale, the photogeneration of singlet oxygen can procure essential building blocks to the synthetic chemist like isatin derivatives and cyclic imides that are obtained *via* the dearomatisation of indole and pyrrole derivatives, respectively. By simply using RB in presence of molecular oxygen, the group of Das synthesized 38 building blocks with yields comprised between 50 and 93 % and accessed pharmaceuticals in two or three steps. The expensive 7-azaisatin was also obtained in one step with a 74 % yield (**Scheme 1.8**). This methodology appeals to the energy and electron transfer (reductive quenching) capabilities of RB.[150] Photooxygenation reactions using dyes are commonly used in organic synthesis for the synthesis of building blocks and natural products.[151–155]

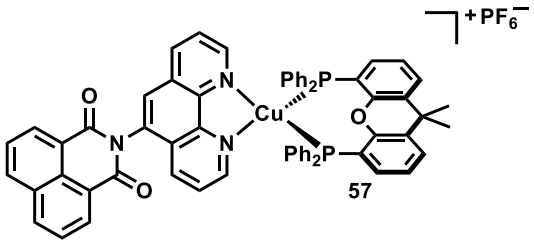


Scheme 1.8. Synthesis of pharmaceuticals *via* dearomatisation of indole derivatives developed by Das's group.[150]

Transition-metal complexes have also shown abilities to produce singlet oxygen. Ruthenium(II)[156–158] and cyclometalated iridium(III)[159–162] complexes have been highly investigated showing interesting singlet oxygen quantum yields, ϕ_Δ = 0.73 and 0.50 for $[Ru(bpy)_3]^{2+}$ and *fac*-$Ir(ppy)_3$, respectively. Oxygen quenching with these species occurs with, in some cases, both energy and electron transfer.[142,160]

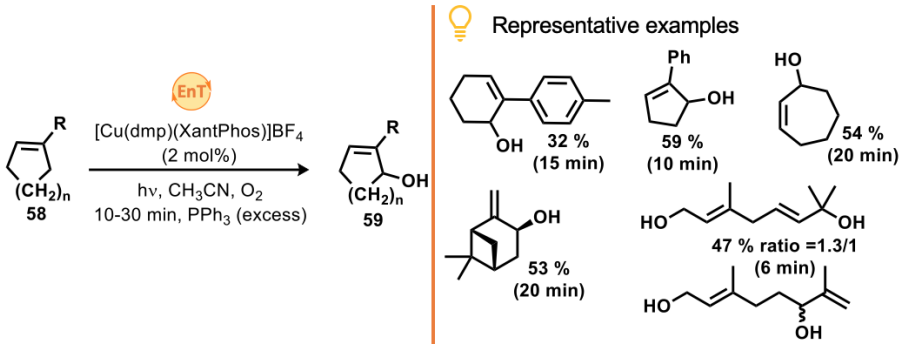
Ruthenium and iridium metal complexes are not alone in their ability to photosensitize oxygen. Recently, copper complexes have gained interest in photooxygenations. The group of Tschierlei investigated the impact of designing new diimine ligands on improving the abilities of Cu to produce $^1O_2$. They developed a new ligand, dmbiipo, which influenced a lot the photophysical and catalytic properties of the copper(I) complex **7** (**Scheme 1.2**). The excited-state lifetime increased to 29 μs and it outperformed the well-established Cu(I) photosensitizer $[Cu(bcp)(XantPhos)]^+$ in the formation

of $^1O_2$.[88] Furthermore, in their research, they studied the ligand NIphen (5-(1,8-naphthalimide)-1,10-phenanthroline) which also had a major impact. $[Cu(NIphen)(XantPhos)]^+$ **57** showed an exceptional photostability, allowing for an efficient and repetitive production of $^1O_2$ with quantum yields of about 0.32 (**Scheme 1.9**).[89]



Scheme 1.9. Chemical structure of $[Cu(NIphen)(XantPhos)]PF_6$.

In 2021, Kallitsakis *et al.* reported for the first time the use of $[Cu(dmp)(XantPhos)]BF_4$ (dmp = dimethylphenanthroline) as a photocatalyst for the selective C–H allylic oxygenation of cycloalkenes **58** into the corresponding allylic hydroperoxides or alcohols **59** in the presence of molecular oxygen (**Scheme 1.10**). This methodology was also applied successfully to several bioactive terpenoids. The authors highlighted the energy transfer mechanism as the addition of DABCO, a well-known $^1O_2$ quencher, prevented the reaction to progress while the use of TEMPO, a radical species, did not significantly affect the reaction progress. Thus, they could underpin an $^1O_2$ generation mechanism, excluding the involvement of other ROS.[163]



Scheme 1.10. Applications of [Cu(dmp)(XantPhos)]BF_4 in photooxygenation of cycloalkenes and terpenoids.

3. Supported homogeneous photocatalysis

Photocatalysts have proven their utility in catalyzing various chemical transformations in homogeneous phase. Nevertheless, organic dyes and transition-metal complexes suffer from several limitations that can hamper their development in large-scale applications. The recoverability and reusability of these PCs are considered challenging although it makes environmental and economic senses to use catalysts and to drive chemical reactions with light. Specifically, Ru(II) and Ir(III) complexes exhibit a high cost, limited availability on Earth of both metals, and poor recycling ability leading to metal contaminations and increasing the processing and waste disposal costs.[164] On the other hand, heteroleptic copper(I) complexes can sometimes suffer from ligand substitution and/or loss depending on the reaction conditions leading to the formation of their homoleptic counterparts that exhibit lower excited-state lifetime decreasing their potential photoactivity. Their (photo)stability is then limited, especially in coordinating solvents.[165–167] Although copper is considered as affordable compared to Ru and Ir, the synthesis of the ligands forming the copper(I) complexes can become expensive. All of these arguments limit the use of transition metal-based complexes in large-scale or industrial applications. Similarly, organic dyes are known to have a notable negative impact on the environment due to

their sluggish degradation, photobleaching and propensity to act as fluorescent pollutants. Moreover, their low photostability is not in their favor.[164] In order to circumvent some of the above-mentioned limitations, heterogenization on a solid support seems to be a promising approach to enable recycling and easy reuse. Some side-benefits can even emerge from that methodology, such as an increased flexibility with the choice of employed solvents, a controlled loading in PC that decreases the self-quenching and, a cooperation with the support that increases the activity and selectivity.[168]

3.1. Immobilization strategies

In order to immobilize a photocatalyst onto a solid matrix, several strategies can be employed (**Figure 1.13**).

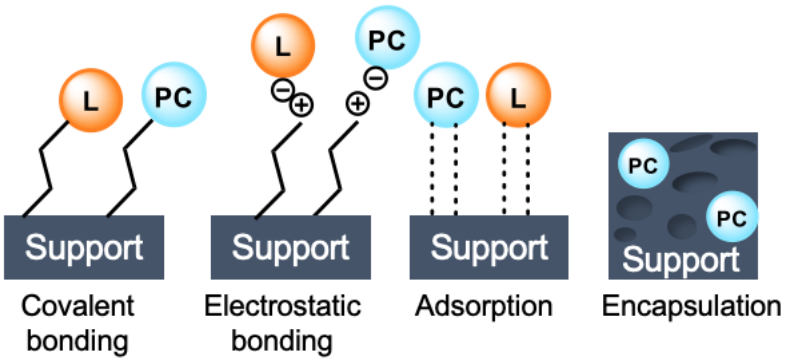


Figure 1.13. The different types of interactions possible between the ligand or the PC and a solid support.

The linkages formed between the photocatalytic species and the solid support can be of different strength and made of either weak interactions such as Van der Waals forces, hydrogen bonding and electrostatic interactions or strong covalent bonding. The nature of the linker is important to attempt to control the rate of leaching (loss of whole or fragments of the surface-bound molecule in solution). There are three fundamental strategies to prepare heterogenized photocatalysts: 1) direct immobilization of the PC meaning that the PC is formed, and/or modified if necessary, entirely before the anchoring step (most general approach); 2) the inverse approach (for metal complexes)

consisting in immobilizing one of the ligands of a complex followed by its complexation with a metal at the surface of the solid (with eventual additional ligands), this approach being able to deliver higher photocatalyst loadings usually; 3) the encapsulation within a (preferably porous) solid matrix.[169] Thanks to the diversity of linkers that can be used and the different strategies, any photocatalyst can find suitable conditions to be heterogenized. This is reinforced by the multitude of solid matrixes available to immobilize photoactive sites, and thus the broad surface chemistry that can be employed, involving materials such as organic polymers, inorganic oxides, graphene or other carbon-based materials, metal organic framework (MOF), natural materials… The ideal solid support has the following properties: i) low cost, ii) inert nature, iii) high (photo)stability, iv) mechanical strength (to avoid abrasion due to stirring), v) easy recovery and reusability and vi) ability to prevent nonspecific adsorption and inactivation.[164]

Although homogeneous supported photocatalysis seems to be appealing, it is not so trivial to achieve fully successfully such methodology. An uneven distribution and leaching of the catalyst are major drawbacks that ultimately lead to a decrease in the activity of (recycled) heterogenized systems.[164] More specifically to photocatalysts, polarity and porosity of solid supports may affect elementary steps involved in a catalytic process such as light absorption, energy transfer, generation of redox intermediates, and adsorption-desorption equilibria of substrates, intermediates, and final products.[169] Furthermore, negative impact of the support can occur on the photogeneration of singlet oxygen for example. Indeed, $^1O_2$ may be lost through interaction with the support, especially for supports exhibiting O–H and C–H oscillators resulting in electronic-to-vibronic energy transfers.[168]

As this methodology is challenging, an intense research effort has been devoted lately towards applications and development of homogeneous supported photocatalysts. Let’s go through some representative examples and

to ease the discussion, we have chosen a classification based on the nature of the support.

3.2. Applications of immobilized photosensitizers

3.2.1. Silica nanoparticles

A common employed support is silica nanoparticles (NPs) that allow various possibilities of linker *via* a rich surface chemistry. Moreover, mesoporous silica NPs, characterized by ordered mesopores (2-50 nm), are interesting supports to explore the effect of nanoconfinement of the PC on its photophysical and catalytic properties although the concerns about photoactive site accessibility and light diffusion remain. Among the most famous mesoporous silica types are MCM-41, MCM-48 (Mobil Composition of Matter) and SBA-15 (Santa Barbara Amorphous) which will be described in more details.

Rose Bengal has been studied a lot for the design of heterogeneous photocatalytic systems. Martins Estevão *et al*. covalently anchored RB onto mesostructured silica NPs *via* a covalent amide bond and evaluated the performances of the system **60** in the photoproduction of singlet oxygen (**Scheme 1.11**). The heterogenized system was as efficient as homogeneous RB and the photobleaching of the dye was stopped when introduced in mesopores.[170] The use of an amide linker is the most common found in the literature for photooxygenation reactions[171–173], carbon-carbon bond formation[174], or for medical and environmental applications with immobilized RB.[175–177] Nevertheless, the phenolate moiety can also be useful to anchor RB as Ronzani *et al.* demonstrated for the photooxygenation of α-terpinenes.[178]

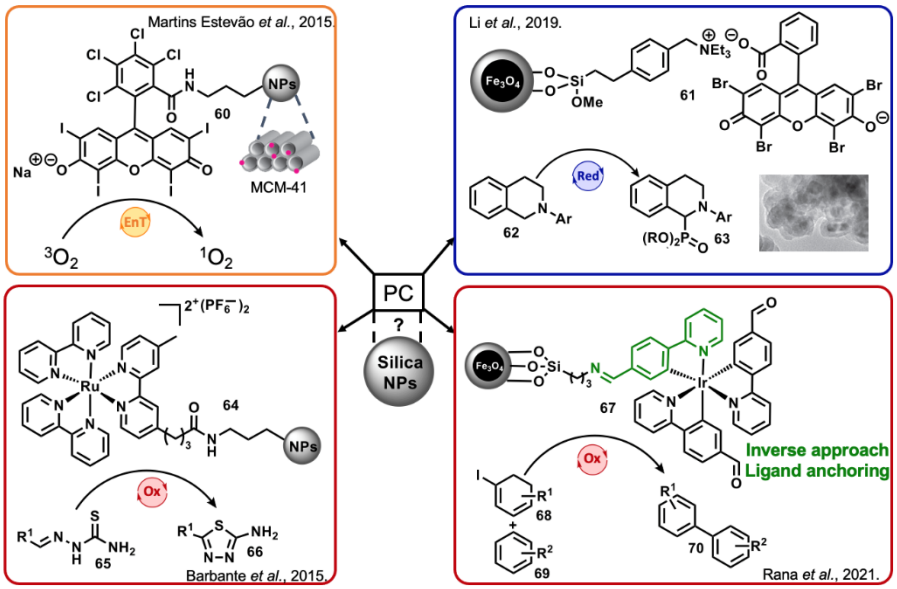
Silica nanoparticles present naturally some negative charges at the surface due to the possible (pH-dependent) deprotonation of silanol groups. The group of Amara exploited this surface chemistry to immobilize non-

covalently, through electrostatic interactions, methylene blue (MB) on non-porous silica NPs used in the photooxidation of citronellol.[148] Eosin Y could also be immobilized with electrostatic interactions onto magnetic silica NPs (made magnetic thanks to an iron oxide core) in order to catalyze a C–P bond formation through a reductive quenching cycle (**Scheme 1.11**). This heterogenized system **61** was recycled at least eight times without a significant loss of activity.[179]

Transition metal-based photocatalysts have also been investigated for their grafting onto silica. Recent work of Rana *et al.* reported the grafting of an iridium complex onto non-porous magnetic silica NPs *via* the inverse approach (ligand first) paving the way towards visible-light driven C–H arylation and cyanation reactions. The ligand was anchored onto the matrix *via* Schiff base condensation forming an imine linker before metal complexation (**Scheme 1.11**). A successful recyclability over 5 runs was obtained.[180] Mori *et al.* employed diverse mesostructured supports to anchor the [Ir(mebib)(ppy)] complex and highlighted the impact of the physical environment onto the photophysical properties such as the emission intensity which increased in the following order: MCM-41 < MCM-48 < SBA-15. This same order was observed for the photocatalytic activity (in photooxidation).[181]

Covalent binding was also investigated for Ru(II) polypyridyl complexes. In 2014, Huang and coworkers have immobilized $[Ru(bpy)_2(abpy)](PF_6)_2$ (abpy = 4-formyl-4'-methyl-2,2'-bipyridine) complex bearing a formyl-substituted bipyridine ligand. The silica NPs with an average diameter of approximately 100 nm were firstly treated with APTMS ((3-aminopropyl)trimethoxysilane) to cover the surface by reactive amino groups, suitable for anchoring the formyl-functionalized Ru(II) complex. A hybrid material, with a catalyst loading of 0.11 mmol g^{-1}, was obtained and involved in the photooxidation of thioanisole in which a negligible leaching was

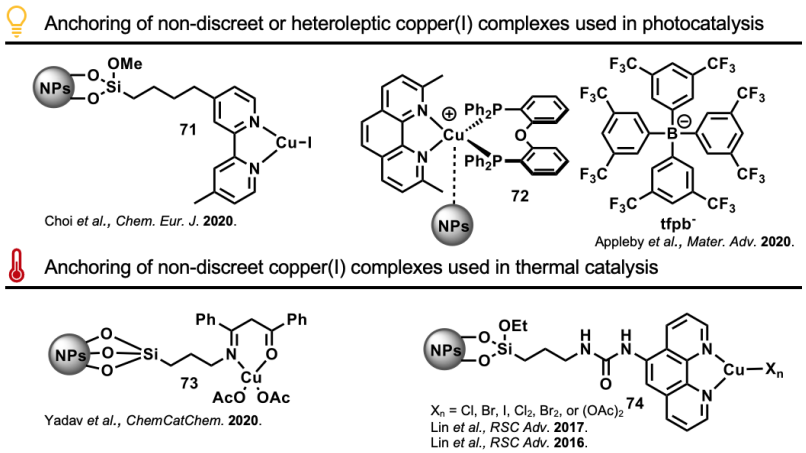
observed.[182] Based on the same strategy, Barbante *et al.* prepared an heterogenized Ru(II) complex by carbodiimide-mediated coupling of amine-functionalized silica beads with a carboxylic acid functionalized ruthenium complex (**Scheme 1.11**). As proof of concept, they used the hybrid material **64** in intramolecular cyclizations of 2-benzylidenehydrazinecarbothioamides **65** to give 5-aryl-1,3,4-thiadiazol-2-amines **66** with an average yield of 65 %.[183]



Scheme 1.11. Organic dyes and organometallic complexes immobilized onto silica NPs and used as immobilized photocatalysts.

Reusable Ru photocatalysts can also be strongly immobilized by simple adsorption on silica surface and this was demonstrated by Amara and coworkers who obtained a $[Ru(bpy)_3]Cl_2$ loading of 2.5 mg g^{-1}. The interaction is considered to be mainly driven by electrostatic interactions and appears stable, even after multiple washings.[184] To further increase this interaction, the silanol groups can be changed into negatively-charged carboxylates. To this end, spherical silica NPs were functionalized with (3-(triethoxysilyl)propyl)succinic acid anhydride that yields to dicarboxylic acid after hydrolysis.[185]

Concerning the immobilization of heteroleptic or homoleptic copper(I) complexes onto silica NPs, this was mainly developed for dye-sensitized solar cells (DSSC)[186–188] or photoproduction of hydrogen[189] but has been scarce as far as we know for photocatalyzed organic transformations (**Scheme 1.12**). In 2020, Choi *et al.* developed a hybrid-copper tri-coordinated catalyst **71** covalently anchored on SBA-15 by derivatizing the bipyridine ligand and was employed in a photoinduced C–H arylation.[190] Other non-discreet copper complexes **73** and **74** were recently heterogenized but their applications involved only thermal reactivity.[191–193] The only example of heteroleptic copper complex immobilization used in photocatalytic applications was described by Appleby *et al.* that used [Cu(xantphos)(dmp)](tfpb) (tfpb = tetrakis(3,5-bis(trifluoromethyl)phenyl)borate) immobilized on chromatography grade silica **72** by simple adsorption. This photoactive surface was then used to produce singlet oxygen upon irradiation with visible light in aqueous media to exterminate bacteria.[194]



Scheme 1.12. Anchoring of non-discreet or heteroleptic copper(I) complexes used in photo- or thermal catalysis.

3.2.2. Zeolites

Zeolites are another inorganic oxide class (usually alumino-silicates) used in supported homogeneous photocatalysis thanks to their so-called

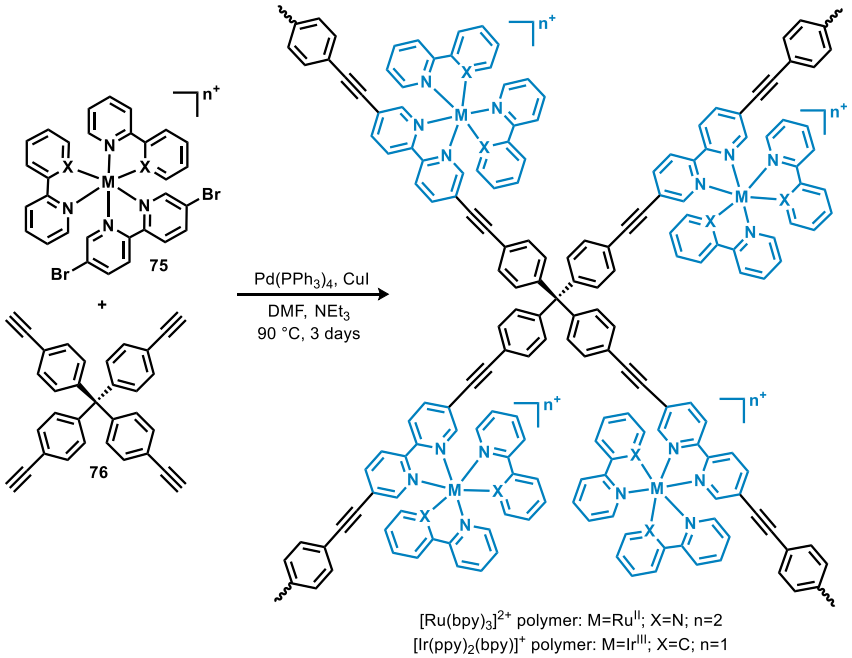
supercages (with a diameter of around 1.3 nm) that can welcome a catalyst using the encapsulation method. 2,4,6-Triphenylpyrylium cation (TPP^+) is a powerful electron-transfer organic dye and it has been encapsulated in zeolite Y (giving TPP-Y) by the "ship-in-a-bottle" synthesis from acetophenone and benzaldehyde using the internal acidic sites of the support as catalyst. TPP-Y showed moderate activity to promote the isomerization of *cis*-stilbene to *trans*-stilbene. The intrazeolite process did not produce byproducts as it was the case in homogeneous conditions.[195] It is also possible to encapsulate TPP^+ in zeolites by simple mixing.[196] This immobilization strategy is highly valuable for TPP^+ as its triplet-state lifetime is enhanced when the cation is confined in zeolites.

3.2.3. Polymers

Various research groups have effectively exploited the potential of polymers as support for heterogenized systems. Synthetic polymers are easily accessible and cost-effective, and their recovery and recycling after purification and isolation are simple.[197] Merrifield resin is a cross-linked polystyrene that carries reactive functional group and is often used for the immobilization of RB. Covalent linkage is possible *via* the reaction between the carboxylate group of the RB and the choloromethyl sidechain of the polymer and demonstrated its efficiency in singlet oxygen generation.[198,199] More interestingly, a non-covalent immobilization onto that resin was also reported in 2019 by converting the chloromethyl moiety into an ammonium site that allows an electrostatic interaction to occur with the negatively charged RB. The newly designed system was efficient in photoredox catalysis for the synthesis of vinyl sulfones with good yields and a broad scope.[200] The anchoring of RB or other PS was reported on other types of polymer and readers are referred to relevant literature.[201–203]

A lot of examples concerning the immobilization of Ru(II) and Ir(III) on various polymers can be found in the literature.[164,169,197] To avoid this section

to be too repetitive, only one strategy will be reviewed: the polymerization of the PC itself to obtain a heterogenized system. Based on two new triscyclometallated iridium complexes containing carbazolyl groups, conjugated microporous polymers were obtained, exhibiting intense phosphorescence and high activity for aza-Henry reaction. One limitation of such system is self-quenching due to a short distance between the photoactive sites. A solution is to co-polymerize the PC with a rigid organic compound such as *para*-substituted tetraphenylmethane derivative **76** that serves as a spacer (**Scheme 1.13**). The latter reacted with $[Ru(bpy)_2(5dbrbpy)]^{2+}$ or $[Ir(ppy)_2(5dbrbpy)]^{2+}$ (5dbrbpy = 5,5'-dibromo-2,2'-bipyridine) according to a Sonogashira cross-coupling reaction to give the corresponding polymers with 76 wt.% of the Ru(II) complex and 71 wt.% of the Ir(III) complex, respectively.[204]



Scheme 1.13. Polymerization reaction of $[Ru(bpy)_3]^{2+}$ and $[Ir(ppy)_2(bpy)]^{+}$ complexes to give solid photocatalysts.[204]

3.2.4. Graphene oxide (GO)

Graphene has attracted considerable interest as a support to prepare heterogenized photocatalysts owing to an advantageous combination of optical, mechanical, thermal and conductive properties.[169] An interesting report relates the immobilization of Eosin Y (EY) on reduced graphene oxide (EY-rGO) and GO (EY-GO) *via* hydrogen bonding and π–π stacking. The immobilization step provoked a red-shift of the absorbance of EY-rGO from 515 nm to 538 nm which may be attributed to π–π interactions. For EY-GO, varying the amount of GO did not induce a spectral shift of EY indicating that the main interaction is hydrogen bonding since GO sheet is strongly oxygenated with carboxylic, hydroxyl, carbonyl, and epoxy groups at the defect and edge sites. Quenching experiments showed a decrease in fluorescence intensity which was higher for EY-rGO, highlighting the possible electron-transfer between EY and the support. Indeed, EY-rGO was efficient in the photoproduction of H_2.[205]

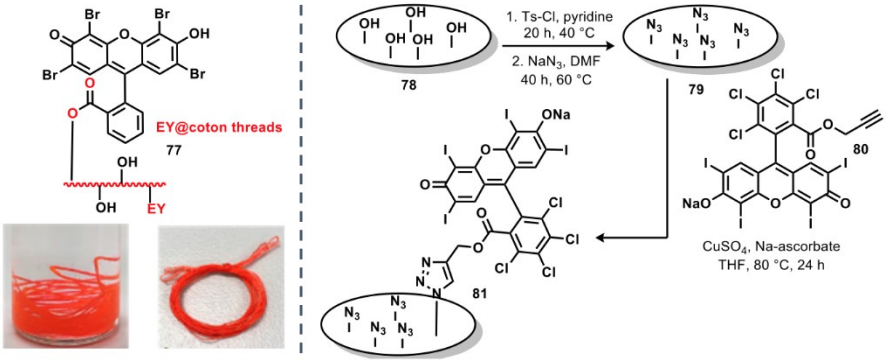
Jain and coworkers prepared rGO samples for the immobilization of iron(II) complex $[Fe(bpy)_3](PF_6)_2$. Weak π–π interactions between bpy ligands and the support are believed to serve as the anchoring force.[206] Using the same solid matrix, $[Ru(bpy)_3]Cl_2$ was immobilized with the difference that rGO was functionalized first covalently with sulfonate moieties. An ion-exchange between Na^+ and Ru(II) complex led to the heterogenized system in which only 27 % of the reactive sites were functionalized with Ru(II) complex due to a low accessibility for this bulky photocatalyst.[207] The heterogenized Ru photocatalyst exhibited excellent catalytic efficiency in visible-light-driven reductive dehalogenation reactions, even for aryl chlorides.

In our group, iridium(III) and ruthenium(II) polypyridyl based PCs have been covalently anchored on GO *via* an esterification reaction and non-covalently fixed on rGO *via* pyrene moieties. The heterogenized complexes exhibited good photocatalytic activities in the radical cyclization of a

malonate and, interestingly, the use of a pyrene-derivatized Ir(III) terpyridine-based complex gave an unexpected "on/off" effect of the photocatalytic activity triggered by the presence or absence of rGO.[208]

3.2.5. Natural supports

More recently, researchers have turned towards the use of natural supports. In 2020, Xu *et al.* immobilized EY onto commercial cotton threads **77**, cellulose being the most abundant and renewable source in nature with low manufacturing costs (**Scheme 1.14**). This is an ideal solid support due to sufficient hydroxyl groups present in the polysaccharide chains. The immobilized EY, obtained by a carbodiimide coupling reaction, is capable of generating singlet oxygen for organic transformations such as the oxidation of thioethers and intervenes efficiently in polymer synthesis. *Via* UV-vis analysis, they determined that one meter of material contains ~2.8 mg of PC. Moreover, a negligible catalyst leaching was observed in multiple solvents (DMSO, DCM, DMF, MeOH, MeCN…), demonstrating the versatility of possible applications.[209] Two years later, Felpin's group immobilized Rose Bengal dye onto simple cellulose paper sheets through copper-catalyzed azide-alkyne click ligation **81** (**Scheme 1.14**).[210] Wool is another natural support that has been used in supported photocatalytic applications as it is available, nontoxic, biodegradable and renewable. Exploiting the natural ammonium groups of wool, Zhang *et al*. immobilized RB with electrostatic interactions and used it in the oxidation of furans with singlet oxygen as the benchmark reaction (90 % yield). Unfortunately, no information was given by the authors concerning the leaching and photobleaching of such system.[211]



Scheme 1.14. Covalent anchoring of Rose Bengal and Eosin Y on cellulose supports; left: cotton and right: paper.

As stated above, it is impossible to review all and every kind of immobilization that have been described with various photosensitizers and supports. Useful reviews are advised to end this section before delving more into the science of silica nanoparticles.[146,164,168,169,197,212]

4. Silica Nanoparticles

Among all supports illustrated in Section 3 of this introduction, silica nanoparticles have been largely used for supported photocatalysts whatever their nature. Silica NPs represent an optimal support as this inorganic oxide possesses i) a high specific surface area which can be tuned by the porosity parameters and particle sizes[213], ii) an easy surface functionalization[214–218], iii) a transparency over a broad range of wavelengths[219], and iv) a high mechanical stability and photostability[213]. Moreover, multiple architectures have been described like nanospheres[220], core-shell[221], hollow spheres or nanofibers[222], urchins or dendritic silica[223]… These available morphologies are a real asset for the use of silica NPs as supports as they can influence the photophysical properties and photoactivity of the photocatalysts.

4.1. Porosity and structures

Based on their pore properties, silica NPs can be classified into non-porous or microporous (pore size < 2 nm) and mesoporous materials (pore size in the range of 2-50 nm). Depending on how their pores organize, different mesoporous silica materials can be obtained (**Figure 1.14**), which are not automatically in the nano-size regime if not effort to control particle size growth is implemented during their synthesis:[216]

- **MCM-41**: two-dimensional hexagonal structure like a honeycomb, with pores comprised between 2 and 5 nm with a volume of ~1 cm^3 g^{-1} and a surface area of ~1000 m^2 g^{-1}.
- **MCM-48**: three-dimensional cubic system of pores that are therefore interconnected. It possesses the same properties as MCM-41.
- **MCM-50**: lamellar structure, is less used than MCM-41 and -48 because it tends to convert into the two other types.
- **SBA-15**: two-dimensional hexagonal structure like a honeycomb structure like MCM-41 but with larger pores comprised between 5 and 30 nm and a thickness of walls of 3-6 nm which makes that structure more robust than MCM-41. However, a lower surface area is displayed (~800 m^2 g^{-1}).
- **KCC-1**: this most recent morphology of silica has been reported with pore sizes in the 50-1200 nm range. The porosity comes from a fibrous structure instead of pores, making the pores easily accessible. The space between two fibers is considered to be of ~5 nm and their thickness ranges from 3.5 to 5.2 nm. Although its fibrous structure can be thought of as fragile, KCC-1 demonstrates a great mechanical stability, even higher than the one of MCM-41.[224] An universal name has not yet been defined in the literature for such silica nanoparticles which are commonly referred to as urchins, dendritic and/or fibrous or radial wrinkle structured silica particles.[224–226]

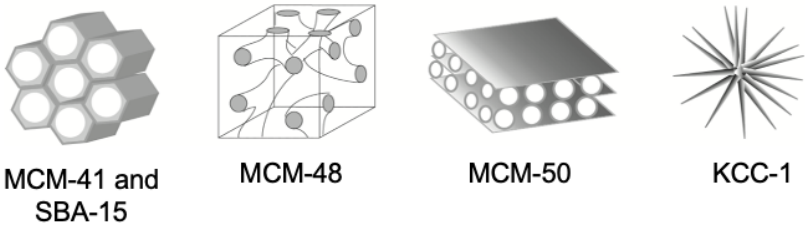


Figure 1.14. Mesoporous silica materials.

4.2. Synthesis

4.2.1. Non-porous silica particles

Different methods are used to synthesize silica nanoparticles but since the seminal work of Stöber, Fink, and Bohn in 1968, the synthesis of silica nanoparticles has relied extensively on ammonia-catalyzed hydrolysis of silicon alkoxides (**eq. 1.6**), in particular tetraethylorthosilicate (TEOS), and subsequent condensation of the resulting silanol monomers (**eq. 1.7** and **1.8**) which is nowadays well-known as the Stöber method. It is also characterized by the use of a low molecular weight alcohol like ethanol as solvent along with the presence of water as hydrolysis agent.[227] According to this method, the size of silica particles obtained can be readily tuned in a wide range from 10 to 500 nm by simply modifying the reaction conditions.

$$Si(OEt)_4 + xH_2O \leftrightharpoons Si(OEt)_{4-x}(OH)_x + xEtOH \quad (1.6)$$

$$2Si(OEt)_{4-x}(OH)_x \leftrightharpoons (EtO)_{8-2x}(Si–O–Si)(OH)_{2x-2} + H_2O \quad (1.7)$$

$$Si(OEt)_4 + Si(OEt)_{4-x}(OH)_x \leftrightharpoons (EtO)_{7-x}(Si–O–Si)(OH)_{x-1} + EtOH \quad (1.8)$$

In the Stöber process, the first step to occur is the hydrolysis of TEOS [$Si(OEt)_4$] into silanol monomers [$Si(OEt)_{4-x}(OH)_x$] as represented in **eq. 1.6**. It involves the nucleophilic substitution of ethoxy group (Si-OEt) by silanol group (Si-OH) *via* a penta-complexation transition state. Ammonia accelerates the hydrolysis rate *via* the generation of OH^- ions which are more

effective nucleophiles compared to H_2O molecules. The degree of hydrolysis can be 1, 2, 3, or 4 depending upon the number of ethoxy groups being converted to hydroxyl groups. The hydrolysis rate escalates when more ethoxy groups are converted into silanols, and this is attributed to the increased positive charge of silicon atoms and the reduced steric hindrance.[227,228] The formation of hydrolyzed monomers at the early stage of the reaction leads to a supersaturation of these intermediates that thermodynamically control the appearance of the first nanostructures.[229] This control depends on the solution chemistry (NH_3, H_2O and solvent).

Subsequently, the second step involves the silanol monomers condensation to generate siloxane bonds according to **eq. 1.7**. Simultaneously, the silanol monomers may also react with the unhydrolyzed ethoxy groups of TEOS according to **eq. 1.8** but this is not favored as fully hydrolyzed silanols tend to be formed under basic conditions and as $Si(OH)_4$ molecules tend to react with each other due to a lower steric hindrance in the absence of ethoxy groups. The rate of condensation is faster than the rate of hydrolysis as a low concentration in silicic acid (depending on hydrolysis and condensation rates) was observed by Bari *et al* as the reaction was proceeding.[230] As such, the silanol monomers are preferentially condensed into large siloxane networks rather than react with other monomers.[228] At this point, the suspension evolves from a sol (small particles in suspension) to a gel (3D connected network with trapped solvent) that can be subsequently dried to recover a powder. This is a very general concept for inorganic oxides synthesis that has been named 'sol-gel method'. It can be followed by a calcination step to increased further the degree of condensation.

Two models, monomer addition and controlled aggregation have been proposed for the growth of silica particles and both involve two important events: nucleation and growth. The two models use different approaches to describe particles growth. The monomer addition model supports a LaMer-

like mechanism[231] where after an initial nucleation, growth occurs through the addition of hydrolyzed monomers to the particle surface. By contrast, the second model, controlled aggregation, claims that nucleation occurs continuously throughout the reaction. These primary particles or nuclei aggregate with one another or larger aggregates to grow into larger particles.[232] For a long time, these two models were independently proven. In the 1990s, both mechanisms were recognized responsible for the growth of particles for which the controlled aggregation occurs for much of the reaction, followed by monomer addition to further enlarge the diameter.[233–235]

There have been many investigations on the kinetics and characterization of Stöber process generated particles in order to precisely control their size, shape, uniformity and polydispersity. The strict control of pH, reaction time, temperature, stirring rate, addition rates and concentration of reactants was deeply investigated to understand their respective impacts.[220,236–242]

4.2.2. Mesoporous materials

The synthesis of nanostructured mesoporous materials relies on the same sol-gel method as Stöber process but requires the additional presence of a structural directing agent, usually in a biphasic medium, as a porogen agent. Surfactants have this ability of pore-forming and are organic molecules with a hydrophilic head and a long hydrophobic hydrocarbon chain. Concerning the MCM-*x* family, cetyltrimethylammonium bromide (CTAB) is the most used surfactant for their synthesis while it is di- or triblock copolymers that are preferred, such as Pluronic P123, for SBA-15 structure. The formation mechanism is based on the supramolecular assemblies of surfactant micelles (when a sufficient concentration of surfactants is reached named critical micellization concentration-CMC) that act as structure directors for the formation of the mesophase. Two pathways are possible (**Figure 1.15**): pathway **a** relies on the organization of cationic or neutral surfactant molecules in hexagonal, lamellar, or cubic structures followed by the

subsequent condensation of anionic silicate species that occurs around that preformed structure. Pathway **b** starts with the condensation of silicate species that occurs at the external surface of the micelles before these latter spontaneously pack into a highly ordered mesoporous material. The formation of a particular case of the MCM-x family depends on the concentration and the nature of the surfactants but also on reaction conditions. To gain the porosity, the surfactants are finally removed from inside the pores by calcination or extraction methods, to rupture the electrostatic interactions that exist between silica walls and the template.[215,216,242]

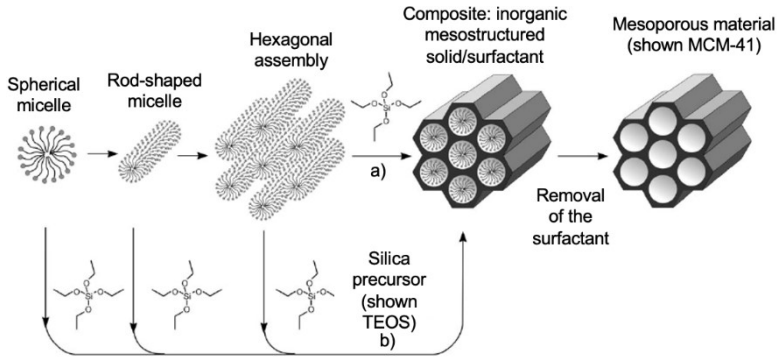


Figure 1.15. Formation of mesoporous materials by structure-directing agents according to the two possible pathways of synthesis.[215]

Silica nanoparticles can also be designed to exhibit non-porous together with mesoporous characteristics by building core-shell particles. Such particles are obtained in two consecutive steps: the first one is the synthesis of the non-porous core where Stöber conditions are used and the second one involves the presence of a surfactant to induce the porosity around the non-porous core that also acts as a template.

4.2.3. Particular case of KCC-1

The first synthesis of KCC-1 was reported by the group of Polshettiwar and was conducted under microwave irradiation using cetylpyridinium bromide (CPB) or cetyltrimethylammonium bromide (CTB) as a template and urea, in a mixture of cyclohexane, pentanol, and water, also based on a sol-gel

process. TEOS is hydrolyzed by urea, followed by assembly of hydrolyzed, negatively charged silicate molecules in the space available between the template molecules in order to aggregate along the free radial directions (**Figure 1.16**). Finally, subsequent condensation occurs to construct the fibrous morphology.[243] In 2016, this same group developed the synthesis of KCC-1 using a simple reflux open-reactor protocol which was easily scaled up and cost effective. The same reactants were used except that CTAB was employed as template.[224,226]

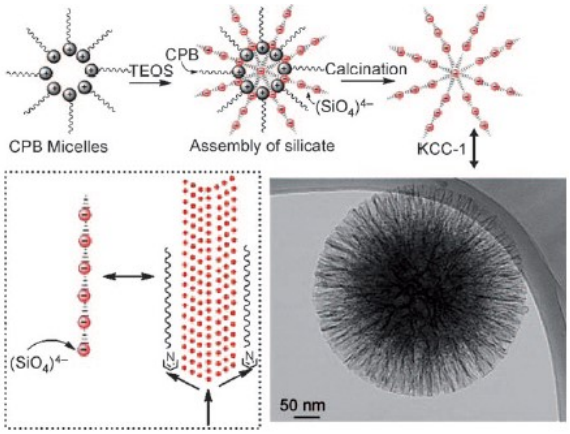


Figure 1.16. Schematic dendritic silica nanoparticles formation.[243]

Dendritic fibrous morphology is especially interesting as photocatalysts support, as the light scattering should be significantly enhanced by this hierarchical structure. Multiple scattering events occur at the solid interfaces, leading to an increase in the light path length between neighboring dendritic fibers which can be of utmost relevance in supported photoredox catalysis.[225]

4.3. Surface chemistry

The surface chemistry of silica particles is governed by the presence of silanol moieties that makes the surface hydrophilic at sufficient concentrations.[244] The concentration (δ_{SiOH}) per gram of silica and the number of silanols (α_{SiOH}) per nm^2 of silica are impacted by the particle size and post-treatments such as drying and calcination temperature. Rahman *et al.*

observed that δ_{SiOH} increases with a decrease in particle size, with a significant increase below 100 nm. The δ_{SiOH} increased ~12 times (from 0.30 to 3.56 mmol g^{-1}) as the particle size reduced from ~130 to ~7 nm. This trend was also obviously observed for specific surface area. Interestingly, α_{SiOH} does not follow that trend and decreases with the decrease in particle size. It can be explained by incomplete or retarded formation of silanol groups at the surface of small particles. 4.5 SiOH groups per nm^2 was found for ~7 nm particles while 5.5 SiOH groups per nm^2 were found for ~130 nm particles.[219] Different types of silanol groups exist at the surface along with the siloxane bonds: isolated, geminal, and vicinal or bridged silanol groups (**Figure 1.17**). The distribution and proportion of these silanols impact the adsorption properties and reactivity of the silica NPs, and can be tuned by thermal treatments.[244] It was observed that the isolated and geminal silanol groups are responsible for the further surface functionalization.

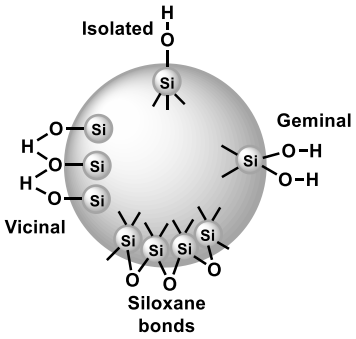


Figure 1.17. Types of silanol groups and siloxane bonds on the surface of silica particles.[244]

4.3.1. Functionalization

A great advantage of using silica particles as a support is that its chemical and physical properties can be easily tuned by functionalizing its outer and/or inner surfaces with various organic moieties. The synthesis of such hybrid materials can be performed *via* two methods: the *in-situ* co-condensation or the post-grafting method.

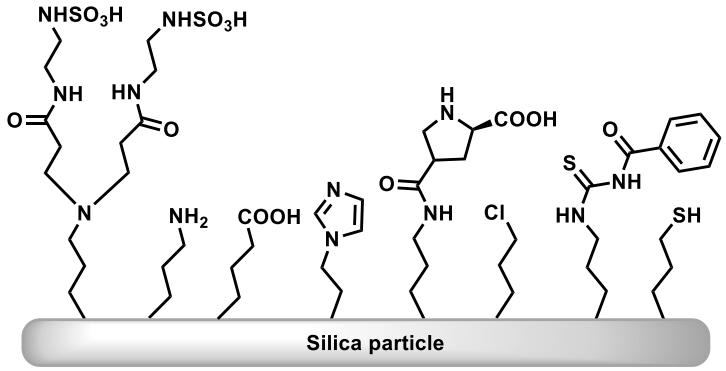
4.3.1.1. Co-condensation method

This one-step method relies on the co-condensation of tetraalkoxysilanes with terminal trialkoxyorganosilanes, which are widely commercially available, in presence of a surfactant (if mesoporous materials are targeted) to yield organically modified silicas with the functionalities projecting into the pores. The main advantage here is that the organic moieties are homogeneously distributed within the materials. However, the terminal silane derivatives can slow down or even hinder the mesoporous matrix formation with consequently a totally disordered product that is obtained. Trialkoxyorganosilanes tend also to condensate with themselves (cross-linking) which does not guarantee a homogeneous distribution and availability of the functionalities. Finally, care must be taken to remove the surfactants in the case of porous structures for which only extraction methods and not high temperature calcination can be used.[215,216,242] Nevertheless, although this functionalization method is not easy to put in place, successful researches were reported about the formation of highly structured mesoporous materials with a good stability after surfactant removal and a well-established functionalization.[245–249]

4.3.1.2. Post-grafting method

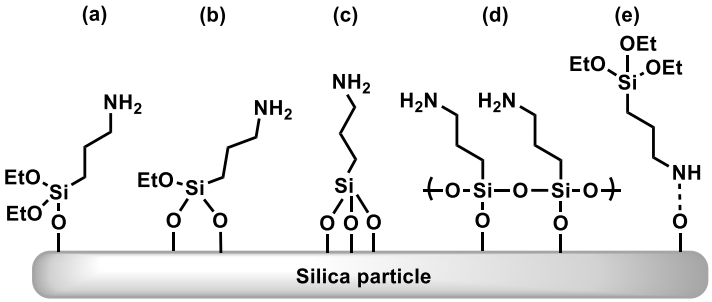
Grafting refers to the subsequent modification (after the formation of the inorganic matrix) with organic groups. This modification method usually occurs under reflux by mixing the inorganic matrix with a silane derivative, in an inert atmosphere and in an appropriate solvent that does not interact with the silanol groups thus favoring the grafting. Compared with the co-condensation method, no structural alterations of the solid matrix occur in most cases and the functionalization occurs almost totally on the external surface and at the entrance of mesoporous channels if the pore size is low. This fact can be attributed to the higher accessibility of the silanol groups localized there. The principal limitations are the low control of

functionalization leading to a non-homogeneous distribution of the organic moieties and the partial porosity blockage that may occur when using bulky binders. Between the possible methods of post-grafting (impregnation, ion-exchange), the formation of a covalent linker between the support and the organic moiety *via* silanization is the most widely used.[215,216,242] A plethora of examples have been reported in the literature to anchor amino, carboxylic acid, thiol, trinitrofluorenone, coumarin, benzene, polythiolactone, enzymes, dendrimers, and many other groups (**Scheme 1.15**).[217,218,250–262]



Scheme 1.15. Examples of functionalization of silica particles.

As terminal trialkoxyorganosilanes are mainly used in post-synthetic modifications, it is important to underline that different orientations of the organic molecule attached at the surface are possible: reaction of only one (a), two (b), or all three ethoxy groups with the silanol-terminated surface (c), cross-linking of the organic molecule (d), or attachment to the surface by electrostatic or H-bond interactions (e). These possibilities are represented in **Scheme 1.16** with aminopropylethoxysilane (APTES) as example.



Scheme 1.16. Possible orientations of the APTES molecule attached to the silanol-terminated silicon surface through the silanization reaction.[217]

This rich surface chemistry allows to consider silica nanoparticles as a suitable support for the anchoring of photocatalysts. The various possibilities of surface functionalization make silica nanoparticles a versatile solid support that can be used to immobilize virtually any kind of photoactive molecule. Moreover, the different types of porosities in silica nanoparticles are an asset as the pores could have an influence on the photophysical properties of the silica-supported photocatalysts by enhancing their photostability and control their aggregation for example.[146,170,181] Nevertheless, a notion of accessibility needs to be kept in mind so that the photocatalysts could still absorb the incoming light, get to their excited state and participate in the bimolecular steps of a photocatalytic cycle.

Chapter 2

Thesis objectives

The main introduction put in evidence the benefit of using photocatalysis as efficient tool to synthesize organic compounds. The versatility of the photocatalysts reinforces the power of photochemistry, in addition to its "green" nature and unique one-electron pathway. Organic dyes and copper complexes have been extensively investigated to replace the expensive and rare ruthenium and iridium metals complexes, but their use is still hampered by their different limitations.

Organic dyes, with their broad structural possibilities, lack of detailed information about the impact of their derivatization onto their photophysical properties (structure-activity relationship). Simple structures such as benzophenazines, are suitable moieties to conduct that kind of investigation but were rarely investigated in this context. Moreover, organic dyes suffer from a low photostability and they are difficult to separate at the end of the reaction. Their anchoring onto a solid support was highlighted as a good solution to increase their photostability but, in most cases, the support was considered inert and very few investigations were dedicated to the impact of the morphology of the support onto a photocatalyzed organic transformation.

In parallel, heteroleptic copper complexes can suffer too from a possible low photostability, due here to ligand exchanges in certain reaction conditions.

Their heterogenization could help to diminish or stop that ligand exchange but, to the best of our knowledge, it has not been yet developed for organic synthesis, neither for homoleptic complexes, and no information is available as to whether the photophysical properties are maintained or not on the support, *i.e.* no spectroscopic analysis with heterogenized systems are found in the literature. Moreover, their heterogenization could facilitate the recovery of traces amounts of metal in effluents which is a current point of attention.[263–265]

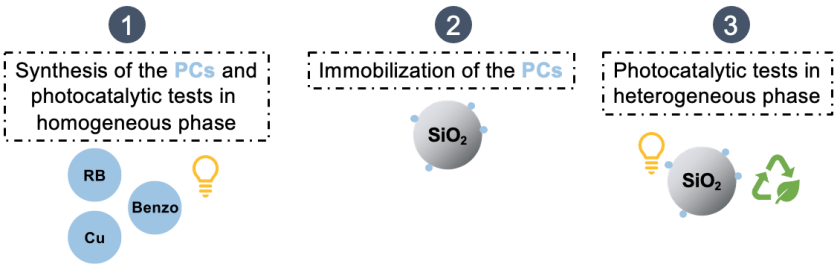
In this context, the main goals of this PhD thesis are **to establish heterogeneous systems based on copper(I) complexes and new or well-established organic dyes that will be deeply characterized at each step of functionalization, to evaluate the impact of immobilizing a photocatalyst onto a support in terms of photophysical properties, photostability, and photoactivity and to investigate how a support, with its intrinsic properties such as specific surface area, particle size, porosity…, can be tuned to enhance the photocatalysts activity and impact the outcome of a reaction.** To fulfill this main goal, different achievements related to sub-objectives need to be pursued within a general methodology:

1. Taking the advantage of having a non-innocent support that influences the course of a reaction, **we aim to develop and compare different morphologies of silica nanoparticles that could impact positively the outcome of an organic transformation**. We would like to highlight the possible impacts that can exist in the multiple steps of a photocatalyst immobilization due to the support itself. Moreover, a fine understanding of the influence of the support could open the door to adequate and optimized supported systems.
2. In order to exploit the versatility of organic dyes, we want to study **the derivatization impact of a simple fully-organic photocatalyst onto its photophysical properties.** The establishment of a structure-activity

relationship is interesting to design the best photosensitizer according to what's necessary for the targeted photochemical reaction. Knowing the characteristics of the excited state and the influence of the functionalization on it, we would be able **to design a grafting approach that is totally neutral towards the photophysical properties** and obtain, ideally, a heterogenized system that is as much or even more robust than its homogeneous counterpart.

3. Finally, we want to assess the benefits of **anchoring copper complexes** onto their photophysical properties and their photostability. We would like to highlight if the ligand exchange mechanism is hindered at the surface of the support based on the idea that an anchored ligand would benefit from a lower degree of freedom and thus would not favor the formation of the homoleptic copper(I) complex. This idea is totally innovative and no precedent in the literature exists to the best of our knowledge. We would like also to assess if some photoredox reactions can still be performed at the solid surface, and if copper complexes can be recycled in multiple runs of organic reactions (without too much leaching).

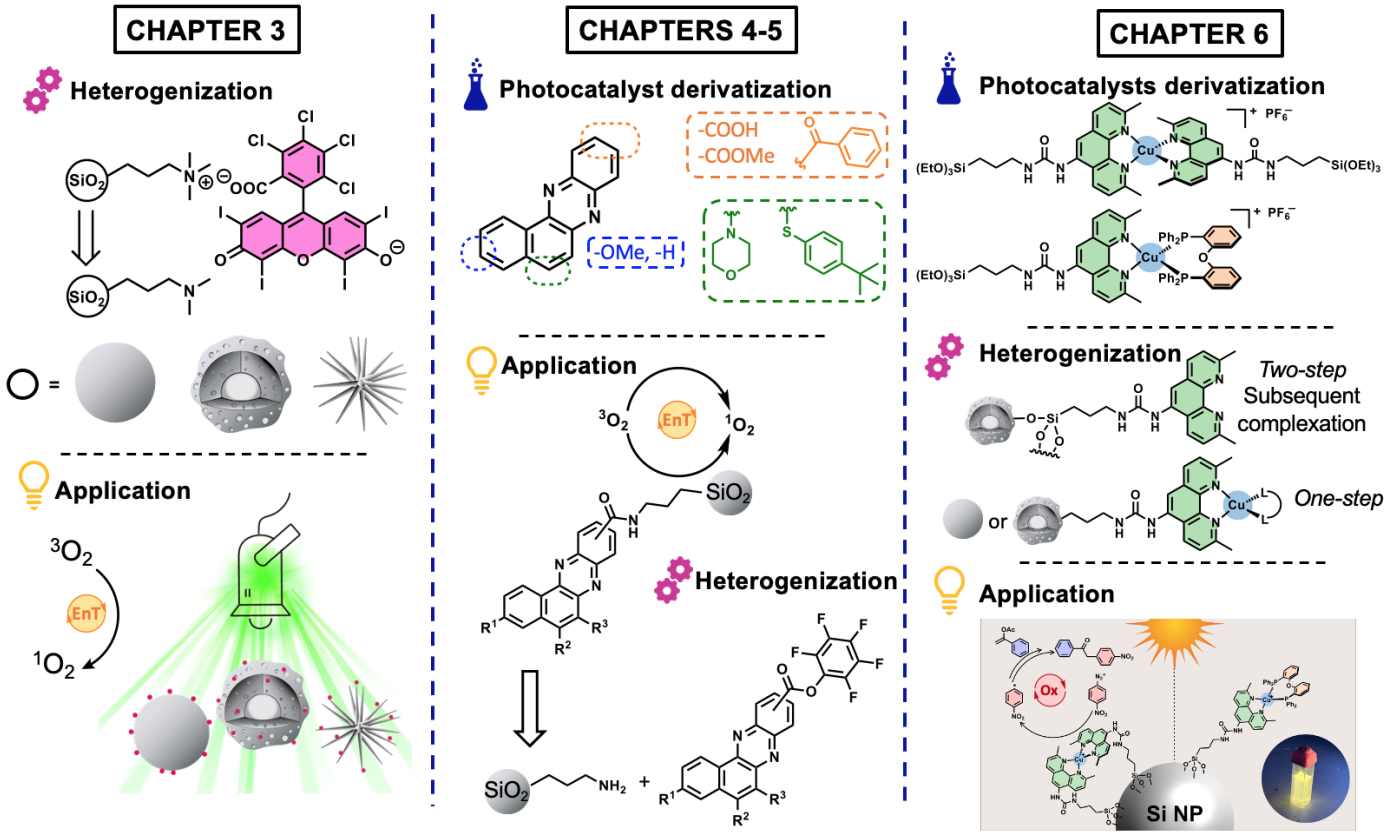
The general methodology (**Scheme 2.1**) involves the obtention or synthesis of selected photocatalysts and their characterization, as well as catalytic testing in homogeneous phase. The second step is their anchoring onto a solid support, which might involve photocatalysts and/or solid particles chemical modifications. The different partners need to be characterized at each step of their elaboration to confirm the success of the procedures and most importantly to confirm the exact nature of the immobilized species. Finally, the heterogenized PCs are tested in the same reaction as in homogeneous phase and compared in terms of performance, stability and recyclability, involving again detailed characterization steps.



Scheme 2.1. General methodology used in this manuscript.

1. Detailed methodologies

In order to accomplish these different sub-objectives, the following detailed methodology has been devised (**Scheme 2.2**):



Scheme 2.2. Objectives and methodology of this PhD thesis.

To tackle objective 1 (development and comparison of the morphology of the support onto a photocatalyzed reaction – Chapter 3):

- Three different structures of silica nanoparticles will be investigated: non-porous nanospheres, core-shell and urchins (KCC-1) particles. The three morphologies will be compared in terms of functionalization rate, PC loadings, light accessibility, diffusion parameters, photoactivity, photostability, and leaching of the immobilized PC.
- Electrostatic interactions will be used to heterogenize an anionic photocatalyst to avoid any covalent functionalization of the PC that could alter its initial photophysical properties. The nanostructured materials will be covalently functionalized with tertiary amines that will be directly alkylated to form ammonium groups allowing the non-covalent interaction between the support and the PC. In this way, the PC is not derivatized and we can focus exclusively on the influence of the support morphology.
- Rose Bengal will be used as the selected negatively charged PC as it is a well-known photosensitizer, especially in the photoproduction of singlet oxygen. Our goal here is not to introduce a new PC catalyzing an innovative chemical reaction with a broad scope but to focus our attention onto the influence of the support texture and we thus need a PC that has already proved its utility in supported homogeneous photocatalysis. A benchmark reaction, developed at industrial scale, will be employed as catalytic test which is the photooxidation of citronellol.

Concerning objective 2 (establishing a structure-activity relationship to allow a neutral covalent grafting approach – Chapter 4):

- A simple all-organic photocatalyst, namely benzophenazine, will be derivatized at its north, south, and west regions with various electro-donating and electro-attractive groups. The excited state of each new derivative will be characterized and each PC will be compared in terms

of absorption, emission, excited-state lifetime, oxygen quenching, photoactivity, and photostability.

- In order to validate our hypothesis of a neutral grafting, an activated ester moiety will be inserted at the neutral region of the best benzophenazine derivative found, to allow the formation of an amide bond with the support surface exhibiting primary amine reactive groups, introduced by APTES grafting onto silica particles. The recyclability of the covalently-bound species along with its properties will be assessed and connected to photocatalytic activity.

Finally, concerning objective 3 (anchoring of copper complexes – Chapter 6), homoleptic and heteroleptic copper(I) complexes, formed with a diimine and diphosphine ligands, will be anchored covalently onto non-porous and porous silica NPs. We selected a core-shell texture for the porosity to limit the diffusion of reactants or the light access issues within fully porous systems. To do so, a new ligand will be synthesized consisting in a siloxane-derivative of the common dimethylphenanthroline (DMP) ligand. Two anchoring methodologies will be compared: a one-step one where the copper complex already formed is grafted at the surface in the last stage, and a two-step one where the diimine ligand is firstly anchored, followed by the copper complexation at the surface. These new heterogeneous systems will be characterized with spectroscopic investigations and evaluated in photoredox applications to obtain useful insight related to our main goal.

2. Characterization methods

The characterization of heterogenized systems calls for the use of relevant techniques to determine their chemical composition and physical properties (**Figure 2.1**). Not one single technique can answer all the questions that might arise along the modifications, immobilization and testing steps. In particular, the loading of a photocatalyst onto a support (that is usually expressed in wt.%) can be quite tricky to determine, especially for organic

dyes which might contain in their structure the same atoms as constituting the support, or at least light atoms that are difficult to quantitatively analyze when present in small amounts within an inorganic matrix. For metal complexes, it is easier thanks to the measurement of metal (even traces) amount by inductively coupled plasma spectroscopy (ICP) after digestion, for example. In addition, it is important to fully characterize a supported homogeneous photocatalyst to confirm its molecular nature, in addition to loading, as the photoactivity is directly impacted by the properties of the heterogenized system. The techniques involved in the characterization of surface species are generally not used by organic chemists and to facilitate the reading of this manuscript, we propose a diagram that link characterization techniques to the chemical composition or physical properties of the supported photocatalyst that we want to determine by using them.

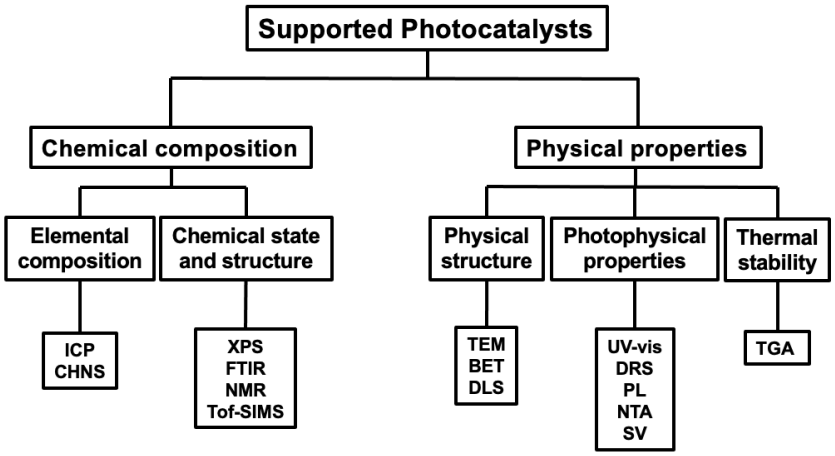


Figure 2.1. Diagram of characterization techniques used to determine the chemical composition and physical properties of supported photocatalysts. ICP = Inductively Coupled Plasma, XPS = X-Ray Photoelectron Spectroscopy, FTIR = Fourier-Transformed Infrared Spectroscopy, NMR = Nuclear Magnetic Resonance spectroscopy, Tof-SIMS = Time of Flight Secondary Ions Mass Spectrometry, TEM = Transmission Electron Microscopy, BET = Brunauer-Emmett-Teller (nitrogen physisorption), DLS = Dynamic Light Scattering, DRS = Diffuse Reflectance UV-vis Spectroscopy, PL = Photoluminescence, NTA = Nanosecond Transient Absorption, SV = Stern-Volmer, TGA = Thermogravimetric analysis. Adapted from literature.[266]

The leaching is another parameter that is important to assess to evaluate the robustness of the heterogenized system along the runs of reaction. Different techniques can used for that purpose. ICP analysis is suitable to quantify the amount of metal from a metallic complex that leached during a catalytic reaction. In the case of photoactive species, UV-vis can also be used to quantify the amount of PC that is not at the solid surface anymore. TGA analysis is the most general technique in this respect, as it can evaluate the lost in weight from the solid and takes into account also the leaching of the ligands for example.

3. Contents of the Manuscript

The introduction and the objectives of this PhD thesis have been covered in chapters 1 and 2, respectively. The results presented in this manuscript will be divided in the next following 4 chapters. Chapters 3, 4 and 6 are in the format of a publication in a peer-reviewed journal (and are published or submitted) while Chapter 5 is an extension of Chapter 4 in which one photocatalyst will be investigated more in depth, but this is not part of a publication. From a practical point of view, the supporting information of each publication is inserted as annexes at the end of this manuscript. Data from these supporting information sections will be referred to as with sentences such as “see SI”. Concerning the computational studies, they were performed by Dr. Corentin Lefebvre and only the pertinent results are discussed in this manuscript but not the methodology for the theoretical developments (for the details, readers are guided to the annexes of the corresponding chapter).

Chapter 3 treats the influence of the support morphology (non-porous nanospheres, mesoporous core-shell and urchins) onto the photooxidation of citronellol by non-covalently immobilized Rose Bengal. The heterogeneous systems are fully characterized and their recycling and leaching are assessed.

Chapter 4 is dedicated to the establishment of a structure-activity relationship for benzophenazine derivatives. The photophysical properties of each derivative (and their respective excited state) are investigated along with their photoactivity in the photogeneration of singlet oxygen. By identifying on which region the functionalization impacts the less the photocatalyst, its covalent anchoring on non-porous silica nanospheres is optimized and the resulting photocatalytic activity is compared with the homogeneous conditions. The recycling is also evaluated.

Chapter 5 is an extension of Chapter 4. One of the benzophenazine derivatives, exhibiting a diethylaniline moiety on the southern region, will be investigated more in depth in order to use it in photoredox applications involving electron transfers.

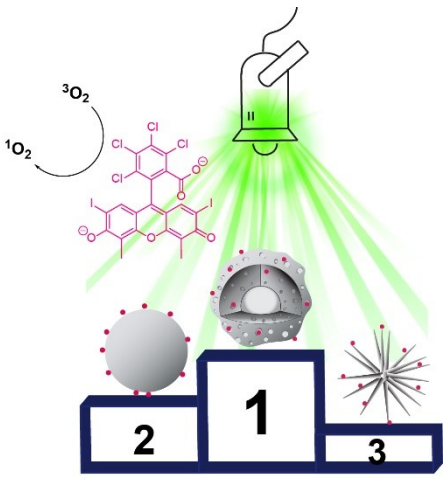
Chapter 6 concerns the covalent grafting of homoleptic and heteroleptic copper(I) complexes on silica NPs. Different methodologies to synthesize such heterogeneous systems are investigated and once optimized, the corresponding supported copper complexes are evaluated in the photocatalyzed α-arylation of an enol acetate. Their photostability and photophysical properties are investigated on the surface of the solid support. This work is completed by the recycling of these photocatalysts.

This manuscript will end with the final chapter, **Chapter 7**, to conclude this PhD thesis and to present the future perspectives of this work, followed by some annexes.

Chapter 3

Impact of silica nanoparticles architectures on the photosensitization of O_2 by immobilized Rose Bengal

N. Body, C. Lefebvre, P. Eloy, T. Haynes, S. Hermans, O. Riant, *Journal of Photochemistry & Photobiology, A: Chemistry* **2023**, *440*, 114648.
DOI: 10.1016/j.jphotochem.2023.114648



Author Statement

Nathalie Body was the principal investigator of this research project. She designed the methodology and performed the investigation and analyses. She also wrote the original draft of this publication. **Corentin Lefebvre** performed the computational experiments. **Pierre Eloy** helped for XPS analyses and interpretation. **Tommy Haynes** helped recording the TEM images by forming and assisting the principal investigator. This research project was realized under the supervision of **Sophie Hermans** and **Olivier Riant** who conceptualized the project, designed the methodology, validated the results and reviewed and edited the publication.

1. Abstract

Transforming light into chemical energy has been widely studied to design ecofriendly, cost-effective and sustainable synthetic approaches. The heterogenization of organic photocatalysts is a well-known strategy providing efficient solid supported catalysts. One of the most suitable solid as support is silica nanoparticles (NPs). This research note highlights the impact of silica nanoparticles morphology on a representative photochemical process that is the photooxidation of citronellol, involving oxygen sensitization. Three architectures of silica NPs were investigated: Nanospheres (NS), Core-Shell (CS) and Urchins (U). Their surfaces were functionalized with ammonium moieties allowing the immobilization of Rose Bengal (RB) by electrostatic interactions. The heterogenized RB on the various supports displayed different activities in the production of singlet oxygen, CS being the best support in terms of activity, recyclability and dye immobilization rate.

2. Introduction

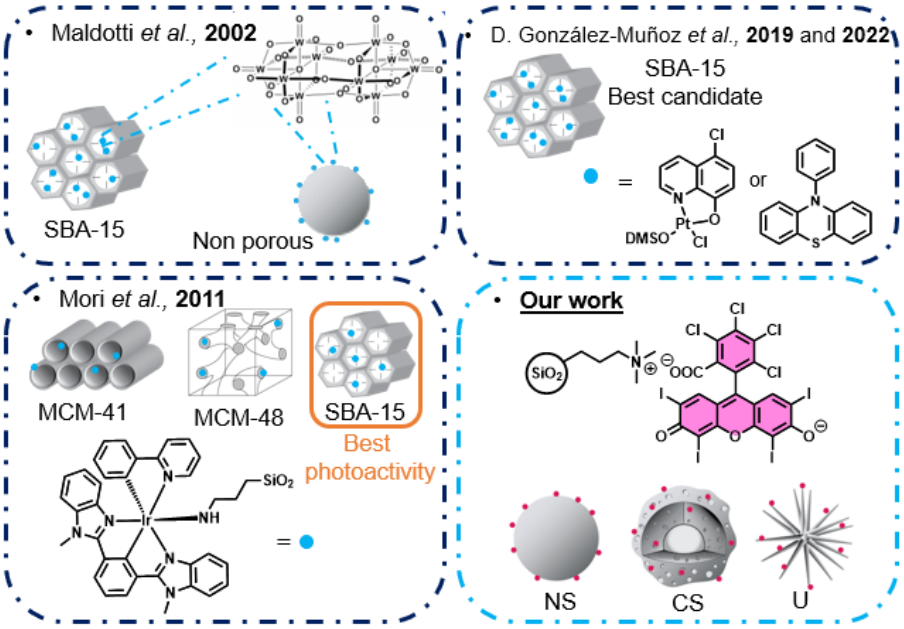
The production of singlet oxygen is one of the most studied photochemical process, since the pioneer work of Foote and Wexler in 1964.[267,268] Singlet oxygen is an important species that can be useful in photodynamic therapy, depollution or even in organic synthesis applications. It is common knowledge that the production of singlet oxygen requires a photosensitizer which absorbs UV or visible light and, after a singlet to triplet intersystem crossing, is enabled to do an energy transfer with the ground triplet state of molecular oxygen.[269] Two main classes of photosensitizers can be distinguished: metallic complexes (based on iridium, ruthenium, or copper centers for example) and organic dyes (e.g. Rose Bengal, Eosin, Methylene Blue).[142] Although these catalysts are highly efficient towards singlet oxygen production, their main drawbacks are their price (especially for metals), multiple steps synthesis, tedious separation from products, photobleaching (especially for dyes) or even toxicity. To solve these problems, their immobilization on a support is an interesting strategy.

Silica nanoparticles are one of the most suitable supports for immobilizing organic photocatalysts. Since decades, silica functionalization with various moieties was developed easily and led to a broad variety of linkages to immobilize molecular species.[250] Moreover, multiple architectures have been described like nanospheres[220], magnetic particles[270], core-shell[221], hollow spheres or nanofibers[222], urchins or dendritic silica[223]… These available morphologies are a real asset for the use of silica nanoparticles. Indeed, numerous examples in the literature described the influence of the texture of inorganic photocatalysts such as TiO_2[38,41,271] or ZnO[43,44] on their photocatalytic activity. It would be interesting to investigate if the morphology of the support can also have an impact on supported organic photocatalysts activity, giving therefore an active role to the support in the photocatalytic process.

To the best of our knowledge, only a few articles are dedicated to this end (**Scheme 3.1**). In 2002, Maldotti *et al.* studied the immobilization of (*n*-$Bu_4N)_4W_{10}O_{32}$ on MCM-41 and amorphous silica NPs. The photocatalytic activity of the decatungstate ion was influenced by the morphology of the support from both the overall yield and the chemoselectivity points of view.[272] González-Muñoz *et al*. dedicated some research efforts to the impact of the size and shape of silica NPs pores on the anchoring of a platinum complex and 10-phenylphenothiazine. They highlighted the best efficiency of SBA-15 materials thanks to an easy access to the catalyst made possible by the large pores and allowing rapid substrate diffusion, compared to materials with hexagonal or wormhole-like pores.[273,274] In 2011, Mori *et al.* anchored the photocatalyst $[Ir(Mebib)(ppy)]^+$ on three different mesoporous silicas namely, SBA-15, MCM-48 and MCM-41. These materials displayed different emission intensities induced by differences in pore dimension and structure of the mesoporous silica supports meaning that the local environment can influence the excited state of the iridium complex. These heterogenized complexes were tested in the photooxidation of *trans*-stilbene and 1-naphtol for which SBA-15 was the best material in terms of photoactivity and turn-over number (TON).[181]

We describe herein the impact of nanostructured silica NPs on the production of singlet oxygen. The anchoring of Rose Bengal (RB), an efficient photosensitizer, on silica NPs has been reported in the literature for applications in photodynamic therapy[175,275,276] and this system is a suitable one to bring light onto the importance of the support. Furthermore, Goddard *et al.* selected this chromophore for covalent grafting on ordered mesoporous silica and showed that up to eight recycling cycles of the supported catalyst was possible on a model photocatalyzed aza-Henry reaction, without any loss in photoactivity.[174] In our design, a non-covalent interaction was chosen as linkage between ammonium groups inserted at the surface and/or in pores of the support and the negative charges of RB (**Scheme 3.1**). This allows

anchoring without photosensitizer chemical modifications and should ensure optimal photocatalytic activity. Moreover, with such electrostatic interaction, the polarity of the solvent used in the future photocatalytic applications is not a limitation as a "boomerang effect" could be envisaged (meaning that with the solvent competition, the photocatalyst could go away from the support before being forced to be immobilized again). Such effect would ensure the best photoactivity as the photocatalyst would be as in homogeneous conditions. The envisaged silica NPs morphologies are NanoSpheres (NS), Core-Shell (CS) and Urchins (U) (dendritic fibrous silica NPs). The heterogenized RB onto these supports are referenced as **RB@NS**, **RB@CS** and **RB@U**.



Scheme 3.1. Study of the silica nanostructure impact on photocatalytic processes: past and present work.

3. Results and discussion

Nanospheres (40 nm) were synthesized according to the famous Stöber sol-gel process.[220] Core-Shell (core = 27 nm, mesoporous layer thickness =

15 nm, total size = 57 nm as measured by TEM) were obtained by adapting the procedure from Yoon *et al*.[221] U NPs were purchased from Strem (40-50 nm). The architectures of Core-Shell and Nanospheres were confirmed by TEM microscopy (**Figure 3.1**). To fully validate the structure of Urchins nanoparticles, a high resolution TEM analysis would have been necessary. XPS (see SI – **Figure 3.11**, **Figure 3.13** and **Figure A.1**) analyses proved that siloxane bonds of SiO_2 were correctly formed (103.4–103.6 eV for Si–O bond) for all structures and that no impurity was present, except for a small amount of unreacted TEOS seen by XPS for NS NPs. The specific surface areas were calculated by using the BET equation on nitrogen physisorption data: NS = 360 $m^2 g^{-1}$; CS = 650 $m^2 g^{-1}$; U = 243 $m^2 g^{-1}$ (see SI – **Figure 3.12, Figure 3.14** and **Figure A.2**). These values are within the expected scale as core-shell NPs were the only mesoporous material. Urchins nanoparticles were expected to be more porous. Concerning the pores size and the porous volume, Barret-Joyner-Halenda (BJH) and Density Functional Theory (DFT) methods were used for mesoporous and microporous materials, respectively. Nanospheres exhibit micropores of mean size 0.7 nm and a porous volume of 0.63 $cm^3 g^{-1}$. Core-Shell nanoparticles possess a combination of mesopores (3.0 nm) and micropores (1.3 nm) with a porous volume of 2.4 $cm^3 g^{-1}$ while the urchins particles presented a broad distribution of pores sizes between 40 and 170 nm.

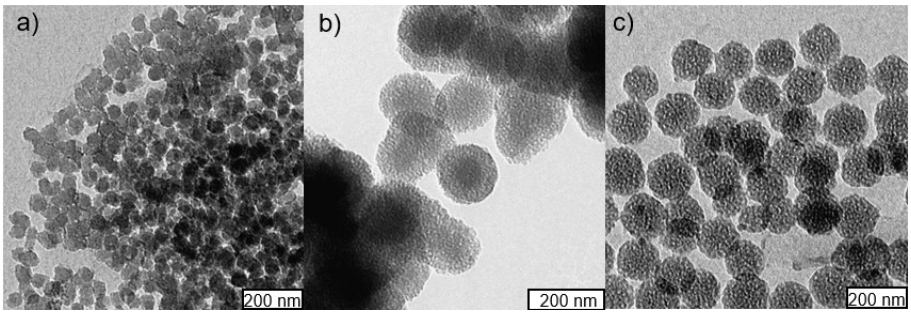
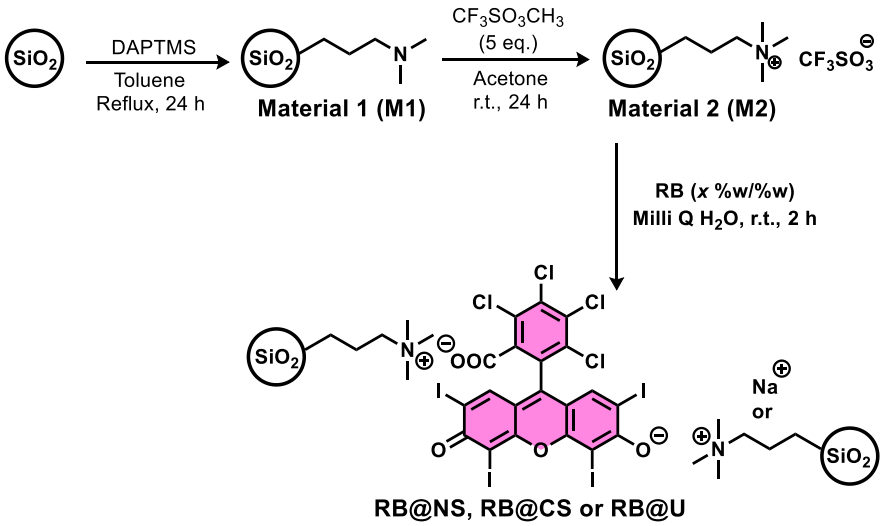


Figure 3.1. TEM images of pristine silica NPs: a) NS, b) CS, c) U.

These three materials present a weakly acidic surface due to the presence of silanol groups with a density generally comprised between 4–6 Si–OH nm^{-2}. A lower density of 1.5–2.5 SiOH nm^{-2} is expected for high-temperature calcinated silica nanoparticles that can be improved followed rehydration.[277] The surface chemistry of silica nanoparticles also governs its hydrophilic/hydrophobic character, that depends on the ability of Si–OH groups to form hydrogen bonds with an adsorbate[244] and on the surface roughness.[278] Sriramulu *et al.* were able to prepare a thin film of unfunctionalized non-porous silica nanoparticles and showed their superhydrophilic character by measuring a water contact angle of 0 °.[279] Mesoporous silica nanoparticles are also hydrophilic with reported water contact angles of 30 ° and 0 ° for MCM-48 and MCM-41, respectively.[278,280] Pristine dendritic mesoporous silica nanoparticles are also known to be hydrophilic materials. A lot of researches focused on increasing their hydrophobicity by implementing alkyl moieties or by applying treatments to remove the silanol groups.[281–283]

In order to immobilize RB non-covalently, a general three-step functionalization method was envisaged (**Scheme 3.2**). The first step was the anchoring of tertiary amines by using of (*N*,*N*-dimethylaminopropyl)trimethoxysilane (DAPTMS) in toluene under reflux for 24 h.[217] This commercial silane allowed the establishment of a 3 carbon-linker which is a good compromise for the photocatalyst to be sufficiently away from the surface support preventing some negative interactions with it. In the same thought, a longer linker could allow the folding of the photocatalyst onto the surface in addition to favoring the possible interactions between neighboring excited photocatalysts leading to their potential quenching by triplet-triplet annihilation. The second step was the methylation of previously anchored amines with $CF_3SO_3CH_3$ to obtain ammonium moieties.[284] Such methylation reagent was used as fluorine atom is easily

detected with a good signal/noise ratio by XPS which would be helpful to validate that step of functionalization. The last step was the immobilization of RB *via* electrostatic interactions by contacting RB with the functionalized support in water.



Scheme 3.2. The three-step functionalization method envisaged to immobilize RB. For **RB@NS**, **RB@CS** and **RB@U**, either a simple or a double electrostatic interaction can take place leading to the presence of a sodium or an ammonium counter cation, respectively. For the double interaction, it can occur with two ammonium sites present on the same silica surface or with two distinct silica particles.

The heterogenized photocatalysts (**RB@NS**, **RB@CS** and **RB@U**) and the intermediate materials (**M1** and **M2**) for each nanostructured support were characterized by XPS, CHN and TGA analyses and the values are reported in the following **Table 3.1**:

Table 3.1. Characterization of the heterogenized photocatalysts and the intermediate materials by XPS, CHN and TGA analyses. *wt.% of N was calculated based on TGA curves (see SI – Annex A).

	NS			CS			U			Pure RB
	M1	**M2**	**RB@NS**	**M1**	**M2**	**RB@CS**	**M1**	**M2**	**RB@U**	-
XPS (atomic%)										
C_{1s}	20.8	17.2	24.7	19.0	17.1	26.1	15.5	15.6	19.1	60.2
O_{1s}	57.1	50.1	45.5	58.1	50.9	48.9	61.9	49	45.4	9.3
Si_{2p}	18.5	19.4	23.2	19.3	18.5	18.5	19.5	25.1	20.4	-
N_{1s}	3.6	2.8	2.1	3.5	2.7	2.2	3.1	2.2	1.9	-
F_{1s}	-	8.4	Traces	-	8.5	Traces	-	7.2	Traces	
S_{2p}	-	2.2	-	-	2.3	-	-	2.0	-	-
I_{3d}	-	-	1.8	-	-	2.2	-	-	3.4	10.5
Cl_{2p}	-	-	2.4	-	-	2.2	-	-	3.1	12.2
Na_{1s}	-	-	0.3	-	-	0.2	-	-	0.7	7.8
O/Si	2.1	2.5	2.0	2.4	2.7	2.6	2.7	2.0	2.0	-
N/Si	0.2	0.1	0.1	0.2	0.2	0.1	0.1	0.1	0.1	-
I/Cl	-	-	0.7	-	-	1	-	-	1.1	0.9
NMe_3^+/Cl	-	-	1.6	-	-	1.6	-	-	1.5	-
CHN (wt.%)										
N	-	1.02	0.90	-	1.44	0.98	-	0.87	0.62	-
TGA (wt.%)										
N*	2.62	1.31	-	2.18	1.46	-	1.47	0.84	-	-

For all XPS analyses, the atomic percentages of oxygen and carbon need to be carefully considered as adventitious carbon contamination exhibiting oxygenated functionalities cannot be avoided during such analysis.

For **M1**, the detection of a nitrogen peak with a 399.6 eV binding energy by XPS proved the efficient anchoring of tertiary amine moieties for the three silica morphologies (**Figure 3.2**).[285]

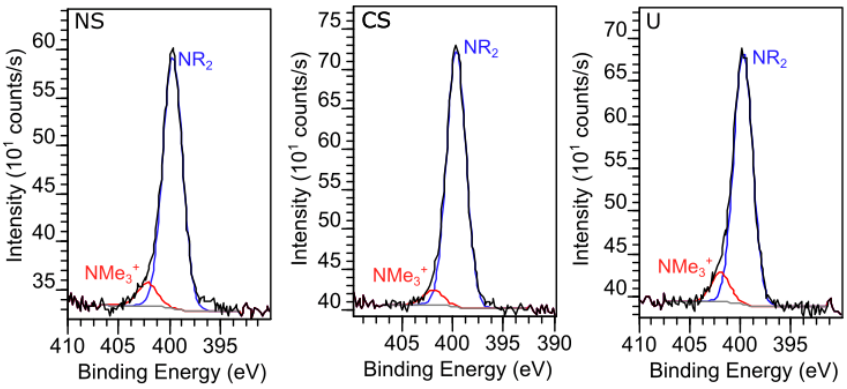


Figure 3.2. N_{1s} XPS spectra of NMe_2-functionalized silica nanoparticles.

The N/Si ratio permits to compare the efficiency of amines anchoring among the three different morphologies. As XPS is a surface analysis, the first few nanometers (5-10 nm) of the material will be analyzed and the core of the particles will not. This feature means that for porous materials, some functionalities will not be detected because they are too deep while for non-porous materials, all functionalities will be detected (**Figure 3.3**). The consequence is that the N/Si ratio is overestimated for NS and slightly underestimated for CS and U NPs, meaning that CS seems to present the best functionalization rate. Another parameter that can influence the surface atomic concentration in nitrogen is the ability of multi(tri)-valent silane (such as DAPTMS) to form infinite, cross-linked siloxane polymer lattices. This phenomenon is well known in the literature [217,286] and lead to multiple layer of DAPTMS with some nitrogen moieties that are not easily accessible for further functionalization steps. This first step was also confirmed by TGA

analysis for which an important loss in mass was observed for NS although this nanostructure is not porous (see SI – **Figure A.3**). We could envisage that for this architecture, the DAPTMS polymerization was favored. The amine loading determined by TGA analysis is 1 mmol g^{-1} for NS (overestimated if DAPTMS polymerization had occurred), 0.9 mmol g^{-1} for CS and 0.6 mmol g^{-1} for U. These loadings are in accordance with the ones used to anchor RB on silica nanoparticles in the literature which are comprised between 1and 1.3 mmol g^{-1}.[170,174,178,287]

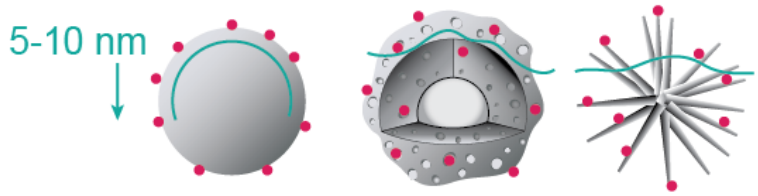


Figure 3.3. XPS depth of analysis sketched for each silica morphology leading to an over- or underestimation of functionalization rate. The photoelectron free path is represented by the green line and tries to consider the different morphologies of silica nanoparticles that will impact the photoelectron free path. A photoelectron travelling in the void between dendrimers of urchins will go further allowing deeper analysis in the sample for example. The pink balls represent some immobilized heteroatoms.

The second step was the formation of ammonium moieties, leading to **M2**.[284] This functionalization step was also evaluated by XPS analyses (**Figure 3.4**, see SI – **Figure A.4** and **Figure A.5**). In all three cases, a N_{1s} peak was observed at around 402 eV corresponding to quaternary amines.[285] Some tertiary amines were still detected at 399.6 eV (7.5 % for NS, 4.7 % for CS and 5.8 % for U of the N_{1s} peak). The higher amount of tertiary amines for NS reinforce the DAPTMS polymerization hypothesis for which nitrogen elements could be buried and not able to be transformed into positively charged moieties. The presence of ammonium functions was also supported by the detection of fluorine and sulfur elements, forming the counter-anion.

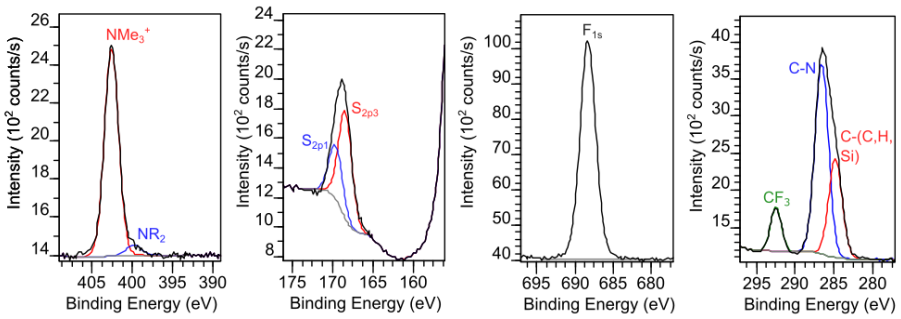


Figure 3.4. N_{1s}, S_{2p}, F_{1s} and C_{1s} XPS spectra of ammonium-functionalized CS NPs.

As the XPS depth of analysis limitation, as discussed above, prevents the quantification, CHN and TGA analyses were performed for the three solids (**Table 3.1**, see SI – **Figure A.6** and **Table A.2**). For TGA analyses, the hypotheses are that the loss in weight is due only to perfectly anchored ammonium arms (no impurity) and that the organic arms are completely calcinated during the TGA analysis. For all supports, TGA and CHN analyses were in agreement, except for NS particles for which a slightly higher amount in nitrogen was assessed by TGA. The loading of ammonium moieties for NS is 0.7 mmol g^{-1}. CS showed the highest level of functionalization (1 mmol g^{-1}) while U showed the worst (0.6 mmol g^{-1}), as expected from their specific surface areas.

FTIR provided further evidence for the anchoring of ammonium moieties. Comparing the spectra of NPs-NMe_3^+ with that of pristine NPs, the presence of a characteristic stretching band of ammonium moieties (1490 cm^{-1}) and, more importantly, of CF_3SO_3 (640 cm^{-1}) validated the successful introduction of desired functionality at the surface of NPs (see SI – **Figure A.10** to **Figure A.12**).

The next step was the immobilization of RB to give heterogenized photocatalysts noted **RB@NS**, **RB@CS** and **RB@U** (**Scheme 3.2**). The hydrophilic head of ammonium-functionalized silica nanoparticles allowed an efficient dispersion of the materials in water in all three cases, indicating that

the hydrophilicity of silica nanoparticles was maintained. The maximal loading of RB was determined by varying the %w/w of RB introduced with silica in several experiments and the resulting bright pink solids were analyzed by TGA while the filtrates were analyzed by UV-vis. M.A. Rauf *et al.* were able to determine experimentally the dipolar moment of Rose Bengal in its fundamental and excited states, namely 1.72 and 2.33 Debye, respectively.[288] This is a small change and if we consider only electrostatic interactions, it would mean that the adsorption of RB would be slightly enhanced when performed in its excited state. We can consider that the difference in Rose Bengal adsorption whether it is performed in the dark or under light is not significant. The most porous structure, CS, gave the highest loading of 19 wt.% (0.19 mmol g^{-1}) followed by U (15 wt.% - 0.15 mmol g^{-1}) and NS (13 wt.% - 0.13 mmol g^{-1}). This agrees with the work of Soria-Castro *et al.* who anchored RB onto SBA-15 with a loading of 0.09 mmol g^{-1}.[174] Although NS and U presented the lowest loadings, it was still quite high compared with CS and taking into account their respective specific surface areas (**Figure 3.5**).

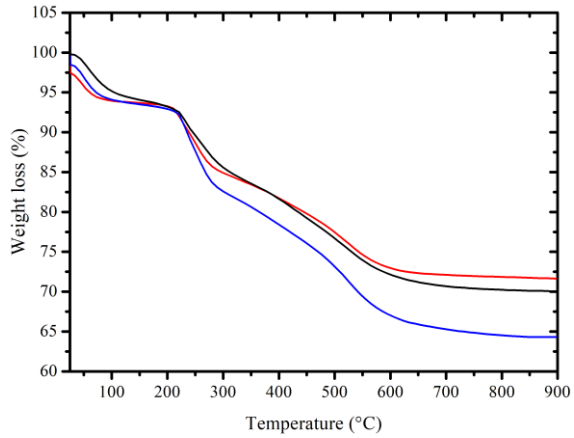


Figure 3.5. TGA curves of **RB@NS** (black), **RB@CS** (blue), and **RB@U** (red).

The heterogenized photocatalysts were analyzed by FTIR-ATR, CHN, XPS and UV-vis to confirm that the structure of RB and its photoactivity were intact after immobilization.

The FTIR spectra of NPs-RB suggested the incorporation of the intact dye onto the materials. Indeed, the characteristic bands of RB observed for the free molecule at 1614, 1543, 1446 and 1340 cm^{-1} (see SI – **Figure A.9**) have been identified after immobilization at 1614, 1548, 1457 and 1342 cm^{-1} in all three cases (see SI – **Figure A.10**, **Figure A.11** and **Figure A.12**).

The heterogenized photocatalysts were also analyzed by XPS. The first thing to check was the stability of our functionalized arms. Ammoniums moieties were still detected but with a lower amount than before the immobilization of RB (**Table 3.1**). This phenomenon was confirmed by CHN analyses (**Table 3.1** and see SI – **Table A.2**) and could be explained by the basicity of the photocatalyst that could induce a Hofmann elimination by losing the ammonium moiety to form a terminal double bond. As an ammonium group is not a good leaving group, such reaction is difficult to achieve but still could explain the decrease in detected nitrogen. However, some CF_3 moieties were still detected by XPS.

The second important information is the detection of chlorine and iodine, which are characteristic elements of the photocatalyst. These elements were spotted by XPS at the same binding energy as the pure powder of RB (see SI – **Figure A.7**) and the atomic concentration ratio I/Cl fitted also to the reference. When analyzing the pure powder of RB, decomposition of the I_{3d} photopeak gave two components: one at 620.6 eV corresponding to I–C bond and the other one at 618.5 eV for 5 % of the amount of iodine corresponding to I^-. It cannot be excluded that the XPS analysis itself causes the breaking of I–C bonds. On the supports, this 618.5 eV component increased to 35 % for CS, 26 % on U, while for NS, this value reached 55 % of the total amount of iodine (**Figure 3.6**).

In addition, the detection of sodium (the counter-ion of RB at the start) on the surface indicates either a simple ion exchange at the carboxylic acid site (sodium cation stays in place at the phenolate site) or the occurrence of a

non-specific physical adsorption of RB, rather than ion-exchange at the ammonium-sites, that cannot be avoided for each material. This non-specific interaction was three times more important on U NPs (Na/Si = 0.03) than on NS and CS nanostructures. A computational study was carried out to assess the energy of interaction between RB and the surface of the modified silica NPs with ammonium moieties and between RB and silica NPs without any ammonium functionalities at the surface and these energies are -74.25 and -46.64 kcal mol^{-1}, respectively. This proves the utility of functionalizing the surface of NPs to enhance the immobilization rate of RB. This adsorption phenomenon was also confirmed experimentally by putting in contact pristine NS (as it possesses the lowest specific surface area) with RB. A loading of 3 wt.% and 4.7 wt.% of RB was measured by UV-vis and TGA, respectively which is much lower than the loadings obtained on ammonium-functionalized NPs.

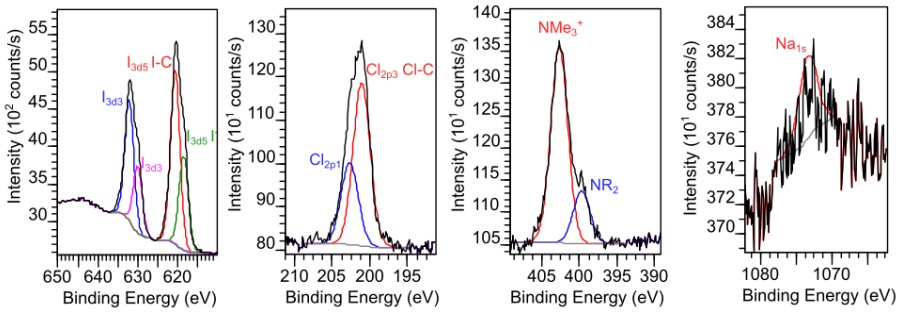
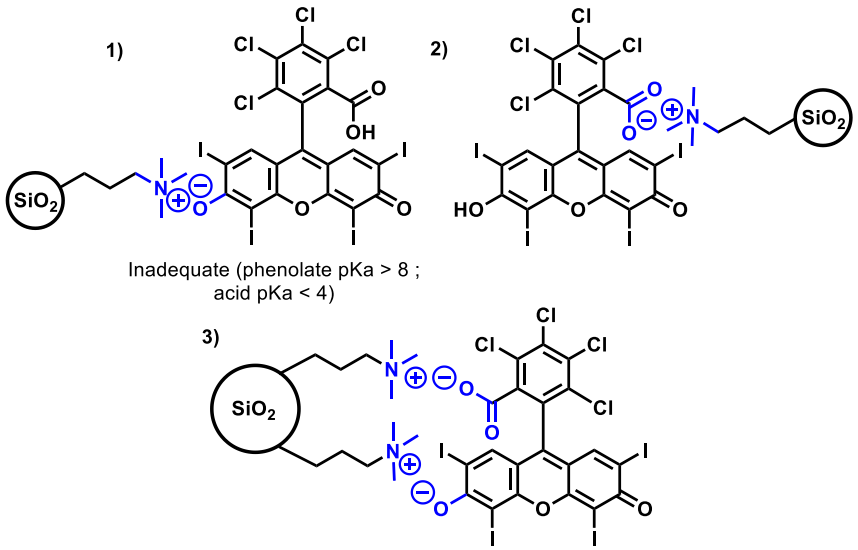


Figure 3.6. I_{3d}, Cl_{2p}, N_{1s} and Na_{1s} XPS spectra of **RB@CS**.

Finally, the NMe_3^+/Cl ratio gave us an idea about how the interaction between RB and the support was realized. If one anionic site of RB was involved in the immobilization, two situations were possible: the electrostatic interaction with the phenolate or with the carboxylate. The first one was inadequate in terms of pKa and, furthermore, a computational study had been carried out, revealing that the second interaction with the carboxylate was the most favored (**Scheme 3.3**). As the NMe_3^+/Cl ratio ranged from 1.6 to 1.8 for the three supports, the situation where the two anionic sites of RB interact with

two distinct ammonium groups needed to be considered. This information given by XPS was supported by TGA from which the ammonium density was calculated. Considering the interacting sphere of one RB molecule with silica NPs modified surface, 2.96, 2.31 and 3.74 ammoniums were available to immobilize one molecule of the dye for NS, CS and U, respectively (see SI – Annex A) leading to a possible double-side interaction. This ammonium density explains the detection of free $CF_3SO_3^-$ moieties by XPS for heterogenized photocatalysts (being the counter-anion of ammonium groups) as an excess of these moieties were present at the surface. Moreover, this double-side interaction was interesting as it prevented RB from being too easily released in the mobile phase and also protected it from photobleaching as it was observed by Terra *et al.*[173] Furthermore, this double-sided interaction diminishes the free ammonium moieties at the surface leading to a decrease in the hydrophilicity of the silica nanoparticles, which is necessary for their correct dispersion in acetonitrile used as solvent in the photooxidation of citronellol.



Scheme 3.3. Three different ways to immobilize RB onto the surface of silica NPs.

Although the results converge to a double-side interaction, we needed to confirm that it was structurally feasible by considering the two perpendicular planes of the RB molecule. Again, a computational study was carried out by implementing the density of ammonium functionalized arms and we could clearly see that two separated ammonium arms can indeed interact with the anionic sites of RB *via* electrostatic interactions (see SI – **Figure A.22**). Some hydrogen bonds were also visualized, reinforcing the interaction with the support.

Photophysical properties of RB@NPs were evaluated by UV-vis spectroscopy (**Table 3.2**). For supported RB, a slight bathochromic shift of the absorbance band was observed in comparison to RB in acetonitrile as already seen in the literature (**Figure 3.7**)[170,176] According to the literature, this red shift can be ascribed to the chemical and polarity environment modification of RB. It has been reported that a more hydrophobic environment (compared to the solvent environment) diminishes the energy gap between the frontier orbitals leading to a red shift in the absorbance of the photocatalyst.[170,289] Heterogenized photocatalyst showed also a decrease in molar absorption coefficient ε due to the presence of solid nanoparticles causing light scattering. **RB@CS** showed the best photophysical properties in terms of molar absorption coefficient and photostability (ΔA) and its ability to produce $^1O_2$ was equivalent to pure RB (**Figure A.13**). Strikingly, the presence of the supports enhances the RB photostability.[171,173] Finally, **RB@NS** had the highest quantum yield of production of $^1O_2$ of 0.94. The direct surface accessibility for light could be an advantage as this silica is non-porous. Such morphology could also decrease the non-radiative deexcitation processes of Rose Bengal, then enhancing the quantum yield of singlet oxygen production. Surprisingly, **RB@U** didn't show the best photophysical properties as we would have expected thanks to the multiple scattering events increasing the light path between neighbouring molecules anchored within the

spikes of the urchins.[225] Indeed, urchins nanoparticles were reported to improve the light-harvesting properties and the photocatalytic activity of several heterogeneous photocatalysts such as TiO_2.[223,290–292] We expected that such phenomena could also be observed with homogeneous supported photocatalysts.

Table 3.2. Photophysical properties of RB and supported RB.

	RB	**RB@NS**	**RB@CS**	**RB@U**
λ_{max} (nm)	557	562	562	562
ε (mol^{-1} cm^{-1})[a]	72.800	15.000	19.300	15.000
ϕ_Δ[b]	0.76	0.94	0.74	0.64
ΔA[c]	0.550	0.034	0.016	0.012

[a] Molar absorption coefficient ε were determined in acetonitrile. [b] ϕ_Δ was determined by anthracene-9,10-divinylsulfonate (AVS) photodegradation in water (see SI - **Figure A.14**, **Figure A.15** and **Figure A.16**).[293] [c] ΔA is the decrease in absorbance of the PC after 15 min of green irradiation.

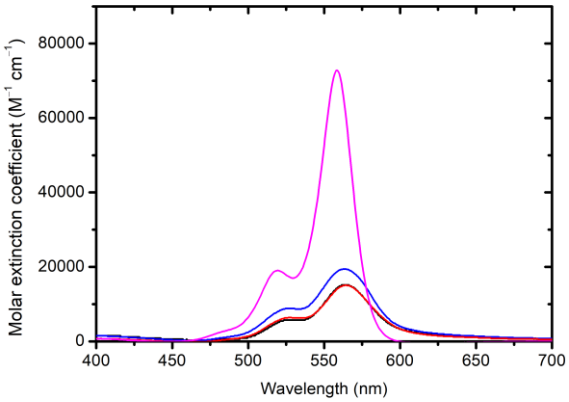
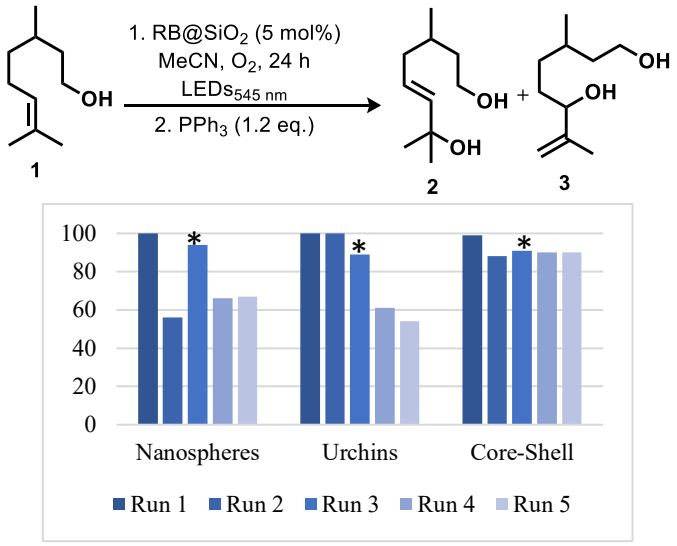


Figure 3.7. Molar extinction coefficient of homogeneous RB (pink) and heterogenized **RB@NS** (black), **RB@CS** (blue) and **RB@U** (red).

To benchmark the reactivity of these immobilized photocatalysts, the materials were tested on the photooxidation of citronellol **1**[270], for which RB in homogeneous phase is known to be effective (**Scheme 3.4**), and which requires singlet oxygen. Control experiments showed that with no light, or no photocatalyst, only traces of products were observed. Using a photocatalyst

loading of 5 mol%, pure RB gave a 94 % yield of the two regioisomers **2** and **3** (ratio 1.1/1) within an irradiation time of 2 h. **RB@NS** was the first heterogenized system to be used to optimize the reaction with the solid catalysts. With an increased irradiation time to 18h (as the diffusion will be slowed down in presence of a solid), an NMR yield of 71 % and a ratio of 1:1 between products **2** and **3** were determined. By increasing the irradiation time to 24 h, a quantitative yield was obtained. These optimized conditions were used with **RB@CS** and **RB@U** and quantitative NMR yields were also obtained, with the same regioisomers ratio.

Recycling runs were then conducted under the same conditions for all supports. The NMR yield with NS dropped by half at the second run, and could be increased again by increasing the catalyst amount in the third run, to counterbalance any recovery losses. **RB@NS** subsequently presented a stable NMR yield of 66 %. Concerning the urchins, the commercial support, a quantitative yield was observed for the first two runs before decreasing and reaching about 50 % for the fourth and fifth runs. The last material, **RB@CS**, was revealed to be the most efficient immobilized photocatalyst, as expected as it showed the best photophysical properties (**Table 3.2**). A quantitative yield was obtained in the first run and the photoactivity of RB was stabilized along five runs (NMR yield in the 5^{th} run = 90 %).



Scheme 3.4. NMR yields (regioisomers **2** and **3**) of photooxidation of citronellol. The internal standard used was dimethylsulfone (see SI – **Scheme 3.5**). In all cases, to conduct run 3, some material arising from run 1 was added to insure same catalyst total mass.

For each run, an evaluation of the RB leaching was realised by UV-vis analysis of the filtrates and TGA of the solids (see SI - **Table A.3**). This leaching could occur by simple loss of RB or loss of ammonium arms. The leaching calculated by TGA after the first run was important for **RB@NS** (4.91 %) and **RB@U** (6.74 %), explaining in part the decrease in photoactivity in the next runs. The RB leaching evaluated by UV-vis gave the same scale for the three different morphologies: 2.75, 2.63 and 8.50 wt.% for **RB@NS**, **RB@CS** and **RB@U**, respectively. Although, a moderate value was obtained for NS NPs comparing to the value obtained by TGA, meaning that the ammonium arms could possibly suffer from light irradiation and stirring.

At this stage, the leaching could be explained by the loss of RB that was weakly immobilized onto silica such as the one that was non-specifically adsorbed (as already discussed above) or the one that was involved in π–π stacking forming multiple layers thanks to the aromatic nature of RB. To validate this last hypothesis, the amount of RB necessary to form a monolayer

was calculated and compared with the quantity of RB introduced. Knowing the ammonium densities and the overall surface area of RB, we could determine that $7.40E^{18}$, $1.34E^{19}$ and $5.01E^{18}$ RB entities were needed to form a monolayer of RB at the surface of the nanoparticles. By comparing these values to the amount of RB immobilized on the supports, the excesses of RB were determined and validated the possibility of having π–π stacking: $5.24E^{17}$, $3.08E^{16}$, $7.77E^{18}$ for NS, CS and U, respectively (see SI, Annex A) The excesses were quite high for **RB@NS** and **RB@U** explaining the leaching of RB during the first run for those supports. Moreover, the important leaching for **RB@U** was understood as the non-specific adsorption phenomenon was also important on that support. This π–π stacking was also a key information to understand the high loadings in RB for all three materials that were obtained compared to what we expected considering the specific surface areas of the different morphologies. Core-Shell structures seems to prevent that interaction as a slight excess of RB and a low leaching were observed.

For the following recycling runs, once the excess of RB was "removed", the photoactivity of **RB@NS** was stable along the runs while for **RB@U**, it kept dropping. **RB@CS** was efficient along the runs (see SI – **Table A.3**).

To understand further the differences in photoactivity, final recycled materials were analysed. Firstly, their morphologies were investigated by TEM and no changes in morphology were observed. Nevertheless, a decrease in size was measured for Nanospheres (34 nm was observed *vs.* diameter of 40 nm at first), which suffered from abrasion. A slighter decrease was also observed for the mesoporous shell of Core-Shell nanoparticles (14 nm instead of 15 nm at first). Urchins nanoparticles remained unchanged as an average diameter of 47 nm was measured, as expected based on their known mechanical stability.[224] All nanostructures were unaltered under photoirradiation and stirring (**Figure 3.8**).

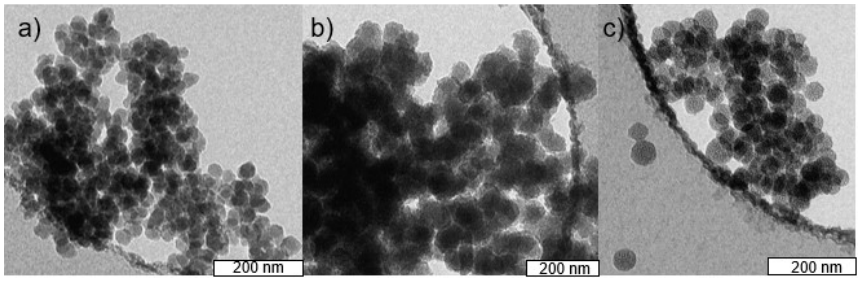


Figure 3.8. TEM images of recycled RB@SiO_2: a) NS, b) CS, and c) U NPs.

Secondly, CHN and XPS analyses were performed to evaluate the robustness of the ammonium-functionalized arm and the chemical structure of RB, respectively. CHN analyses proved the stability of the functionalized arm for two materials as no loss of nitrogen was detected in the cases of CS (0.96 and 0.98 %wt. N) and U (0.62 and 0.68 %wt. N, before and after 5 runs of photooxidation, respectively). On the contrary, NS showed a slight decrease in nitrogen content from 0.89 to 0.74 %wt. N after 5 runs. Functionalization of simple silica spheres seemed to suffer from light and abrasion while the other architectures being porous and allowing internal functionalization acted as a shield for the anchored arms.

Concerning the photocatalyst, XPS analyses showed an important loss in iodine and chlorine elements. The ratio I/Cl was unbalanced, explained by the accentuated loss in iodine (**Table 3.3**, **Figure 3.9**). The formation of iodide increased under light reaching 85 % of total iodine in all cases. Furthermore, the photobleaching of C–Cl bond occurred along the runs and chloride was detected up to 61 % of the total amount of chlorine while none was detected before photocatalytic runs. It would have been interesting to conduct homogeneous photocatalytic runs with Rose Bengal (no silica nanoparticles involved) and recover it by precipitation for example, to highlight if that photobleaching is inherent to Rose Bengal itself or accentuated by the presence of the support. As the whole structure was not analysed by XPS in the case of U and CS because of the depth of analysis limitation, the RB buried deep in the pores could not be detected by XPS, so the extent of

photobleaching was clearly overestimated. These known photobleaching phenomena [294–296] could also partially explain the decrease in photoactivity for **RB@NS** for which these photodegradations could happen more rapidly than for **RB@CS** and **RB@U**. The commercial support suffered from a high leaching explaining the decreased photoactivity. In Core-Shell structure, RB seemed to be protected for a longer time from photobleaching, as indicated by the photophysical characterization reported in **Table 3.2**. Finally, the expected absorption band was still distinguishable in the absorption curves obtained by UV-vis analysis of the solids after 5 runs, in line with retained photoactivity (**Figure 3.10**). All in all, this demonstrated the superiority of the core-shell structure and the ammonium immobilization strategy.

Table 3.3. XPS analysis of final materials after five runs of photooxidation. The values are expressed in atomic concentration percentage.

	C_{1s}	O_{1s}	Si_{2p}	N_{1s}	I_{3d}	Cl_{2p}	O/Si	I/Cl
RB@NS	17.0	53.3	26.7	1.9	0.2	0.8	2.0	0.3
RB@CS	23.6	50.4	23.1	1.6	0.2	0.7	2.2	0.3
RB@U	23.0	50.0	24.6	1.8	0.3	0.7	2.0	0.4

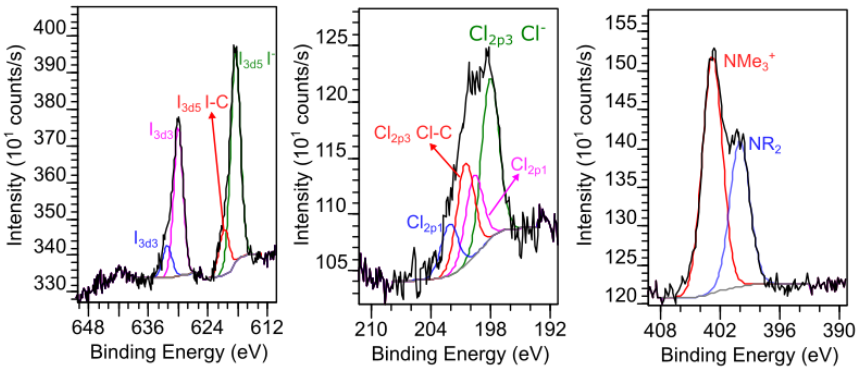


Figure 3.9. I_{3d}, Cl_{2p} and N_{1s} XPS spectra of **RB@CS** after five catalytic runs. For XPS spectra of **RB@NS** and **RB@U**, see SI – **Figure A.17** and **Figure A.18**.

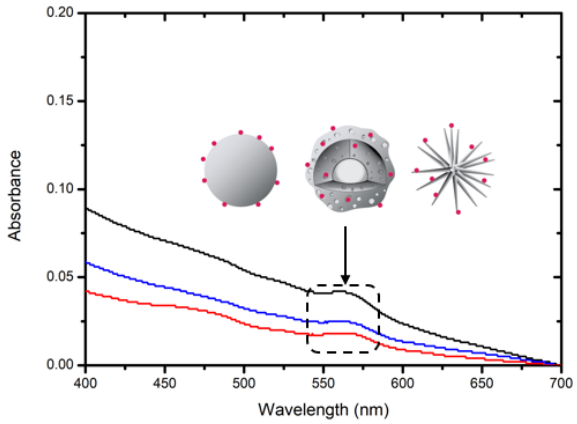


Figure 3.10. Absorption spectra of highly diluted recycled **RB@NS** (black), **RB@CS** (blue), and **RB@U** (red).

4. Conclusion

Rose Bengal was immobilized *via* electrostatic interactions onto three different morphologies of silica nanoparticles, namely Nanospheres (NS), Core-Shell (CS) and Urchins (U). The impact of these different architectures was studied on the production of singlet oxygen for application in citronellol photooxidation.

To allow the dye immobilization, a general three-step methodology was used to functionalize the materials: the anchoring of tertiary amines followed by their methylation, leading to ammonium moieties that can immobilize RB by ion-exchange. For all supports, the presence of these positively charged groups was proven by XPS and IR. The immobilization of RB was successful, reaching the highest loading of 19 wt.% on CS (0.19 mmol g^{-1}) which is of similar magnitude than the loadings reported by Martins Estevão *et al.* (**Scheme 1.11** – 0.07 mmol g^{-1})[170] and Ronzani *et al.* (0.19 mmol g^{-1})[178] highlighting that the non-covalent immobilization is as performant as the one using a covalent amide linker between RB and the support. The photophysical properties of immobilized RB were determined for each solid and CS particles were determined as the best support with photophysical properties similar to

that of pure RB. Similar quantum yield of $^1O_2$ production and protection from photobleaching was obtained with CS as the one found in the literature[170,178] but with less anchored RB meaning that our system could further be improved by varying the content of the photocatalyst without working all the time at maximal loading. This could be beneficial to limit the auto-quenching process that can happen at the solid support surface. Nevertheless, Martins Estevão *et al.* did not conduct recycling runs and no information about leaching is found in their report.[170] The possibility of double ion interaction between the support and RB increased even further the robustness of our methodology, which allowed organic dye immobilization without any modification to the active molecule.

The citronellol photooxidation was used as benchmark reaction to test the efficiency of the heterogenized photocatalysts. All immobilized photosensitizers were active and could be recycled at least 5 times. XPS analyses demonstrated the occurrence of a photobleaching on all supports (breaking of C–Cl and C–I bonds) but the activity was maintained. **RB@NS** and **RB@U** suffered from leaching explaining the decrease in photoactivity, reaching 65 and 53 % NMR yield in the fifth run, respectively. Moreover **RB@NS** showed a decrease in nitrogen content *via* CHN analysis, indicating that some ammoniums moieties were also lost, due to the non-porous nature of this support and the presence of functional groups at the external surface rendering them more fragile. The best results were obtained with **RB@CS**, in which case the leaching was moderate thanks to limited π–π stacking multi-layer interactions, giving an average 90 % NMR yield throughout the five runs. Our system is more efficient than the one developed by Terra *et al.* (covalent amide linker used in their work) for which a drastic decrease in photoactivity was observed at the second recycling run when using nanospheres that do not limit the photobleaching.[173]

In conclusion, there is a clear influence of the architecture of silica nanoparticles onto the production of singlet oxygen by immobilized RB. The Core-Shell morphology seemed to be the best choice in terms of photophysical properties, activity and recycling of the surface-bound molecule. Although some photobleaching was detected at the surface for this material, we could hypothesize that the porous structure acts as a shield and protects RB in the pores explaining its high photoactivity along the five runs.

5. Experimental section

5.1. Chemicals and materials

Toluene was distilled on MBraun MBSPS5 device before use. Ethanol (99 % V/V euro denaturated with 1 % of isopropanol, VWR), acetone (> 98 %, VWR), acetonitrile (HPLC-water content below 30 ppm, VWR), tetraethylorthosilicate (TEOS, ≥ 99 %, Sigma-Aldrich), ammonium hydroxide ($NH_4.OH$, 25 % solution in water, Acros Organics), hexadecyltrimethylammonium bromide (CTAB, ≥ 99 %, Sigma-Aldrich), urchins nanoparticles (Strem, catalog reference: 14-6310), 3-(*N*,*N*-Dimethylamino)propyl]trimethoxysilane (DAPTMS, > 96 %, TCI, kept safe from air and moisture), methyl triflate ($CF_3SO_3CH_3$, 97 %, Alfa Aesar), Rose Bengal (RB, 85 %, Acros Organics, kept under dark), citronellol (> 95 %, Sigma-Aldrich), triphenylphosphine (PPh_3, 99 %, Fluorochem) and dimethylsulfone (DMS, 99 %, Alfa Aesar) were used as received. Photocatalytic tests were performed using 513 nm green LEDs strips purchased from HUBO stores.

5.2. Characterization methods

Nuclear Magnetic Resonance (NMR). NMR spectra were recorded on BRUKER spectrometers (300 MHz for ^1H). Chemical shifts are reported in δ ppm relative to the residual solvent peak for $CDCl_3$ (δ = 7.26 ppm).

X-Ray Photoelectron Spectroscopy (XPS). XPS analyses were carried out at room temperature with a SSI X-probe (SSX 100/206) photoelectron spectrometer (55° angle) from Surface Science Instruments (USA) equipped with a monochromatized microfocus Al X-ray source. Samples were stuck onto small sample holders with double-face adhesive tape and then placed on an insulating home-made ceramic carousel (Macor®, Switzerland). Charge effects were avoided by placing a nickel grid above the samples and using a flood gun set at 8 eV. The binding energies were calculated with respect to the Si_{2p} peak fixed at 103.5 eV. Data treatment was performed with the CasaXPS program (Casa Software Ltd., UK). The peaks were decomposed into a sum of Gaussian/Lorentzian (85/15) after subtraction of a Shirley type baseline. The XPS analyses were performed only once for each sample which prevent to assess the experimental error that can be quite important for several elements. Indeed, the peak selection is performed by the experimenter and can cause large variations in the peak area measured for smaller peak sizes. Elements with a low photoelectron cross-section, such as nitrogen, are particularly susceptible to errors. For most elements with moderate to strong photoelectron cross-sections, precision may vary by only a few tenths of a percent which is considered as a minor amount only if the element is mostly present at the surface (10 – 100 at%) but becomes a larger error as the element amount decreases.[285]

UV-vis. UV-vis absorption spectra were recorded on a Shimadzu UV-1700 instrument using 1 cm large cuvettes in quartz.

Thermogravimetric Analysis (TGA). Thermograms were recorded on a TGA/SDTA 851e simultaneous DSC-TGA instrument from METTLER TOLEDO. These analyses were carried out with a heating ramp of 10 °C min^{-1} and under air flow (100 ml min^{-1}) with the samples (3 – 20 mg) placed into alumina containers.

Transmission Electron Microscopy (TEM). TEM images were obtained with a LEO 922 OMEGA energy filter transmission electron microscope. The powder samples were suspended in ethanol under ultrasonic treatment, then a few drops of the supernatant were deposited on a holey carbon film supported on a copper grid (Protochips, 1.2 micron hole diameter, 1.3 micron hole spacing, 200 mesh copper grid), which was dried for a few hours under vacuum at room temperature before analysis.

Elemental analysis. CHN analyses were carried out on a FlashSmart device from Thermo Scientific. The reactor temperature was set at 950 °C and the one from GC oven at 65 °C. The gas flows for vector and reference He and O_2 were 140, 100 and 250 mL min^{-1}, respectively. A packed column CHNS/NCS (PTFE, 2 m, 6X5 mm) was used with a katharometer as a detector. 1-2 mg of each samples were precisely weighed and put in a tin cupule. The quantification was based on a calibration curve (4 points).

Fourier-Transformed Infrared-Attenuated Total Reflectance spectroscopy. FTIR-ATR spectra were recorded on Perkin Elmer Spectrum Two-UATR Two by depositing the powder onto the diamond equipped with a mechanical press. The bands are reported in cm^{-1} and the following abbreviations have been used: br (broad), s (strong), m (medium), w (weak).

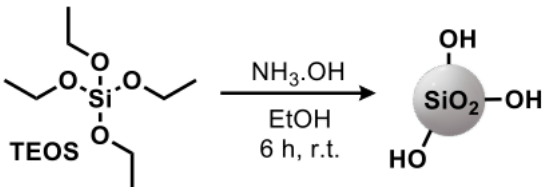
Centrifuge. A Biofuge Stratos Heraeus Instrument was used as centrifuge. 50 ml in polypropylene (PP) tubes were purchased from VWR (525-1098).

Nitrogen physisorption. The specific surface areas were measured by nitrogen adsorption-desorption isotherms. The measurements were achieved using a Micromeritics ASAP 2020 analyser at -196 °C. Before analysis, the samples (~ 200 mg) were degassed for 2 h at 200 °C with a heating ramp of 10 °C min^{-1} under 0.133 Pa pressure. The analysis of the isotherms provided

specific surface areas calculated with the Brunauer-Emmett-Teller (BET) equation.

5.3. Experimental protocols

Silica nanospheres – NS (40 nm).[220]



150 mL of ethanol (99.9 % denaturated) were introduced in a 500 mL Erlenmeyer. Under vigorous stirring, 6 mL of $NH_4.OH$ were added quickly. The reaction mixture was stirred for 5 min at room temperature. Then, 10 mL of tetraethylorthosilicate (TEOS) were added dropwise with a syringe pump at a rate of 59 mL $hour^{-1}$. The solution was left under stirring for 6 hours at room temperature. The silica nanoparticles were recovered by centrifugation (9.500 rpm for 40 min) and washed with ethanol several times. The nanoparticles were dried in the oven at 100 °C overnight subsequently grinded to obtain a fine white/beige powder.

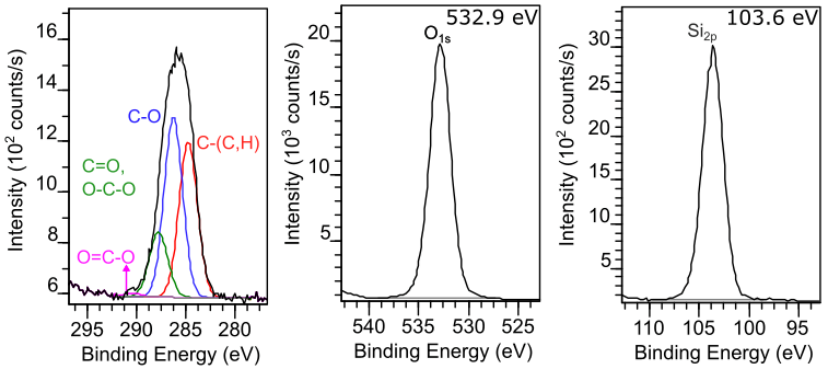


Figure 3.11. XPS spectra of pristine NS NPs: C_{1s}, O_{1s} and Si_{2p} peaks with the corresponding energy binding.

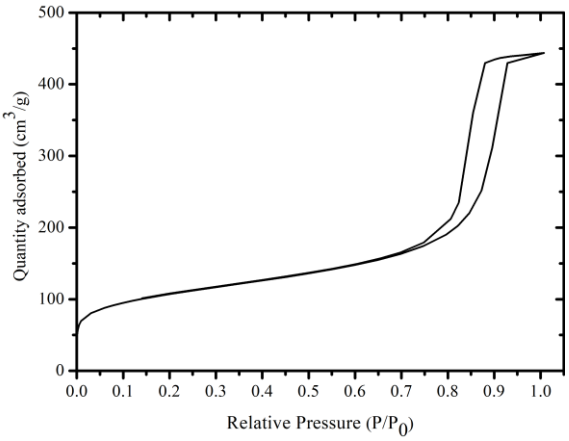
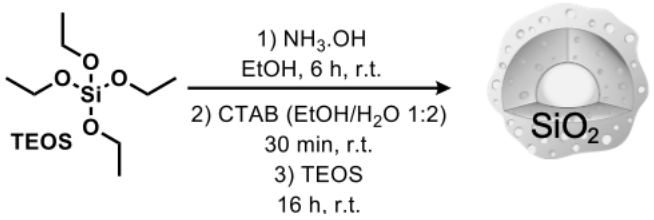


Figure 3.12. N_2 adsorption-desorption isotherms at 77 K of silica NS NPs.

Core-Shell nanoparticles – CS (50 nm).[221]



150 mL of ethanol (99.9 % denaturated) were introduced in a 500 mL Erlenmeyer. Under vigorous stirring, 6 mL of NH_4.OH were added quickly. The reaction mixture was stirred for 5 min at room temperature. Then, 10 mL of tetraethylorthosilicate (TEOS) were added dropwise with a syringe pump at a rate of 59 mL hour^{-1}. The solution was left under stirring for 6 hours at room temperature. 380 mL of Milli-Q water and 30 mL of a hexadecyltrimethylammonium bromide (CTAB) solution (1.2 g of CTAB dissolved in 20 mL H_2O/10 ml EtOH) were added at once and the solution was left under stirring for 30 min. 2.15 mL of TEOS were added with a rate of 59 mL hour^{-1} and the mixture was stirred overnight (200 rpm). The silica nanoparticles were recovered by centrifugation (6000 rpm for 50 min) subsequently dried in the oven at 100 °C. Finally, the inorganic oxide was calcinated by heating at 500 °C for 5 hours at rate of 10 °C min^{-1} (3 g of silica nanoparticles were recovered).

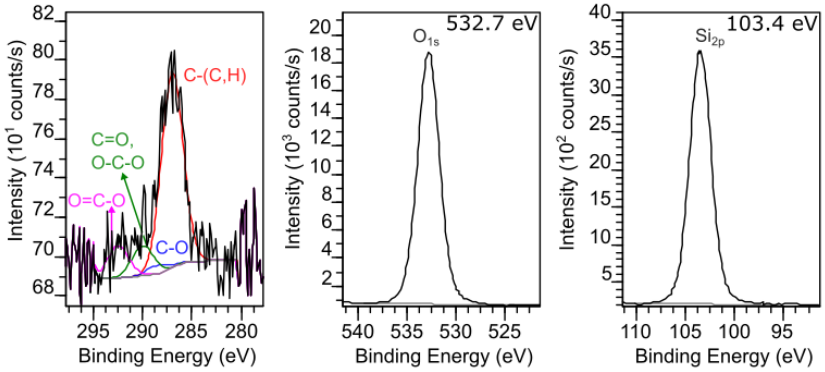


Figure 3.13. XPS spectra of pristine CS NPs: C_{1s}, O_{1s} and Si_{2p} peaks with the corresponding energy binding.

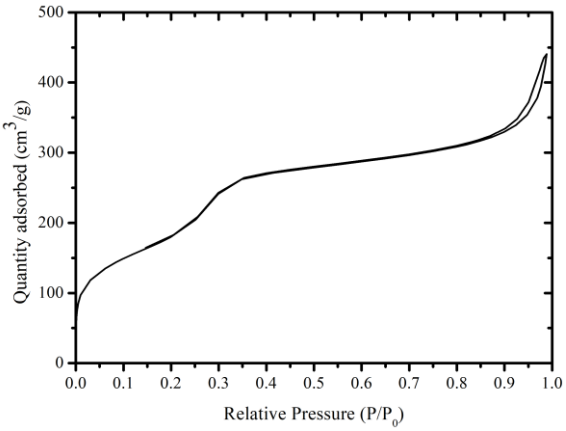
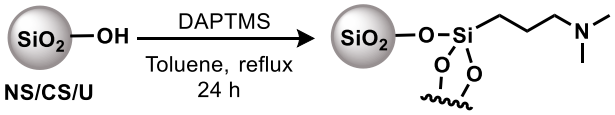


Figure 3.14. N_2 adsorption-desorption isotherms at 77 K of silica CS NPs.

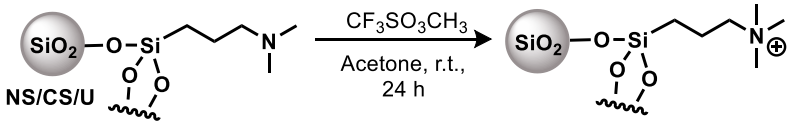
Amine anchoring.[217]



Nanospheres, Core-Shell, and Urchins silica nanoparticles were functionalized with the same protocol. 100 mg of silica nanoparticles were added in a 25 mL flame-dried round-bottom flask and 3 cycles vacuum/argon were applied. 10 mL of dry toluene was added and the resulting suspension was sonicated for 15 min at power 3 on a VWR ultrasonic bath. [3-(*N*,*N*-Dimethylamino)propyl]trimethoxysilane (DAPTMS) (0.5 eq., 0.83 mmol,

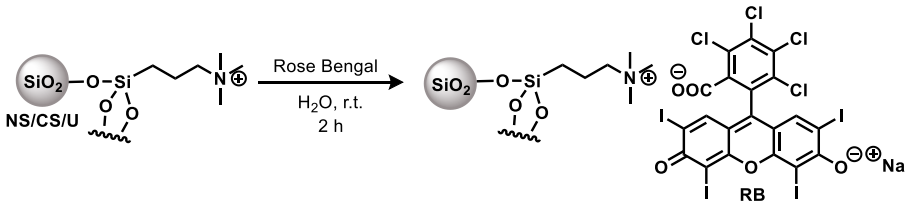
184.2 mg, 0.19 mL) was added dropwise and the suspension was refluxed at 120 °C for 24 h. Filtration on a PVDF Millipore Membrane (0.1 µm) allowed the recovery of the solid. The white/beige powder was washed with 3X100 mL of ethanol.

Ammonium functionalization.[284]



100 mg of NMe_2-functionalized silica nanoparticles were inserted into a 25 mL flame-dried round bottom flask and 3 cycles vacuum/argon were applied. 10 mL of acetone were injected by syringe through a septum and the resulting suspension was sonicated for 15 min at power 3 on a VWR ultrasonic bath. $CF_3SO_3CH_3$ (5 eq. with regard to the number of amine functions estimated by TGA in 100 mg of NMe_2-silica nanoparticles) was added dropwise and the suspension was stirred at room temperature for 24 h during which a yellow/orange coloration was observed. Filtration on a PVDF Millipore Membrane (0.1 µm) allowed the recovery of the solid. The white/beige powder was washed with 3X100 mL of acetone.

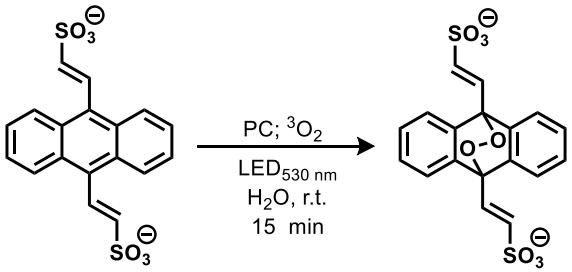
Rose Bengal immobilization.



100 mg of NMe_3^+-functionalized silica nanoparticles were dispersed in 40 mL of Milli-Q water. Different tests of immobilization were conducted on each nanostructure to find the maximal amount of RB that the materials can immobilize (amount from which a pink filtrate was recovered meaning that an excess of RB was introduced). These amounts vary, depending on the specific surface area of the materials. We could determine that 15, 25 or 20 mg of RB

(for NS, CS and U, respectively) were necessary and added to the dispersed silica nanoparticles. The dark pink mixture was stirred for 2 h at room temperature before being cooled to 0 °C. The solid was recovered by filtration on a PVDF Millipore Membrane (0.1 μm) and washed with cold DCM (2X50 mL). The solid was dried under vacuum overnight before being analyzed by TGA, elemental analysis, FTIR, UV-vis and XPS.

Singlet oxygen quantum yield.[293]



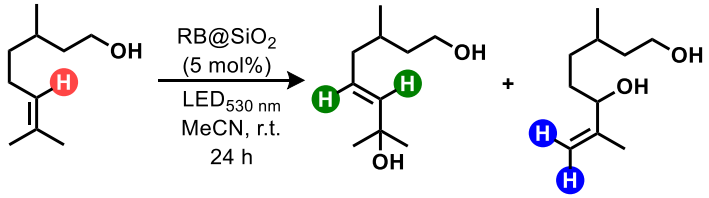
Determined for **RB@NS**, **RB@CS** and **RB@U** in water by monitoring the decomposition of a $^1O_2$ trap (AVS = Anthracene-9,10-divinylsulfonate) on a time range extending from 0 to 15 minutes. Practically, a O_2 balloon was bubbled in the cuvette for 15 minutes containing AVS (Absorbance = ~ 1 at 397 nm) and the photosensitizer (Absorbance = ~ 0.05 at 530 nm). The cuvette was irradiated at 530 nm and at regular intervals, an absorption spectrum was taken. The decomposition of AVS was then determined by analyzing the absorption decay of AVS at 397 nm. This protocol was repeated three times for each heterogenized material. The reference used was pure RB for which a singlet oxygen quantum yield of 0.76 in water is known [170]. Singlet oxygen quantum yields were determined based on the following equation:

$$\phi_{sam} = \phi_{ref}*[(m_{sam}/m_{ref})*(L_{ref}/L_{sam})]$$

where ϕ_{sam} and ϕ_{ref} are $^1O_2$ quantum yields of RB@SiO_2 heterogenized photocatalysts and RB, respectively, m_{sam} and m_{ref} are slopes in the plots of ΔA at the photoabsorption maximum wavelength of AVS (397 nm) against photoirradiation time, and L_{sam} and L_{ref} are light harvesting efficiencies, which

are given by L = 1-10^{-A} ("A" is the absorbance at the photoirradiation wavelength).

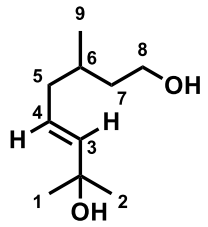
Citronellol photooxidation.[270]



The quantity of RB needed for the reaction equals 4.9 mg to 5 mol%. The quantities of solid materials to introduce in the medium were determined by considering the loadings determined by TGA for each material: 4.9/0.13 = 38 mg for **RB@NS**, 4.9/0.19 = 26 mg for **RB@CS** and 4.9/0.16 = 30 mg for **RB@U** (the partial degradation of RB was not taken into account). The heterogenized photocatalyst was added in a 50 mL round-bottom flask, followed by 20 mL of MeCN. The resulting suspension was sonicated for 15 min at power 3 on a VWR ultrasonic bath. Citronellol (0.1 mmol, 1 eq., 15 mg, 18 µl) was added and O_2 was bubbled in the mixture. The medium was stirred and illuminated with green LEDs for 24 h. PPh_3 (0.12 mmol, 1.2 eq., 30.2 mg) was added and the mixture was stirred for 5 min. The solvent was evaporated under high vacuum, DCM was added and the medium was cooled to 0 °C for 15 min. Filtration on a PVDF Millipore Membrane (0.1 µm) allowed the recovery of the solid. The pink powder was washed with 3X25 mL of DCM. The resulting powder was finally dried under vacuum. The filtrate was recovered and the solvent was evaporated. Dimethylsulfoxide (DMS) was added to allow quantitative NMR analysis.

The recycling runs were conducted as explained above, except that for each run, the recovered materials were weighted again to ensure the same quantity of photocatalyst and if not, this quantity was corrected by adding materials from after the first run (but not fresh heterogenized photocatalyst as

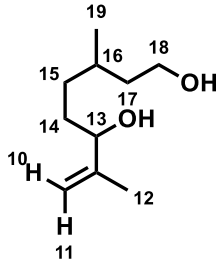
this would too strongly influence the results). The added amount was never more than 10 % of the total. This has been only necessary for run 3.



CAS: /

Formula: $C_{10}H_{20}O_2$

Molecular weight: 172.27 g mol^{-1}

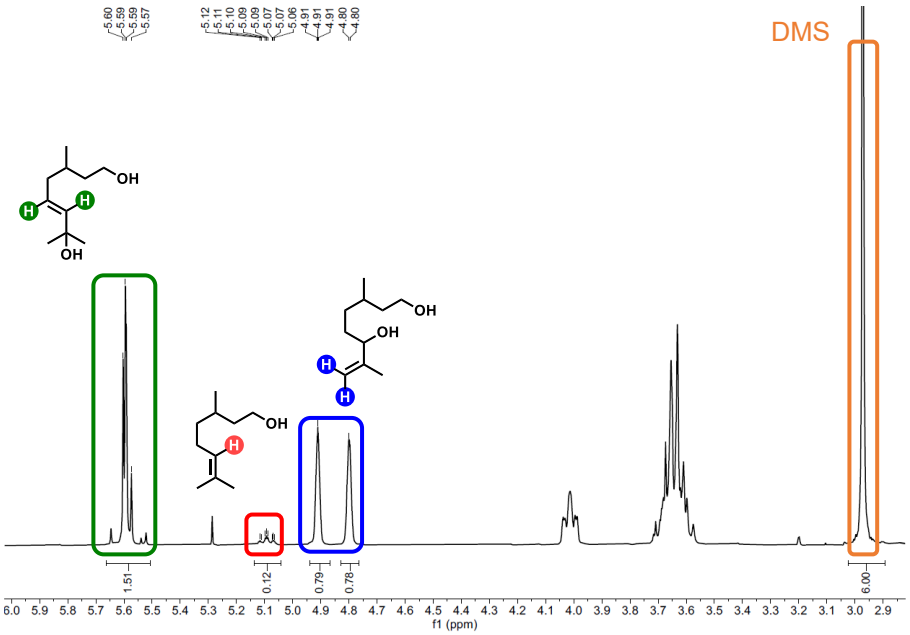


CAS: /

Formula: $C_{10}H_{20}O_2$

Molecular weight: 172.27 g mol^{-1}

^{1}H NMR (300 MHz, $CDCl_3$) δ 5.65 – 5.44 (m, 2H, H_3 and H_4), 4.89 (s, 1H, H_{10} or H_{11}), 4.78 (s, 1H, H_{10} or H_{11}), 3.99 (t, J = 6.4 Hz, 1H, H_{13}), 3.75 – 3.50 (m, 4H, H_8 and H_{18}), 2.39 (bs, 4H, OH), 2.04 – 1.82 (m, 2H), 1.68 (s, 3H), 1.61 – 1.51 (m, 6H), 1.41 – 1.31 (m, 4H), 1.28 (s, 6H), 0.87 (d, J = 2.3 Hz, 3H), 0.84 (d, J = 1.0 Hz, 3H).

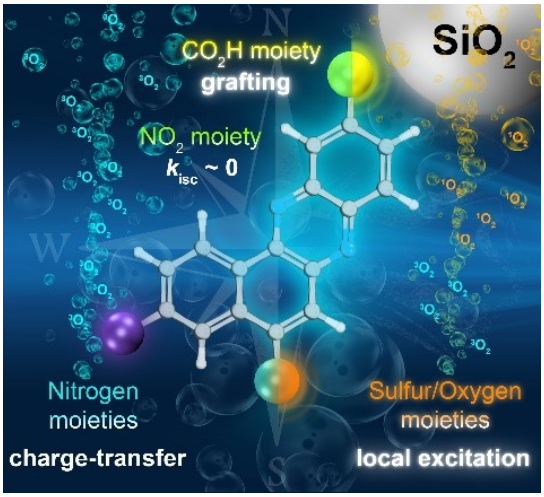


Scheme 3.5. Quantitative NMR spectrum of a filtrate after photooxidation of citronellol using heterogenized **RB@CS** (third run).

Chapter 4

Structure-activity relationship investigation of new benzophenazine derivatives as homogeneous and heterogenized photooxygenation catalyst

N. Body, C. Lefebvre, S. Eeckhout, A.-S. Léonard, L. Troian-Gautier, S. Hermans, O. Riant, *in preparation.*



Author statement

Nathalie Body was the principal investigator of this research project. She designed the methodology and performed the investigation and analyses. She supervised the experimental work of S. Eeckhout and A.-S. Léonard. She also wrote the original draft of this publication. **Corentin Lefebvre** performed the theoretical calculations and their interpretation. He also participated partly in the writing of the experimental results in the publication. **Sarah Eeckhout** and **Anne-Sophie Léonard** performed some of the investigation and analyses. **Ludovic Troian-Gautier** participated in the design of the methodology. He realized with the principal investigator the steady-state and time-resolved photoluminescence experiments and helped in the results interpretation. This research project was realized under the supervision of **Sophie Hermans** and **Olivier Riant** who conceptualized the project, designed the methodology, validated the results and reviewed and edited the publication.

1. Abstract

Singlet oxygen is a valuable oxidant in various domains, such as organic synthesis, medicine, and environmental remediation. Photosensitizers are commonly used to generate this reactive species by exchanging energy with triplet oxygen. We describe here new benzophenazine derivatives as a promising class of photosensitizers due to their facile synthesis and versatile derivatization that enables to span a range of photophysical properties. In this study, we investigated their structure-activity relationship in order to be able to immobilize them onto a solid support while maintaining their photophysical properties. To do so, firstly, the southern fragment was functionalized with either aromatic or alkyl tertiary amines, aromatic and alkyl sulfur groups, or cyclic ethers. Enhanced triplet lifetime, absorption wavelength, triplet state energy or $^1O_2$ production quantum yield were obtained with cyclic ether and sulfur groups. Conversely, the presence of an amine moiety was detrimental for the PCs. The western and northern fragments were then investigated and slightly negative or negligible changes in photophysical properties, respectively, were observed, in most cases. In consequence, it can be concluded that the southern fragment of the molecules influences the most the behavior of the PCs. Among the functional groups investigated for that part, the cyclic ether one exhibiting interesting photophysical properties along with the best photostability was selected to conduct photosensitization experiments in heterogeneous phase, by immobilizing it on silica nanoparticles. We have successfully synthesized a covalent linker by reacting amino groups at the surface of the support with an activated ester on the northern fragment of the PC. The resulting heterogeneous system has been evaluated for its photoactivity in the citronellol photooxidation reaction. A high yield in desired product was obtained, with only a slight decrease over recycling runs. These results provide insights into the design of efficient photosensitizers for singlet oxygen generation, and the development of heterogeneous systems.

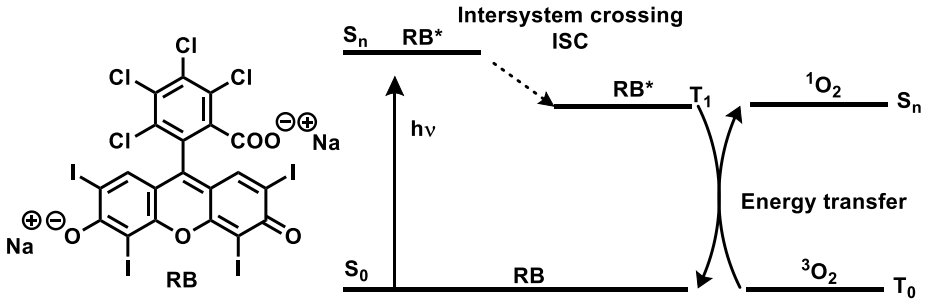
2. Introduction

Dioxygen (O_2) molecules participate actively in the Earth's atmosphere chemistry and in diverse chemical reactions and biological processes.[297] Indeed, natural occurring triplet dioxygen is necessary for the anabolism of aerobic living beings whereas by contrast other reactive oxygen species are involved in cells damage leading to organism aging and the development of cancers.[298,299] Reactive oxygen species (ROS) are photogenerated according to two mechanisms. The type I mechanism involves hydrogen-atom abstraction or electron-transfer between an excited photosensitizer PS* (9,10-dicyanoanthracene (DCA) for example) and a substrate (electron rich alkenes), yielding free radicals that react with oxygen to produce ROS, such as the superoxide radical anion. In the type II mechanism, an energy transfer happens between an excited photosensitizer and triplet oxygen forming singlet oxygen.[142,299]

Singlet oxygen ($^1O_2$) is a powerful reactant with many applications in the environmental domain where it can be used in water disinfection[300–302] or pollutant degradations,[303–305] in medicine with photodynamic therapy[306–313] and bacterial disinfection[314–316] or even in organic synthesis such as in photooxidations.[151,317,318] Such oxidations are applied at industrial scale for the production of rose oxide developed by Symrise company[147] or the photooxygenation of dihydroartemisinic acid in the synthesis of artemisinin investigated by Sanofi.[149]

Singlet oxygen can be easily photosynthesized, according to a type II mechanism, using photosensitizers which, by absorption of light, are excited to their singlet state S_1. Thanks to an efficient intersystem crossing (ISC), a triplet state T_1 is generated allowing an energy transfer with fundamental state triplet oxygen: the photosensitizer is therefore regenerated in its fundamental singlet state S_0 and the oxygen is excited, forming singlet oxygen (**Scheme 4.1**).[147] Diverse (metal-)organic photosensitizers have shown singlet oxygen

generating ability. Transition metal complexes based on ruthenium[156–158,319,320], iridium[159–162] or even copper[88,89,163] centers are potential candidates but the use of organic dyes is predominant. Among them, xanthenes (Rose Bengal (RB)[170,172,321–324], eosin Y[325–327]), phenothiazines (methylene blue)[148,328–331], tetrapyrroles (porphyrins, phtalocyanines, chlorins, bacteriochlorins…)[332–336], (aza)-boron-dipyrromethene ((aza)-BODIPY)[337–341] or (benzo)phenazine families[293,342–345] of compounds are identified as effective and known photosensitizers.



Scheme 4.1. Schematic representation of $^1O_2$ photoproduction using Rose Bengal as photocatalyst according to a type II mechanism.

Although organic dyes demonstrate a great potential to photogenerate singlet oxygen used for various purposes, these photocatalysts suffer mainly from a low photostability due to photobleaching that may be fast, an agglomeration tendency leading to self-quenching and a harsh elimination at the end of a reaction.[146,164] Intense researches have proved that immobilizing such photocatalysts onto a solid support allows to circumvent or diminish those drawbacks while maintaining a high efficiency, even obtaining an increased one, in generating singlet oxygen. Additionally, the use of immobilized PC allows the recovery and the reuse of the PC that has obvious environmental and economic positive impacts. An easy separation of the reaction products from the catalyst facilitates the work-up and a flexibility in terms of reaction conditions leads to the use of various solvents.[142]

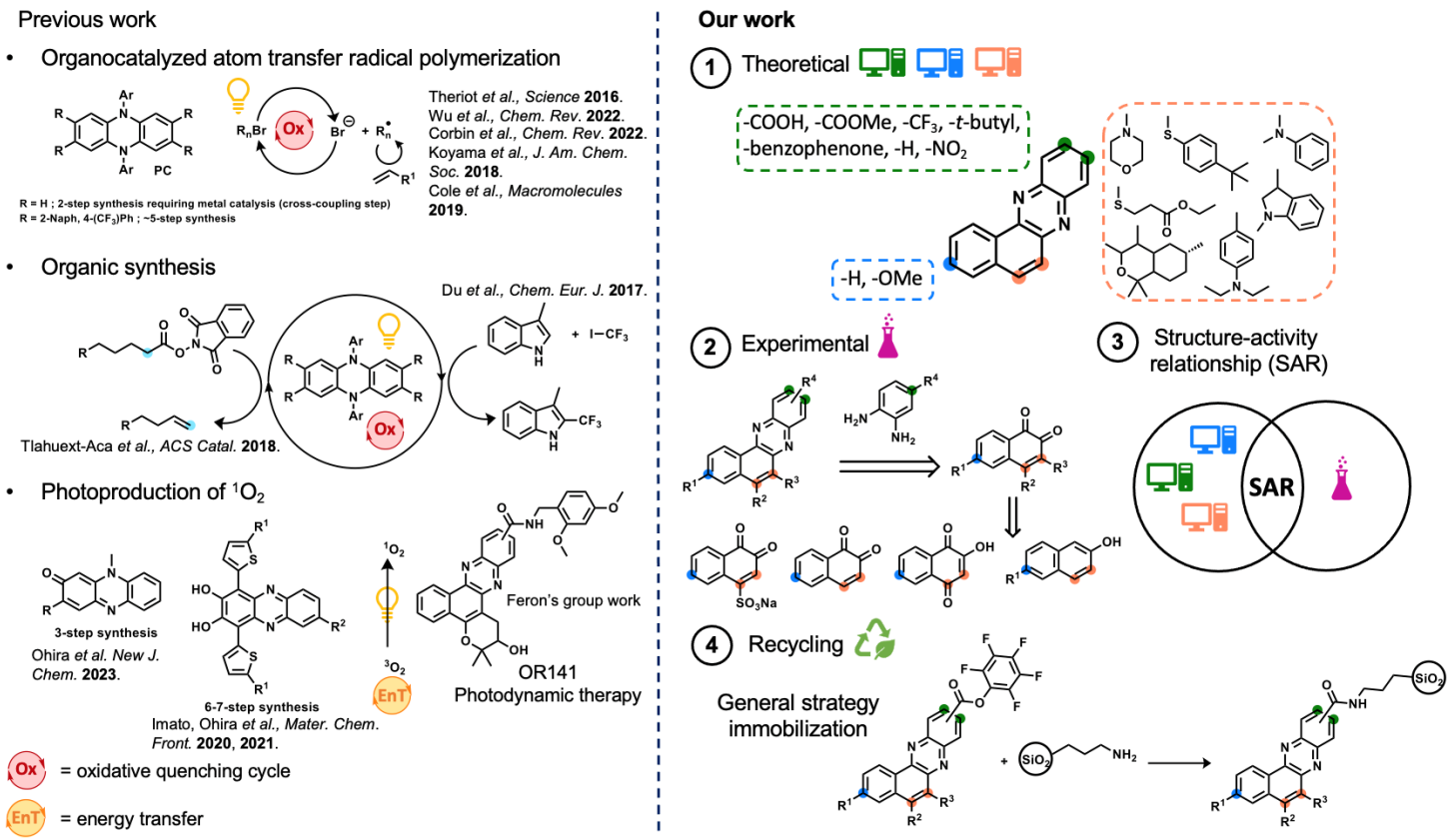
Silica nanoparticles represent one of the best supports for photocatalysts immobilization since this cheap inorganic oxide possesses i) a high specific surface area which can be tuned by the porosity parameters,[213] ii) an easy surface functionalization[214,216–218,346], iii) a transparency over a broad range of wavelengths[219] and iv) a high mechanical and (photo)stability.[213] In the generation of singlet oxygen, Rose Bengal was immobilized covalently or non-covalently onto silica nanoparticles which acted as a shield to prevent the photobleaching thus increasing the photostability of RB and allowing its recyclability.[170,173,176,275,347] Methylene blue (MB) is another dye that has been immobilized onto silica nanoparticles leading to higher photostability in heterogeneous conditions.[148,348] Zinc phthalocyanines suffer from severe aggregation in aqueous medium thereby losing their singlet oxygen generation efficiency. By loading such PC into the modified mesopores of silica nanoparticles, the phthalocyanines could generate singlet oxygen efficiently.[349] This immobilization strategy to increase the potential of organic dyes has been successfully reported in the literature for many other photosensitizers concerning singlet oxygen production[142,146,168,197] used in organic synthesis[148,173,323,347] or in medicinal applications.[276,321,331]

Nevertheless, the strong immobilization of an organic dye *via* a covalent linker is not trivial to achieve as it usually requires its derivatization that may alter its photophysical properties and/or excited state and thus, its photoreactivity and/or performances. To the best of our knowledge, the investigation of the impact of the functionalization of the molecular skeleton of a dye onto its fundamental and excited state properties in order to immobilize the PC without impacting its properties has been non-existent. By displaying various positions prone to simple functionalization, (benzo)phenazines are an interesting motif to consider for such structure-activity establishment, besides being easily synthesized in a few steps or in one-pot from available and affordable starting materials.[350–353] Only investigations in homogeneous phase to find the best photophysical properties

to generate singlet oxygen has been conducted with (benzo)phenazines. Ohira, Imato and coworkers developed several derivatives of phenazines to increase their efficiency in producing singlet oxygen.[293,343,345] In 2015, Tathe and Sekar also synthesized benzophenazine derivatives to study the effect of functionalization onto their absorption and emission in different solvents.[354] Surprisingly, such simple dye has not been yet investigated much for O_2 photosensitization applied in organic synthesis. So far, biological applications, such as photodynamic therapy, have been mainly targeted as highlighted by **OR141** photocatalyst which has been developed in our laboratory.[311,342,355–359]

In this work, we have synthesized a series of benzo[*a*]phenazines for the production of singlet oxygen and their use in organic synthesis, ultimately in heterogeneous phase. Our methodology relies on the synthesis of various benzo[*a*]phenazine derivatives targeting the functionalization of three key fragments of the molecular backbone: the northern, the southern and the western parts (**Scheme 4.2**). By introducing relevant moieties at different positions, we have first computationally investigated the structure-activity relationship (SAR) of the benzo[*a*]phenazines and have identified which fragment influences the most the fundamental and excited states and which kind of functionalization strategy ensures the best photophysical properties for the production of singlet oxygen. The influence of the nature of the functionalization (electron-withdrawing or attractive groups) was also investigated in order to identify if derivatization for immobilization could impact the photocatalyst. These results were confirmed with experimental results in homogeneous phase photocatalysis, *i.e.* citronellol photooxidation chosen as simple and fast proof-of-concept reaction used at an industrial scale for the production of rose oxide. Then, we have considered to extend our methodology towards the heterogenization of benzophenazines on silica nanoparticles. The fragment of the molecular backbone identified theoretically and experimentally as the one impacting the less the fundamental

and excited states was used to synthesize the linker between the photoactive species and the support. Such investigation of a structure-activity relationship in order to maintain the photophysical properties upon photocatalyst heterogenization is totally innovative. Once grafted on a solid support, the immobilized PC was again tested in the same reaction and the possibility of recycling was investigated.

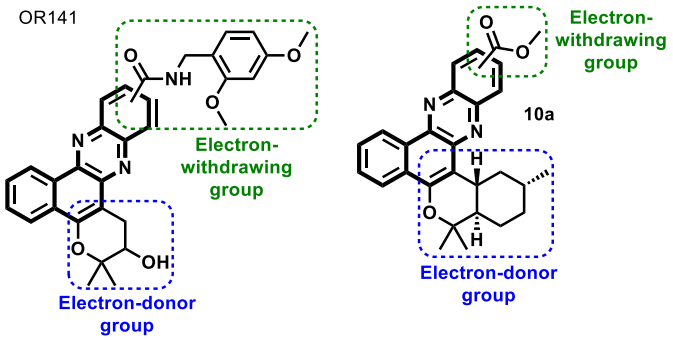


Scheme 4.2. State of the art of (benzo)phenazine derivatizations for singlet oxygen applications and strategy of this work.

3. Results and discussion

3.1. Cyclic ether case

Based on our envisaged methodology, a first benzo[*a*]phenazine derivative (cyclic ether **10a**) was targeted. Such motif was already known and investigated for biological applications as stated in recent publications[360–362] making its synthesis optimized and straightforward in a very few steps.[353] The first step of synthesis consisted in the combination of lawsone and *R*-citronellal allowing the introduction of a pyrane moiety on the southern fragment of the benzophenazine. From this reaction, a 1,2-benzoquinone (product of interest) and a 1,4-benzoquinone were produced in a 1:1 ratio, which were separated by silica-gel chromatography purification (see SI – Annex B).[360] The second and final step for our starting organic chromophore's synthesis consisted in condensing the synthesized methyl 3,4-diaminobenzoate with 1,2-benzoquinone to form the benzophenazine structure and insert an ester function on the northern fragment of the molecular skeleton which should be extremely useful for future photocatalyst immobilization (**Scheme 4.3**).[354] This first benzophenazine structure was envisaged as a close structure compared to efficient **OR141** photosensitizer.[342,355–357]



Scheme 4.3. Structures of **OR141** and cyclic ether **10a** presenting a benzo[*a*]phenazine core.

The photophysical properties of this new chromophore were investigated by UV-vis spectroscopy and steady-state photoluminescence. An absorption in the blue region of the visible-light spectrum (427 nm, ε = 7840 M^{-1} cm^{-1}) and an emission at around 516 nm were observed (**Figure 4.1**).

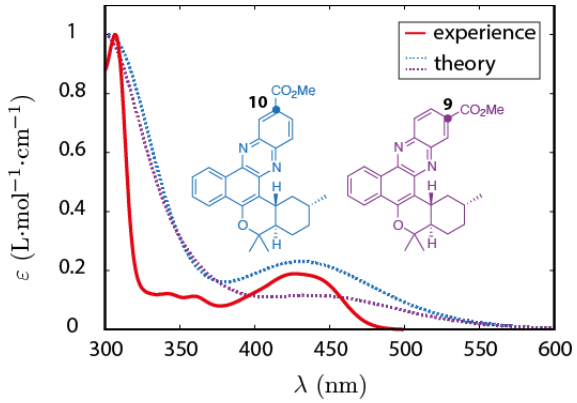
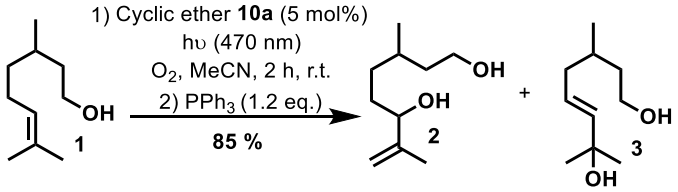


Figure 4.1. Comparison between the experimental (both regioisomers together) and the theoretical UV-visible absorption spectra of regioisomers of cyclic ether **10a**: influence of the position of the –CO_2Me functional group on the first monoelectronic excitation $S_0 \rightarrow S_1$.

It should be noted that during the condensation step, two regioisomers were produced, as positions 9 and 10 of the benzophenazine structure can hold the carboxylate group (identified by * in following schemes). These regioisomers are difficult to separate or are even inseparable in most cases. This is not a problem as the absorption and emission properties are expected to be similar. Previous work in our group investigated their separation and these regioisomers exhibited the same absorption wavelength while the excited state displayed a difference in energy of 0.03 eV based on fluorescence spectra which can be negligible. Tathe and Sekar, who synthesized benzophenazines using the same methodology than the one used in this work, did not separate the isomers neither and the photophysical properties were investigated with both regioisomers.[354] Furthermore, the negligible impact of the carboxylate function position was observed with theoretical experiments (*vide infra*).

To evaluate the ability of this dye to produce singlet oxygen, the photooxidation of citronellol was used as a benchmark reaction (**Scheme 4.4**). Performing this reaction in the presence of cyclic ether **10a** afforded the corresponding diols **2** and **3** (in a 1:1 ratio) with a 85 % NMR yield identifying cyclic ether **10a** as an efficient producer of singlet oxygen. In order to understand how this process can be influenced, the characteristics of its excited state have then been investigated.



Scheme 4.4. Photooxidation of citronellol used as benchmark reaction for assessing the photoactivity of the synthesized photosensitizers.

For this purpose, the first monoelectronic excitations $S_0 \rightarrow S_n$ (n = 100) have been calculated *via* time dependent DFT with the hybrid generalized gradient approximation functional mPWPW91 recommended for organic molecules[363] and selected *via* a benchmark (see SI – Annex B for details). The triple-ζ Alhrichs basis set Def2-TZVP[364] has been employed with implicit solvation (solvation model based on density (SMD), acetonitrile ($\epsilon = 35.688\ \mathrm{F \cdot m^{-1}}$)) with the use of Gaussian 16 RevB.01.[365] The theoretical UV-visible spectrum of cyclic ether **10a** with the two possible positions of –CO_2Me group compared to the experimental one is represented in **Figure 4.1** with normalization. Interestingly, the position of this functional group has a marginal effect on the theoretical absorption value associated to the monoelectronic excitation $S_0 \rightarrow S_1$ with a slight difference of 0.05 eV, except its intensity is multiplied by 1.73 when the –CO_2Me is placed at the position 10.

This result then leads to consider only one of these positions, *i.e.* the position 10 in the following computational study. A slight difference of 0.06 eV between experience and theory has been detected for the lowest singlet

excited-state excitation, with an absorption centered around 427 nm and 431 nm for experience and theory, respectively. The nature of the first excited state of cyclic ether **10a** has been determined to be of local excitation type *via* the calculation of the charge transfer length D_{index} for which the value corresponds to 2.04 Å and the τ_{index} being negative (see SI – Annex B).[366] The former is characterized by a monoelectronic transfer from HOMO to LUMO of mainly $\pi \rightarrow \pi^*$ nature as depicted by a canonical molecular orbitals analysis performed with the NBO 7.0 software.[367] As a matter of fact, this analysis revealed a contribution of 37 % from the π(C(12)—C(13)) bond composing the HOMO and a 38 % contribution of the π^*(C(11)—N(15)) and π^*(C(14)—N(16)) natural bond orbitals (NBOs) constituting the LUMO, as shown in **Figure 4.2**. To be even more precise on the location of the orbitals involved in the electronic transitions, the localization of the electron and holes density would have been also interesting to determine computationally.

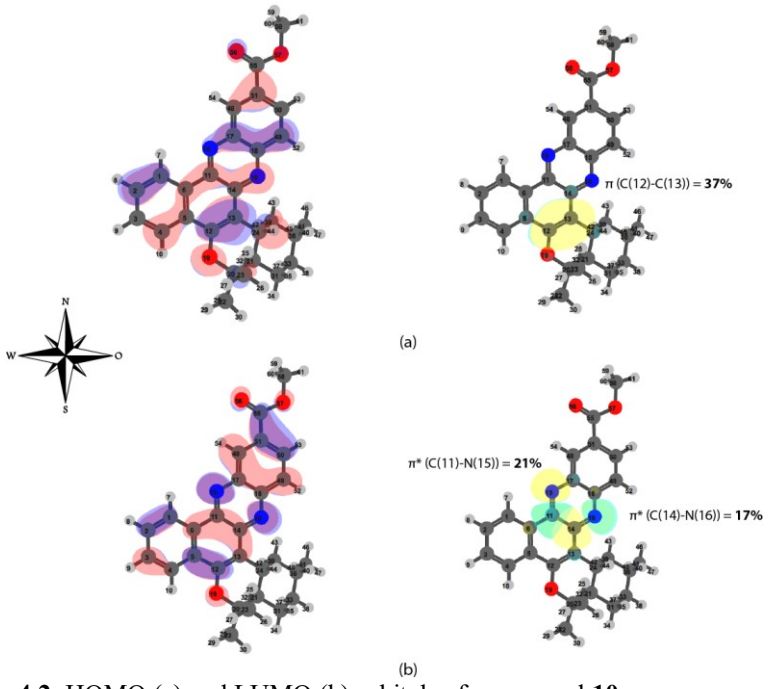
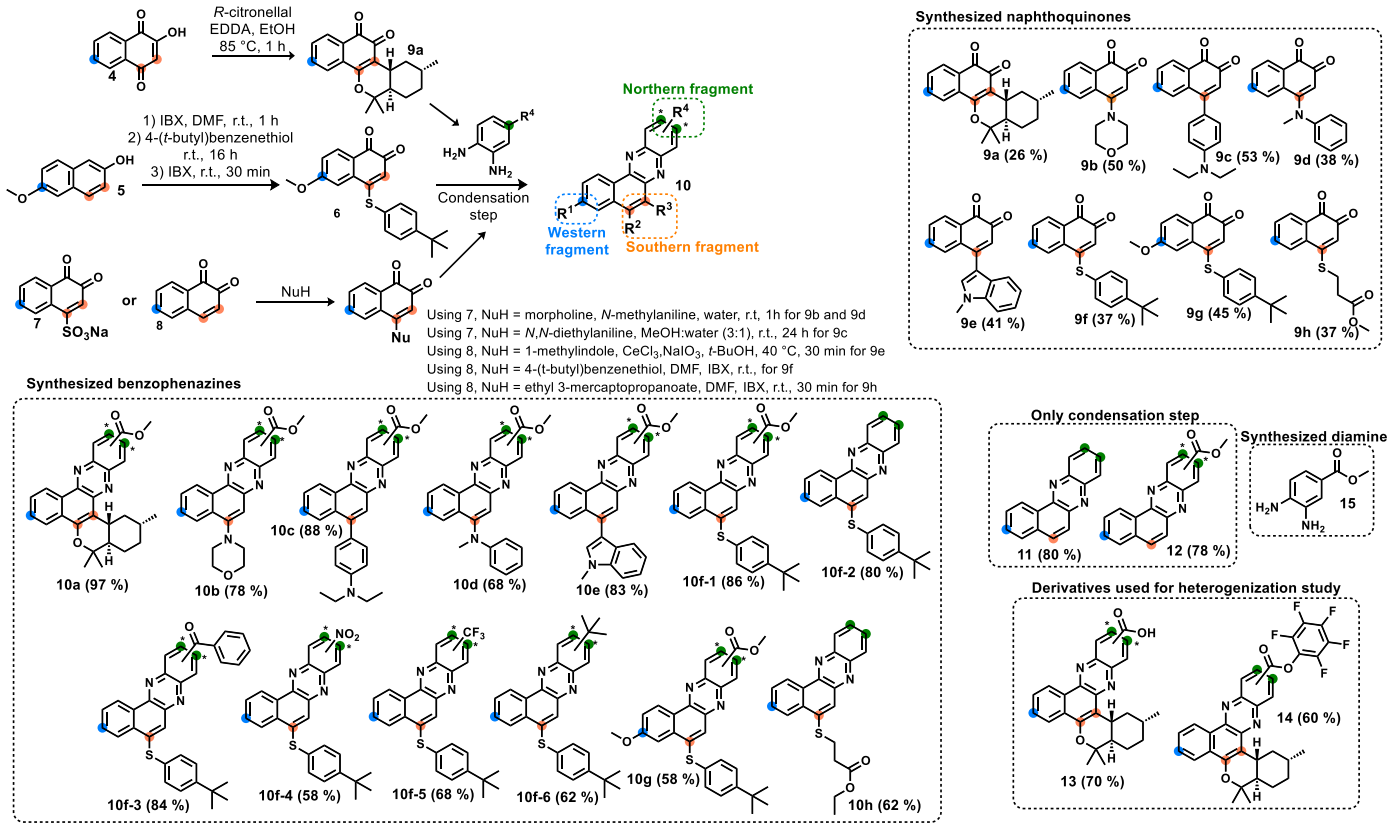


Figure 4.2. HOMO (a) and LUMO (b) orbitals of compound **10a** are represented on the left with positive (red) and negative (blue) orbitals along with their decomposition in their principal natural bond orbitals (NBOs) on the right.

The triplet energy of cyclic ether **10a** has been evaluated *via* the *Δ*SCF consisting in taking the energy difference between the optimized ground-state geometry and the optimized triplet one in acetonitrile. A value of 40.6 kcal mol^{-1} has been determined at 25 °C, justifying the observed successful triplet-triplet energy transfer with $^3O_2$ whose first singlet excited-state energy ($^1\Delta_g$) has been experimentally measured at 22.5 kcal mol^{-1} above its triplet ground state ($^3\Sigma_g^-$).[142] As a matter of fact, the Dexter energy transfer between the photosensitizer and $^3O_2$ is thermodynamically guided by the triplet energy of the chromophore. This last value can therefore be predicted prior to the synthesis of the envisaged benzophenazine derivatives. Indeed, the benzophenazine core is highly functionalizable in positions that can have an influence on the energy of the orbitals involved in the $S_0 \rightarrow S_1$ transition and thus, the absorption wavelength will be varied, in particular when the northern, southern and western fragments of the benzophenazine are modified (**Figure 4.2**), where the frontier orbitals are mainly located.

3.2. Computational prediction of the absorption wavelengths and the triplet energy of benzophenazine derivatives

A list of synthetically accessible benzophenazine derivatives has been considered towards the establishment of a SAR in order to identify the impact of such functionalization onto the fundamental and excited states of the photocatalysts. This SAR could also highlight the kind of moieties needed to optimize the required properties of a visible-light absorbing photosensitizer, *i.e.* an ability to absorb a low-energy photon while still having a high triplet energy excited state (**Scheme 4.5)**. Therefore, different functionalizations addressing the areas of interest of the benzophenazine core have been considered starting with the southern fragment.



Scheme 4.5. Naphthoquinone and benzophenazine structures envisaged and synthesized in this work to conduct the SAR study.

In comparison with the north-ester-functionalized benzophenazine **12**, the considered modifications trigger a bathochromic effect of the absorption wavelength associated with the $S_0 \rightarrow S_1$ transition (**Table 4.1**). This effect is particularly enhanced when using highly conjugated moieties notably in the cases of diethylaniline **10c** and indole **10e**, for which an absorption in the green region of the visible spectrum is predicted. This red-shift can be naturally explained by the nature of the monoelectronic transition. Like in the case of cyclic ether **10a**, the first singlet excited state is attributed to an electron transfer from the HOMO to the LUMO. The HOMO being mainly constituted of the π C–C bond on which the functionalization is carried out, the extension of the conjugation causes the decrease of the HOMO-LUMO gap resulting in a less energetic $S_0 \rightarrow S_1$ transition. However, the nature of the excitation has been identified to be a charge transfer type for diethylaniline **10c**, methylaniline **10d** and indole **10e** unlike cyclic ether **10a**, suggesting a different behavior of these derivatives at the excited state and particularly for the triplet energy transfer mechanism (**Table 4.1**). The functionalization on the southern fragment of the benzophenazine core leads also to a stabilization of the triplet excited state. It is noteworthy that this impact is relatively smaller in the case of morpholine **10b** and that all the derivatives are still predicted to thermodynamically favor the triplet energy transfer with $^3O_2$ in the light of this computed property.

Table 4.1. Influence of the functionalization of the benzophenazine core on the absorption wavelength associated to $S_0 \rightarrow S_1$ transition, the triplet energy and the nature of the monoelectronic excitation (level of theory: DFT(mPWPW91/Def2-TZVP) in acetonitrile).

Functionalized benzophenazines	**Computed absorption wavelength (nm)**	**Triplet energy ($kcal \cdot mol^{-1}$)**	**$S_0 \rightarrow S_1$ transition type**
12–10b–10f-1–10f-2–10f-3–10f-4–10f-5–10f-6–10g–10h	394–479–427–413–431–449–419–415–421–414	43.9–34.2–40.7–41.5–40.0–38.8–41.5–41.0–40.8–41.1	Local excitation, HOMO to LUMO ($\pi \rightarrow \pi^*$)
10c–10d–10e	567–464–502	33.6–36.7–36.2	Charge transfer, HOMO to LUMO ($\pi \rightarrow \pi^*$)

Consequently, the derivatives presenting a nitrogen atom on the southern part of the benzophenazine, except morpholine **10b**, are likely to be unsuitable for the photooxidation reaction due to the nature of the excitation, even though their absorption wavelength and their triplet energy are favorable for this kind of reaction. The north-ester benzophenazine **12** is also not appropriate because of its near UV absorption, despite its important triplet energy. The functionalization on the northern fragment of the benzophenazine has then been conducted with aromatic sulfur **10f-2**, one of the two derivatives exhibiting the highest triplet energy, an absorption in the blue region of the visible spectrum and an identical nature of local excitation when compared with cyclic ether **10a**.

By opposition to the functionalization on the southern fragment of the benzophenazine, the northern one had a minor effect on the computed parameters, *i.e.*, compared to aromatic sulfur **10f-2**, the absorption wavelength was red-shifted with electron-withdrawing groups with a maximum variation of 36 nm for nitro **10f-4** while being nearly unchanged with electron-donating *t*-butyl group. The triplet energies were only slightly impacted after modifications, remaining always above 38 kcal mol^{-1}, as presented in **Table 4.1**. This result is in accordance with what has been observed for the frontier orbitals of cyclic ether **10a** in **Figure 4.2**: unlike the HOMO mostly located in

the region where the southern functionalization is performed, the LUMO is not principally located in the region of the northern functionalization and thus, the impact of the implementation of different chemical groups is marginal.

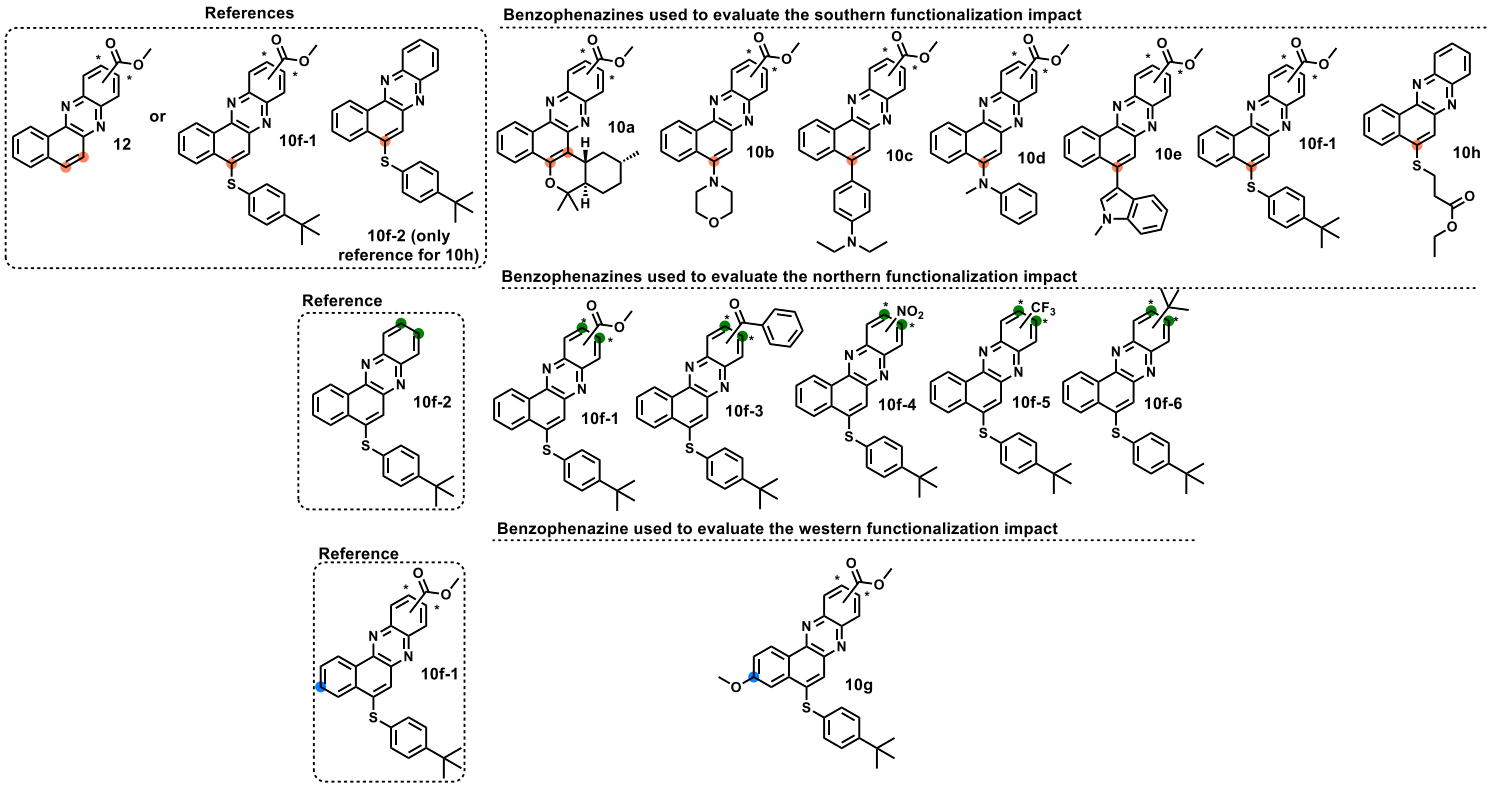
Hence, this result fosters the use of the $–CO_2Me$ group on the northern fragment of the benzophenazine as it does not interplay on the excited-state properties of interest and would facilitate the subsequent anchoring reaction of the photosensitizer over silica nanoparticles. The western fragment of the north-ester and south-aromatic sulfur **10f-1** has also been explored *via* the west-OMe **10g** (**Scheme 4.5**) with no strong incidence on the absorption wavelength and the triplet energy. In parallel, another available sulfur compound **10h**, bearing an aliphatic sulfur containing an ester group for potential further modification or grafting has been studied, revealing in the same manner, no improvements on the absorption wavelength and the triplet energy.

In order to validate the computational studies, we have conducted the synthesis of the different chromophores, using the same two-step procedure as described above. At first, we tackled the southern fragment variations of the benzophenazine core in order to introduce various substitutions with heteroatoms (O, N, S: **9a, 9b, 9d, 9f-h**) and carbon-based electron conjugated systems with electron–donating atoms (N: **9c and 9e**) (**Scheme 4.5**), using adapted reported procedures from the literature.[352,353,360,368] In most cases, a Michael addition with an heteroatom or carbon-based nucleophile on the corresponding naphthoquinone **8**, or its sulfonate adduct **7**, allowed to access the desired 1,2-naphthoquinone in a single step. For the 6-methoxy-derivative **9g**, the starting 2-naphthoquinone **6** was generated *in situ* by IBX (2-iodoxybenzoic acid) oxidation of the corresponding 6-methoxynaphthalen-2-ol **5**.[353] Finally, naphthoquinone **9a** was easily prepared by condensation of hydroxynaphthoquinone **4** with *R*-citronellal *via* well-known reported

procedures.[360] These photosensitizers were obtained in the range of 21 and 47 % yields over two steps.

3.3. Experimental photophysical properties of benzophenazine derivatives

In order to establish a structure-activity relationship, references were needed to evaluate strictly the impact of the functionalization on one of the key fragments of the molecular skeleton of benzophenazines. For the southern fragment, north-ester benzophenazine **12** was used to evaluate the impact on the fundamental and excited states, north-ester and south-aromatic sulfur **10f-1** for the influence on the generation of singlet oxygen and aromatic sulfur **10f-2** was used as reference only for the aliphatic sulfur **10h** to assess the impact of the presence of aromatic or aliphatic sulfur. For the northern fragment, aromatic sulfur **10f-2** was the reference and north-ester and south-aromatic sulfur **10f-1** was the one for the western fragment (**Scheme 4.6**).



Scheme 4.6. References used to evaluate the impact of functionalization on key fragments of benzophenazines.

The first parameter to be investigated was the absorption in acetonitrile (**Table 4.2**). The main reference for the southern fragment, north-ester benzophenazine **12**, absorbed mostly in the UV range and had a contribution in the visible range with a maximum centered at 408 nm that tailed until 435 nm with a corresponding molar absorption coefficient ε of 13.200 M^{-1} cm^{-1}. The considered functionalizations on the southern fragment led to a bathochromic shift in the absorption wavelengths which was more important for diethylaniline **10c**, methylaniline **10d** and indole **10e**, as expected for diethylaniline **10c** and indole **10e** based on the computational results. While enhancing the ability to absorb in the visible range, the functionalization on the southern fragment generally decreased the molar extinction coefficient which was particularly intense for methylaniline **10d**, indole **10e** and cyclic ether **10a** (below 10.000 M^{-1} cm^{-1}). Aliphatic sulfur **10h**, used to present a second way of future heterogenization by exploiting the aliphatic sulfur, had marginal effect compared to aromatic sulfur **10f-2**. The northern fragment had a moderate impact on the photophysical properties of the benzophenazines with a maximum variation of 15 nm for nitro **10f-4**. The introduction of the slightly electron-donating *t*-butyl group had no impact at all on absorption properties while electron-withdrawing groups tended to give bathochromic shifts. For molar absorption coefficients, the impact of functionalization was stronger and of outmost importance for the NO_2 moiety for which it was divided by more than half. This result with NO_2 is quite surprising as the CF_3 motif did not give such decrease for ε. The western fragment derivatization had also a detrimental effect on the molar absorption coefficient while the absorption wavelength was unchanged (**Figure 4.3**). Based on these findings, it can be concluded that all functionalizations whatever the fragment considered led to a decrease in molar absorption coefficient while the absorption wavelength was impacted the most by the southern fragment as expected based on computational studies identifying the location of the HOMO on that part of the molecule.

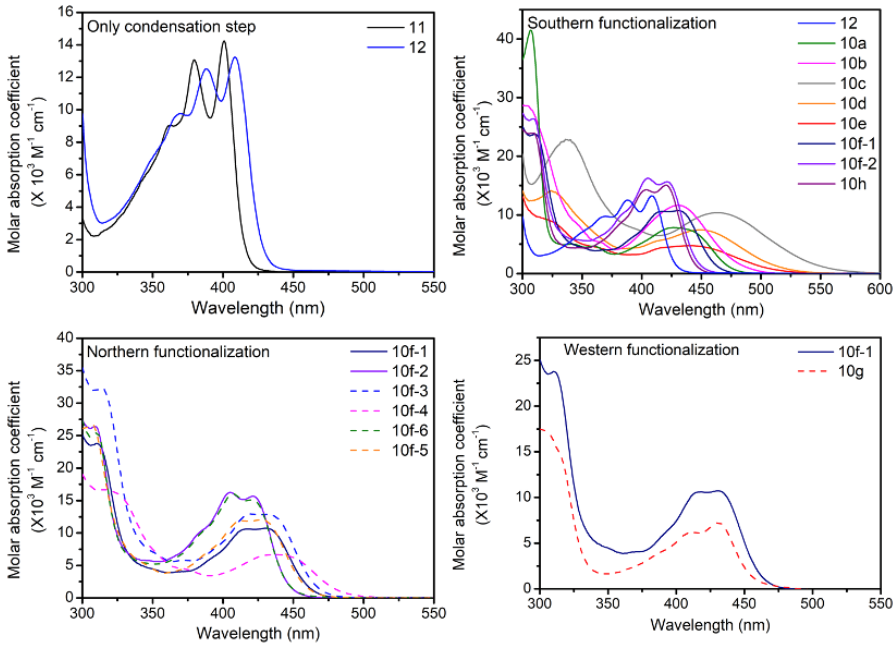


Figure 4.3. UV-vis absorption spectra of benzophenazine derivatives recorded at room temperature in acetonitrile.

The second photophysical property investigated was emission. The influence of derivatization on emission properties is the first insight into the changes that can suffer the excited state of a photocatalyst upon functionalization. Visible-light excitation of benzophenazine derivatives led to steady-state photoluminescence (SSPL) centered between 469 and 609 nm for fluorescence signals (**Figure B.1**). A red-shifted emission was observed for benzophenazine derivatives functionalized on their southern fragment whatever the nature of functionalization. When comparing aromatic sulfur **10f-2** and aliphatic sulfur **10h**, aromatic sulfur seems to stabilize the singlet excited state as their fluorescence wavelengths are 529 and 477 nm, respectively. The modifications on the northern fragment, irrespective of the presence of an electron-donating or withdrawing group, provoked a blue-shifted emission of ~40 nm. The western fragment had only a slight influence on emission properties (red-shifted emission of 10 nm for west-OMe **10g**).

To further characterize this singlet excited state, time-resolved photoluminescence (TRPL) measurements in acetonitrile were conducted to determine the fluorescence lifetime. The measurements were well described by first-order kinetics which yielded short singlet excited-state lifetimes of around 5 ns. For sulfur-based derivative compounds, the fluorescence lifetime could not be measured as it was below the instrument response factor. These short singlet excited-state lifetimes can be due to a fast intersystem crossing (ISC) leading to a triplet state from which a phosphorescence signal can be emitted. If an ISC quantum yield of 1 would be effective, no fluorescence at all would have been observed. Such hypothesis is interesting as the triplet state is the state of interest involved in the photosensitization of $^3O_2$. It would explain the short singlet excited-state lifetime of sulfur-based compounds as the sulfur atom favors the spin-orbit coupling and thus, the ISC quantum yield as described in the literature.[369]

To investigate this triplet excited state, *i.e.* the phosphorescence signal, the photoluminescence intensity was measured 100 ns after the laser pulse, when no fluorescence emission could be detected anymore due to its short lifetime. An emission signal was indeed detected and could be attributed to a phosphorescence signal which was comprised between 482 and 609 nm (**Figure B.2**). The southern fragment had no rational influence on the phosphorescence signal. On the northern fragment, the electron-withdrawing groups caused a red-shifted emission while the *t*-butyl group caused a blue-shifted one, highlighting that electron-donating groups could lead to an increased triplet excited-state energy. The −OMe functionalization on the western fragment displayed also a quite important blue-shifted phosphorescence emission compared to north-ester and south-aromatic sulfur **10f-1**. These maxima values of emission can be used to approximate the experimental triplet energy value (by converting the wavelength of emission into an energy value). With emission wavelength comprised between 482 and

609 nm, all compounds have a high triplet energy that is enough to photosensitize O_2 and allow the energy transfer, as predicted by computational study. Based on the scale of energy (**Table 4.2** and **Figure B.4**), indole **10e**, aliphatic sulfur **10h** and west-OMe **10g** are identified as the best compounds to photosensitize oxygen as the differences with the most stable excited state of oxygen are the most important. Surprisingly, for compounds methylaniline **10d** and indole **10e**, the triplet state was higher in energy than the singlet state, leading to a positive singlet-triplet energy gap. This inverted energy gap is mainly investigated for organic light-emitting diodes (OLED) to increase the quantum efficiency.[370–372] This positive gap is peculiar as for the vast majority of molecular systems, T_1 state lies energetically below the S_1 state due to exchange interactions which stabilize triplets and destabilize singlets.[370] When the HOMO and the LUMO are spatially nonoverlapping, these exchange interactions can become very small and can lead to inverted gaps. This applies, in particular, for internal charge-transfer excitation that minimizes the exchange interactions.[372] Based on our computational results, methylaniline **10d** and indole **10e** derivatives possess a S_0 to S_1 internal charge transfer and this could explain this anomaly. As an inverted gap is highly difficult to obtain experimentally, another hypothesis needs to be considered. Indeed, the time-delayed emission spectra are not of high quality (very broadened) and could suggest that different electronic transitions, such as $\pi - \pi^*$and an internal charge transfer from the donor nitrogen, proceed under irradiation leading to different excited state with different energies. Such combinations of excited states could potentially explain this anomaly. Computations could intervene to determine the excited-state energies of both electronic transitions in order to validate or not our hypothesis. This hypothesis of a mixture of excited states can be reinforced when taking a look at the phosphorescence emission of north-ester and south-aromatic sulfur **10f-1** and west-OMe 10g which differ by 75 nm. That difference is too important to be only due to the introduction of a methoxy group on the western fragment

of the benzophenazine and could be explained by the presence of a mixture of excited states.

Having a high triplet excited-state energy is important to photosensitize oxygen but it is not sufficient as the photosensitizer needs also a long triplet excited-state lifetime to perform energy transfer during that time range. Hence, triplet excited-state lifetimes were measured 100 ns after the laser pulse (again to avoid any fluorescence contribution) by integrating the signal at different time intervals (**Figure B.3**). These measured lifetimes were of the order of a few microseconds in most cases, with the lowest values exhibited by diethylaniline **10c**, methylaniline **10d** and indole **10e**. These lifetimes are long enough to allow energy or electron transfer (**Table 4.2**). The functionalization on the southern fragment was valuable for the triplet excited-state lifetime. Indeed, the presence of heavy atoms, such as sulfur which are known to enhance the ISC quantum yield, led to a phosphorescence lifetime of 4.5 μs for north-ester and south-aromatic sulfur **10f-1** while it dropped below 2 μs when nitrogen moieties were present.[373] Thus, indole **10e**, methylaniline **10d** and diethylaniline **10c** derivatives are identified as possibly less efficient PCs. Moreover, the computational study had revealed the different nature of their excited states which reinforces our hypothesis. The use of an aliphatic sulfur as southern fragment (**10h**) enhanced the phosphorescence lifetime by nearly doubling its value compared to its reference aromatic sulfur **10f-2**. Interesting triplet excited-state lifetimes were also reached with morpholine **10b** and cyclic ether **10a**, although no heavy atom was introduced. The derivatization of the northern fragment of molecular skeleton had a positive impact on the triplet excited-state lifetimes as the presence of electron-withdrawing or -donating groups increased these values from 2.2 μs for the reference **10f-2** (aromatic sulfur) to a maximum value of 5.4 μs for nitro **10f-4** which is the longest triplet lifetime of all the benzophenazines synthesized in this work. The introduction of a methoxy

group on the western fragment (**10g**) negatively impacted the phosphorescence lifetime.

Table 4.2. Photophysical properties of benzophenazine derivatives. Steady-state and time-resolved photoluminescence spectra were recorded in argon-purged acetonitrile. Phosphorescence signals were recorded 100 ns after the laser pulse at different time intervals. R points out the references.

	λ_{abs} (nm)	ε ($M^{-1}cm^{-1}$)	Fluo./ Phospho. (nm)	Fluo. lifetime (ns)	Phospho. lifetime (μs)	Triplet state energy (kcal mol^{-1})
Southern fragment functionalization						
R. 12	408	13.200	469/561	n.d.	n.d.	50.9
R. 10f-2	421	15.600	529/539	< IRF	2.2	53.0
10a	427	7840	516/516	2.6	3.0	**55.4**
10b	431	11.650	609/609	6.9	**4.6**	46.9
10c	**463**	10.380	500/564	5.1	0.3	50.7
10d	**449**	7450	569/538	5.3	0.8	53.1
10e	**440**	4760	530/482	4.7	1.1	**59.3**
10f-1	431	10.730	476/569	< IRF	**4.5**	50.2
10h	420	15.060	477/477	< IRF	**3.9**	**59.9**
Northern fragment functionalization						
R. 10f-2	421	15.600	529/539	< IRF	2.2	53.0
10f-1	431	10.730	476/569	< IRF	**4.5**	50.2
10f-3	432	12.870	475/572	< IRF	2.6	50.0
10f-4	436	6660	481/549	< IRF	5.4	52.1
10f-5	427	12.050	476/578	< IRF	2.6	49.5
10f-6	421	15.110	483/522	< IRF	3.0	**54.8**
Western fragment functionalization						
R. 10f-1	431	10.730	476/569	< IRF	4.5	50.2
10g	431	7240	486/494	< IRF	3.0	**57.9**

Although having a long triplet excited-state lifetime could increase the efficiency of a photosensitizer, the triplet state also needs to be highly populated to ensure a strong O_2 photosensitization. An ISC quantum yield

close to the unity leads to an efficient and fast access to triplet state which is highly populated by excited molecules and is translated by an intense phosphorescence intensity. **Figure 4.4** shows that all sulfur benzophenazine derivatives exhibited the strongest photoluminescence intensity which was expected as heavy atoms increase the spin-orbit coupling and, thus the ISC as already stated.[374] ISC quantum yield depends also on the energy gap existing between S_1 and T_1 (ΔE_{ST}) and small ΔE_{ST} values are more conducive to increase the ISC quantum yield.[373] This dependency is observed with aliphatic sulfur **10h** exhibiting the most important intensity of phosphorescence among all sulfur-based PCs together with the smallest ΔE_{ST}. Exception was made for nitro **10f-4** and west-OMe **10g** for which the presence of a NO_2 moiety on the northern fragment and the presence of a methoxy group on the western one were detrimental, respectively, and lowered the efficiency of the ISC conversion. Despite having the longest phosphorescence lifetime, the photoactivity of NO_2 benzophenazine derivative **10f-4** could be low as the triplet state is not occupied enough inducing that only a small fraction of excited molecules could transfer energy with triplet oxygen. This peculiar behavior is interesting as average photophysical properties were obtained with CF_3 moiety (**10f-5**) which is also an efficient electron-withdrawing group, confirming again the specific impact of a NO_2 moiety onto the photophysical properties. Cyclic ether **10a** is promising as it exhibited the second most intense photoluminescence with an average triplet lifetime. Although no heavy atom is present, the ΔE_{ST} is small and could explain this observed high ISC quantum yield. On the contrary, benzophenazines with a nitrogen moiety on the southern fragment showed poor results and reinforce the hypothesis of being non-suitable triplet oxygen photosensitizers.

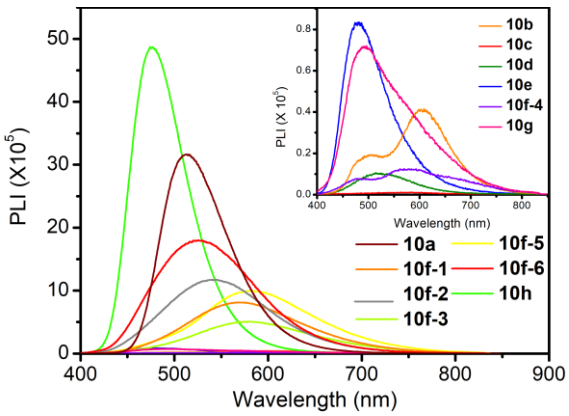
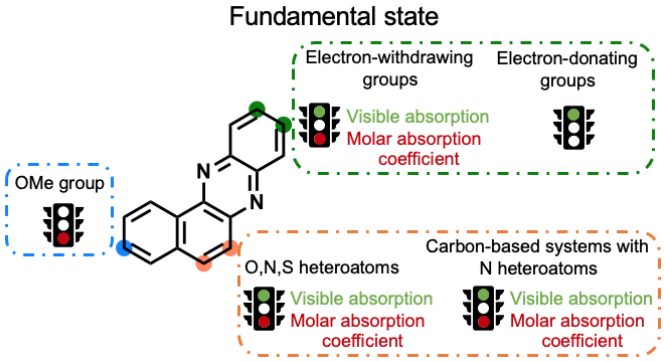
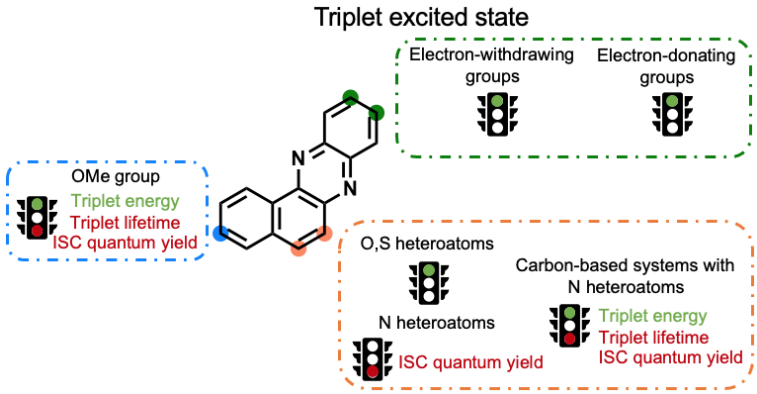


Figure 4.4. Photoluminescence intensity spectra of benzophenazine derivatives. Inset: zoom in case of low PLI.

Based on these results, we observed that the southern fragment derivatization led to a decrease of the molar absorption coefficient. The presence of N heteroatoms or carbon-based systems with N heteroatoms on that fragment was detrimental for the triplet excited state (ISC quantum yield and triplet lifetime). On the other hand, the introduction of O and S heteroatoms led to an efficient triplet excited state. The northern fragment, which was functionalized with electron-withdrawing or -donating groups, had a weaker influence on both the fundamental and excited states. This functionalization did not or slightly change the photophysical properties of the PCs which can be useful for future immobilization while maintaining their properties and reactivity intact. Finally, the western fragment had negative influence on both states (**Scheme 4.7**).





Scheme 4.7. Impact of the functionalization of the different fragments onto the fundamental (absorption wavelength and molar absorption coefficient) and triplet excited states (energy, lifetime and ISC quantum yield). The nitro **10f-4** with the NO_2 moiety was not considered for the northern fragment as it behaves differently from all others.

3.4. $^3O_2$ photosensitization

Optimal photophysical properties are vital to synthesize an efficient PS but it is also important to evaluate the capacity of a PS to interact with oxygen and produce reactive oxygen species. In this work, the photogeneration of singlet oxygen by using excited photosensitizers is targeted. All synthesized benzophenazines have a triplet energy that is higher than the first triplet excited state of oxygen, ensuring that the energy transfer is possible. To highlight that interaction, phosphorescence emission measurements were performed under argon and under O_2 to evaluate the O_2 quenching by calculating the ratios of areas of corresponding emission curves (**Table 4.3** and **Figure B.5**). A high argon/O_2 photoluminescence ratio indicates an efficient quenching with oxygen and thus a possible photoproduction of reactive oxygen species. The southern derivatization with O and S heteroatoms (cyclic ether **10a**, north-ester and south-aromatic sulfur **10f-1**, aromatic sulfur **10f-2** and aliphatic sulfur **10h**) led to efficient oxygen quenching with ratios comprised between 51.5 and 75.8, confirming their potential photosensitizing capabilities. The group of nitrogen

benzophenazines (morpholine **10b**, diethylaniline **10c**, methylaniline **10d** and indole **10e**) were disappointing with ratios that did not exceed the 11.4 value. The presence of electron-withdrawing groups on the northern fragment decreased the phosphorescence ratio under argon or oxygen compared to the reference **10f-2** (aromatic sulfur), with a very low value observed for nitro **10f-4**, which again highlights the peculiar behavior of this PC with a NO_2 moiety. On the contrary, the electron-donating *t*-butyl group enhanced this ratio. The western fragment impacted strongly in a negative way the ratio.

It is known that the photosensitization of oxygen leads to the production of reactive oxygen species, such as O_2^{-}, hydroxyl radical, H_2O_2, singlet oxygen…[373,375] The O_2 quenching efficiency estimated from the phosphorescence spectra is not selective for singlet oxygen only and a high ratio value does not implicate having an efficient photoproduction of $^1O_2$. In order to evaluate the selective production of singlet oxygen, quantum yields (ϕ_Δ) for $^1O_2$ generation by benzophenazine derivatives were evaluated by monitoring the changes in absorption of anthracene-9,10-divinylsulfonate (AVS), the anthracene-based fluorescence probes being known as selective for singlet oxygen (**Figure B.6**).[143] At regular intervals, the absorption spectra of AVS in presence of a given PS and under irradiation was measured in DMSO and the difference in absorption was plotted against time to determine the quantum yields for $^1O_2$ generation. This experiment was conducted three times for each different molecule. The same trend was observed as before, the sulfur-based derivatives and compound **10a** exhibiting quantum yields comprised between 0.84 and 0.59 (the highest one being attributed to the aliphatic sulfur compound **10h**) which is in the same range as Rose Bengal, famous $^3O_2$ PS, which was used as reference ($\phi_\Delta = 0.76$ in water, **Figure B.7**).[170] The oxygen quantum yields obtained are also comparable to methylene blue (ϕ_Δ = 0.51), $[Ru(bpy)_3]^{2+}$ (bpy = bipyridine, ϕ_Δ = 0.73), tetraphenylporphyrin (ϕ_Δ = 0.78) or 4-phenylbenzophenone (ϕ_Δ = 0.75)[146]

which highlights the good performances of our new synthesized photosensitizers. On the southern fragment, the family of nitrogen derivatives were poorly active: 0.05 and 0.04 for indole **10e** and diethylaniline **10c** derivatives, respectively, or non-active at all (methylaniline **10d** showed a decrease in absorbance of AVS identical to the control test which consisted in irradiating AVS alone (**Figure B.8**)). The singlet oxygen quantum yield for morpholine derivative **10b** could not be measured due to incompatibility in reaction conditions. The southern fragment is again identified as having a lot of influence on the reactivity of our photosensitizers. The use of electron-withdrawing groups on the northern fragment increased the singlet oxygen quantum yield while the use of *t*-butyl electron donating group changed only slightly the value. Exception made for the peculiar photosensitizer bearing a NO_2 motif which decreased ϕ_Δ as nearly none singlet oxygen was produced (ϕ_Δ = 0.07) and confirmed that its behavior is different from the sulfur derivatives. The western fragment had no influence on the production of singlet oxygen by the photocatalyst.

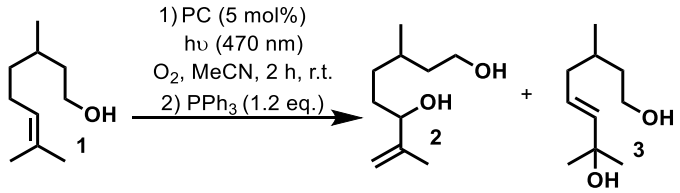
Table 4.3. Investigated parameters in the $^3O_2$ photosensitization by benzophenazine derivatives.

	Ratio Phospho. Argon/O_2	ϕ_Δ[a]	Citronellol photooxidation (%)[b]
Southern fragment functionalization			
Reference 10f-1	**51.5**	**0.80**	**98**
Reference 10f-2	**67.8**	**0.59**	**98**
10a	**73.1**	**0.70**	**85**
10b	7.8	-	83
10c	4.0	0.04	7
10d	4.3	0	15
10e	11.4	0.05	34
10h	**75.8**	**0.75**	**92**
12	n.d.	n.d.	96[c]
Northern fragment functionalization			
Reference 10f-2	**67.8**	**0.59**	**98**
10f-1	**51.5**	**0.80**	**98**
10f-3	**50.7**	**0.84**	**99**
10f-4	9.2	0.07	32
10f-5	**43.4**	**0.83**	**93**
10f-6	**80.8**	**0.64**	**98**
Western fragment functionalization			
Reference 10f-1	**51.5**	**0.80**	**98**
10g	33.6	**0.82**	**95**

[a] The singlet oxygen quantum yield was corrected taking into account the degradation of AVS alone under blue irradiation with blue Thorlabs lamp. [b] NMR yield determined with dimethylsulfone as internal standard. [c] Two LED IP FL-30 (eurolite) with an emission wavelength of ~390 nm were used.

Finally, all benzophenazine derivatives were evaluated in the photooxidation of citronellol, in the same reaction conditions as presented on **Scheme 4.8** for which the simultaneous presence of PS and light was highlighted as necessary with control tests. Based on the photophysical properties and the ability to perform energy transfer with oxygen, sulfur

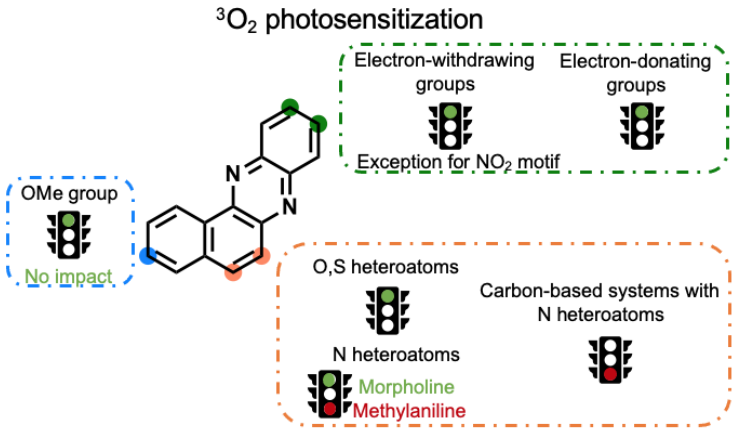
derivatives (except for nitro **10f-4**) were expected to be efficient and indeed, a high NMR yield in desired products was obtained, comprised between 99 and 92 %, which is similar to the photoactivity of cyclic ether **10a**. The presence of electron-donating or -withdrawing groups on the northern fragment had no influence on the activity. The morpholine derivative **10b**, with its long phosphorescence lifetime, was performant and a NMR yield of 83 % was determined. This compound is the only one in the family of nitrogen derivatives that exhibits an activity in the photoproduction of singlet oxygen. As expected from the computational study and above experimental results, indole **10e**, methylaniline **10d** and diethylaniline **10c** derivatives were not efficient in the photooxidation of citronellol with NMR yields of 34, 15 and 7 %, respectively. West-OMe **10g** was as performant as the reference **10f-1** (north-ester and south-aromatic sulfur) highlighting the inertness of the western fragment for the production of singlet oxygen. The generation of singlet oxygen was reproducible as the citronellol photooxidation was performed three times with morpholine **10b**, cyclic ether **10a** and aliphatic sulfur **10h** with an average NMR yield of 79±7, 86±1 and 94±4 %, respectively.



Scheme 4.8. Photooxidation of citronellol used as a benchmark reaction to evaluate and compare the performances of benzophenazine derivatives to photogenerate singlet oxygen. Two blue Thorlabs lamps (470 nm, 4.0 mW cm^{-2}, output power of 253 mW) were used in that reaction to irradiate the PCs.

For future photocatalysts immobilization in order to obtain a recyclable and robust system photogenerating singlet oxygen, the best fragment to use for that purpose is the northern one as it impacted the less the photophysical properties and the reactivity of the PCs. Moreover, the presence of electron-withdrawing groups on that fragment can even increase the capabilities of

oxygen quenching which is a valuable information as an amide linker is envisaged in our immobilization methodology (**Scheme 4.9**). The southern fragment nature impacted too much the reactivity of the PCs and the western one had no influence but is more complicated to derivatize synthetically reinforcing the choice of the northern fragment for the immobilization step.



Scheme 4.9. Impact of the functionalization of the different fragments onto the abilities of benzophenazine derivatives to photosensitize $^3O_2$ (considered parameters: $^1O_2$ quantum yield and citronellol photooxidation).

3.5. Photostability investigation

Inherent to ensure an excellent PS, the photostability is an important characteristic to evaluate and is of utmost importance when considering immobilizing a PC as it necessitates its irradiation for many hours. The NO_2 **10f-4**, diethylaniline **10c**, indole **10e** and methylaniline **10d** derivatives being not efficient PS, the functionalization of west-OMe **10g** having no strong positive impact on its photophysical properties and its photoactivity, and the functionalization of aliphatic sulfur **10h** being located on the southern fragment that could alter a lot the photophysical properties of a PC with further modifications, the photostability of these compounds were not assessed. The photostabilities of north-ester and south-aromatic sulfur **10f-1** (**Figure 4.6**), morpholine **10b** (**Figure B.9**) and cyclic ether **10a** (**Figure 4.5**) were evaluated by monitoring their absorption and emission spectra under different

reaction conditions, *i.e.* under irradiation, under irradiation in presence of oxygen and under irradiation in presence of oxygen and citronellol. A difference or changes in absorbance along with a decrease in photoluminescence intensity would be the sign of a photodegradation. North-ester and south-aromatic sulfur **10f-1** showed a very slight decrease in absorbance when it was irradiated alone meaning that no photodegradation was induced by light. The difference in absorbance was more important in presence of oxygen but decreased when citronellol was also present in the mixture. The PS was slightly sensitive to singlet oxygen but is considered photostable when another molecule that can react with singlet oxygen is present. The same trend was observed with the emission spectra. We went one step further by analyzing the filtrates by HRMS with north-ester and south-aromatic sulfur **10f-1** to be sure that the structure of the PS was not altered. In all three cases, the characteristic peak of the PS was observed and no other peaks were found at higher *m/z* ratio, excluding the hypothesis of forming a sulfoxide or sulfone moiety onto the PS structure in presence of singlet oxygen. Morpholine **10b** was also photostable but the presence of citronellol did not decrease its photodegradation meaning that this PS was more sensitive than north-ester and south-aromatic sulfur **10f-1** but was still highly photostable. Finally, the photostability of cyclic ether **10a** was investigated and nearly no photodegradation was observed on absorption and emission spectra under the three different conditions tested.

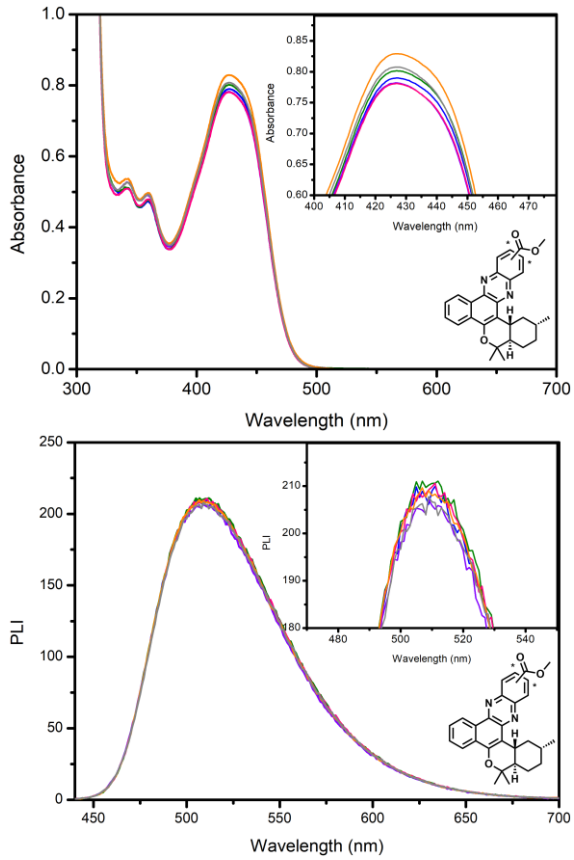


Figure 4.5. Absorption (top) and steady-state photoluminescence (bottom) spectra of cyclic ether **10a** before (blue) and after (purple) 2 hours of irradiation, before (green) and after (pink) 2 hours of irradiation in presence of oxygen and before (orange) and after (grey) 2 hours of irradiation in presence of oxygen and citronellol. The insets correspond to a zoom of the zone of interest.

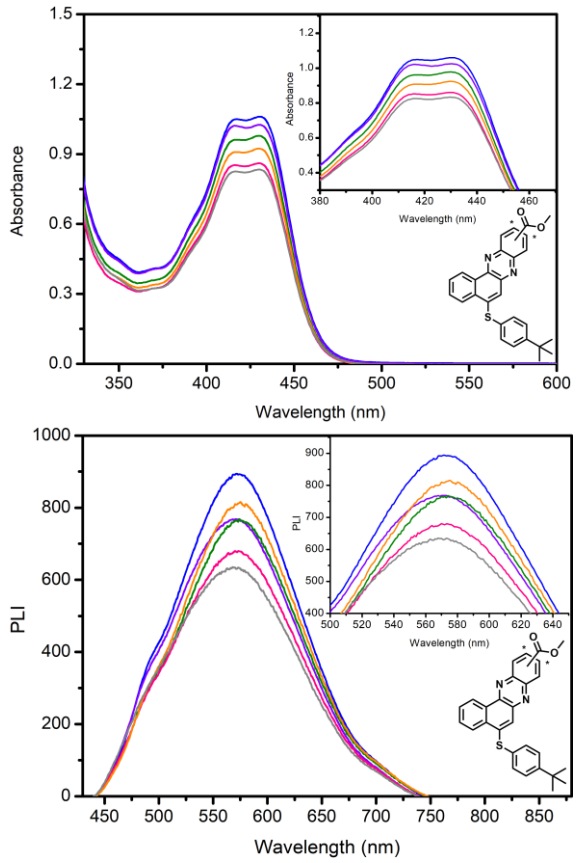
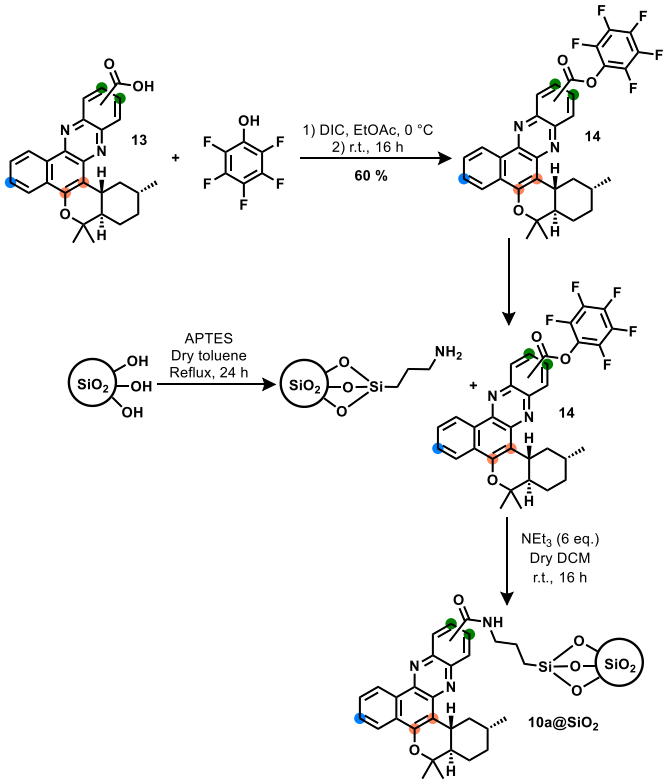


Figure 4.6. Absorption (top) and steady-state photoluminescence (bottom) spectra of north-ester and south-aromatic sulfur **10f-1** before (blue) and after (purple) 2 hours of irradiation, before (green) and after (pink) 2 hours of irradiation in presence of oxygen and before (orange) and after (grey) 2 hours of irradiation in presence of oxygen and citronellol. The insets correspond to a zoom of the zone of interest.

So far, the sulfur-based photocatalysts were the best to produce singlet oxygen. However, north-ester and south-aromatic sulfur **10f-1** did not exhibit the highest photostability which is a crucial characteristic in heterogeneous photocatalysis, in order to be able to reuse the PC with no, or little, decrease in photoactivity. Indeed, more photodegradation was observed for north-ester and south-aromatic sulfur **10f-1** compared to cyclic ether **10a** for each tested condition. For this reason, cyclic ether **10a** was selected for the heterogenization study as it displayed excellent efficiency in producing singlet oxygen together with high stability.

3.6. Benzophenazine heterogenization on silica nanoparticles

We have identified that the northern fragment functionalization of a benzophenazine has little impact on the photophysical properties or the photoactivity of the PS and we can then, therefore, take advantage of a carboxylic acid derivative to carry out the heterogenization of the PS on silica nanoparticles. Such electron-withdrawing group can even increase the efficiency of producing singlet oxygen as observed with the above results. Cyclic ether **10a** was the PS of choice to conduct this recyclability study as explained above. The envisaged methodology is to add an activated ester on the northern fragment of cyclic ether **10a** that could react with amino-functionalized silica nanoparticles to form a photostable covalent amide linker (**Scheme 4.10**).



Scheme 4.10. Envisaged methodology for the heterogenization of cyclic ether **10a**.

The first step towards the heterogenization of cyclic ether **10a** was the synthesis of the activated ester derivative **14** that would allow the formation of covalent bond with the modified silica surface. An acid-derivative **13** was needed which was easily obtained in the same two steps as cyclic ether **10a**, exception made of the use of 3,4-diaminobenzoic acid. The presence of the acid moiety on the northern fragment allows now the formation of the activated ester. The acid-derivative **13** reacted with pentafluorophenol in presence of *N*,*N*'-diisopropylcarbodiimide (DIC) in ethyl acetate to afford the corresponding activated ester with a 60 % isolated yield.

With the activated ester photosensitizer **14** in hands, we sought to develop the synthesis of silica nanoparticles for efficient surface immobilization. Nanospheres (NS) were targeted as these represent a standard morphology that prevents potential pore-diffusion issues, as commonly observed in heterogeneous catalysis.[347,376–380] Nanospheres were obtained by adapting the procedure of Stöber *et al.* based on the sol-gel process to access a 40 nm diameter size.[220] The size and morphology of these NS nanoparticles were confirmed by transmission electron microscopy (TEM) (**Figure 4.7**) and dynamic light scattering (DLS) (**Figure 4.8**). Specific surface area of 360 m^2 g^{-1} was calculated using the Brunauer-Emmett-Teller (BET) equation on nitrogen physisorption data (**Figure 4.13**).

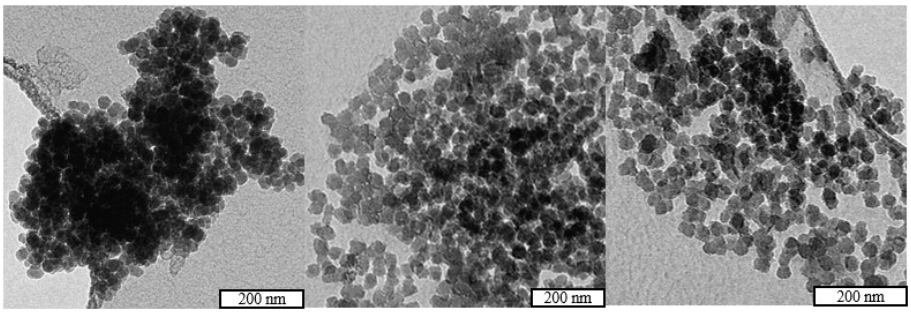


Figure 4.7. TEM images of pristine silica nanoparticles of spherical shapes (NS).

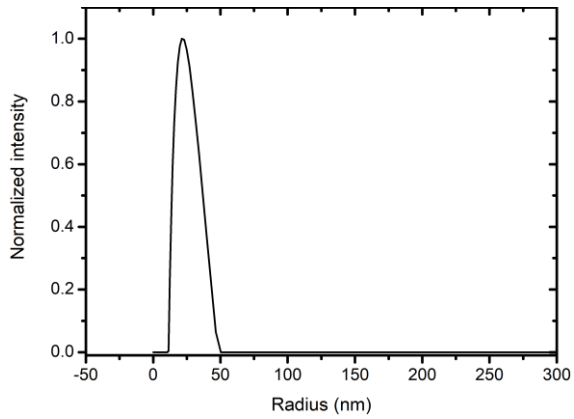


Figure 4.8. Dynamic light scattering analysis of pristine silica NS.

In order to form the covalent bond between the support and the PS, some amino-functions were needed at the surface of NS nanoparticles. *Via* the silanol chemistry of these NS nanoparticles, aminopropyltriethoxysilane (APTES) was grafted onto the surface using inert conditions to avoid the fast and possible polymerization of this silane.[217] The efficient grafting of amine functions was confirmed by X-Ray photoelectron spectroscopy (XPS) where a peak at 399.8 eV was observed, which is characteristic of amine moieties (**Figure B.10**). As XPS is a semi-quantitative surface analysis, a thermogravimetric analysis (TGA) was recorded to quantify the loading of amino groups at the surface of the support (**Figure 4.9**). The thermogram showed a loss in weight of about 12 wt.% which corresponds to 0.10 mmol of amino functions per 100 mg of material which is in accordance with the loadings reported in the literature as stated in Chapter 3.[170,178]

The NS nanoparticles with amine moieties immobilized at their surfaces were dispersed in dichloromethane and allowed to react with the activated ester **14** in presence of triethylamine during 16 h to afford the heterogenized photosensitizer denoted **10a@SiO$_2$**. This afforded a yellowish powder. Material **10a@SiO$_2$** was analyzed by XPS to check if the PC was indeed anchored onto the solid support. All expected elements were detected at correct binding energy by XPS (**Figure 4.11**). The atomic ratio N/C (0.13)

was close to the theoretical one (0.10) corroborating that the organic dye's structure was intact. Surprisingly, fluorine was detected on the surface and the XPS signal was decomposed into two components: one at 689.3 eV which is also present for the activated ester **14** and can be attributed to a Teflon contamination due to the stirring bar and one at 686.9 eV that could arise from the adsorption of pentafluorophenolate, leaving group formed during the synthesis of the amide bond between the PS and the support (**Figure 4.11**). The adsorption of an unreacted activated ester **14** is not envisaged as this molecule presents a binding energy of 688.3 eV for the F_{1s} signal (**Figure B.11**). A TGA thermogram was recorded to evaluate the quantity of grafted PS and showed a loss in weight of about 20 wt.% (**Figure 4.9**). By calculating the difference between the loss in weight of the amino-functionalized NS nanospheres and the one of grafted PS, we determined that a 7.8 wt.% loading in PS was present which corresponds to 0.02 mmol of PS per 100 mg of material.

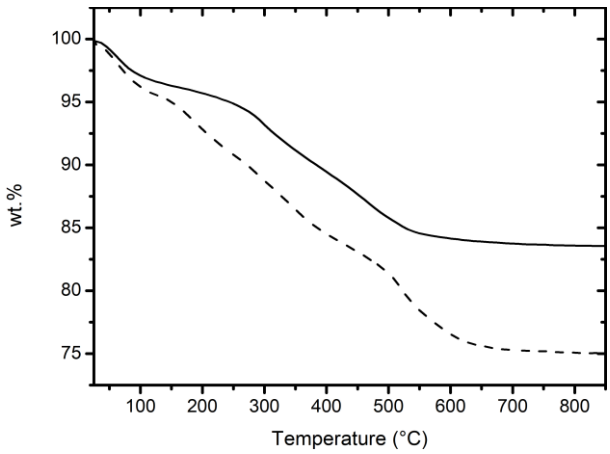


Figure 4.9. TGA thermograms of amino functionalized silica nanoparticles (solid) and of heterogenized **10a@SiO₂** photosensitizer on silica NS (dashed).

The photocatalytic activity of **10a@SiO₂** was then investigated using the citronellol photooxidation benchmark reaction. Knowing the adsorption/desorption equilibria that occurs before and after the reaction and the potential loss of singlet oxygen through interaction with the support, the

time of reaction was increased to 16 h. The first run of reaction gave a very satisfying 97 % NMR yield which proved that the photophysical properties were maintained after heterogenization. For a strict comparison with homogenous catalysis, the citronellol photooxidation must have been realized under 2 hours of irradiation. Such reaction conditions could also give insights into the kinetics of reaction if it was time-followed by NMR or GC analysis. A kinetic study could help to strictly compare the heterogenized system with its homogeneous counterpart. A bright yellow powder was recovered at the end of the reaction which was promising for future recyclability tests. Three consecutive recycling runs were conducted and 96, 91 and 85 % NMR yield were obtained for second, third and fourth run, respectively (**Figure 4.10**).

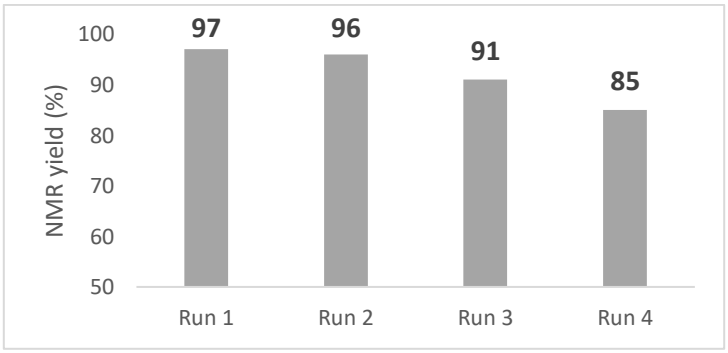


Figure 4.10. NMR yields of desired products obtained with the grafted and recycled **10a@SiO$_2$** used in the photooxidation of citronellol. Conditions: citronellol ($5X10^{-3}$ M), **10a@SiO$_2$** (5 mol%, 28 mg), bubbling O_2, MeCN, 470 nm irradiation, r.t., 16 h.

To understand the slight decrease in activity of the heterogenized PS along the runs, the final material was analyzed by XPS (**Figure 4.11**). Nitrogen, which is the characteristic element of our dye, was still detected with an atomic percentage (at.%) of 3 at an appropriate binding energy of 400 eV. Based on this, we could calculate an approximative leaching of 25 %, which could explain the decrease in photoactivity. This leaching is overestimated if some amine moieties that did not react with the activated ester **14** are leached which could explain, partly, the decrease in NR_4^+ component in the N_{1s} signal after 4 runs. Another explanation for this component decrease

is that primary amines can interact with silanol groups through H-bonds. Such interaction is impacted by the solvent polarity and decrease in the presence of a polar solvent. In our case, the use of polar acetonitrile could then explain the lower amount of detected quaternary amines. Moreover, the N/C ratio (0.15) was similar to the initial one (0.13), indicating that the PS may have conserved its molecular skeleton and remained intact. Concerning the F_{1s} signal, the same two components (as in starting material) were observed. The amount of detected pentafluorophenolate molecule is decreased after 4 runs of reactions as it can be washed away from the support along the runs.

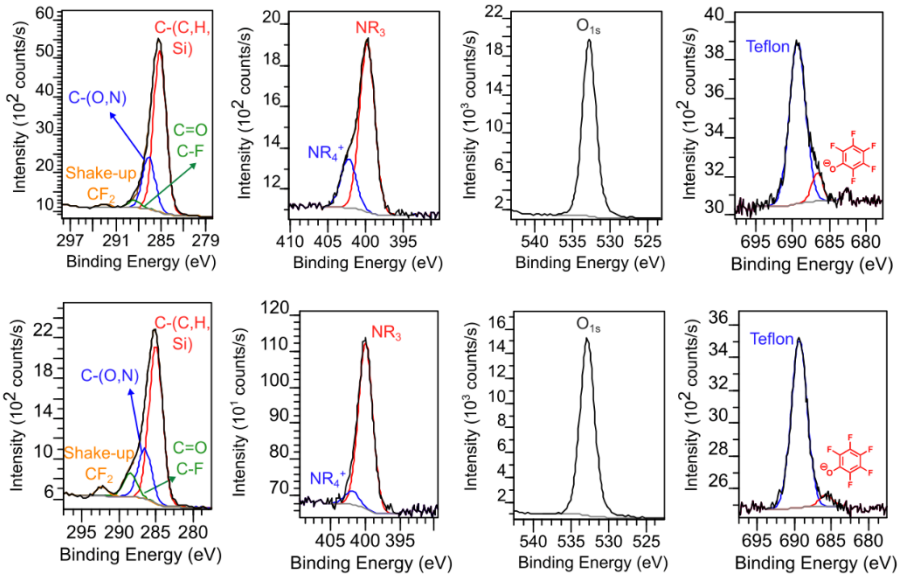


Figure 4.11. XPS spectra for C_{1s}, N_{1s}, O_{1s} and F_{1s} elements for heterogenized **10a@SiO₂** on silica nanospheres (top) and heterogenized **10a@SiO₂** on silica nanospheres after 4 runs of reaction (bottom).

Our new heterogenized system is competitive with the ones found in the literature. Indeed, porphyrin and methylene blue were immobilized onto silica nanocomposites and were efficient in the photoproduction of singlet oxygen and recyclable over 3 and 4 runs, respectively. The amount of immobilized PS was in the same range as for the porphyrin and methylene blue photosensitizers.[348,381] A maximal loading was targeted at first for our new photoactive system but it would be interesting to optimize the loading as we

could obtain an even increased photoactivity by diminishing the loading. Our system is even more efficient than the ones developed by Terra *et al.* for citronellol photooxidation in which Rose Bengal immobilized on magnetic silica nanoparticles showed a drastic decrease in conversion in the first reuse cycle. On the other hand, $[Ru(bpy)_2]^{2+}$ could be used in 3 reuse cycles (85 % conversion) with minimal loss in activity, but at the fifth run the activity dropped to 65 % conversion only.[173] In the Chapter 3, we also highlighted the photobleaching of Rose Bengal immobilized on non-porous silica structures demonstrating a drastic decrease in photoactivity from the first reuse cycle.[347] In this same work, the use of core-shell silica nanoparticles with a mesoporous shell acted as a shield to reduce the photobleaching of Rose Bengal. As the photooxidation of citronellol was also photocatalyzed in that case, we could envisage to use here such silica structures in the future to further improve our system in terms of recyclability.

4. Conclusions

Benzophenazine molecules were easily and diversely functionalized leading to the establishment of a structure-activity relationship by derivatizing three identified zones of the molecular backbone: the southern, the western and the northern ones. Based on computational results, relevant moieties were identified along with the understanding of the nature of the first excited state. These results highlighted the probable inertness of the northern fragment on photophysical properties and the different energy transfer mechanisms that can occur depending on the functionalization of the southern fragment.

The series of benzophenazines investigated computationally were synthesized easily in two steps from affordable and available starting materials. The photophysical properties, the ability to interact with oxygen and the photostability were assessed. The southern part had a huge impact on the PS activity. Cyclic ether **10a** and sulfur-based derivatives (aromatic or

aliphatic sulfur) exhibited incredible properties such as high phosphorescence lifetime (~3.5 μs), populated and energetic triplet state, high $^1O_2$ quantum yield (~0.75), citronellol conversion (nearly quantitative) and photostability. The low ΔE_{ST} and heavy atom effect could explain their incredible efficiencies. Functionalizing the southern fragment with a morpholine moiety led to a peculiar PS with contrasted properties but a good activity in citronellol photooxidation. This was the only nitrogen function that was efficient on the southern part as the others gave dramatic results and were not efficient in the production of singlet oxygen. The functionalization on the western fragment had no significant impact and was detrimental for certain photophysical properties. Finally, the northern one was not quite useful to tune the properties of the PS but highlighted the negative impact of a nitro moiety onto the $^3O_2$ photosensitization.

With the nearly inertness of the northern fragment, compound **10a** could be advantageously modified and grafted onto silica nanospheres by an amide linker. An activated ester was synthesized to favor the formation of the covalent bond with the amino groups introduced at the surface of the support. XPS and TGA analysis proved the successful anchoring of the PS with a loading of 7.8 wt.% The heterogenized system was performant in the citronellol photooxidation and was robust in recyclability tests as it could be engaged in three recycling runs with only slightly decreased yields in desired products being obtained. This opens the door for versatile photocatalyst immobilization as our methodology is efficient and involves basic functional groups that can be present on various molecular skeleton and supports. Our supported system could be employed in different applications such as photodynamic therapy, natural products synthesis, depollution, flow chemistry and the real extent of its potential is still to be discovered.

5. Experimental section

5.1. Chemicals

Commercial reagents were used as received. Methanol (> 98 %, VWR), ethanol (99% V/V euro denaturated with 1 % of isopropanol, VWR or absolute), acetonitrile (water content below 30 ppm, VWR), dimethylformamide (DMF, anhydrous, 99.8 %, Sigma-Aldrich), tetraethylorthosilicate (TEOS, ≥ 99 %, Sigma-Aldrich), ammonium hydroxide (NH_4.OH, 25 % solution in water, Acros Organics) (3-Aminopropyl)triethoxysilane (APTES, 99 %, Sigma-Aldrich), 1,2-naphthoquinone sulfonic acid sodium salt (97 %, Sigma-Aldrich), morpholine (> 99 %, Alfa Aesar), *N*-methylaniline (98 %, Janssen), *N,N*-diethylaniline (> 99 %, Sigma-Aldrich), 1,2-naphthoquinone (97 %, Sigma-Aldrich), 1-methylindole (> 96 %, TCI), cerium(III) chloride (99.9 %, Acros organics), sodium iodate (> 99 %, Acros organics), *tert*-butanol (> 99 %, Merck), ethylene diamine (> 99 %, Acros organics), 2-hydroxy-1,4-naphthoquinone (97 %, Sigma-Aldrich), (*R*)-citronellal (> 95 %, TCI), 6-methoxynaphthalen-2-ol (> 97 %, Sigma-Aldrich), 2-iodoxybenzoic acid (45 %wt., Sigma-Aldrich), 4-(*tert*-butyl)benzenethiol (97 %, Sigma-Aldrich), ethyl 3-mercaptopropanoate (> 97 %, Fluorochem), benzene-1,2-diamine (99.5 %, flaked, Sigma-Aldrich), 4-nitrobenzene-1,2-diamine (95 %, Fluorochem), 4-(trifluoromethyl)benzene-1,2-diamine (95 %, Fluorochem), 4-(*tert*-butyl)benzene-1,2-diamine (97 %, Fluorochem), 3,4-diaminobenzoic acid (97 %, Acros organics), pentafluorophenol (> 99 %, Sigma-Aldrich), citronellol (> 95 %, Sigma-Aldrich), triphenylphosphine (99 %, Fluorochem), triethylamine (99 %, Acros organics), *N*-*N*'-diisopropylcarbodiimide (DIC, for synthesis, Merck). Ethylenediammonium diacetate (EDDA) was synthesized according to a published procedure, and its purity was confirmed by IR and NMR.[382]

5.2. Characterization methods

Nuclear Magnetic Resonance (NMR). NMR spectra were recorded on BRUKER spectrometers (300 MHz for ^{1}H, 75 MHz for ^{13}C, 282 MHz for ^{19}F.). Chemical shifts are reported in δ ppm relative to the residual solvent peak for $CDCl_3$ (δ = 7.26 ppm, 77.16 ppm), D_2O (δ = 4.79 ppm) or for CD_2Cl_2 (δ = 5.30 ppm, 53.5 ppm). The following abbreviation have been used: δ (chemical shift), *J* (coupling constant expressed in hertz), br (broad), s (singlet), d (doublet), t (triplet), q (quadruplet) and m (multiplet).

X-Ray Photoelectron Spectroscopy (XPS). XPS analyses were carried out at room temperature with a SSI X-probe (SSX 100/206) photoelectron spectrometer (55° angle) from Surface Science Instruments (USA) equipped with a monochromatized microfocus Al X-ray source. Samples were stuck onto small sample holders with double-face adhesive tape and then placed on an insulating home-made ceramic carousel (Macor®, Switzerland). Charge effects were avoided by placing a nickel grid above the samples and using a flood gun set at 8 eV. The binding energies were calculated with respect to the Si_{2p} peak fixed at 103.5 eV. Data treatment was performed with the CasaXPS program (Casa Software Ltd., UK). The peaks were decomposed into a sum of Gaussian/Lorentzian (85/15) after subtraction of a Shirley type baseline. The XPS analyses were performed only once for each sample which prevent to assess the experimental error that can be quite important for several elements. Indeed, the peak selection is performed by the experimenter and can cause large variations in the peak area measured for smaller peak sizes. Elements with a low photoelectron cross-section, such as nitrogen, are particularly susceptible to errors. For most elements with moderate to strong photoelectron cross-sections, precision may vary by only a few tenths of a percent which is considered as a minor amount only if the element is mostly present at the surface (10 – 100 at%) but becomes a larger error as the element amount decreases.[285]

UV-vis. UV-vis absorption spectra were recorded on a Shimadzu UV-1700 instrument using 1 cm large cuvettes in quartz. The UV-vis spectra were measured each 0.5 nm. An absorption range of 0.2-0.8 was targeted to measure a spectrum.

Fourier-transform Infrared Total Attenuated reflectance spectroscopy (FTIR-ATR). FTIR-ATR spectra were recorded on Perkin Elmer Spectrum Two-UATR by depositing the powder onto the diamond equipped with a mechanical press. The bands are reported in cm^{-1} and the following abbreviations have been used: br (broad), s (strong), m (medium), w (weak).

Photoluminescence. Time-resolved photoluminescence spectra were recorded on a previously described LP980-K spectrometer from Edinburgh Instruments.[81] Briefly, the latter consisted in a LP980-K spectrometer equipped with an iCCD detector from Andor (DH320T). The excitation source was a tunable Nd:YAG Laser NT342 Series from EKSPLA. The third harmonic (355 nm) at 150 mJ was directed into an optical parametric oscillator (OPO) to enable wavelength tuning starting from 410 nm. The laser power was then attenuated to reach appreciable signal/noise and the integrity of the samples was verified by UV–Vis measurements. The LP980-K is equipped with a symmetrical Czerny-Turner monochromator. For single wavelength absorption changes, a 1800 g mm^{-1} grating, blazed at 500 nm is used, which affords wavelength coverage from 200 to 900 nm. For spectral mode (iCCD), a 150 g mm^{-1} grating, blazed at 500 nm is used, offering a wavelength coverage of 540 nm over the full wavelength range extending from 250 to 900 nm. Single wavelength absorption changes were monitored using a PMT LP detector (Hamamatsu R928) which covers the spectral range from 185 to 870 nm. The probe was a 150 W ozone-free xenon short arc lamp (OSRAM XBO 150W/CR OFR) that was pulsed at the same frequency than the laser. The optically diluted samples were excited with pulsed light and the excited-state

lifetime was measured on a PMT LP detector (Hamamatsu R928) which covers the spectral range from 185 to 870 nm. An average of 30 scans per measurement was used.

Thermogravimetric analysis (TGA). Thermograms were recorded on a TGA/SDTA 851e simultaneous DSC-TGA instrument from METTLER TOLEDO. These analyses were carried out with a heating ramp of 10 °C min^{-1} and under air flow (100 mL min^{-1}) with the samples (3 – 20 mg) placed into alumina containers.

Transmission Electron Microscopy (TEM). TEM images were obtained with a LEO 922 OMEGA energy filter transmission electron microscope. The powder samples were suspended in ethanol under ultrasonic treatment, then a few drops of the supernatant were deposited on a holey carbon film supported on a copper grid (Protochips, 1.2 micron hole diameter, 1.3 micron hole spacing, 200 mesh copper grid), which was dried for a few hours under vacuum at room temperature before analysis.

Cyclic voltammetry (CV). Experiments were performed with an Autolab PGSTAT 100 potentiostat using a standard three-electrode-cell, *i.e.* a glassy carbon disk working electrode (approximated area = 0.03 cm^2), a platinum wire counter electrode and an aqueous Ag/AgCl reference electrode (salt bridge: 3 M KCl/saturated AgCl). Experiments were performed in 0.1 M tetrabutylammonium hexafluorophosphate acetonitrile electrolyte, and the samples were purged with argon before each measurement.

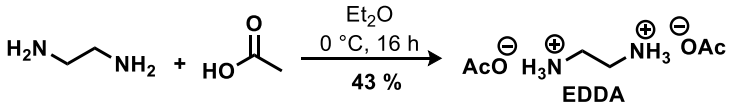
Mass spectrometry. HRMS were recorded on a Q-Extractive orbitrap from ThermoFisher. Samples were ionized by ESI (capillary temperature: 250 °C, vaporizer temperature: 250 °C, sheath gas flow rate: 20).

Nitrogen physisorption. The specific surface area was measured by nitrogen adsorption-desorption isotherms. The measurement was achieved using a Micromeritics ASAP 2020 analyzer at –196 °C. Before analysis, the

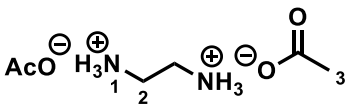
sample (~ 200 mg) was degassed for 2 h at 200 °C with a heating ramp of 10 °C min^{-1} under 0.133 Pa pressure. The analysis of the isotherm provided specific surface area calculated with the Brunauer-Emmett-Teller (BET) equation.

5.3. Experimental protocols

Synthesis of ethylenediammonium diacetate (EDDA)



Acetic acid (11.4 mL, 0.2 mol, 2 eq.) was added dropwise to a solution of diethylamine in diethyl ether (10mL) at 0 °C in a 250 mL flask. As the acid was added, white fumes were released, and a white precipitate formed. After 5 min, the flask was put into contact with air with an ongoing fume release and left to stir overnight. A yellow solid was subsequently filtered and washed with diethyl ether. The precipitate was dissolved in a minimal amount of methanol and recrystallized. Pale yellow to white acicular crystals were collected (7.58 g, 43 %).



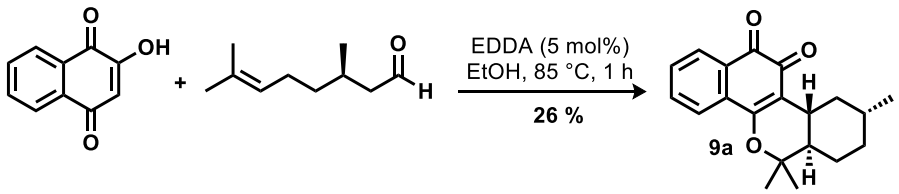
CAS: 38734-69-9

Formula: $C_6H_{16}N_2O_4$

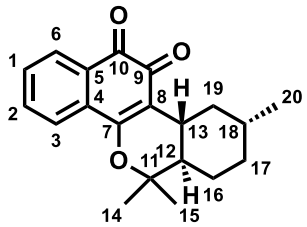
Molecular weight: 180.19 g mol^{-1}

^{1}H NMR (300 MHz, D_2O) δ= 3.32 (s, 4H, H_2), 1.89 (s, 6H, H_3).

Synthesis of (6a*S*,9*R*,10a*S*)-6,6,9-trimethyl-6a,7,8,9,10,10a-hexahydro-6*H*-dibenzo[*c,h*]chromene-11,12-dione (9a)



The method[383] reported for the preparation of compound **9a** was modified as such: 2-hydroxy-1,4-naphthoquinone (500 mg, 2.9 mmol, 1 eq.) was dissolved in 50 mL of absolute ethanol and *R*-citronellal (1.55 mL, 8.6 mmol, 3 eq.) was added. An ethylenediammonium diacetate (EDDA) solution (25.5 mg, 0.14 mmol, 5 mol% in 2 mL of absolute ethanol) was added dropwise which caused a deep red color to be observed. The mixture was heated at 85 °C for one hour. The solvent was evaporated and the crude residue was purified by column chromatography with a gradient of petroleum ether: ethyl acetate (95/5 to 80/20). A red solid was recovered after evaporation (230 mg, 26 % yield).



CAS: 106927-62-2

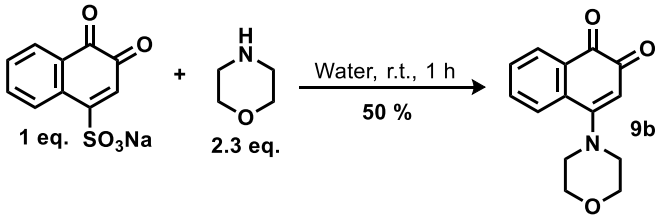
Formula: $C_{20}H_{22}O_3$

Molecular weight: 310.39 g mol^{-1}

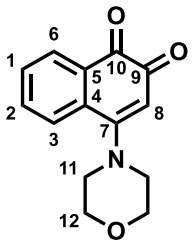
^{1}H NMR (300 MHz, $CDCl_3$) δ= 7.94 (dd, *J* = 7.6, 1.4 Hz, 1H, H_6), 7.76 (dd, *J* = 7.8, 1.1 Hz, 1H, H_3), 7.58 (td, *J* = 7.6, 1.5 Hz, 1H, H_1), 7.42 (td, *J* = 7.5, 1.2 Hz, 1H, H_2), 2.84 (m, 1H, H_{19a}), 2.33 (td, *J* = 11.1, 3.0 Hz, 1H, H_{13}), 1.86 – 1.72 (m, 2H, H_{16a} and H_{17a}), 1.64 – 1.52 (m, 1H, H_{18}), 1.49 (s, 3H, H_{14} or H_{15}), 1.38 (td, *J* = 11.3, 2.6 Hz, 1H, H_{12}), 1.16 (s, 3H, H_{14} or H_{15}), 1.13 – 0.93 (m, 2H, H_{16b} and H_{17b}), 0.86 (d, *J* = 6.6 Hz, 3H, H_{20}), 0.62 – 0.45 (m, 1H, H_{19b}).
^{13}C NMR (75 MHz, $CDCl_3$) δ= 180.3 (C_{10}), 179.0 (C_9), 161.5 (C_7), 134.8 (C_1), 132.9 (C_4 or C_5), 130.5 (C_2), 130.3 (C_4 or C_5), 128.1 (C_6), 124.4 (C_3), 116.7 (C_8), 82.5 (C_{11}), 48.0 (C_{12}), 38.0 (C_{19}), 35.3 (C_{16} or C_{17}), 33.9 (C_{13}), 32.3 (C_{18}), 27.4 (C_{16} or C_{17}), 27.1 (C_{14} or C_{15}), 22.3 (C_{20}), 20.0 (C_{14} or C_{15}).
IR (cm^{-1}) $\tilde{\nu}$ = 2921 (m, alkyl), 1694 (m, aromatic), 1641 (s, C=O), 1565 (s, C=O), 1489 (m, alkyl), 1456 (m, alkyl), 1360 (m, C=O), 1284 (m, C=O), 1232 (s, C–O–C), 1096 (m, aromatic), 782 (s, aromatic).

HRMS (ESI) *m/z* calcd for $C_{20}H_{22}O_3$ + H^+: 311.1642 $[M + H]^+$; found: 311.1639.

Synthesis of 4-morpholinonaphthalene-1,2-dione (9b)



The method[350] reported for the preparation of compound **9b** was modified as such: 1,2-naphthoquinone-4-sulfonic acid sodium salt (1.3 g, 5 mmol, 1 eq.) was dissolved in 30 mL of demineralized water. Morpholine (1 mL, 1 g, 11.5 mmol, 2.3 eq.) was added dropwise and, immediately, a dark red mixture was obtained. The medium was left under stirring for one hour at room temperature during which a precipitate was formed. The solid was recovered by filtration, washed with water and dried under vacuum. The title compound **9b** was obtained as a red solid (616 mg, 50 %).



CAS: 4569-83-9

Formula: $C_{14}H_{13}NO_3$

Molecular weight: 243.26 g mol^{-1}

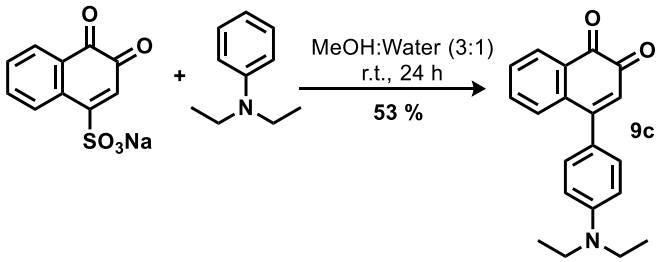
^{1}H NMR (300 MHz, $CDCl_3$) δ= 8.11 (dd, *J* = 7.5, 1.0 Hz, 1H, H_6), 7.70 – 7.60 (m, 1H, H_3), 7.60 – 7.49 (m, 2H, H_1 and H_2), 5.98 (s, 1H, H_8), 3.99 – 3.86 (m, 4H, H_{12}), 3.40 – 3.29 (m, 4H, H_{11}).

^{13}C NMR (75 MHz, $CDCl_3$) δ= 180.4 (C_9 or C_{10}), 179.0 (C_9 or C_{10}), 163.4 (C_7), 134.3 (C_3), 132.3 (C_4 or C_5), 132.2 (C_4 or C_5), 131.0 (C_1 or C_2), 129.9 (C_6), 126.8 (C_1 or C_2), 110.1 (C_8), 66.35 (C_{12}), 51.77 (C_{11}).

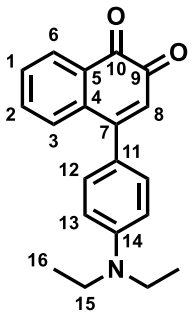
IR (cm^{-1}) $\tilde{\nu}$ = 2975 (m, alkyl), 1686 (s, C=O), 1620 (s, C=O), 1578 (m, aromatic), 1363 (m, C=O), 1293 (m, C=O), 1205 (m, NR_3), 1117 (s, O–C–O), 1096 (m, aromatic), 1023 (m, aromatic), 781 (s, aromatic).

HRMS (ESI) *m/z* calcd for $C_{14}H_{13}O_3N + H^+$: 244.0968 $[M + H]^+$; found: 244.0966.

Synthesis of 4-(4-(diethylamino)phenyl)naphthalene-1,2-dione (9c)



The method[350] reported for the preparation of compound **9c** was modified as such: 1,2-naphthoquinone-4-sulfonic acid sodium salt (660 mg, 2.52 mmol, 1 eq.) was introduced into a 20 mL flask followed by an 8 mL methanol:water (3:1) mixture. To the orange solution, *N,N*-diethylaniline (0.52 mL, 485 mg, 3.25 mmol, 1.3 eq.) was added dropwise which caused the solution to darken. After 24 h, the solution turned to a dark blue. The product was extracted with dichloromethane and then purified *via* flash chromatography (PE:EtOAc 80:20). The compound **9c** was recovered as a blue solid (409 mg, 53 %).



CAS: 123135-53-5

Formula: $C_{20}H_{19}NO_2$

Molecular weight: 305.38 g mol^{-1}

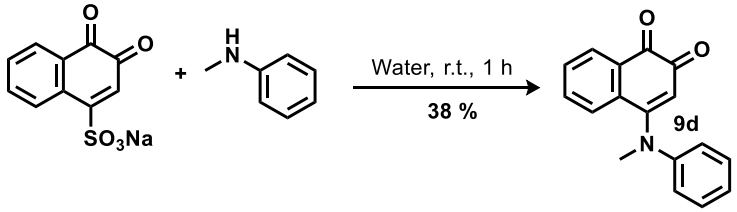
^{1}H NMR (300 MHz, $CDCl_3$) δ= 8.16 (dd, *J* = 7.4, 1.1 Hz, 1H, H_6), 7.62 – 7.56 (m, 2H, H_1 and H_2), 7.54 – 7.45 (m, 1H, H_3), 7.42 – 7.31 (m, 2H, H_{13}), 6.74 (m, 2H, H_{12}), 6.42 (s, 1H, H_8), 3.44 (q, *J* = 7.1 Hz, 4H, H_{15}), 1.23 (t, *J* = 7.1 Hz, 6H, H_{16}).

^{13}C NMR (75 MHz, $CDCl_3$) δ= 180.6 (C_9 or C_{10}), 180.3 (C_9 or C_{10}), 157.5 (C_7), 149.4 (C_{14}), 135.5 (C_4 or C_5), 134.8 (C_1 or C_2), 132.1 (C_4 or C_5), 130.5 (C_3), 130.4 (C_{13}), 130.3 (C_6), 130.0 (C_1 or C_2), 125.5 (C_8), 122.6 (C_{11}), 111.1 (C_{12}), 44.6 (C_{15}), 12.7 (C_{16}).

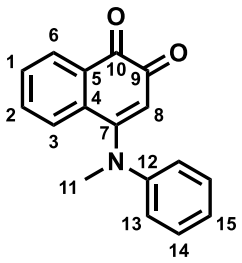
IR (cm^{-1}) $\tilde{\nu}$ = 2962 (m, alkyl), 1695 (m, aromatic), 1642 (C=O), 1598 (s, C=O), 1404 (m, alkyl), 1342 (s, NR_3 aromatic), 1278 (m, C=O), 1263 (m, C=O), 1078 (m, aromatic), 969 (m, aromatic), 819 (s, aromatic).

HRMS (ESI) *m/z* calcd for $C_{20}H_{19}O_2N + H^+$: 306.1489 $[M + H]^+$; found: 306.1487.

Synthesis of 4-(methyl(phenyl)amino)naphthalene-1,2-dione (9d)



The methods[368,384] reported for the preparation of compound **9d** were modified as such: 1,2-naphthoquinone-4-sulfonic acid sodium salt (1.3 g, 5 mmol, 1 eq.) was dissolved in 50 mL of demineralized water. *N*-Methylaniline (1.25 mL, 1.24 g, 11.5 mmol, 2.3 eq.) was added dropwise and, immediately, a dark red mixture was observed. The medium was left under stirring for one hour at room temperature during which a red precipitate was formed. The solid was recovered by filtration, washed with water and dried under vacuum. The title compound **9d** was obtained as a red solid (490 mg, 38 %).



CAS: 17672-02-5

Formula: $C_{17}H_{13}NO_2$

Molecular weight: 263.30 g mol^{-1}

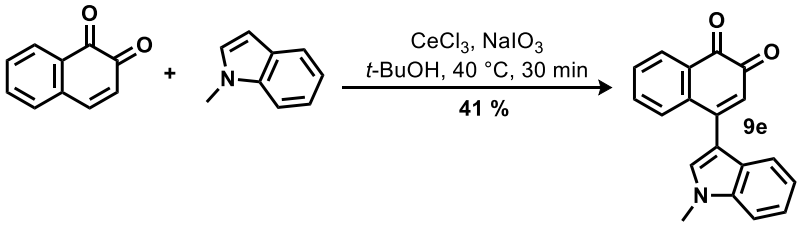
^{1}H NMR (300 MHz, $CDCl_3$) δ= 8.04 (d, J = 6.1 Hz, 1H, H_6), 7.33 (m, 3H, H_1 or H_2 and H_{13} or H_{14}), 7.20 (m, 2H, H_1 or H_2 and H_{15}), 7.10 (m, 2H, H_{13} or H_{14}), 7.01 (d, J = 8.0 Hz, 1H, H_3), 6.26 (s, 1H, H_8), 3.48 (s, 3H, H_{11}).

^{13}C NMR (75 MHz, $CDCl_3$) δ= 180.9 (C_{10}), 178.6 (C_9), 159.7 (C_7), 147.9 (C_{12}), 133.4 (C_1 or C_2), 132.7 (C_4 or C_5), 132.2 (C_4 or C_5), 130.1 (C_1 or C_2), 130.0 (C_{13} or C_{14}), 129.2 (C_6), 129.0 (C_3), 126.5 (C_{15}), 125.5 (C_{13} or C_{14}), 110.9 (C_8), 44.3 (C_{11}).

IR (cm^{-1}) $\tilde{\nu}$ = 3050 (w, aromatic), 2976 (m, alkyl), 1688 (m, aromatic), 1613 (s, C=O), 1528 (s, C=O), 1374 (m, C=O), 1314 (m, C=O), 1285 (s, NR_3 aromatic), 1127 (m, aromatic), 1101 (m, aromatic), 776 (s, aromatic), 694 (s, aromatic).

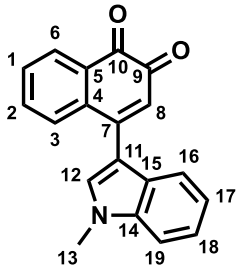
HRMS (ESI) *m/z* calcd for $C_{17}H_{13}O_2N + H^+$: 264.1019 $[M + H]^+$; found: 264.1018.

Synthesis of 4-(1-methyl)-1*H*-indol-3-yl)naphthalene-1,2-dione (9e)



The compound **9e** was prepared according to known literature procedure.[385] 1,2-naphtoquinone (320 mg, 2 mmol, 1 eq.), indole (270 mg, 2 mmol, 1 eq.), cerium chloride (480 mg, 2 mmol, 1 eq.) and sodium iodate (390 mg, 2 mmol, 1 eq.) were dissolved in *t*-butanol (30 mL). The mixture was stirred at 40 °C for 30 min during which a purple precipitate was formed and

recovered by filtration. The crude residue was purified *via* flash chromatography (PE:EtOAc 50:50). The compound **9e** was recovered as a purple solid (10 mg, 17 %).



CAS: /

Formula: $C_{19}H_{13}NO_2$

Molecular weight: 287.32 g mol^{-1}

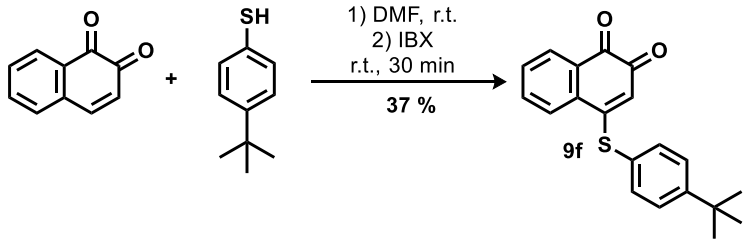
^{1}H NMR (300 MHz, $CDCl_3$) δ= 8.21 (m, 1H, H_6), 7.84 – 7.78 (m, 1H, H_3), 7.68 (dt, *J* = 8.0, 1.0 Hz, 1H, H_{17} or H_{18}), 7.60 (td, *J* = 7.5, 1.8 Hz, 1H, H_1 or H_2), 7.54 (td, *J* = 7.4, 1.5 Hz, 1H, H_1 or H_2), 7.44 (s, 1H, H_{12}), 7.45 – 7.41 (m, 1H, H_{19}), 7.40 – 7.32 (m, 1H, H_{17} or H_{18}), 7.25 – 7.20 (m, 1H, H_{16}), 6.70 (s, 1H, H_8), 3.93 (s, 3H, H_{13}).

^{13}C NMR (75 MHz, $CDCl_3$) δ= 180.5 (C_9 or C_{10}), 180.3 (C_9 or C_{10}), 151.1 (C_7), 137.8 (C_{14}), 135.3 (C_4 or C_5), 134.9 (C_1 or C_2), 132.2 (C_4 or C_5), 131.0 (C_{19}), 130.8 (C_1 or C_2), 130.4 (C_6), 129.5 (C_3), 126.8 (C_{15}), 125.7 (C_8), 123.4 (C_{17} or C_{18}), 121.4 (C_{16}), 121.0 (C_{17} or C_{18}), 112.0 (C_{11}), 110.3 (C_{12}), 33.6 (C_{13}).

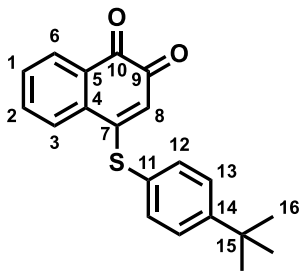
IR (cm^{-1}) $\tilde{\nu}$ = 3052 (w, aromatic), 1687 (m, aromatic), 1617 (s, C=O), 1582 (s, C=O), 1372 (s, NR_3), 1294 (m, C=O), 1214 (m, C=O), 1136 (m, aromatic), 1074 (m, aromatic), 741 (s, aromatic).

HRMS (ESI) *m/z* calcd for $C_{19}H_{13}O_2N + H^+$: 288.1019 $[M + H]^+$; found: 288.1018.

Synthesis of 4-((4-(*tert*-butyl)phenyl)thio)naphthalene-1,2-dione (9f)



The method[353] reported for the preparation of compound **9f** was modified as such: a solution of 4-(*tert*-butyl)benzenethiol (1.25 g, 7.5 mmol, 1.2 eq.) in dimethylformamide was added dropwise to a solution of naphthalene-1,2-dione (1 g, 6.3 mmol, 1 eq.) in dimethylformamide. The mixture was left under stirring at room temperature and was monitored by TLC. After reaction, 2-iodoxybenzoic acid (IBX) (45 wt.%, 1.96 g, 3.15 mmol, 0.5 eq.) was added and the solution was left under stirring for 30 minutes. Water was added (5 times the volume of dimethylformamide) and the aqueous phase was extracted three times with ethyl acetate. The organic phases were combined, washed with brine, dried over $MgSO_4$ and the solvent was removed under reduced pressure. The crude residue was purified by column chromatography using petroleum ether: ethyl acetate (80/20) as eluent. Compound **9f** was obtained as an orange/red solid (0.8 g, 37 % yield).



CAS: /

Formula: $C_{20}H_{18}N_2S$

Molecular weight: 322.42 g mol^{-1}

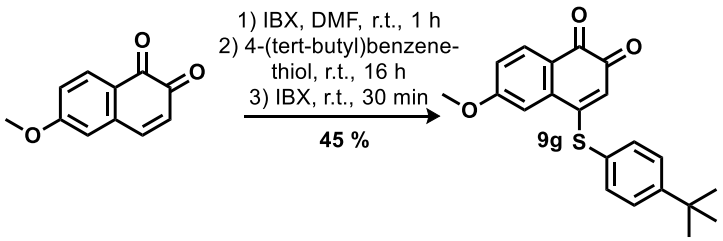
^{1}H NMR (300 MHz, $CDCl_3$) δ= 8.18 (dd, *J* = 7.6, 1.0 Hz, 1H, H_6), 7.96 (dd, *J* = 7.8, 0.8 Hz, 1H, H_3), 7.73 (td, *J* = 7.7, 1.5 Hz, 1H, H_1), 7.60 (td, *J* = 7.6, 1.1 Hz, 1H, H_2), 7.55 – 7.46 (m, 4H, H_{12} and H_{13}), 5.95 (s, 1H, H_8), 1.37 (s, 9H, H_{16}).

^{13}C NMR (75 MHz, $CDCl_3$) δ= 179.8 (C_9 or C_{10}), 176.9 (C_9 or C_{10}), 162.2 (C_7), 154.9 (C_{11}), 135.8 (C_{12}), 135.20 (C_1), 133.7 (C_4 or C_5), 131.4 (C_2), 130.5 (C_4 or C_5), 129.6 (C_6), 127.7 (C_{13}), 125.2 (C_3), 122.8 (C_{14}), 121.4 (C_8), 35.2 (C_{15}), 31.3 (C_{16}).

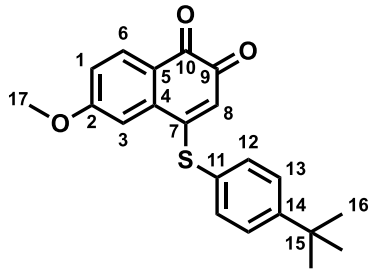
IR (cm^{-1}) $\tilde{\nu}$ = 2964 (m, alkyl), 1697 (m, aromatic), 1639 (s, C=O), 1538 (s, C=O), 1449 (m, alkyl), 1318 (m, C=O), 1288 (m, C=O), 1014 (m, aromatic), 772 (s, aromatic), 663 (s, S–C).

HRMS (ESI) *m/z* calcd for $C_{20}H_{19}O_2{}^{32}S + H^+$: 323.1100 $[M + H]^+$; found: 323.1096.

Synthesis of 4-((4-(*tert*-butyl)phenyl)thio)-6-methoxynaphthalene-1,2-dione (9g)



6-methoxynaphthalen-2-ol (87 mg, 0.5 mmol, 1 eq.) was dissolved in 3 mL of dry dimethylformamide and IBX (45 wt.%, 342 mg, 0.55 mmol, 1.1 eq.) was added. The mixture was stirred at room temperature for 1 h. 4-(*tert*-butyl)benzenethiol (0.1 mL, 0.6 mmol, 1.2 eq.) was added and the solution was left under stirring for 16 h at room temperature. IBX (156 mg, 0.25 mmol, 0.5 eq.) was added and the mixture was stirred for 30 min at room temperature. After reaction, 10 mL of demineralized water were poured along with 10 mL of ethyl acetate. The aqueous phase was extracted three times with ethyl acetate and the organic phases were combined, washed with $NaHCO_3$ (10 %), saturated NaCl and LiCl (10 %) and dried over $MgSO_4$. The crude residue was purified by column chromatography with petroleum ether: ethyl acetate (85/15). The corresponding naphthoquinone **9g** was obtained (79 mg, 45 % yield).



CAS: /

Formula: $C_{21}H_{20}O_3S$

Molecular weight: 352.45 g mol^{-1}

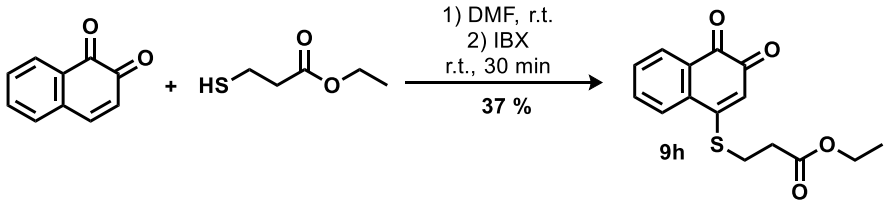
^{1}H NMR (300 MHz, $CDCl_3$) δ= 8.12 (d, *J* = 8.6 Hz, 1H, H_6), 7.55 – 7.43 (m, 4H, H_{12} and H_{13}), 7.38 (d, *J* = 2.4 Hz, 1H, H_3), 6.99 (dd, *J* = 8.6, 2.4 Hz, 1H, H_1), 5.90 (s, 1H, H_8), 3.94 (s, 3H, H_{17}), 1.35 (s, 9H, H_{16}).

^{13}C NMR (75 MHz, $CDCl_3$) δ= 178.2 (C_{10}), 177.5 (C_9), 165.1 (C_2), 161.1 (C_7), 154.8 (C_{14}), 135.8 (C_{12} or C_{13}), 135.7 (C_4 or C_5), 132.5 (C_6), 127.6 (C_{12} or C_{13}), 124.0 (C_4 or C_5), 122.7 (C_{11}), 121.9 (C_8), 115.0 (C_1), 111.9 (C_3), 56.1 (C_{17}), 35.1 (C_{15}), 31.2 (C_{16}).

IR (cm^{-1}): $\tilde{\nu}$ = 2955 (m, alkyl), 1681 (m, aromatic), 1634 (s, C=O), 1586 (s, C=O), 1459 (m, alkyl), 1269 (s, C–O–C), 1098 (m, aromatic), 1023 (s, C–O–C), 950 (m, aromatic), 866 (s, aromatic), 850 (s, aromatic), 631 (s, S–C).

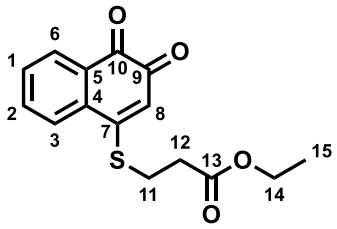
HRMS (ESI) *m/z* calcd for $C_{21}H_{20}O_3{}^{32}S + H^+$: 353.1206 $[M + H]^+$; found 353.1204.

Synthesis of ethyl 3-((3,4-dioxo-3,4-dihydronaphthalen-1-yl)thio)propanoate (9h)



A solution of ethyl 3-mercaptopropanoate (0.55 mL, 4.3 mmol, 1.2 eq.) in dimethylformamide was added dropwise to a solution of naphthalene-1,2-dione (550 mg, 3.5 mmol, 1 eq.) in dimethylformamide. The mixture was left under stirring at room temperature and was monitored by TLC. After reaction,

IBX (1.96 g, 3.15 mmol, 0.5 eq.) was added and the solution was left under stirring for an additional 30 minutes. Water was added (5 times the volume of dimethylformamide) and the aqueous phase was extracted three times with ethyl acetate. The organic phases were combined, washed with brine, dried over $MgSO_4$ and the solvent was removed under reduced pressure. The crude residue was purified by column chromatography using petroleum ether: ethyl acetate (80/20) as eluent. A dark orange solid corresponding to compound **9h** was obtained (0.8 g, 37 % yield).



CAS: /

Formula: $C_{15}H_{14}O_4S$

Molecular weight: 290.33 g mol^{-1}

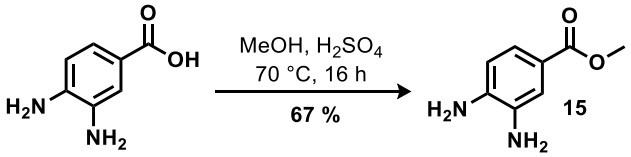
^{1}H NMR (300 MHz, $CDCl_3$) δ= 8.15 (dd, *J* = 7.5, 1.2 Hz, 1H, H_6), 7.82 – 7.78 (m, 1H, H_3), 7.67 (td, *J* = 7.7, 1.6 Hz, 1H, H_1 or H_2), 7.56 (td, *J* = 7.5, 1.2 Hz, 1H, H_1 or H_2), 6.41 (s, 1H, H_8), 4.20 (q, *J* = 7.1 Hz, 2H, H_{14}), 3.32 (t, *J* = 7.1 Hz, 2H, H_{11}), 2.81 (t, *J* = 7.1 Hz, 2H, H_{12}), 1.29 (t, *J* = 7.1 Hz, 3H, H_{15}).

^{13}C NMR (75 MHz, $CDCl_3$) δ= 179.5 (C_{10}), 176.4 (C_9), 170.7 (C_{13}), 159.0 (C_7), 135.2 (C_1 or C_2), 133.6 (C_4 or C_5), 131.4 (C_1 or C_2), 130.6 (C_4 or C_5), 129.5 (C_6), 125.3 (C_3), 119.8 (C_8), 61.5 (C_{14}), 32.5 (C_{11} or C_{12}), 26.5 (C_{11} or C_{12}), 14.3 (C_{15}).

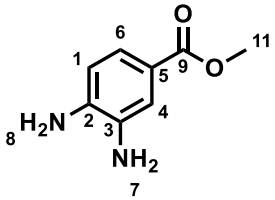
IR (cm^{-1}): $\tilde{\nu}$ = 2915 (m, alkyl), 1714 (s, O=C–O), 1646 (s, C=O), 1581 (m, alkyl), 1545 (s, C=O), 1375 (m, C=O), 1186 (s, COOEt), 940 (m, aromatic), 768 (s, aromatic), 658 (s, S–C).

HRMS (ESI) *m/z* calcd for $C_{15}H_{14}O_4{}^{32}S + H^+$: 291.0686 $[M + H]^+$; found 291.0686.

Synthesis of methyl-3,4-diaminobenzoate (15)



The method[386] reported for the preparation of methyl-3,4-diaminobenzoate was modified as such: diamino benzoic acid (520 mg, 3.4 mmol, 1 eq.) was added to a 25 mL two-necked flask with 10 mL of methanol. Sulfuric acid (1 mL, 5.7 eq.) was added dropwise to the resulting suspension, which gave a dark brown coloration to the reaction mixture. The latter was then heated at 70 °C and left under stirring for 16 h. After reaction, the medium was concentrated and the acidity was neutralized with a 1 M sodium hydroxide solution. The organic phase was then extracted with dichloromethane, dried over $MgSO_4$ and filtered. Methyl-3,4-diaminobenzoate was obtained as a white-brown solid (380 mg, 67 % yield).



CAS: 36692-49-6

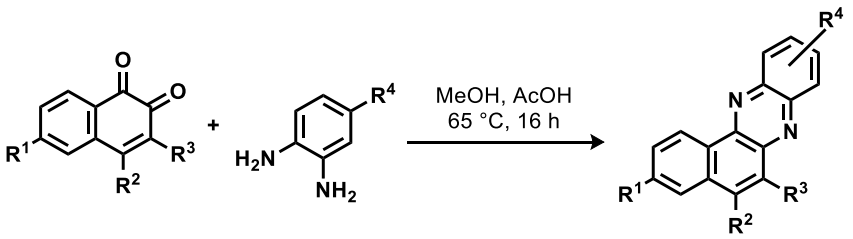
Formula: $C_8H_{10}N_2O_2$

Molecular weight: 166.18 g mol^{-1}

^{1}H NMR (300 MHz, $CDCl_3$) δ= 7.46 (dd, *J* = 8.1, 1.9 Hz, 1H, H_6), 7.40 (d, *J* = 1.9 Hz, 1H, H_4), 6.66 (d, *J* = 8.1 Hz, 1H, H_1), 3.84 (s, 3H, H_{11}), 3.56 (bs, 4H, H_7 and H_8).

^{13}C NMR (75 MHz, $CDCl_3$) δ= 167.5 (C_9), 140.5 (C_2 or C_3), 133.2 (C_2 or C_3), 123.4 (C_6), 121.2 (C_5), 118.4 (C_4), 115.0 (C_1), 51.8 (C_{11}).

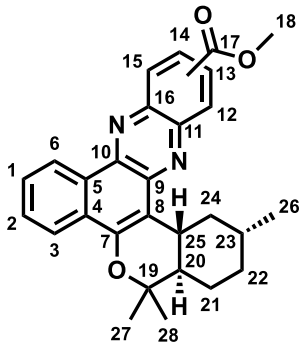
General procedure for the benzo[*a*]phenazine compounds synthesis and its description for each compound



A solution of diamine (0.33 mmol, 1.1 eq., C = ~ 0.15 M) was added dropwise to a suspension of naphthoquinone (0.3 mmol, 1 eq.) in dry methanol (2 mL), followed by the addition of glacial acetic acid (5 drops). The mixture was heated at 65 °C for 16 h. After a few minutes, a precipitate was formed. After reaction, the suspension was cooled down slowly to room temperature. The precipitate was recovered by filtration and washed with 50 mL of methanol.

The NMR characterization is difficult due to the presence of two regioisomers. The attributions are done as far as possible. The ratios of regioisomers are determined with the $COOCH_3$ signal or the singlet signal of H_8. For particular cases, H_{12} needs to be considered.

Methyl (2R,4aR,16cR)-2,5,5-trimethyl-1,3,4,4a,5,16c-hexahydro-2H-benzo[a]isochromeno[3,4-c]phenazine-13,14-carboxylate ***(10a)*** was synthesized from naphthoquinone **4** (200 mg, 0.64 mmol) and methyl 3,4-diaminobenzoate **15** (120 mg, 0.72 mmol) by following the general procedure described above. The desired compound was obtained as a yellow powder. Yield: 97 %.



CAS: /

Formula: $C_{28}H_{28}N_2O_3$

Molecular weight: 440.54 g mol^{-1}

Regioisomers ratio: 55/45 (H_{18})

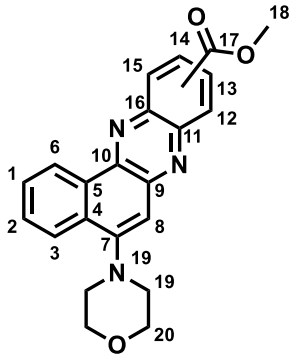
^{1}H NMR (300 MHz, $CDCl_3$) δ= 9.37 – 9.24 (m, 2H, H_6), 9.01 (m, 1H), 8.98 (m, 1H), 8.97 – 8.92 (m, 1H), 8.39 – 8.20 (m, 6H), 7.84 – 7.71 (m, 4H,), 4.05 (s, 3H, H_{18}), 4.04 (s, 3H, H_{18}), 3.67 (m, 2H), 3.13 (m, 2H), 2.06 – 1.92 (m, 4H), 1.81 – 1.67 (m, 2H), 1.63 (s, 6H), 1.46 – 1.32 (m, 4H), 1.25 (s, 6H), 1.22 – 1.12 (m, 2H), 1.00 (m, 6H), 0.72 (q, J = 11.6 Hz, 2H).

^{13}C NMR (75 MHz, $CDCl_3$) δ= 166.9 (C_{17}), 152.3, 141.4, 132.5, 131.8, 130.4, 130.2, 130.0, 129.6, 129.2, 128.9, 128.6, 128.1, 127.9, 127.2, 125.4, 125.1, 122.6, 113.4, 79.6, 79.4, 52.6 (C_{18}), 50.0, 50.0, 40.5, 36.1, 36.0, 33.0, 28.1, 27.6 (C_{27} or C_{28}), 22.7 (C_{26}), 19.2 (C_{27} or C_{28}).

IR (cm^{-1}): $\tilde{\nu}$ = 2981 (m, alkyl), 1717 (s, COOEt), 1388 (m, NR_3), 1254 (s, COOEt), 1211 (s, O–C–O), 1140 (s, aromatic), 1090 (m, COOEt), 724 (s, aromatic).

HRMS (ESI) *m/z* calcd for $C_{28}H_{28}O_3N_2 + H^+$: 441.2173 $[M + H]^+$; found 441.2171.

Methyl 5-morpholinobenzo[a]phenazine-9,10-carboxylate ***(10b)*** was synthesized from 4-morpholinonaphthalene-1,2-dione **9b** (243 mg, 1 mmol) and methyl 3,4-diaminobenzoate **15** (183 mg, 1.1 mmol) by following the general procedure described above. The desired compound was obtained as a bright yellowish powder. Yield: 78 %.



CAS: /

Formula: $C_{22}H_{19}N_3O_3$

Molecular weight: 373.41 g mol^{-1}

Regioisomers ratio: 81/19 (H_{18})

85/15 (H_8)

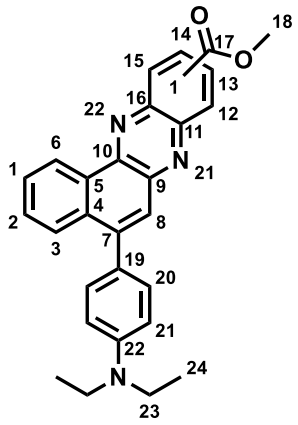
^{1}H NMR (300 MHz, $CDCl_3$) δ= 9.47 – 9.37 (m, 2H, H_6), 9.04 (m, 1H), 8.92 (m, 1H), 8.35 (m, 4H), 8.21 (m, 2H), 7.87 – 7.76 (m, 4H), 7.42 (s, 1H, H_8), 7.41 (s, 1H, H_8), 4.07 (m, 8H, H_{20}), 4.04 (s, 6H, H_{18}), 3.32 (s, 8H, H_{19}).

^{13}C NMR (75 MHz, $CDCl_3$) δ= 166.6 (C_{17}), 153.8, 145.5, 142.9, 142.7, 142.1, 131.9, 131.6, 131.0, 130.8, 130.2, 129.9, 128.3, 128.0, 126.5 (C_6), 124.5, 112.6 (C_8), 67.1 (C_{20}), 53.0 (C_{19}), 52.7 (C_{18}).

IR (cm^{-1}): $\tilde{\nu}$ = 2981 (m, alkyl), 1714 (s, COOEt), 1361 (s, NR_3), 1264 (s, COOEt), 1188 (s, aromatic), 1117 (s, C–O–C), 1089 (m, COOEt), 778 (s, aromatic).

HRMS (ESI) *m/z* calcd for $C_{22}H_{19}O_3N_3 + H^+$: 374.1499 $[M + H]^+$; found 374.1498.

*Methyl 5-(4-(diethylamino)phenyl)benzo[a]phenazine-9,10-carboxylate **(10c)*** was synthesized from 4-(4-(diethylamino)phenyl)naphthalene-1,2-dione **9c** (380 mg, 1.2 mmol) and methyl 3,4-diaminobenzoate **15** (230 mg, 1.38 mmol) by following the general procedure described above. The desired compound was obtained as an orange powder. Yield: 88 %.



CAS: /

Formula: $C_{28}H_{25}N_3O_2$

Molecular weight: 435.53 g mol^{-1}

Regioisomers ratio: 70/30 (H_{18})

71/29 (H_8)

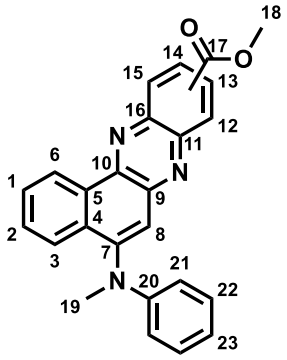
^{1}H NMR (300 MHz, $CDCl_3$) δ= 9.53 – 9.42 (m, 2H, H_6), 9.06 (m, 1H), 9.00 – 8.92 (m, 1H), 8.37 (m, 4H), 8.19 – 8.09 (m, 2H, H_3), 7.89 (s, 1H, H_8), 7.88 (s, 1H, H_8), 7.85 – 7.69 (m, 4H, H_1 and H_2), 7.51 (d, *J* = 8.9 Hz, 4H, H_{20} or H_{21}), 6.84 (m, 4H, H_{20} or H_{21}), 4.05 (s, 3H, H_{18}), 4.04 (s, 3H, H_{18}), 3.47 (q, *J* = 7.1 Hz, 8H, H_{23}), 1.27 (t, *J* = 7.1 Hz, 12H, H_{24}).

^{13}C NMR (75 MHz, $CDCl_3$) δ= 166.7 (C_{17}), 147.9, 147.3, 146.5, 145.0, 144.6, 143.7, 143.4, 143.3, 142.3, 140.8, 133.8, 133.4, 132.9, 132.2, 131.5, 131.4, 131.0 (C_{20} or C_{21}), 130.4, 130.2, 130.0, 129.3, 129.1, 128.5, 128.0, 127.9, 127.6, 126.2, 126.1, 126.0, 125.9, 125.7 (C_8), 111.4 (C_{20} or C_{21}), 52.7 (C_{18}), 44.5 (C_{23}), 12.8 (C_{24}).

IR (cm^{-1}): $\tilde{\nu}$ = 2970 (m, alkyl), 1717 (s, COOEt), 1354 (s, NR_3), 1268 (s, COOEt), 1194 (s, aromatic), 1092 (m, COOEt), 751 (s, aromatic).

HRMS (ESI) *m/z* calcd for $C_{28}H_{26}O_2N_3$ $[M + H]^+$ 436.2020, found 436.2020.

*Methyl 5-(methyl(phenyl)amino)benzo[a]phenazine-9,10-carboxylate **(10d)*** was synthesized from 4-(methyl(phenyl)amino)naphthalene-1,2-dione **9d** (170 mg, 0.64 mmol) and methyl 3,4-diaminobenzoate **15** (117 mg, 0.7 mmol) by following the general procedure described above. The desired compound was obtained as a red powder. Yield: 68 %.



CAS: /

Formula: $C_{25}H_{19}N_3O_2$

Molecular weight: 393.45 g mol^{-1}

Regioisomers ratio: 80/20 (H_{18})
82/18 (H_8)

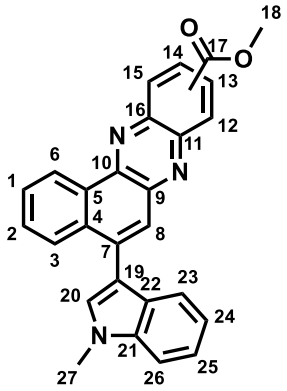
^{1}H NMR (300 MHz, $CDCl_3$) δ= 9.53 – 9.39 (m, 1H, H_6), 9.08 (m, 1H), 8.97 – 8.93 (m, 1H), 8.49 – 8.34 (m, 4H), 7.97 – 7.84 (m, 1H, H_3), 7.80 – 7.74 (m, 1H, H_1 or H_2), 7.76 (s, 2H, H_8), 7.63 (m, 2H, H_1 or H_2), 7.26 – 7.19 (m, 4H), 7.03 – 6.83 (m, 6H), 4.06 (s, 3H, H_{18}), 4.05 (s, 3H, H_{18}), 3.62 (s, 3H, H_{19}), 3.61 (s, 3H, H_{19}).

^{13}C NMR (75 MHz, $CDCl_3$) δ= 166.7 (C_{17}), 151.0, 150.1, 145.6, 143.2, 142.3, 132.1, 131.9, 131.2, 130.3, 130.1, 129.4, 128.4, 128.3, 126.3 (C_6), 125.9 (C_3), 121.2, 119.8, 119.6, 119.0, 52.8 (C_{18}), 42.2 (C_{19}).

IR (cm^{-1}): $\tilde{\nu}$ = 2982 (m, alkyl), 1714 (s, COOEt), 1385 (m, NR_3), 1256 (s, COOEt), 1191 (s, aromatic), 1088 (m, COOEt), 774 (s, aromatic), 757 (s, aromatic), 694 (s, aromatic).

HRMS (ESI) *m/z* calcd for $C_{25}H_{19}O_2N_3$ + H^+: 394.1550 $[M + H]^+$; found 394.1550.

*Methyl 5-(1-methyl-1H-indol-3-yl)benzo[a]phenazine-9,10-carboxylate **(10e)*** was synthesized from 4-(1-methyl)-1*H*-indol-3-yl)naphthalene-1,2-dione **9e** (100 mg, 0.35 mmol) and methyl 3,4-diaminobenzoate **15** (45 mg, 0.39 mmol) by following the general procedure described above. The desired compound was obtained as an orange powder. Yield: 83 %.



CAS: /

Formula: $C_{27}H_{19}N_3O_2$

Molecular weight: 417.47 g mol^{-1}

Regioisomers ratio: 70/30 (H_{18})

75/25 (H_8)

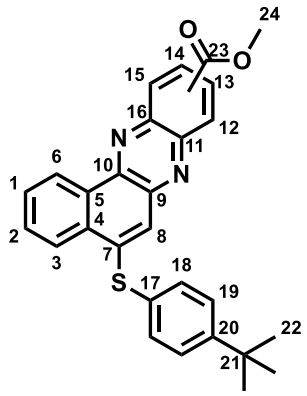
^{1}H NMR (300 MHz, $CDCl_3$) δ= 9.54 (m, 2H, H_6), 9.12 (m, 1H), 9.06 (m, 1H), 8.49 – 8.34 (m, 4H), 8.33 – 8.23 (m, 2H, H_3), 8.11 (s, 1H, H_8), 8.10 (s, 1H, H_8), 7.89 – 7.80 (m, 2H, H_1 or H_2), 7.78 – 7.72 (m, 1H, H_1 or H_2), 7.68 (m, 2H), 7.53 – 7.45 (m, 2H), 7.45 (s, 2H, H_{20}), 7.36 (m, 2H), 7.19 (m, 2H), 4.07 (s, 3H, H_{18}), 4.05 (s, 3H, H_{18}), 3.98 (s, 6H, H_{27}).

^{13}C NMR (75 MHz, $CDCl_3$) δ= 166.7 (C_{17}), 144.7, 143.8, 143.5, 142.4, 139.5, 137.3, 133.9, 132.9, 132.3, 131.5, 131.1, 130.3, 130.1, 129.3, 128.6, 128.1, 127.8, 127.7, 127.0 (C_8), 126.2 (C_6), 126.0, 122.6, 120.8, 120.4, 113.9, 109.9 (C_{20}), 52.8 (C_{18}), 33.3 (C_{27}).

IR (cm^{-1}): $\tilde{\nu}$ = 2980 (m, alkyl), 1728 (s, COOEt), 1372 (m, NR_3), 1255 (s, COOEt), 1193 (s, aromatic), 1089 (m, COOEt), 725 (s, aromatic).

HRMS (ESI) *m/z* calcd for $C_{27}H_{19}O_2N_3$ + H^+: 418.1550 $[M + H]^+$; found 418.1550.

*Methyl 5-((4-(tert-butyl)phenyl)thio)benzo[a]phenazine-9,10-carboxylate **(10f-1)*** was synthesized from 4-((4-(*tert*-butyl)phenyl)thio)naphthalene-1,2-dione **9f** (530 mg, 1.6 mmol) and methyl 3,4-diaminobenzoate **15** (300 mg, 1.8 mmol) by following the general procedure described above. The desired compound was obtained as a yellow powder. Yield: 86 %.



CAS: /

Formula: $C_{28}H_{24}N_2O_2S$

Molecular weight: 452.57 g mol^{-1}

Regioisomers ratio: 65/35 (H_{24})
62/38 (H_8)

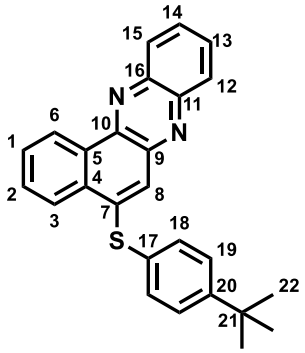
^{1}H NMR (300 MHz, $CDCl_3$) δ= 9.49 – 9.40 (m, 2H, H_6), 9.01 (m, 1H), 8.86 (m, 1H), 8.46 – 8.38 (m, 2H, H_3), 8.38 – 8.28 (m, 3H), 8.13 (m, 1H), 7.93 – 7.81 (m, 4H, H_1 and H_2), 7.62 (m, 4H, H_{18} or H_{19}), 7.54 (m, 4H, H_{18} or H_{19}), 7.43 (s, 1H, H_8), 7.40 (s, 1H, H_8), 4.04 (s, 3H, H_{24}), 4.01 (s, 3H, H_{24}), 1.58 (s, 9H, H_{22}), 1.41 (s, 9H, H_{22}).

^{13}C NMR (75 MHz, $CDCl_3$) δ (ppm) 166.5, 166.5, 153.4, 153.3, 146.3, 145.0, 144.6, 144.5, 144.1, 143.2, 143.1, 142.8, 142.0, 140.5, 135.5, 135.3, 132.8, 131.9, 131.8, 131.5, 131.2, 130.7, 130.5, 130.4, 130.0, 129.3, 129.0, 128.9, 128.7, 128.4, 127.5, 127.5, 126.2, 126.2, 126.0, 124.4, 124.3, 122.6, 122.2, 52.7 (C_{24}), 35.1 (C_{21}), 31.4 (C_{22}).

IR (cm^{-1}): $\tilde{\nu}$ = 2965 (m, alkyl), 1720 (s, COOEt), 1369 (s, NR_3), 1254 (s, COOEt), 1197 (s, aromatic), 1090 (m, COOEt), 766 (s, aromatic), 755 (s, aromatic).

HRMS (ESI) *m/z* calcd for $C_{28}H_{24}O_2N_2{}^{32}S + H^+$: 453.1631 $[M + H]^+$; found 453.1631.

*5-((4-(tert-butyl)phenyl)thio)benzo[a]phenazine (**10f-2**)* was synthesized from 4-((4-(*tert*-butyl)phenyl)thio)naphthalene-1,2-dione **9f** (84 mg, 0.26 mmol) and commercially available benzene-1,2-diamine (31.4 mg, 0.29 mmol) by following the general procedure described above. The desired compound was obtained as a yellow powder. Yield: 80 %.



CAS: /

Formula: $C_{26}H_{22}N_2S$

Molecular weight: 394.54 g mol^{-1}

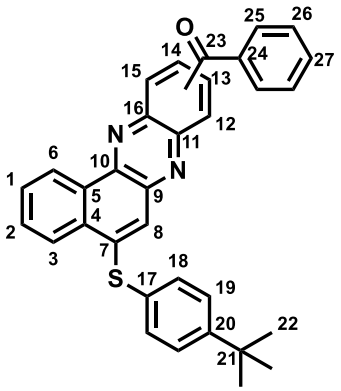
^{1}H NMR (300 MHz, $CDCl_3$) δ= 9.50 – 9.40 (m, 1H, H_6), 8.47 – 8.36 (m, 1H, H_3), 8.34 – 8.25 (m, 1H, H_{12} or H_{15}), 8.18 – 8.07 (m, 1H, H_{12} or H_{15}), 7.88 – 7.81 (m, 2H, H_1 and H_2), 7.81 – 7.74 (m, 2H, H_{13} and H_{14}), 7.65 – 7.57 (m, 2H, H_{18}), 7.55 – 7.49 (m, 2H, H_{19}), 7.48 (s, 1H, H_8), 1.40 (s, 9H, H_{22}).

^{13}C NMR (75 MHz, $CDCl_3$) δ (ppm) 153.0 (C_{20}), 143.9 (C_7 or C_{10}), 143.4 (C_7 or C_{10}), 143.0 (C_{11} or C_{16}), 142.0 (C_9), 141.6 (C_{11} or C_{16}), 135.1 (C_{18}), 131.6 (C_4 or C_5), 130.9 (C_4 or C_5), 130.3 (C_1, C_2, C_{13} or C_{14}), 130.1 (C_1, C_2, C_{13} or C_{14}), 129.8 (C_{12} or C_{15}), 129.4 (C_1, C_2, C_{13} or C_{14}), 128.8 (C_{12} or C_{15}), 128.5 (C_1, C_2, C_{13} or C_{14}), 127.4 (C_{19}), 126.6 (C_{17}), 125.8 (C_6), 124.4 (C_3), 123.3 (C_8), 35.0 (C_{21}), 31.4 (C_{22}).

IR (cm^{-1}): $\tilde{\nu}$ = 2965 (m, alkyl), 1491 (m, aromatic), 1363 (s, NR_3), 1012 (m, aromatic), 753 (s, aromatic).

HRMS (ESI) *m/z* calcd for $C_{26}H_{22}N_2{}^{32}S + H^+$: 395.1577 $[M + H]^+$; found 395.1579.

*5-((4-(tert-butyl)phenyl)thio)benzo[a]phenazine-9,10-yl)(phenyl)methanone **(10f-3)*** was synthesized from 4-((4-(*tert*-butyl)phenyl)thio)naphthalene-1,2-dione **9f** (150 mg, 0.47 mmol) and commercially available (3,4-diaminophenyl)(phenyl)methanone (110.4 mg, 0.52 mmol) by following the general procedure described above. The desired compound was obtained as a yellow powder. Yield: 84 %.



CAS: /

Formula: $C_{33}H_{26}N_2OS$

Molecular weight: 498.64 g mol^{-1}

Regioisomers ratio: 80/20 (H_8)

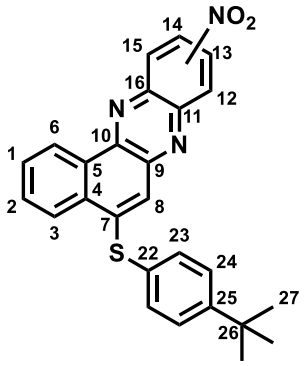
^{1}H NMR (300 MHz, $CDCl_3$) δ= 9.50 – 9.42 (m, 1H, H_6), 9.40 – 9.34 (m, 1H, H_6), 8.65 (d, *J* = 1.8 Hz, 1H), 8.47 (d, *J* = 1.8 Hz, 1H), 8.43 – 8.33 (m, 4H), 8.28 (dd, *J* = 8.9, 1.9 Hz, 1H), 8.20 (d, *J* = 8.9 Hz, 1H), 8.00 – 7.78 (m, 8H), 7.60 (m, 8H), 7.54 – 7.46 (m, 6H), 7.42 (s, 1H, H_8), 7.38 (s, 1H, H_8), 1.41 (s, 9H, H_{22}), 1.38 (s, 9H, H_{22}).

^{13}C NMR (75 MHz, $CDCl_3$) δ (ppm) 196.0 (C_{23}), 153.3, 145.3, 144.2, 143.3, 143.0, 141.8, 138.3, 137.3, 135.4, 132.8, 132.5, 131.8, 130.7, 130.5, 130.2, 128.9, 128.8, 128.6, 127.5, 126.2, 126.0, 124.4, 122.3, 35.1, 35.0 (C_{21}), 31.4 (C_{22}).

IR (cm^{-1}): $\tilde{\nu}$ = 2968 (m, alkyl), 1661 (s, C=O), 1582 (m, aromatic), 1367 (s, NR_3), 1313 (m, C=O), 767 (s, aromatic), 731 (s, aromatic), 711 (s, aromatic).

HRMS (ESI) *m/z* calcd for $C_{33}H_{26}O_2N_2{}^{32}S + H^+$: 499.1839 $[M + H]^+$; found 499.1840.

*5-((4-(tert-butyl)phenyl)thio)-9,10-nitrobenzo[a]phenazine (**10f-4**)* was synthesized from 4-((4-(*tert*-butyl)phenyl)thio)naphthalene-1,2-dione **9f** (100 mg, 0.31 mmol) and commercially available 4-nitrobenzene-1,2-diamine (52 mg, 0.34 mmol) by following the general procedure described above. The desired compound was obtained as a yellow powder. Yield: 58 %.



CAS: /

Formula: $C_{26}H_{21}N_3O_2S$

Molecular weight: 439.53 g mol^{-1}

Regioisomers ratio: 75/25 (H_8)

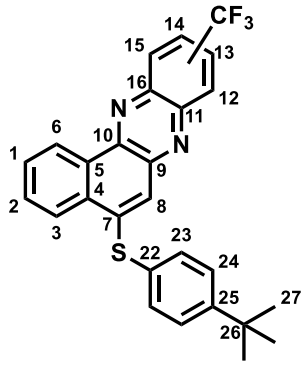
^{1}H NMR (300 MHz, CD_2Cl_2) δ= 9.46 – 9.36 (m, 2H, H_6), 9.14 (d, *J* = 2.6 Hz, 1H), 8.95 (d, *J* = 2.5 Hz, 1H), 8.53 – 8.33 (m, 6H), 7.96 – 7.84 (m, 4H), 7.68 – 7.50 (m, 8H), 7.30 (s, 1H, H_8), 7.26 (s, 1H, H_8), 1.52 (s, 9H, H_{27}), 1.40 (s, 9H, H_{27}).

^{13}C NMR (75 MHz, CD_2Cl_2) δ (ppm) 153.6, 147.9, 146.4, 144.8, 143.9, 143.3, 141.4, 135.4, 135.2, 132.0, 131.2, 130.2, 129.0, 127.4, 126.2, 125.9, 125.4, 124.4, 122.1, 122.0, 34.8 (C_{26}), 31.0 (C_{27}).

IR (cm^{-1}): $\tilde{\nu}$ = 2969 (m, alkyl), 1585 (m, aromatic), 1514 (m, NO_2), 1369 (m, NR_3), 1339 (s, NO_2), 839 (s, aromatic), 765 (s, aromatic), 737 (s, aromatic).

HRMS (ESI) *m/z* calcd for $C_{26}H_{21}O_2N_3{}^{32}S + H^+$: 440.1427 $[M + H]^+$; found 440.1429.

*5-((4-(tert-butyl)phenyl)thio)-9,10-(trifluoromethyl)benzo[a]phenazine **(10f-5)*** was synthesized from 4-((4-(*tert*-butyl)phenyl)thio)naphthalene-1,2-dione **9f** (100 mg, 0.31 mmol) and commercially available 4-(trifluoromethyl)benzene-1,2-diamine (60 mg, 0.34 mmol) by following the general procedure described above. The desired compound was obtained as a yellow powder. Yield: 68 %.



CAS: /

Formula: $C_{27}H_{21}F_3N_2S$

Molecular weight: 462.53 g mol^{-1}

Regioisomers ratio: 60/40 (H_8)

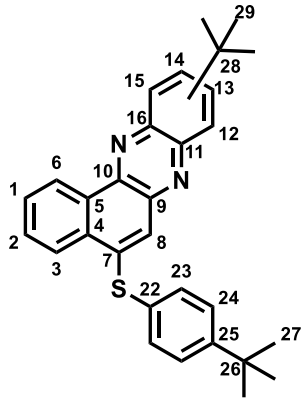
^{1}H NMR (300 MHz, $CDCl_3$) δ= 9.49 – 9.37 (m, 2H, H_6), 8.63 – 8.17 (m, 6H), 7.93 (m, 2H), 7.90 – 7.83 (m, 4H, H_1 and H_2), 7.63 (m, 4H, H_{23}), 7.54 (m, 4H, H_{24}), 7.40 (s, 1H, H_8), 7.39 (s, 1H, H_8), 1.41 (s, 9H, H_{27}).

^{13}C NMR (75 MHz, $CDCl_3$) δ= 153.5, 146.6, 145.9, 144.4, 143.5, 142.2, 141.7, 140.2, 135.5, 135.4, 131.9, 131.7, 131.1, 130.9, 130.7, 130.4, 130.1, 129.0, 128.9, 127.5, 127.0, 126.2, 126.0, 126.0, 124.6, 124.5, 122.2, 122.0, 35.1 (C_{26}), 31.4 (C_{27}).

IR (cm^{-1}): $\tilde{\nu}$ = 2965 (m, alkyl), 1581 (m, aromatic), 1338 (s, NR_3), 1128 (s, CF_3), 836 (s, aromatic), 767 (s, CF_3).

HRMS (ESI) *m/z* calcd for $C_{27}H_{21}N_2F_3{}^{32}S + H^+$: 463.1450 $[M + H]^+$; found 463.1454.

9,10-(tert-butyl)-5-((4-(tert-butyl)phenyl)thio)benzo[a]phenazine ***(10f-6)*** was synthesized from 4-((4-(*tert*-butyl)phenyl)thio)naphthalene-1,2-dione **9f** (100 mg, 0.31 mmol) and commercially available 4-(*tert*-butyl)benzene-1,2-diamine (56 mg, 0.34 mmol) by following the general procedure described above. The desired compound was obtained as a yellow powder. Yield: 62 %.



CAS: /

Formula: $C_{30}H_{30}N_2O_2S$

Molecular weight: 450.64 g mol^{-1}

Regioisomers ratio: 55/45 (H_8)

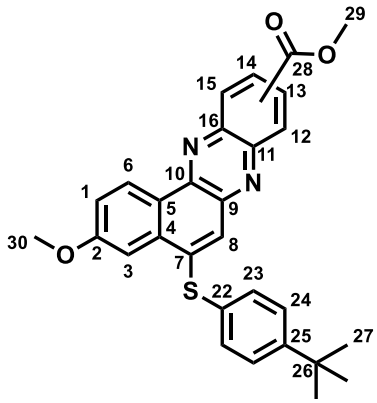
^{1}H NMR (300 MHz, $CDCl_3$) δ= 9.53 – 9.42 (m, 2H, H_6), 8.47 – 8.39 (m, 2H, H_3), 8.24 (dd, *J* = 5.0, 3.4 Hz, 2H), 8.12 – 8.04 (m, 1H), 7.92 (dt, *J* = 9.0, 2.0 Hz, 2H), 7.85 (m, 4H, H_1 and H_2), 7.60 (m, 4H, H_{23}), 7.54 – 7.47 (m, 6H, H_{24} and H_8), 1.50 (s, 9H, H_{29}), 1.46 (s, 9H, H_{29}), 1.40 (s, 9H, H_{27}), 1.39 (s, 9H, H_{27}).

^{13}C NMR (75 MHz, $CDCl_3$) δ= 153.8, 153.0, 152.9, 152.9, 143.4, 143.1, 143.0, 142.9, 142.0, 141.7, 141.6, 140.3, 135.1, 135.0, 131.6, 131.5, 131.0, 129.9, 129.8, 129.1, 129.0, 128.4, 128.2, 127.4, 127.3, 126.9, 126.8, 125.7, 124.6, 124.5, 124.4, 123.8, 123.7, 123.4, 35.6, 35.5, 35.0, 31.4, 31.2.

IR (cm^{-1}): $\tilde{\nu}$ = 2956 (m, alkyl), 1582 (m, aromatic), 1363 (s, NR_3), 832 (s, aromatic), 771 (s, aromatic).

HRMS (ESI) *m/z* calcd for $C_{30}H_{30}N_2O_2{}^{32}S + H^+$: 451.2203 $[M + H]^+$; found 451.2203.

*Methyl 5-((4-(tert-butyl)phenyl)thio)-3-methoxybenzo[a]phenazine-9,10-carboxylate (**10g**)* was synthesized from 4-((4-(*tert*-butyl)phenyl)thio)-6-methoxynaphthalene-1,2-dione **9g** (92 mg, 0.26 mmol) and methyl 3,4-diaminobenzoate **15** (48 mg, 0.29 mmol) by following the general procedure described above. The desired compound was obtained as a yellow powder. Yield: 58 %.



CAS: /

Formula: $C_{29}H_{26}N_2O_3S$

Molecular weight: 482.60 g mol^{-1}

Regioisomers ratio: 60/40 (H_{24})

58/42 (H_8)

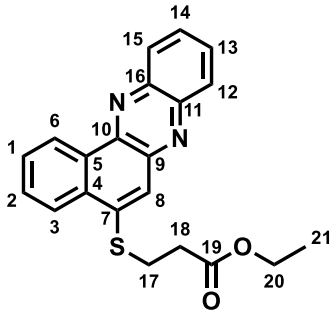
^{1}H NMR (300 MHz, $CDCl_3$) δ= 9.34 (d, *J* = 8.9 Hz, 2H, H_6), 8.98 (m, 1H), 8.85 (m, 1H), 8.39 – 8.21 (m, 4H), 7.79 (d, *J* = 2.5 Hz, 1H), 7.67 – 7.50 (m, 8H), 7.49 – 7.40 (m, 4H), 4.04 (m, 6H, H_{29} or H_{30}), 4.01 (s, 6H, H_{29} or H_{30}), 1.41 (s, 9H, H_{27}).

^{13}C NMR (75 MHz, $CDCl_3$) δ= 166.6, 161.8, 161.6, 153.2, 145.4, 144.9, 144.2, 143.4, 143.2, 141.5, 135.3, 135.1, 133.7, 133.3, 132.6, 131.9, 130.7, 130.4, 129.7, 129.0, 128.8, 128.5, 128.0, 127.4, 126.4, 124.2, 123.7, 123.3, 117.6, 106.7, 55.8 (C_{29} or C_{30}), 52.7 (C_{29} or C_{30}), 35.0 (C_{26}), 31.4 (C_{27}).

IR (cm^{-1}): $\tilde{\nu}$ = 2953 (m, alkyl), 1716 (s, COOEt), 1362 (s, NR_3), 1260 (s, COOEt), 1197 (s, C–O–C), 1091 (m, COOEt), 1046 (m, C–O–C), 831 (s, aromatic), 751 (s, aromatic).

HRMS (ESI) *m/z* calcd for $C_{29}H_{27}O_3N_2{}^{32}S + H^+$: 483.1737 $[M + H]^+$; found 483.1739.

*Ethyl 3-(benzo[a]phenazin-5-ylthio)propanoate (**10h**)* was synthesized from ethyl 3-((3,4-dioxo-3,4-dihydronaphthalen-1-yl)thio)propanoate **9h** (100 mg, 0.34 mmol) and commercially available benzene-1,2-diamine (40 mg, 0.37 mmol) by following the general procedure described above. The desired compound was obtained as a yellow powder. Yield: 62 %.



CAS: /

Formula: $C_{21}H_{18}N_2O_2S$

Molecular weight: 362.45 g mol^{-1}

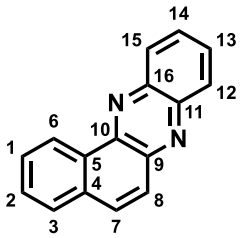
^{1}H NMR (300 MHz, $CDCl_3$) δ= 9.41 (m, 1H, H_6), 8.28 (m, 2H, H_2 and H_{12} or H_{13} or H_{14} or H_{15}), 8.23 – 8.14 (m, 1H, H_3), 7.90 – 7.75 (m, 4H, H_1 and 3H of $H_{12\text{-}15}$), 7.74 (s, 1H, H_8), 4.21 (q, J = 7.1 Hz, 2H, H_{20}), 3.51 (t, J = 7.3 Hz, 2H, H_{17}), 2.88 (t, J = 7.3 Hz, 2H, H_{18}), 1.28 (t, J = 7.1 Hz, 3H, H_{21}).

^{13}C NMR (75 MHz, $CDCl_3$) δ= 171.5 (C_{19}), 143.2 (C_{11} or C_{16}), 143.0 (C_{11} or C_{16}), 141.9 (C_9 or C_{10}), 141.8 (C_9 or C_{10}), 141.3 (C_7), 131.9 (C_4 or C_5), 130.8 (C_4 or C_5), 130.4 (C_1 and C_{12} or C_{13} or C_{14} or C_{15}), 130.0 (C_1 and C_{12} or C_{13} or C_{14} or C_{15}), 129.9 (C_2 or C_{12} or C_{13} or C_{14} or C_{15}), 129.5 (C_1 and C_{12} or C_{13} or C_{14} or C_{15}), 129.0 (C_3), 128.5 (C_1 and C_{12} or C_{13} or C_{14} or C_{15}), 125.8 (C_6), 124.5 (C_2 or C_{12} or C_{13} or C_{14} or C_{15}), 121.6 (C_8), 61.2 (C_{20}), 33.6 (C_{18}), 26.9 (C_{17}), 14.4 (C_{21}).

IR (cm^{-1}): $\tilde{\nu}$ = 2973 (m, alkyl), 1724 (s, COOEt), 1352 (m, NR_3), 1175 (s, COOEt), 1062 (m, COOEt), 957 (m, alkyl), 767 (s, aromatic).

HRMS (ESI) *m/z* calcd for $C_{21}H_{18}O_2N_2{}^{32}S + H^+$: 363.1162 $[M + H]^+$; found 363.1160.

*Benzo[a]phenazine (**11**)* was synthesized from naphthalene-1,2-dione (557 mg, 3.5 mmol) and benzene-1,2-diamine (427 mg, 2.57 mmol) by following the general procedure described above. The desired compound was obtained as a yellowish powder. Yield: 80 %.



CAS: 225-61-6

Formula: $C_{16}H_{10}N_2$

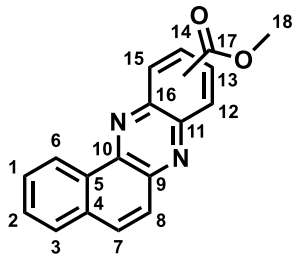
Molecular weight: 230.27 g mol^{-1}

^{1}H NMR (300 MHz, $CDCl_3$) δ= 9.46 – 9.34 (m, 1H, H_6), 8.42 – 8.32 (m, 1H, H_{12} or H_{15}), 8.32 – 8.23 (m, 1H, H_{12} or H_{15}), 8.03 – 7.93 (m, 2H, H_7 and H_8), 7.93 – 7.82 (m, 3H, H_3, H_{13} and H_{14}), 7.81 – 7.73 (m, 2H, H_1 and H_2).

^{13}C NMR (75 MHz, $CDCl_3$) δ= 143.7 (C_9 or C_{10}), 142.8 (C_{11} or C_{16}), 142.8 (C_9 or C_{10}), 142.1 (C_{11} or C_{16}), 133.4 (C_4 or C_5), 133.4 (C_7 or C_8), 131.3 (C_4 or C_5), 130.2 (C_{13} or C_{14}), 130.0 (C_{13}, C_{14}, C_1, or C_2), 129.9 (C_{13}, C_{14}, C_1, or C_2), 129.9 (C_{12} or C_{15}), 129.3 (C_{12} or C_{15}), 128.3 (C_1 or C_2), 128.1 (C_3), 127.3 (C_7 or C_8), 125.5 (C_6).

IR (cm^{-1}): $\tilde{\nu}$ = 1496 (m, aromatic), 1474 (m, aromatic), 1353 (s, NR_3), 1198 (m, aromatic), 838 (s, aromatic), 755 (s aromatic).

*Methyl benzo[a]phenazine-9,10-carboxylate (**12**)* was synthesized from naphthalene-1,2-dione **8** (162 mg, 1 mmol) and methyl 3,4-diaminobenzoate **15** (190 mg, 1.1 mmol) by following the general procedure described above. The desired compound was obtained as a brown/yellowish powder. Yield: 70 %.



CAS: /

Formula: $C_{18}H_{12}N_2O_2$

Molecular weight: 288.31 g mol^{-1}

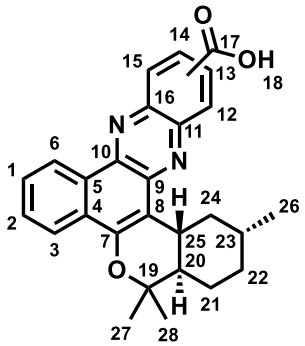
Ratio regioisomers: 55/45 (H_{18})

^{1}H NMR (300 MHz, $CDCl_3$) δ= 9.41 – 9.30 (m, 2H, H_6), 9.04 (m, 1H), 8.97 (m, 1H), 8.44 – 8.24 (m, 4H), 8.06 – 7.97 (m, 2H), 7.96 – 7.86 (m, 4H), 7.84 – 7.75 (m, 4H), 4.05 (s, 3H, H_{18}), 4.04 (s, 3H, H_{18}).

^{13}C NMR (75 MHz, $CDCl_3$) δ= 166.5 (C_{17}), 144.9, 144.5, 144.3, 143.9, 143.6, 141.8, 141.0, 134.8, 134.0, 133.7, 133.4, 132.8, 132.3, 131.2, 131.1, 130.9, 130.6, 130.4, 130.0, 129.5, 129.2, 129.0, 128.5, 128.3, 127.2, 127.1, 125.9 (C_6), 125.6 (C_6), 52.8 (C_{18}).

IR (cm^{-1}): $\tilde{\nu}$ = 1723 (s, COOEt), 1360 (s, NR_3), 1262 (s, COOEt), 1190 (m, aromatic), 1092 (s, COOEt), 748 (s, aromatic).

Methyl (2R,4aR,16cR)-2,5,5-trimethyl-1,3,4,4a,5,16c-hexahydro-2H-benzo[a]isochromeno[3,4-c]phenazine-13,14-carboxylic acid ***(13)*** was synthesized from **9a** (200 mg, 0.65 mmol) and commercially available 3,4-diaminobenzoic acid (110 mg, 0.71 mmol) by following the general procedure described above. The desired compound was obtained as a yellow powder. Yield: 70 %.



CAS: /

Formula: $C_{27}H_{26}N_2O_3$

Molecular weight: 426.52 g mol^{-1}

Regioisomers ratio: 55/45 ($H_{12\text{-}15}$)

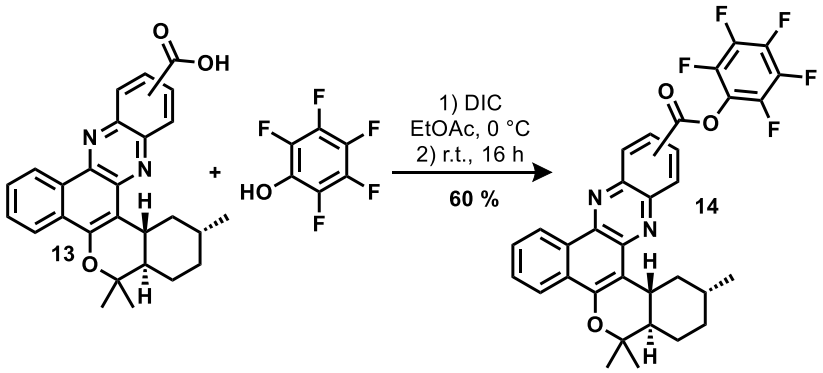
^{1}H NMR (300 MHz, CD_2Cl_2) δ (ppm) 9.37 – 9.24 (m, 2H, H_6), 9.07 (m, 1H), 9.00 (m, 1H), 8.43 – 8.23 (m, 6H), 7.85 – 7.76 (m, 4H), 3.70 (m, 2H), 3.13 (m, 2H), 2.02 (s, 2H), 2.00 (m, 4H), 1.82 – 1.70 (m, 2H), 1.64 (s, 6H), 1.47 – 1.30 (m, 4H), 1.25 (s, 6H), 1.23 – 1.18 (m, 2H), 1.01 (m, 6H), 0.73 (q, J = 11.4 Hz, 2H).

^{13}C NMR (75 MHz, $CDCl_3$) δ (ppm) 207.2, 171.4, 153.4, 152.4, 146.3, 145.7, 143.9, 142.2, 141.4, 138.0, 133.6, 132.9, 130.6, 130.5, 130.0, 129.8, 129.7, 129.1, 128.7, 128.2, 128.0, 127.3, 125.5, 125.2, 122.6, 113.5, 49.9, 40.5, 36.2, 36.0, 33.0, 31.0, 28.1, 27.6, 22.8, 19.3.

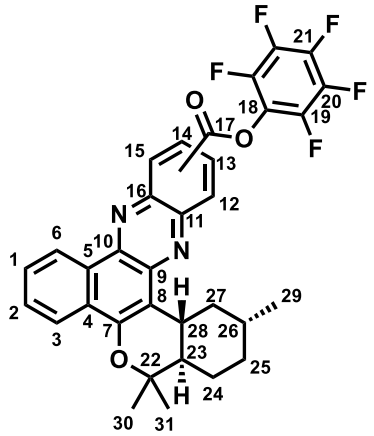
IR (cm^{-1}): $\tilde{\nu}$ = 2920 (m, alkyl), 1694 (m, COOH), 1407 (m, COOH), 1380 (s, NR_3), 1210 (s, O–C–O), 1137 (s, aromatic), 764 (s, aromatic).

HRMS (ESI) *m/z* calcd for $C_{27}H_{27}O_3N_2$ $[M + H]^+$ 427.2016, found 427.2016.

Synthesis of activated ester (14)



A 50 mL round-bottom flask was filled with 20 mL of ethyl acetate, pentafluorophenol (70 mg, 0.4 mmol, 1 eq.) and compound **13** (150 mg, 0.4 mmol, 1 eq.). The resulting solution was cooled to 0 °C and *N*-*N*'-diisopropylcarbodiimide (DIC) (0.06 mL, 0.44 mmol, 1.1 eq.) was added dropwise. The mixture was stirred at room temperature for 16 h. After reaction, the solvent was evaporated under reduced pressure and the crude residue was purified by column chromatography (10 % ethyl acetate in petroleum ether). The activated ester was obtained as a yellow powder (142 mg, 60 % yield).



CAS: /

Formula: $C_{33}H_{25}F_5N_2O_3$

Molecular weight: 592.57 g mol^{-1}

Regioisomers ratio: 50/50 ($H_{12\text{-}15}$)

^{1}H NMR (300 MHz, $CDCl_3$) δ= 9.36 – 9.28 (m, 2H, H_6), 9.24 (m, 1H), 9.15 (t, *J* = 1.3 Hz, 1H), 8.48 – 8.39 (m, 2H), 8.37 – 8.30 (m, 4H), 7.87 – 7.75 (m, 4H, H_1 and H_2), 3.68 (d, *J* = 12.4 Hz, 2H, H_{27a}), 3.16 (m, 2H, H_{28}), 2.01 (m, 2H, H_{26} and H_{25a}), 1.83 – 1.70 (m, 2H, H_{23}), 1.65 (d, *J* = 2.2 Hz, 6H, H_{30} or H_{31}), 1.47 – 1.33 (m, 4H, H_{24}), 1.28 (d, *J* = 3.6 Hz, 6H, H_{30} or H_{31}), 1.19 (m, 2H, H_{25b}), 1.08 – 0.97 (m, 6H, H_{29}), 0.83 – 0.65 (m, 2H, H_{27b}).

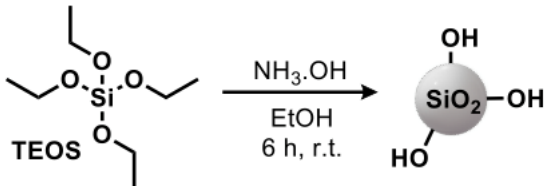
^{19}F NMR (282 MHz, $CDCl_3$) δ= -152.2 (t, *J* = 19.9 Hz, 2F), -157.7 (q, *J* = 22.2 Hz, 1F), -162.4 (m, 2F).

^{13}C NMR (75 MHz, $CDCl_3$) δ= 162.5 (C_{17}), 153.9, 152.8, 146.5, 145.9, 144.1, 142.4, 142.0, 141.7, 140.4, 139.7, 138.2, 134.5, 133.7, 130.6, 130.5, 130.3, 130.3, 129.7, 129.6, 128.5, 128.3, 128.1, 127.1, 126.9, 125.6, 125.5, 125.2, 122.7, 113.5, 113.3, 79.8, 79.6, 49.9, 49.8, 40.5, 40.4, 36.1, 35.9, 35.9, 33.0, 29.1, 28.1, 27.5, 22.7, 19.3, 19.2.

IR (cm^{-1}): $\tilde{\nu}$ = 2942 (m, alkyl), 1755 (s, C=O), 1518 (s, aromatic), 1410 (m), 1234 (m, C=O), 1189 (s, C–O–C), 1140 (s, C–F), 992 (s, aromatic).

HRMS (ESI) *m/z* calcd for $C_{33}H_{25}O_3N_2F_5 + H^+$: 593.1858 $[M + H]^+$; found 593.1859.

Silica nanospheres (NS) synthesis



Reaction conditions were adapted from the work of Stöber *et al.* to yield bigger quantities of 40 nm diameter silica nanospheres.[220] 150 mL of ethanol (99.9 % denaturated) were introduced in a 500 mL Erlenmeyer. Under vigorous stirring, 6 mL of NH_4OH were added. The reaction mixture was stirred for 5 min at room temperature. Then, 10 mL of tetraethylorthosilicate (TEOS) were added dropwise with a syringe pump at a rate of 59 mL $hour^{-1}$. The solution was left under stirring for 6 hours at room temperature. The silica

nanoparticles were recovered by centrifugation (9.500 rpm for 40 min) and washed three times with 40 mL of ethanol. The nanoparticles were dried in the oven at 100 °C overnight and subsequently grinded to obtain a fine white/beige powder. This material was characterized by TEM, XPS and BET.

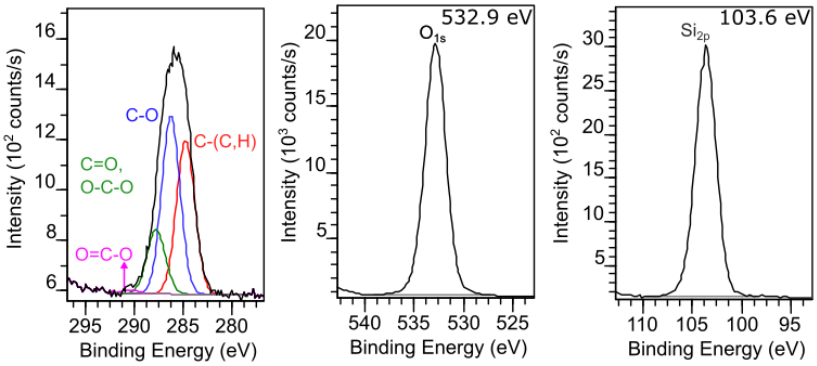


Figure 4.12. XPS spectra of silica nanospheres: C_{1s}, O_{1s} and Si_{2p} signals.

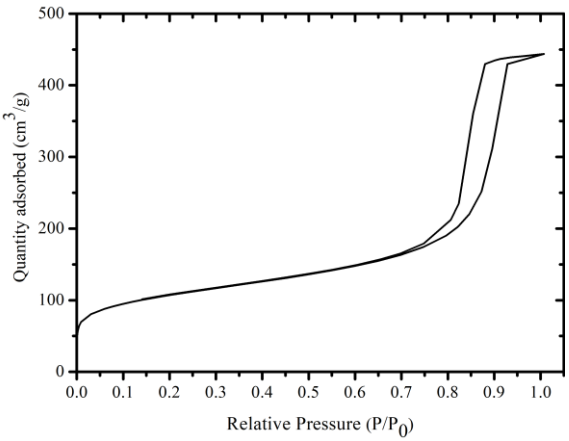
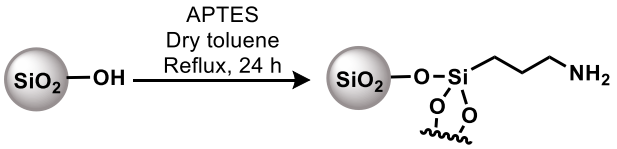


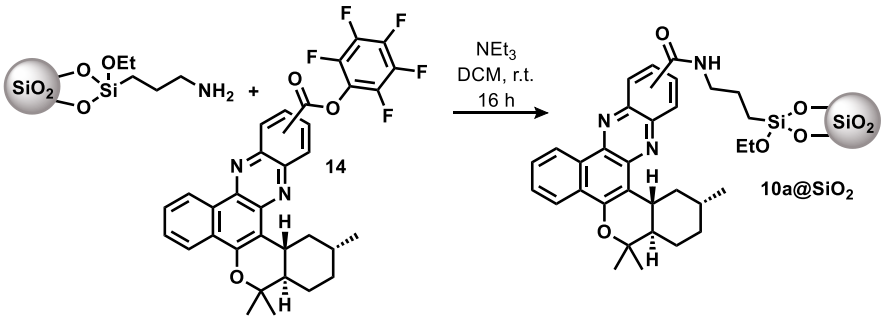
Figure 4.13. N_2 adsorption-desorption isotherms at 77 K of silica nanospheres. BET calculated surface area of 360 $m^2\ g^{-1}$.

Functionalization of silica nanospheres with aminopropylethoxysilane (APTES)



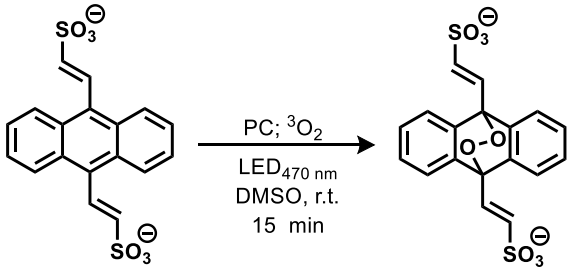
In a 50 mL flame-dried two-neck round-bottom flask, silica nanospheres (250 mg) were introduced. The flask was placed under static vacuum for 10 minutes before being filled with argon. 30 mL of dry toluene were added and the resulting suspension was sonicated for 15 minutes at power 2 on a VWR ultrasonic bath. Aminopropylethoxysilane (APTES, 0.4 mL) was added dropwise to the silica suspension which was refluxed for 24 h. After reaction, the mixture was cooled to room temperature and filtered on a PVDF Millipore Membrane (0.1 μm). The powder was recovered and washed three times with 50 mL of ethanol. The solid was dried under vacuum for several hours and was characterized by TGA and XPS.

Synthesis of heterogenized photocatalyst 10a@SiO_2



Amino-functionalized silica nanospheres (100 mg) were introduced in a 50 mL flame-dried round-bottom flask. The flask was placed under static vacuum for 10 minutes before being filled with argon. 15 mL of dry dichloromethane were added and the resulting suspension was sonicated for 15 minutes at power 2 on a VWR ultrasonic bath. A solution of compound **14** (60 mg, 1 mmol, 1 eq.) in dichloromethane (5 mL) was added dropwise to the solution followed by triethylamine (0.7 mL, 6 mmol, 6 eq.). The resulting mixture was stirred at room temperature for 16 h. After reaction, the mixture was filtered on a PVDF Millipore Membrane (0.1 μm). The powder was recovered and washed three times with 10 mL of dichloromethane. The yellowish solid was dried under vacuum for several hours and was characterized by XPS.

$^1O_2$ production quantum yield determination

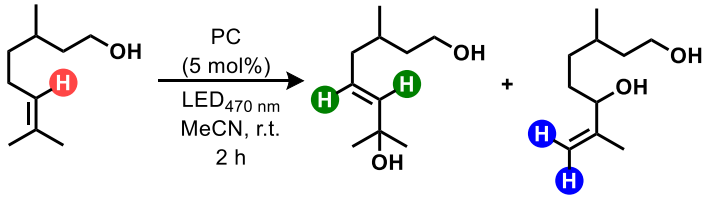


Singlet oxygen production quantum yields obtained with the benzophenazine derivatives were determined in dimethylsulfoxide (DMSO) by monitoring the decomposition of a $^1O_2$ trap (AVS = Anthracene-9,10-divinylsulfonate) on a time range extending from 0 to 10 minutes. Practically, a O_2 balloon was bubbled through a septum in the cuvette for 15 minutes containing AVS (Absorbance = ~ 1 at 390 nm) and the photosensitizer (Absorbance = ~ 0.05 at 470 nm or 459 nm when the PC absorbance was red-shifted). The cuvette was irradiated at 470 nm with a blue Thorlabs LED lamp (4.0 mW cm^{-2}, output power of 253 mW, placed at ~5 cm of the cuvette) and an absorption spectrum was taken at regular intervals. The decomposition of AVS was then determined by analyzing the absorption decay of AVS at 390 nm. This protocol was repeated three times for each compound. The reference used was Rose Bengal for which a singlet oxygen quantum yield of 0.76 in water is known[170]. Singlet oxygen quantum yields were determined based on the following equation:

$$\phi_{sam} = \phi_{ref}*[(m_{sam}/m_{ref})*(L_{ref}/L_{sam})]$$

where ϕ_{sam} and ϕ_{ref} are $^1O_2$ quantum yields of benzophenazine derivatives and RB, respectively, m_{sam} and m_{ref} are slopes in the plots of ΔA at the photoabsorption maximum wavelength of AVS (390 nm) against photoirradiation time, and L_{sam} and L_{ref} are light harvesting efficiencies, which are given by $L = 1\text{-}10^{-A}$ ("A" is the absorbance at the photoirradiation wavelength).

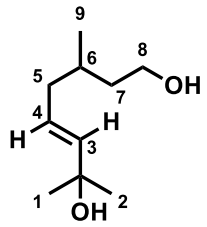
Citronellol photooxidation in homogeneous conditions





In a 50 mL two-necks round-bottom flask the photosensitizer ($5*10^{-3}$ mmol, 5 mol%) was added with 20 mL of acetonitrile under air. Citronellol (18 µL, 0.1 mmol, 1 eq.) was added dropwise. A balloon of oxygen was placed through a septum on one exit and a tap was placed on the second exit to control the bubbling of O_2. A slow bubbling was applied throughout the reaction which was stirred at room temperature for 2 h and irradiated with two LIU470A 470 nm blue LEDs purchased from Thorlabs (intensity = 4.0 mW/cm^2; total output power = 253 mW; supply voltage = 24 V). After reaction, triphenylphosphine (30.2 mg, 0.12 mmol, 1.2 eq.) was added to form the alcohols and the mixture was stirred for an additional 5 minutes. The solvent was removed under reduced pressure at 40 °C (Note: do not exceed that temperature to avoid product degradation). Dimethylsulfone (DMS) was used as internal standard to determine the yield by NMR: the signal at 5.6 ppm was used for tertiary alcohol, the signal at 4.9 ppm was used for secondary alcohol and the signal at 5.1 ppm was used for the remaining citronellol

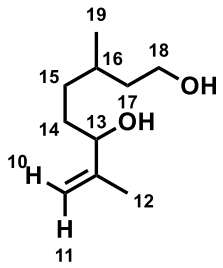
fraction. In the case of control tests, the same protocol was applied with either no irradiation (in the dark) or no photosensitizer.



CAS: /

Formula: $C_{10}H_{20}O_2$

Molecular weight: 172.27 g mol^{-1}

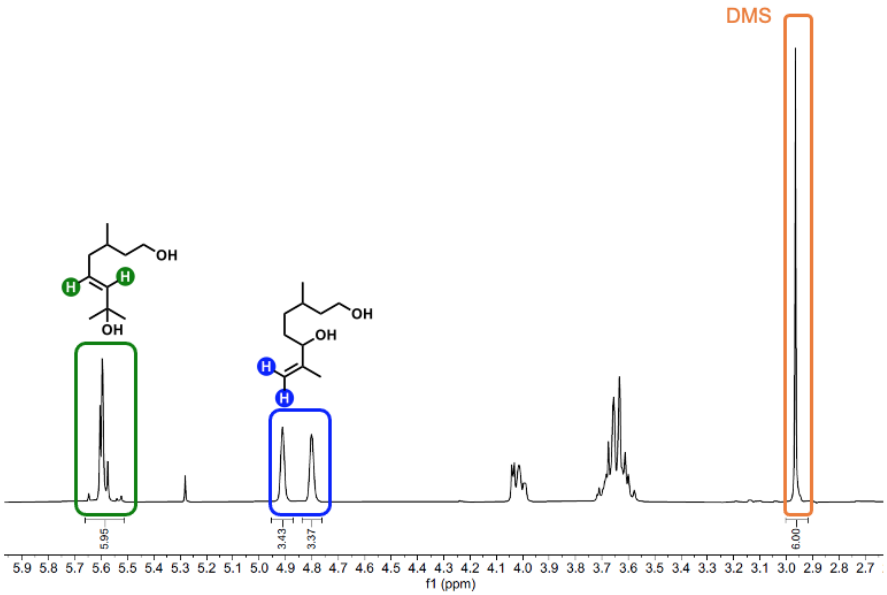


CAS: /

Formula: $C_{10}H_{20}O_2$

Molecular weight: 172.27 g mol^{-1}

^{1}H NMR (300 MHz, $CDCl_3$) δ= 5.70 – 5.50 (m, 2H, H_3 and H_4), 4.93 (s, 1H, H_{10} or H_{11}), 4.82 (s, 1H, H_{10} or H_{11}), 4.09 – 3.96 (m, 1H, H_{13}), 3.78 – 3.55 (m, 4H, H_8 and H_{18}), 2.33 (bs, 4H, OH), 2.09 – 1.85 (m, 2H), 1.72 (s, 3H), 1.65 – 1.52 (m, 6H), 1.45 – 1.35 (m, 4H), 1.32 (s, 6H, H_1 and H_2), 0.94 – 0.86 (m, 6H).



Scheme 4.11. Quantitative NMR spectrum of a filtrate after photooxidation of citronellol using heterogenized compound **10a**.

Citronellol photooxidation in heterogeneous conditions

In a 50 mL two-necks round-bottom flask, the heterogenized photosensitizer **10a@SiO$_2$** (28 mg, 5*10^{-3} mmol, 5 mol%) was added with 20 mL of acetonitrile under air. The resulting suspension was sonicated for 15 minutes at power 2 on a VWR ultrasonic bath. Citronellol (18 µL, 0.1 mmol, 1 eq.) was added dropwise. A balloon of oxygen was placed through a septum on one exit of the flask and a tap was placed on the second exit to control the bubbling of O_2. A slow bubbling was applied as much as possible throughout the reaction which was stirred at room temperature for 16 h and irradiated with two LIU470A 470 nm blue LEDs purchased from Thorlabs (intensity = 4.0 mW/cm^2; total output power = 253 mW; supply voltage = 24 V). After reaction, triphenylphosphine (30.2 mg, 0.12 mmol, 1.2 eq.) was added to form the alcohols and the mixture was stirred for an additional 5 minutes. The mixture was filtered on a PVDF Millipore Membrane (0.1 µm). The powder was recovered and washed three times with 10 mL of dichloromethane. The white yellowish solid was dried under vacuum for several hours. The filtrate

was concentrated under reduced pressure at 40 °C (Note: do not exceed that temperature to avoid product degradation). DMS was used as internal standard to perform quantitative NMR as detailed above.

The recycling runs were conducted as explained above, except that for each run, the recovered solid material was weighted again to guarantee the same quantity of photocatalyst in each test and if not, the quantity of citronellol was adapted to have always a loading of 5 mol% in photocatalyst. This adaptation has been necessary from run 3.

Chapter 5

The diethylaniline photocatalyst

1. Introduction

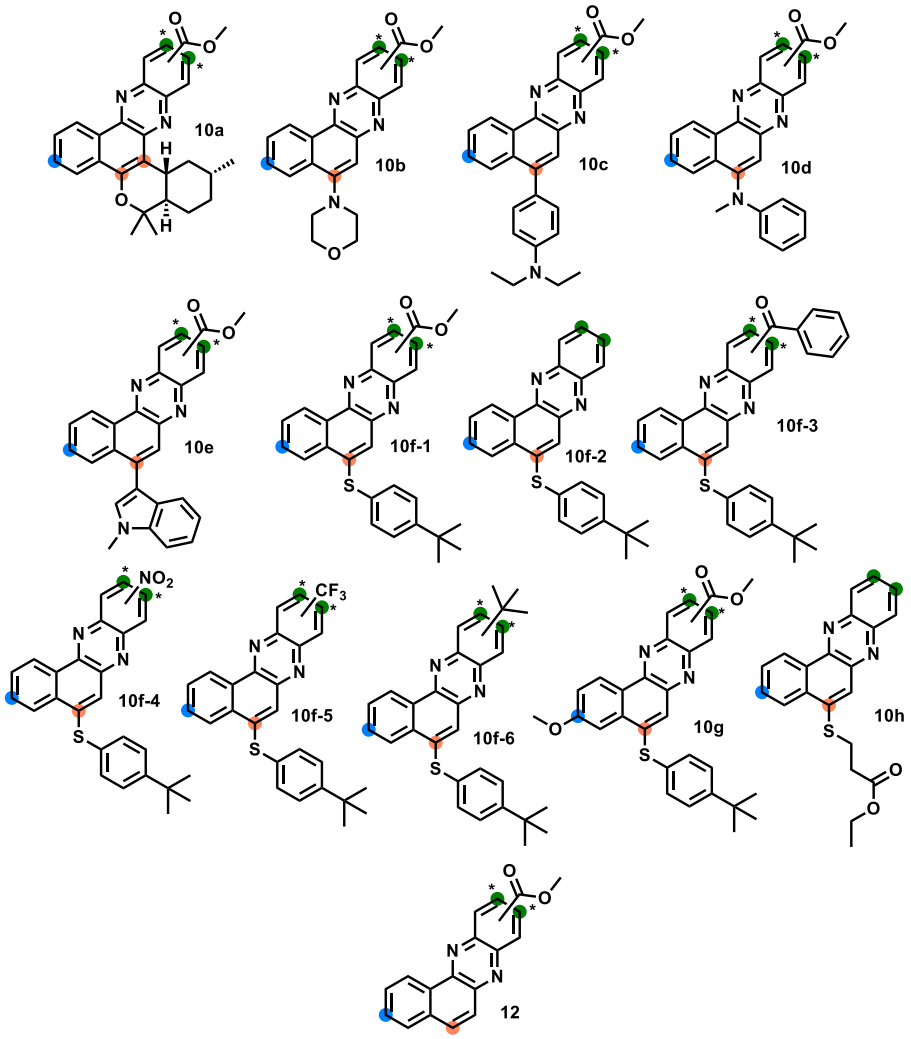
In Chapter 4, we investigated the impact of the functionalization of a benzophenazine skeleton on its photophysical properties in order to determine how to heterogenize the PC without disturbing its photoactivity. The northern fragment was identified as the best anchor point as this region does not quite impact the excited state of benzophenazine derivatives. Photocatalysts exhibiting a sulfur, cyclic ether or morpholine moiety on the southern part displayed excellent photophysical properties and reactivity (strong absorption in the visible range, long phosphorescence lifetime, high triplet energy state, high singlet oxygen quantum yield, high photostability) and were revealed to be efficient for the photoproduction of singlet oxygen. On the other hand, when nitrogen-based functions were employed such as diethylaniline, indole or methylaniline motifs, the photoactivity of these photosensitizers decreased completely and exhibited very low efficiency for $^1O_2$ production. Still, these nitrogen-based photocatalysts showed interesting properties such as an absorption in the visible range, a fluorescence lifetime of a few nanoseconds and a high triplet state energy. The photosensitization of oxygen was maybe simply not the best photocatalyzed reaction to use with these chromophores.

In this Chapter, we are interested in evaluating the capacity of benzophenazine derivatives to perform electron transfer in photoredox applications, as the lifetime of their singlet excited state is enough to perform photoredox reactions. The envisaged methodology is to determine their excited-state redox potentials and find a suitable photoreaction to assess their activity in an electron transfer process.

2. Results and discussion

2.1. Electrochemical properties

Each benzophenazine derivative used in Chapter 4 was also used here and **Scheme 5.1** reminds their different chemical structure. As stated above, their lifetime is sufficient to allow electron transfer but interesting excited-state redox potentials are also necessary so that these benzophenazine derivatives can find an interest in photoredox catalysis.



Scheme 5.1. Benzophenazine derivatives evaluated for electron transfer.

The electrochemical properties of benzophenazine derivatives were measured by cyclic voltammetry in acetonitrile containing 0.1 M $TBAPF_6$ electrolyte (**Table 5.1**). For all benzophenazine derivatives, an irreversible oxidation wave was observed (**Figure C.1**), except for compound **10c** bearing a diethylaniline motif which exhibited a reversible one. The values for the oxidation peak were comprised between 1.07 and 1.99 V *vs* NHE with lowest values observed for nitrogen-based PCs. Note that the oxidation potential of some derivatives was not observed in the investigated electrochemical

window. All of these values highlight the fact that the nature of functionalization on the southern fragment impacts also the redox potentials. Thus, the oxidation redox process involved potentially the southern fragment of the benzophenazines as the nitrogen-based and sulfur-based compounds exhibit an oxidation potential in a tight range of values in these families of compounds. This was already described by Singh *et al.* who observed different oxidation peak values (between 0.9 and 1.29 V *vs* NHE) for amine-substituted benzophenazines depending on the donor strength of the amine segment.[352] The northern fragment had no influence, except with the introduction of a NO_2 moiety which led to a peculiar behavior with no oxidation peak observed in the investigated electrochemical window. The western functionalization did not change the redox properties.

Concerning the reduction potentials, these were comprised between –0.78 and –1.04 V *vs* NHE (apart from NO_2 derivative **10f-4**). Whatever the functionalization nature and place, the reduction waves were found in a tight range of values as the reduction is localized on the phenazine core, moiety that tends to be easily reduced. Under specific reaction conditions, the back-electron transfer from the phenazine could be favored, explaining its reversibility. Using the Rehm-Weller equation[387], excited-state redox potentials $E_{1/2}(PS^{*/-})$ between 1.52 and 1.96 V *vs* NHE (still, derivative **10f-4** is not considered) and $E_{1/2}(PS^{*/+})$ between –0.72 and –1.60 V *vs* NHE were determined (**Figure 5.1**).

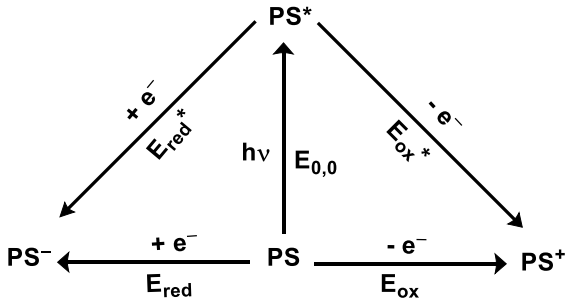


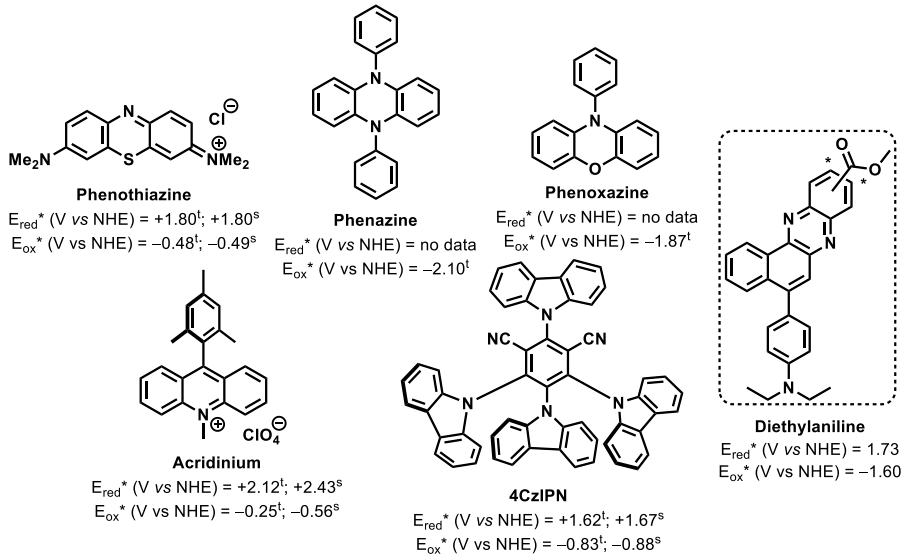
Figure 5.1. Modified Latimer diagram showing the ground-state and excited-state redox processes of a photosensititzer (PS). Adapted from the literature.[388]

Table 5.1. Redox potentials of benzophenazine derivatives in the fundamental and excited states. The $E_{0,0}$ energy was determined using the intersection between absorption and emission spectra (**Figure C.2**).

	E_{ox} (V) *vs* NHE	E_{red} (V) *vs* NHE	E_{ox}^* (V) *vs* NHE	E_{red}^* (V) *vs* NHE	$E_{0,0}$ (eV)
10a	-	–1.02	-	1.62	2.64
10b	1.36	–0.94	–1.10	1.52	2.46
10c	1.07	–0.88	–1.60	1.73	2.61
10d	1.57	–0.87	–0.99	1.69	2.56
10e	1.52	–0.88	–1.00	1.62	2.51
10f-1	1.84	–0.79	–0.86	1.92	2.71
10f-2	1.99	–0.99	–0.82	1.82	2.81
10f-3	1.83	–0.78	–0.72	1.93	2.71
10f-4	-	–0.57	-	2.13	2.70
10f-5	1.83	–0.80	–0.93	1.96	2.76
10f-6	1.99	–1.04	–0.83	1.78	2.82
10g	1.99	–0.82	–0.77	1.94	2.76
10h	1.79	–1.02	–1.03	1.80	2.82

Most photocatalysts exhibit average excited-state redox potentials comparable to known photocatalysts (**Scheme 5.2**) but could only be used in reducing quenching cycles as the reduction wave is the only one to be reversible. Diethylaniline compound **10c** is the only exception and stands out

as a promising candidate for photoredox catalysis, as reversible oxidation and reduction waves were observed with high values in the excited state (–1.60 and 1.73 V *vs* NHE, respectively) (**Figure 5.2**) making it an efficient reducer and oxidant photocatalyst in its excited state. These values are in the same range as highly efficient and well-known photosensitizers[388] (**Scheme 5.2**) reinforcing the potential of compound **10c**. Nevertheless, being an efficient reducer and oxidant can be a problem if internal charge transfer occurs leading to a fast quenching and/or possible photodegradation.



Scheme 5.2. Excited-state redox potentials of well-known photosensitizers and compound **10c**. s: values for the singlet excited state; t: values for the triplet excited state.

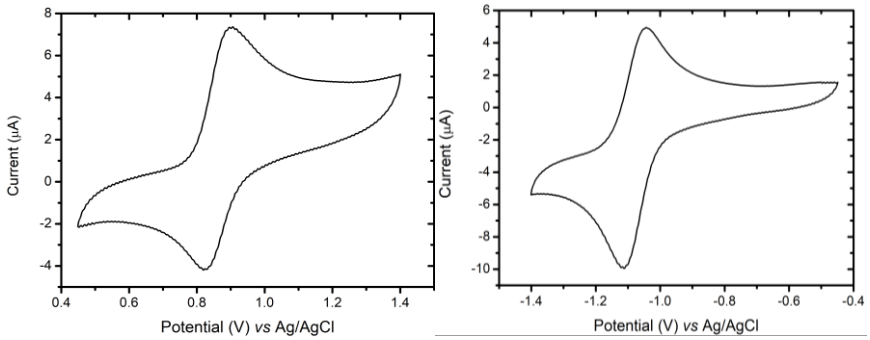
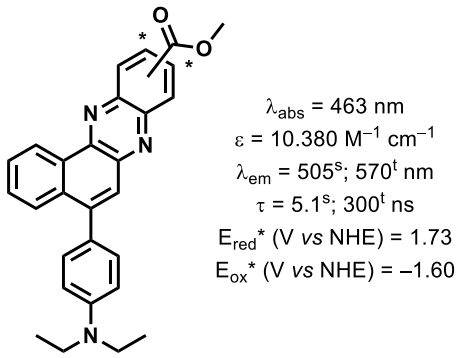


Figure 5.2. Cyclic voltammetry (CV) of compound **10c**.

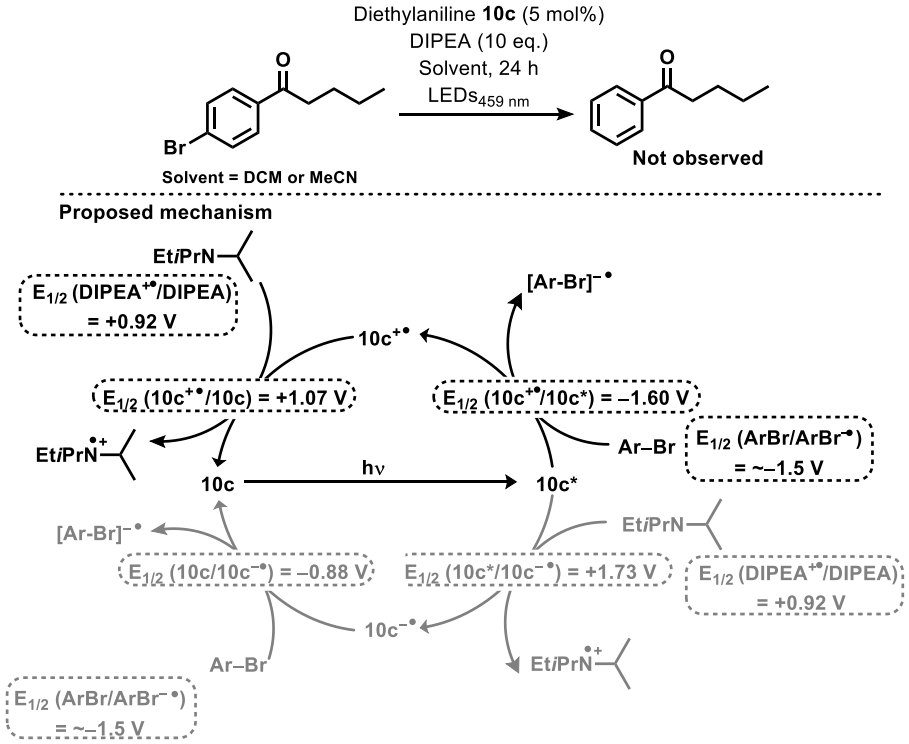
Moreover, in the previous Chapter, this photosensitizer **10c** showed a strong absorption in the visible range, a large molar absorption coefficient and a triplet excited-state lifetime of 300 ns in acetonitrile, which is in line with the timescale for bimolecular electron transfer (**Scheme 5.3**). For these reasons, only the diethylaniline compound, named here "**10c**", is investigated for photoredox applications in this Chapter.



Scheme 5.3. Summary of the photophysical properties of compound **10c** investigated partly in the previous chapter. Acetonitrile was used as solvent. s: values for the singlet excited state; t: values for the triplet excited state.

2.2. Excited-state and photoreactivity investigation

The photophysical properties of **10c** in acetonitrile are suitable for photoredox applications and thus, its photoactivity was first evaluated in the photodebromination of bromovalerophenone (**Scheme 5.4**). Indeed, according to the excited-state redox potentials, an oxidative quenching can be performed to reduce an aryl bromide. A reductive quenching cycle is not envisaged as the ground-state reduction potential of **10c** is not negative enough to reduce such bromide derivative (**Scheme 5.4**). Unfortunately, no conversion was observed in acetonitrile. The solvent was changed to dichloromethane but the result was identical. As this lack of reactivity was quite surprising, we decided to further characterize the fundamental and excited states.



Scheme 5.4. Photodebromination of bromovalerophenone used to assess the photoactivity of **10c** and its proposed mechanism. Redox potentials are expressed *vs* NHE.

2.2.1. Characterization in dichloromethane

The photophysical properties of **10c** were evaluated in dichloromethane. The absorption was slightly red-shifted compared to the one in acetonitrile, with an absorption maximum at 470 nm (**Figure 5.3**). Visible-light excitation of the photosensitizer led to steady-state photoluminescence (SSPL) centered at 600 nm.

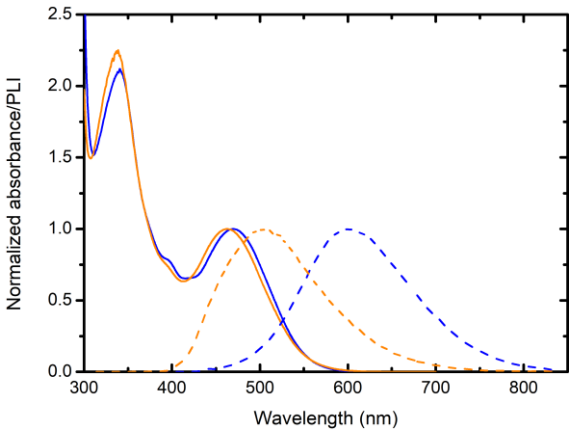


Figure 5.3. Normalized absorption (solid) and photoluminescence (dashed) spectra of diethylaniline photocatalyst in acetonitrile (orange) and dichloromethane (blue).

Time-resolved photoluminescence (TRPL) measurements in dichloromethane were well-described by first-order kinetics which yielded excited-state lifetime of 1.75 µs under argon atmosphere (**Figure 5.4**). This excited-state lifetime is higher than in acetonitrile (5.1 ns for singlet state and 0.3 µs for triplet state) and could therefore favor electron transfer reactivity. Oddly, a blue-shifted emission centered at 453 nm on **Figure 5.4** was observed compared to the fluorescence spectra in dichloromethane centered at 600 nm. This would need further investigations to find an explanation. The hypothesis about the formation of different excited states due to different possible electronic transitions stated in Chapter 4 can be considered again to explain such discrepancy.

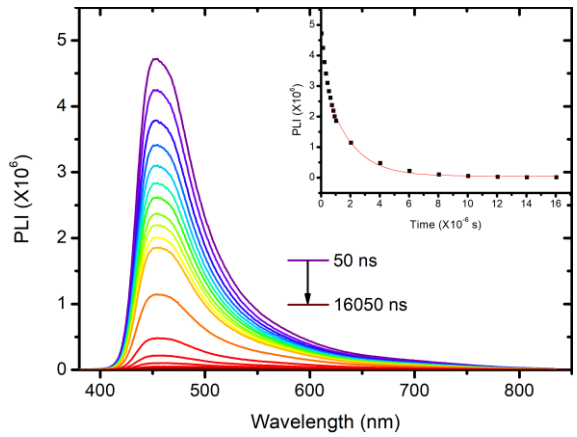


Figure 5.4. Delay map of the photoluminescence spectra of compound **10c** measured in dichloromethane between 50 ns and 16.05 µs after the laser pulse at regular intervals. The inset corresponds to the PLI intensity at 453 nm.

2.2.2. Excited-state photostability

As the excited-state lifetime, excited-state redox potentials, and the visible-light absorption are adequate to promote an electron transfer in photoredox applications, the excited state was characterized to determine the reasons why the photocatalyst displayed no photoactivity in the photodebromination of bromovalerophenone.

Nanosecond transient absorption spectroscopy (TA) was used to characterize the excited state of **10c**. This technique relies on the observation of transient species such as excited states, radicals, ions… with short lifetime. To detect those species, a laser pulse (or pump pulse) with a shorter time than the lifetimes of the transient species is used. Transient absorption spectroscopy records any change in the absorption spectrum of a molecule as a function of wavelength or time. It gives a difference spectrum between the sample absorption with and without laser pulse (Δ in absorbance (ΔA) for the y axis).[118]

To correctly understand the transient absorption spectra that can be obtained, let's consider first two specific absorption spectra (**Figure 5.5**). The absorbance of the solid black curve corresponds to the molecules existing in

their fundamental state S_0 and the absorbance of the dashed black curve (which was recorded at a time *t* in the range of excited-state lifetime after an excitation pulse) corresponds to the sum of absorbance of molecules in their excited state and the molecules that are still in their fundamental state. If we determine the difference absorption spectra to obtain ΔA and get the transient absorption spectra, such "ideal" spectrum represented on **Figure 5.5** would be obtained.

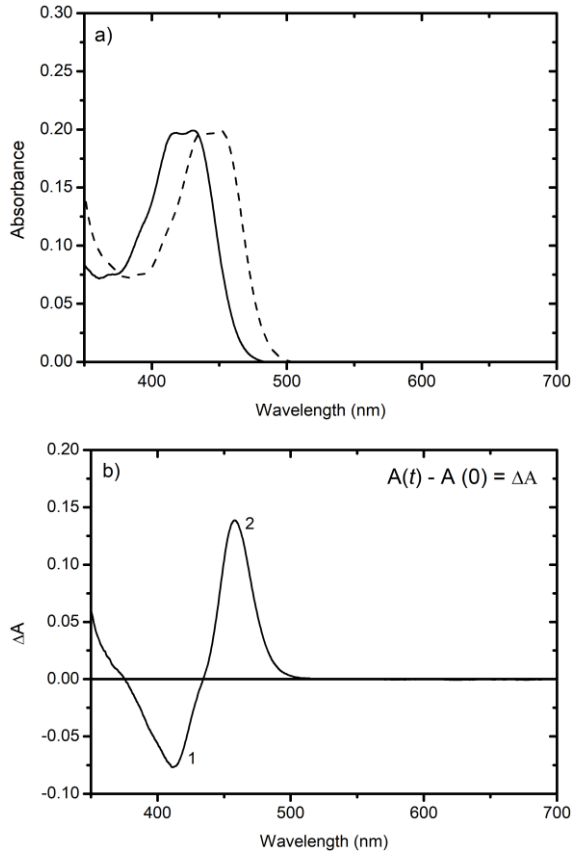


Figure 5.5. a) Absorption spectra of a photocatalyst without laser pulse (*t* = 0, solid) and with laser pulses (*t*, dashed). b) Difference absorption spectrum of a photocatalyst. Those spectra were imagined for didactic purpose.

The intensity of negative signal **1** is proportional to the amount of molecules that still exist in their fundamental state and is referred to as the ground-state bleaching and the intensity of the positive signal **2** is proportional

to the fraction of molecules that were promoted to their excited state and corresponds to the absorption of the excited state in the ideal case. Any new absorption feature that would result from excited-state electron transfer generated *via* photo-induced electron transfer would also manifest in novel absorption features that could be detected by TA spectroscopy. Having in mind the characteristics of a transient absorption spectrum, we can now investigate the excited state of **10c**.

Excitation at 450 nm in acetonitrile and recording the transient absorption spectra 10 ns after the laser pulse led to no significant absorption changes, *i.e.* no excited species or intermediates were detected in that time range which is confirmed by a ΔA near 0 value (**Figure 5.6**). The absorption spectra at $t = 0$ or $t = 10$ ns are identical. This is in line with a short singlet excited-state lifetime of 5.1 ns in acetonitrile that completely returns to the ground state within 10 ns in acetonitrile and/or with a rapid quenching. This transient absorption analysis confirms that no side reaction occurred with acetonitrile and that no intermediates were formed on that timescale.

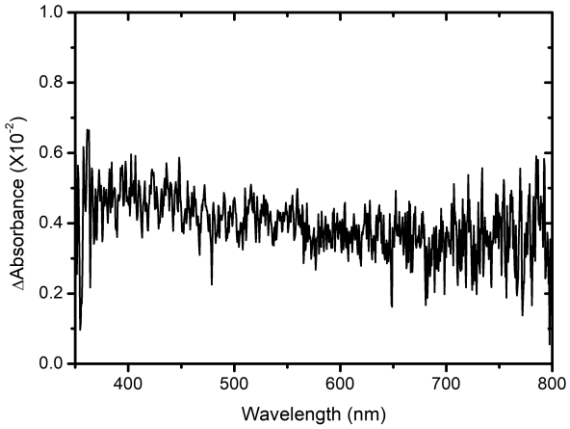


Figure 5.6. Nanosecond transient absorption spectrum of **10c** in acetonitrile. The spectrum was recorded 10 ns after the laser pulse (450 nm) and integrated for 10 ns (30 scans) under argon atmosphere.

On the other hand, when the same analysis was performed in dichloromethane, a novel intense absorption feature was observed around 470

nm (**Figure 5.7**). This was quite surprising as we could have expected to obtain the same spectra in acetonitrile or in dichloromethane. To check the photostability of this transient species, the time of measurement was extended to 100 ns (instead of 10 ns) and a completely different transient absorption spectra was recorded. Indeed, an intense negative signal at around 460 nm and a ΔA of ~0.50 above 550 nm were obtained. The positive absorbance above 550 nm could be attributed to a reduced phenazine as reported in the literature.[389]

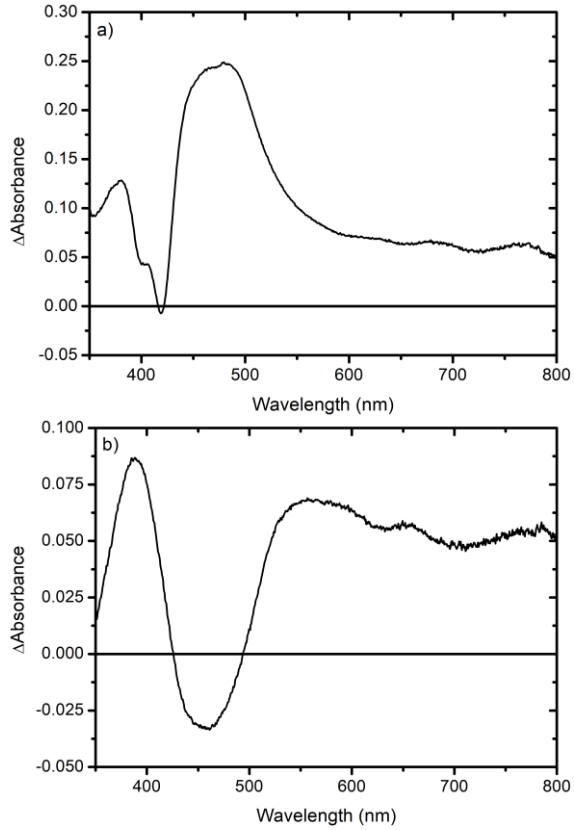
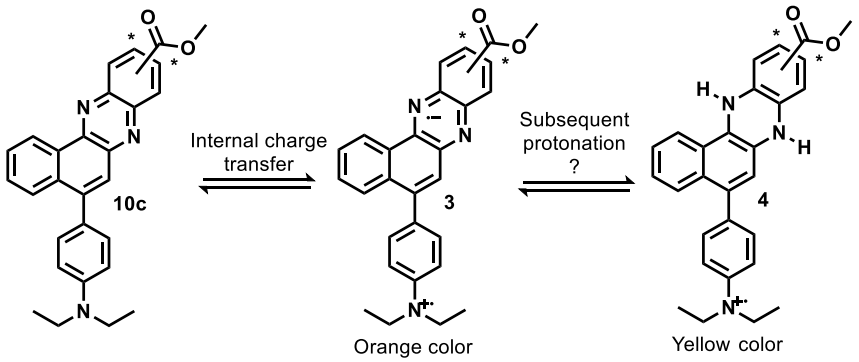


Figure 5.7. Nanosecond transient absorption spectra of **10c** in DCM. Spectrum a: recorded 10 ns after the laser pulse (450 nm) and integrated for 10 ns (30 scans). Spectrum b: recorded 100 ns after the laser pulse (450 nm) and integrated for 10 ns (30 scans). Both spectra were recorded under argon atmosphere.

Based on these results, we clearly see that the excited state of **10c** evolves over time and is thus not photostable as the signal shape is changing at

different time intervals. If the spectra corresponded solely to excited-state absorption, then identical absorption features of different intensity would have been observed. The signal obtained after 10 ns is hard to attribute and may not correspond only to the excited state of compound **10c**.

The photodegradation seen with the transient absorption spectra was also supported by a color change occurring through the TA analysis. At the beginning, the compound **10c** displayed an orange color in dichloromethane while at the end of the experiment, the color had changed to a pale-yellow solution. Such observations are probably in line with the undesired internal charge transfer, previously mentioned, that may occur giving an orange color to the solution (**Scheme 5.5**). Indeed, as **10c** exhibits a reducing function, *i.e.* the diethylamine that has the same molecular structure as common sacrificial donors used in photoredox applications, and an oxidant one which is the phenazine, the amine moiety can reduce the phenazine core by transferring intramolecularly an electron to form compound **3** which tends to get protonated before performing the back-electron transfer. The formation of this new species **4** could explain the yellow color observed at the end of the TA analysis. This protonation event could be promoted in the presence of an acid that would come from the dichloromethane as it contains naturally acid traces and could explain the different behaviors observed in the two solvents. In acetonitrile, as no acid traces are present, the reduced phenazine would not be protonated after the intramolecular electron transfer and may quickly undergo the back-electron transfer explaining that no signal was observed by transient spectroscopy.



Scheme 5.5. Internal charge transfer that may occur in dichloromethane followed by a possible subsequent protonation of the phenazine core.

To substantiate this hypothesis of internal charge transfer and subsequent protonation event, the nanosecond transient absorption spectra of **10c** were recorded in the presence of triflic acid. In this case, whether the signal was recorded 10 or 100 ns after the laser pulse, the spectra were identical with an intense negative signal around 460 nm. This corresponds to the spectrum recorded during 100 ns in absence of triflic acid, suggesting that the hypothesis of the formation of a photoproduct obtained by internal charge transfer and protonation in dichloromethane may be possible (**Figure 5.8**). Moreover, the transient species formed in the presence of triflic acid is probably also a permanent photoproduct as no sign of recovery towards the baseline was observed, even after 3 μs (**Figure 5.9**). Spectro-electrochemistry would be the suitable tool to use in the future to prove definitely if an internal charge transfer occurs and to identify the partners involved by following their absorbance according to their redox potentials.

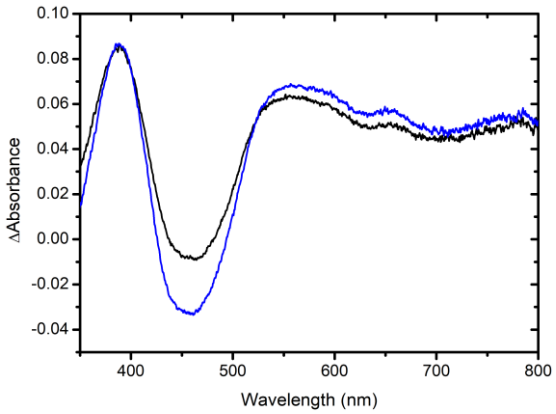


Figure 5.8. Nanosecond transient absorption spectra of diethylaniline in dichloromethane in the presence of triflic acid. The spectra were recorded (30 scans) 10 ns after the laser pulse (450 nm) for 10 ns (black) and 100 ns (blue) under argon atmosphere.

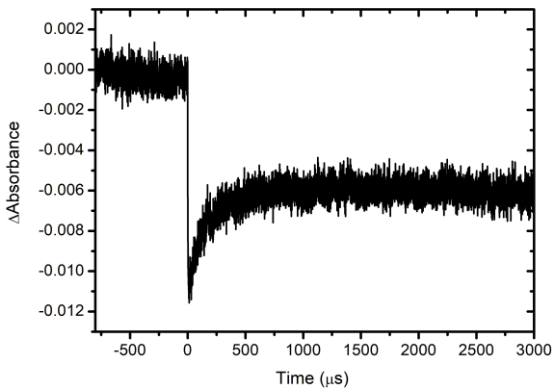


Figure 5.9. Single wavelength absorption changes recorded at 460 nm in argon purged dichloromethane.

In addition, the presence of triflic acid immediately provoked a change of color of **10c** (**Figure 5.10**) reinforcing our hypothesis of internal charge transfer and protonation. As already mentioned, dissolved **10c** gives an orange solution when the internal charge transfer occurs. When the triflic acid was added, the diethylamine group could get protonated thus hampering the internal charge transfer or the phenazine core got protonated and became a more powerful oxidant which led to the rapid disappearance of the orange color and the appearance of a yellow one.



Figure 5.10. Change of color observed with **10c** when the addition of triflic acid was performed.

2.2.3. Photoproduct identification

Nanosecond transient absorption spectroscopy was consistent with the formation of a permanent photoproduct upon irradiation in dichloromethane. To gain further insight into that process, we carried out steady-state absorbance and photoluminescence measurements before and after transient absorption spectroscopy to see if any structural changes may have occurred. The absorbance of **10c** was recorded in dichloromethane with and without triflic acid, before and after TA. After TA, a drastically different absorption spectrum was observed. Indeed, the spectrum became vibronically resolved and the maxima blue-shifted to 416 and 396 nm (**Figure 5.11**). Surprisingly, the absorbance spectra after TA looked quite the same as the one of the benzophenazine derivative **12** that has no southern function. This observation clearly demonstrates the formation of a photoproduct yielding to a yellow solution. The strict identification of this photoproduct would have had required HPLC analysis or its isolation and subsequent NMR analysis. Still, some hypotheses can be made.

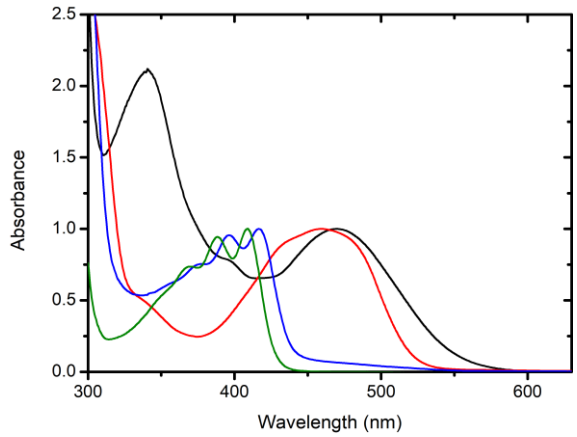
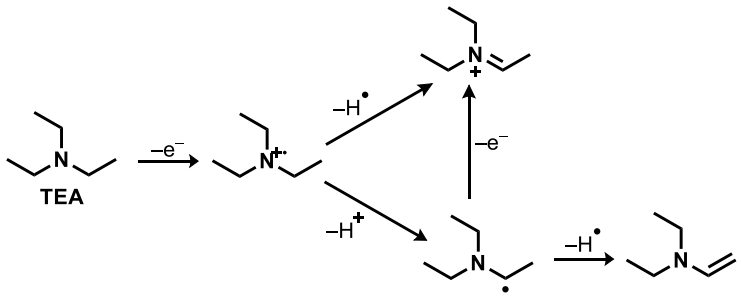


Figure 5.11. Absorption spectra of **10c** in dichloromethane (black), in the presence of triflic acid (red), after TA in the presence of triflic acid (blue) and in comparison with absorption spectrum of compound **12** (green).

As the product of photodegradation exhibits an absorption quite similar to compound **12**, we could envisage that the southern fragment in **10c** suffers from changes. It is known in the literature that sacrificial donors, such as triethylamine (TEA), undergo cascade chemistry once they have been oxidized by one electron (**Scheme 5.6**).[390–392] Such reaction pathways can be envisaged for the diethylamine moiety which can further be lost when the back-electron transfer is performed. The loss of the entire southern fragment, *i.e.* the diethylaniline motif, could be also envisaged but the breaking of a C–C bond necessitates more energy than for a C–N bond (82.7 and 70.0 kcal mol^{-1}, respectively) and can be considered as less favorable.



Scheme 5.6. Cascade chemistry associated with cationic radical TEA when TEA is oxidized by one electron.

The photodegradation of **10c** was also observed by emission spectroscopy (**Figure 5.12**). A blue-shifted emission was observed at 504 nm after TA while an emission wavelength of 548 nm was displayed before TA.

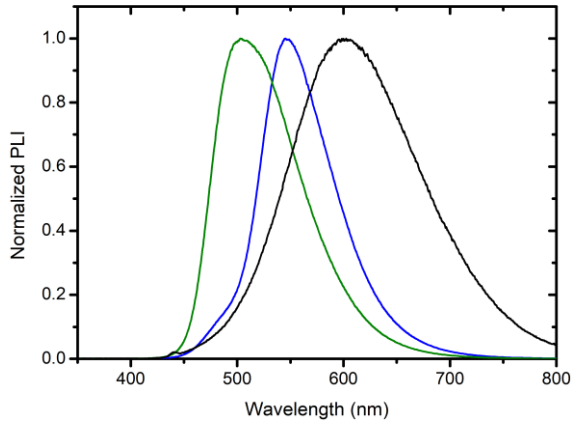


Figure 5.12. Normalized emission spectra of **10c** in dichloromethane (black), with triflic acid (blue) and with triflic acid after TA (green).

The photostability was also assessed under 24 h of irradiation (two blue Thorlabs lamps, less energetic than the laser pulse) in presence of acetic acid (A), TEA (C), TFA (D) in excess or by itself (B) and the final solutions were analyzed by thin layer chromatography (TLC) (solution D was neutralized with TEA before doing the TLC). In presence of acetic acid, some degradation of compound **10c** was observed (supported by lower NMR integrals, see **Figure C.3**) with the formation of a more polar species while in presence of a stronger acid neutralized at the end of irradiation (TFA, D), the solution went darker and an orange spot identical to the photocatalyst was observed. In presence of triethylamine (C) or just by itself (B), the same spot as the photocatalyst was observed and compound **10c** seemed unchanged (**Figure 5.13**). This observation was supported by a NMR analysis which showed no photodegradation of compound **10c** after 24 h of irradiation (**Figure C.3**). The difference in light irradiation (power, photon flux) could explain the stability of compound **10c** observed here and it would have been interesting to control each solution by UV-vis to detect any change in photophysical properties.

Nanosecond transient absorption would have been also interesting to conduct in basic conditions to see if a photoproduct may form under these conditions also.

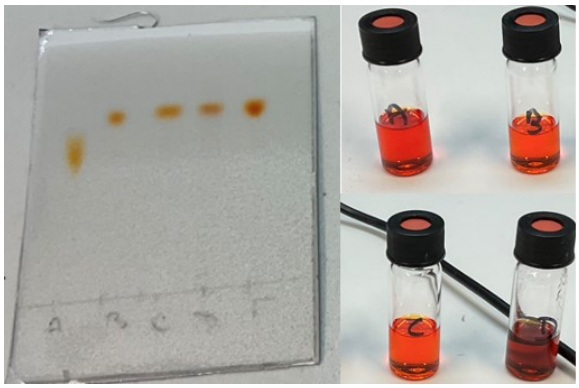


Figure 5.13. Photostability assessed in DCM with an excess of acetic acid (A), TEA (C), TFA with neutralization (D) or just compound **10c** by itself (B) and the corresponding TLC analysis.

2.2.4. Comparison with another benzophenazine derivative

We went one step further by investigating the excited state of the benzophenazine derivative **10f-1** bearing a sulfur-based motif on the southern fragment of the molecular skeleton to avoid the presence of a donor fragment. This photocatalyst was selected as it was proven to exhibit a great photostability in the previous Chapter. The goal with such photocatalyst is to highlight if the low photostability observed with compound **10c** is specific to it or due to the oxidant character of benzophenazine skeleton.

The TA spectra (with or without triflic acid) were recorded and were identical, displaying an intense negative signal around 430 nm corresponding to the absorption of the fundamental state and an intense positive signal at 503 nm corresponding to the absorption of the excited state (**Figure 5.14**). Such excited state had a lifetime of 3.3 and 2.3 µs without or with triflic acid, respectively. The possibility of protonating the phenazine core could explain the lower excited-state lifetime but the influence of acidity needs further investigations to be fully understood. With sulfur-based derivative, a strong

absorbing excited state was immediately formed after the laser pulse and the transient species was not impacted by acidic conditions proving that such photocatalyst seem to be photostable under these conditions.

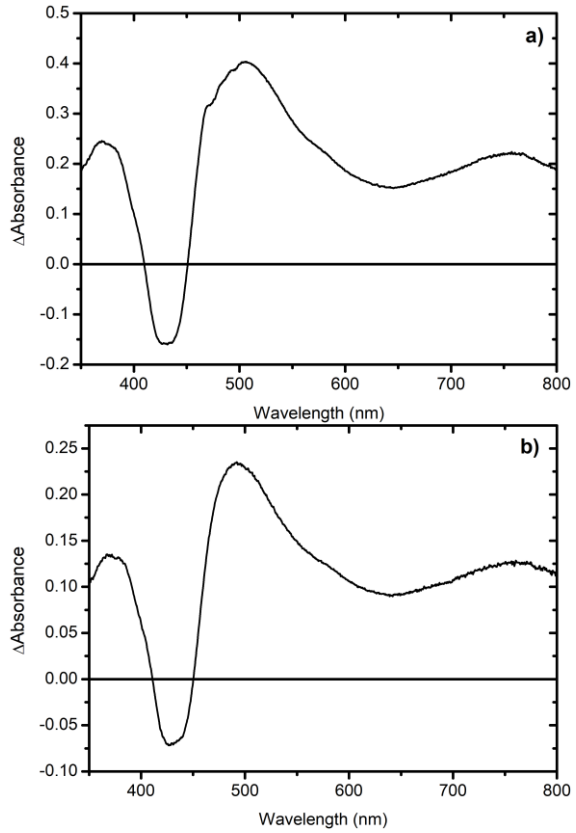


Figure 5.14. Transient absorption spectrum of **10f-1** in dichloromethane, without (a) and with triflic acid (b) under argon atmosphere. Excitation at 430 nm.

The emission spectra (**Figure 5.15**) were also nearly not impacted by the presence of triflic acid as a maximum of around 550 nm was observed in both cases, which is another proof that the sulfur-based benzophenazine **10f-1** is (photo)stable while the emission of **10c** was shifted in acidic conditions.

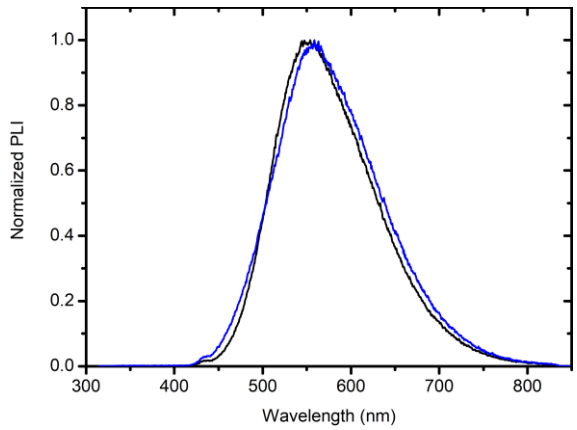


Figure 5.15. Normalized emission spectra of sulfur-based benzophenazine **10f-1** in dichloromethane without (black) and in the presence of triflic acid (blue).

3. Conclusions and perspectives

The compound **10c** was selected as a possible suitable photoredox catalyst as it possesses reversible reduction potentials. Unfortunately, this photocatalyst was revealed to be inefficient for the photodebromination of bromovalerophenone and thus, its excited state was investigated by nanosecond transient spectroscopy.

Transient absorption spectra of **10c** were different whether they were recorded in acetonitrile or in dichloromethane. In acetonitrile, no excited-state absorption could be observed in the time range used suggesting that the excited-state lifetime is short or that a rapid quenching occurs in acetonitrile. In dichloromethane, depending on the time scale used during the analysis, the transient absorption spectra were different and showed the formation of a long-lived transient species that we hypothesized to be a photoproduct formed by an internal charge transfer and a subsequent protonation. The use of triflic acid proved this possible protonation as the transient absorption spectra were unchanged over time and fitted with the evolution of **10c** excited-state.

The photoproduct formation hypothesis was finally confirmed by UV-vis and emission spectroscopies. Completely different spectra were obtained for

both techniques after performing TA analysis and the shape and position of absorbance band was close to the benzophenazine **12** case without a southern functionalization demonstrating that, due to protonation or even back-electron transfer, the diethylamine or diethylaniline moiety was lost to form the photoproduct.

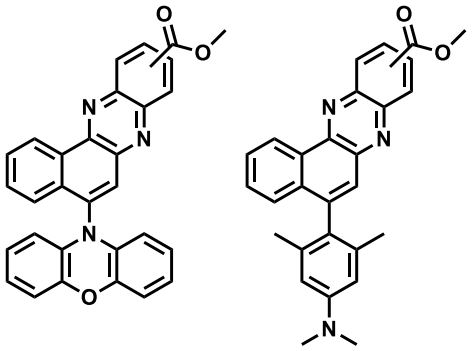
The sulfur-based benzophenazine **10f-1** was employed in order to investigate if such photodegradation was specific to compound **10c** or to the benzophenazine molecular skeleton. The sulfur-based derivative **10f-1** proved to be (photo)stable under acidic conditions as transient absorption was unchanged along with the emission wavelength. The photodegradation and the formation of the photoproduct seems to be specific to the compound **10c**.

The low photostability of **10c** is maybe not the only reason why compound **10c** was not efficient in the reduction of an aryl bromide. The establishment of the excited-state redox potentials may not be correct. Indeed, if the amine motif is not spectroscopically active in the transition used in photoredox applications, the fundamental-state oxidation wave was not the correct one to use to determine the excited-state oxidation potential, thus the latter could be overestimated and could explain the inability of compound **10c** to reduce bromovalerophenone.

A lot of investigations still need to be done to confirm and prove the internal charge transfer and protonation events. Spectro-electrochemistry would be a suitable technique to identify the partners involved in the electron transfer (if one occurs). Moreover, different observations are still not understood such as an emission wavelength that is shifted from 600 nm to 450 nm 50 ns after the laser pulse when performing the delay map or the strict impact of acidity onto the photocatalysts as an hypsochromic shift in absorption and emission was observed with compound **10c** while the absorption of **10f-1** remained unchanged. This could highlight that the

different functionalizations of the benzophenazine core can ease or not its protonation.

In order to obtain an efficient and photostable photocatalyst, it would be interesting to add another nitrogen-based southern fragment, like a phenoxazine or a tetramethylaniline (**Scheme 5.7**) which are more sterically hindered, inducing an orthogonality between the donor and the acceptor groups. Such geometry would reduce the electronic communication between these two fragments as the overlap between the HOMO and LUMO orbitals would be small.[393–395] The internal charge transfer may then be hampered or at least less effective. This orthogonality could be one solution to use a nitrogen-based benzophenazine derivative as efficient photoredox catalyst.



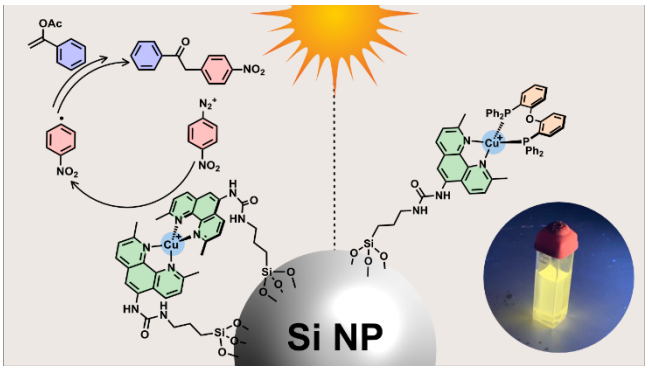
Scheme 5.7. Other southern fragments envisaged to design an efficient benzophenazine photoredox catalyst.

In conclusion, compound **10c** is not photostable under the conditions used in this Chapter and further investigations need to be done to fully understand the reasons of its low photostability and to characterize better its excited state if this photocatalyst can still be considered as valuable.

Chapter 6

Photo-catalyzed α-arylation of enol acetate using recyclable silica-supported heteroleptic and homoleptic copper(I) photosensitizers

N. Body, R. Bevernaegie, C. Lefebvre, I. Jabin, S. Hermans, O. Riant, L. Troian-Gautier, *under soumission process.*



Author statement

Nathalie Body was the principal investigator of this research project. She designed the methodology and performed the entire investigation and analyses. **Robin Bevernaegie** and **Corentin Lefebvre** participated in the methodology of ligand synthesis and anchoring. **Ivan Jabin** participated in the conceptualization of the project, gave advice about the methodology and reviewed and edited the publication. This research project was realized under the supervision of **Sophie Hermans** and **Olivier Riant** who conceptualized the project, designed the methodology, and reviewed and edited the publication. **Ludovic Troian-Gautier** designed the methodology, conducted the experiments concerning the excited-state reactivity with the principal investigator, assisted in the results interpretation and reviewed and edited the publication.

1. Abstract

Earth-abundant photosensitizers are highly sought after for light-mediated applications, such as photoredox catalysis, depollution and energy conversion schemes. Homoleptic and heteroleptic copper(I) complexes are promising candidates in this field, as copper is abundant and the corresponding complexes are easily obtained in smooth conditions. However, some heteroleptic copper(I) complexes suffer from low (photo)stability that leads to the gradual formation of the corresponding homoleptic complex. Such degradation pathways are detrimental, especially when recyclability is desired. In here, we report a novel approach for the heterogenization of homoleptic and heteroleptic Cu complexes on silica nanoparticles. In both cases, the photophysical properties upon surface immobilization were only slightly affected. Excited-state quenching with aryl diazonium derivatives occurred efficiently (10^8-10^{10} M^{-1} s^{-1}) with heterogeneous and homogeneous photosensitizers. Moderate but almost identical yields were obtained for the α-arylation of enol acetate using the homoleptic complex in homogeneous or heterogeneous conditions. Importantly, the silica-supported photocatalysts were recycled with moderate loss in photoactivity over multiple experiments. Transient absorption spectroscopy confirmed that excited-state electron transfer occurred from the homogeneous and heterogeneous homoleptic copper(I) complexes to aryl diazonium derivatives, generating the corresponding copper(II) center that persisted for several hundreds of microseconds, compatible with photoredox catalysis applications.

2. Introduction

Visible-light photoredox catalysis has emerged as an efficient tool to develop novel reaction pathways using mild and ecofriendly conditions. Despite being the most efficient organometallic photocatalysts, ruthenium(II) and iridium(III) complexes suffer from limitations in terms of sustainability and scalability. Alternatives based on organic and Earth-abundant photosensitizers, such as those based on iron, zinc or copper, have recently emerged.[68,74–90,390,396]

Homoleptic copper complexes $[Cu(NN)_2]^+$, where NN is a bidentate diimine ligand, were the first copper(I) complexes to be developed in photocatalysis. In the late 1980s, Kern and Sauvage reported the synthesis of $[Cu(dap)_2]^+$ (dap = 2,9-dianisyl-1,10-phenanthroline) and its application in the homocoupling of *p*-nitrobenzyl bromide.[25] Drawbacks such as the low excited-state lifetime of homoleptic complexes limited their applications, which led to their gradual disuse compared to Ru(II) and Ir(III) analogues.[83] $[Cu(NN)_2]^+$ have nonetheless experienced a recent upsurge due to their notable reducing properties and the development of new diimine ligands enhancing the photophysical properties of such copper complexes.[75,76,91–98,397] In an effort to improve the photophysical properties of these latter, new derivatives of 1,10-phenanthroline ligands bearing bulky substituents were developed to prevent excited-state geometry changes *via* pseudo Jahn-Teller distortion.[99,100] In 2002, McMillin and coworkers drastically improved the field of copper photocatalysis by associating these sterically hindered diimine ligands with a diphosphine POP ligand (POP = bis[2-(diphenylphosphino)phenyl] ether). This led to the development of a new family of heteroleptic photocatalysts with excited-state lifetimes that can exceed those of ruthenium and iridium photocatalysts with blue-shifted absorbances.[101] Since then, heteroleptic copper complexes have been tremendously developed and their potential was demonstrated in multiple

organic synthesis applications.[83,86,102–105,398–400] However, it has been reported that heteroleptic copper complexes can sometimes suffer from ligand substitution and/or loss depending on the reaction conditions. This possible low (photo)stability leads to the formation of their homoleptic counterparts *via* a ligand association-dissociation mechanism that occurs more rapidly in coordinating solvents than in non-coordinating ones for example.[165–167] This process can also occur upon oxidation of Cu(I) to Cu(II), either photochemically or electrochemically.[401–403] This association-dissociation mechanism also occurs in homoleptic complexes but the impact of such process is evidently less detrimental.[140]

Combining bulky ligands around the copper center is a solution to ensure a long-lived excited state and a (photo)stable photocatalyst in solution, but it is not always sufficient to suppress that ligand exchange mechanism in coordinating solvents, as observed for [Cu(bcp)(DPEPhos)]PF_6 (bcp = bathocuproine, DPEPhos = bis[(2-diphenylphosphino)phenyl] ether) which rapidly forms the corresponding [$Cu(bcp)_2$]PF_6 complex under irradiation.[87] Heterogenization on solid particles seems to be a promising approach to circumvent some of the above-mentioned limitations. Indeed, such an approach would restrict the degrees of freedom of the photosensitizers and potentially inhibits the association-dissociation mechanism. Moreover, we believe that developing approaches to recycle photosensitizers is paramount in the current energy and environmental landscape. Indeed, despite the low cost of heteroleptic copper(I) complexes such as [Cu(bcp)(DPEPhos)]PF_6 (2.5 times less expensive than $[Ru(bpy)_3]^{2+}$ (bpy = bipyridine) and 32 times less than [$Ir(ppy)_3$] (ppy = phenylpyridine)), developing versatile approaches to recover and isolate the metal is highly desirable to implement circular economy.[263–265] An added benefit in photoredox catalysis would also be the efficient separation of the heterogenized copper complexes that could be easily recovered by filtration from the reaction media.

Photocatalysts heterogenization has been extensively studied as a powerful tool towards sustainable organic synthesis, amongst others.[164,197] Silica nanoparticles represent an optimal support as this inorganic oxide possesses i) a high specific surface area which can be tuned by the porosity parameters,[213] ii) an easy surface functionalization[214,216–218,346], iii) a transparency over a broad range of wavelengths[219] and iv) a high mechanical and (photo)stability.[213] In organic photocatalysis, the heterogenization on silica supports has been developed mainly for organic dyes such as Rose Bengal[170,171,173,178,404,405], Eosin Y[179,406] or BODIPY[337] as well as rare Earth ruthenium(II)[169,183,270,407] and iridium(III) complexes.[180,408] To the best of our knowledge, there is only a handful of examples of well-defined copper complexes heterogenized on silica nanoparticles. For example, Cai and coworkers recently heterogenized a non-discreet copper complex $[Cu(NN)X_n]^+$ (X = I, Br, Cl, OAc or SO_4) on mesoporous silica nanoparticles for the thermal reactivity in organic synthesis.[192,193,409,410] Hosseinzadeh *et al.* anchored a phenanthroline-Cu(I) catalyst on nanocellulose which was used in thermal C–N and C–O cross-couplings reactions.[411]

The main photocatalytic domain for which copper complexes immobilization was developed is dye-sensitized solar cells (DSSC).[186–188] Numerous heteroleptic and homoleptic copper(I) complexes were immobilized on TiO_2 surfaces and revealed to be efficient for solar energy conversion.[83] Efficient surface anchoring is achieved *via* the introduction of carboxyl[412] or phosphonate[413] groups on the chelating diimine ligand for example. The anchoring of heteroleptic copper(I) complexes was also applied for the photocatalytic hydrogen production by the Beller group.[189] Using sulfonated photosensitizers also anchored on TiO_2 composites along with $[Fe_3(CO)_{12}]$ as water reduction catalyst, a TON of 2452 could be reached in the photoproduction of H_2. For photocatalytic organic transformations, the immobilization of copper complexes has been rare. In 2020, Choi *et al.*

developed a hybrid-copper catalyst anchored on SBA-15 silica nanoparticles.[190] By derivatizing the bipyridine ligand, a covalent bond was formed between the photoactive species and the support. This heterogenized system was then used in a photo-induced C–H arylation. Note however that no heteroleptic or homoleptic copper complex was involved, only a non-discreet complex. The only example of heteroleptic copper complex immobilization used in photocatalytic applications was described by Appleby *et al*. that used [Cu(xantphos)(dmp)](tfpb) (dmp = dimethylphenanthroline; tfpb = tetrakis(3,5-bis(trifluoromethyl)phenyl)borate) immobilized on chromatography grade silica by simple adsorption. These photoactive surfaces were then used to produce singlet oxygen upon irradiation with visible light in aqueous media to exterminate bacteria.[194] To the best of our knowledge, the immobilization of homoleptic or heteroleptic copper(I) complexes for photoredox applications is overlooked so far.

In here, we present an innovative approach for the heterogenization of heteroleptic and homoleptic Cu(I) complexes on silica nanoparticles and their use in the photo-catalyzed α-arylation of enol acetate using aryl diazonium derivatives. Unambiguous heterogenization was confirmed by XPS, TEM, Time of Flight Secondary Ion Mass Spectrometry (Tof-SIMS) as well as by Diffuse Reflectance UV-vis spectroscopy (DR-UV-vis). Comprehensive mechanistic details were garnered by steady-state and time-resolved spectroscopic techniques, which included transient absorption spectroscopy. The latter was used to determine that the heterogenized Cu(I) complexes were competent for excited-state electron transfer to the aryl-diazonium derivatives with electron transfer rate constants that were in the 10^8-10^{10} M^{-1} s^{-1} range. Importantly, the supported photocatalyst could be efficiently recovered and the photocatalytic activity only slowly decreased from 40 to 18 % over 5 runs.

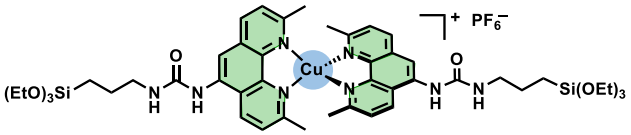
3. Results and discussion

3.1. Synthesis

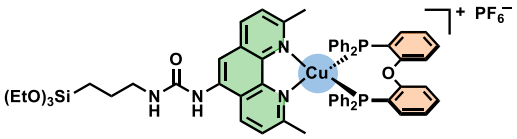
Siloxane moieties were considered to derivatize 1,10-phenanthroline-type ligands in order to achieve the final goal of immobilizing copper(I) complexes onto silica nanostructures. These anchoring moieties are suitable functions as they form strong anchor points with silica nanoparticles. In addition, the present study also investigated two different approaches to efficiently anchor copper(I) complexes, *i.e.* a one-step anchoring of well-defined homoleptic and heteroleptic copper(I) complexes and a two-step procedure where the heteroleptic complex was gradually assembled on the silica nanoparticles.

The targeted ligand functionalized with siloxane moieties (DMP-Si) was synthesized in three steps starting from the commercial 2,9-dimethyl-1,10-phenanthroline (DMP) that underwent nitration in a mixture of concentrated sulfuric acid and fuming nitric acid to yield the corresponding 5-nitro-2,9-dimethyl-1,10-phenanthroline (DMP-NO_2). Subsequent reduction using hydrazine hydrate and carbon-supported palladium afforded the corresponding amine (DMP-NH_2). The last step was the formation of the ureido group through the reaction of DMP-NH_2 with triethoxy(3-isocyanatopropyl)silane to obtain the final DMP-Si ligand with an overall yield of 31 %. This ligand was then used for the synthesis of the corresponding homoleptic and heteroleptic copper complexes (**Scheme 6.1**). The homoleptic complex **(Cu-1)** was formed by dissolving the DMP-Si ligand in 2:1 ratio with $[Cu(MeCN)_4]PF_6$ in dichloromethane. For the heteroleptic complex **(Cu-2)**, DMP-Si was reacted in 1:1 ratio with a previously synthesized diphosphine copper complex ($[Cu(DPEPhos)_2]PF_6$) in DCM at room temperature for 3 hours. The homoleptic (**Cu-1**) and heteroleptic (**Cu-2**) complexes were obtained with isolated yields of 57 % and 61 %, respectively, and were

characterized by NMR, Differential Pulse Voltammetry (DPV), XPS, FTIR-ATR and HRMS (see SI – Annex D).



[Cu(DMP-Si)$_2$]PF$_6$ **(Cu-1)**



[Cu(DMP-Si)(DPEPhos)]PF$_6$ **(Cu-2)**

Scheme 6.1. Structures of the homo- and heteroleptic copper complexes **Cu-1** and **Cu-2**, respectively.

With the two complexes in hands, we sought to develop the synthesis of silica nanoparticles for efficient surface immobilization. Nanospheres (NS) nanoparticles were first targeted as they represent a standard morphology that prevents potential pore-diffusion issues, as commonly observed in heterogeneous catalysis.[376,377,379] Nanospheres nanoparticles were obtained by adapting the procedure of Stöber *et al.* based on the sol-gel process to access a 40 nm diameter size.[220] Core-Shell (CS) silica nanoparticles were also targeted as this architecture offers a high specific surface area while limiting the diffusion of chemical species. Core-Shell silica nanoparticles, with a core of 28 nm and a mesoporous layer of 16 nm, were obtained by adapting the procedure from Yoon *et al* also based on the sol-gel process.[221] The size and morphology of these NS and CS nanoparticles were confirmed by TEM (**Figure 6.1**). XPS analysis proved that the siloxane bonds of SiO_2 were correctly formed, and that no impurities were present, with the exception for NS for which a small amount of unreacted or partially reacted tetraethylorthosilicate (TEOS) was observed. Specific surface areas of 360 m^2 g^{-1} and 650 m^2 g^{-1} were calculated using the Brunauer-Emmett-Teller (BET) equation on nitrogen physisorption data for NS and CS, respectively.

Concerning the pores size and the porous volume, Barret-Joyner-Halenda (BJH) and Density Functional Theory (DFT) methods were used for mesoporous and microporous materials, respectively. Nanospheres exhibit micropores of 0.7 nm and a porous volume of 0.63 $cm^3\ g^{-1}$. Core-Shell nanoparticles possess a combination of mesopores (3.0 nm) and micropores (1.3 nm) with a porous volume of 2.4 $cm^3\ g^{-1}$.

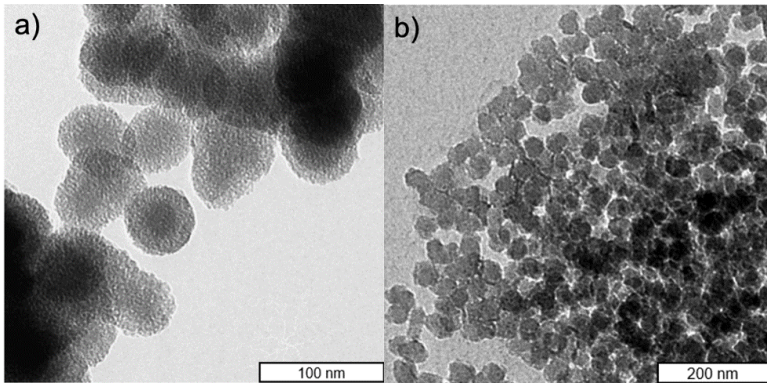
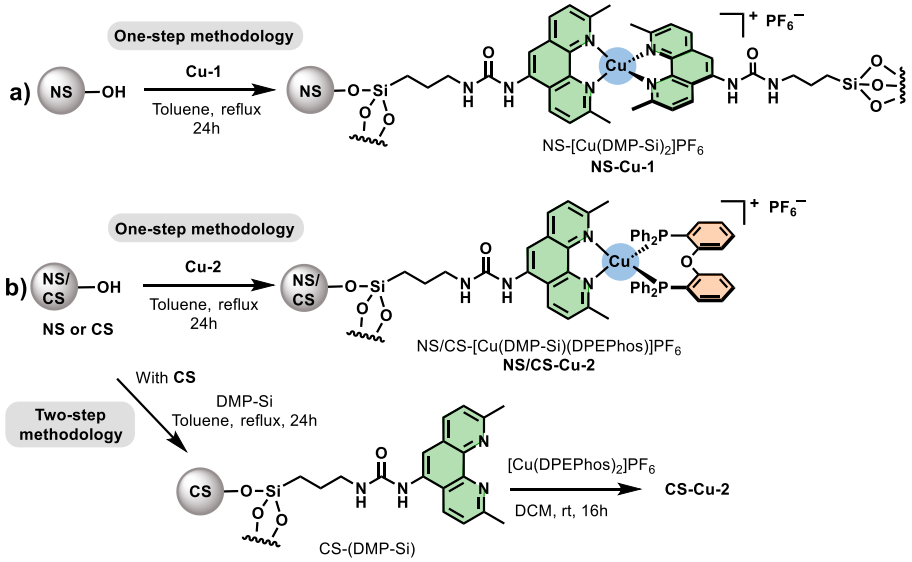


Figure 6.1. TEM images of pristine silica core-shell (CS) nanoparticles (a) and nanospheres (NS) (b).

First, the grafting of $[Cu(DMP\text{-}Si)_2]PF_6$ **Cu-1** was investigated on silica nanospheres. **Cu-1** was allowed to react with silanol functions of silica nanospheres in toluene under reflux over 24 hours (**Scheme 6.2a**). This afforded a deep orange-colored powder that was characterized by XPS and TGA. All expected elements were detected at correct binding energies by XPS (**Figure 6.2**). The atomic ratios were in agreement with the one of pure **Cu-1** (**Figure D.1**) corroborating that the complex's structure remained intact on the silica surface (**Table 6.1**). Nevertheless, two unexpected components were observed for the F_{1s} signal by XPS, indicating that two types of fluorine environments were detected. The first one was attributed to PF_6^- appearing at a binding energy of 686.5 eV while the second one, with a binding energy of 688.3 eV, was attributed to F–(O, Si) bonds. The latter could come from the hydrolysis of PF_6^- that yields hydrofluoric acid which is a known reagent able to passivate the silica surface by forming Si-F bonds.[414,415] When the

temperature is elevated from about 40 °C, although the amount of H_2O is very low, the hydrolysis of PF_6^- could happen. The thermal degradation of PF_6^- was quite well investigated with $LiPF_6$ as its low stability is a recognized issue in Li-ion battery research field.[416,417] To bring that degradation into light, $[Cu(DPEPhos)_2]PF_6$ was stirred in DCM at room temperature in the presence of pristine NS silica. After several washing steps, the silica nanoparticles were analyzed by XPS where a fluorine signal was detected at 688.1 eV, though in a lower amount compared to the elevated temperature experiment implemented in the anchoring of **Cu-1** (**Figure D.19**). This observation is in line with the possible hydrolysis of PF_6^- and the passivation of silica surface. As XPS is a semi-quantitative surface analysis, a TGA thermogram was recorded to quantify the loading of **Cu-1** at the surface of the support. The thermogram showed a loss in weight of about 15.6 wt.% which corresponds to 0.015 mmol of complex per 100 mg of material (**Figure D.11**). This is consistent with standard loading values of copper comprised between 0.3–0.75 mmol g^{-1} found in the literature when considering the specific surface area ratios.[191–193,418]



Scheme 6.2. The one- or two-step methodologies investigated to anchor the homoleptic (a) and heteroleptic (b) copper(I) complexes on nanospheres (NS) and core-shell (CS) silica nanoparticles. Note that both anchoring points of **NS-Cu-1** complex are probably located on the same silica nanosphere.

Table 6.1. XPS atomic ratios determined for the grafting of **Cu-1** and **Cu-2** onto CS or NS nanoparticles, in comparison with pure compounds. The theoretical ratio (in parenthesis) was calculated based on the molecular structure of **Cu-1** and **Cu-2**.

	Cu-1	**NS-Cu-1**	**Cu-2**	**CS-Cu-2**		**NS-Cu-2**
				Two steps[a]	One step[a]	One step[a]
N/Si	3.60 (4)	0.09	4.2 (4)	0.38	0.13	0.11
N/C	0.17 (0.17)	0.13	0.06 (0.07)	0.12	0.08	0.08
Cu/C	0.02 (0.02)	0.018	0.01 (0.02)	0.02	0.02	0.02
Cu/N	0.15 (0.13)	0.14	0.24 (0.25)	0.14	0.26	0.32
Cu/P	1.15 (1)	-	0.38 (0.5)[b]	0.89[b]	0.70[b]	1.40[b]
Cu/F	0.14 (0.17)	0.23	0.14 (0.17)	0.28	0.19	0.25
P/F[c]	0.12 (0.17)	-	0.15 (0.17)	0.07	0.08	0.04

[a] "One step" and "two steps" refer to the one- and two-step methodologies used for the preparation of the supported complexes (**Scheme 6.2**). [b] Only the phosphine component was used. [c] Only the phosphorus component arising from the counter anion was used.

Similar conditions were used to anchor the heteroleptic complex **Cu-2** on nanospheres and core-shell nanoparticles (**Scheme 6.2b**). XPS results were encouraging in both cases as all of the expected elements were detected at

correct binding energies (**Figure 6.2** and **Figure D.12**) and all the atomic ratios were close to those of the pure copper complex (**Table 6.1**, **Figure D.4**). The only mismatch came from Cu/P ratio that highlighted a slight deficiency of phosphine ligand and the P/F ratio, as described before, which was larger on NS than on CS nanoparticles. The loading was different from one support to the other, as expected based on the various specific surface areas. *Via* TGA, a loading of 0.014 mmol per 100 mg (wt.% = 14.8) and of 0.020 mmol per 100 mg (wt.% = 20.8) of material were determined for NS and CS, respectively (**Figure D.13**). Inductively coupled plasma optical emission spectroscopy (ICP-OES) also corroborated the calculated loading obtained by TGA (wt.% in Cu = 0.82%, wt.% in **Cu-2** = 14.6 %). As for the anchoring of **Cu-1**, these values are encouraging as the same range was found in the literature when considering the specific surface area ratios.[191–193,418] Hence, this one-step anchoring procedure seemed efficient to preserve the copper complex's architecture. Smoother reaction conditions were also attempted with **Cu-2** (EtOH at room temperature instead of toluene at reflux) but only 0.03 at.% of Cu were detected by XPS (*vs* 0.7 at.% in toluene).

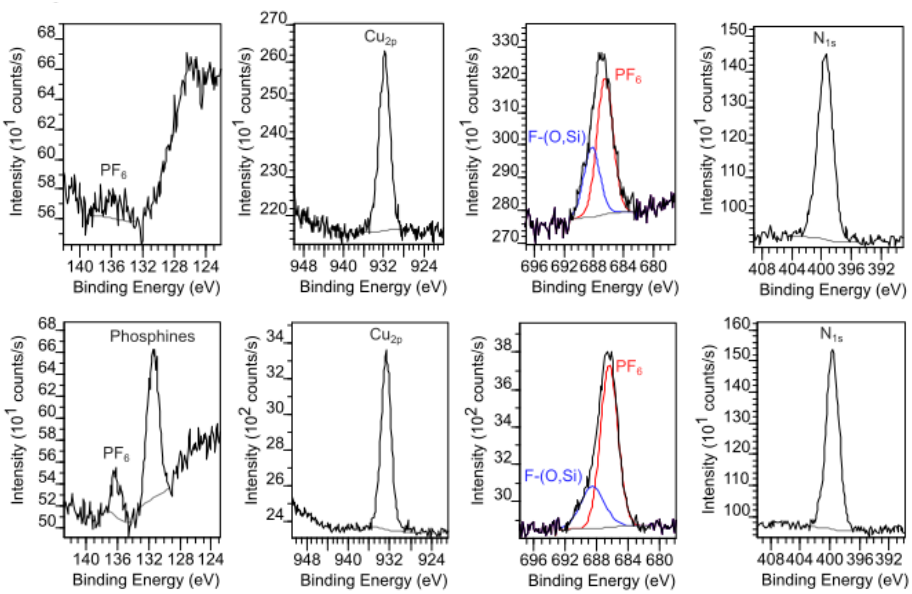
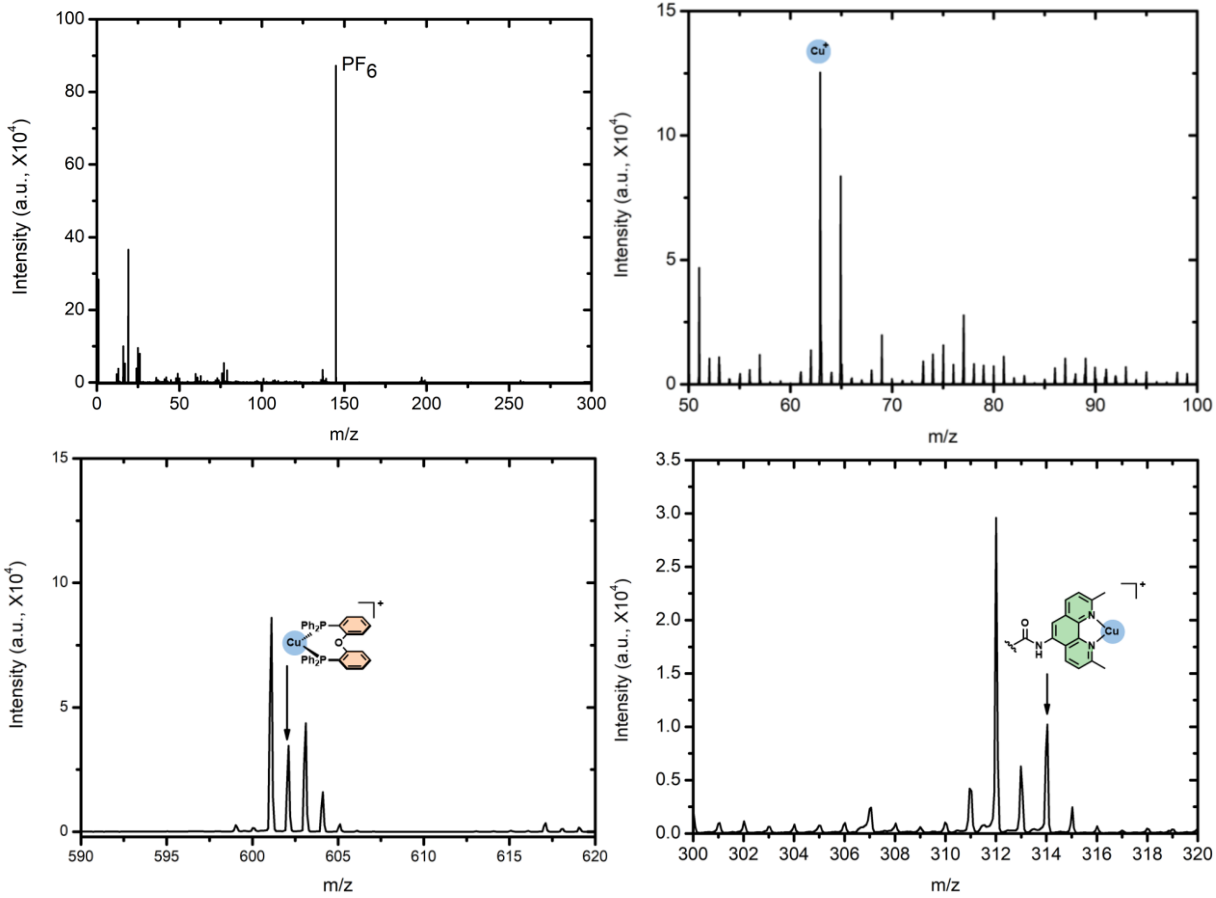


Figure 6.2. P_{2p}, Cu_{2p}, F_{1s} and N_{1s} XPS spectra of immobilized **NS-Cu-1** (top) and **NS-Cu-2** (bottom) obtained through the one-step methodology.

ToF-SIMS analysis was performed on **NS-Cu-2** to further confirm the efficient immobilization of complex **Cu-2**. In ToF-SIMS, surface sputtering with a focused primary ion beam generates the ejection of secondary ions that are easily collected and analyzed and provide molecular information. All the important fragments were detected by ToF-SIMS in negative (PF_6) and positive modes (Cu, Cu+DPEPhos, Cu+DMP-Si, Cu+DPEPhos+DMP-Si) (**Figure 6.3**) which, in combination with the results obtained by XPS, unambiguously confirm the efficient immobilization of unaltered **Cu-2** at the surface of nanoparticles and highlights the efficiency of the proposed methodology.


PF6
Intensity (a.u., X10^4)
m/z
Cu+
Cu
Ph2P
PPh2
O
N
H

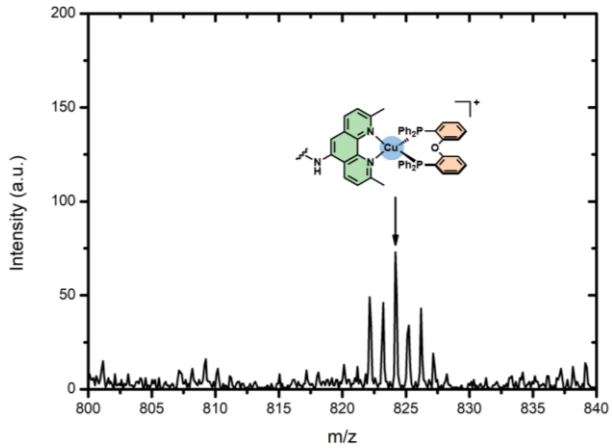


Figure 6.3. ToF-SIMS spectra of **NS-Cu-2** obtained with the one-step methodology and the color-coded identified fragments, *i.e*. PF_6 (black, m/z = 145), Cu (blue, m/z = 63), Cu+DPEPhos (blue-orange, m/z = 602), Cu+DMP-Si (blue-green, m/z = 314) and Cu+DPEPhos+DMP-Si (orange-blue-green, m/z = 824).

In an effort to increase versatility of the silica support and expand the range of possible coordination reactions, a two-step methodology was also optimized where the ligand was anchored prior to being reacted with $[Cu(DPEPhos)_2]PF_6$ in dichloromethane at room temperature (**Scheme 6.2b**). The DMP-Si ligand was anchored onto CS by reacting the dense layer of silanols with the DMP-Si siloxane moieties. The formation of the CS supported ligand, *i.e.* CS-(DMP-Si), was confirmed by XPS analysis that showed a nitrogen peak at 399.4 eV corresponding to aromatic and urea nitrogen (**Figure D.14**).[4] An experimental N/C atomic ratio of 0.19 was determined, which agreed well with the theoretical one of 0.22. In addition, TGA was also used to evaluate the ligand loading at the surface that showed a loss in weight of wt.% = 21.3, corresponding to a loading of 0.045 mmol of ligand per 100 mg of material, assuming that the calcinated organic part was only due to the presence of the DMP-Si ligand (**Figure D.15**). With the efficient covalent immobilization of DMP-Si confirmed, we investigated the formation of the heteroleptic complex **Cu-2**. CS-(DMP-Si) was dispersed in DCM and a solution of $[Cu(DPEPhos)_2]PF_6$ in DCM was added dropwise. After an overnight reaction, a yellow powder was recovered and analyzed by XPS which confirmed the efficient formation of the immobilized heteroleptic complex **CS-Cu-2**, as emphasized by the presence of copper and diphosphine ligand peaks (**Figure D.16**). Similar observations as in the anchoring of **Cu-1** were made for the F_{1s} signal indicating once again the interaction between the counter anion and the silica support. The atomic ratios were investigated to confirm that the expected structure was obtained (**Table 6.1**). Firstly, the N/Si ratio did not change compared to CS-(DMP-Si), confirming that the DMP-Si ligand was not altered or lost during reaction. The Cu/N was smaller than the theoretically predicted one, indicating that either some of the DMP-Si ligand was left unreacted, or that some homoleptic complex was also formed. This last hypothesis was reinforced by the lower than predicted percentage of phosphorus element. Finally, a loading of photoactive compound of 0.02

mmol of [Cu] per 100 mg of material was determined by TGA (**Figure D.17**) which is slightly higher than the one obtained with the previously described methodology. Hence, the one-step methodology seems more suitable to preserve the structure of heteroleptic complex **Cu-2**.

3.2. Photophysical and electrochemical properties

The photophysical (**Table 6.2**) and electrochemical properties of $[Cu(DMP\text{-}Si)_2]PF_6$ (**Cu-1**) and $[Cu(DMP\text{-}Si)(DPEPhos)]PF_6$ (**Cu-2**) were first evaluated in homogeneous conditions. **Cu-2** absorbed moderately in the visible range with a maximum centered at 389 nm that tailed until 470 nm. A molar absorption coefficient around 2800 $M^{-1}\,cm^{-1}$ was determined at 389 nm which is in line with $[Cu(dmp)(DPEPhos)]BF_4$ (ε = 2700 $M^{-1}\,cm^{-1}$ in DCM).[419] Visible-light excitation of **Cu-2** led to steady-state photoluminescence centered at 537 nm. Time-resolved photoluminescence measurements in dichloromethane were well described by first-order kinetics which yielded excited-state lifetimes of 13.2 µs and 283 ns under argon and under O_2 saturated solution, respectively. **Cu-2** was also luminescent in acetonitrile with excited-state lifetimes of 2220 ns and 20 ns under argon and under O_2 saturated solution, respectively. Complex **Cu-1** exhibited a more intense and red-shifted absorption with a maximum centered at 464 nm with a corresponding molar absorption coefficient of 11000 $M^{-1}cm^{-1}$ in DCM which is in accordance with values for $[Cu(bcp)_2]PF_6$ (ε = 13200 $M^{-1}cm^{-1}$ in DCM)[420]. SSPL was observed at 708 nm in DCM under argon with a corresponding excited-state lifetime of 41 ns (**Figure 6.4**). The electrochemical properties of **Cu-1** and **Cu-2** were measured by differential pulse voltammetry in MeCN containing 0.1 M $TBAPF_6$ electrolyte. For **Cu-2**, a metal-centered oxidation and ligand-centered reduction were recorded at 1.46 and –1.11 V *vs* NHE, respectively (**Figure D.5**). Using the Rehm-Weller equation,[387] excited-state redox potentials $E_{1/2}(Cu^{+*/0}) = 1.09$ and $E_{1/2}(Cu^{2+*/+})$ = –0.74 V *vs* NHE were determined for **Cu-2**. These excited-state redox

potentials are in line with the prototypical [Cu(bcp)(DPEPhos)]PF_6,[87] highlighting that the introduction of a siloxane anchoring group did not change the fundamental properties of the complex. Concerning **Cu-1**, a metal-centered oxidation and ligand-centered reduction were recorded at 0.91 V and –1.12 V *vs* NHE (**Figure D.2**), respectively, which yielded excited-state redox potentials of 0.64 V and –0.85 V *vs* NHE for $E_{1/2}(Cu^{+*/0})$ and $E_{1/2}(Cu^{2+*/+})$, respectively.

Table 6.2. Photophysical properties of **Cu-1** and **Cu-2** recorded in DCM.

Complex	Absorption (nm)	PL (nm)	ε ($M^{-1}cm^{-1}$)	Excited-state lifetime (ns)
Cu-1	464	704	11000	41 (Ar)
Cu-2	389	560	2830	13200 (Ar); 283 (O_2)

Similar photophysical properties were observed for the heterogenized copper complexes. The absorption profile was first assessed to confirm proper immobilization of the copper complexes without significant changes in their fundamental properties. To do so, diffuse reflectance UV-vis spectroscopy with a Kubelka-Munk treatment was performed. Anchored or not, the complexes showed the same absorption profile (**Figure 6.4**) and corresponding photoluminescence upon blue light excitation (**Figure D.18**). Importantly, different diffuse reflectance spectra were obtained for **CS-Cu-2** whether the immobilization of the copper complex was performed in one or two steps. When a one-step immobilization approach was used, the diffuse reflectance spectra agreed well with the absorption spectra of **Cu-2** recorded in DCM. However, when the two-step procedure was used, a shoulder at 415 nm and a higher absorbance at 450 nm was observed which could potentially be attributed to the partial formation of **Cu-1**, albeit with the maxima slightly shifted compared to homogeneous conditions. This observation reinforces the previously proposed hypothesis that a portion of homoleptic complex was formed at the solid surface when a two-step methodology was used.

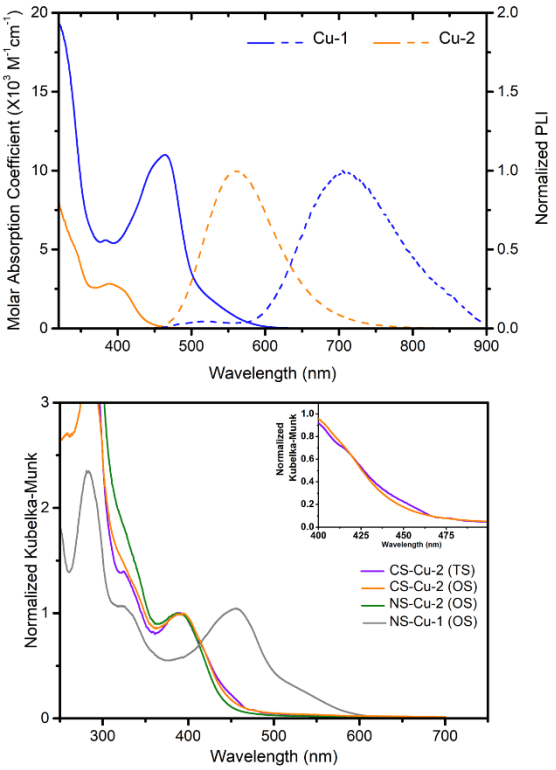


Figure 6.4. Top: UV-vis absorption (solid) and steady-state photoluminescence spectra of **Cu-1** and **Cu-2** recorded in argon-purged DCM. Bottom: Diffuse reflectance spectra of **Cu-1** and **Cu-2** heterogenized on silica core-shell (CS) or nanospheres (NS) nanoparticles. OS = one-step methodology; TS = two-step methodology.

The SSPL spectra in DCM of **NS-Cu-2** functionalized nanoparticles were recorded following pulsed 410 nm light excitation. A very small shift of 6 nm was observed under argon atmosphere, with maxima centered at 561 and 555 nm in homogeneous and heterogeneous conditions, respectively. In the presence of oxygen, the PL intensity was almost completely quenched, indicating that this material is competent for $^1O_2$ photosensitization. In addition, this also highlights that, even if immobilized, the photoactive compound is still capable of undergoing excited-state reactivity. An excited-state lifetime of 3.8 μs was determined in heterogenous conditions, indicating that surface immobilization leads to additional excited-state deactivation processes.

We were then interested in investigating the stability of the heteroleptic complex in the dark and under irradiation. Indeed, even if heteroleptic complexes represent a widely used class of photosensitizers for photoredox catalysis, their stability over the course of a reaction is not always investigated. It is also known that heteroleptic copper complexes can suffer from a lack of (photo)stability leading to the formation of their homoleptic counterparts *via* a ligand association-dissociation mechanism that occurs more rapidly in coordinating solvents than in non-coordinating ones for example.[165–167] This is proper to heteroleptic copper(I) complexes but such light-induced degradation also occurs in prototypical Ru(II) photosensitizer where the dissociative ligand-field states can be easily populated.[421–426] In the dark or under irradiation, these heteroleptic Cu(I) complexes undergo ligand exchange to yield the corresponding homoleptic complexes which tend to be less effective in photoredox reactions. Strategies to mitigate these problems have been proposed over the years, the most famous one being the use of bulky substituents around the copper center. In the present case, **Cu-2** did not undergo ligand exchange over 24 h in the dark in dimethylformamide, as evidenced by ^{1}H NMR (**Figure D.7**). The photostability of this complex was then evaluated under 470 nm irradiation (Blue Thorlabs LED) in dimethylformamide, a suitable solvent for photoredox catalysis applications (*vide infra*). To do so, different concentrations of **Cu-2** were prepared to verify the zero-order ligand exchange reaction and the absorption spectra were recorded at specific time intervals following irradiation with Blue Thorlabs LED. As can be observed from **Figure 6.5**, the presence of an isosbestic point at 420 nm coupled to the gradual increase of an absorption band at 475 nm is in line with the formation of the corresponding homoleptic complex **Cu-1**. Based on molar absorption coefficients, we estimated that 12 % of **Cu-1** was formed after 4 hours of irradiation. In addition, it should be pointed out that this conversion was independent of the concentrations of photosensitizer and hence evolved according to a zero-order reaction. Similar experiments could

not be performed on the heterogenized surfaces that require diffuse reflectance measurements, but those spectra were recorded following photoredox catalysis reactions (*vide infra*). Formation of the homoleptic complex **Cu-1** was also confirmed by ^{1}H NMR with similar conclusions as in the photostability study (55 % of **Cu-1** formation after 24 h of irradiation) (**Figure D.8**). Photostability of **Cu-1** was also assessed using the same irradiation setup which showed that **Cu-1** is photostable throughout 10 h of constant irradiation (**Figure 6.5**).

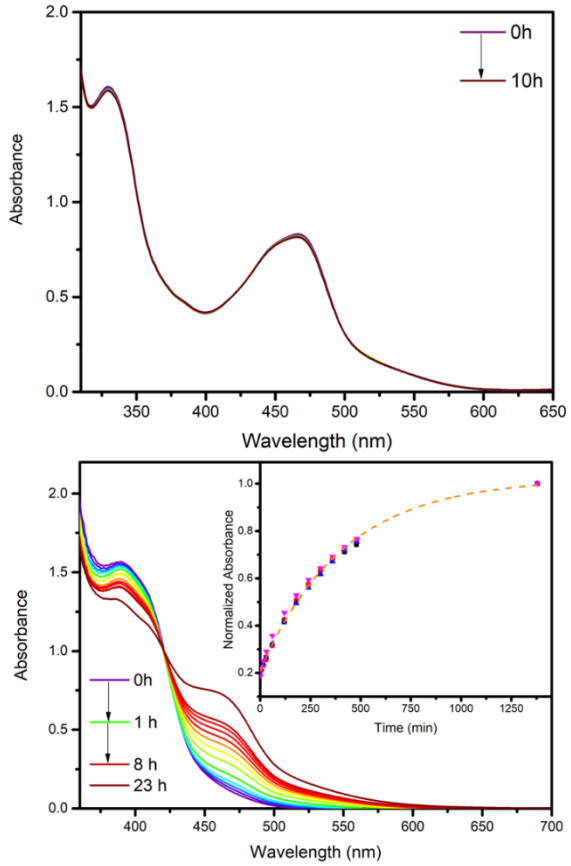


Figure 6.5. Photostability study of the homoleptic complex (**Cu-1**) and of the heteroleptic complex **Cu-2**. Since degradation was observed for **Cu-2**, experiments were carried out at different concentrations (1.19×10^{-4} M = black square; 2.51×10^{-4} M = red circle; 3.47×10^{-4} M = blue triangle; 4.57×10^{-4} M = pink triangle) and the corresponding exponential fit (dashed orange line).

3.3. Excited-state reactivity

With a clear understanding of the ground and excited-states properties of the homogeneous and heterogenized copper complexes, we sought to investigate excited-state reactivity with an electron donor (*N*,*N*-diisopropylethylamine (DIPEA)) and an electron acceptor (4-nitrobenzene diazonium tetrafluoroborate). To do so, we performed excited-state quenching experiments following a Stern-Volmer approach. In homogeneous conditions using **Cu-2**, a quenching rate constant (k_q) of 4.1×10^7 M^{-1} s^{-1} was determined with DIPEA in acetonitrile. This represents a very inefficient quenching process, and probably stems from the moderate driving force for electron transfer (–0.13 eV). When 4-nitrobenzene diazonium tetrafluoroborate was used, a much larger quenching rate constant of 2.0×10^9 M^{-1} s^{-1} was determined in acetonitrile along with a very favorable driving force for electron transfer (–1.14 eV) (**Figure 6.6**). This value is very close to the solvent diffusion limit and highlights the efficiency for potential excited-state oxidative quenching. The Stern-Volmer experiments were more difficult to perform on **Cu-1** due to the short excited-state lifetime. No quenching rate constant could be determined with DIPEA or 4-nitrobenzene diazonium tetrafluoroborate in acetonitrile due to low emission intensity. These Stern-Volmer experiments were also conducted in dichloromethane on **Cu-2** and **Cu-1**. The low solubility of the tetrafluoroborate diazonium salt makes such analysis more difficult than in acetonitrile. For the quenching of **Cu-1**, this low solubility combined with a short excited-state lifetime of **Cu-1** makes the analysis even more complicated, explaining the low number of points recorded at the higher concentrations of diazonium. In both cases, the copper complexes were efficiently quenched by 4-nitrobenzene diazonium tetrafluoroborate with quenching rate constant of 1.0×10^9 M^{-1} s^{-1} and 5.5×10^{10} M^{-1} s^{-1} for **Cu-2** and **Cu-1**, respectively. No significant degradation was observed over the course of these experiments.

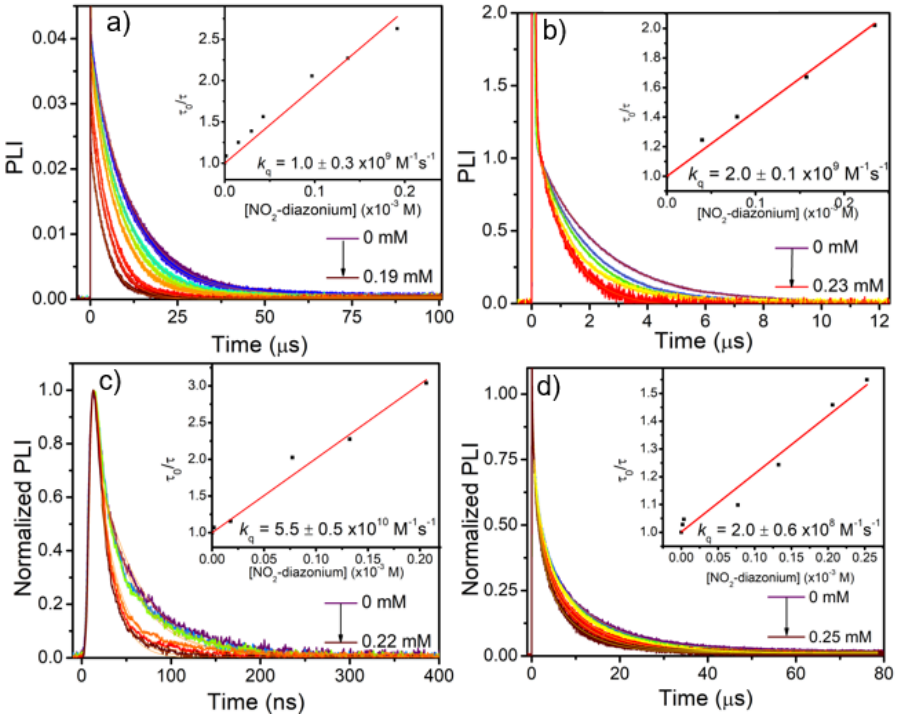


Figure 6.6. Excited-state quenching of **Cu-2** (a, b) and **Cu-1** (c) with increasing amounts of 4-nitrobenzene diazonium tetrafluoroborate in acetonitrile (b) and dichloromethane (a, c). Similar experiments were carried out with **NS-Cu-2** and 4-nitrobenzene diazonium tetrafluoroborate in dichloromethane (d). All experiments were carried out in argon purged solutions.

To corroborate the photoredox catalysis experiments (*vide infra*), nanosecond transient absorption experiments were also conducted in DMF. Unfortunately, **Cu-2** did not exhibit sufficient photostability to obtain unambiguous transient absorption results. Indeed, when **Cu-2** was irradiated at 410 nm with ~10 mJ pulse^{-1} laser fluence, a positive signal gradually appeared at wavelengths consistent with the formation of the homoleptic complex. However, **Cu-1** was particularly well-suited for these transient absorption measurements. The photosensitizers were short lived in DMF, as in acetonitrile. Excitation at 470 nm and recording the transient absorption spectra 200 ns after the laser pulse led to no significant absorption changes, setting the baseline for these experiments and confirming that no side reaction occurred with DMF on that timescale (**Figure 6.7**), unlike **Cu-2**. Identical

measurements were performed in the presence of 10 mM of 4-nitrobenzene diazonium tetrafluoroborate. In that case, an intense negative signal was observed around 490 nm, consistent with the loss of MLCT transition *via* oxidative electron transfer associated with the excited-state oxidation of Cu(I) into Cu(II) and the corresponding reduction of the aryl diazonium derivative. Note that the reduced aryl radical does not absorb in that wavelength range. To confirm our hypothesis, absorption spectra of a Cu(II) compound and the reduced diazonium derivative are needed to correctly assign the absorption bands visualized in transient absorption spectroscopy. In addition, at these concentrations, the transient species perdured on the millisecond timescale, which is very promising for photocatalytic applications.

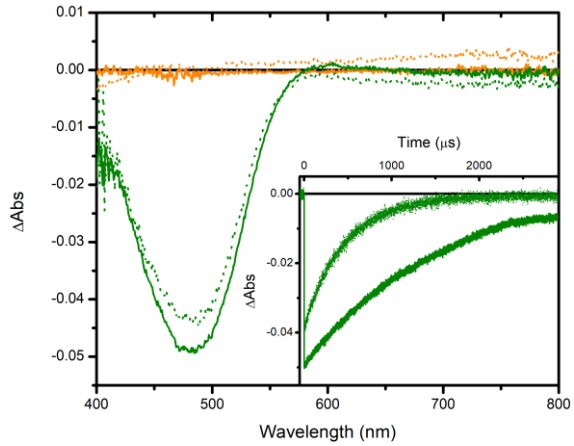


Figure 6.7. Nanosecond transient absorption spectroscopy recorded in DMF 200 ns after pulsed 470 nm light excitation of **Cu-1** (solid) and **NS-Cu-1** (dashed) without (orange) and with (green) 10 mM of 4-nitrobenzene diazonium tetrafluoroborate. The inset represents the single wavelength absorption changes recorded at 490 nm following pulsed 470 nm excitation for **Cu-1** (solid) and **NS-Cu-1** (dotted) in the presence of 10 mM of 4-nitrobenzene diazonium tetrafluoroborate. All experiments were carried out in argon purged solutions.

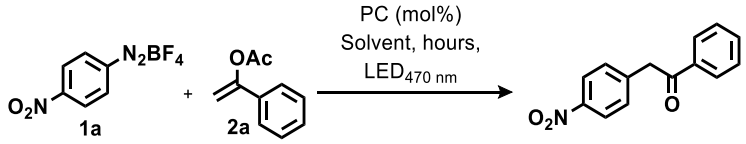
In heterogeneous conditions, a similar quenching rate constant with 4-nitrobenzene diazonium tetrafluoroborate was determined in acetonitrile, *i.e.* 3×10^9 M^{-1} s^{-1}. The main challenge associated with these experiments was the dispersion efficiency of the silica nanoparticles which impacts the intensity of the photoluminescence. In addition, aggregation of silica nanoparticles could

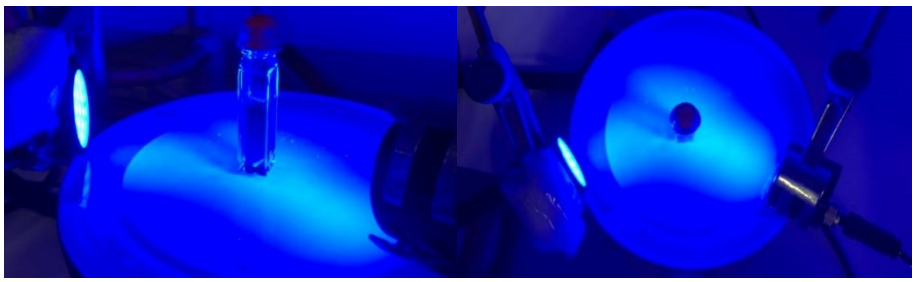
impair the photocatalyst's availability to engage in excited-state reactivity. When an effective dispersion was assured (*i.e.* no persistent solid aggregates), the heterogenized photocatalyst was capable of reacting with the aryl diazonium and thus, induced photochemical reaction at the solid surface which is, to the best of our knowledge, one of the first example in the literature using copper(I) complexes. At this stage, it should be noted that for heterogeneous photoredox catalysis application, an oxidative quenching generating an oxidized photosensitizer might be preferable compared to a reductive pathway. Indeed, in a classical reductive pathway, the excited state is reduced by large amount of sacrificial electron donor, whose sole purpose is to ensure a high yield of formation of the reduced species. In solution, this reduced photosensitizer then diffuses until it encounters a suitable reactive substrate, yielding the original photosensitizer and reduced substrate. This therefore depends on diffusion properties of the (reduced) photosensitizer. When heterogenized, the reduced photosensitizer does not have the possibility to diffuse, and chances of encountering the substrate are hence less probable. However, in oxidative electron transfer, the oxidized photosensitizer is formed as well as the corresponding reduced substrate, which can then diffuse out of the support and be used to drive further reactivity. If sufficiently stable, the oxidized copper can rest in that oxidized state until it finds a suitable regeneration pathway. Transient absorption experiments were also realized in heterogenous conditions and the same profile as in homogeneous conditions was observed. This is interesting as it shows that the immobilization does not seem to have an impact on the photoactivity of the complex and highlights that Cu(II) can be transiently formed. The recombination process seemed to occur faster in heterogeneous conditions than in homogeneous ones, but still lasts for several hundreds of microseconds.

3.4. Photocatalytic tests

The photoactivity of both homogeneous and heterogeneous copper complexes were investigated. To do so, an already established $[Ru(bpy)_3]^{2+}$-photocatalyzed reaction was transposed and optimized under heterogenized conditions to assess the efficiency of these copper(I) complexes for such reactions, as well as to evaluate the recyclability efficiency. The α-arylation of an enol acetate (**2a**) using 4-nitrobenzene diazonium tetrafluoroborate **1a** mediated by visible light was used as a benchmark reaction (**Table 6.3**). This reaction was reported by the Burkhard König's group to work efficiently in DMF using $[Ru(bpy)_3]^{2+}$ as photosensitizer.[427] In here, we used a LED with an emission distributed between 435 and 500 nm with a maximum centered at 470 nm (**Figure D.9**). This allowed to sufficiently excite both photosensitizers as higher-energy wavelength LED led to some undesired reactivity of the substrate. We were able to reproduce the reaction using $[Ru(bpy)_3]^{2+}$ as photosensitizer which yielded the desired product in 88 % yield following 2 hours of irradiation. Smaller yields of 55 % were obtained after 2 hours in homogeneous conditions when **Cu-2** was used as photosensitizer. This yield was increased to 78 % when the irradiation time was increased to 4 hours (**entry 3**). In DCM, the photoactivity dropped completely, probably due to the poor solubility of 4-nitro-benzene diazonium tetrafluoroborate (**entry 4**). Moderate yields of 45 % were obtained when **Cu-1** was used (**entry 6**). Control experiments highlighted that both a light source and the photosensitizer were needed for an efficient reaction to occur (**entries 8** and **9**). These results showcase the efficiency of the newly reported **Cu-2** for the α-arylation reaction while the corresponding homoleptic **Cu-1** exhibited only moderate activity in 4 hours.

Table 6.3. Photoactivity evaluation of homogeneous and immobilized copper complexes and the irradiation setup used.[a]





Entry	Photocatalyst (PC)	PC (mol%)	Time (h)	Yield[b] (%)
1	$[Ru(bpy)_3](PF_6)_2$	2	2	88
2	**Cu-2**	5	2	55
3	**Cu-2**	5	4	78
4	**Cu-2**	5	4	8[c]
5	**Cu-1**	5	2	22
6	**Cu-1**	5	4	45
7	**Cu-1**	5	16	50
8	No light	5	4	3[d]
9	No photocatalyst	-	4	1[d]
10	**CS-Cu-2**	5	16	14
11	**NS-Cu-2**	5	16	33
12	**NS-Cu-2** (Run 2)	5	16	24
13	**NS-Cu-1**	5	16	40
14	**NS-Cu-1** (Run 2)	5	16	39
15	**NS-Cu-1** (Run 3)	5	16	31
16	**NS-Cu-1** (Run 4)	5	16	27
17	**NS-Cu-1** (Run 5)	5	16	18

[a] The reaction was performed using 0.15 mmol of **1a**, 10 equiv. of **2a** and two blue Thorlabs lamps (470 nm, 4.0 mW/cm^2, output power of 253 mW). The picture relates to the set-up in heterogeneous conditions. [b] Isolated yields. [c] In dichloromethane. [d] NMR yield using dimethylsulfone as internal standard.

Encouraged by these results, we transposed the best reaction conditions to the heterogenized copper complexes. To do so, we kept the respective ratios of photosensitizers and reagents unchanged but increased the volume of

reaction from 0.4 to 10 mL to ensure optimal dispersion of the silica-supported photosensitizers. The heteroleptic copper complex immobilized on core-shell nanostructures **CS-Cu-2** gave disappointing results in the first run of reaction as only a 14 % isolated yield for the product was obtained (**entry 10**). CS nanostructures are probably not the most suitable support as the diffusion of the reactants and the light path to the pores seem to be limiting factors in this reaction. Moreover, chemical transformations at the solid surface depend on adsorption/desorption equilibria that can also lower the overall apparent rate of the reaction compared to homogeneous conditions. Even more concerning was the orange coloration of silica nanoparticles that was clearly visualized during the nanoparticle's dispersion step, meaning that the homoleptic complex could possibly be formed just by applying ultrasound (**Figure 6.8**). Heterogenized photocatalyst on nanospheres **NS-Cu-2** gave better isolated yields of 33 % (**entry 11**). However, the orange color of the silica nanoparticles at the end of the reaction indicated the probable formation of the homoleptic complex at the solid surface (**Figure 6.9**), as it is the case in homogeneous conditions where the ligand exchange also occurs. Both CS and NS recovered solids were analyzed by XPS to check the presence of all elements and verify the proposed hypothesis about homoleptic complex formation (**Table 6.4**). Indeed, phosphorus was no longer detected and only the inelastic component of Si_{2p} was visualized (**Figure 6.10**). Hence, it seems that the DPEPhos ligand was completely removed during the course of the photoredox catalytic reaction. Under oxidative conditions, Fischer *et al.* demonstrated that a heteroleptic copper complex decomposed by the dissociation of the sterically demanding phosphine ligand (elongation of the Cu–P bond and a decrease in the bite angle value). A second diimine ligand is then able to coordinate to form the homoleptic copper complex.[428] This dynamic ligand exchange was also reported by Kaeser *et al.*[165] Another reason for the loss in phosphorus element could be the oxidation of the DPEPhos ligand that would no longer be coordinating. The atomic ratios after

the first run corresponded to the theoretical ratios expected for the homoleptic complex, validating the previously formulated hypothesis. A leaching of copper was also observed for which its surface atomic concentration was divided by half. This is consistent with the formation of the homoleptic photocatalyst as two anchored ligands are needed for one copper center. Therefore, it seems that the homoleptic complex was formed, irrespective of the morphology of the support. A regeneration attempt on NS was performed by adding fresh DPEPhos ligand at the solid surface but this approach was unfortunately not successful as no phosphorus element could be detected by XPS.

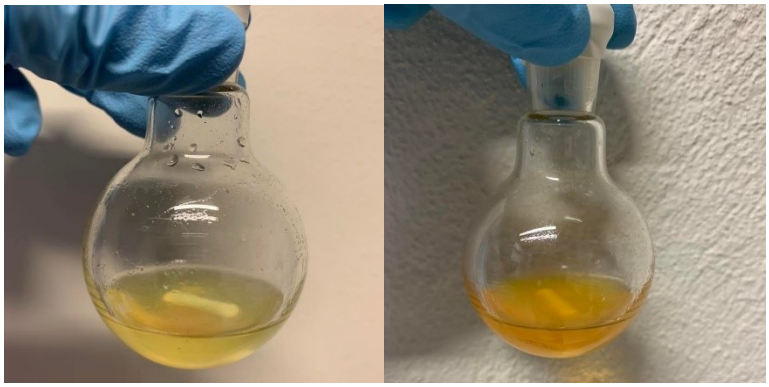


Figure 6.8. CS-Cu-2 in dry DMF (yellow suspension on the left) and after 15 minutes of applying ultrasound (orange suspension on the right).



Figure 6.9. NS-Cu-2 (yellow powder on the right) and the recovered solid after one photocatalytic run (orange powder on the left).

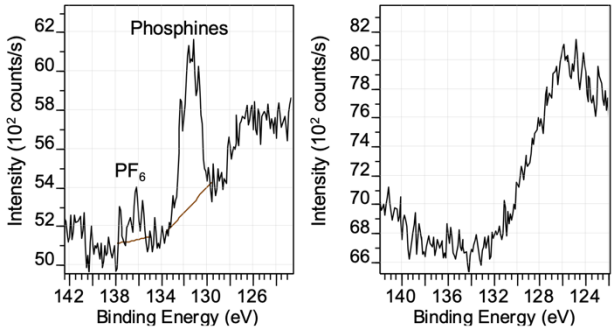


Figure 6.10. P_{2p} XPS spectra of **NS-Cu-2** (left) and **NS-Cu-2** after photocatalyzed α-arylation of enol acetate **2a** (right).

Table 6.4. XPS atomic ratios of **NS-Cu-1** and **NS-Cu-2** and of the recovered heterogenized heteroleptic and homoleptic complexes after the first run of reaction.

Atomic ratios	NS-Cu-1	NS-Cu-1 Run 1	NS-Cu-2	NS-Cu-2 Run 1
N/Si	0.09	0.07	0.11	0.08
N/C	0.13	0.19	0.08	0.15
Cu/C	0.018	0.013	0.02	0.03
Cu/N	0.14	0.07	0.32	0.18
Cu/P	-	-	1.40[a]	-
Cu/F	0.23	0.04	0.25	0.04
P/F[b]	-	-	0.04	-

[a] Only the phosphine component was used. [b] Only the phosphorus component arising from the counter anion was used.

Heterogeneous tests were carried out using the immobilized homoleptic complex **NS-Cu-1**. In otherwise identical conditions, 40 % isolated yields were obtained (**entry 13**), emphasizing that the homoleptic complex is competent for that reaction, with yields close to the one obtained in homogeneous conditions. **NS-Cu-1** were then recycled by simple filtration at the end of the reaction. The solid was washed with ~ 50 mL of diethyl ether and dried for several hours under high vacuum before being used in the next run of reaction. When the anchored homoleptic complex **NS-Cu-1** was used in a second run of reaction, a 39 % isolated yield was obtained which is similar to the first run (**entry 14**). This photoactivity was maintained over 4 runs before dropping by half on the fifth run (**entries 15-17**). **NS-Cu-2** was used in

a recycling run and a 24 % isolated yield was obtained (**entry 12**), which is consistent with the activity of the anchored homoleptic complex, albeit with a smaller surface loading. The heterogenized homoleptic complex remained stable throughout these experiments as copper and nitrogen were still detected by XPS after these runs (**Figure D.20**). However, a loss in these elements was observed when comparing to the initial atomic percentages of **NS-Cu-1** before use. It seems that 25 % of the initial copper was still present at the surface while the leaching of the ligand was much less important as 70 % of the initial nitrogen was detected. Hence, the lower amount of copper present at the NS surface explains the smaller isolated yields in the fifth run.

All samples were also characterized by DR-UV-vis to further prove our hypothesis of the *in-situ* formation of homoleptic complex. After one run of reaction using the heterogenized heteroleptic complex, an absorption profile similar to that of the homoleptic complex was clearly observed (**Figure 6.11**).

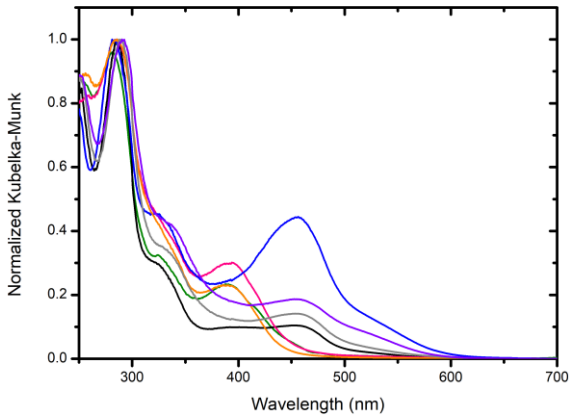


Figure 6.11. Diffuse reflectance UV-vis spectra of anchored **CS-Cu-2** obtained with the two-step methodology (green), **CS-Cu-2** obtained with the one-step methodology (pink), **NS-Cu-2** obtained with the one-step methodology (orange), recycled **NS-Cu-2** after the first run (grey), **NS-Cu-2** after applying ultrasound (black) and of **NS-Cu-1** (blue) and recycled **NS-Cu-1** after the first run (purple).

4. Conclusions

In conclusion, a robust strategy for the functionalization of silica nanospheres with homoleptic and heteroleptic copper(I) complexes was reported. In one step, heterogenized copper complexes were obtained that maintained photophysical properties compatible with excited-state reactivity. Stern-Volmer analysis revealed that aryl diazonium derivatives were suitable reagents for excited-state oxidative electron transfer that were used to trigger a reported α-arylation of enol acetate reaction. The homogeneous and heterogeneous homoleptic complexes were able to perform that reaction with moderate yields. Importantly, the supported photocatalyst could be efficiently recovered and the photocatalytic activity was maintained with slightly altered yields over 4 runs. Unfortunately, the heteroleptic complex, whether in homogeneous solution or heterogenized on silica nanospheres did not exhibit sufficient photostability and underwent the well-known ligand exchange to form the corresponding homoleptic derivatives. Other ligands need to be envisaged in starting Cu(I) complexes to ensure a good photostability in homogeneous conditions that would be transposed to heterogeneous conditions.

Nanosecond transient absorption spectroscopy revealed that both **Cu-1** and **NS-Cu-1** were competent for excited-state electron transfer to 4-nitrobenzene diazonium tetrafluoroborate that generated the corresponding Cu(II) analogue that persisted on the millisecond timescale. The nearly retained photophysical properties of the anchored homoleptic complex are promising for other applications in photoredox catalysis and solar fuel productions. In addition, photocatalytic yields were almost unchanged in homogeneous and heterogenous conditions. That aspect, coupled to the developed methodology that yields robust functionalized surfaces, highlight that the anchoring methodology is optimal but that better copper(I)

photosensitizer could be useful to burst the door open to efficient and recyclable photocatalysts.[397]

5. Experimental section

5.1. Chemicals and materials

All reactions were carried out using flame-dried glassware and magnetic stirring under an argon atmosphere unless otherwise stated. Commercial reagents were used as received while dichloromethane and toluene were distilled on MBraun MBSPS5 device before use. Ethanol (99 % V/V euro denaturated with 1 % of isopropanol), tetraethylorthosilicate (TEOS, ≥ 99 %, Sigma-Aldrich), ammonium hydroxide (NH_4OH, 25 % solution in water, Acros Organics), hexadecyltrimethylammonium bromide (CTAB, ≥ 99 %, Sigma Aldrich), anhydrous chloroform (≥ 99 % with 0.5-1.0 % ethanol as stabilizer, Sigma-Aldrich), anhydrous dimethylformamide (99.8 %, Sigma-Aldrich), 2,9-dimethyl-1,10-phenanthroline (≥ 98 %, Sigma-Aldrich), palladium on activated carbon (5 % Pd, Acros Organics), hydrazine hydrate ($N_2H_4.H_2O$, 99.9 %, Acros Organics), triethoxy(3-isocyanatopropyl)silane (95 %, ABCR), DPEPhos (99 %, Acros Organics), tetrakis(acetonitrile)copper(I) hexafluorophosphate (> 97 %, TCI), acetophenone (98 %, Acros Organics), isopropenyl acetate (99 %, Sigma-Aldrich), *p*-toluenesulfonic acid (*p*-TsOH, > 98 %, Sigma-Aldrich), 4-nitrobenzenediazonium tetrafluoroborate (> 98 %, TCI) were commercially available and used as received. 2,9-dimethyl-5-nitro-1,10-phenanthroline (DMP-NO_2)[429], 2,9-dimethyl-5-amino-1,10-phenanthroline (DMP-NH_2)[429], [Cu(DPEPhos)$_2$]PF_6[430] and 1-phenylvinyl acetate[427] were synthesized according to published literature.

5.2. Characterization methods

Nuclear Magnetic Resonance (NMR). NMR spectra were recorded on BRUKER spectrometers (300 MHz for ^{1}H, 75 MHz for ^{13}C, 121 MHz for ^{31}P).

Chemical shifts are reported in δ ppm relative to either the residual solvent peak of $CDCl_3$ (δ = 7.26 ppm) or the signal of PF_6^- (δ = –144.30 ppm). The following abbreviations have been used: δ (chemical shift), *J* (coupling constant expressed in hertz), br (broad), s (singlet), d (doublet), t (triplet), q (quadruplet) and m (multiplet).

X-Ray Photoelectron Spectroscopy (XPS). XPS analyses were carried out at room temperature with a SSI X-probe (SSX 100/206) photoelectron spectrometer (55 ° angle) from Surface Science Instruments (USA) equipped with a monochromatized microfocus Al X-ray source. Samples were stuck onto small sample holders with double-face adhesive tape and then placed on an insulating home-made ceramic carousel (Macor®, Switzerland). Charge effects were avoided by placing a nickel grid above the samples and using a flood gun set at 8 eV. The binding energies were calculated with respect to the Si_{2p} peak fixed at 103.5 eV. Data treatment was performed with the CasaXPS program (Casa Software Ltd., UK). The peaks were decomposed into a sum of Gaussian/Lorentzian (85/15) after subtraction of a Shirley type baseline. The XPS analyses were performed only once for each sample which prevent to assess the experimental error that can be quite important for several elements. Indeed, the peak selection is performed by the experimenter and can cause large variations in the peak area measured for smaller peak sizes. Elements with a low photoelectron cross-section, such as nitrogen, are particularly susceptible to errors. For most elements with moderate to strong photoelectron cross-sections, precision may vary by only a few tenths of a percent which is considered as a minor amount only if the element is mostly present at the surface (10 – 100 at%) but becomes a larger error as the element amount decreases.[285]

UV-vis. UV-vis absorption spectra were recorded on a Shimadzu UV-1700 instrument using 1 cm large cuvettes in quartz.

Photoluminescence. Time-resolved photoluminescence spectra were recorded on a LP980-K spectrometer from Edinburgh Instruments (see nanosecond transient absorption for full description). The optically diluted samples were excited with pulsed light and the excited-state lifetime was measured on a PMT LP detector (Hamamatsu R928) which covers the spectral range from 185 to 870 nm. An average of 30 scans per measurement was used.

Differential Pulse Voltammetry (DPV). Experiments were performed with an Autolab PGSTAT 100 potentiostat using a standard three-electrode-cell, *i.e.* a glassy carbon disk working electrode (approximated area = 0.03 cm^2), a platinum wire counter electrode and an aqueous Ag/AgCl reference electrode (salt bridge: 3 M KCl/saturated AgCl). Experiments were performed in 0.1 M tetrabutylammonium hexafluorophosphate acetonitrile electrolyte, and the samples were purged with argon before each measurement.

Nanosecond transient absorption. Nanosecond transient absorption measurements were recorded on a previously described apparatus.[81] Briefly, the latter consisted in a LP980-K spectrometer from Edinburgh Instruments equipped with an iCCD detector from Andor (DH320T). The excitation source was a tunable Nd:YAG Laser NT342 Series from EKSPLA. The third harmonic (355 nm) at 150 mJ was directed into an optical parametric oscillator (OPO) to enable wavelength tuning starting from 410 nm. The laser power was then attenuated to reach appreciable signal/noise and the integrity of the samples was verified by UV–Vis measurements. The LP980-K is equipped with a symmetrical Czerny-Turner monochromator. For single wavelength absorption changes, a 1800 g mm^{-1} grating, blazed at 500 nm is used, which affords wavelength coverage from 200 to 900 nm. For spectral mode (iCCD), a 150 g mm^{-1} grating, blazed at 500 nm is used, offering a wavelength coverage of 540 nm over the full wavelength range extending from 250 to 900 nm. Single wavelength absorption changes were monitored using a PMT LP detector (Hamamatsu R928) which covers the spectral range from 185 to 870

nm. The probe was a 150 W ozone-free xenon short arc lamp (OSRAM XBO 150W/CR OFR) that was pulsed at the same frequency of the laser. The excitation wavelength depended on the photosensitizers but in all cases the concentration at the excitation wavelength was adjusted to reach absorbance values between 0.3 and 0.5. All measurements were performed in argon-purged solvents at room temperature. An average of 30 to 90 scans per measurement was used.

Stern-Volmer. Stern-Volmer experiments were performed in a quartz cuvette equipped with a 24/32 joint. Cuvettes were sealed with Teflon tape, a septum and parafilm. All samples were purged with dried argon that was passed through a bubbler containing the solvent of interest, for at least 15 minutes. *p*-Nitrobenzenediazonium tetrafluoroborate stock solutions with a concentration of ~ 11 mM were prepared in 10 mL of dry acetonitrile and were purged with argon for 15 minutes. In dichloromethane, the concentration was ~ 0.6 mM as the *p*-nitrobenzenediazonium tetrafluoroborate is only slightly soluble. A photosensitizer solution with an absorbance of ~ 0.2 at the excitation wavelength was prepared in dry acetonitrile or dichloromethane and was purged with argon for 15 minutes. The desired *p*-nitrobenzenediazonium tetrafluoroborate quencher was then gradually added to the photosensitizer cuvette. The excited-state quenching was monitored by time-resolved spectroscopy using the LP980-K spectrometer from Edinburgh Instruments (see above). The decrease of excited-state lifetime is directly related to the concentration of quencher and the respective Stern-Volmer plots were extrapolated using the following equation. The quenching rate constant (k_q) was then determined by dividing the slope by the initial lifetime without any quencher.

$$\frac{\sum(PLI_0)}{\sum(PLI)} = \frac{\tau_0}{\tau} = 1 + K_{SV}[Q] \ = 1 + k_q\tau_0[Q]$$

Thermogravimetric analysis (TGA). Thermograms were recorded on a TGA/SDTA 851e simultaneous DSC-TGA instrument from METTLER

TOLEDO. These analyses were carried out with a heating ramp of 10 °C min^{-1} and under air flow (100 mL min^{-1}) with the samples (3 – 20 mg) placed into alumina containers.

Transmission Electron Microscopy (TEM). TEM images were obtained with a LEO 922 OMEGA energy filter transmission electron microscope. The powder samples were suspended in ethanol under ultrasonic treatment, then a few drops of the supernatant were deposited on a holey carbon film supported on a copper grid (Protochips, 1.2 micron hole diameter, 1.3 micron hole spacing, 200 mesh copper grid), which was dried for a few hours under vacuum at room temperature before analysis.

Fourier-transform Infrared_Total Attenuated reflectance spectroscopy (FTIR-ATR). FTIR-ATR spectra were recorded on Perkin Elmer Spectrum Two-UATR by depositing the powder onto the diamond equipped with a mechanical press. The bands are reported in cm^{-1} and the following abbreviations have been used: br (broad), s (strong), m (medium), w (weak).

Diffuse Reflectance-UV-vis (DR-UV-vis). DR-UV-vis spectra were recorded on a Shimadzu 2600plus device from 800 to 200 nm using a harrick praying mantis modulus. Spectralon was used to record the baseline prior to powder samples measurements.

Time of flight secondary ion mass spectrometry (ToF-SIMS). Chemical characterisation of samples were carried out by using a TOF.SIMS 5 instrument (IONTOF GmbH, Münster, Germany). A pulsed Bi^{5+} metal ion source was used to produce a primary beam using an acceleration voltage of 30 kV. An AC target current of 0.05 pA with a bunched pulse width lower than 1 ns was used. Both positive and negative secondary ion species were analysed. For spectra, a raster of 128 x 128 data points over an area of 300 x 300 μm^2 was recorded. The total primary ion beam dose for each analysed

area was always kept below $4X10^{10}$ ions.cm^{-2}, ensuring static conditions. Lateral resolution of ~ 3 µm and mass resolution m/Δm > 5000 at 41 m/z were maintained for positive and negative spectra acquisition. Charge compensation was done by an interlaced electron flood gun (E_k = 20 eV). All data analyses were carried out using the software supplied by the instrument manufacturer, SurfaceLab (version 6.8). Sample powders were simply pressed onto the adhesive part of Post-it® papers before introduction in the instrument.

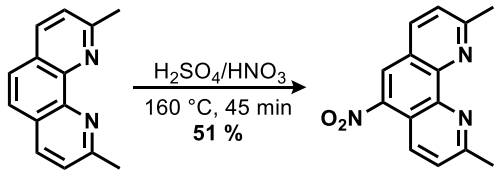
Inductively Coupled Plasma Optical Emission Spectroscopy (ICP-OES). These analyses were performed by MEDAC LTD company using Varian Vista MPX ICP-OES system. The sample was digested using a combination of HNO_3 and HF acids and the mixture was made up to 100 mL of de-ionised water. A matrix blank was prepared at the sample time.

High Resolution Mass Spectrometry (HRMS). HRMS were recorded on a Q-Extractive orbitrap from ThermoFisher. Samples were ionized by Electrospray Ionization (ESI) (capillary temperature: 250 °C, vaporizer temperature: 250 °C, sheath gas flow rate: 20).

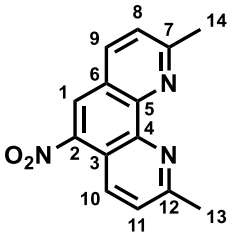
Nitrogen physisorption. The specific surface areas were measured by nitrogen adsorption-desorption isotherms. The measurements were achieved using a Micromeritics ASAP 2020 analyzer at –196 °C. Before analysis, the samples (~ 200 mg) were degassed for 2 h at 200 °C with a heating ramp of 10 °C min^{-1} under 0.133 Pa pressure. The analysis of the isotherms provided specific surface areas calculated with the Brunauer-Emmett-Teller (BET) equation.

5.3. Experimental protocols

Synthesis of 2,9-dimethyl-5-nitro-1,10-phenanthroline[429]



Fuming HNO_3 (5 mL) was added dropwise to 15 mL of ice-cold H_2SO_4 kept under air. A round-bottom flask containing 2,9-dimethyl-1,10-phenanthroline (5 g, 0.024 mol) was placed in an ice bath and the mixture of acids was added dropwise. The mixture was then gradually heated to 160 °C and kept at that temperature for 45 minutes. After reaction, the solution was brought to room temperature and poured onto ice (± 100 mL). The pH was adjusted to 5-6 by the addition of NaOH (30 %). The mixture containing a yellow precipitate was extracted 3 times with dichloromethane. The organic phases were combined, dried on $MgSO_4$ and concentrated under reduce pressure to obtain a black/yellow oil. The crude residue was washed with diethylether several times by applying ultrasound until the supernatant was colorless. The NO_2-dimethylphenanthroline was obtained as a yellow/white powder (3.11 g, 51 % yield).



CAS: 118752-27-5

Formula: $C_{14}H_{11}N_3O_2$

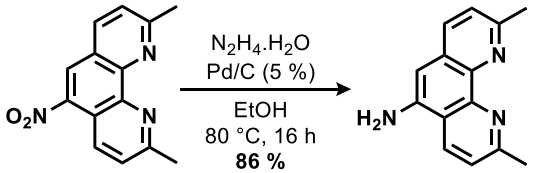
Molecular weight: 253.26 g mol^{-1}

^{1}H NMR (300 MHz, $CDCl_3$) δ= 8.91 (d, *J* = 8.8 Hz, 1H, H_{10}), 8.60 (s, 1H, H_1), 8.28 (d, *J* = 8.2 Hz, 1H, H_9), 7.65 (dd, *J* = 12.8, 8.6 Hz, 2H, H_8 and H_{11}), 3.00 (s, 3H, H_{13} or H_{14}), 2.98 (s, 3H, H_{13} or H_{14}).

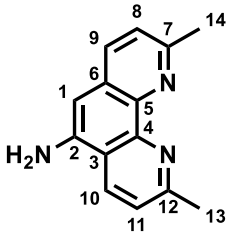
^{13}C NMR (75 MHz, $CDCl_3$) δ= 163.7 (C_7), 161.2 (C_{12}), 147.1 (C_5), 145.5 (C_4), 143.8 (C_2), 138.1 (C_9), 132.7 (C_{10}), 125.2 (C_8 or C_{11}), 125.1 (C_8 or C_{11}), 124.7 (C_1), 123.8 (C_6), 119.4 (C_3), 26.5 (C_{13} or C_{14}), 26.0 (C_{13} or C_{14}).

IR (cm^{-1}) $\tilde{\nu}$ = 1517 (s, NO_2).

Synthesis of 2,9-dimethyl-5-amino-1,10-phenanthroline[429]



Pd/C 5 % (426 mg, 0.2 mmol, 0.1 eq.) and 2,9-dimethyl-5-nitro-1,10-phenanthroline (500 mg, 1.97 mmol, 1eq.) were added in a two-neck round-bottom flask along with 15 mL of absolute ethanol. The mixture was heated at 80 °C under air and once this temperature was reached, hydrazine hydrate (1 mL, 20 mmol, 10 eq.) was added dropwise. The mixture was kept under reflux overnight. After reaction, the medium was brought to room temperature and filtered on celite. The filtrate was recovered and concentrated under reduce pressure. The crude residue was washed with diethylether several times to obtain 2,9-dimethyl-5-amino-1,10-phenanthroline as a brown/yellow powder (380 mg, 86 % yield).



CAS: 118752-28-6

Formula: $C_{14}H_{13}N_3$

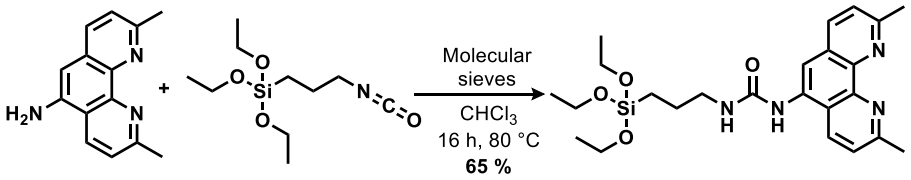
Molecular weight: 223.28 g mol^{-1}

^{1}H NMR (300 MHz, $CDCl_3$) δ= 8.17 (d, J = 8.4 Hz, 1H, H_{10}), 7.88 (d, J = 8.2 Hz, 1H, H_9), 7.49 (d, J = 8.5 Hz, 1H, H_{11}), 7.37 (d, J = 8.2 Hz, 1H, H_8), 6.89 (s, 1H, H_1), 2.91 (s, 3H, H_{13}), 2.84 (s, 3H, H_{14}).

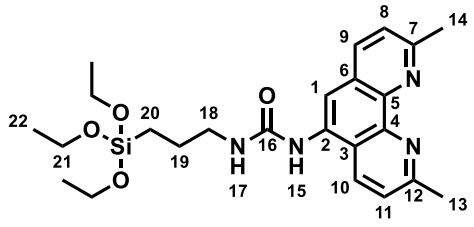
^{13}C NMR (75 MHz, $CDCl_3$) δ= 159.2 (C_{12}), 155.9 (C_7), 145.9 (C_4), 141.4 (C_5), 139.3 (C_2), 134.2 (C_9), 129.9 (C_{10}), 128.0 (C_6), 123.9 (C_8), 122.8 (C_{11}), 120.3 (C_3), 105.4 (C_1), 25.8 (C_{13} or C_{14}), 25.6 (C_{13} or C_{14}).

IR (cm^{-1}) $\tilde{\nu}$ = 3296 (w, NH_2), 3188 (m, NH_2), 1606 (m, NH_2), 855 (s, NH_2).

Synthesis of 2,9-dimethylphenanthroline-siloxane ligand (DMP-Si)



2,9-dimethyl-5-amino-1,10-phenanthroline (100 mg, 0.45 mmol, 1 eq.) and molecular sieves were added in a 25 mL two-neck round-bottom flask. The flask was placed under static vacuum for 10 minutes and filled with argon. 5 mL of dry chloroform were added followed by the dropwise addition of triethoxy(3-isocyanatopropyl)silane (0.11 mL, 0.45 mmol, 1 eq.). The reaction mixture was heated at 80 °C for 16 h. After reaction, the solvent was evaporated under reduced pressure and the crude residue was purified by silica flash chromatography (DCM/MeOH, 100:0 to 95:5). The DMP-Si ligand was obtained as a brown oil (138 mg, 65 % yield).



CAS: /

Formula: $C_{24}H_{34}N_4O_4Si$

Molecular weight: 470.65 g mol^{-1}

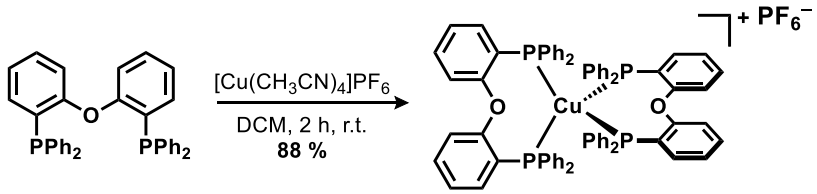
^{1}H NMR (300 MHz, $CDCl_3$): δ= 9.07 (br, 1H, H_{15} or H_{17}), 8.42 (s, 1H, H_1), 8.24 (d, J = 8.6 Hz, 1H, H_{10}), 8.09 (d, J = 8.3 Hz, 1H, H_9), 7.42 (d, J = 8.3 Hz, 1H, H_{11}), 6.77 (m, 2H, H_8 and H_{15} or H_{17}), 3.62 (q, J = 7.0 Hz, 6H, H_{21}), 3.30 (m, 2H, H_{18}), 2.78 (s, 3H, H_{13} or H_{14}), 2.51 (s, 3H, H_{13} or H_{14}), 1.54 (m, 2H, H_{19}), 1.06 (t, J = 7.0 Hz, 9H, H_{22}), 0.49 (t, J = 8.4 Hz, 2H, H_{20}).

^{13}C NMR (75 MHz, $CDCl_3$): δ= 158.6 (C_{12}), 157.7 (C_{16}), 156.9 (C_7), 145.4 (C_4), 142.2 (C_5), 136.4 (C_9), 132.9 (C_2), 131.0 (C_{10}), 127.7 (C_6), 124.3 (C_{11}), 122.8 (C_8), 122.5 (C_3), 114.5 (C_1), 58.4 (C_{21}), 42.7 (C_{18}), 24.8 (C_{13} or C_{14}), 24.5 (C_{13} or C_{14}), 23.7 (C_{19}), 18.3 (C_{22}), 7.7 (C_{20}).

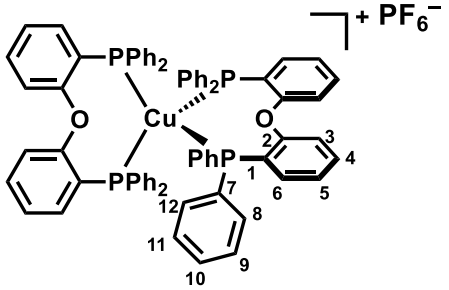
FTIR-ATR (cm^{-1}): $\tilde{\nu}$ = 3322 (m, NH–C=O–NH), 2926 (m, alkyl), 1656 (s, NH–C=O–NH), 1102 (s, SiOEt), 1078 (s, SiOEt), 954 (m, aromatic), 775 (m, alkyl).

HRMS (ESI) *m/z* calcd for $C_{24}H_{34}O_4N_4{}^{28}Si+ H^+$: 471.2422 $[M + H]^+$; found: 471.2424.

Synthesis of $[Cu(DPEPhos)_2]PF_6$



This compound was prepared according to the literature.[430] In a flame-dried round-bottom flask, $[Cu(MeCN)_4]PF_6$ (186 mg, 0.5 mmol, 1 eq.) and DPEPhos (539 mg, 1 mmol, 2 eq.) were introduced. The flask was placed under static vacuum for 10 minutes and filled with argon. 12 mL of dry dichloromethane were added and the reaction mixture was left under stirring for 2 h in the dark. After reaction, the mixture was filtered on celite. The solvent was evaporated under reduced pressure and the crude residue was precipitated in cold diethylether. $[Cu(DPEPhos)_2]PF_6$ was recovered as a white powder (567 mg, 88 %).



CAS: /

Formula: $C_{72}H_{56}CuO_2P_5F_6$

Molecular weight: 1285.64 g mol^{-1}

^{1}H NMR (300 MHz, $CDCl_3$) δ= 7.31 – 7.20 (m, 8H, H_{10}), 7.14 (m, 4H, H_4), 6.99 (t, J = 7.6 Hz, 20H, H_5 and H_9), 6.82 – 6.69 (m, 20H, H_6 and H_8), 6.50 – 6.39 (m, 4H, H_3).

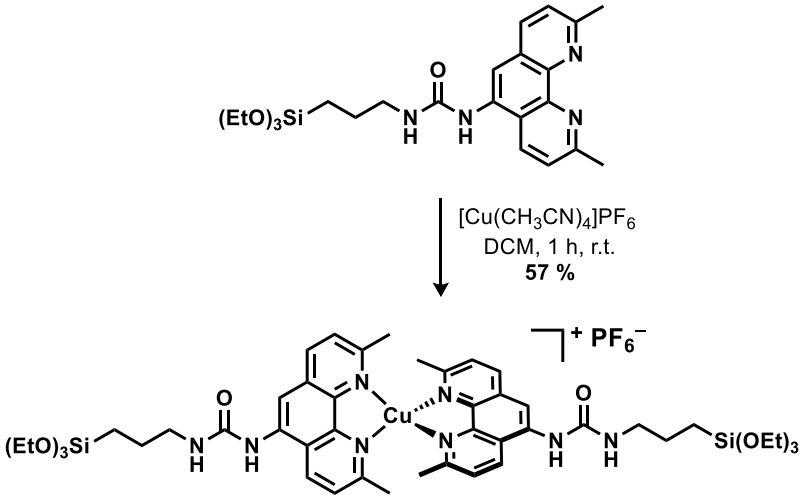
^{31}P NMR (121 MHz, $CDCl_3$) δ= -13.69, -132.60, -138.46, -144.32, -150.19, -156.05.

^{13}C NMR (75 MHz, $CDCl_3$) δ= 158.2 (C_2), 134.4 (C_9 or C_{11}), 133.8 (C_8 or C_{12}), 133.3 (C_8 or C_{12}), 133.6 (C_6), 132.2 (C_4), 131.0 (C_1), 130.4 (C_{10}), 128.8 (C_9), 124.8 (C_5), 124.7 (C_7), 119.3 (C_3).

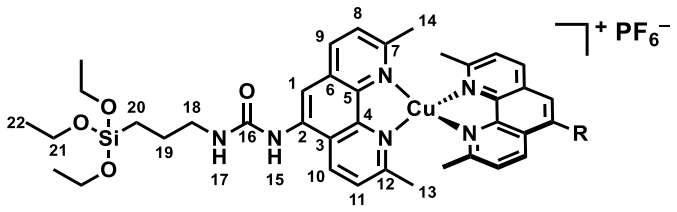
FTIR-ATR (cm^{-1}) $\tilde{\nu}$ = 1435 (m, PC_6H_5), 1219 (m, C–O–C), 1093 (m, PC_6H_5), 1064 (m, C–O–C), 1025 (w, PC_6H_5), 998 (w, PC_6H_5), 833 (s, aromatic), 742 (m, aromatic), 694 (s, aromatic).

HRMS (ESI) *m/z* calcd for $C_{72}H_{56}{}^{63}CuO_2P_4$: 1139.2521 $[M - PF_6]^+$; found: 1139.2511.

Synthesis of $[Cu(DMP\text{-}Si)_2]PF_6$ (Cu-1)



$[Cu(MeCN)_4]PF_6$ (37 mg, 0.1 mmol, 1 eq.) was added in a 50 mL flame-dried round-bottom flask. The flask was placed under static vacuum for 10 minutes and filled with argon. 13 mL of dry dichloromethane was added and a solution of DMP-Si (94 mg, 0.2 mmol, 2 eq.) in dichloromethane was added dropwise. A red color was observed that went darker along the time of reaction. The reaction mixture was left under stirring for 1 hour under the dark. After reaction, the solvent was evaporated under reduced pressure. The crude residue was dissolved in a minimum amount of dichloromethane and added dropwise in 100 mL of *n*-hexane previously cooled to 0 °C. An orange/red powder corresponding to complex **Cu-1** was recovered by filtration (65 mg, 57 % yield).



CAS: /

Formula: $C_{48}H_{68}CuN_8O_8Si_2PF_6$

Molecular weight: 1149.80 g mol^{-1}

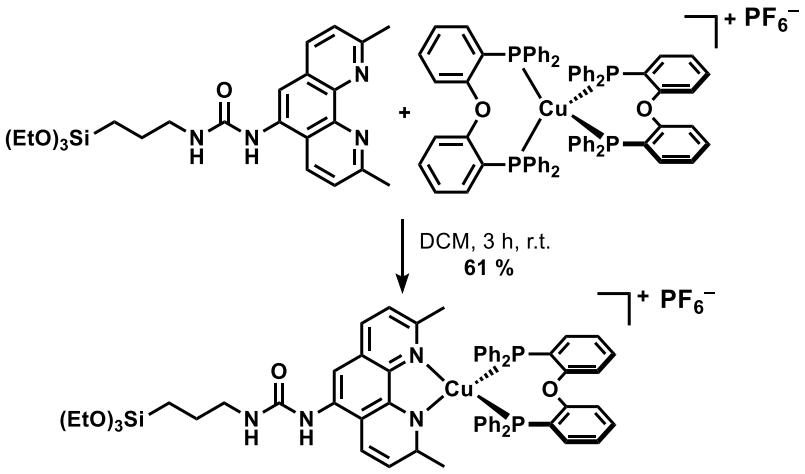
^{1}H NMR (300 MHz, $CDCl_3$): δ= 8.72 (br, 2H, H_{10} or H_9), 8.37 (s, 2H, H_1), 8.23 (br, 2H, H_{10} or H_9), 7.78 (br, 2H, H_{15} or H_{17}), 7.57 (m, 4H, H_8 and H_{11}), 5.97 (br, 2H, H_{15} or H_{17}), 3.83 (q, J = 7.0 Hz, 12H, H_{21}), 3.33 (br, 4H, H_{18}), 2.34 (s, 6H, H_{13} or H_{14}), 2.25 (s, 6H, H_{13} or H_{14}), 1.74 (m, 4H, H_{19}), 1.21 (t, J = 7.0 Hz, 18H, H_{22}), 0.72 (m, 4H, H_{20}).

^{13}C NMR (75 MHz, $CDCl_3$): δ= 156.9 (C_7 or C_{12}), 156.0 (C_{16}), 155.4 (C_7 or C_{12}), 143.4 (C_4 or C_5), 140.1 (C_4 or C_5), 136.4 (C_9 or C_{10}), 133.4 (C_2), 132.3 (C_9 or C_{10}), 128.1 (C_6 or C_3), 125.4 (C_8 or C_{11}), 124.9 (C_8 or C_{11}), 119.6 (C_6 or C_3), 115.2 (C_1), 58.5 (C_{21}), 43.1 (C_{18}), 25.7 (C_{13} or C_{14}), 25.4 (C_{13} or C_{14}), 23.4 (C_{19}), 18.3 (C_{22}), 7.6 (C_{20}).

FTIR-ATR (cm^{-1}): $\tilde{\nu}$ = 3373 (m, NH–C=O–NH), 2927 (m, alkyl), 1655 (s, NH–C=O–NH), 1102 (s, SiOEt), 1073 (s, SiOEt), 956 (s, aromatic), 835 (s, aromatic), 775 (s, alkyl).

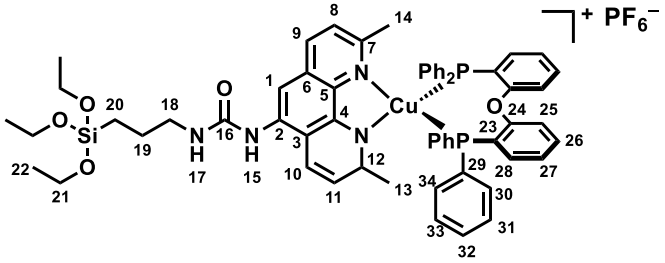
HRMS (ESI): *m/z* calcd for $C_{48}H_{68}O_8N_8{}^{63}Cu^{28}Si_2$: 1003.3989 $[M - PF_6]^+$; found: 1003.3986.

Synthesis of [Cu(DMP-Si)(DPEPhos)]PF_6 (Cu-2)



In two flame-dried 25 mL round-bottom flasks, $[Cu(DPEPhos)_2]PF_6$ (140 mg, 0.3 mmol, 1 eq.) and DMP-Si ligand (386 mg, 0.3 mmol, 1 eq.) were added separately. The flasks were placed under static vacuum for 10 minutes and filled with argon. The copper complex was dissolved in 20 mL of dry

dichloromethane and a minimum amount of dichloromethane was added to solubilize the DMP-Si ligand. The solution of DMP-Si was cannula-transferred to the copper solution leading to an immediate orange/yellow color. The reaction medium was left under stirring for one hour under the dark. After reaction, the mixture was added dropwise to 100 mL of *n*-hexane previously cooled to 0°C. The yellow precipitate was recovered by filtration. If free DPEPhos was still observed by NMR spectroscopy, the copper complex was purified by silica flash chromatography (3 % methanol in dichloromethane). The title compound **Cu-2** was obtained as a yellow solid (95 mg, 61 % yield).



CAS: /

Formula: $C_{60}H_{63}CuN_4O_5SiP_3F_6$

Molecular weight: 1218.73 g mol^{-1}

^{1}H NMR (300 MHz, $CDCl_3$): δ= 8.75 (d, *J* = 8.7 Hz, 1H, H_{10}), 8.35 (s, 1H, H_1), 8.11 (d, *J* = 8.3 Hz, 1H, H_9), 7.69 (s, 1H, H_{15} or H_{17}), 7.54 (d, *J* = 8.6 Hz, 1H, H_{11}), 7.35 (d, *J* = 8.2 Hz, 1H, H_8), 7.33 – 7.28 (m, 2H, H_{28}), 7.25 – 7.13 (m, 8H, H_{25}, H_{27} and H_{32}), 7.08 – 6.87 (m, 18H, H_{26}, H_{30}, H_{31}, H_{33} and H_{34}), 5.92 (t, *J* = 5.8 Hz, 1H, H_{15} or H_{17}), 3.84 (q, *J* = 7.0 Hz, 6H, H_{21}), 3.33 (q, *J* = 6.7 Hz, 2H, H_{18}), 2.37 (s, 3H, H_{14}), 2.34 (s, 3H, H_{13}), 1.75 (m, 2H, H_{19}), 1.23 (t, *J* = 7.0 Hz, 9H, H_{22}), 0.80 – 0.68 (m, 2H, H_{20}).

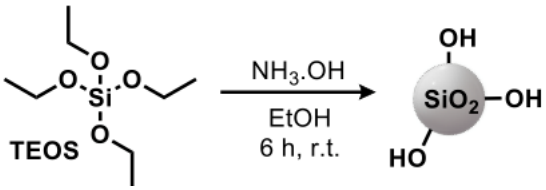
^{31}P NMR (121 MHz, $CDCl_3$): δ= –13.33, –126.66, –132.54, –138.42, –144.30, –150.18, –156.06, –161.94.

^{13}C NMR (75 MHz, $CDCl_3$): δ= 158.5 (C_{24}), 158.38 (C_{12}), 156.18 (C_7), 155.98 (C_{16}), 143.39 (C_4), 140.21 (C_5), 137.21 (C_9), 133.92 (C_{26}, $C_{30,}$ C_{31}, C_{33} or C_{34}), 133.80 (C_2), 133.22 (C_{25}, C_{27} or C_{32}), 133.12 (C_{10}), 132.77 (C_{26}, $C_{30,}$ C_{31}, C_{33} or C_{34}), 132.22 (C_{28}) 131.68 (C_{23}), 130.08 (C_{25}, C_{27} or C_{32}), 128.73 (C_{26}, $C_{30,}$ C_{31}, C_{33} or C_{34}), 128.67 (C_{26}, $C_{30,}$ C_{31}, C_{33} or C_{34}), 128.4 (C_6), 125.74 (C_{29}), 125.29 (C_{25}, C_{27} or C_{32}), 125.15 (C_{11}), 125.0 (C_8), 123.35 (C_3), 120.20 (C_{26}, $C_{30,}$ C_{31}, C_{33} or C_{34}), 114.21 (C_1), 58.5 (C_{21}), 43.2 (C_{18}), 27.09 (C_{14}), 26.95 (C_{13}), 23.4 (C_{19}), 18.5 (C_{22}), 7.6 (C_{20}).

FTIR-ATR (cm^{-1}): $\tilde{\nu}$ = 3427, (br), 2926 (m), 1657 (s), 1462 (m), 1435 (s), 1097 (s), 1066 (s), 956 (s), 833 (s), 740 (s), 697 (s).

HRMS (ESI): *m/z* calcd for $C_{60}H_{62}O_5N_4{}^{63}CuP_2{}^{28}Si$: 1071.3255 [M – PF_6]$^+$; found: 1071.3272.

Silica nanospheres (NS) synthesis



Reaction conditions were adapted from the work of Stöber *et al.* to yield bigger quantities of silica nanospheres.[220] 150 mL of ethanol (99.9 % denaturated) were introduced in a 500 mL Erlenmeyer. Under vigorous stirring, 6 mL of NH_4OH were added. The reaction mixture was stirred for 5 min at room temperature. Then, 10 mL of tetraethylorthosilicate (TEOS) were added dropwise with a syringe pump at a rate of 59 mL hour^{-1}. The solution was left under stirring for 6 hours at room temperature. The silica nanoparticles were recovered by centrifugation (9.500 rpm for 40 min) and washed three times with 40 mL of ethanol. The nanoparticles were dried in the oven at 100 °C overnight and subsequently grinded to obtain a fine white/beige powder. This material was characterized by TEM, XPS and BET.

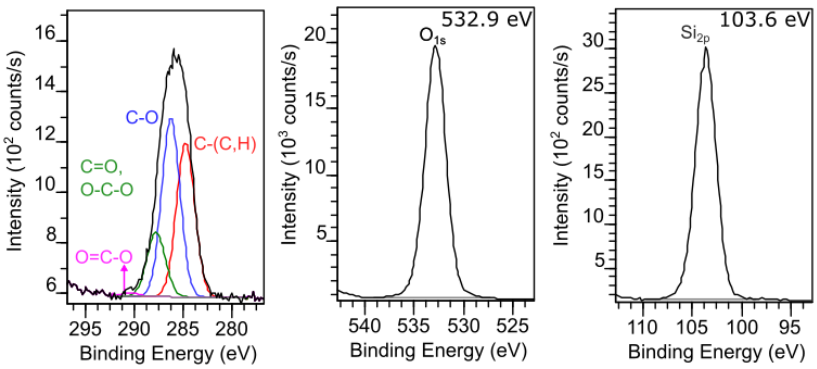


Figure 6.12. XPS spectra of silica nanospheres: C_{1s}, O_{1s} and Si_{2p} signals.

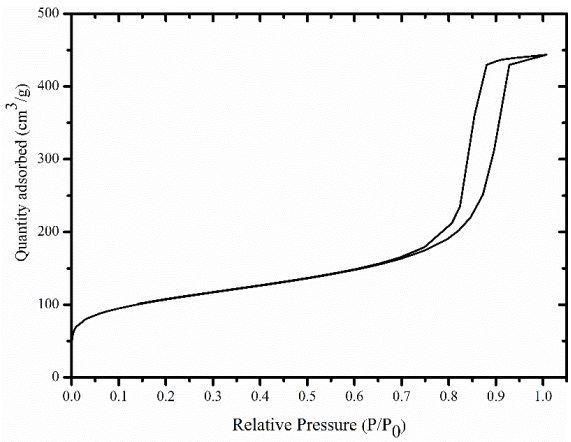
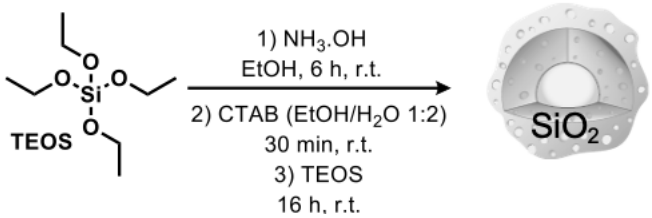


Figure 6.13. N_2 adsorption-desorption isotherms at 77 K of silica nanospheres. BET calculated surface area of 360 m^2 g^{-1}.

Silica Core-Shell (CS) nanoparticles synthesis



Reaction conditions were adapted from the work of Yoon *et al.* to yield smaller nanoparticles.[221] 150 mL of ethanol (99.9 % denaturated) were introduced in a 500 mL Erlenmeyer. Under vigorous stirring, 6 mL of NH_4OH were added. The reaction mixture was stirred for 5 min at room temperature. Then, 10 mL of tetraethylorthosilicate (TEOS) were added dropwise with a

syringe pump at a rate of 59 mL hour^{-1}. The solution was left under stirring for 6 hours at room temperature. 380 mL of Milli-Q water and 30 mL of a hexadecyltrimethylammonium bromide (CTAB) solution (1.2 g of CTAB dissolved in 20 mL H_2O/10 mL ethanol) were added at once and the solution was left under stirring for 30 min. 2.15 mL of TEOS were added at a rate of 59 mL hour^{-1} and the mixture was stirred overnight (200 rpm). The silica nanoparticles were recovered by centrifugation (6000 rpm for 50 min) and washed three times with 40 mL of ethanol. The nanoparticles were dried in the oven at 100 °C and finally calcinated by heating at 500 °C for 5 hours at a rate of 10 °C min^{-1} (3 g of silica nanoparticles were recovered). This material was characterized by TEM, XPS and BET.

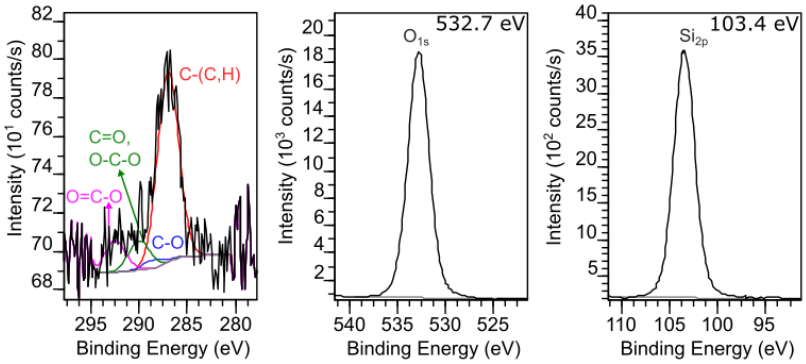


Figure 6.14. XPS spectra of CS nanoparticles: C_{1s}, O_{1s}, and Si_{2p} peaks.

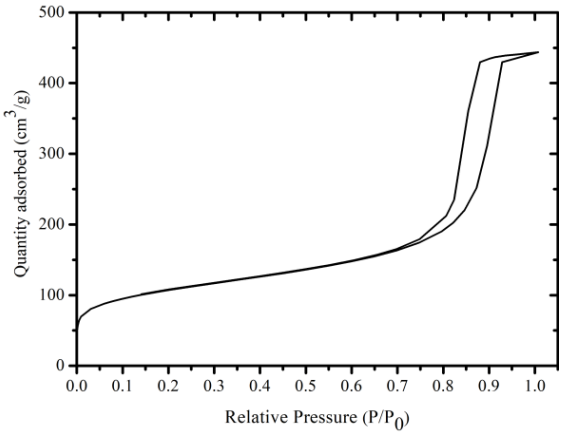
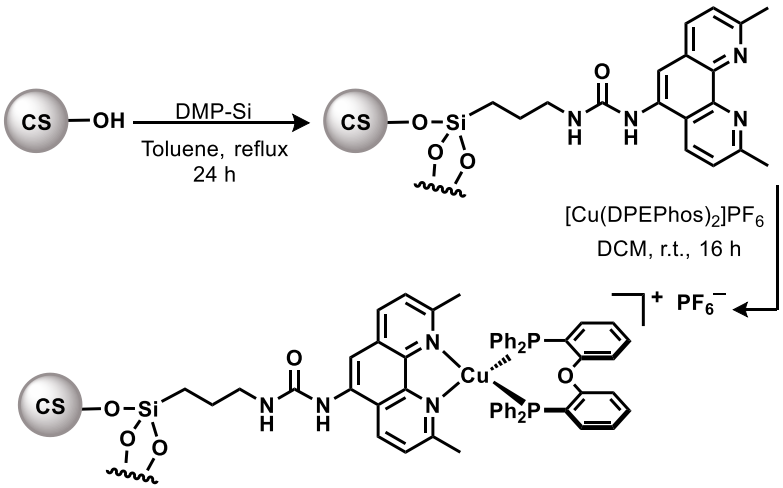


Figure 6.15. N_2 adsorption-desorption isotherms at 77 K of CS nanoparticles. BET calculated surface area of 650 m^2 g^{-1}.

Anchoring of [Cu(DMP-Si)(DPEPhos)]PF_6 (Cu-2) according to a two-step procedure

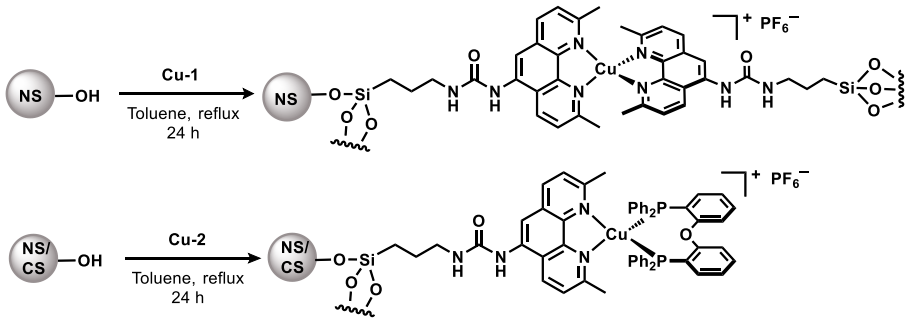


In a flame-dried 25 mL two-neck round-bottom flask were inserted silica core-shell nanoparticles (100 mg). The flask was placed under static vacuum for 10 minutes and filled with argon. 5 mL of dry toluene were added and the resulting suspension was sonicated for 15 min at power 3 on a VWR ultrasonic bath. DMP-Si ligand (94 mg, 0.2 mmol, 0.12 eq.) was dissolved in 5 mL of toluene before being added dropwise at a rate of 8 mL $hour^{-1}$. The reaction mixture was refluxed at 120 °C for 24 h. Filtration on a PVDF Millipore Membrane (0.1 μm) allowed the recovery of a yellowish solid which was washed several times with absolute ethanol.

The functionalized core-shell nanoparticles were then added in a 25 mL flame-dried round-bottom flask. The flask was placed under static vacuum for 10 minutes and filled with argon. 8.5 mL of dry dichloromethane was added to the silica nanoparticles and the resulting suspension was sonicated for 15 minutes at power 2 on a VWR ultrasonic bath. $[Cu(DPEPhos)_2]PF_6$ (93 mg, 0.07 mmol) was placed in a round-bottom flask and the latter was placed under static vacuum for 10 minutes and filled with argon. 1.5 mL of dry dichloromethane were added and this solution was added dropwise to the

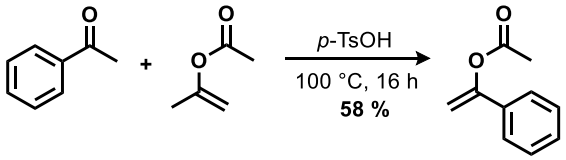
silica nanoparticles suspension that was stirred at ambient temperature for an additional 16 h. The solid was recovered by filtration on a PVDF Millipore Membrane (0.1 μm) and washed three times with 10 mL of dichloromethane. The resulting yellowish powder was dried under vacuum for several hours.

General one-step procedure for the anchoring of copper complexes

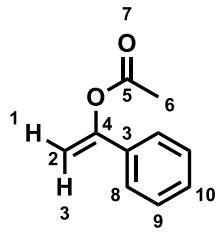


In a 50 mL flame-dried two-neck round-bottom flask, nanospheres or core-shell nanoparticles (140 mg) were introduced. The flask was placed under static vacuum for 10 minutes before being filled with argon. 30 mL of dry toluene were added and the resulting suspension was sonicated for 15 minutes at power 2 on a VWR ultrasonic bath. The homoleptic or heteroleptic copper complexes (90 mg and 100 mg, respectively, 0.08 mmol) were dissolved in a minimum amount of dry toluene and added dropwise to the silica suspension. The suspension was refluxed for 24 h. After reaction, the mixture was cooled to room temperature and filtered on a PVDF Millipore Membrane (0.1 μm). The powder was recovered and washed three times with 10 mL of dichloromethane. The solid was dried under vacuum for several hours.

Synthesis of 1-phenylvinyl acetate[427]



In a 50 mL flame-dried two-neck round-bottom flask were introduced acetophenone (2.9 mL, 25 mmol, 1 eq.) and 2-propenyl acetate (14 mL, 125 mmol, 5 eq.). *p*-Toluenesulfonic acid monohydrate (342 mg, 1.8 mmol, 0.7 eq.) was added and the mixture was refluxed at 100 °C for 16 h. After reaction, the mixture was brought to room temperature and the solvent was evaporated under reduced pressure. Diethylether (50 mL) was added and the organic layer was subsequently washed with H_2O (3x25 mL), dried over $MgSO_4$ and concentrated *in vacuo*. The crude residue was purified by column chromatography on SiO_2 (50 % dichloromethane in *n*-hexane) and a yellowish oil was recovered (2.33 g, 58 % yield).



CAS: 2206-94-2

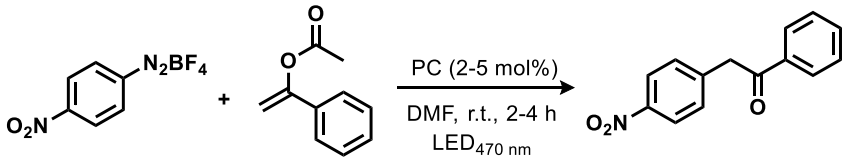
Formula: $C_{10}H_{10}O_2$

Molecular weight: 162.19 g mol^{-1}

^{1}H NMR (300 MHz, $CDCl_3$) δ= 7.54 – 7.45 (m, 2H, H_8), 7.41 – 7.28 (m, 3H, H_9 and H_{10}), 5.50 (dd, J = 2.2, 0.9 Hz, 1H, H_1 or H_3), 5.05 (dd, J = 2.2, 0.9 Hz, 1H, H_1 or H_3), 2.28 (s, 3H, H_6).

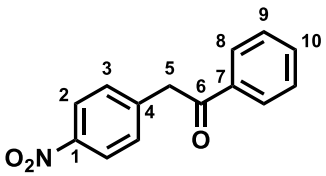
^{13}C NMR (75 MHz, $CDCl_3$) δ= 169.1 (C_5), 153.0 (C_4), 134.3 (C_3), 129.0 (C_{10}), 128.6 (C_9), 124.9 (C_8), 102.2 (C_2), 21.0 (C_6).

Use of homogeneous photocatalysts for the α-arylation of 1-phenylvinyl acetate 2a



In a 3 mL oven-dried vial were dissolved 4-nitrobenzene diazonium tetrafluoroborate **1a** (35.5 mg, 0.15 mmol, 1 eq.), 1-phenylvinyl acetate **2a** (243 mg, 1.5 mmol, 10 eq.) and the photocatalyst (2-5 mol%) in 0.4 mL of dry

dimethylformamide. Argon was bubbled for 15 min and the solution was irradiated for 2 or 4 hours (depending on the photocatalyst) with two LIU470A 470 nm blue LEDs purchased from Thorlabs (intensity = 4.0 mW/cm^2; total output power = 253 mW; supply voltage = 24 V). After reaction, 5 mL of distilled water were added and the aqueous phase was washed three times with 10 mL of diethylether. The organic phases were combined, dried over $MgSO_4$, filtered and the solvent was evaporated under reduced pressure. The crude residue was purified over silica flash chromatography using NextGen CombiFlash device along with 12 g silica column (*n*-hexane/ethyl acetate). The following gradient in ethyl acetate was used: 0 to 2.5 % (2 min), 2.5 % (1 min), 2.5 to 5 % (1 min), 5 % (2 min), 5 to 7.5 % (1 min), 7.5 % (1 min), 7.5 to 10 % (1 min), 10 % (2 min). The product was recovered as a white powder.



CAS: 3769-82-2

Formula: $C_{14}H_{11}NO_3$

Molecular weight: 241.25 g mol^{-1}

^{1}H NMR (300 MHz, $CDCl_3$): δ= 8.25 – 8.14 (m, 2H, H_2), 8.06 – 7.96 (m, 2H, H_8), 7.66 – 7.56 (m, 1H, H_{10}), 7.55 – 7.47 (m, 2H, H_9), 7.45 – 7.40 (m, 2H, H_3), 4.42 (s, 2H, H_5).

^{13}C NMR (75 MHz, $CDCl_3$): δ= 196.1 (C_6), 147.2 (C_1), 142.2 (C_4), 136.3 (C_7), 133.9 (C_{10}), 130.8 (C_3), 129.0 (C_9), 128.6 (C_8), 123.9 (C_2), 45.1 (C_5).

IR (cm^{-1}): $\tilde{\nu}$ = 2922 (w, alkyl), 1683 (s, C=O), 1599 (m, NO_2), 1514 (s, NO_2), 1108 (m, aromatic), 761 (s, aromatic), 733 (s, aromatic), 690 (s, aromatic).

Use of heterogeneous photocatalysts for the α-arylation of 1-phenylvinyl acetate 2a

In a 50 mL flame-dried round-bottom flask, the heterogenized copper complex (50 mg for homoleptic and 65 mg for heteroleptic) was introduced and placed under static vacuum for 10 minutes before being filled with argon. 8-10 mL of degassed (freeze-pump-thaw) dry dimethylformamide were added

and the resulting suspension was sonicated for 15 minutes at power 2 on a VWR ultrasonic bath. 4-nitrobenzene diazonium tetrafluoroborate **1a** (35.5 mg, 0.15 mmol, 1 eq.) and 1-phenylvinyl acetate **2a** (243 mg, 1.5 mmol, 10 eq.) were added and the suspension was left under stirring for 16 h at room temperature under blue irradiation. After reaction, the heterogenized copper complex was recovered by filtration on a PTFE Millipore Membrane (0.1 μm) and the solid was washed three times with 10 mL of diethylether. To the filtrate was added 20 mL of distilled water and the aqueous phase was washed three times with 20 mL of diethylether. The organic phases were combined, washed with saturated NaCl (20 mL) and LiCl 10 % (20 mL), dried over $MgSO_4$, filtered and the solvent was evaporated under reduced pressure. The white powder was finally dried under vacuum.

Chapter 7

Conclusions and perspectives

1. General conclusions

In this manuscript, we put in evidence the benefit of using photocatalysis as efficient tool to synthesize organic compounds. The versatility of the photocatalysts reinforces the power of photochemistry, in addition to its "green" nature and unique one-electron pathway. Organic dyes and copper complexes have been extensively investigated to replace the expensive and rare ruthenium and iridium metals complexes, but their use is still hampered by their different limitations.

The main goal of this PhD thesis was to establish heterogeneous systems based on copper(I) complexes and new or well-established organic dyes by immobilization on solid supports. The obtained heterogenized systems should be deeply characterized at each step of functionalization and anchoring, to evaluate the impact of immobilizing a photocatalyst onto a support in terms of photophysical properties, photostability, and photoactivity and to investigate how a support, with its intrinsic properties such as specific surface area, particle size, porosity…, can be tuned to enhance the photocatalysts activity and impact the outcome of a reaction.

To fulfill such goal, three sub-objectives were targeted:

1. The development and comparison of different morphologies of silica nanoparticles that may impact the outcome of a photocatalyzed reaction. The targeted information in this first part of the project was to highlight the influence of a solid material architecture onto a photocatalyzed reaction (Chapter 3).
2. The second part focused onto the derivatization of a simple dye to establish a structure-activity relationship in order to design a grafting approach that was as neutral as possible towards the photophysical properties and reactivity of the investigated photosensitizers (Chapters 4 and 5).
3. The final project, based on heterogenized heteroleptic and homoleptic copper(I) complexes, was dedicated to evaluating the benefits of immobilization to limit, or even stop, the ligand exchange that copper complexes may suffer from, leading to a decrease in photostability. The excited state once grafted could also be characterized and compared to the one in homogeneous phase.

The outcome of these endeavors will now be summarized below. Firstly, in **Chapter 3**, we investigated the influence of three morphologies (nanospheres, core-shell and urchins) of silica nanoparticles onto the photogeneration of singlet oxygen by Rose Bengal. This well-known organic dye-based system was used for citronellol photooxidation. To focus only on the architecture of the solid support and avoid any negative functionalization impacts onto the PC's photophysical properties and/or reactivity, RB was immobilized non-covalently, *via* electrostatic interactions with ammonium moieties anchored beforehand at the surface of silica nanoparticles. A clear influence of the architecture of the solid support onto the production of $^1O_2$ by immobilized RB was observed and the core-shell morphology seemed to be the best structure. Indeed, RB could be immobilized on CS nanoparticles with a high loading of 19 wt.% and this immobilized system exhibited a $^1O_2$ production quantum yield of 0.74 (similar to pure RB), a diminished

photobleaching, and an excellent activity and recyclability over 5 runs in the photooxidation of citronellol.

Secondly, in **Chapters 4** and **5**, benzophenazines were functionalized with relevant moieties on their southern, northern and western parts to establish a structure-activity relationship and identify which fragment of the molecular structure influences the most their photophysical properties and reactivity. Such simple dyes were selected as they are easily accessible and modifiable and were not largely investigated for the photoproduction of singlet oxygen used in organic synthesis so far. The southern fragment impacted a lot the photocatalysts depending on the nature of functionalization: O and S heteroatoms boosted the generation of singlet oxygen while the presence of N heteroatom was detrimental. The western fragment had no significant impact but its functionalization was more complicated. Finally, the northern fragment was revealed to be the one influencing the least the photocatalysts whether electron-withdrawing or -donating groups were inserted. This fragment was used to immobilize the cyclic ether-based derivative on nanospheres silica nanoparticles and its activity upon immobilization could be maintained over 4 recyclability runs.

The benzophenazine derivatives were also investigated for photoredox applications based on their respective excited-state redox potentials. The derivative exhibiting a diethylaniline motif on the southern fragment was the only one showing interesting reversible oxidation and reduction waves by cyclic voltammetry. It was applied in the photodebromination of bromovalerophenone in dichloromethane or acetonitrile in presence of DIPEA as sacrificial donor but no product could be isolated. Some photostability issues were encountered with the formation of a persistent photoproduct that was highlighted by nanosecond transient and UV-vis spectroscopies. Further investigations are needed to fully understand what is happening with this diethylaniline-based photocatalyst.

Finally, in **Chapter 6**, heteroleptic and homoleptic copper(I) complexes were covalently anchored onto silica nanoparticles with an efficient methodology based on the formation of an urea linker. In both cases, the photophysical properties upon surface immobilization were only slightly affected. Excited-state quenching with an aryl diazonium derivative occurred efficiently (10^8-10^{10} M^{-1} s^{-1}) with heterogeneous and homogeneous copper complexes. Unfortunately, the immobilization of the heteroleptic copper complex could not hamper the ligand exchange and the formation of the corresponding homoleptic complex occurred quickly at the surface of silica nanoparticles. Nevertheless, transient absorption spectroscopy confirmed that excited-state electron transfer occurred from the homogeneous and heterogeneous homoleptic copper(I) complexes to aryl diazonium derivatives. This heterogenized homoleptic copper system could be efficiently recovered and the photocatalytic activity for the α-arylation of enol acetate was maintained with slightly altered yields over 4 runs. *Via* this study, we could gain direct insights into the immobilization impact onto the excited state of copper complexes and thus, on their photoreactivity.

In conclusion, the results presented in this work sustain the fact that designing heterogeneous systems is relevant. This research field is worth investigating to increase the performances and recyclability of photocatalysts which makes sense in terms of economic and environmental aspects. We have accomplished to prove that the solid support itself can play a role in the photoactivity of a photocatalyst and can be tuned to increase the efficiency of a photochemical process. We were able to underline that the functionalization of a photoactive species is not without consequences onto its photophysical properties. Most of the time, in the literature, such functionalization is performed to design the best photocatalyst possible but this derivatization is rarely, even non-existent, dedicated towards the immobilization of photocatalysts in order to maintain their photophysical properties. It is

important to fully characterize a PC to anchor it onto a solid support, at each step of the procedure, to avoid identifying the immobilization procedure as the problem in case a heterogeneous system would not be photoactive. The grafting approach was also efficiently applied to heteroleptic and homoleptic copper(I) complexes. Transient absorption spectroscopy could clearly demonstrate that the immobilization step did not hamper the possibility of electron transfer and thus, photoredox applications. Such result is totally innovative as the excited state of immobilized homoleptic or heteroleptic copper complexes has not been investigated so far in the literature, to the best of our knowledge. This work allowed to gain insights on the possibilities of designing robust heterogeneous systems and appeal for further improvements in terms of versatility, photostability, leaching, large-scale applications and recyclability.

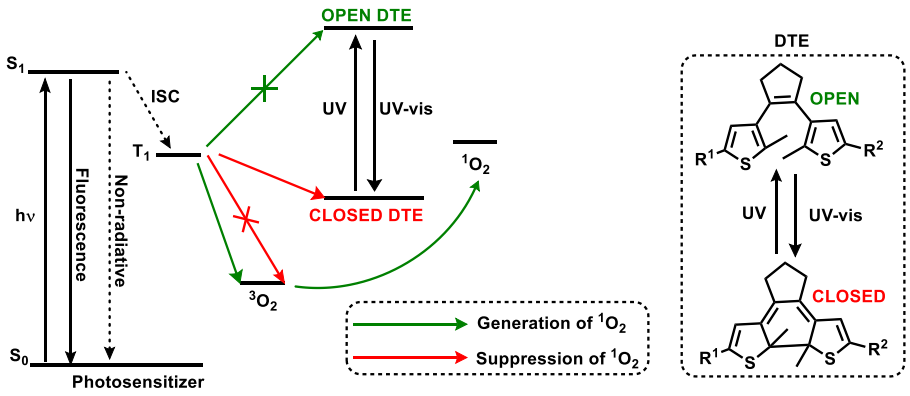
2. Perspectives of this work

In this work, we proved that the immobilization of organic dyes, either covalently or non-covalently, could allow their reuse and recyclability by protecting them from an intense and rapid photobleaching. To limit even more such photodegradation, applications under flow chemistry could be a real asset to valorize our heterogenized systems under such reaction conditions, necessitating in most cases less time of irradiation. Moreover, flow chemistry would permit to control the incoming flux of pure oxygen and thus, controlling the local concentration of oxygen which is a key parameter in the production of singlet oxygen.[171,172]

We proved also that the generation of singlet oxygen can be increased depending on the morphology of silica nanoparticles used. A solid support made of core-shell silica nanoparticles revealed to be the best architecture to use in the case of Rose Bengal. Their usage to anchor benzophenazine derivatives would be interesting to see if such result is generalizable and could enhance the photoactivity of different types of photosensitizers. If so, the

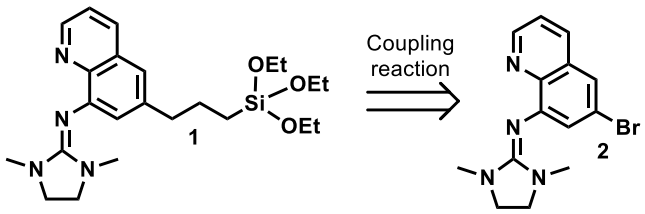
synthesis of value-added organic molecules, rather than testing in benchmark reactions, could be considered to highlight the full potential of the core-shell solid support.

About the structure-activity relationship of benzophenazine derivatives, this needs to be enlarged with electron-donating groups on the western and northern fragments to gain further insights into the impact of functionalization. Benzophenazines are a common motif used in biological applications[311,342,355–359] and we could envision to immobilize our photocatalysts onto biomolecules such as antibody to make a selective drug used in photodynamic therapy, which is a current theme of investigation mainly based on tetrapyrrolic photosensitizers.[431–434] It would also be interesting to derivatize further our benzophenazine derivatives with a photoswitch to control the reversible production of singlet oxygen. Such strategy would allow the elaboration of cascade reactions in a one-pot system for example. A well-known photoswitch, dithienylethene (DTE)[435–437], could be attached to our PCs by exploiting the activated ester strategy developed in this work while the anchoring onto silica nanoparticles could be tried with the southern fragment bearing a mercaptopropanoic acid. Such carboxylic acid could be deprotonated to allow a non-covalent immobilization of the photocatalyst with ammonium groups anchored at the surface of silica nanoparticles. If a stronger linker is needed, a covalent one can be envisaged by transforming the carboxylic acid into an acyl chloride that could react with amine moieties grafted at the surface of the solid material. By applying UV or UV-vis light, the open and closed systems could control the photoproduction of singlet oxygen making our heterogenized systems much more attractive (**Scheme 7.1**). This perspective would need to investigate if the energy transfer between our photocatalysts and the envisaged switch would be possible and if the use of UV light would not lead to photodegradation of the PC or its leaching from the solid support.



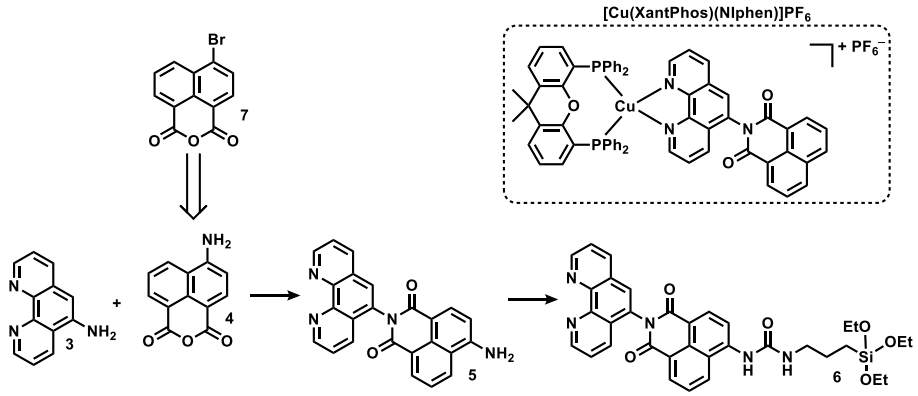
Scheme 7.1. Reversible generation of singlet oxygen with the use of DTE as photoswitch. Adapted from the literature.[437]

Concerning the heterogenized systems based on copper complexes, further investigations on the functionalization of diimine ligands need to be performed to hamper the ligand exchange occurring at the silica surface for the heteroleptic complex. Recent researches have demonstrated that the introduction of new diimine ligands could increase the photophysical properties and photostability of these complexes. In 2019, the group of Poisson designed a new heteroleptic copper complex based on 1,3-dimethyl-N-(quinoline-8-yl)imidazolidine-2-imine (DMEGqu) ligand which exhibited a good photostability over 12 hours of intense blue irradiation by monitoring the photochemical stability by NMR.[138] Such ligand would be interesting to derivatize with siloxane moieties (**1**) to allow future immobilization on silica nanoparticles (**Scheme 7.2**). The same linker length as the one used in this work would be accessed. This could be accomplished by synthesizing a bromine derivative of DMEGqu ligand **2** that opens the door for coupling reactions such as the Negishi one for example.



Scheme 7.2. Derivatization of a diimine ligand developed by the group of Poisson to allow the anchoring of a copper(I) complex.

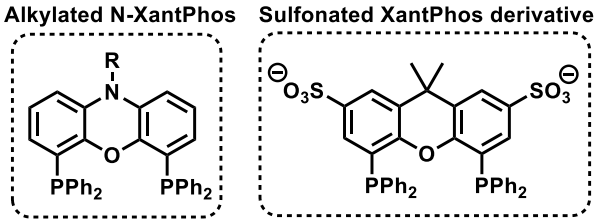
Last year, the group of Tschierlei reported a new copper complex [Cu(XantPhos)(NIphen)PF_6] which displayed an outstanding photostability measured over a period of 8.5 hours in dry acetonitrile.[89] The same anchoring methodology as the one used in this work could be envisioned: an amide linker made by the reaction between a primary amine and an isocyanate moiety. Indeed, the NIphen functionalized with a primary amine **5** can be possibly synthesized from the reaction between compounds **3** and **4**[438], the latter being obtained from commercially available 4-bromo-1,8-napthalic anhydride **7**[439], as illustrated in **Scheme 7.3**. An increased photostability in homogenous phase before any immobilization steps could be the key to achieve the heterogenization of heteroleptic copper complexes while maintaining their photophysical properties.



Scheme 7.3. Synthesis of a NIphen ligand derivative.

It would also be interesting to investigate the immobilization of copper complexes, not by derivatizing their diimine ligand which is mainly

responsible for their photophysical properties, but by modifying the diphosphine ligand. Such methodology is more restricted as diphosphine compounds are less prone to functionalization and can be easily oxidized, in which case they cannot be coordinated anymore to a copper center. The simplest idea would be to alkylate the N-XantPhos[440,441] (**Scheme 7.4**) ligand, but unfortunately, to our experience, such functionalization give poor yields and the subsequent purification is highly difficult to achieve. Another idea based on non-covalent immobilization would be to introduce sulfonate moieties on the XantPhos ligand[442,443] (**Scheme 7.4**) that would participate in an electrostatic interaction with ammonium groups at the surface of silica nanoparticles which are known to immobilize strongly a negatively charged photocatalyst (as demonstrated in Chapter 3). The challenge here would be to be able to obtain the disulfonated compound and not a mixture of no, mono- or disulfonated compounds that would be impossible to purify. Another pitfall could be that a repulsion interaction would occur between the copper center and the ammonium moieties, thus hampering the immobilization.



Scheme 7.4. Possibilities of diphosphine ligands functionalizations.

Finally, for both heteroleptic and homoleptic copper(I) complexes, their quenching with other compounds than aryl diazonium derivatives would be valuable to study. The diazonium compounds are known to be highly reactive and the heterogenized systems could gain in interest if more difficult electron transfer could be achieved at the surface of a solid support, leading to the synthesis of exotic building blocks used in organic synthesis for example.

Annex A

Supporting information – Chapter 3

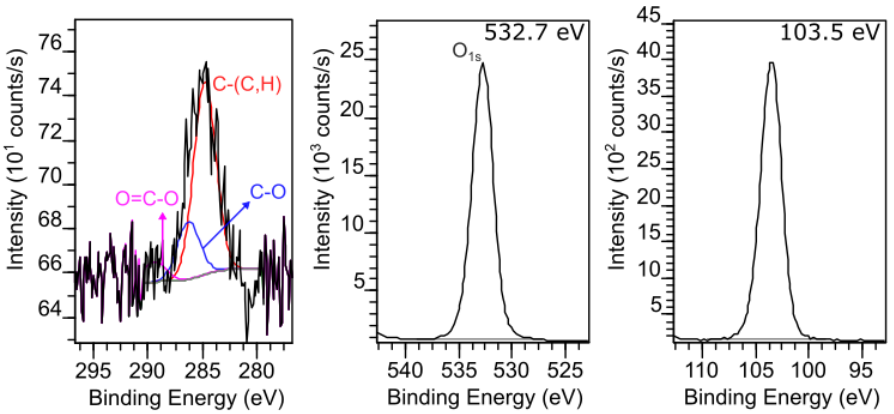


Figure A.1. XPS spectra of pristine U NPs: C_{1s}, O_{1s} and Si_{2p} peaks with the corresponding energy binding.

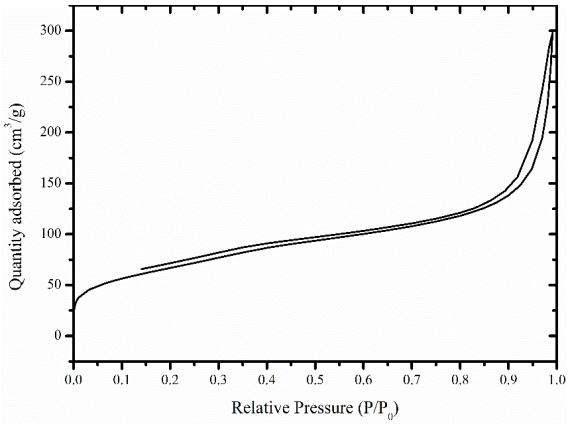


Figure A.2. N_2 adsorption-desorption isotherms at 77 K of silica U NPs.

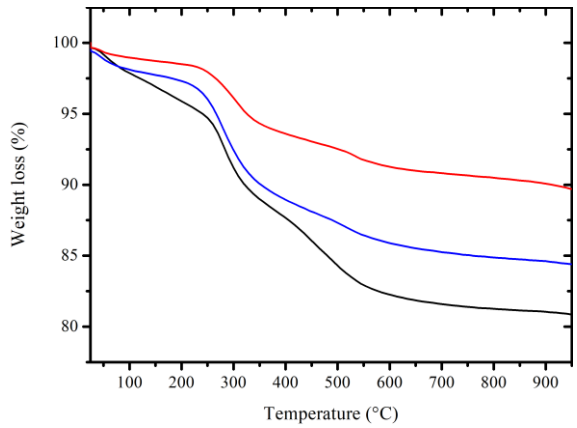


Figure A.3. TGA curves of tertiary amine-functionalized NPs: NS (black), CS (blue) and U (red).

The amount of nitrogen was calculated based on TGA curves. The loss in weight from 150 °C to 900 °C was attributed to the decomposition of organic part: $C_5H_{12}N$. The nitrogen represents 16.3 % (MM_N/MM_{C5H12N}) of the total weight of the organic part. If we take NS nanoparticles as an example, the TGA curve showed a weight loss of 16.06 %, meaning that 2.62 % corresponded to the weight of nitrogen.

Table A.1. XPS analysis of ammonium-functionalized silica NPs. The values are expressed in atomic concentration percentage.

	C_{1s}	O_{1s}	Si_{2p}	N_{1s}	F_{1s}	S_{2p}	O/Si	F/S	CF_3/N
NS	17.2	50.1	19.4	2.8	8.4	2.2	2.6	3.9	0.75
CS	17.1	50.9	18.5	2.7	8.5	2.3	2.8	3.8	0.75
U	15.6	49.0	25.1	2.2	7.2	2.0	2.0	3.6	0.85

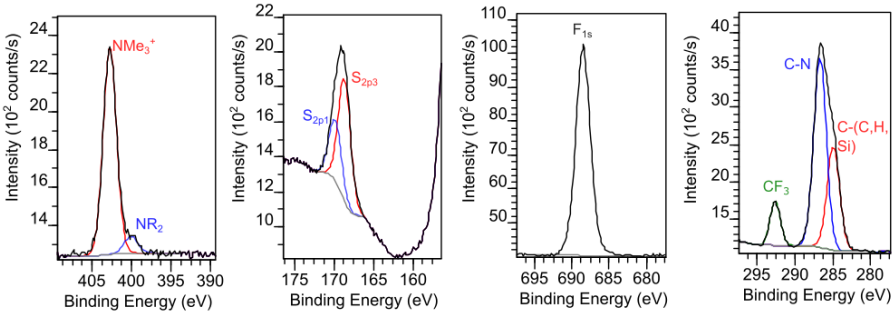


Figure A.4. N_{1s}, S_{2p}, F_{1s} and C_{1s} XPS spectra of ammonium-functionalized NS NPs.

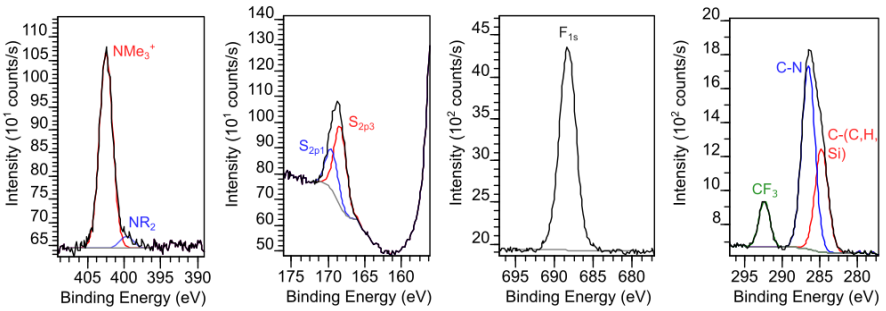


Figure A.5. N_{1s}, S_{2p}, F_{1s} and C_{1s} XPS spectra of ammonium-functionalized U NPs.

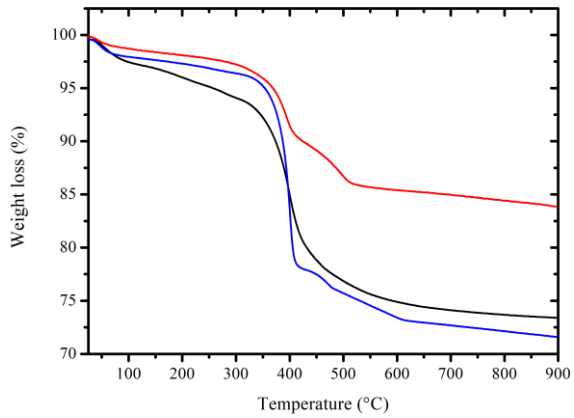


Figure A.6. TGA curves of ammonium-functionalized NS (black), CS (blue) and U (red) NPs.

The amount of nitrogen was calculated based on TGA curves. The loss in weight from 150 °C to 900 °C was attributed to the decomposition of organic part: $C_6H_{15}N^+$ $CF_3SO_3^-$. The cation represents 40 % of the total weight and the anion, 60 % of the total weight of the organic part. If we take NS

nanoparticles as an example, the TGA curve showed a weight loss of 23.5618 %, meaning that 9.42 % corresponded to the weight of the cation. Multiplying 9.42 % by the ratio $N/C_6H_{15}N^+$ gave the amount of nitrogen due to the desired function (9.42*0.1386 = 1.31 %N).

The density of ammonium moieties could also be determined by using CHN analyses. If we take NS nanoparticles as an example, CHN analysis revealed a 1.02 wt.% in nitrogen (0.103 mmol of nitrogen/100 mg of SiO_2). By using Avogadro number, we can determine the number of entities: $1.03E^{-4}*6.022E^{23} = 6.20E^{19}$ entities. Knowing the specific surface area that was determined by BET, we calculate the density of ammoniums which is, in this case, 1.22 ammoniums nm^{-2}.

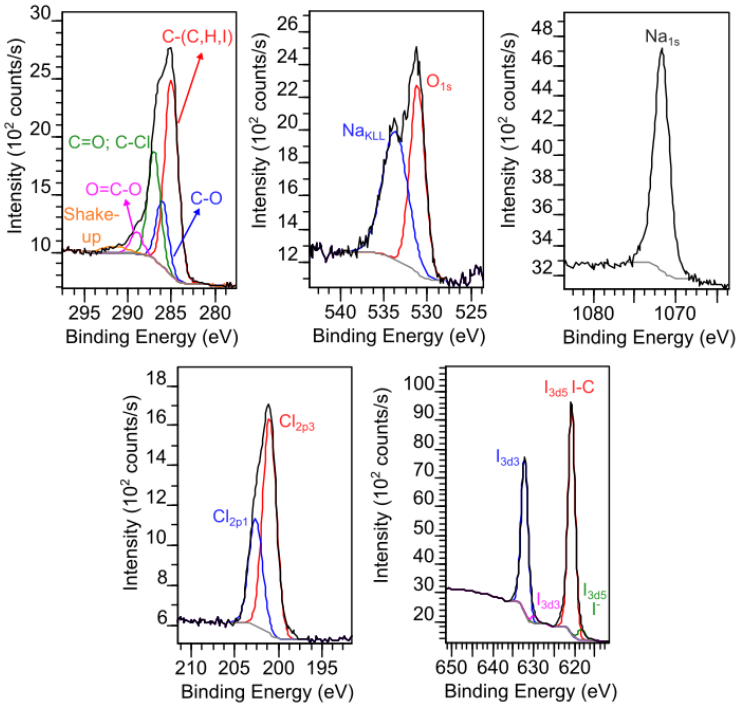


Figure A.7. C_{1s}, O_{1s}, Na_{1s}, Cl_{2p} and I_{3d} XPS spectra of pure Rose Bengal powder.

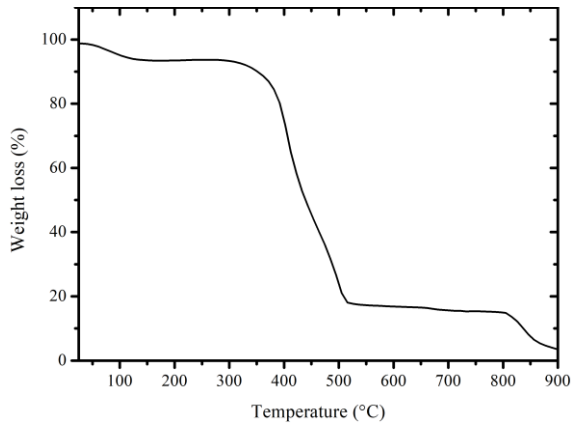


Figure A.8. TGA curve of pure Rose Bengal powder.

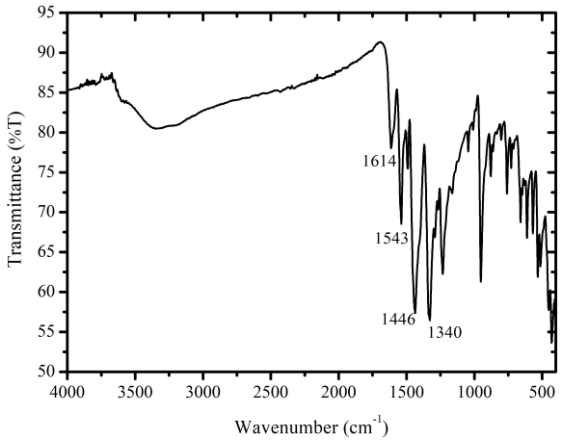


Figure A.9. FTIR-ATR spectrum of pure and solid Rose Bengal dye.

Table A.2. Elemental analyses of ammonium-, RB-functionalized and recycled materials.

	Carbon (%)	**Nitrogen (%)**	**Hydrogen (%)**
Nanospheres particles			
NS-NMe_3^+	7.16	1.02	2.00
NS-RB	7.94	0.90	1.64
NS-RB Run 5	6.02	0.74	1.59
Core-Shell nanoparticles			
CS-NMe_3^+	8.25	1.44	1.89
CS-RB	8.89	0.96	1.67
CS-RB Run 5	9.97	0.98	1.52
Urchins nanoparticles			
U-NMe_3^+	5.04	0.87	1.13
U-RB	7.05	0.62	0.97
U-RB Run 5	6.80	0.68	1.74

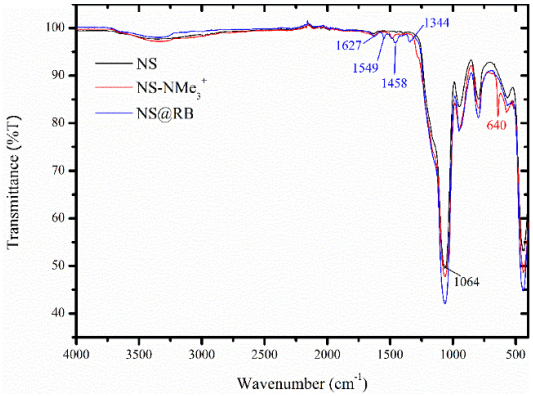


Figure A.10. FTIR-ATR spectra of pristine NS, ammonium- and RB-functionalized NS. The solids were dried at 100 °C overnight and kept under inert atmosphere before doing the analysis.

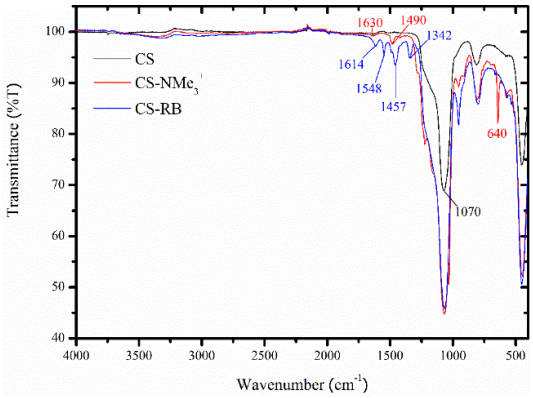


Figure A.11. FTIR-ATR spectra of pristine CS, ammonium- and RB-functionalized CS. The solids were dried at 100 °C overnight and kept under inert atmosphere before doing the analysis.

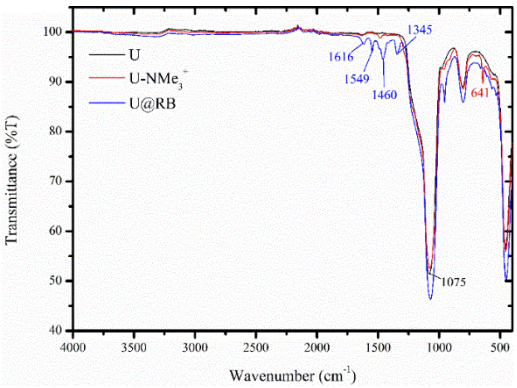


Figure A.12. FTIR-ATR spectra of pristine U, ammonium- and RB-functionalized U. The solids were dried at 100 °C overnight and kept under inert atmosphere before doing the analysis.

As the density of ammonium was determined by CHN analyses and the overall surface area of one RB molecule was calculated by a computational study (486.85 $Å^2$), we could determine how many ammonium arms were available to immobilize one RB molecule. As only half of the molecule can interact with the support because of its perpendicular plane, (we consider that the RB is symmetric), we used a surface of 242.93 $Å^2$ (the other half of the surface can participate in π–π stacking). In the case of NS NPs presenting an ammonium density of 1.22 ammonium nm^{-2}, 2.96 ammonium arms are available to immobilize one RB molecule.

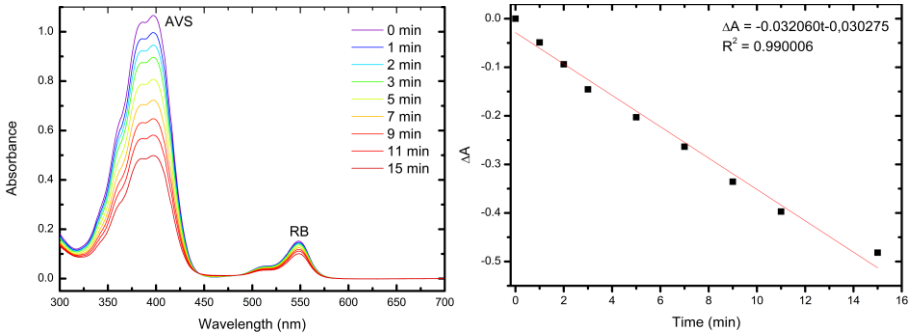


Figure A.13. Degradation of AVS (397 nm) by RB followed by UV-vis analysis and its plot *vs* time.

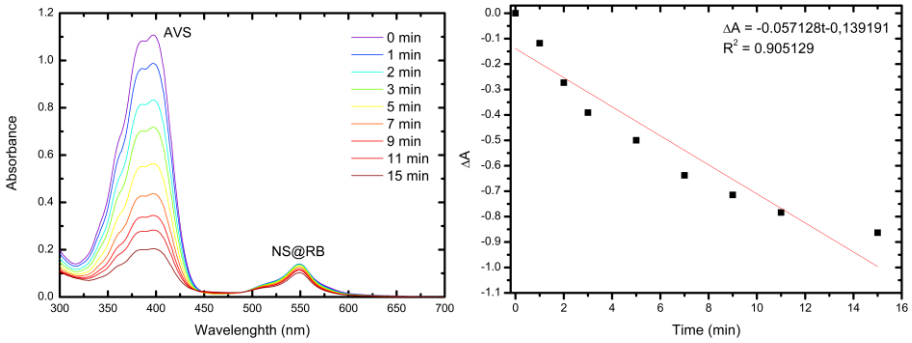


Figure A.14. Degradation of AVS (397 nm) by **RB@NS** followed by UV-vis analysis and its plot *vs* time.

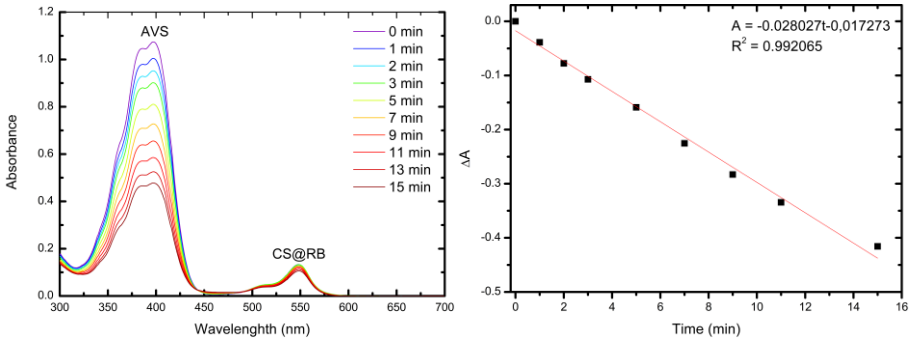


Figure A.15. Degradation of AVS (397 nm) by **RB@CS** followed by UV-vis analysis and its plot *vs* time.

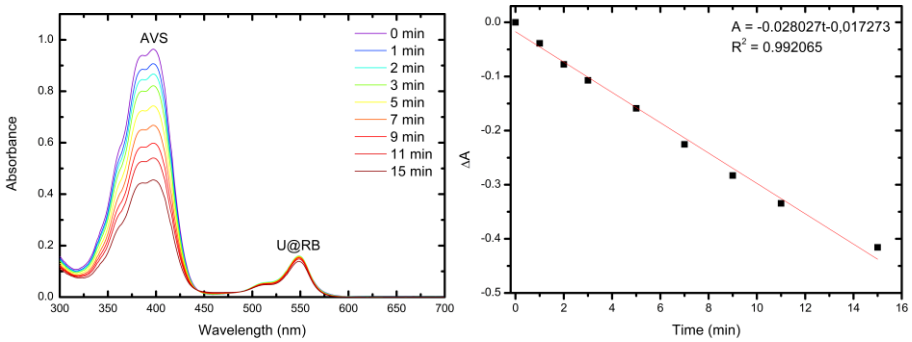


Figure A.16. Degradation of AVS (397 nm) by **RB@U** followed by UV-vis analysis and its plot *vs* time.

Table A.3. Leaching of RB evaluated after each run. The filtrates were analyzed by UV-vis and the resulting solids by TGA. The values are expressed in wt.% of RB.

	NS		**CS**		**U**	
	UV-vis	**TGA**	**UV-vis**	**TGA**	**UV-vis**	**TGA**
Run 1	2.75	4.91	2.63	0.81	8.50	6.74
Run 2	0.36	2.04	1.39	1.05	4.02	n.d.
Run 3	3.14[a]	1.34[a]	3.07[a]	2.24[a]	1.53[a]	1.19[a]
Run 4	1.17	0	0.42	0	0.14	0.18
Run 5	n.d.	0.54	0.13	0	0.12	0

[a] Recharge with materials from Run 1 to keep constant the loading in RB.

The leaching was supposed to arise mainly from multilayers of RB formed at the surface of the nanoparticles thanks to the aromatic nature of RB that can induce π–π stacking. To validate this hypothesis, we determined the amount of RB needed to form one monolayer at the surface of the

nanoparticles. In this case, the entire surface of RB is used (485.86 $Å^2$) as the entire surface can participate in π–π stacking. Knowing the ammonium density and the surface of RB, in the case of NS particles, $4.39E^{19}$ ammonium entities were determined to be present for a surface of 4.86 nm^2 leading to $7.403E^{18}$ entities of RB needed to form a monolayer. As $8.85E^{18}$ RB entities were introduced in the immobilization step and $9.23E^{17}$ RB entities were recovered in the filtrate of this same step, we could conclude that $7.927E^{18}$ RB entities were immobilized. An excess of $5.24E^{17}$ was calculated and proved the possibility of having π–π stacking.

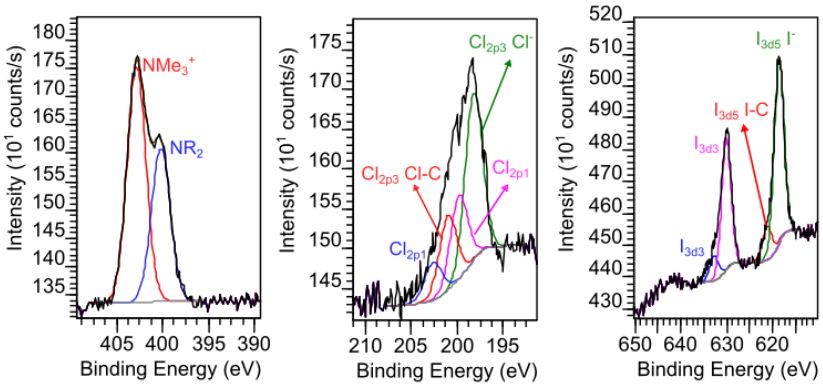


Figure A.17. N_{1s}, Cl_{2p}, and I_{3d} XPS spectra of recycled **RB@NS** used in five runs.

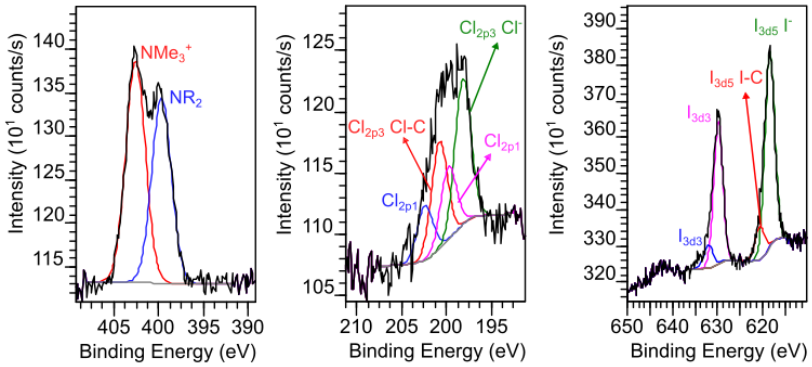
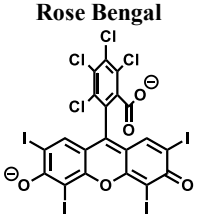


Figure A.18. N_{1s}, Cl_{2p}, and I_{3d} XPS spectra of recycled **RB@U** used in five runs.

Computational details (realized by Dr. Corentin Lefebvre)

- Optimized geometry coordinates and thermochemical properties (298 K, 1 bar).

Rose Bengal



E = -4170.90373760 Hartree DFT(M06-2X/Def2-TZVP)
Zero-point correction = 0.168144 (Hartree/Particle)
Thermal correction to Energy = 0.199340
Thermal correction to Enthalpy = 0.200284
Thermal correction to Gibbs Free Energy = 0.096463
Sum of electronic and zero-point Energies = -4170.735593
Sum of electronic and thermal Energies = -4170.704398
Sum of electronic and thermal Enthalpies = -4170.703454
Sum of electronic and thermal Free Energies = -4170807275

Charge = -2, Multiplicity = 1

C	-2.39258888	0.90170893	0.07215745
C	-3.61607191	0.33913272	-0.01468781
C	-3.85282160	-1.10884480	-0.08694692
C	-2.63065823	-1.89134647	-0.03970938
C	-1.39113865	-1.31997055	0.04263270
C	-1.21698889	0.09513654	0.08615261
O	-0.30870722	-2.13226757	0.05066698
C	0.07771171	0.60762657	0.09787683
C	0.95736528	-1.65419255	0.09197705
C	1.17991793	-0.25085299	0.12771561
C	1.99293275	-2.55042448	0.07111898
C	2.52825156	0.19564140	0.16961793
C	3.55302717	-0.68484063	0.14715719
C	3.38433305	-2.14127616	0.08665133
H	2.71391294	1.25907706	0.23925733
I	5.52938218	-0.00357622	0.19888097
O	4.33027644	-2.92339829	0.05141281
I	1.62057589	-4.59465898	-0.01117537
H	-2.28031814	1.97312899	0.16952197
I	-5.32799806	1.53809390	-0.04414843
O	-4.97312143	-1.59902286	-0.17964991
I	-2.83735397	-3.95847023	-0.13335894
O	-1.38211551	2.47513343	2.76695708
C	-0.19325854	2.29464110	2.47991271
C	0.20038767	2.90133054	1.10592312
C	0.29807799	2.08086622	-0.01532640
O	0.73509017	1.72203354	3.05765606
C	0.60406197	2.63364783	-1.25860227
C	0.44638825	4.26199507	0.96868618
C	0.77518923	4.81626127	-0.26392853
C	0.84550184	3.99873975	-1.39137346
Cl	0.35113404	5.27404422	2.36465889
Cl	1.09132138	6.50669858	-0.41264984
Cl	1.22784791	4.67495117	-2.93135710
Cl	0.67517835	1.61868857	-2.65522015

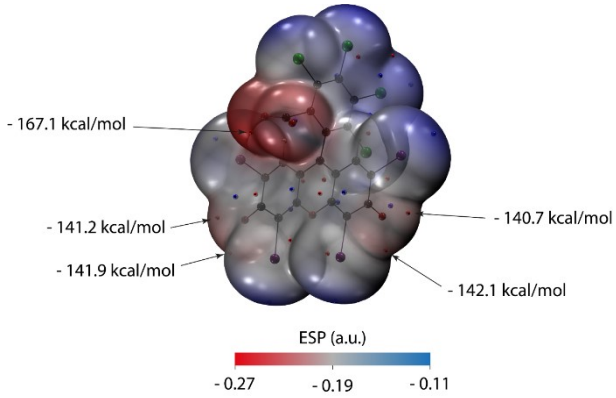


Figure A.19. Representation of the electrostatic potential (ESP) and its extrema (minima in red spheres and maxima in blue spheres) over the van der Waals surface (ρ = 0.001 a.u.) of the Rose Bengal molecule (level of theory: M06-2X/Def2-TZVP in gaz phase).

Fictive Rose Bengal	*E* = -3899.20521300 Hartree DFT(M06-2X/Def2-TZVP) Zero-point correction = 0.179415 (Hartree/Particle) Thermal correction to Energy = 0.212172 Thermal correction to Enthalpy = 0.213116 Thermal correction to Gibbs Free Energy = 0.106287 Sum of electronic and zero-point Energies = -3899.025798 Sum of electronic and thermal Energies = -3899.993041 Sum of electronic and thermal Enthalpies = -3899.992097 Sum of electronic and thermal Free Energies = -3899.098926

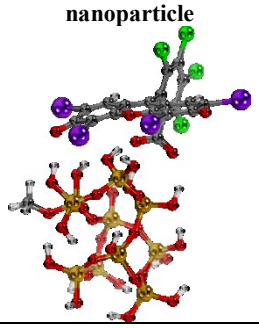
Charge = -3, Multiplicity = 1

C	0.37526927	4.18104714	-1.14150508
C	0.39147647	2.79217015	-1.15891280
C	0.00020978	2.11373640	0.00001656
C	-0.39091322	2.79227612	1.15893658
C	-0.37440929	4.18114670	1.14150296
C	0.00050400	4.88316981	-0.00000849
C	-0.83351602	2.03111375	2.43582693
O	0.09074872	1.48258977	3.05142754
C	0.00005895	0.61780238	0.00002681
C	-1.21052942	-0.08689331	-0.01694477
C	-1.18223441	-1.50695699	-0.03985523
O	-0.00022485	-2.16171487	0.00002129
C	1.18191640	-1.50719662	0.03989602
C	1.21050344	-0.08713993	0.01698052
C	-2.49050380	0.53391036	-0.05925499
C	-3.61846605	-0.20711069	-0.13375375
C	-3.65294107	-1.66916442	-0.16653137
C	-2.33182434	-2.25443052	-0.10900498
C	2.49060699	0.53339889	0.05926383
C	3.61841704	-0.20785674	0.13374720
C	3.65258917	-1.66991872	0.16652605
C	2.33134887	-2.25490930	0.10902721
I	-5.48937156	0.73766873	-0.20300021
O	-4.69532384	-2.32375370	-0.23639358
I	-2.23470998	-4.33687646	-0.14549928
I	2.23378449	-4.33733372	0.14552178
I	5.48952222	0.73653365	0.20293571
O	4.69483558	-2.32472547	0.23638516

C	0.83395467	2.03090427	-2.43578347
Cl	-0.81246554	5.05572613	2.57954347
Cl	0.00071615	6.62118306	-0.00001220
Cl	0.81356563	5.05550219	-2.57954678
O	-2.05262077	2.07844255	2.65827836
H	2.53792104	1.61192056	0.01489551
H	-2.53759747	1.61244189	-0.01489987
O	-0.09040839	1.48257236	-3.05140640
O	2.05308855	2.07789750	-2.65814747

Estimated overall surface area in condensed phase (ρ = 0.002 a.u.):

485.86 Å^2

Rose Bengal & Surface of silica nanoparticle 	*E* = -9300.18200884 Hartree DFT(M06-2X/Def2-TZVP) Zero-point correction = 0.538512 (Hartree/Particle) Thermal correction to Energy = 0.619696 Thermal correction to Enthalpy = 0.620640 Thermal correction to Gibbs Free Energy = 0.414432 Sum of electronic and zero-point Energies = -9299.643497 Sum of electronic and thermal Energies = -9299.562313 Sum of electronic and thermal Enthalpies = -9299.561368 Sum of electronic and thermal Free Energies = -9299.767576

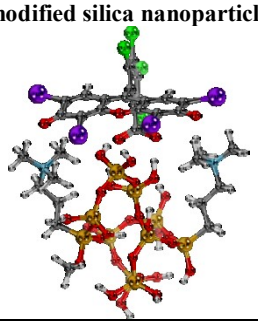
Charge = -2, Multiplicity = 1

Si	7.54817264	1.58860809	-0.70215916
O	6.19775003	2.06851559	-1.43844905
Si	4.61039442	1.83389644	-1.12219906
O	4.34686897	2.48755686	0.33732104
Si	4.96662256	3.00991371	1.73452911
O	5.99460052	1.85731768	2.30018451
Si	1.76837564	0.83267194	1.28926541
Si	6.15610473	0.91858939	3.62900362
Si	4.22386806	-0.82494440	2.24501598
O	5.07605788	-0.29614599	3.52589143
O	3.23541736	0.36247544	1.79849740
O	0.72564640	-0.35919368	1.65002104
Si	-0.05931718	-1.50872933	0.81488966
O	0.82616440	-2.87821027	0.83206146
Si	2.03505740	-3.25236058	-0.20301350
O	5.30006057	-1.22595846	1.11047026
Si	6.76324090	-1.28777929	0.43262774
O	7.32450079	0.17071639	0.04224918
O	4.37430904	0.23087457	-1.13567474
Si	3.46431997	-0.98410554	-1.68865855
O	2.80943649	-1.82880876	-0.47299161
O	-0.15701325	-1.09944306	-0.75471848
H	-0.46599653	-0.20488475	-1.00172528
O	1.52877413	-3.94658466	-1.55950187
H	0.65811863	-3.77968402	-1.97008963
O	7.83866978	-1.80233583	1.57393716
H	7.71050755	-2.70423706	1.87754674
O	3.39035848	-2.17150116	2.63380215
H	2.42732535	-2.10360501	2.61792099
O	7.66676306	0.33525021	3.67833421
H	7.86398573	-0.39937843	3.07837277

O	5.92672830	1.80353270	4.96919446
O	3.76240518	2.57432291	-2.28027517
H	2.84433603	2.28778540	-2.34423288
O	3.84250795	3.30361475	2.85468906
H	2.92665174	3.01103392	2.68416987
O	8.03429491	2.64694717	0.45149301
H	7.77698952	2.36844677	1.34245977
O	8.70186710	1.52360247	-1.84602521
H	9.59995630	1.42871756	-1.52457752
O	6.76177762	-2.32077184	-0.80114784
H	6.03683130	-2.23006321	-1.45114195
O	5.83076534	4.37143489	1.52009746
H	6.60844767	4.26878251	0.95879213
O	4.56631943	-1.92558388	-2.47127388
O	2.33287187	-0.52423218	-2.75251113
O	1.82167850	1.15052747	-0.29542901
H	0.94468978	1.34373706	-0.72690008
O	1.40350468	2.16266759	2.16910812
H	0.54327477	2.52666947	1.89570747
O	3.08356203	-4.27402655	0.50204058
H	3.53163930	-3.87206920	1.25736720
O	-1.46596002	-1.72698500	1.58273916
H	-1.96480882	-2.53594400	1.42161145
C	4.17006046	-3.09435951	-3.18043884
H	4.93705785	-3.30875512	-3.92418514
H	3.21153609	-2.94116980	-3.67885545
H	4.07452874	-3.94076214	-2.49779427
H	5.17833586	2.40868746	4.91369982
H	1.41752736	-0.61663197	-2.45489806
I	-2.54518932	-4.67289016	-0.50362131
O	-0.90241559	-3.51253699	-2.96048555
I	-5.35542881	-3.26340385	2.71468095
C	-2.59917748	-2.83143184	-1.46557858
C	-1.71717756	-2.65850709	-2.59503095
O	-4.00727008	-1.99905076	0.20297757
C	-3.28774792	-1.78167055	-0.92206723
C	-1.85505679	-1.36391730	-3.26003114
I	-0.73307788	-1.09638620	-4.99566278
C	-5.24679015	-1.29877198	2.05251979
C	-4.56840636	-0.98989116	0.91054500
C	-3.23119549	-0.47735809	-1.48632503
C	-2.53524775	-0.32881869	-2.71802793
O	-6.53582788	-0.53957516	3.88317122
C	-5.90273451	-0.28926041	2.86745880
C	-4.44696245	0.35252367	0.44020260
C	-3.79760553	0.58173219	-0.76728916
H	-2.50988309	0.64689819	-3.18423622
Cl	-6.25074925	1.59597368	-2.14326476
C	-5.73109084	1.08014277	2.35301902
C	-5.04753465	1.37711554	1.22930462
O	-0.56032534	1.52294755	-1.35112817
C	-3.71552151	1.97491840	-1.29989005
C	-4.82275304	2.53736521	-1.93624956
C	-1.28711633	2.14759897	-0.52700539
H	-4.94446616	2.40459382	0.90605921
I	-6.62424678	2.59185114	3.47935673
C	-2.55406270	2.73100150	-1.15567939
C	-4.78561293	3.84522227	-2.41387597
Cl	-6.15814206	4.52640431	-3.19424118
O	-1.08167250	2.34916031	0.66687172
C	-2.51649352	4.03617678	-1.63278446

C	-3.62517286	4.60160755	-2.25636649
Cl	-1.06796560	4.94915833	-1.45726722
Cl	-3.56645936	6.21743161	-2.83875687

Rose Bengal & Surface of modified silica nanoparticle



E = -9732.98634895 Hartree DFT(M06-2X/Def2-TZVP)
Zero-point correction = 0.935640 (Hartree/Particle)
Thermal correction to Energy = 1.032595
Thermal correction to Enthalpy = 1.032595
Thermal correction to Gibbs Free Energy = 0.797903
Sum of electronic and zero-point Energies = -9732.050709
Sum of electronic and thermal Energies = -9731.953754
Sum of electronic and thermal Enthalpies = -9731.952810
Sum of electronic and thermal Free Energies = -9732.188446

Charge = 0, Multiplicity = 1

Si	7.64800627	-0.44749632	1.56820482
O	6.56546604	0.36680093	2.44708004
Si	4.99285064	0.77624576	2.38879772
O	4.14014258	-0.59288549	2.45546654
Si	4.36438180	-2.20841828	2.48243535
O	5.00020324	-2.64451353	1.04612522
Si	1.69848193	-0.44254701	0.19105961
Si	5.24549886	-3.27529780	-0.41991400
Si	4.11843990	-0.75056328	-1.61902019
O	4.73741185	-2.25113639	-1.58479705
O	3.24132450	-0.56887291	-0.27749426
O	0.83400540	-0.19580591	-1.17201728
Si	-0.07764930	1.04473671	-1.72582560
O	0.91089783	2.18738101	-2.32301745
Si	2.41159443	2.77812844	-2.36659537
O	5.35358939	0.28388017	-1.73367358
Si	6.95349097	0.15413538	-1.43964339
O	7.14921279	-0.49122342	0.02729400
O	4.71344965	1.62774015	1.04692323
Si	4.27875267	2.85343496	0.09399297
O	3.15778091	2.35966733	-0.98434954
O	-0.90385446	1.71924958	-0.50671539
H	-1.20956530	1.13487980	0.21204369
O	2.36852060	4.41145713	-2.38770422
H	2.09211773	4.83344052	-3.20486833
O	7.64709079	-0.95814123	-2.41324023
H	7.71347798	-0.77727330	-3.35308700
O	3.18746470	-0.51541051	-2.93915316
H	2.23908161	-0.65534178	-2.81493032
O	6.85282188	-3.51744344	-0.59433185
H	7.29699733	-2.93859323	-1.23051035
C	4.22029052	-4.81810139	-0.58515459
O	4.61420923	1.75937752	3.62572017
H	4.63390942	1.38838767	4.51062728
O	2.93753305	-2.92371056	2.73650291
H	2.20820611	-2.48696543	2.25917412
O	7.76230977	-2.00620832	2.04946401
H	7.53677289	-2.65278287	1.36371641
O	9.05487182	0.32203982	1.77202340
H	9.86772152	-0.13769646	1.55563787
O	7.63630102	1.59953040	-1.61953884
H	7.11684778	2.31868102	-1.22038338

O	5.37896032	-2.65823759	3.65734984
H	6.31773827	-2.54759416	3.45411967
O	5.64388317	3.33130013	-0.68746568
C	3.53649961	4.28809263	1.01186546
O	1.51571722	0.78106852	1.24818535
H	0.67751957	0.65106536	1.72711726
O	1.24384204	-1.85204531	0.85372114
H	0.23661856	-1.95351837	1.05107033
O	3.22557724	2.28676632	-3.67433592
H	3.35615380	1.33130965	-3.75641483
O	-0.95164193	0.37700859	-2.90039265
H	-1.66547085	0.86170578	-3.33289150
H	3.13005223	4.93893652	0.22915702
H	4.31451215	4.86302225	1.51906767
C	2.43817498	3.88073521	2.00955333
H	1.95747370	2.95314236	1.69575375
C	1.38436431	4.95935873	2.26039035
H	2.91030492	3.63363800	2.96021664
H	1.07876587	4.98945361	3.30632211
N	0.09771564	4.78796825	1.48743056
H	1.76797165	5.94435816	1.99089815
C	-0.65804854	3.60793443	2.00166937
C	0.35232530	4.59327410	0.02895292
H	0.93842428	5.43148063	-0.34007037
H	-0.61097465	4.53686091	-0.47873278
H	0.88990083	3.65912621	-0.10539180
H	-0.92134028	3.78849252	3.04154807
H	-0.04215801	2.72119884	1.89825951
H	-1.55262663	3.49048859	1.39889596
C	-0.73905403	6.01142683	1.66776469
H	-0.92115812	6.15030659	2.73165065
H	-1.68047632	5.87022043	1.13565382
H	-0.19081482	6.86002726	1.26366965
C	5.60164324	4.22302380	-1.80026980
H	6.60970854	4.60010240	-1.96532468
H	4.93413612	5.06509665	-1.60729351
H	5.26099975	3.69614298	-2.69400969
H	4.42891281	-5.31105285	-1.53813544
C	2.74263705	-4.40825750	-0.48295950
H	4.47873213	-5.52086375	0.21159911
H	2.50379986	-3.71832552	-1.29530370
H	2.58947509	-3.86285763	0.44744359
C	1.81399621	-5.60708508	-0.54223880
H	1.81073832	-6.04711634	-1.54102358
N	0.36765776	-5.31183524	-0.20909808
H	2.12763968	-6.37317763	0.16888397
C	-0.16813639	-4.18492418	-1.03811498
C	0.21968172	-4.97212056	1.24009015
H	-0.03404055	-4.43439874	-2.08927656
H	0.36133008	-3.27367716	-0.77737987
H	-1.22675909	-4.06789840	-0.81152436
H	0.51106081	-5.84100122	1.82625558
H	-0.81753288	-4.70138727	1.42419579
H	0.85313448	-4.12543359	1.47804988
C	-0.43178034	-6.53704107	-0.48837808
H	-0.41277155	-6.73401360	-1.55792196
H	-1.45678314	-6.36243179	-0.17200677
H	0.00413846	-7.36958167	0.06000113
I	-2.97011119	3.61712673	-3.02671529
O	-3.14983115	5.04199190	-0.19218677
I	-3.69947270	-0.48885359	-4.90577745

C	-3.62661062	2.94643428	-1.17637130
C	-3.58410534	3.88896944	-0.08559228
O	-3.80636005	0.77437407	-2.03129631
C	-3.87546233	1.61616311	-0.97171339
C	-4.04721475	3.34289990	1.19064540
I	-4.25295504	4.69023680	2.77225919
C	-3.81677487	-1.34406379	-3.02060078
C	-3.87482441	-0.57403440	-1.89910057
C	-4.12135078	1.09556722	0.32541738
C	-4.24029725	2.01886293	1.39486006
O	-3.69839595	-3.52285241	-3.93355977
C	-3.81104520	-2.79949888	-2.95769931
C	-3.99159756	-1.14301280	-0.59048532
C	-4.12725265	-0.29406411	0.49591701
H	-4.48413674	1.64583324	2.38097362
Cl	-6.86915107	-0.56294737	1.71441480
C	-3.94994846	-3.33629342	-1.59115933
C	-4.02314709	-2.56606304	-0.48843565
O	-1.20174564	0.03422843	1.69088581
C	-4.20242395	-0.85877824	1.87242048
C	-5.42204365	-1.01378089	2.52473860
C	-1.69257784	-1.10775483	1.79699468
H	-4.12499727	-3.01102723	0.49270615
I	-4.07815779	-5.41484139	-1.45025445
C	-3.02689141	-1.23902064	2.51214411
C	-5.47419698	-1.53102441	3.81917554
Cl	-6.97949157	-1.71509427	4.61500329
O	-1.19421435	-2.17850000	1.38034323
C	-3.07329028	-1.75394814	3.80053000
C	-4.29108857	-1.89771084	4.46341747
Cl	-1.60447468	-2.19559615	4.58382174
Cl	-4.33937541	-2.52317150	6.05771682

- Analysis of the molecular interactions between RB and silica nanoparticles

Atoms in Molecules (AIM), Natural Bond Orbitals (NBO) and Intrinsic Bond Strength Index (IBSI) analysis:

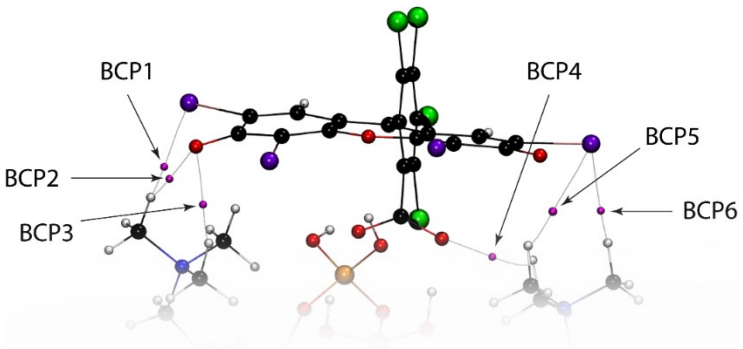


Figure A.20. Representation of the bond critical points (BCP) and their associated bond path for electrostatic interactions between Rose Bengal and ammonium moieties

Table A.4. Value of electron density (ρ), laplacian of electron density ($\nabla^2\rho$), ratio between absolute value of potential energy V and lagrangian kinetic energy G at the considered BCP. Bond ellipticity ε, second order perturbation theory analysis with NBO $E^{(2)}$ associated with the donor-acceptor transfer (LP = lone pair, σ* = antibonding σ bond) and IBSI are also given.

Label	ρ (a.u.)	$\nabla^2\rho$ (a.u.)	$\lvert V\rvert/G$	ε	$E^{(2)}$ (kcal/mol)	Donor → acceptor transfer	IBSI
BCP1	0.006226	0.017743	0.813322	1.085430	0.19	LP(I109) → σ*(C72—H74)	0.007
BCP2	0.016692	0.066354	0.799541	0.047133	3.50	LP(O102) → σ*(C72—H74)	0.042
BCP3	0.007286	0.025060	0.755361	0.138888	0.17	LP(O102) → σ*(C65—H67)	0.018
BCP4	0.008484	0.034980	0.764019	0.491545	0.25	LP(O131) → σ*(C90—H95)	0.013
BCP5	0.008506	0.021530	0.839242	0.136714	1.67	LP(I127) → σ*(C97—H99)	0.017
BCP6	0.006124	0.016705	0.811856	0.594046	0.36	LP(I127) → σ*(C89—H93)	0.015

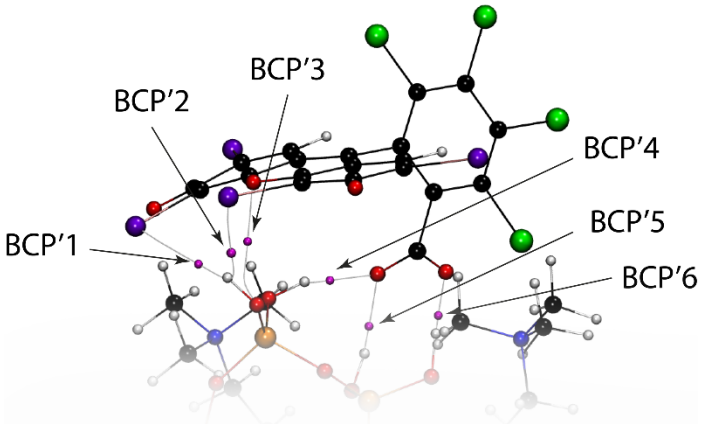


Figure A.21. Representation of the bond critical points (BCP) and their associated bond path for hydrogen bonding between Rose Bengal and the surface of the silica nanoparticle.

Table A.5. Value of electron density (ρ), laplacian of electron density ($\nabla^2\rho$), ratio between absolute value of potential energy V and lagrangian kinetic energy G at the considered BCP. Bond ellipticity ε, second order perturbation theory analysis with NBO $E^{(2)}$ associated with the donor-acceptor transfer and IBSI are also given.

Label	ρ (a.u.)	$\nabla^2\rho$ (a.u.)	$\lvert V\rvert/G$	ε	$E^{(2)}$ (kcal mol^{-1})	Donor → acceptor transfer	IBSI
BCP'1	0.007492	0.019808	0.796758	0.291741	1.44	LP(I101) → σ*(O53—H54)	0.017
BCP'2	0.009386	0.029741	0.779752	0.231399	1.59	LP(I103) → σ*(O53—H54)	0.020
BCP'3	0.008910	0.040168	0.722436	0.701803	0.10	LP(O106) → σ*(O53—H54)	0.013
BCP'4	0.028163	0.110110	0.966212	0.055071	14.26	LP(O122) → σ*(O22—H23)	0.082
BCP'5	0.022560	0.090667	0.890477	0.099641	6.72	LP(O122) → σ*(C47—H48)	0.051
BCP'6	0.080323	0.114352	1.535180	0.013475	63.79	LP(O131) → σ*(O49—H50)	0.272

Evaluation of the molecular interactions and their energy with the Independent Gradient-Model (IGM) δg descriptor and EDA-NOCV analysis:

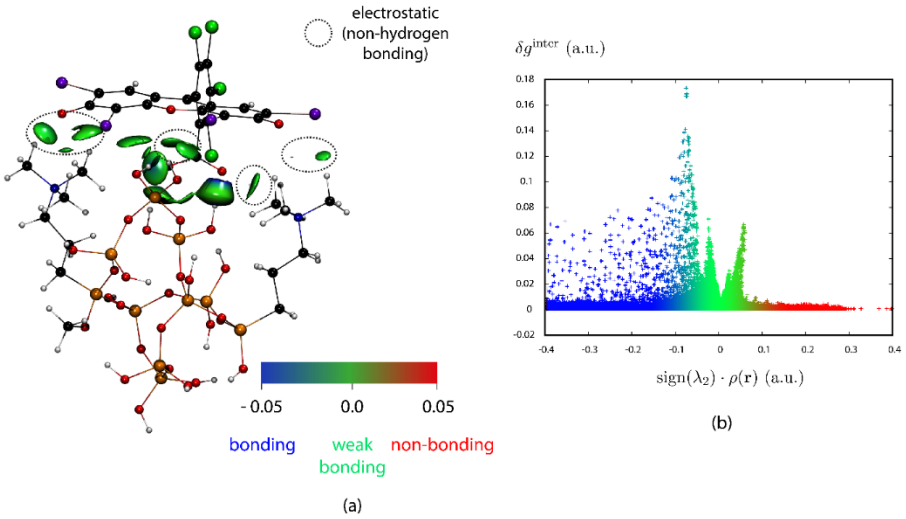


Figure A.22. IGM analysis for the molecular interactions between Rose Bengal and the surface of the modified silica nanoparticle with ammonium moieties. Electrostatic interactions (non-hydrogen bonding) are indicated by dotted black circles in (a). Blue-Green-Red (BGR) color range for the value of $\mathrm{sign}(\lambda_2) \cdot \rho(\mathbf{r})$ (λ_2 standing for the second eigenvalue of the hessian matrix of electron density) is given with $\delta g^{inter} = 0.05$ a.u. in (a) and in the signature of molecular interactions in (b).

Determined energy of interaction between Rose Bengal and the surface of the modified silica nanoparticle with ammonium moieties:

-74.25 kcal/mol

to be compared to the energy of interaction between Rose Bengal and the surface of the nanoparticle without ammonium functionalization:

-46.64 kcal/mol

Annex B

Supporting information – Chapter 4

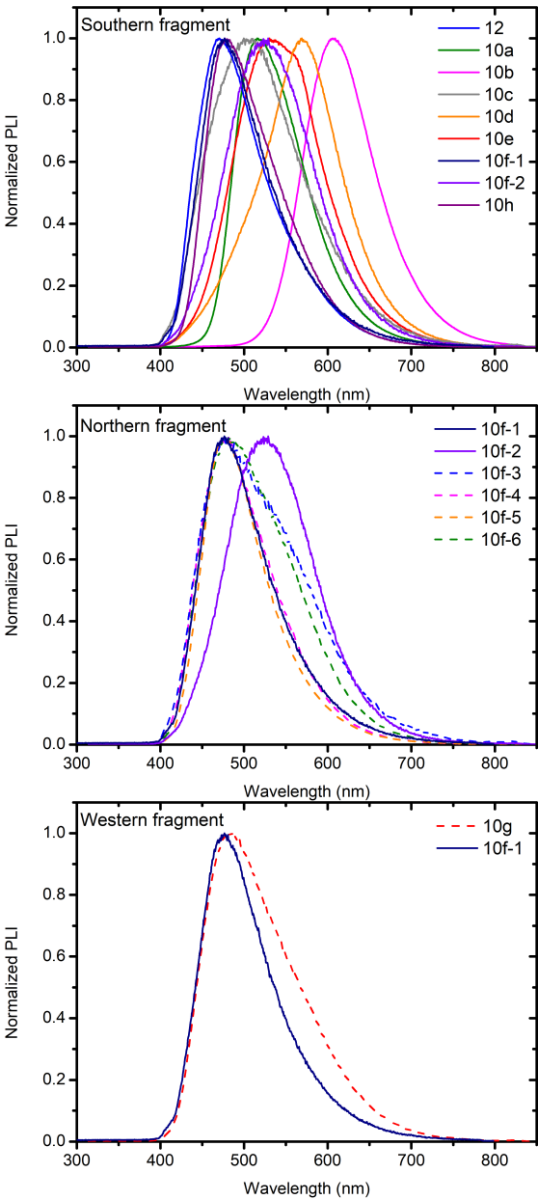


Figure B.1. Fluorescence spectra of benzophenazine derivatives.

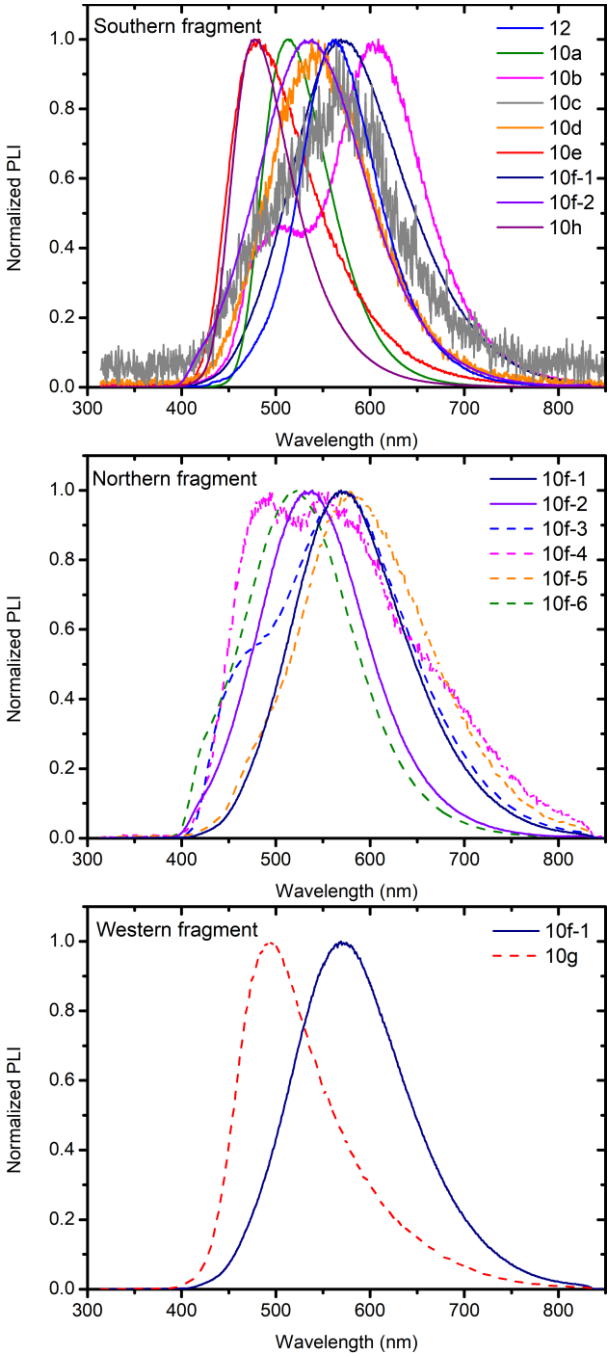
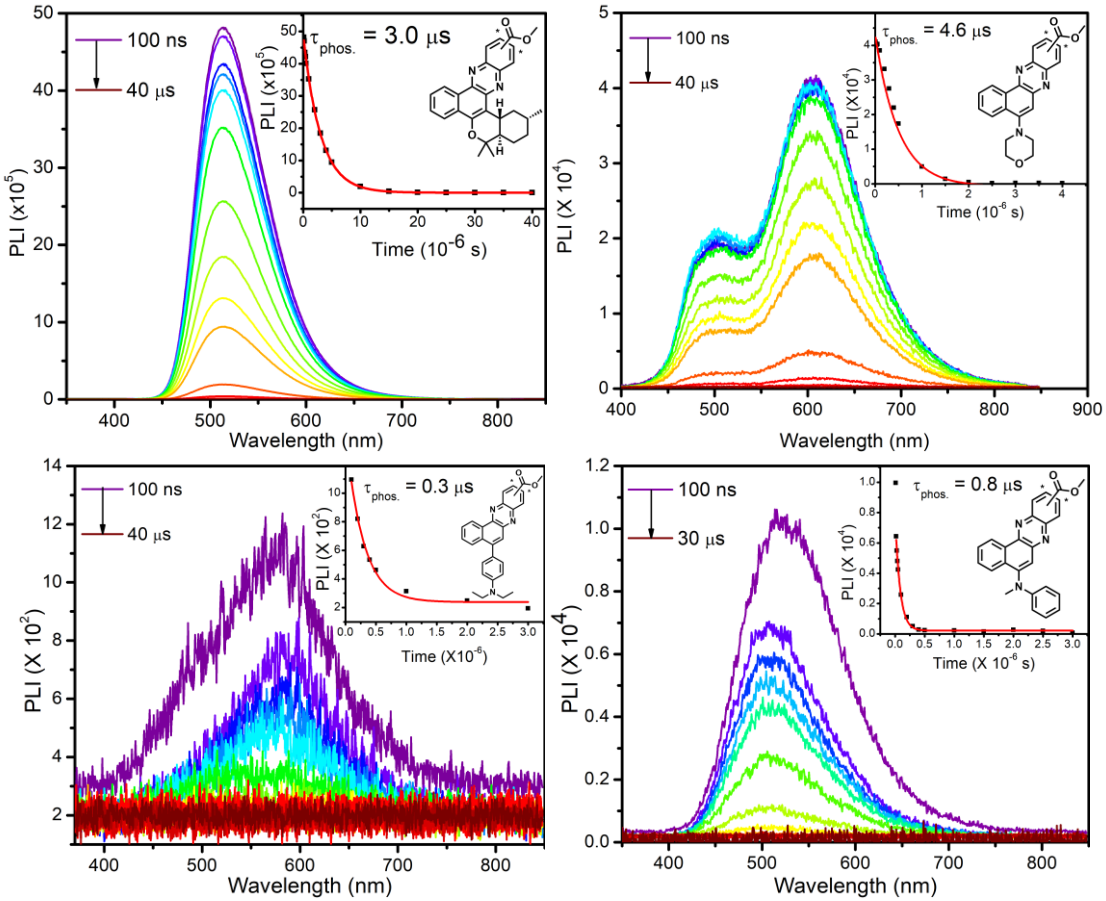
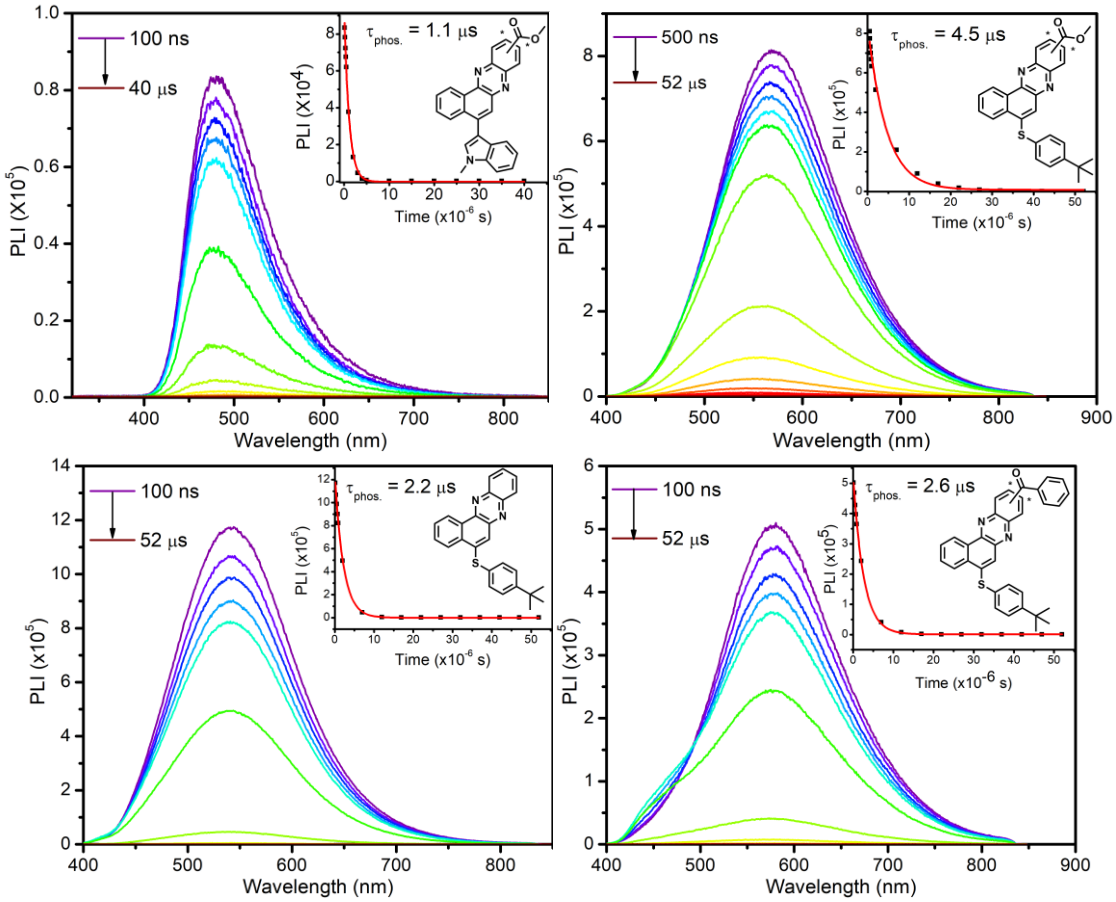
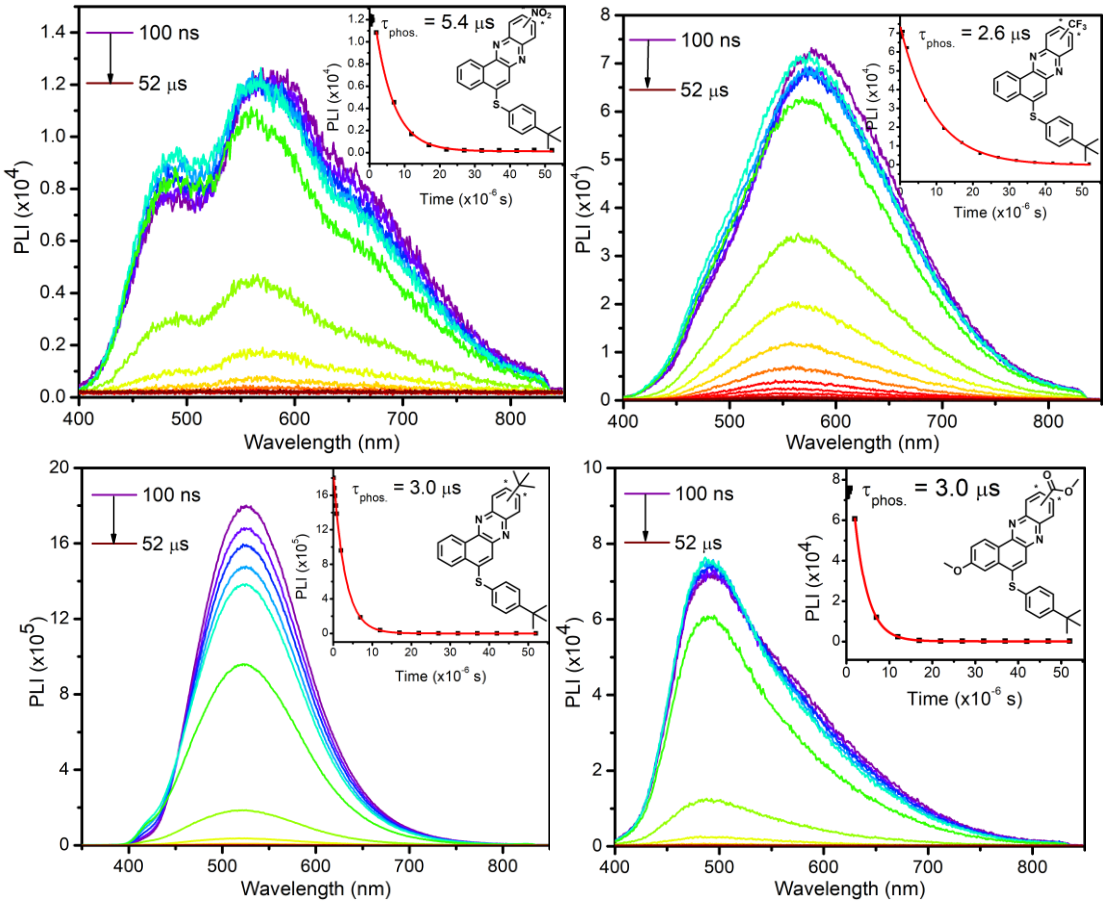


Figure B.2. Phosphorescence spectra of benzophenazine derivatives.


100 ns
40 μs
PLI (x10^5)
Wavelength (nm)
τ phos. = 3.0 μs
Time (10^-6 s)
100 ns
40 μs
PLI (X 10^4)
Wavelength (nm)
τ phos. = 4.6 μs
Time (10^-6 s)
100 ns
40 μs
PLI (X 10^2)
Wavelength (nm)
τ phos. = 0.3 μs
Time (X10^-6)
100 ns
30 μs
PLI (X 10^4)
Wavelength (nm)
τ phos. = 0.8 μs
Time (X 10^-6 s)


100 ns
40 μs
PLI (X10^5)
Wavelength (nm)
τphos. = 1.1 μs
PLI (X10^4)
Time (x10^-6 s)
500 ns
52 μs
τphos. = 4.5 μs
100 ns
52 μs
τphos. = 2.2 μs
100 ns
52 μs
τphos. = 2.6 μs


100 ns
52 μs
PLI (x10^4)
Wavelength (nm)
τ phos. = 5.4 μs
Time (x10^-6 s)
100 ns
52 μs
PLI (x10^4)
Wavelength (nm)
τ phos. = 2.6 μs
Time (x10^-6 s)
100 ns
52 μs
PLI (x10^5)
Wavelength (nm)
τ phos. = 3.0 μs
Time (x10^-6 s)
100 ns
52 μs
PLI (x10^4)
Wavelength (nm)
τ phos. = 3.0 μs
Time (x10^-6 s)

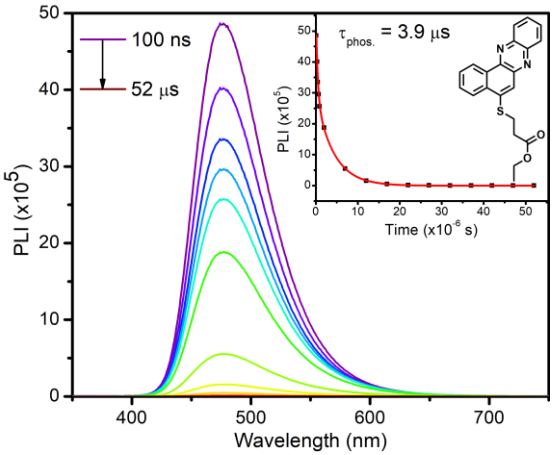


Figure B.3. Delay map of the phosphorescence spectra of benzophenazine derivatives measured between 100 ns and 30 µs after the laser pulse at regular intervals. The inset corresponds to the photoluminescence intensity at 514 **(10a)**, 605 **(10b)**, 584 **(10c)**, 519 **(10d)**, 480 **(10e)**, 570 **(10f-1)**, 540 **(10f-2)**, 579 **(10f-3)**, 564 **(10f-4)**, 577 **(10f-5)**, 526 **(10f-6)**, 490 **(10g)** and 476 **(10h)** nm according to time with the exponential fit (red).

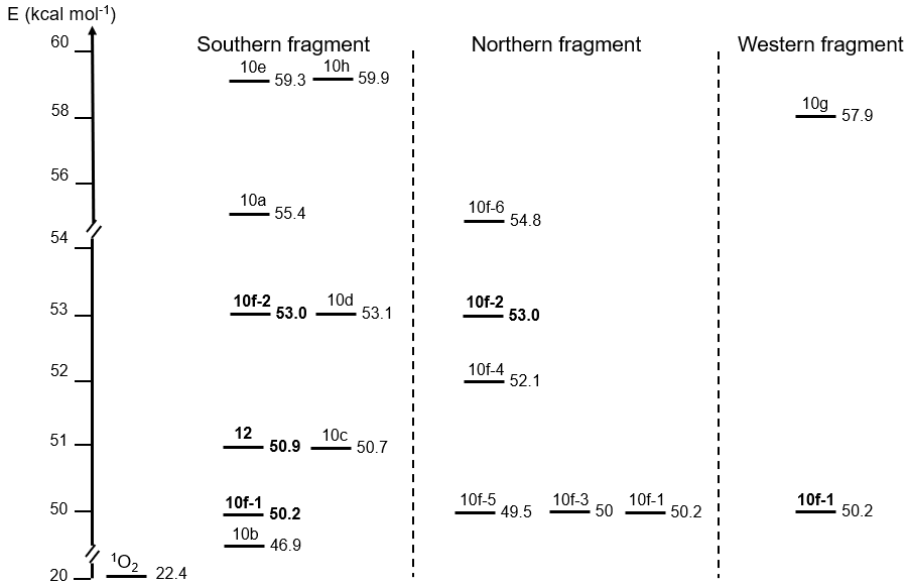
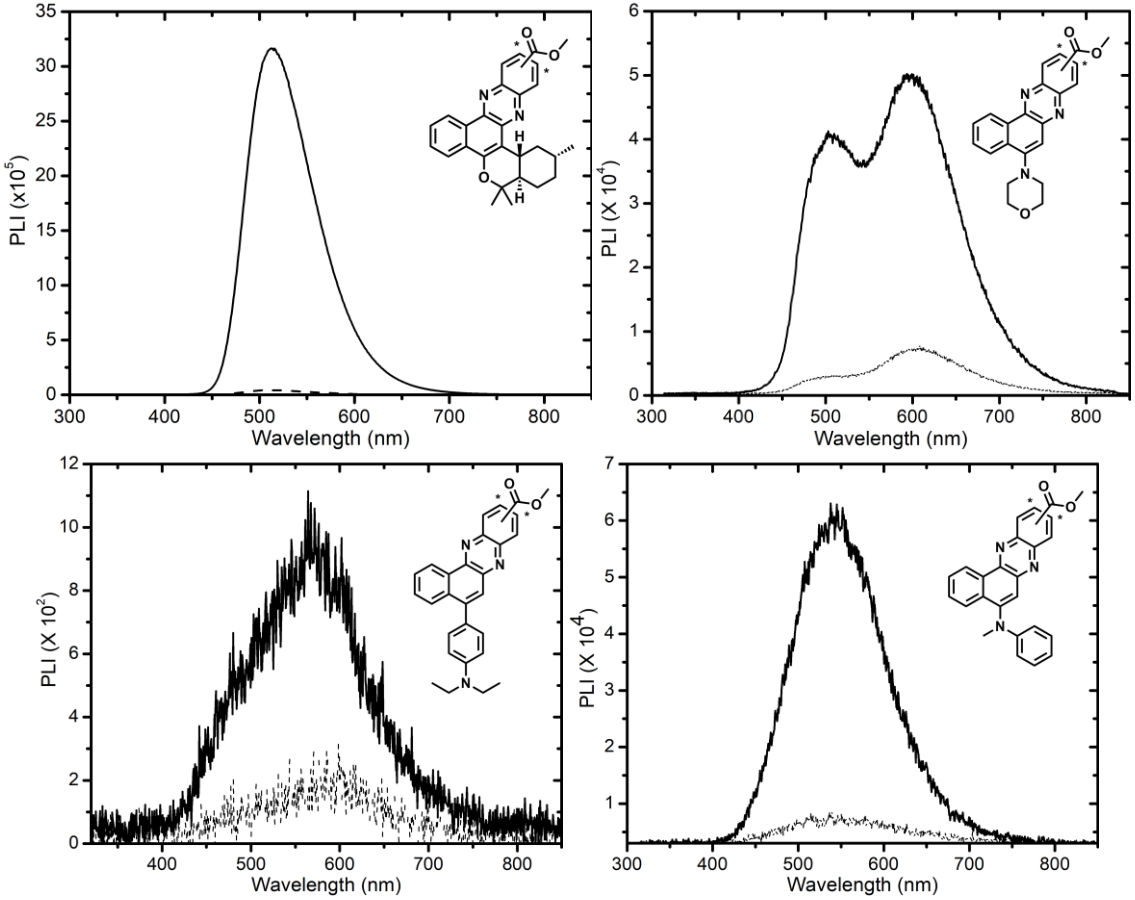
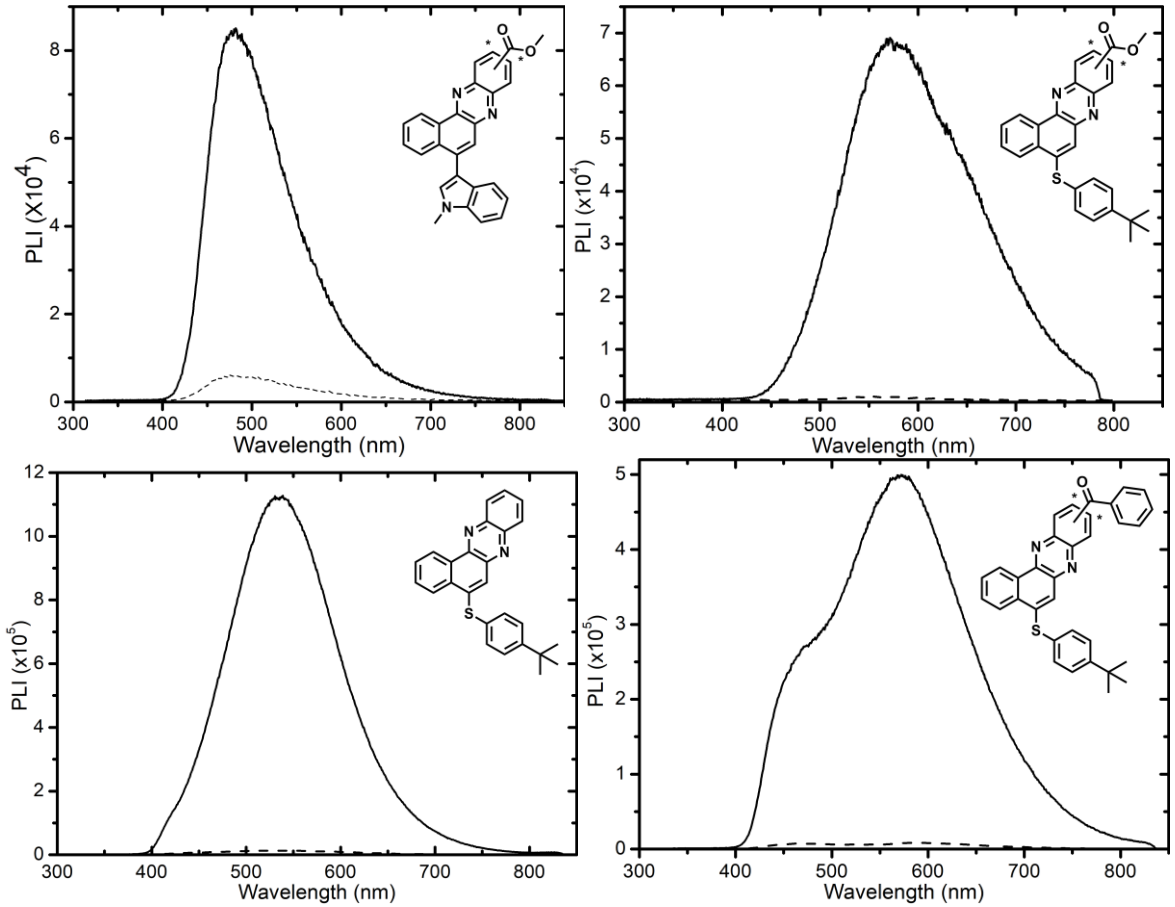
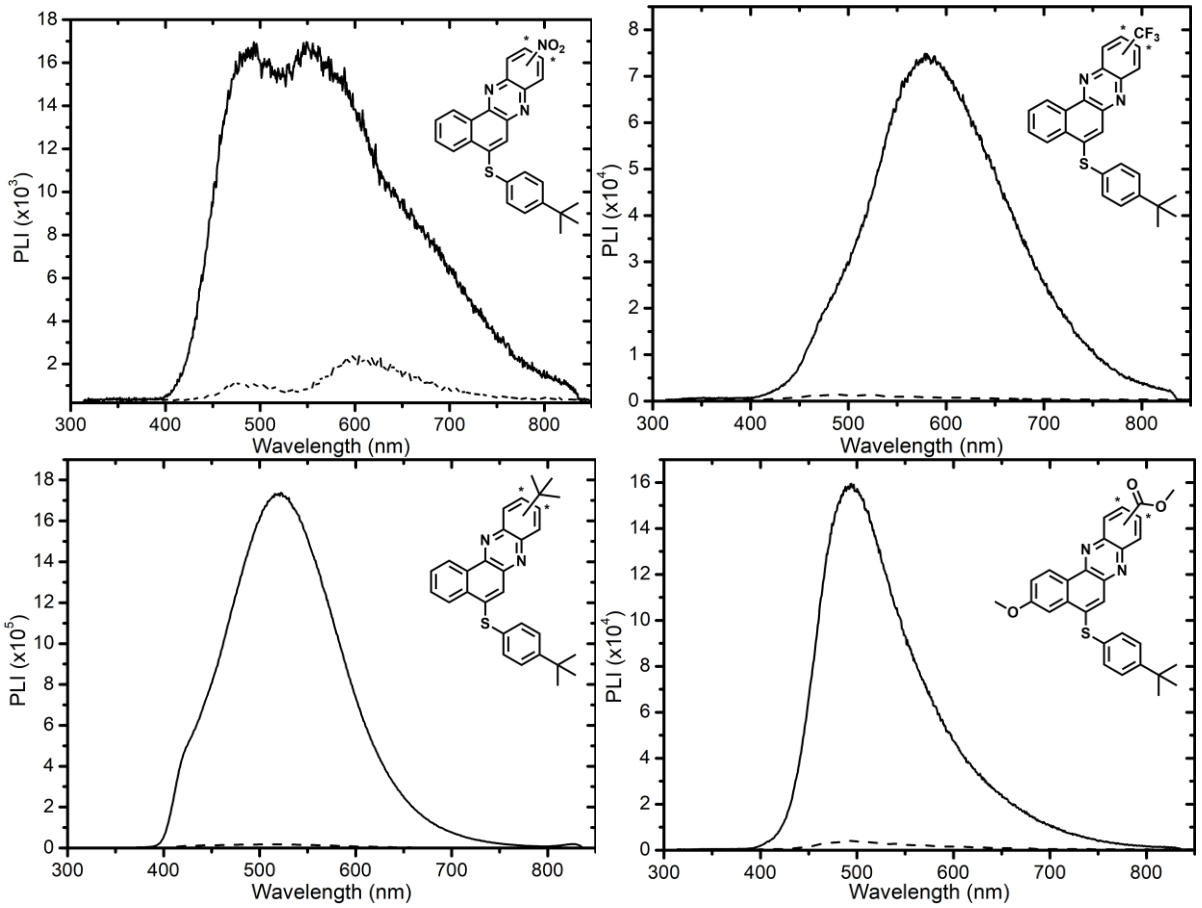


Figure B.4. Triplet energy scale of benzophenazine derivatives arising from experimental phosphorescence spectra.


PLI (x10^5)
Wavelength (nm)
PLI (X 10^4)
Wavelength (nm)
PLI (X 10^2)
Wavelength (nm)
PLI (X 10^4)
Wavelength (nm)


PLI (X10^4)
Wavelength (nm)
PLI (x10^4)
Wavelength (nm)
PLI (x10^5)
Wavelength (nm)
PLI (x10^5)
Wavelength (nm)


PLI (x10^3)
Wavelength (nm)
NO2
PLI (x10^4)
Wavelength (nm)
CF3
PLI (x10^5)
Wavelength (nm)
PLI (x10^4)
Wavelength (nm)
O
O
O
N
N
S

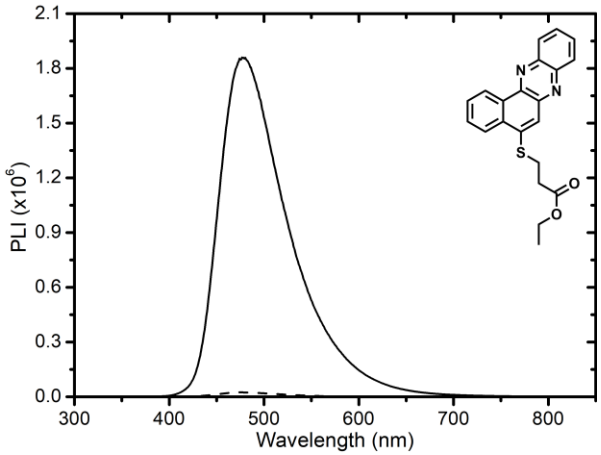
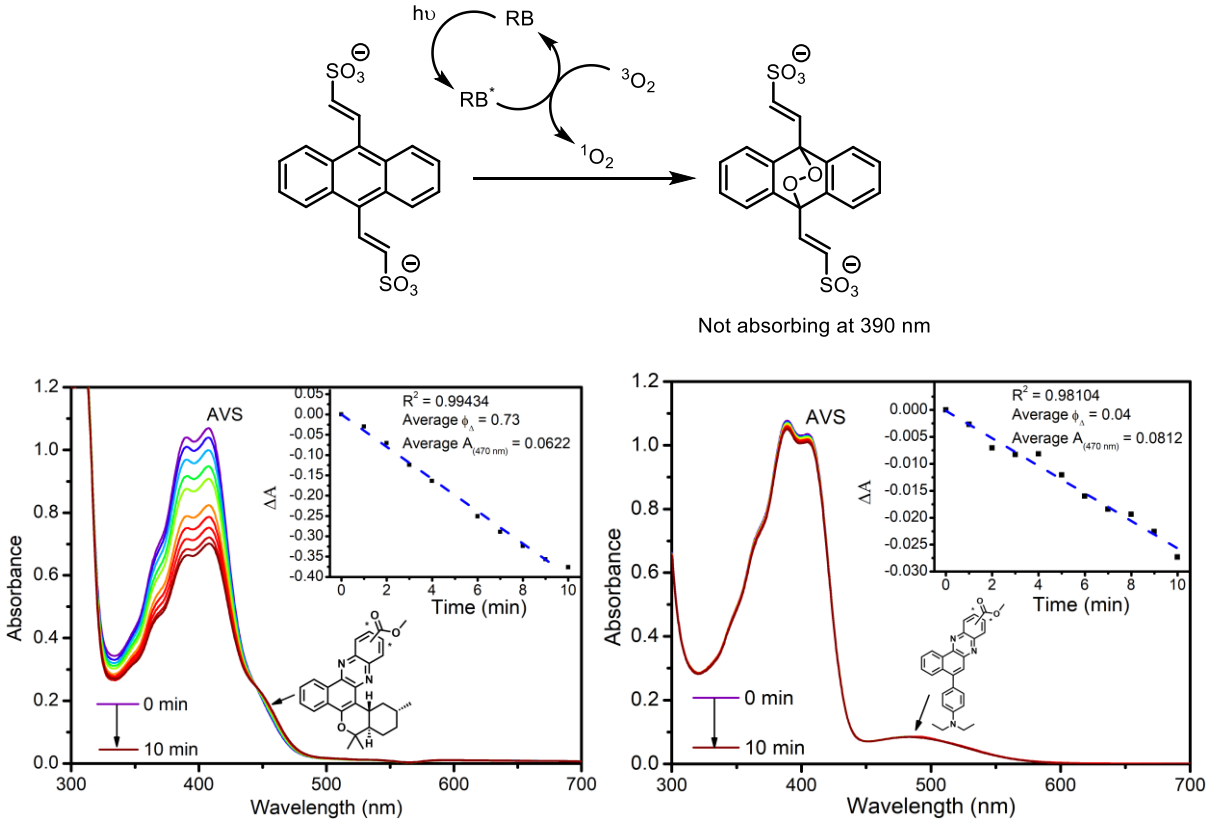
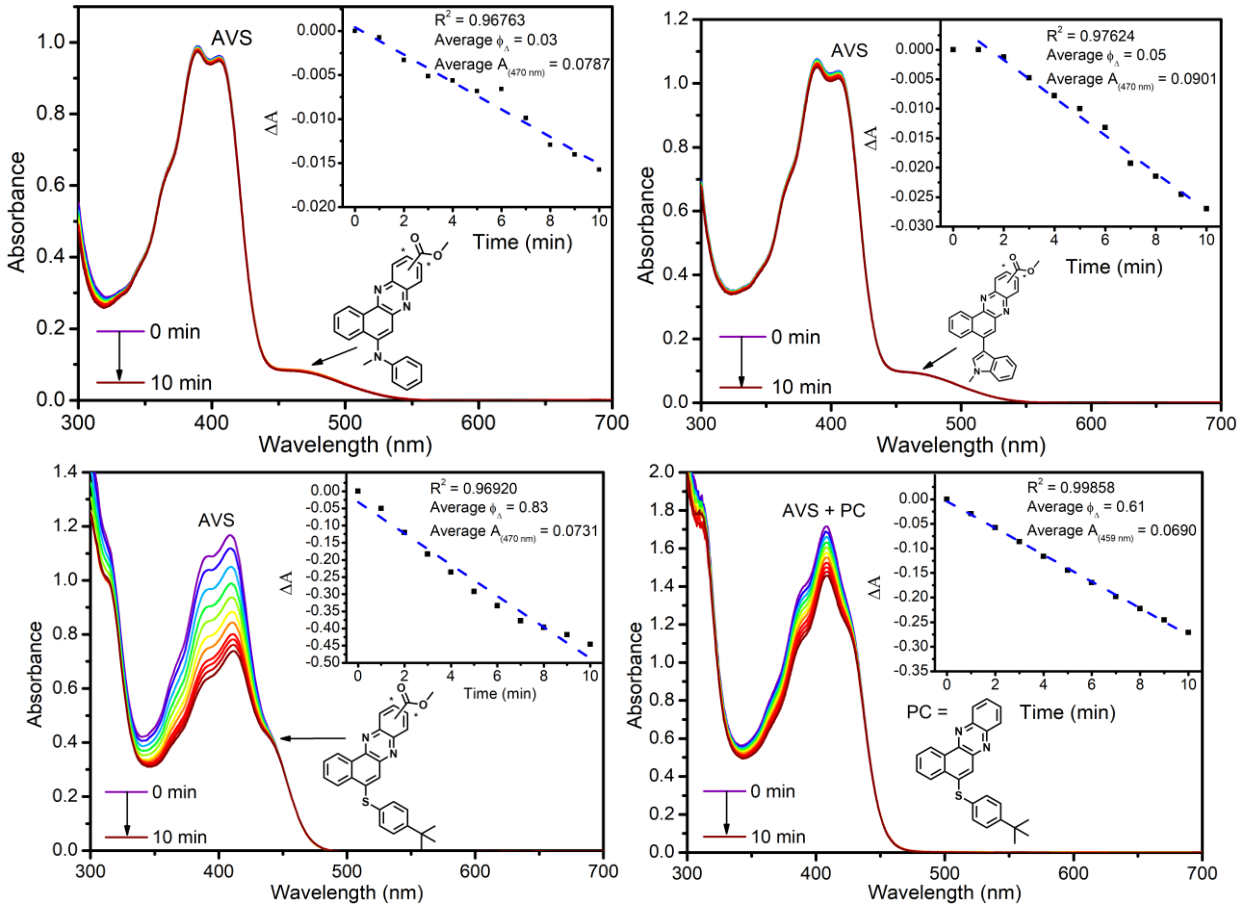
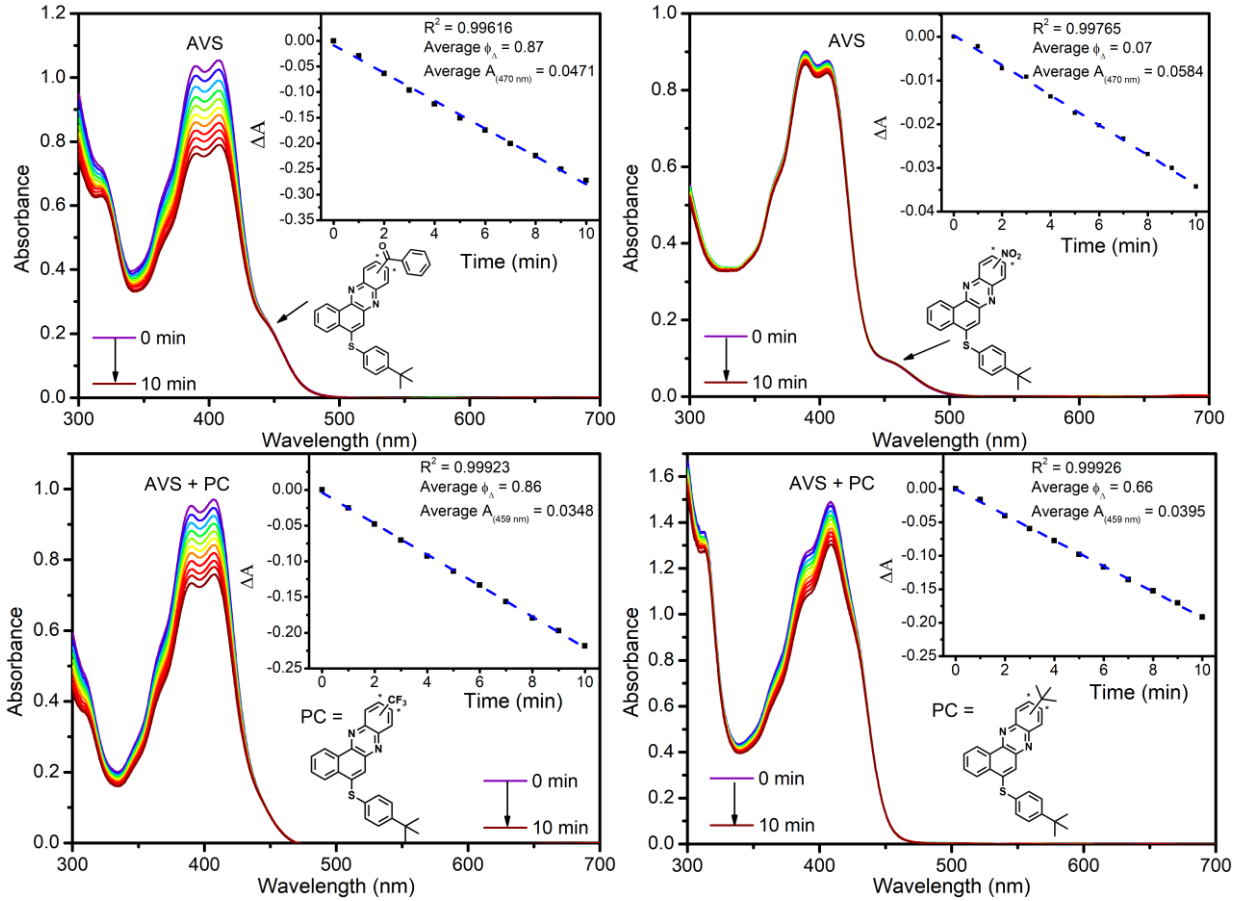


Figure B.5. Phosphorescence spectra of benzophenazine derivatives under argon (solid) or under O_2 (dashed).


hυ
RB
RB*
$^3O_2$
$^1O_2$
SO_3^-
Not absorbing at 390 nm
AVS
0 min
10 min
Absorbance
Wavelength (nm)
ΔA
Time (min)
R^2 = 0.99434
Average ϕ_Δ = 0.73
Average $A_{(470\ nm)}$ = 0.0622
R^2 = 0.98104
Average ϕ_Δ = 0.04
Average $A_{(470\ nm)}$ = 0.0812


AVS
Absorbance
Wavelength (nm)
0 min
10 min
ΔA
Time (min)
R² = 0.96763
Average φΔ = 0.03
Average A(470 nm) = 0.0787
AVS
Absorbance
Wavelength (nm)
0 min
10 min
ΔA
Time (min)
R² = 0.97624
Average φΔ = 0.05
Average A(470 nm) = 0.0901
AVS
Absorbance
Wavelength (nm)
0 min
10 min
ΔA
Time (min)
R² = 0.96920
Average φΔ = 0.83
Average A(470 nm) = 0.0731
AVS + PC
Absorbance
Wavelength (nm)
0 min
10 min
ΔA
Time (min)
PC =
R² = 0.99858
Average φΔ = 0.61
Average A(459 nm) = 0.0690


AVS
R² = 0.99616
Average ϕΔ = 0.87
Average A(470 nm) = 0.0471
ΔA
Time (min)
0 min
10 min
Absorbance
Wavelength (nm)
AVS
R² = 0.99765
Average ϕΔ = 0.07
Average A(470 nm) = 0.0584
ΔA
Time (min)
0 min
10 min
Absorbance
Wavelength (nm)
AVS + PC
R² = 0.99923
Average ϕΔ = 0.86
Average A(459 nm) = 0.0348
ΔA
Time (min)
PC =
0 min
10 min
Absorbance
Wavelength (nm)
AVS + PC
R² = 0.99926
Average ϕΔ = 0.66
Average A(459 nm) = 0.0395
ΔA
Time (min)
PC =
0 min
10 min
Absorbance
Wavelength (nm)

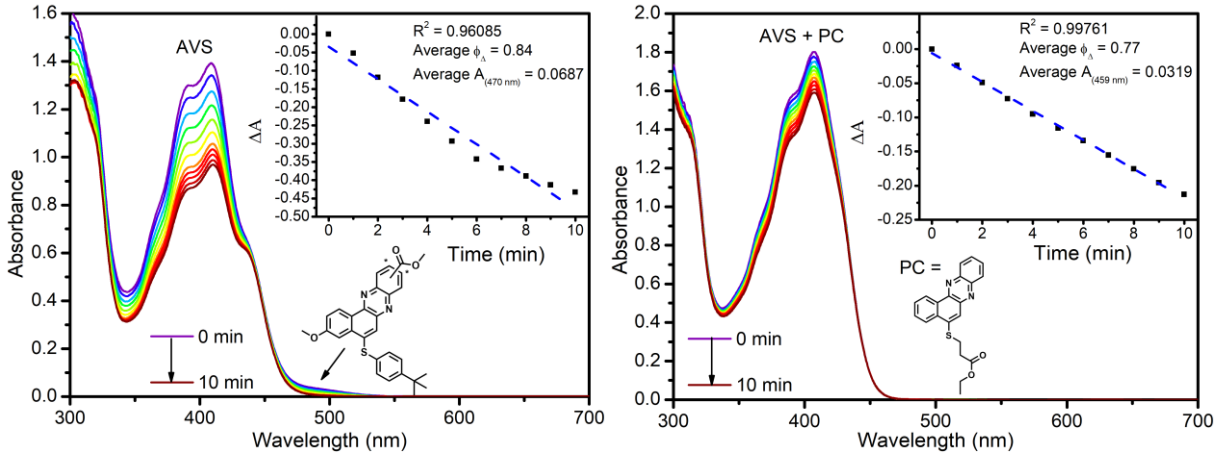


Figure B.6. Degradation of anthracene-9,10-divinylsulfonate (AVS) (390 nm) by benzophenazine derivatives followed by UV-vis analysis. The inset corresponds to the decrease in absorbance *vs* time with a linear fit in blue.

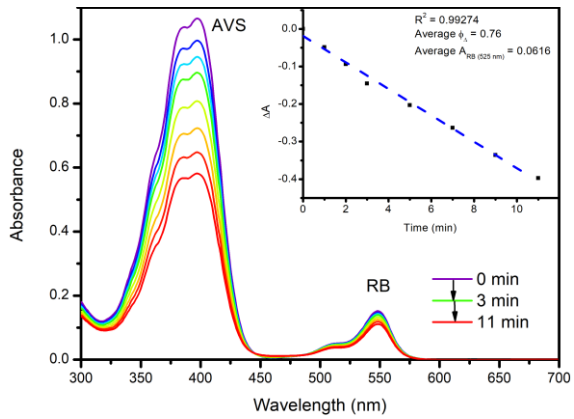


Figure B.7. Degradation of AVS (390 nm) by Rose Bengal (RB) followed by UV-vis analysis. The inset corresponds to the decrease in absorbance vs time with a linear fit in blue.

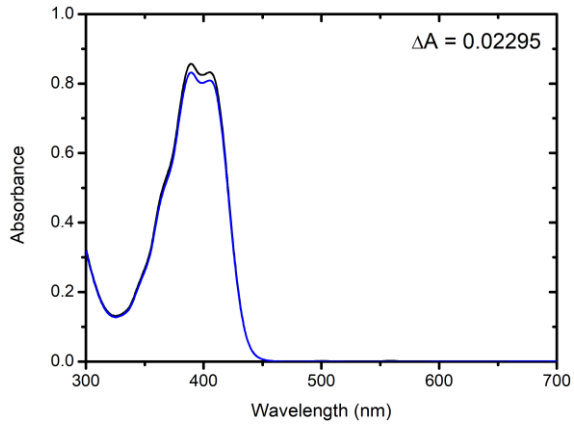


Figure B.8. Absorbance of AVS before (black) and after 10 min of irradiation at 470 nm (blue).

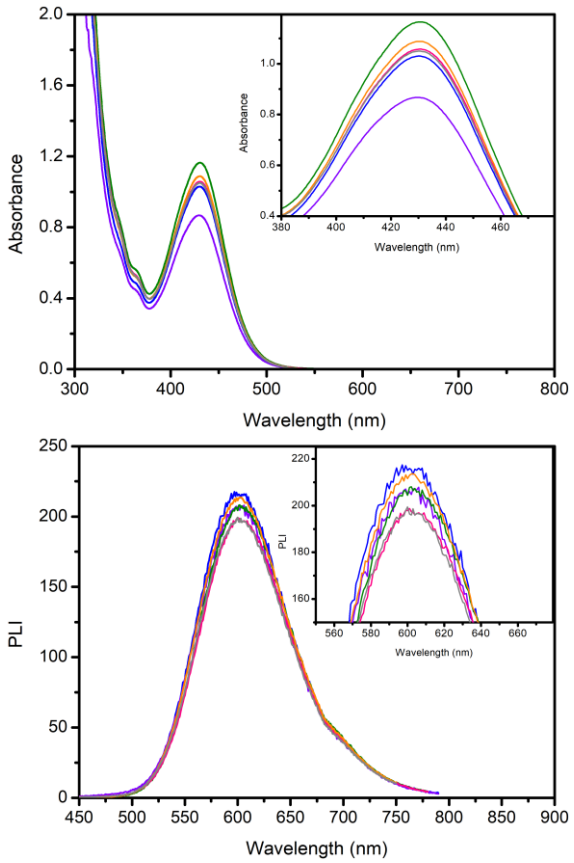


Figure B.9. Absorption (left) and steady-state photoluminescence (right) spectra of morpholine **10b** before (blue) and after (purple) 2 hours of irradiation, before (green) and after (pink) 2 hours of irradiation in presence of oxygen and before (orange) and after (grey) 2 hours of irradiation in presence of oxygen and citronellol.

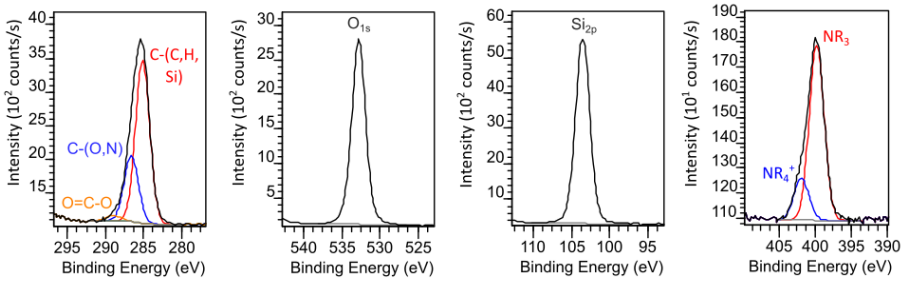


Figure B.10. C_{1s}, O_{1s}, Si_{2p} and N_{1s} XPS spectra of amino-functionalized NS.

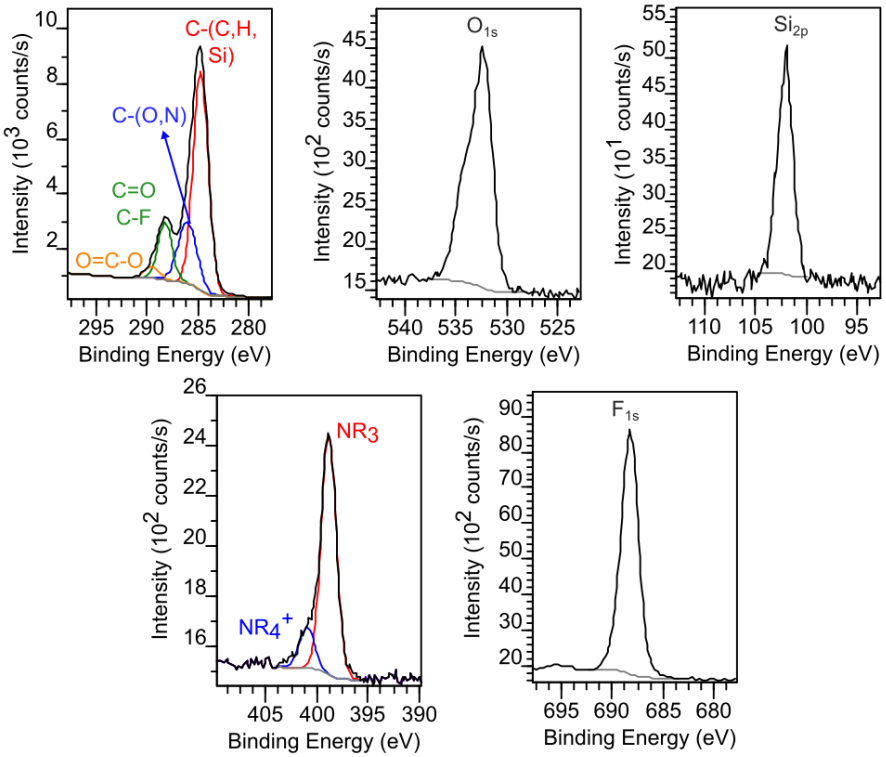


Figure B.11. C_{1s}, O_{1s}, Si_{2p}, N_{1s} and F_{1s} XPS spectra of organic activated ester **14** (no silica).

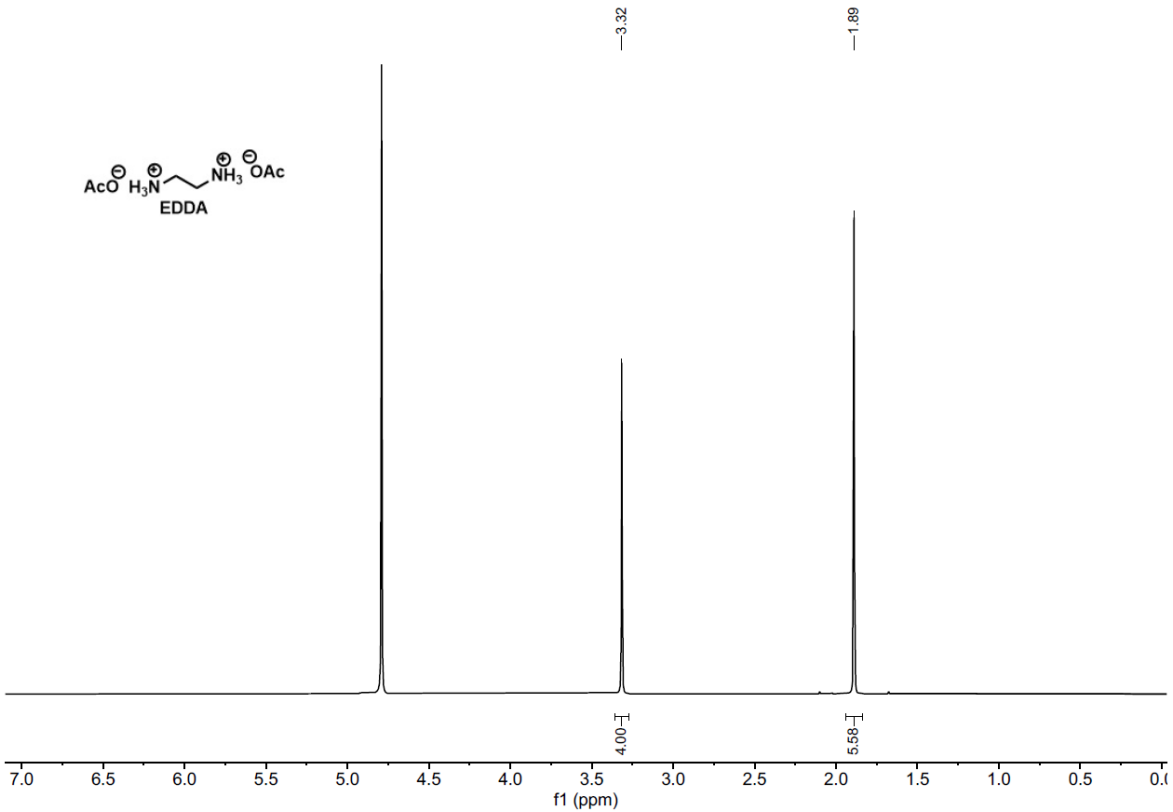


Figure B.12. ^{1}H NMR of EDDA recorded in D_2O at 300 MHz and 298 K.

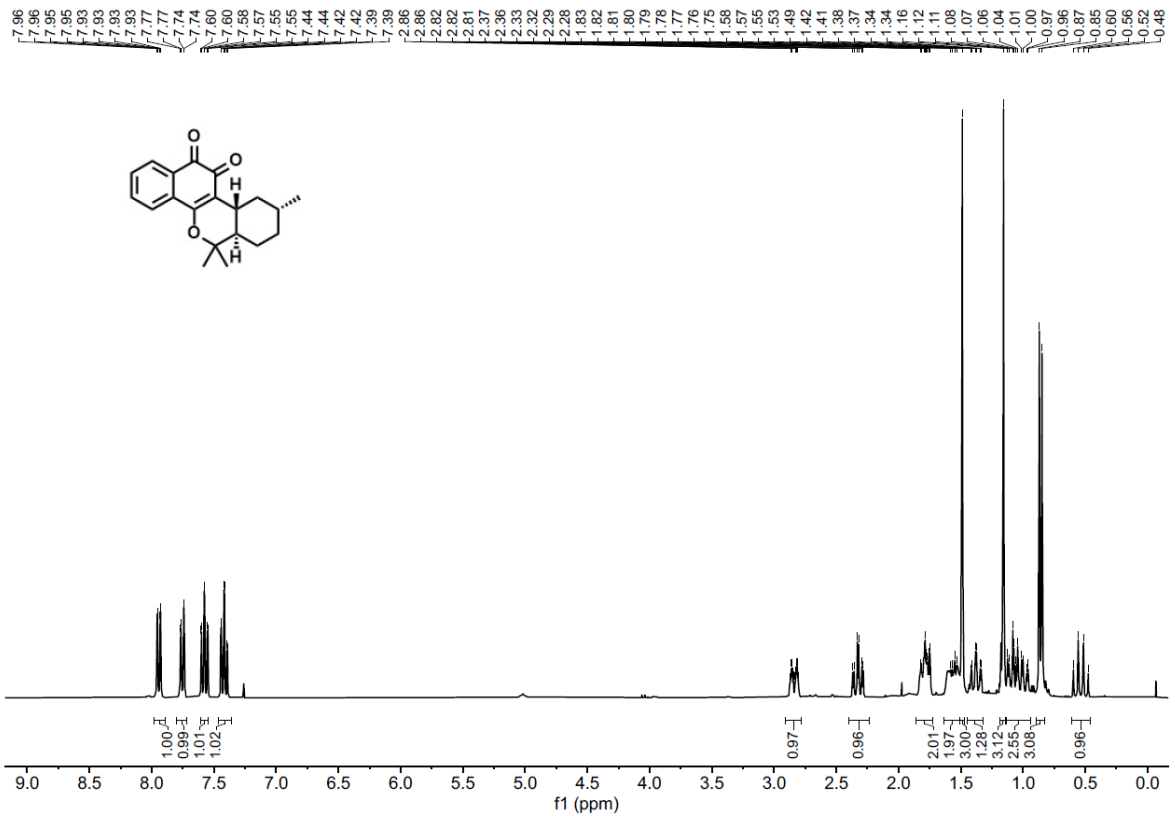


Figure B.13. ^{1}H NMR of compound **9a** recorded in $CDCl_3$ at 300 MHz and 298 K.

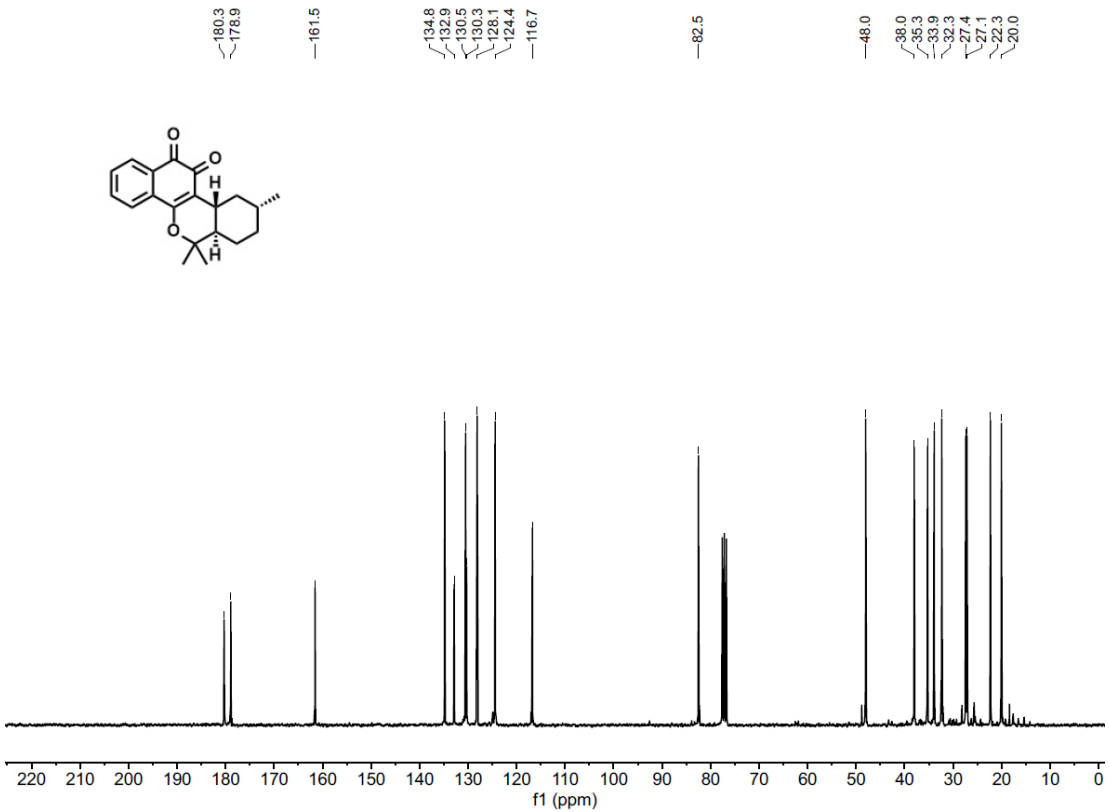


Figure B.14. ^{13}C NMR of compound **9a** recorded in $CDCl_3$ at 75 MHz and 298 K.

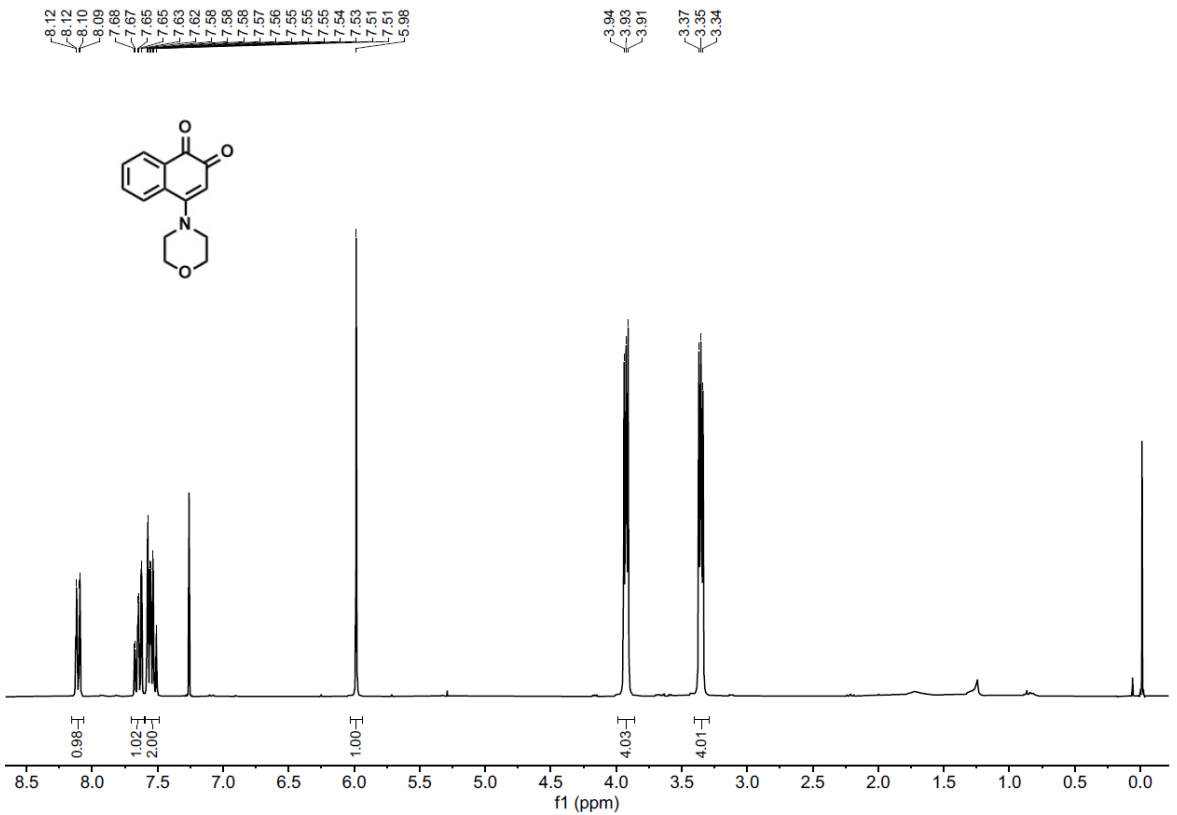


Figure B.15. ^{1}H NMR of compound **9b** recorded in $CDCl_3$ at 300 MHz and 298 K.

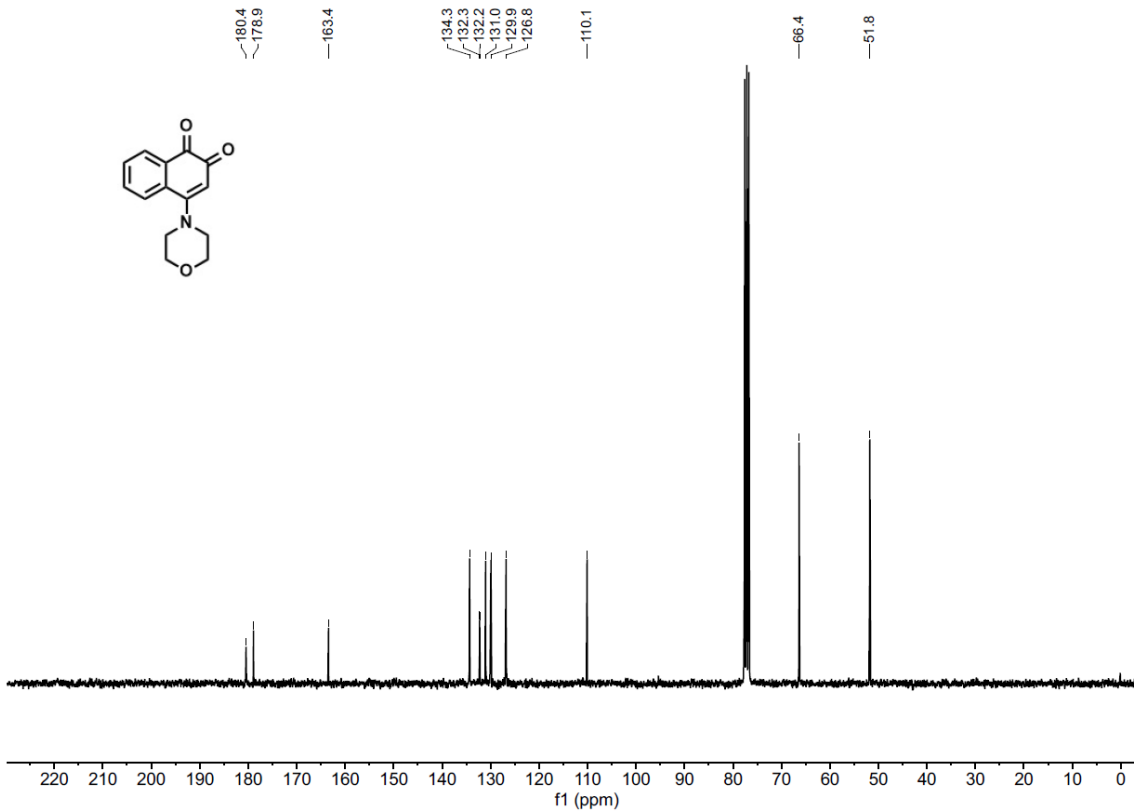


Figure B.16. ^{13}C NMR of compound **9b** recorded in $CDCl_3$ at 75 MHz and 298 K.

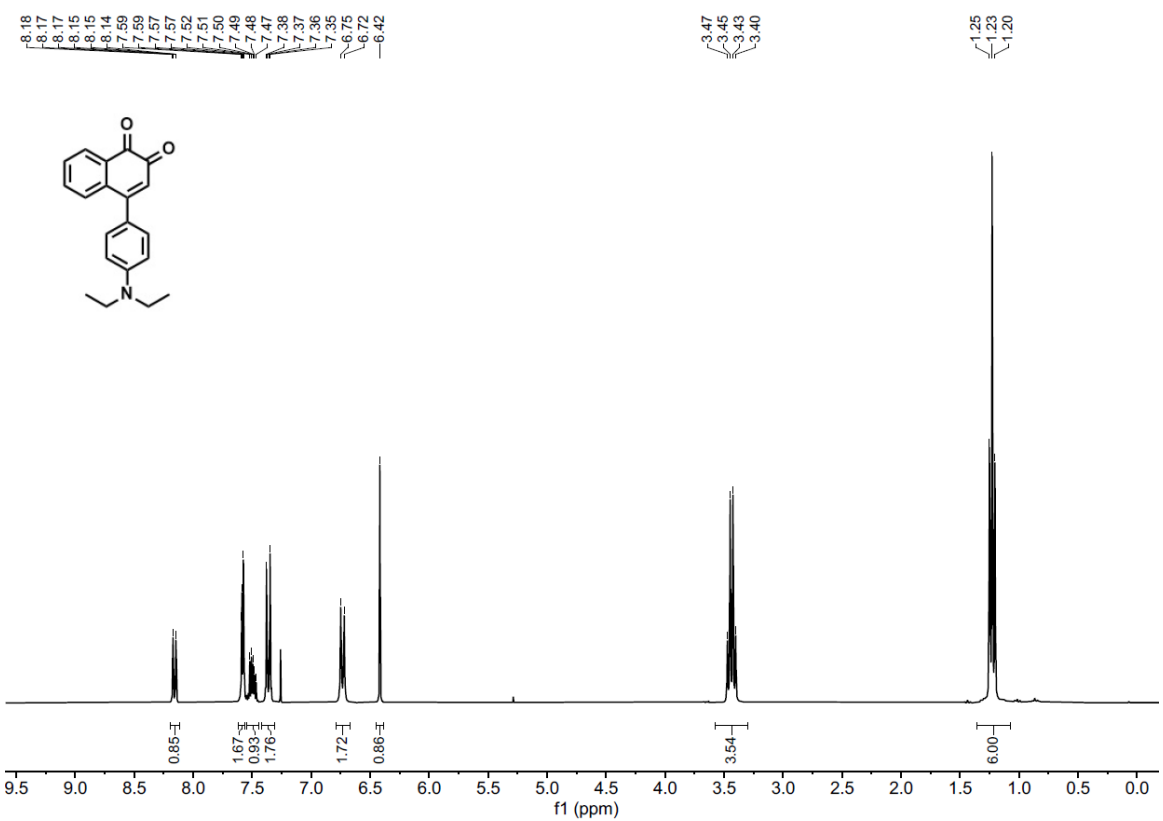


Figure B.17. ^{1}H NMR of compound **9c** recorded in $CDCl_3$ at 300 MHz and 298 K.

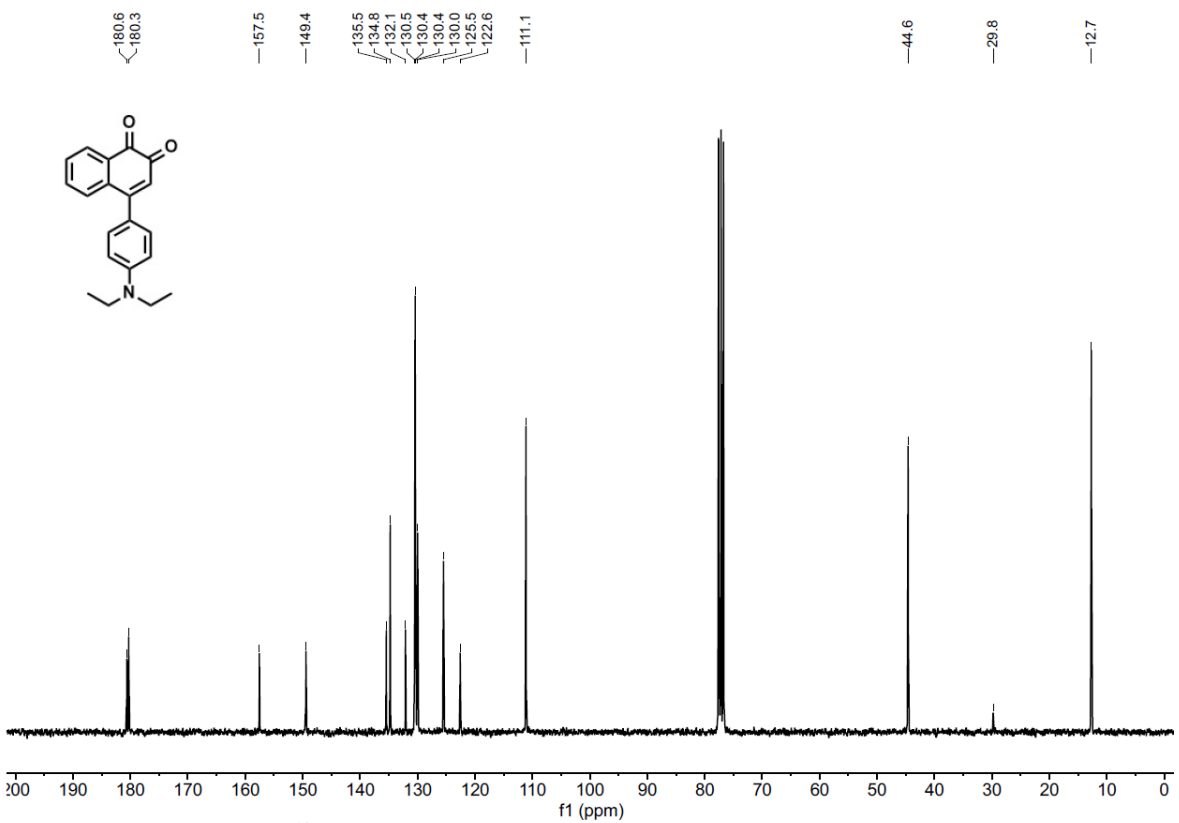


Figure B.18. ^{13}C NMR of compound **9c** recorded in $CDCl_3$ at 75 MHz and 298 K.

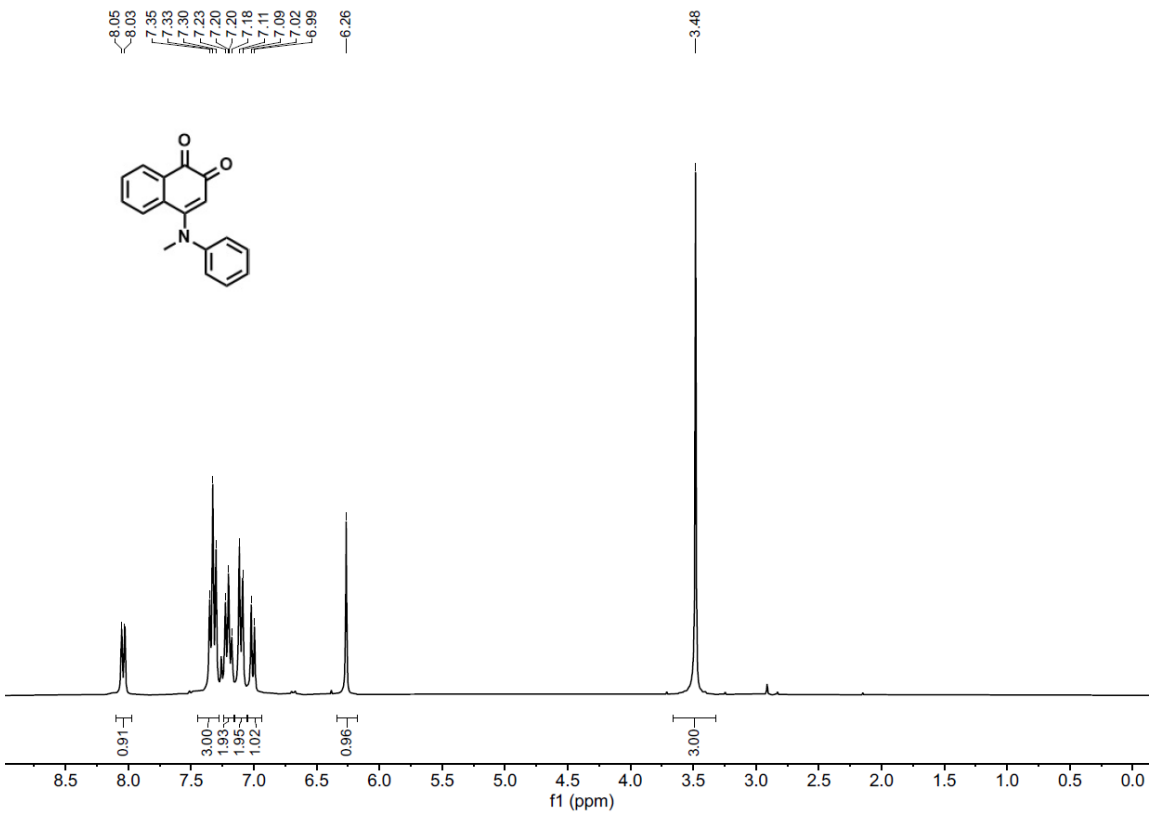


Figure B.19. ^{1}H NMR of compound **9d** recorded in $CDCl_3$ at 300 MHz and 298 K.

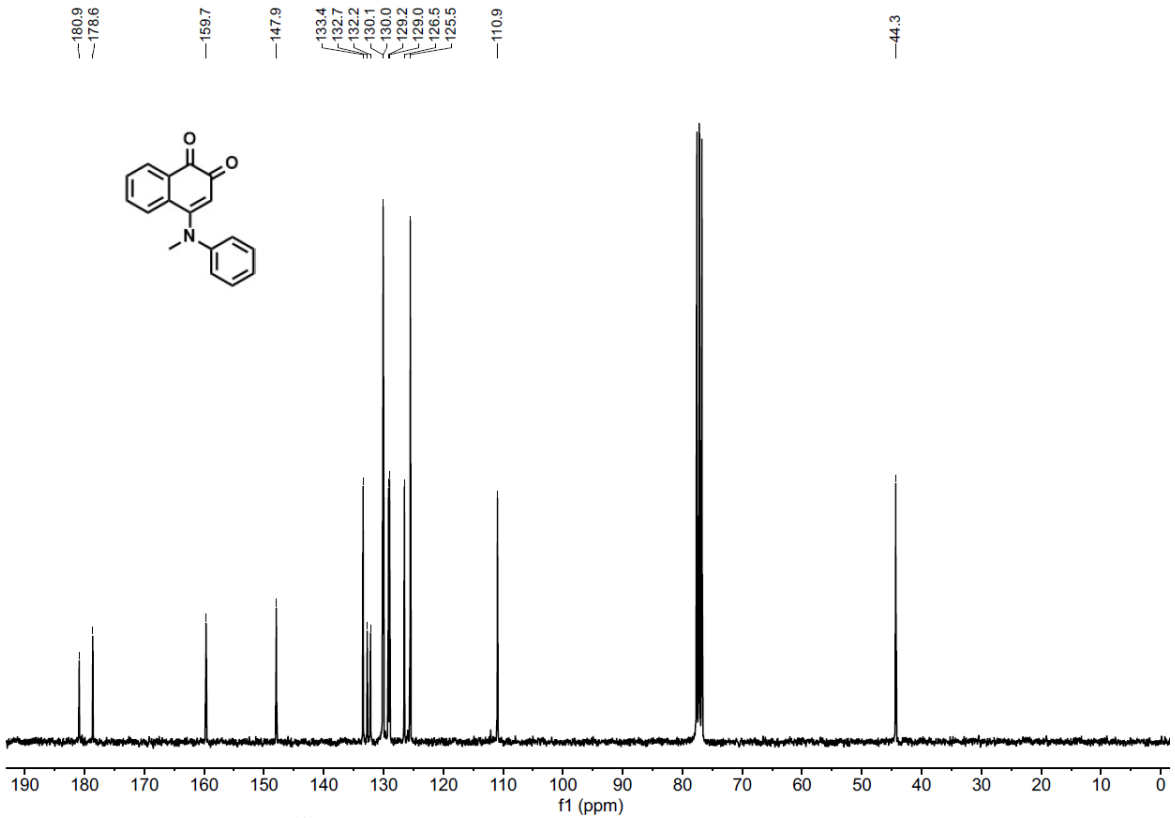


Figure B.20. ^{13}C NMR of compound **9d** recorded in $CDCl_3$ at 75 MHz and 298 K.

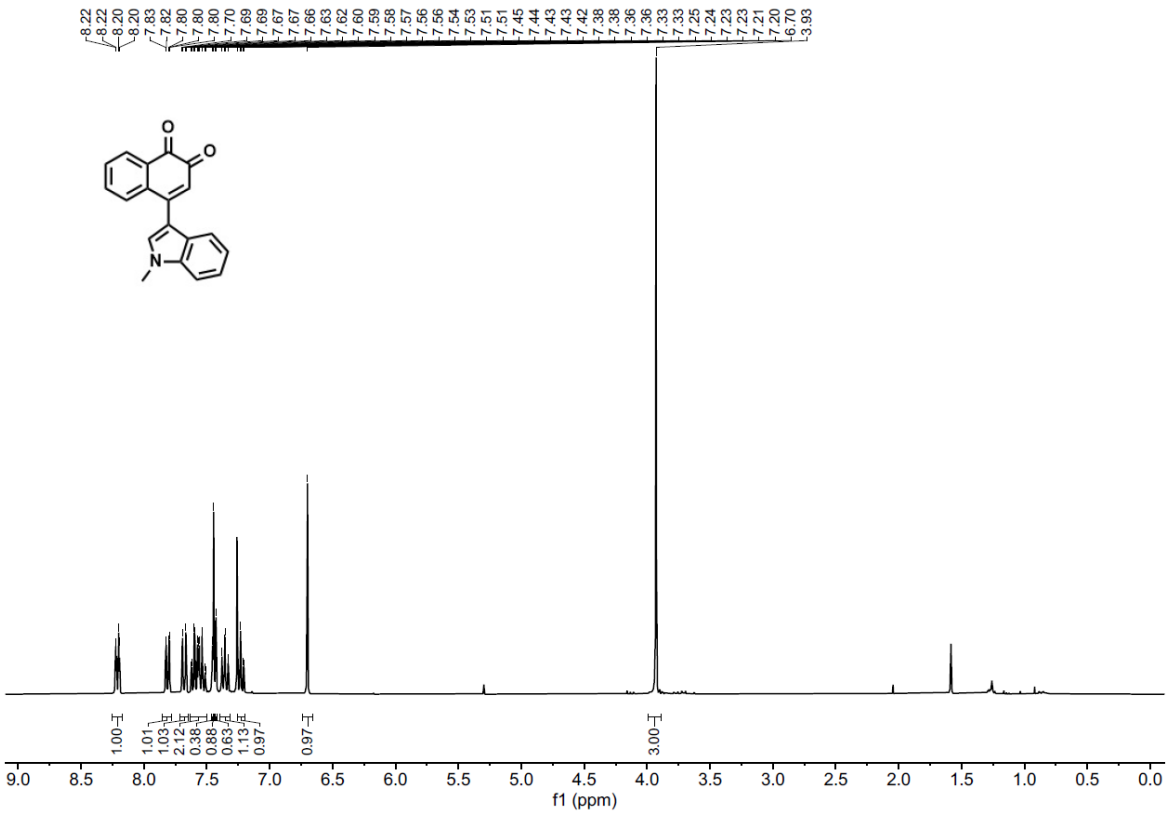


Figure B.21. ^{1}H NMR of compound **9e** recorded in $CDCl_3$ at 300 MHz and 298 K.

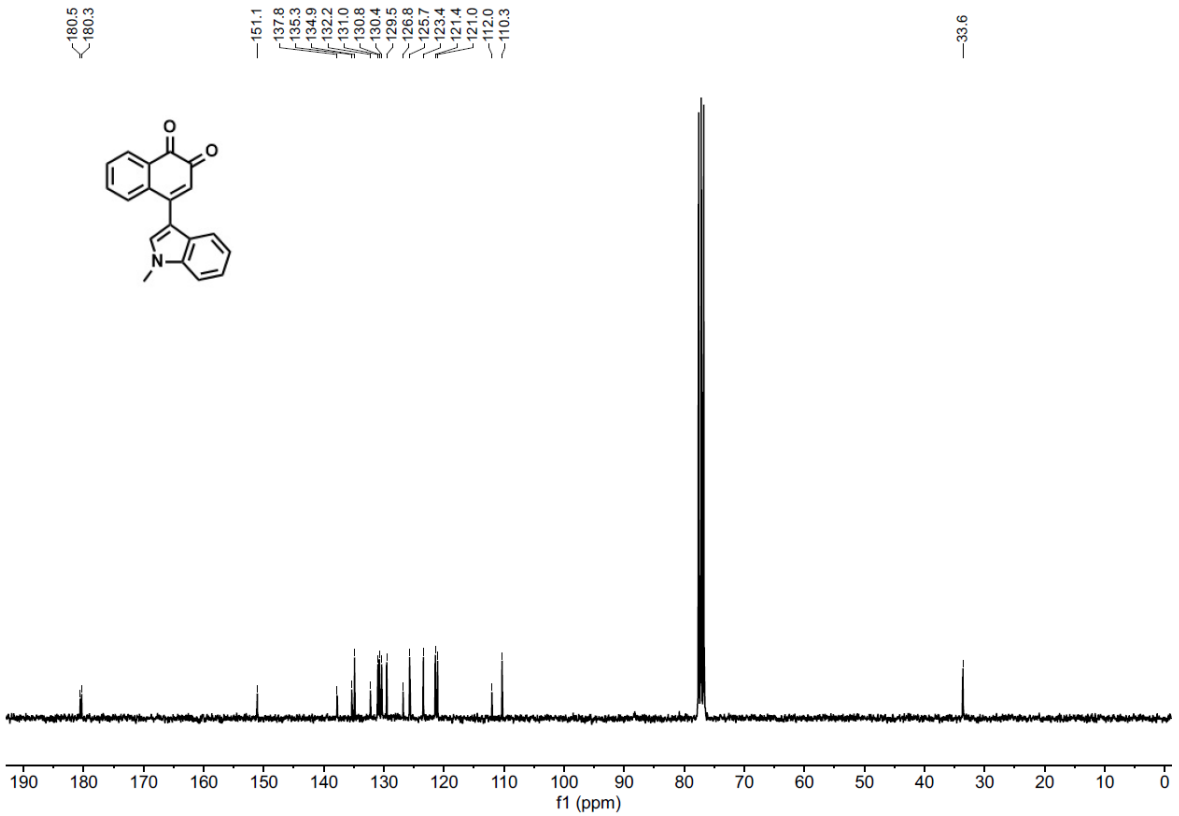


Figure B.22. ^{13}C NMR of compound **9e** recorded in $CDCl_3$ at 75 MHz and 298 K.

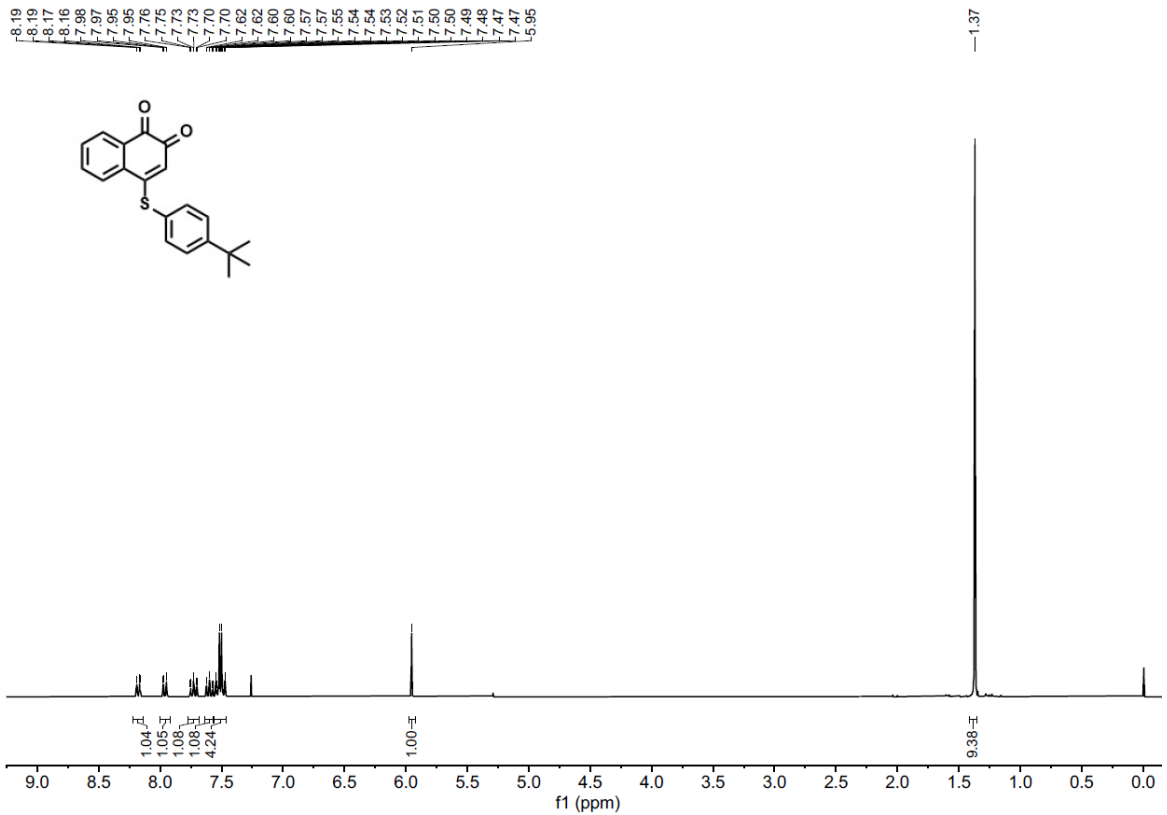


Figure B.23. ^{1}H NMR of compound **9f** recorded in $CDCl_3$ at 300 MHz and 298 K.

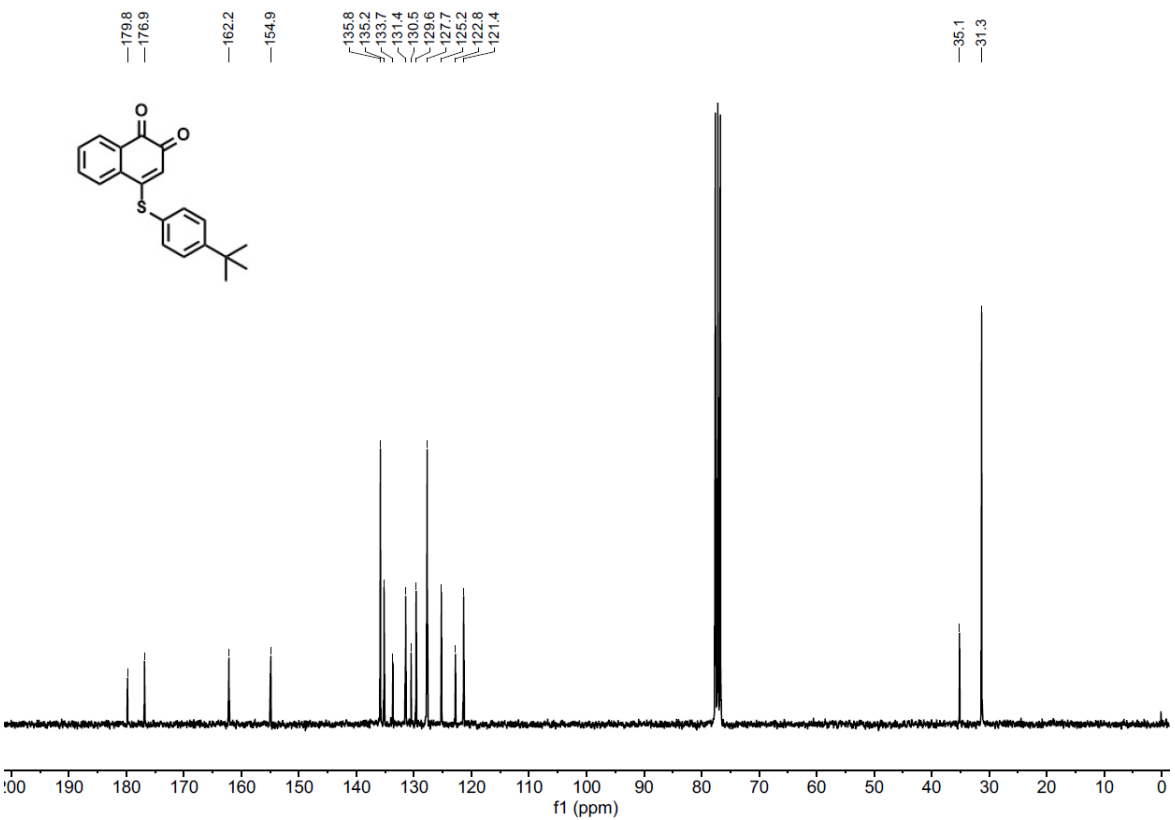


Figure B.24. ^{13}C NMR of compound **9f** recorded in $CDCl_3$ at 75 MHz and 298 K.

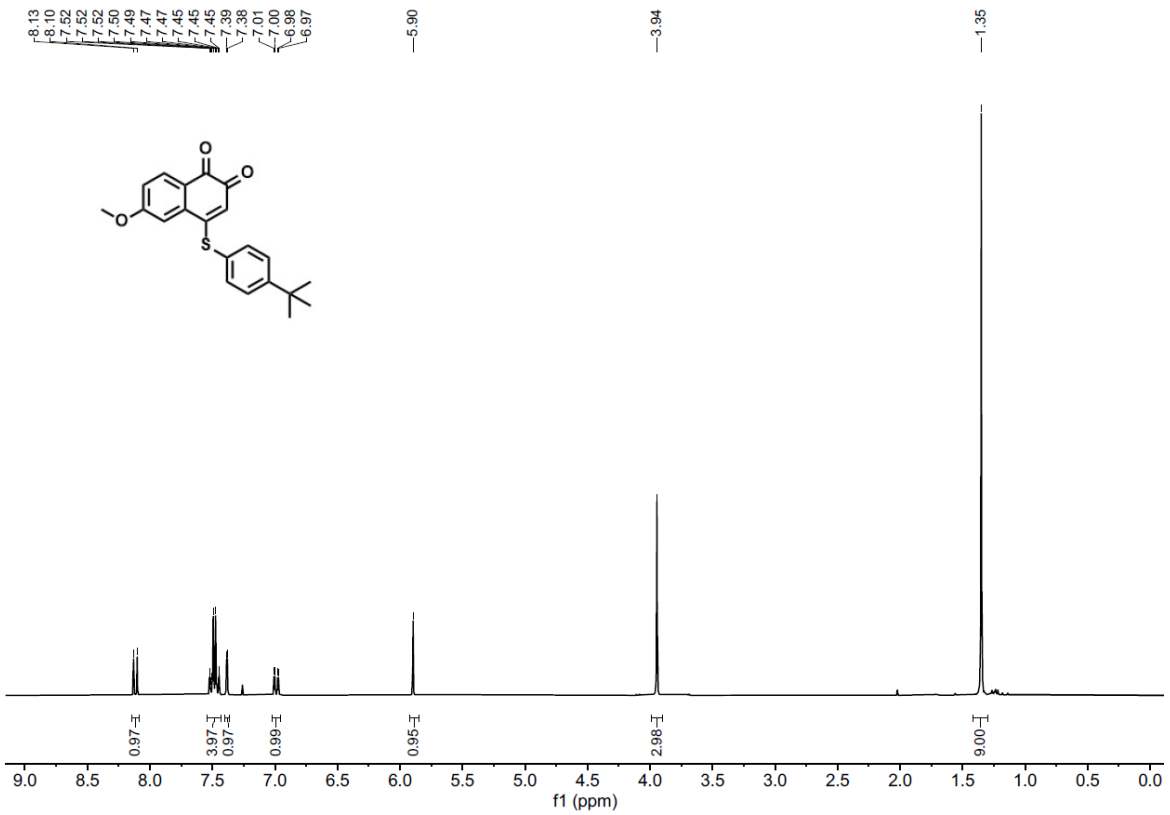


Figure B.25. ^{1}H NMR of compound **9g** recorded in $CDCl_3$ at 300 MHz and 298 K.

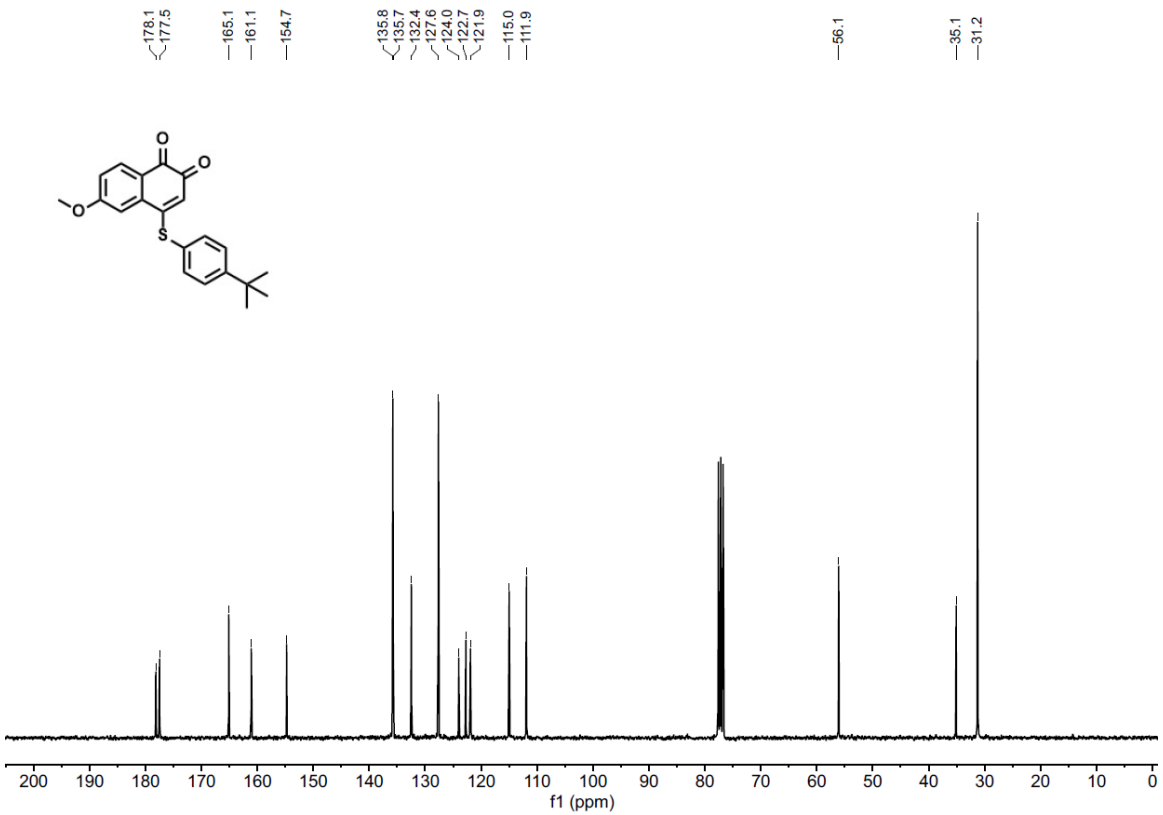


Figure B.26. ^{13}C NMR of compound **9g** recorded in $CDCl_3$ at 75 MHz and 298 K.

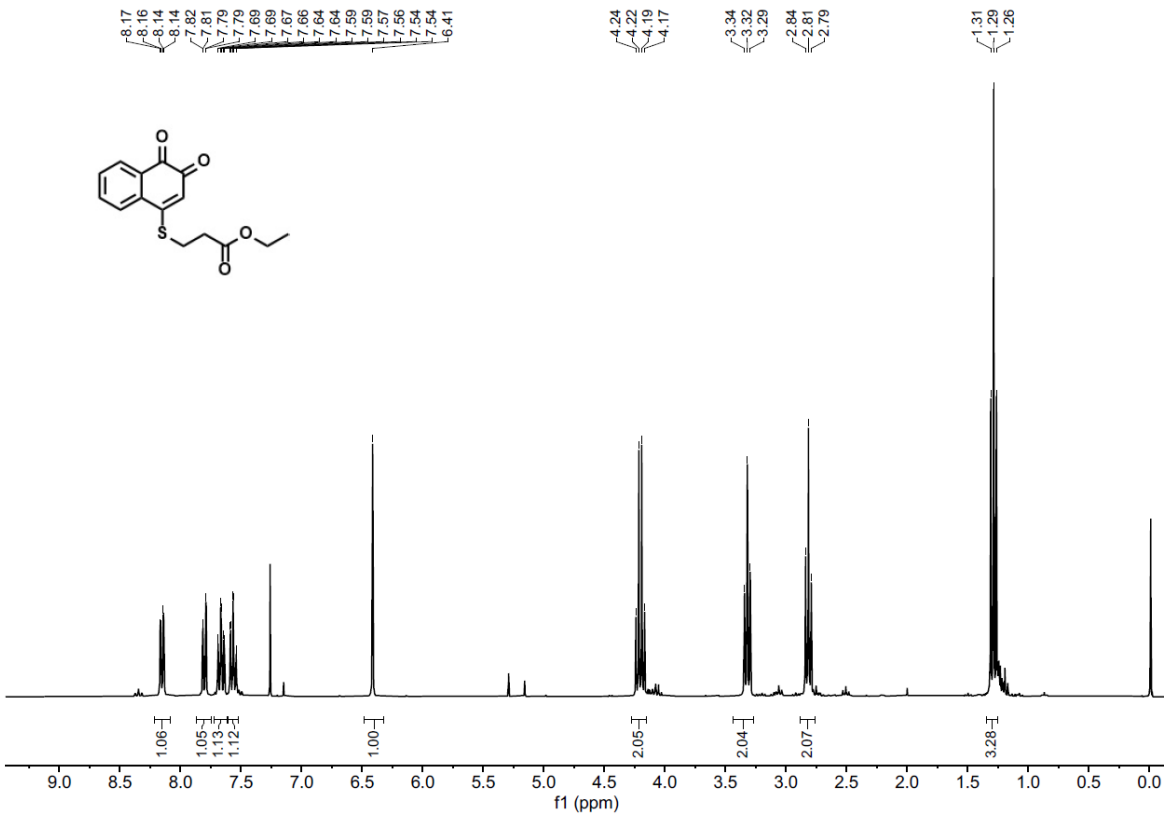


Figure B.27. ^{1}H NMR of compound **9h** recorded in $CDCl_3$ at 300 MHz and 298 K.

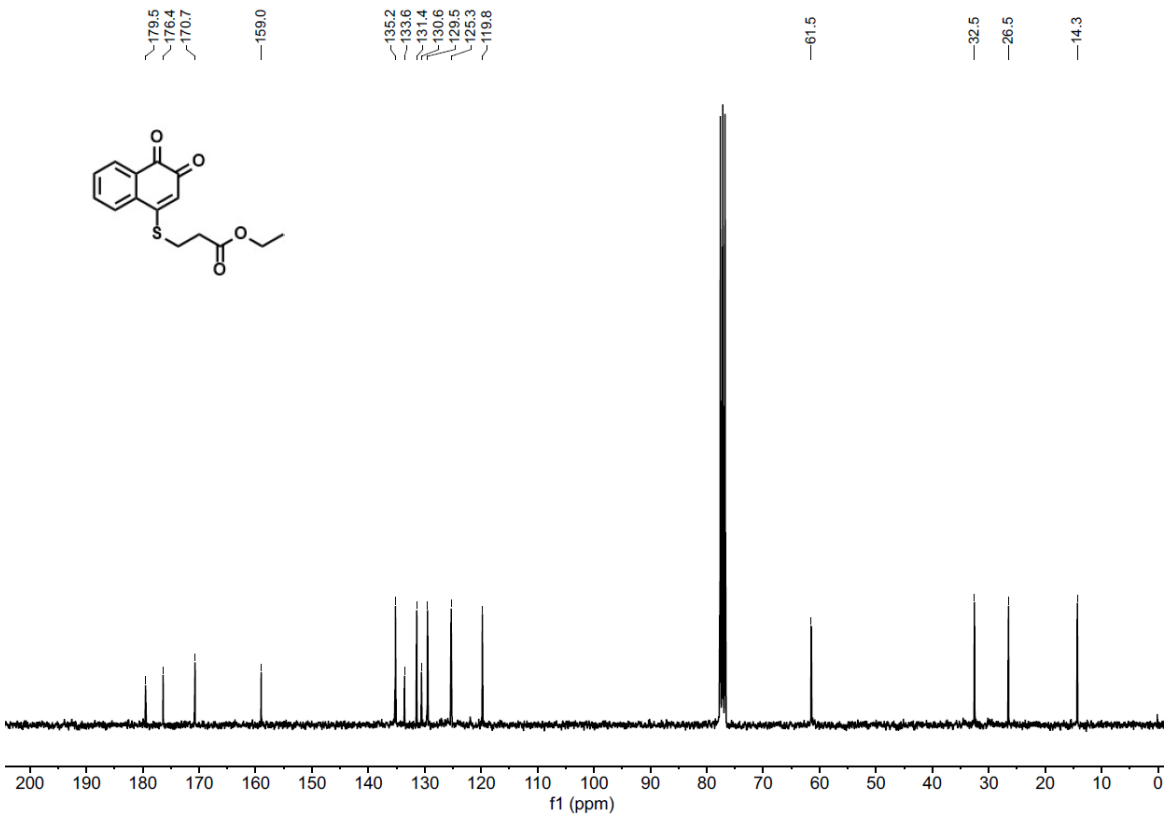


Figure B.28. ^{13}C NMR of compound **9h** recorded in $CDCl_3$ at 75 MHz and 298 K.

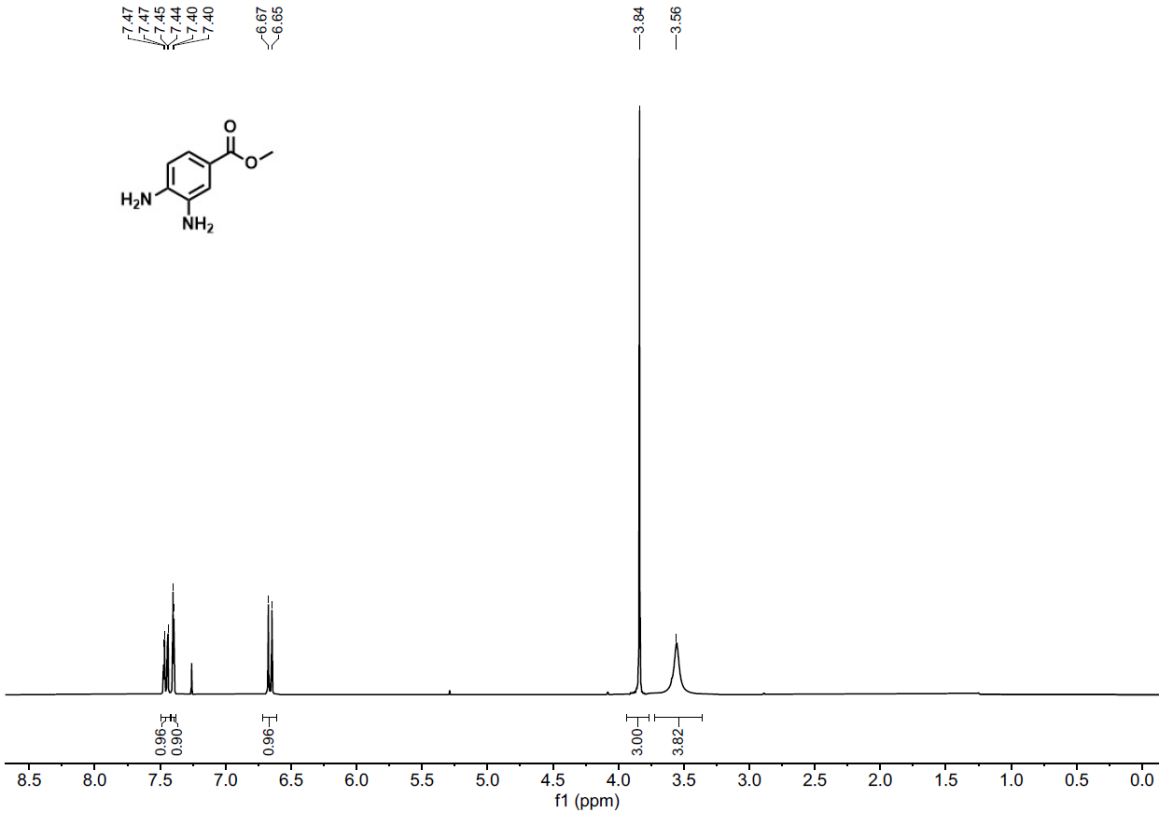


Figure B.29. ^{1}H NMR of compound **15** recorded in $CDCl_3$ at 300 MHz and 298 K.

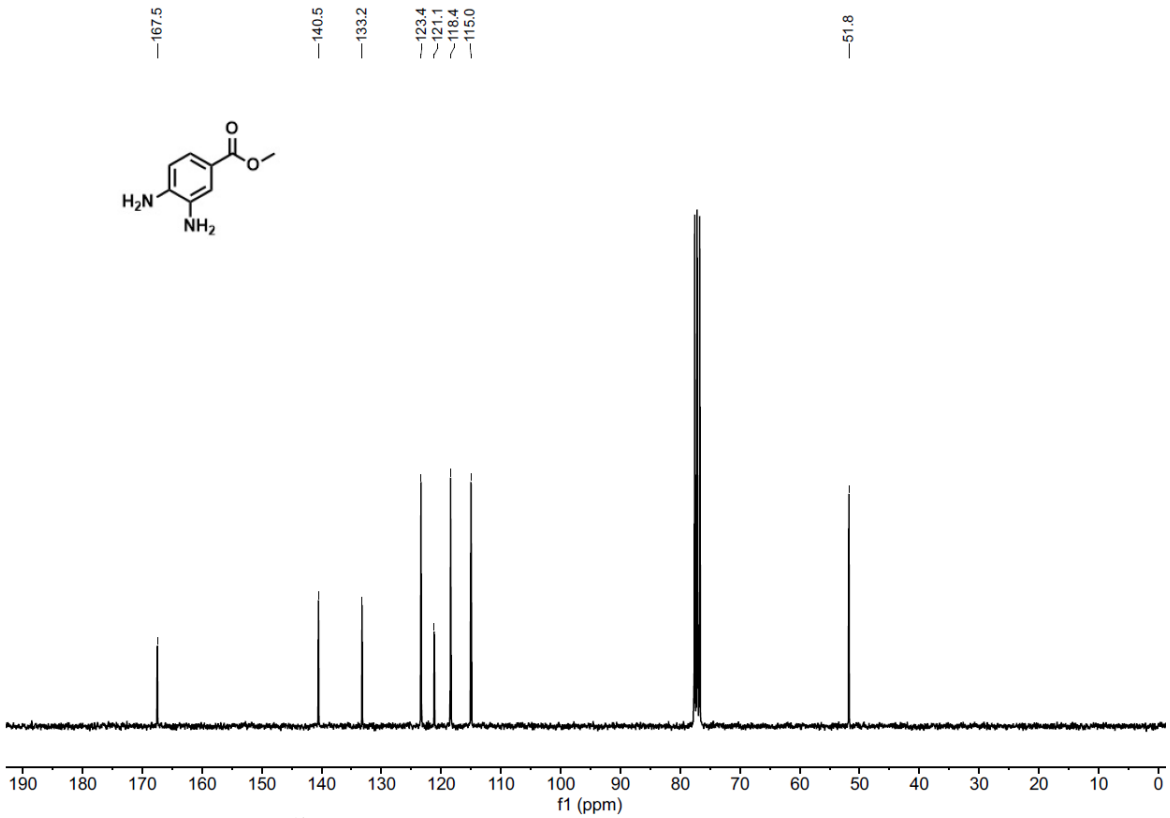


Figure B.30. ^{13}C NMR of compound **15** recorded in $CDCl_3$ at 75 MHz and 298 K.

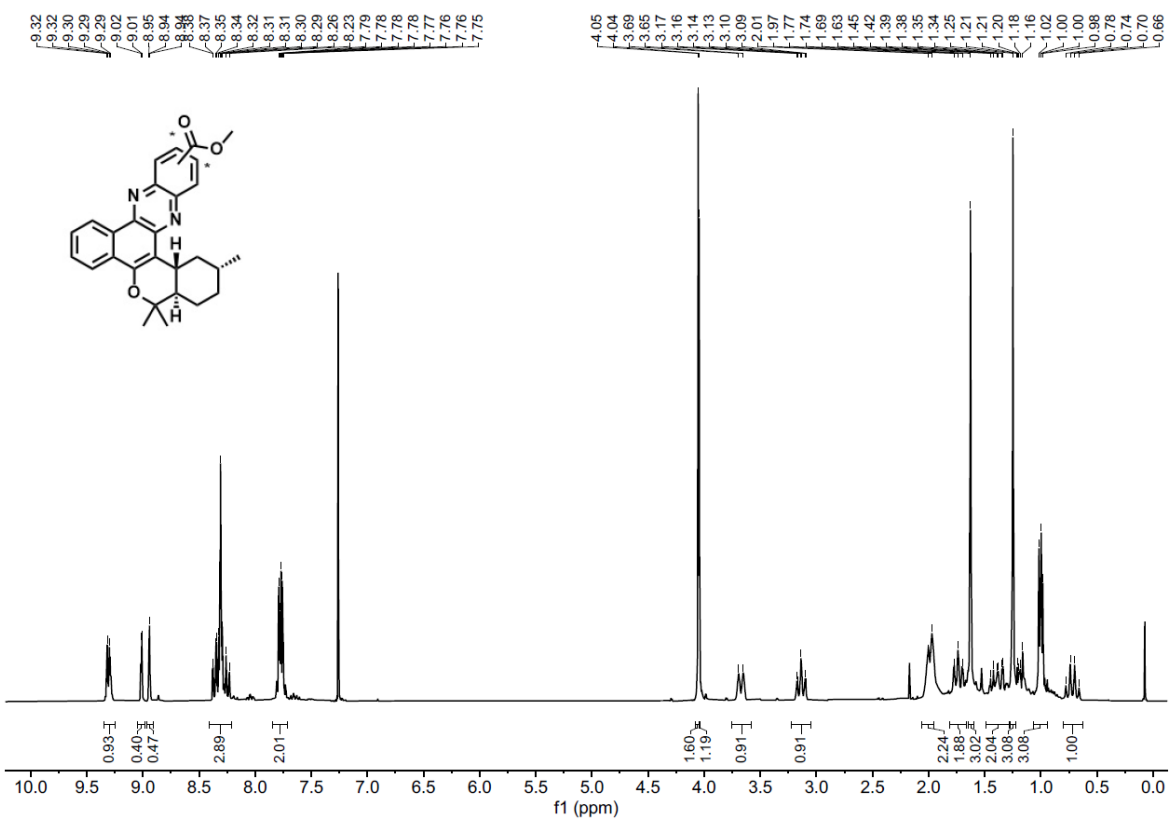


Figure B.31. ^{1}H NMR of cyclic ether **10a** recorded in $CDCl_3$ at 300 MHz and 298 K.

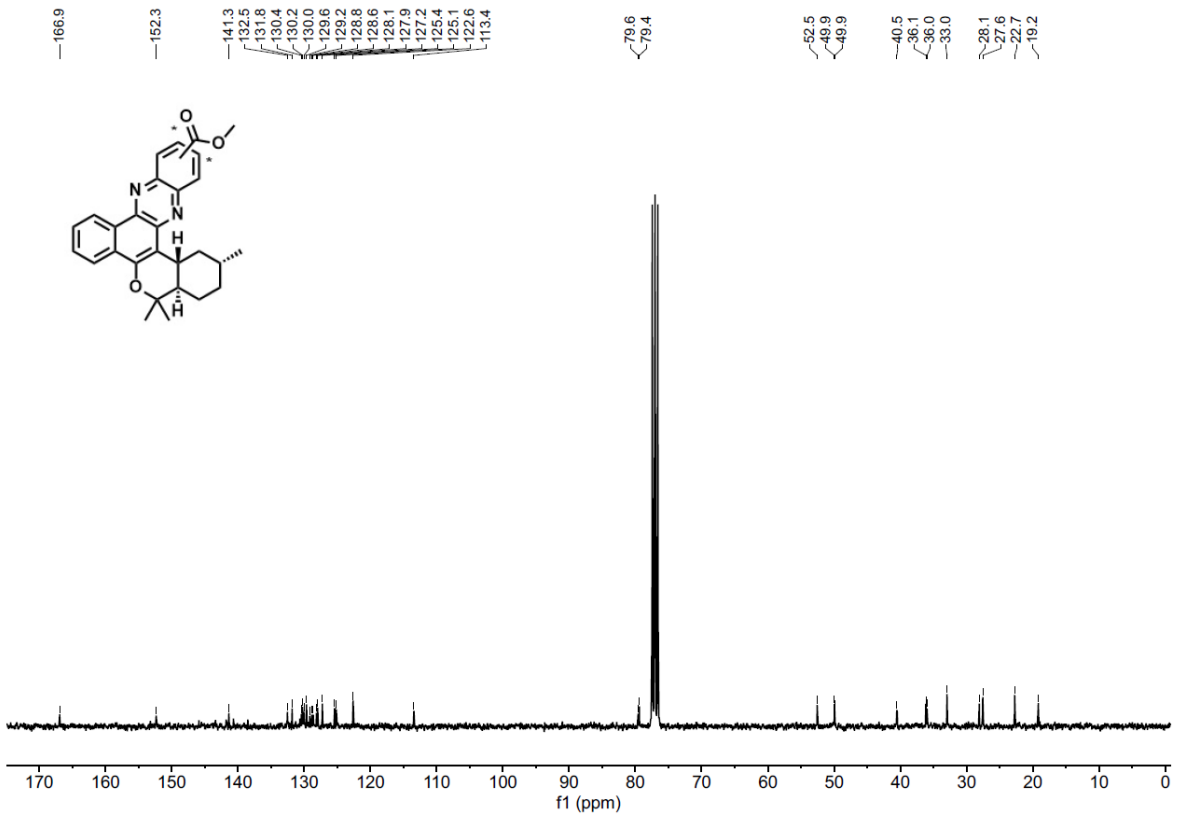


Figure B.32. ^{13}C NMR of cyclic ether **10a** recorded in $CDCl_3$ at 75 MHz and 298 K.

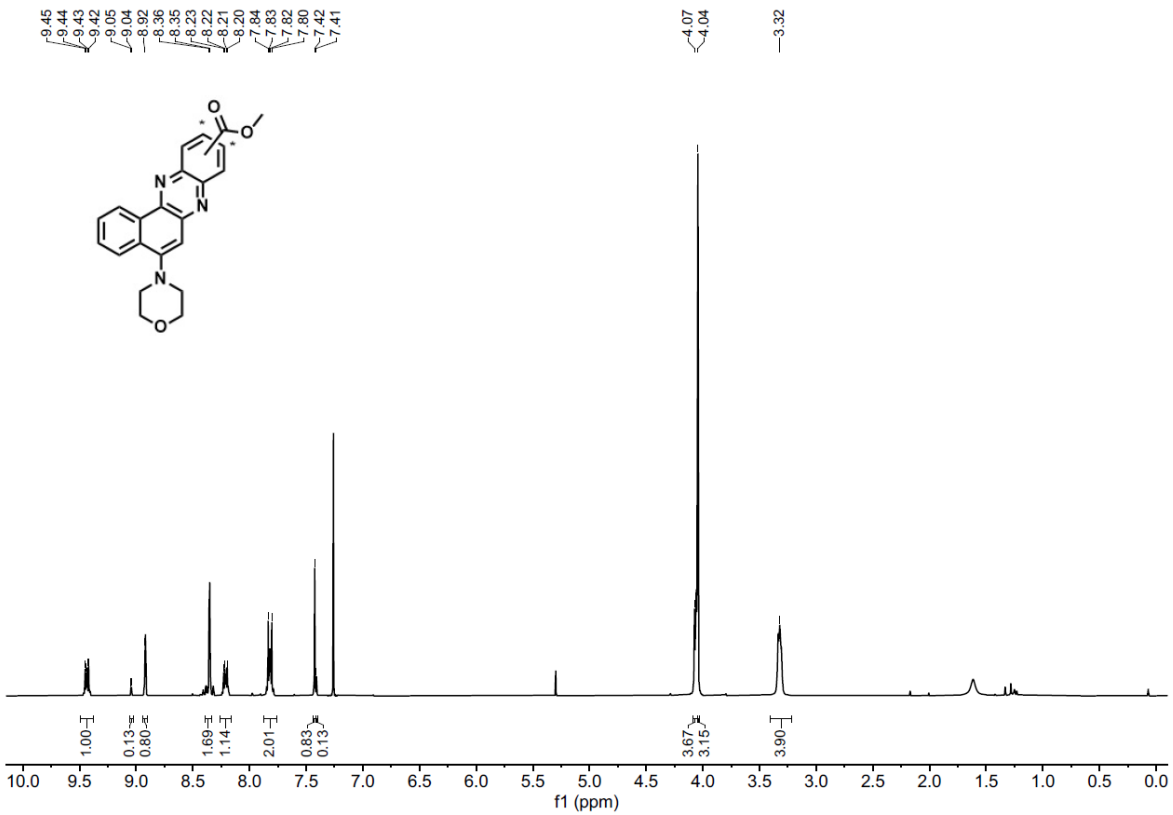


Figure B.33. ^{1}H NMR of morpholine **10b** recorded in $CDCl_3$ at 300 MHz and 298 K.

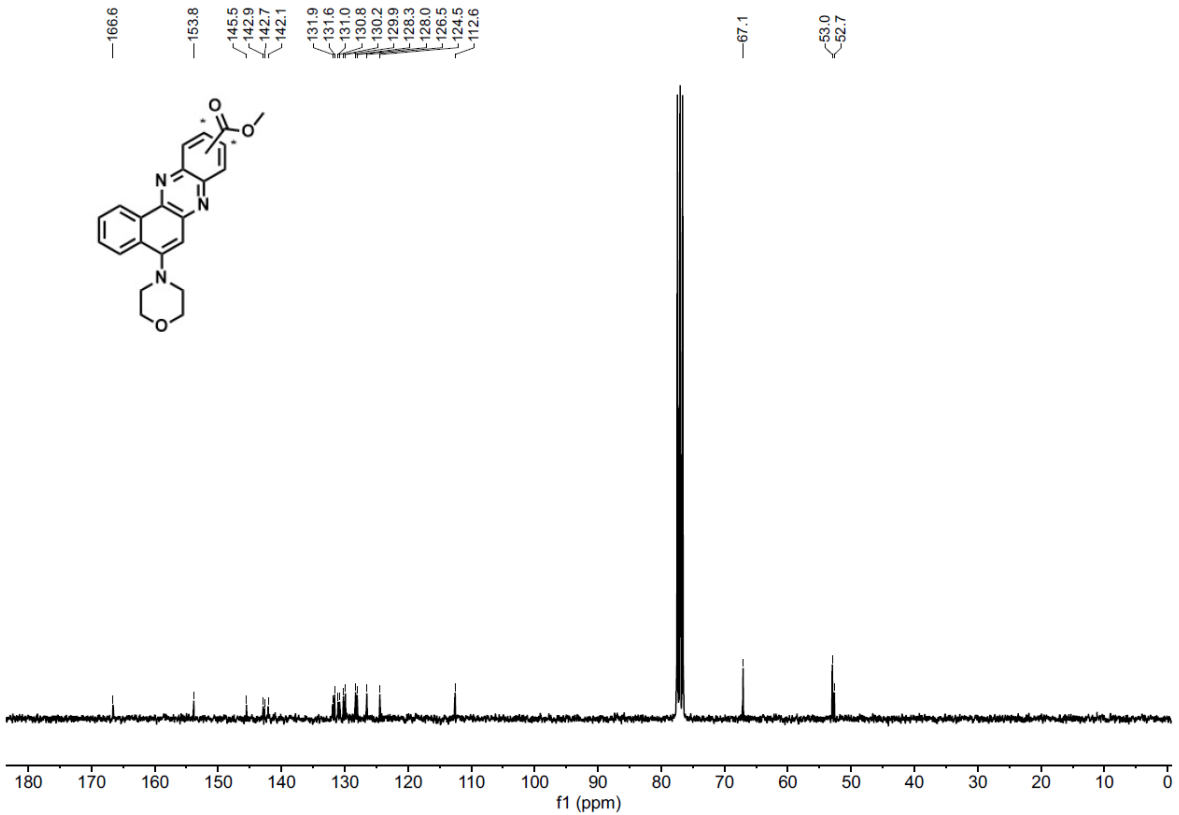


Figure B.34. ^{13}C NMR of morpholine **10b** recorded in $CDCl_3$ at 75 MHz and 298 K.

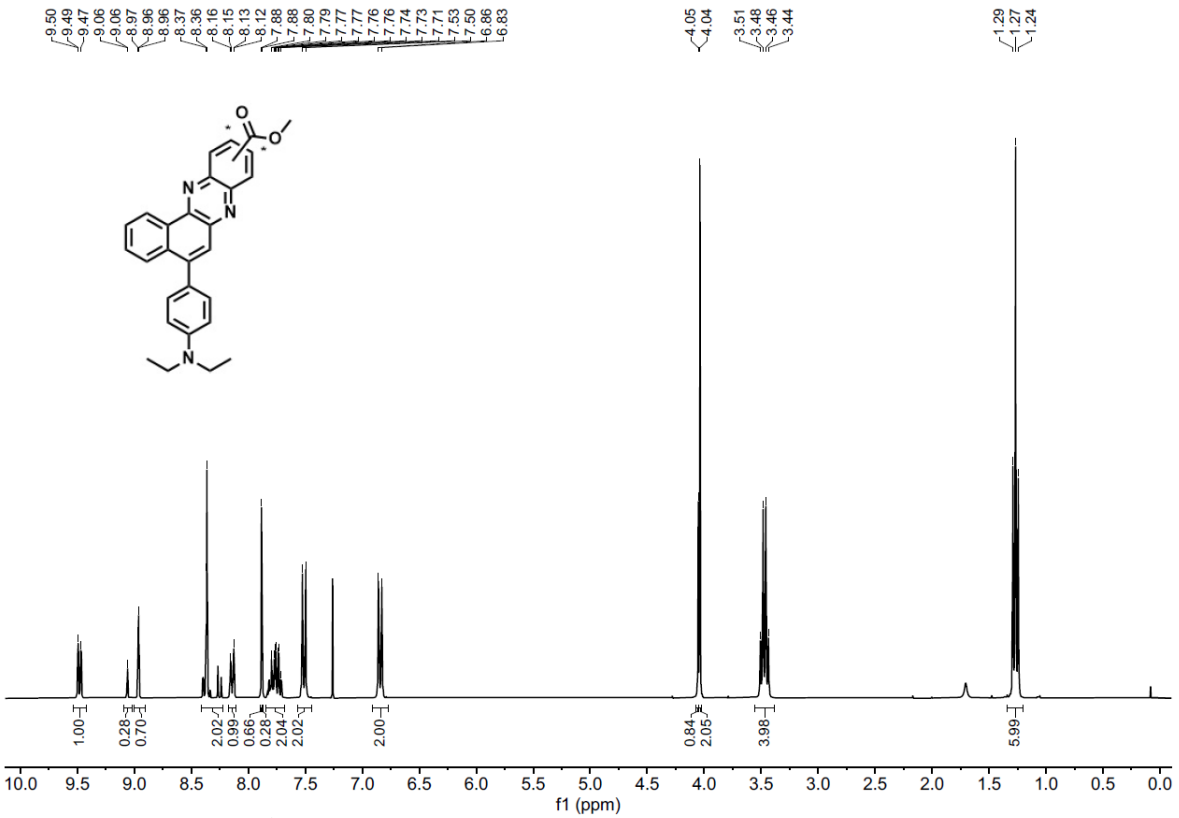


Figure B.35. ^{1}H NMR of diethylaniline **10c** recorded in $CDCl_3$ at 300 MHz and 298 K.

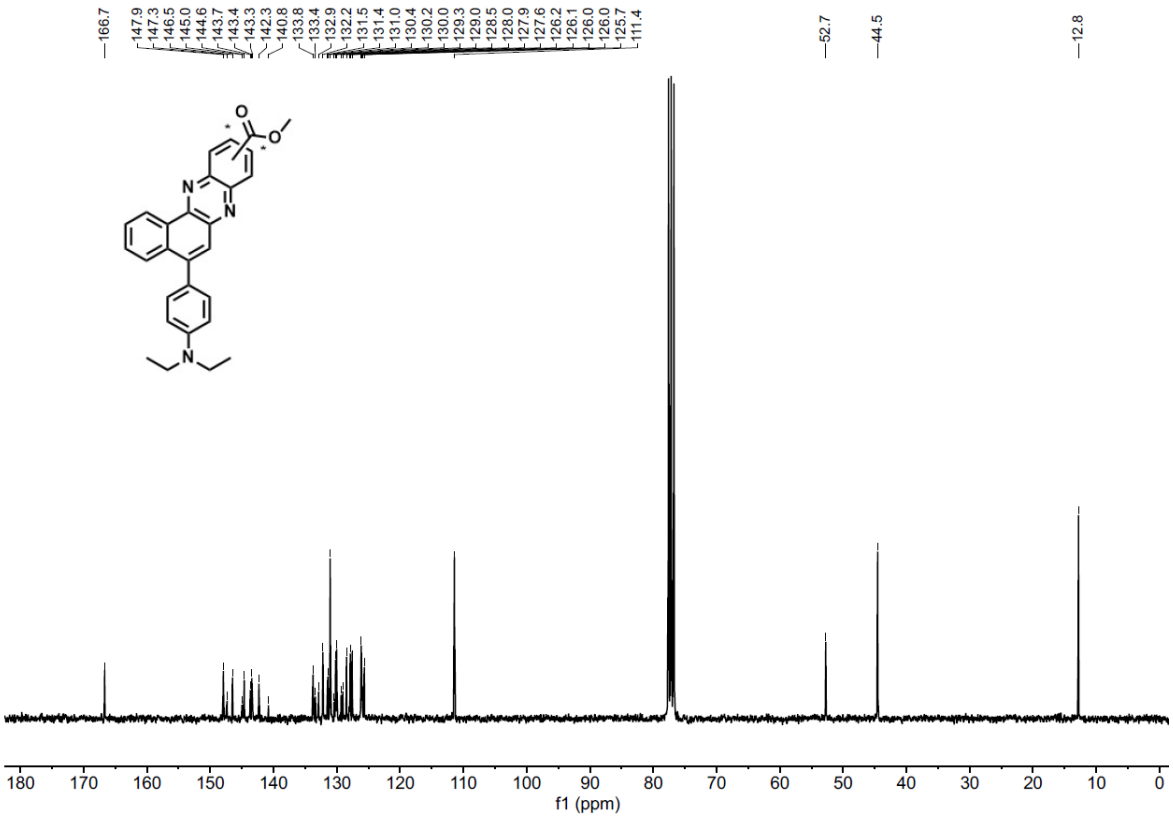


Figure B.36. ^{13}C NMR of diethylaniline **10c** recorded in $CDCl_3$ at 75 MHz and 298 K.

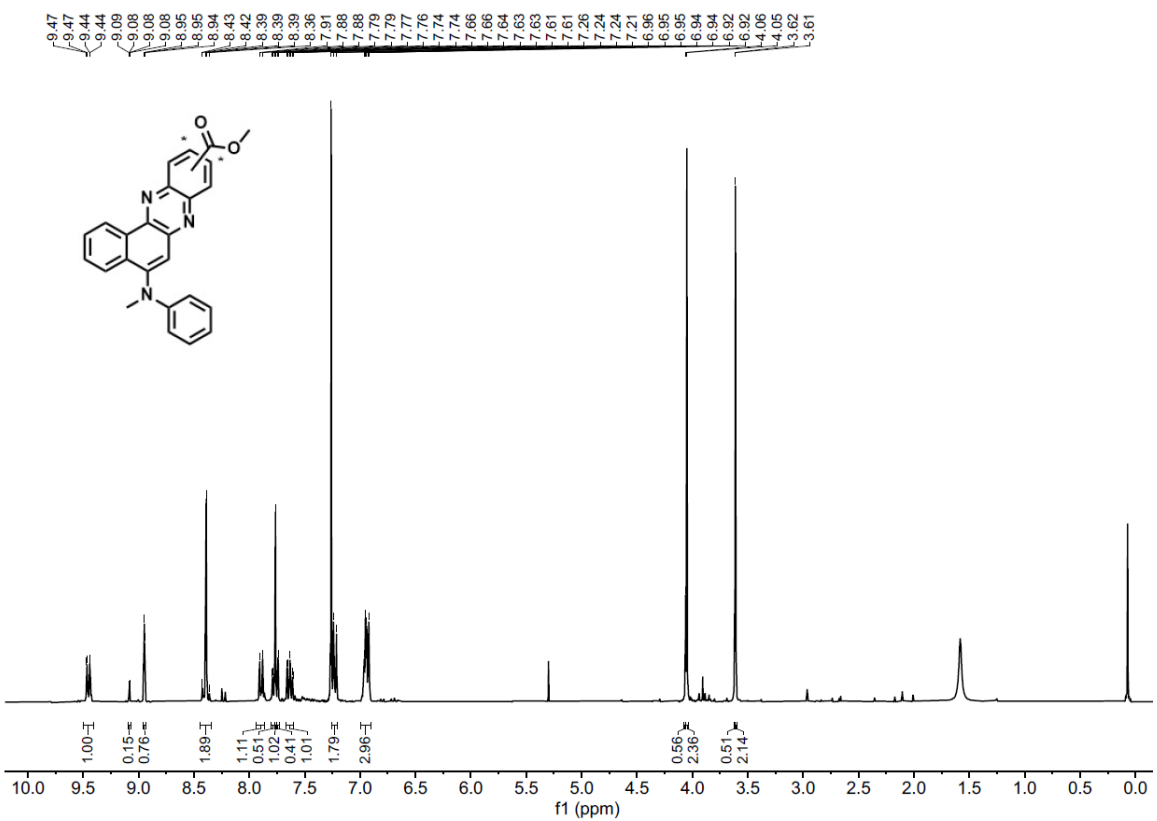


Figure B.37. ^{1}H NMR of methylaniline **10d** recorded in $CDCl_3$ at 300 MHz and 298 K.

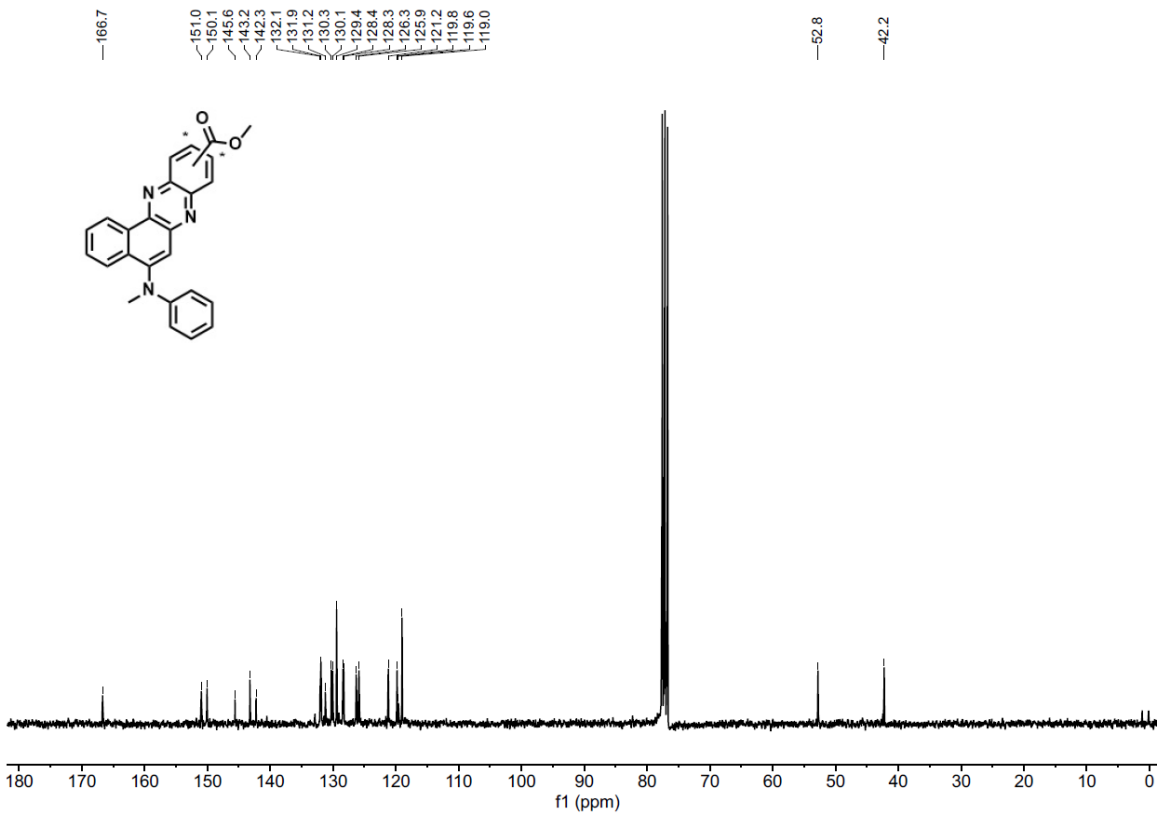


Figure B.38. ^{13}C NMR of methylaniline **10d** recorded in $CDCl_3$ at 75 MHz and 298 K.

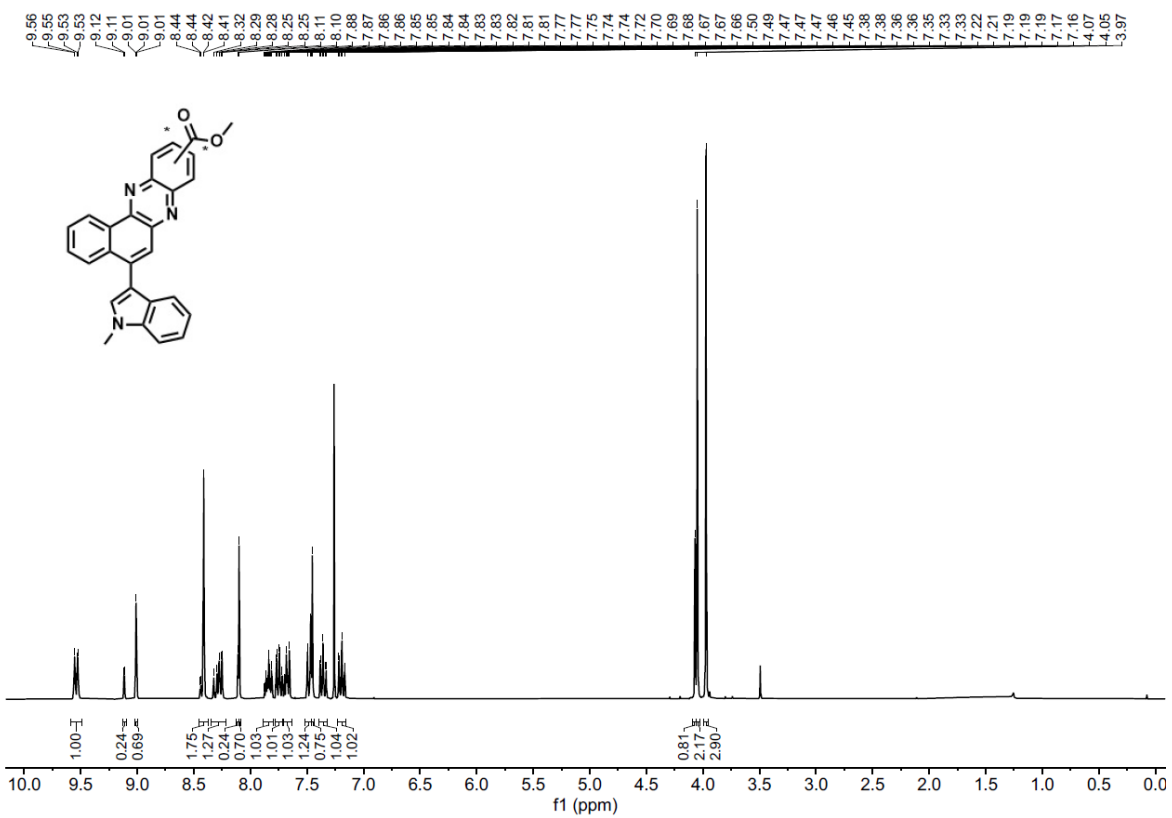


Figure B.39. ^{1}H NMR of indole **10e** recorded in $CDCl_3$ at 300 MHz and 298 K.

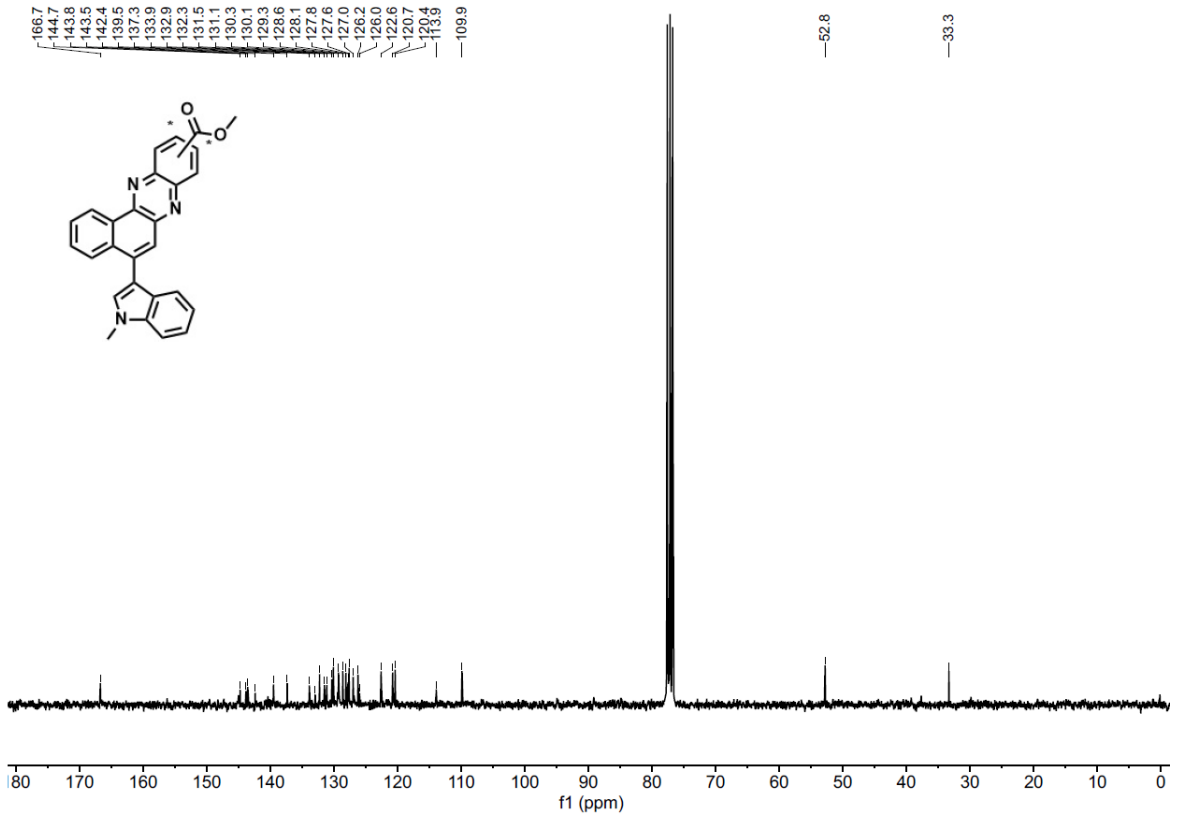


Figure B.40. ^{13}C NMR of indole **10e** recorded in $CDCl_3$ at 75 MHz and 298 K.

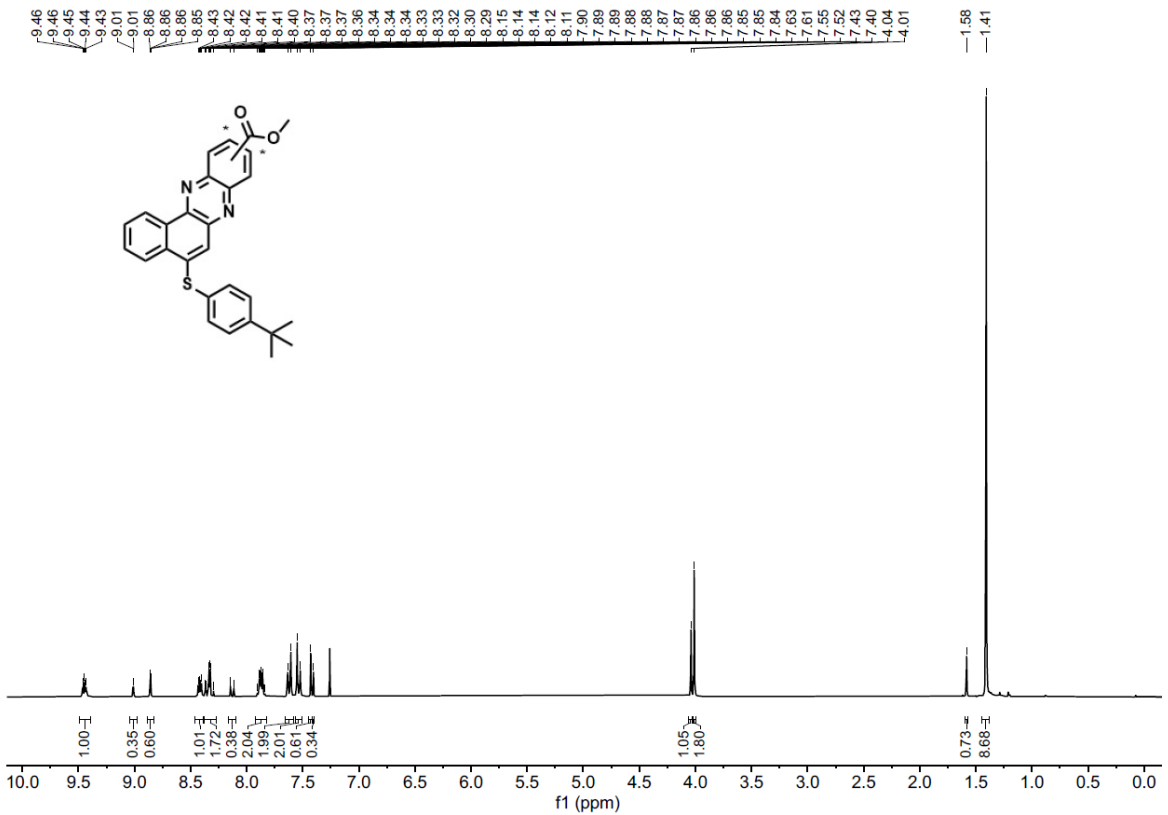


Figure B.41. ^{1}H NMR of north-ester and south aromatic sulfur **10f-1** recorded in $CDCl_3$ at 300 MHz and 298 K.

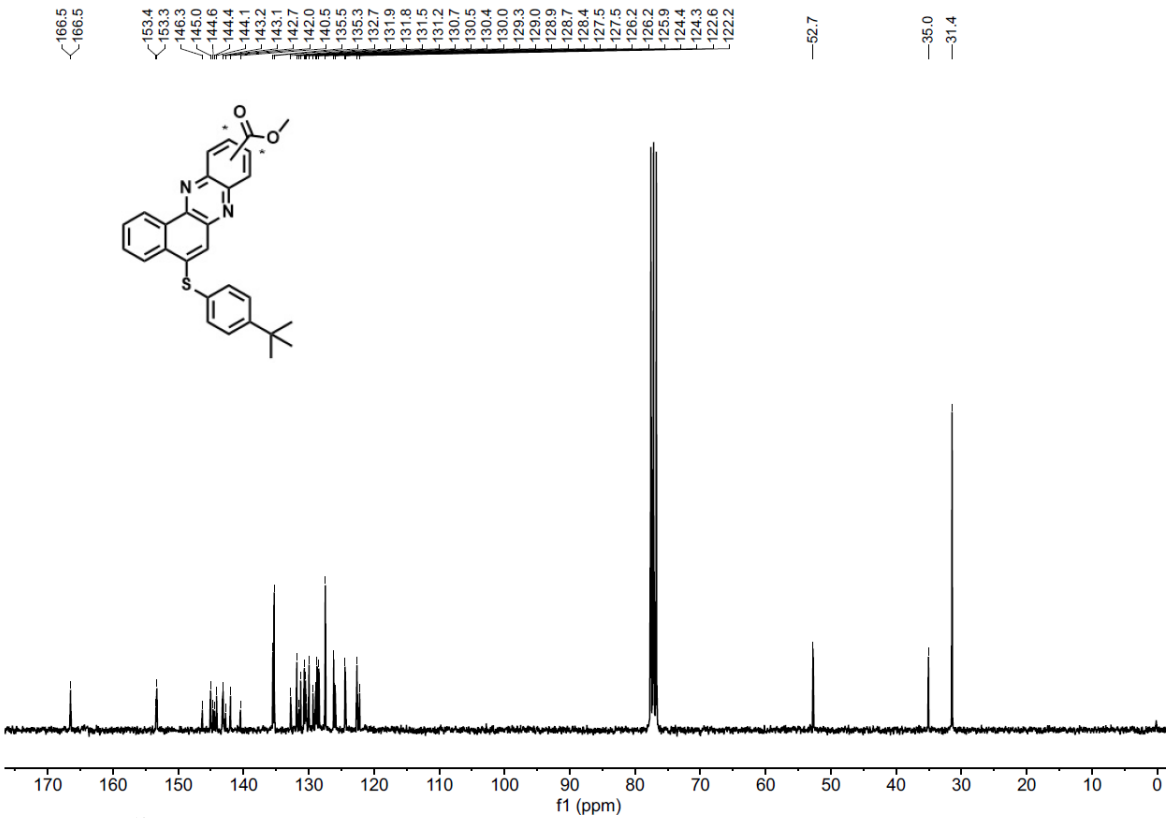


Figure B.42. ^{13}C NMR of north-ester and south aromatic sulfur **10f-1** recorded in $CDCl_3$ at 75 MHz and 298 K.

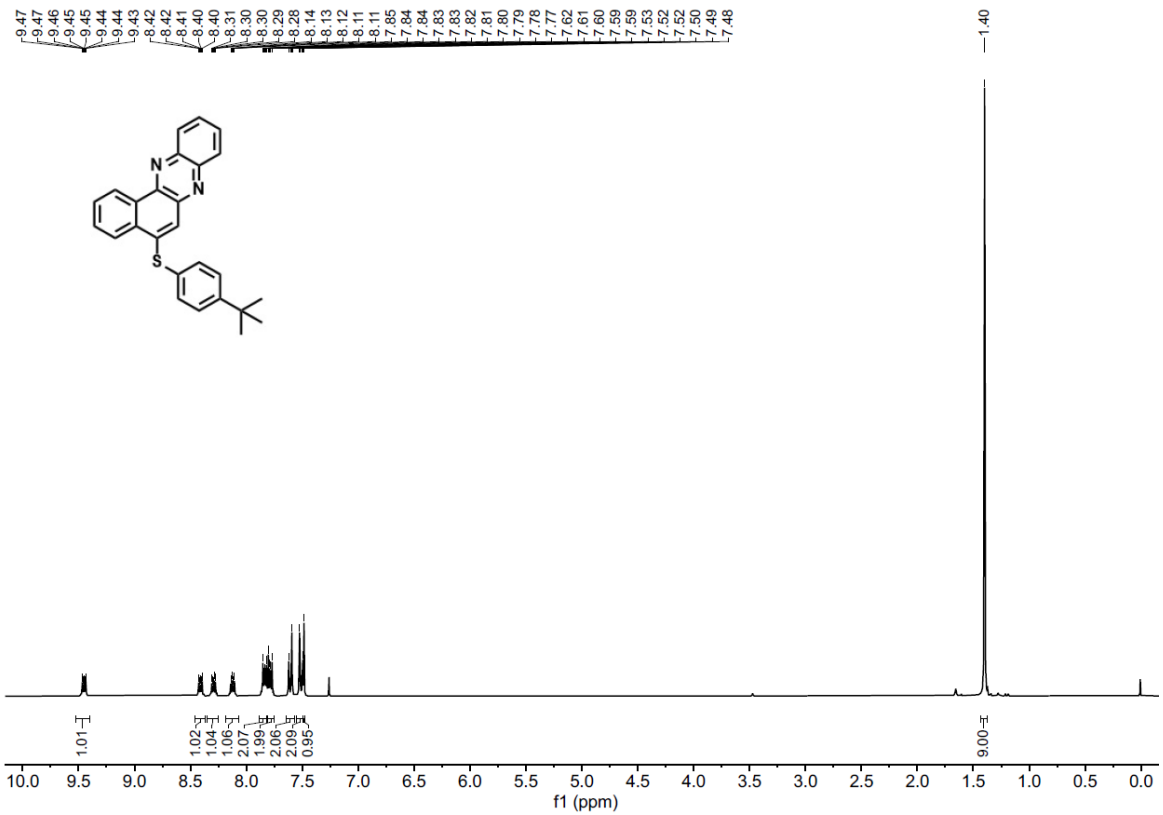


Figure B.43. ^{1}H NMR of aromatic sulfur **10f-2** recorded in $CDCl_3$ at 300 MHz and 298 K.

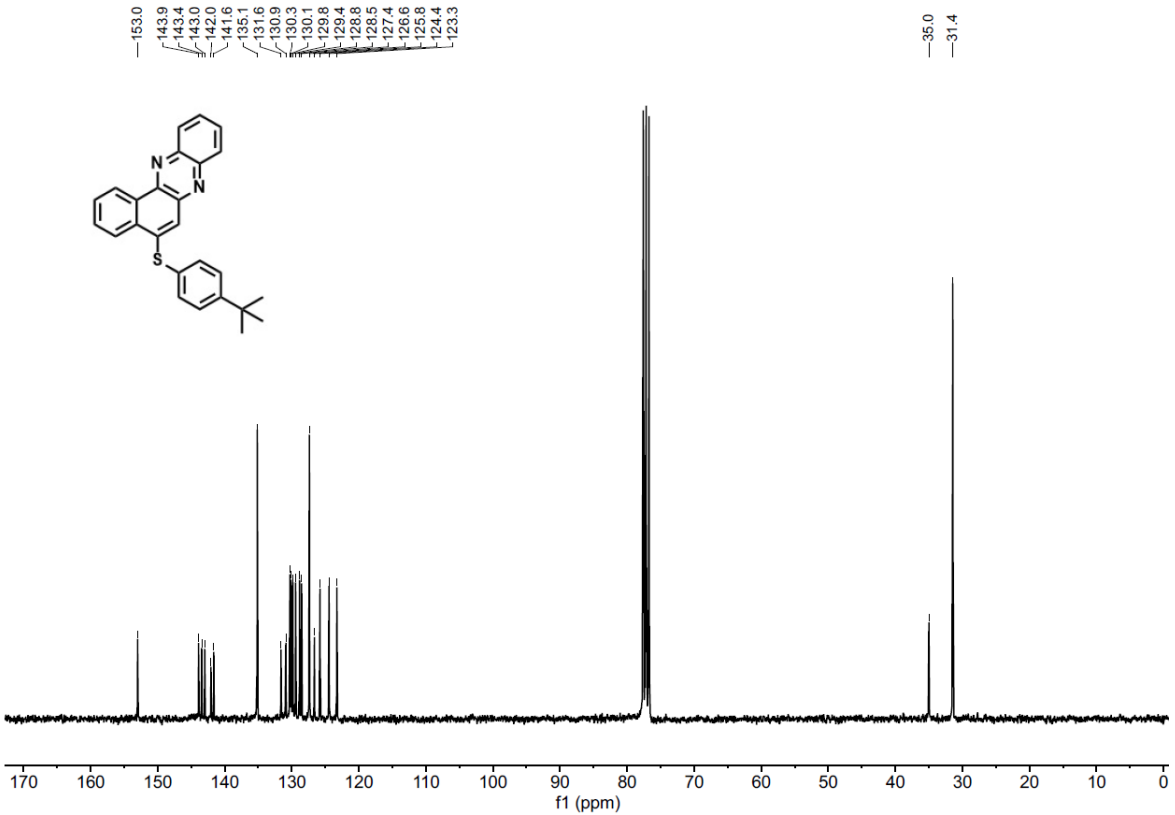


Figure B.44. ^{13}C NMR of aromatic sulfur **10f-2** recorded in $CDCl_3$ at 75 MHz and 298 K.

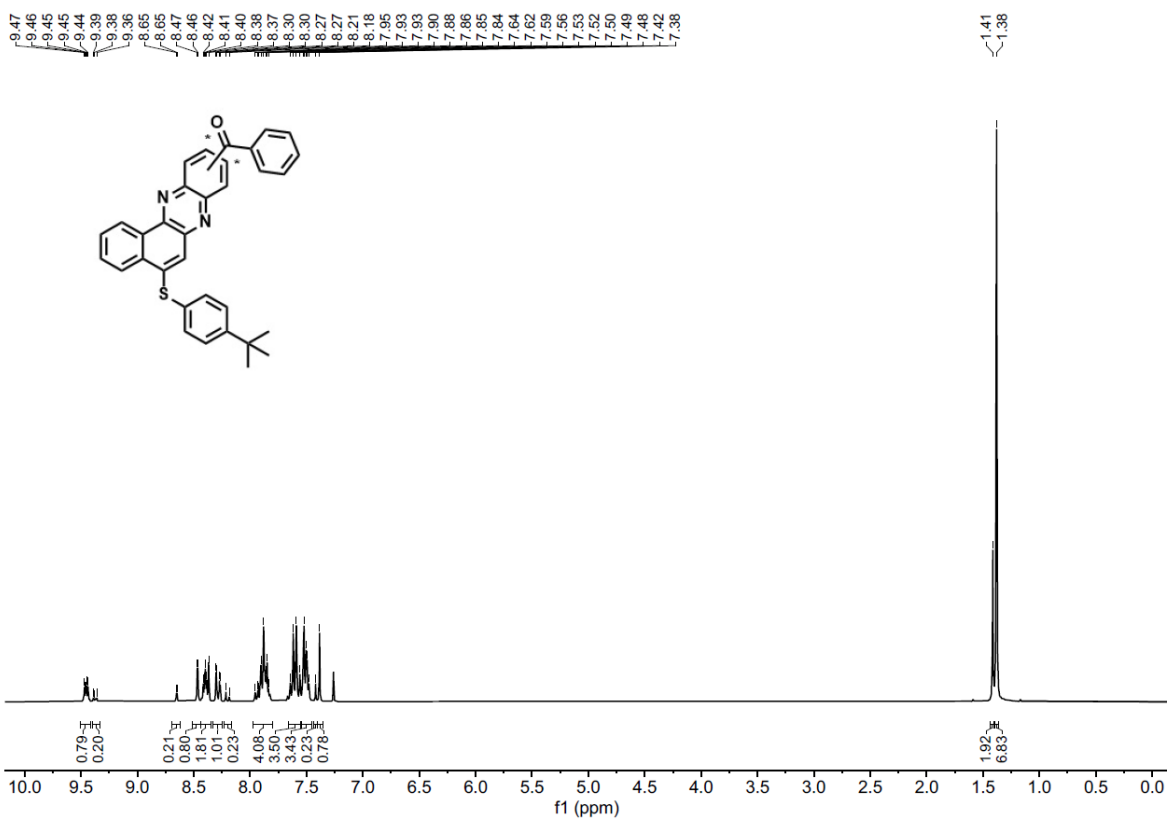


Figure B.45. ^{1}H NMR of benzophenone **10f-3** recorded in $CDCl_3$ at 300 MHz and 298 K.

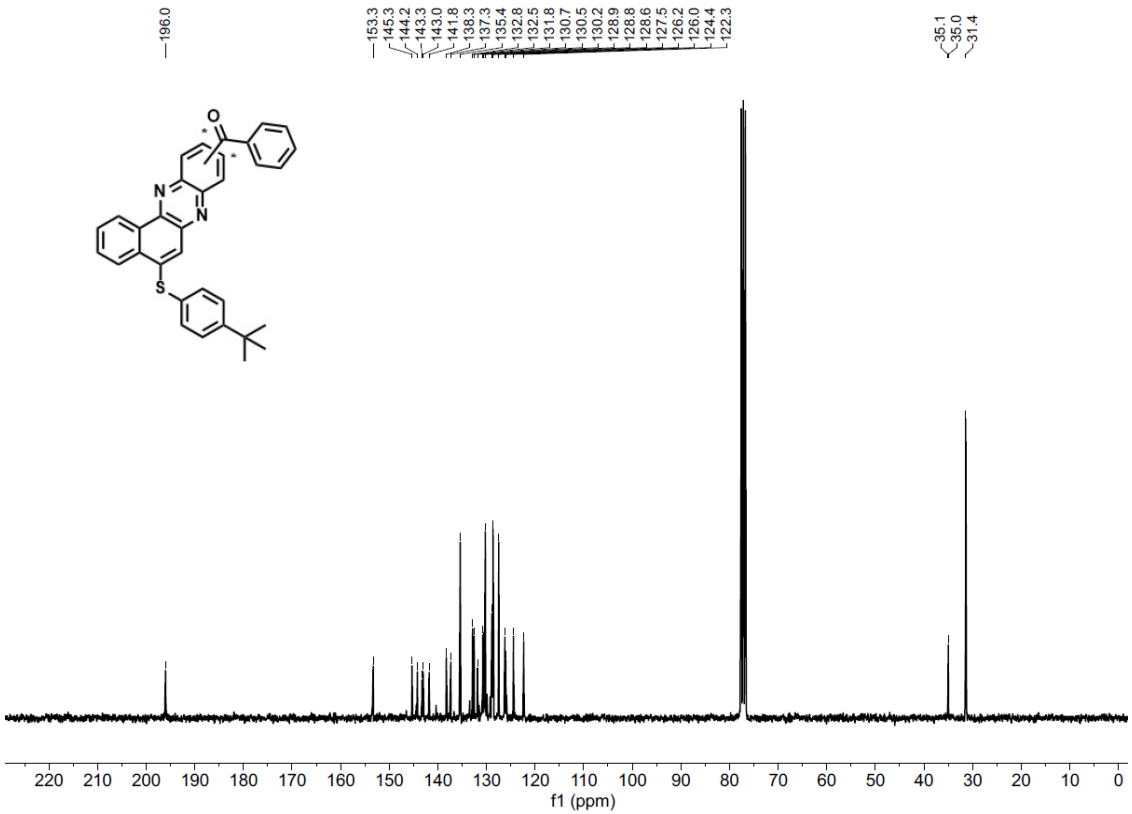


Figure B.46. ^{13}C NMR of benzophenone **10f-3** recorded in $CDCl_3$ at 75 MHz and 298 K.

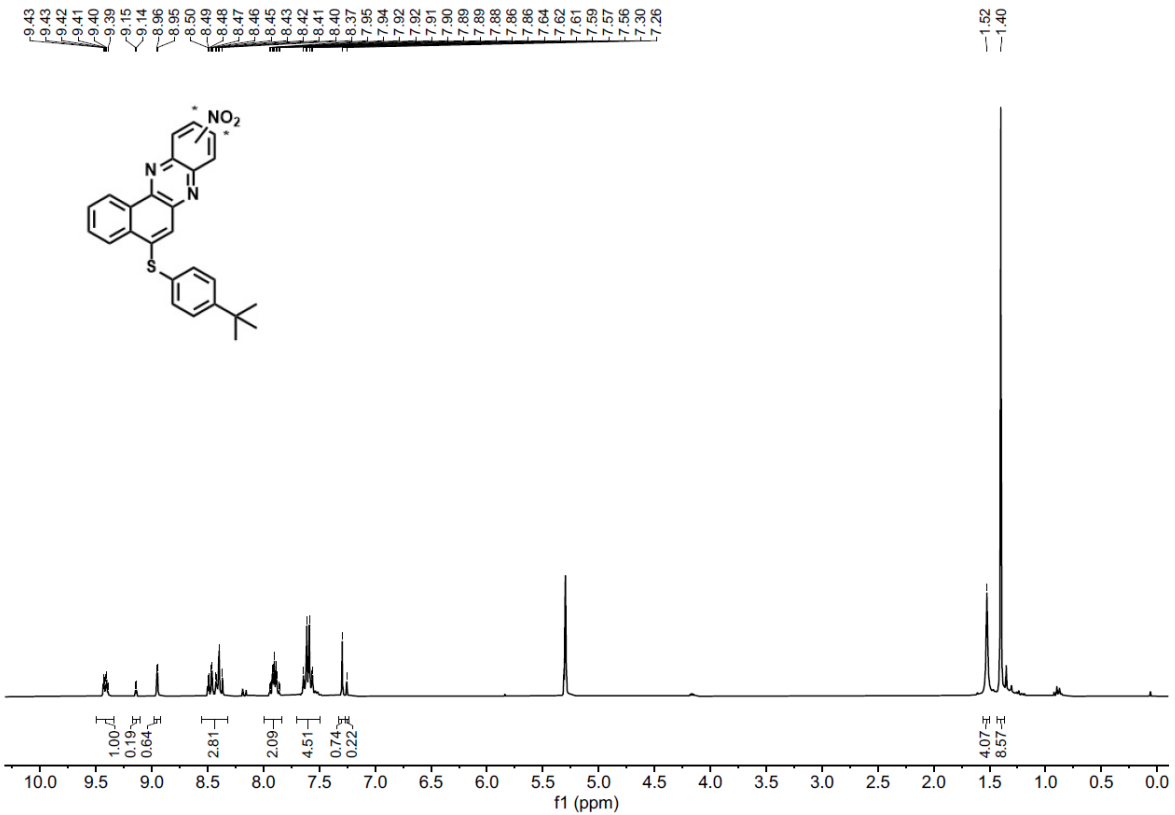


Figure B.47. ^{1}H NMR of nitro **10f-4** recorded in CD_2Cl_2 at 300 MHz and 298 K.

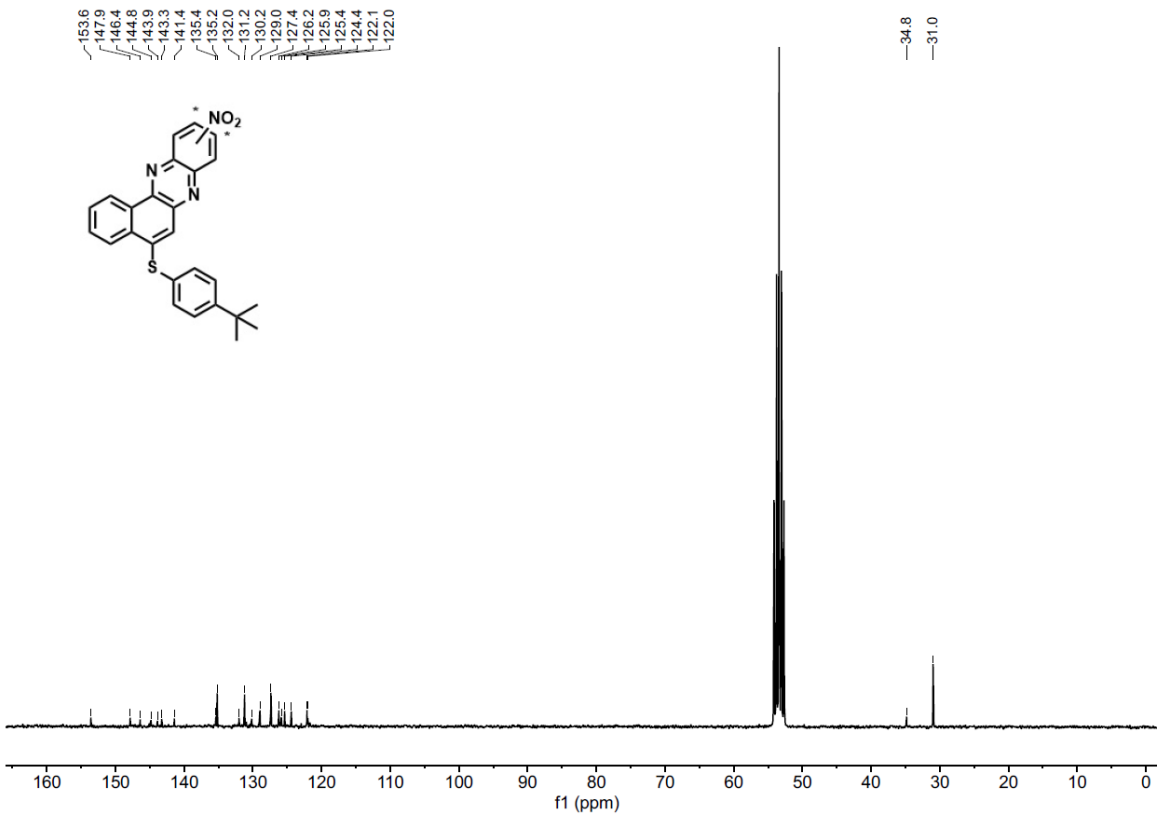


Figure B.48. ^{13}C NMR of nitro **10f-4** recorded in CD_2Cl_2 at 75 MHz and 298 K.

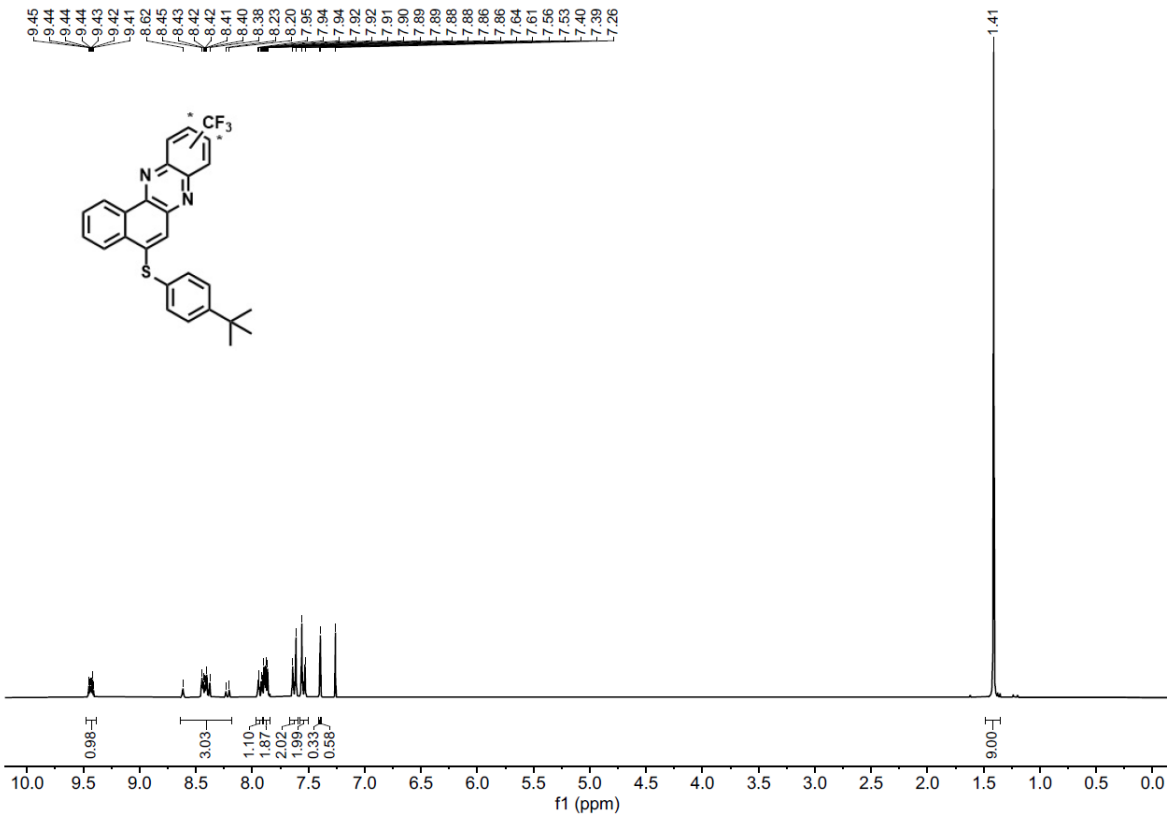


Figure B.49. ^{1}H NMR of trifluoro **10f-5** recorded in $CDCl_3$ at 300 MHz and 298 K.

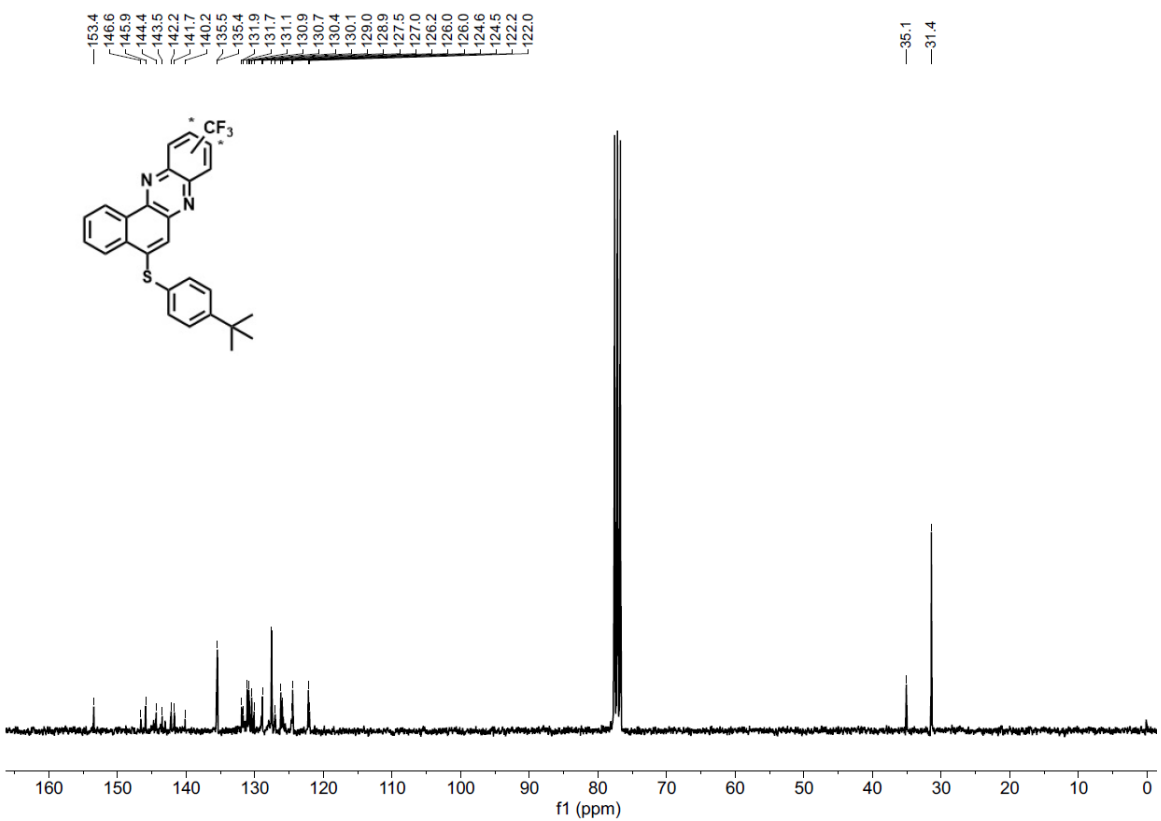


Figure B.50. ^{13}C NMR of trifluoro **10f-5** recorded in $CDCl_3$ at 75 MHz and 298 K.

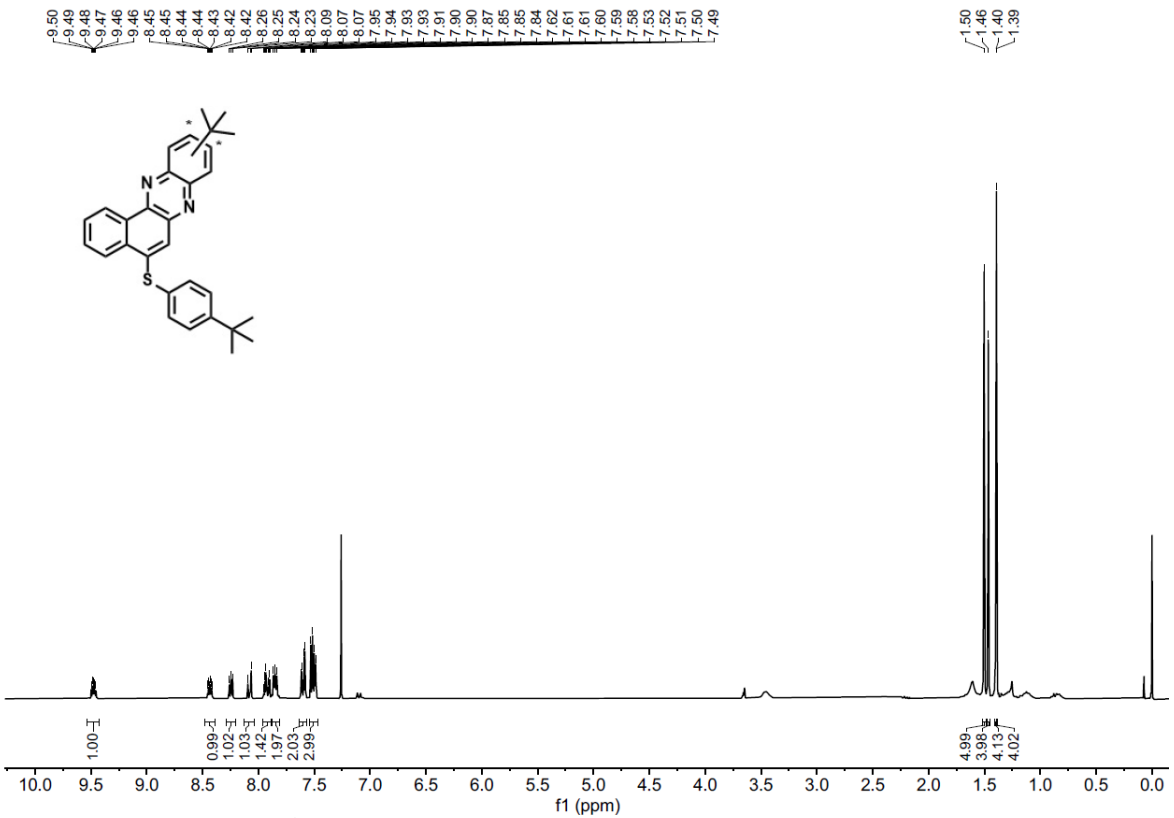


Figure B.51. ^{1}H NMR of *t*-butyl **10f-6** recorded in $CDCl_3$ at 300 MHz and 298 K.

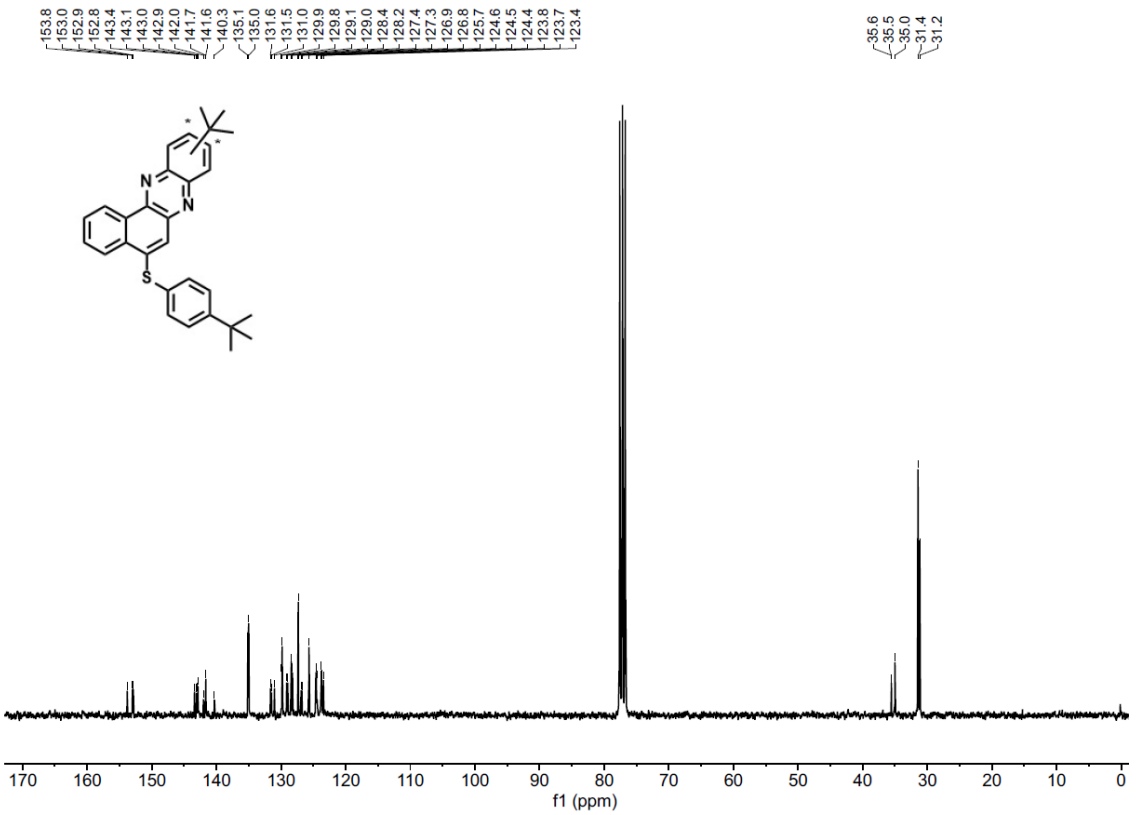


Figure B.52. ^{13}C NMR of *t*-butyl **10f-6** recorded in $CDCl_3$ at 75 MHz and 298 K.

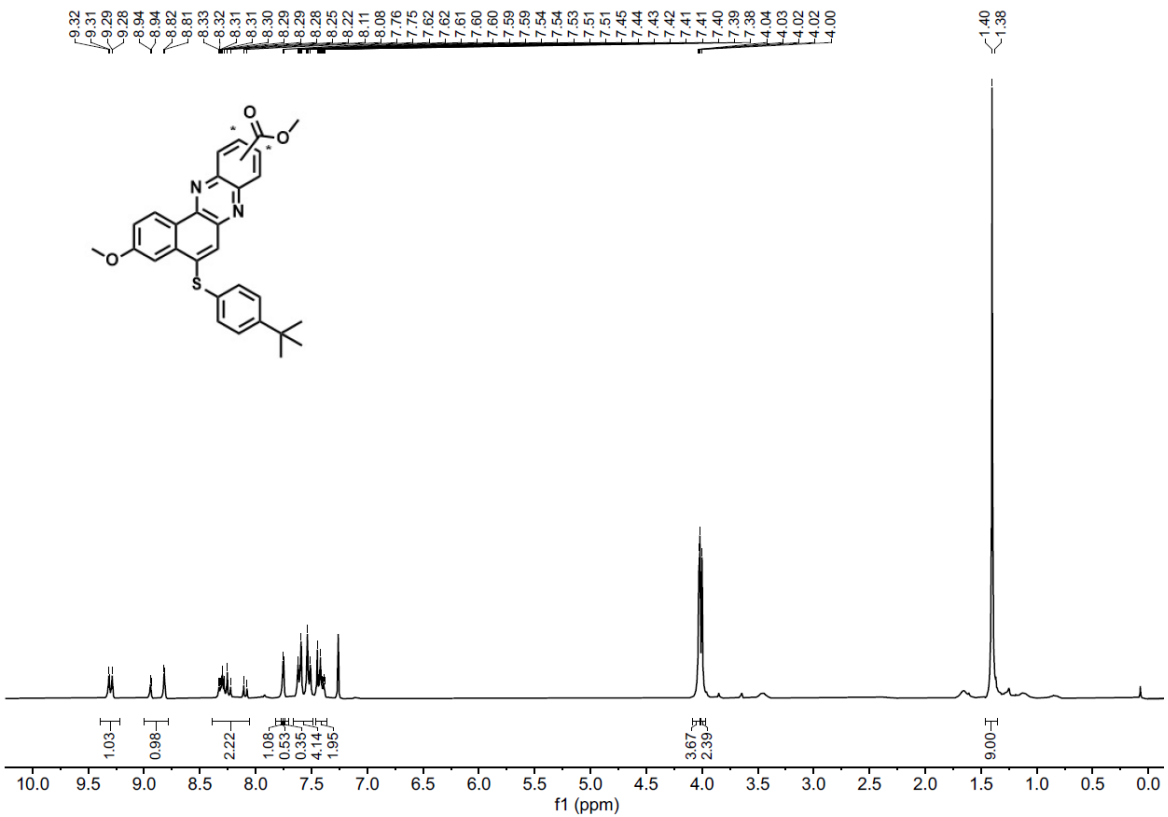


Figure B.53. ^{1}H NMR of west-OMe **10g** recorded in $CDCl_3$ at 300 MHz and 298 K.

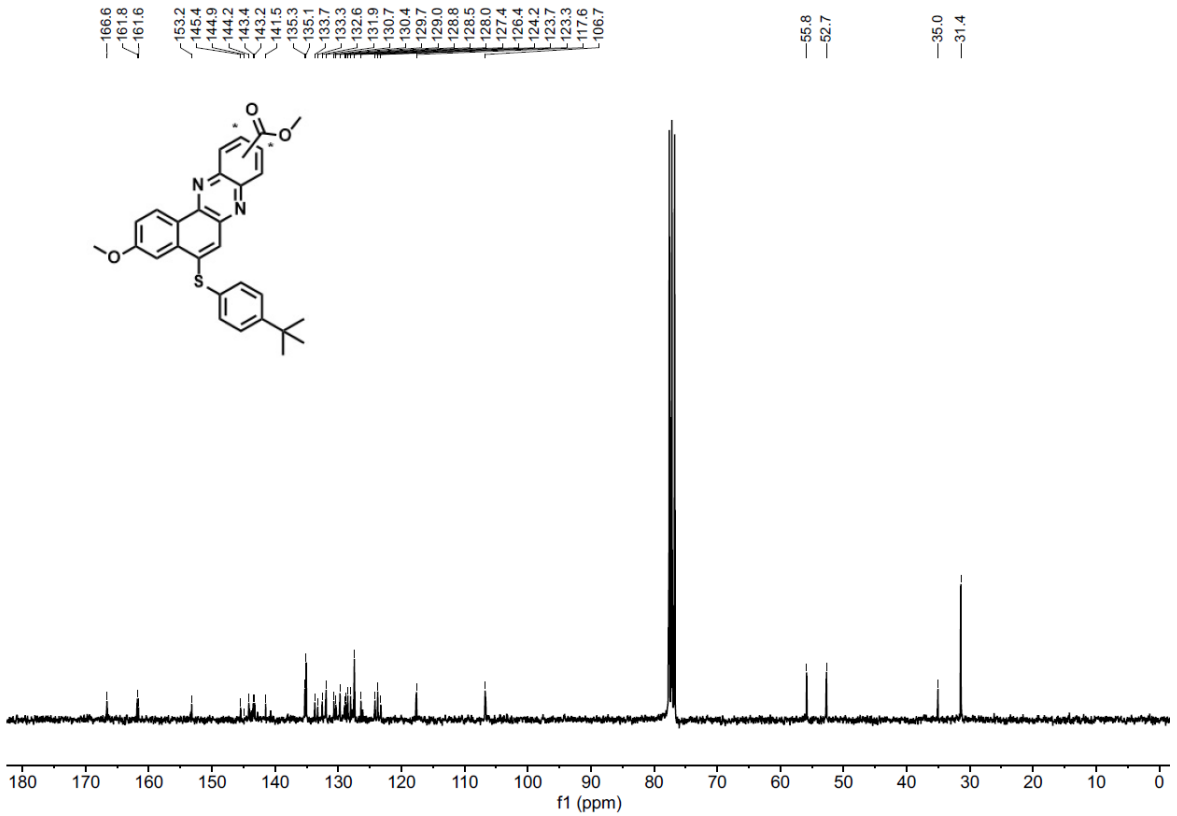


Figure B.54. ^{13}C NMR of west-OMe **10g** recorded in $CDCl_3$ at 75 MHz and 298 K.

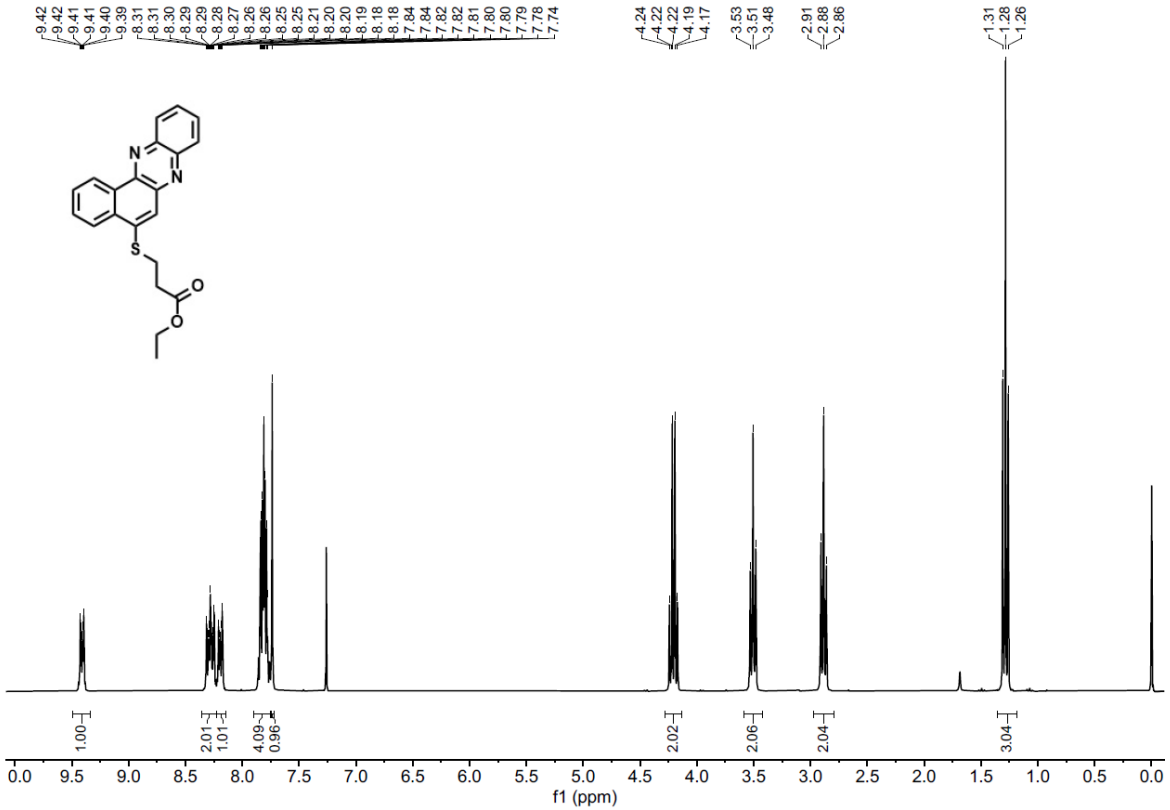


Figure B.55. ^{1}H NMR of aliphatic sulfur **10h** recorded in $CDCl_3$ at 300 MHz and 298 K.

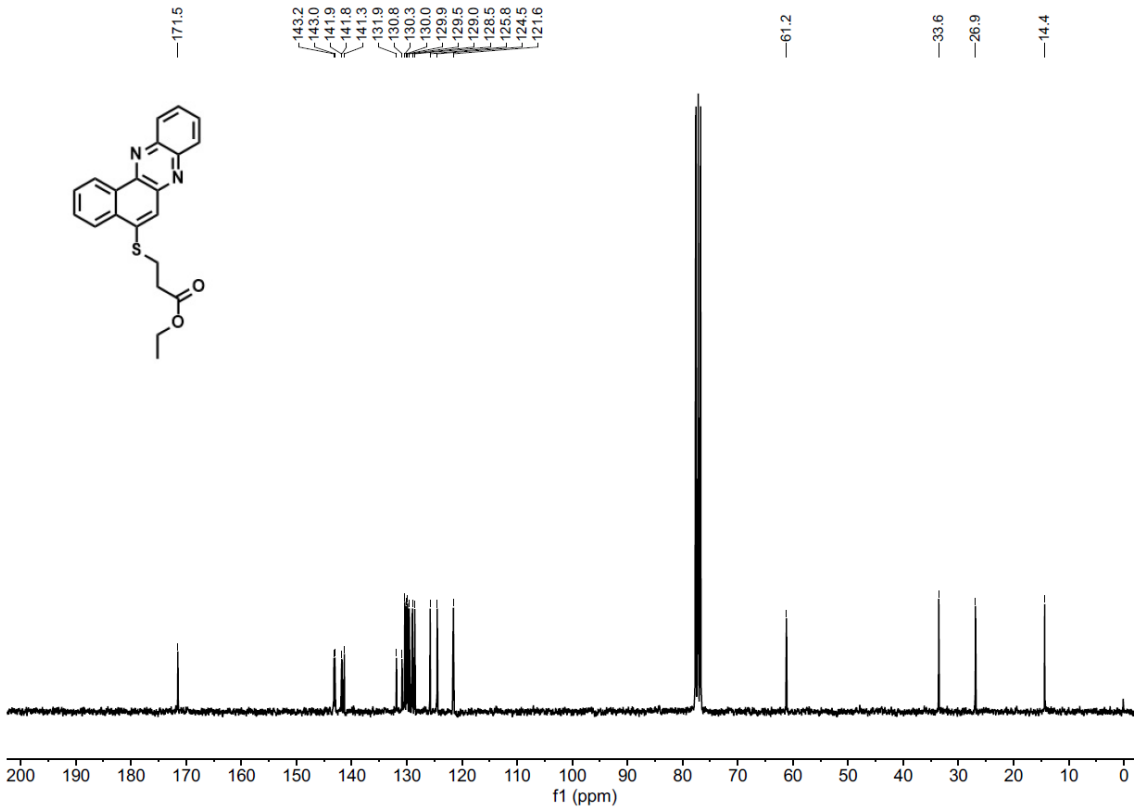


Figure B.56. ^{13}C NMR of aliphatic sulfur **10h** recorded in $CDCl_3$ at 75 MHz and 298 K.

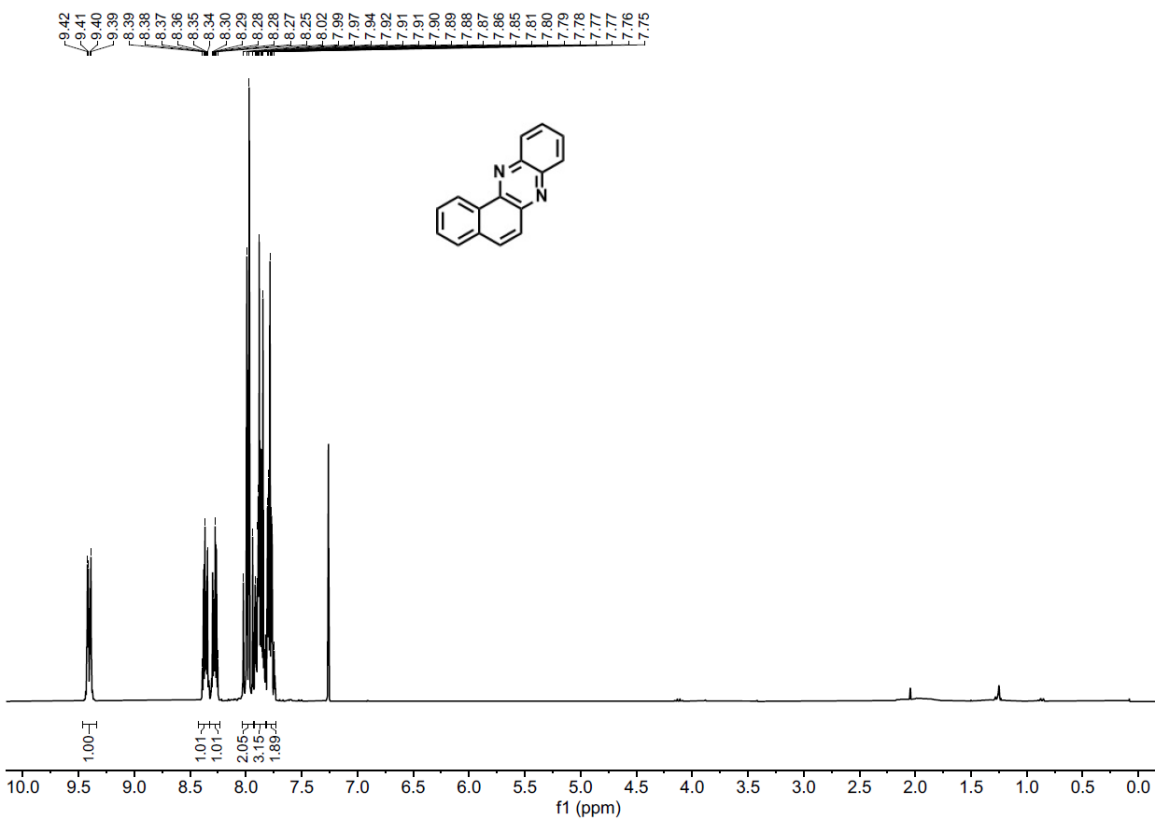


Figure B.57. ^{1}H NMR of benzophenazine **11** recorded in $CDCl_3$ at 300 MHz and 298 K.

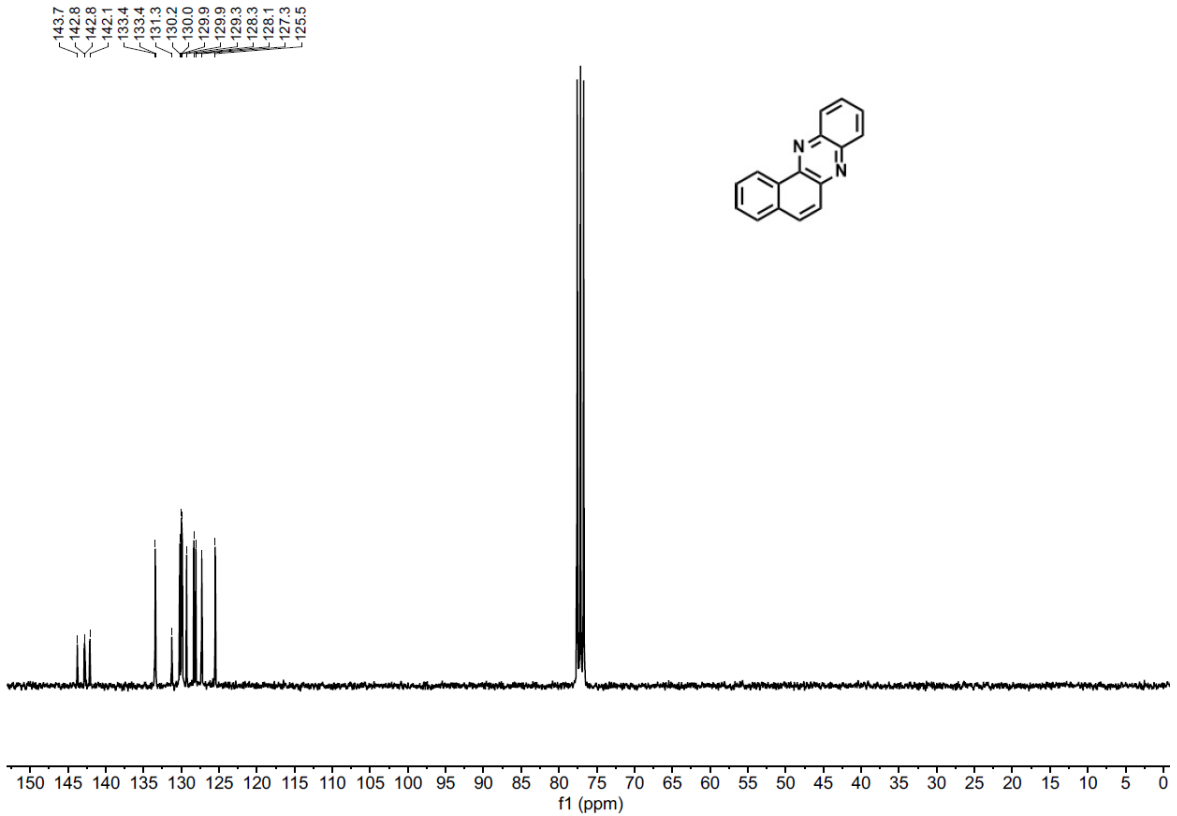


Figure B.58. ^{13}C NMR of benzophenazine **11** recorded in $CDCl_3$ at 75 MHz and 298 K.

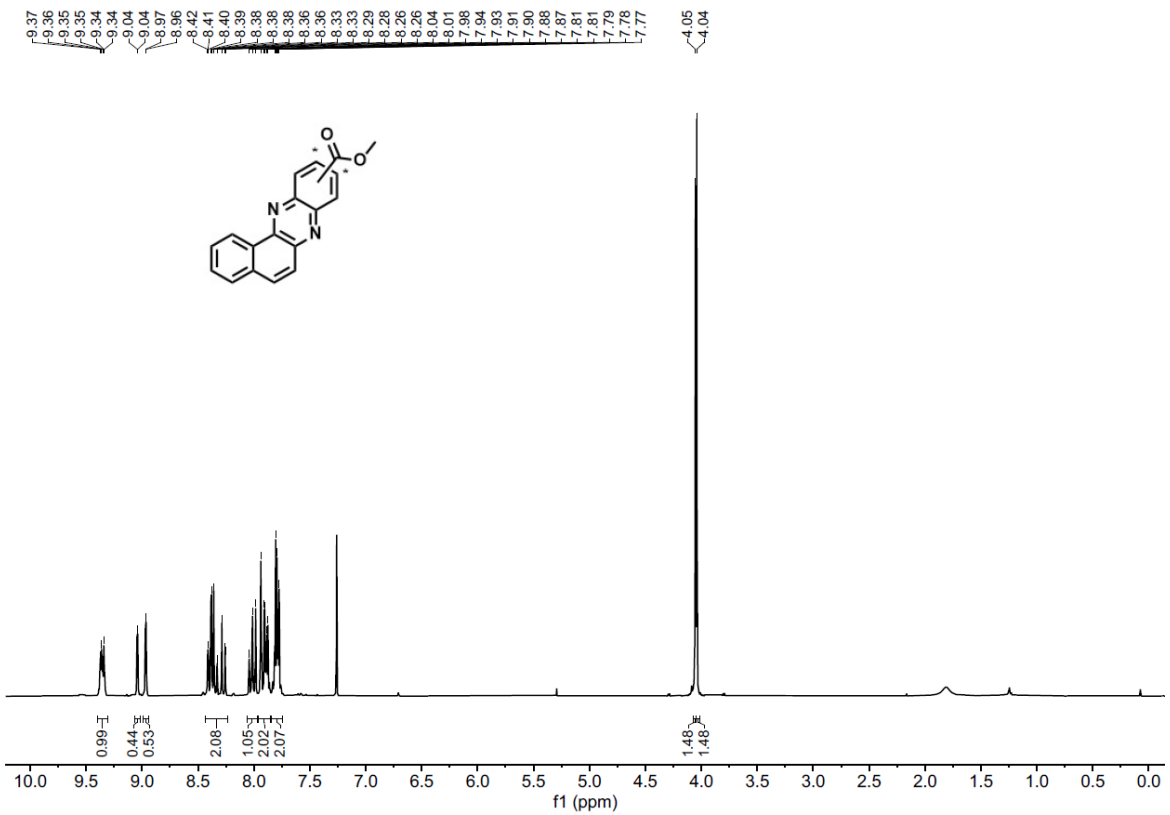


Figure B.59. ^{1}H NMR of north-ester benzophenazine **12** recorded in $CDCl_3$ at 300 MHz and 298 K.

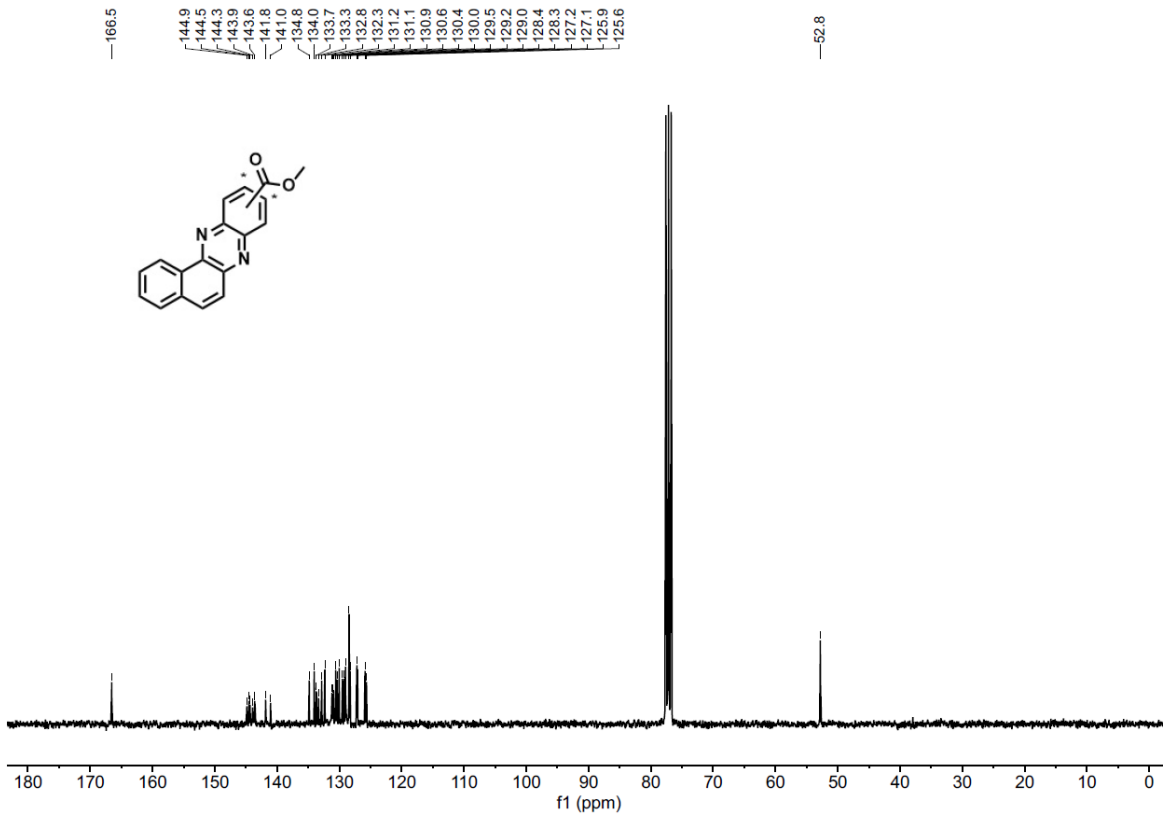


Figure B.60. ^{13}C NMR of north-ester benzophenazine **12** recorded in $CDCl_3$ at 75 MHz and 298 K.

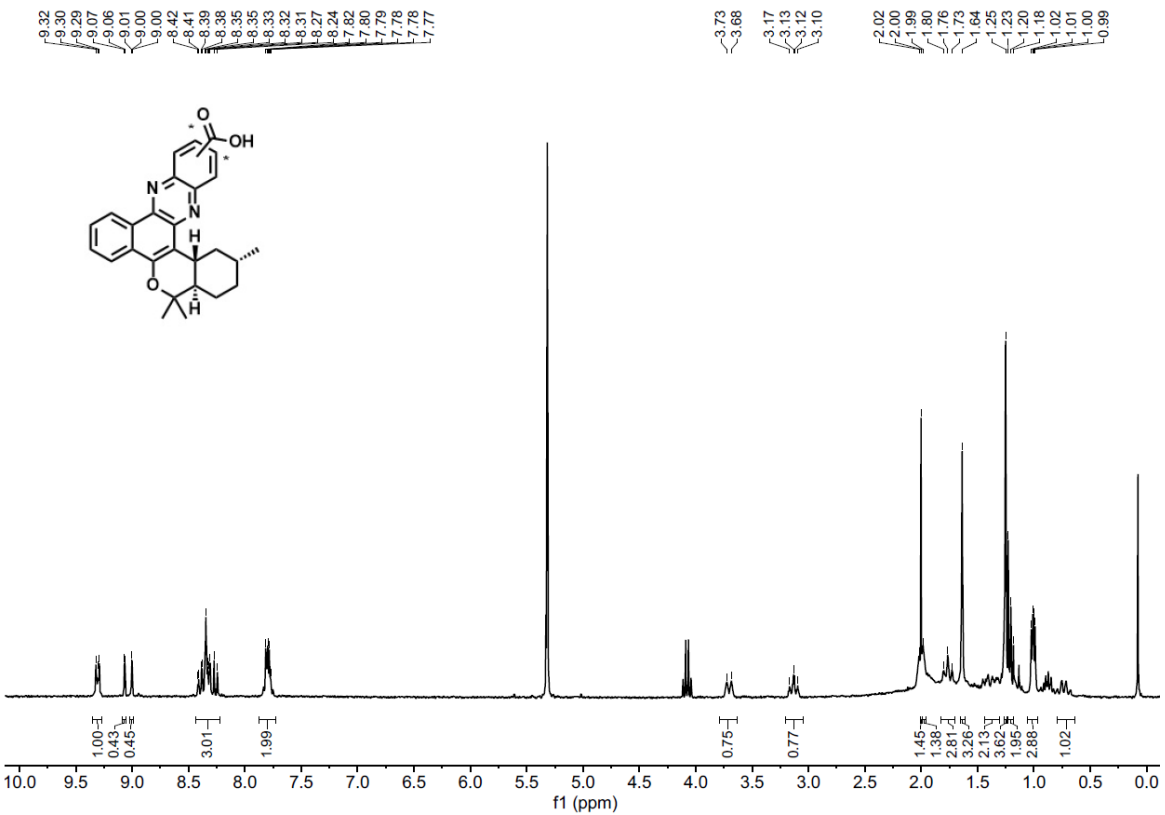


Figure B.61. ^{1}H NMR of acid-derivative **13** recorded in CD_2Cl_2 at 300 MHz and 298 K.

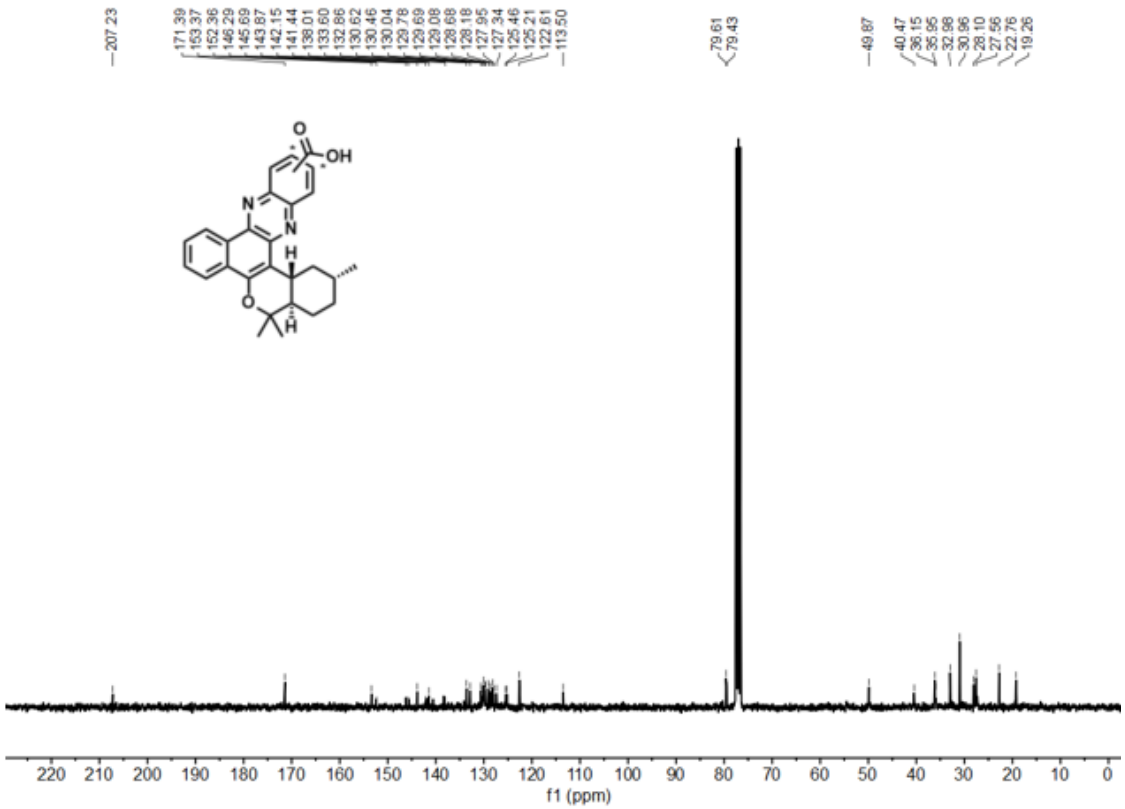


Figure B.62. ^{13}C NMR of acid-derivative **13** recorded in $CDCl_3$ at 75 MHz and 298 K.

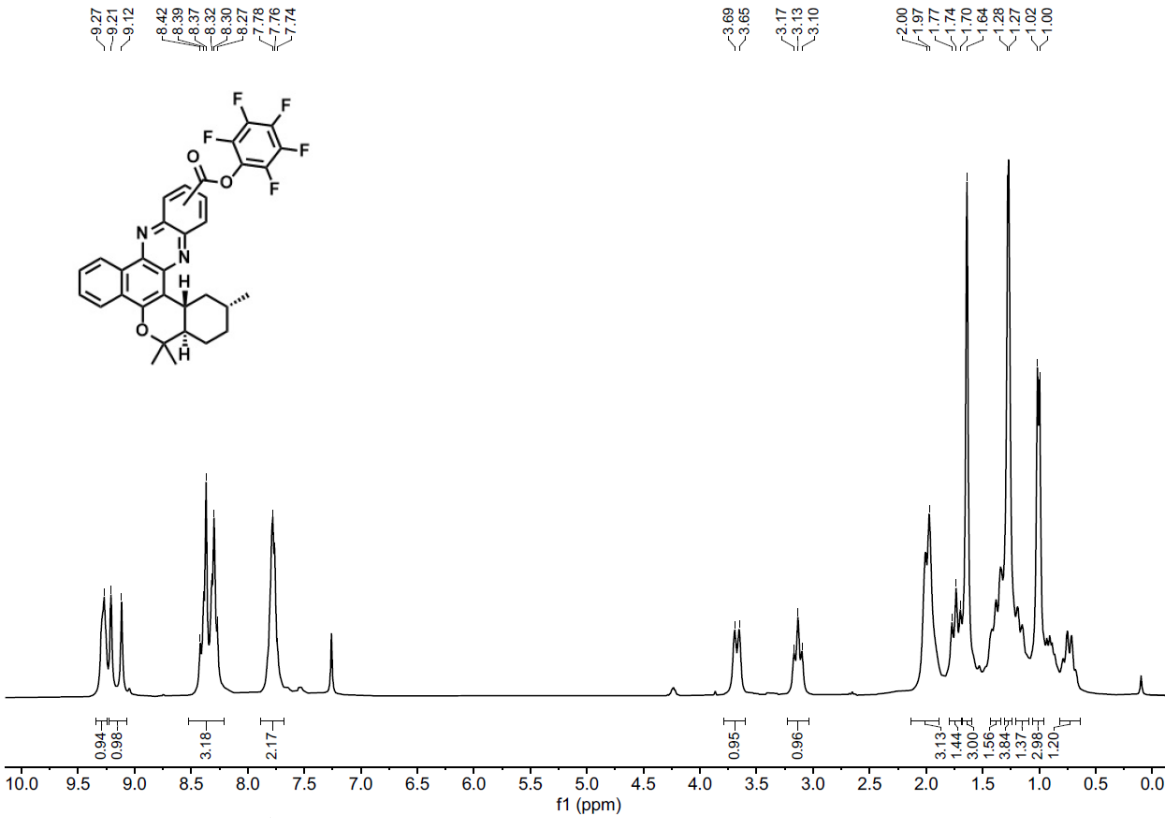


Figure B.63. ^{1}H NMR of activated ester **14** recorded in $CDCl_3$ at 300 MHz and 298 K.

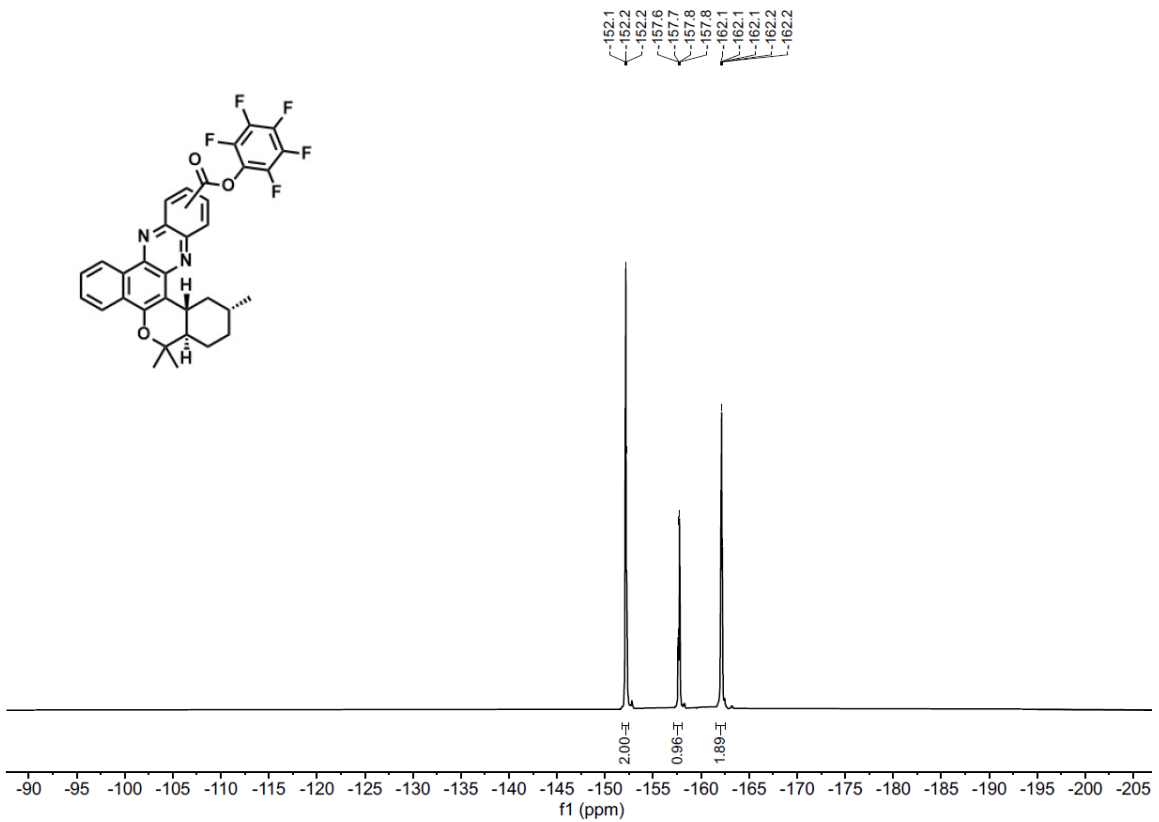


Figure B.64. ^{19}F NMR of activated ester **14** recorded in $CDCl_3$ at 282 MHz and 298 K.

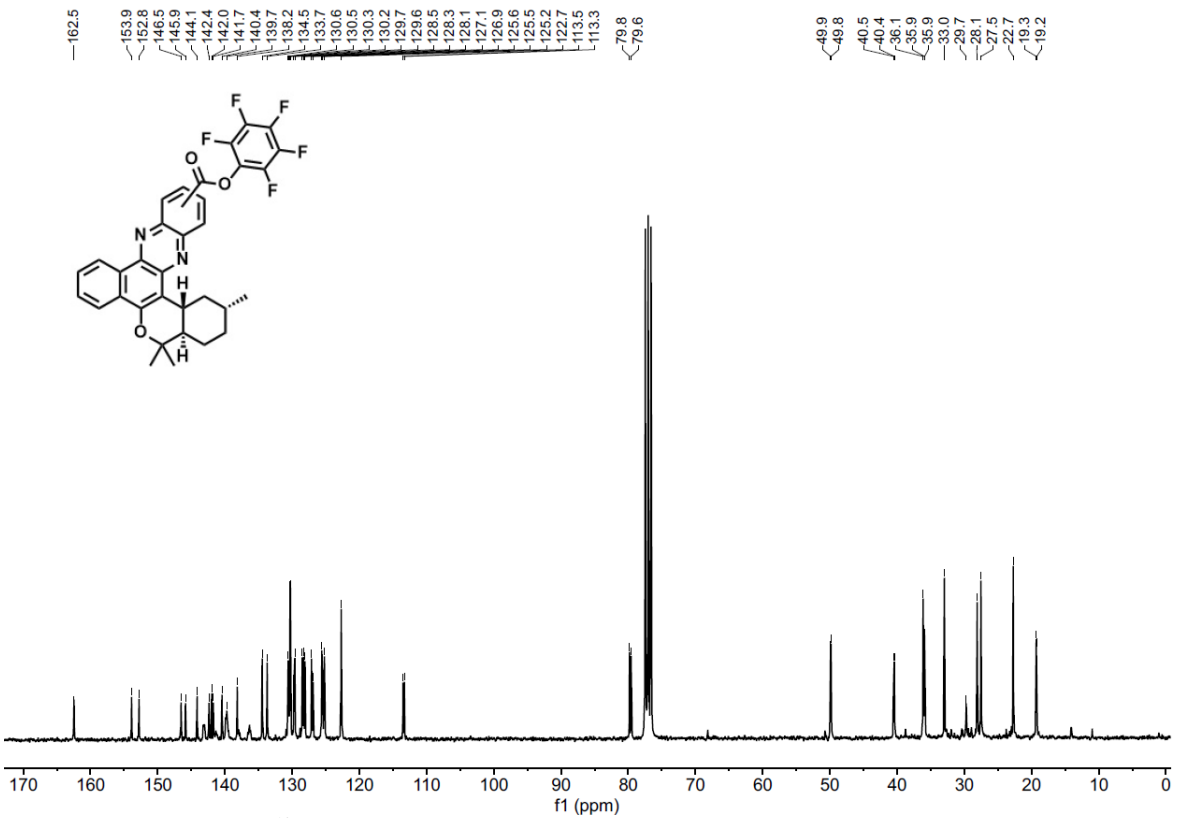


Figure B.65. ^{13}C NMR of activated ester **14** recorded in $CDCl_3$ at 75 MHz and 298 K.

Computational details (realized by Dr. Corentin Lefebvre)

Gaussian 16 Revision B.01[365] was used for geometry optimization calculations at the DFT(mPWPW91/Def2-TZVP) level of theory using implicit solvation (Solvation Model based on Density (SMD), Acetonitrile, ε = 35.688 D). Systematically, harmonic frequency analysis has been performed to verify each obtained optimized geometry corresponds to a minimum (no imaginary frequency). The first 100 singlet excited-state excitations have been calculated with Time-Dependent Density Functional Theory (TD-DFT) which has been carried out without the Tamm-Dancoff approximation at the same level of theory of geometry optimization. ORCA 4.2.1[444] has been used to incorporate the spin-orbit correction for the north-ester and south-aromatic sulfur **10f-1** at the same level of theory of Gaussian, without revealing any difference without it (see SI). Multiwfn[445] has been used for electron excitation analysis as well as NBO 7.0[446] program to give the major natural bond orbital (NBO) contributions in the excited-state of interest. IQMol[447] has been used for graphical outputs.

- Benchmark study of the functionals

11 different functionals have been benchmarked against the experimental UV-visible spectrum of the north-ester and south-aromatic sulfur **10f-1** (**Figure B.66**). The computational study has revealed no clear contribution of the spin-orbit coupling (SOC) correction to the prediction of the UV-visible spectrum. The best result concerning the position and the intensity of the absorption of interest has been given by the use of the mPW1PW91 functional thus employed for the study of the other benzophenazine derivatives.

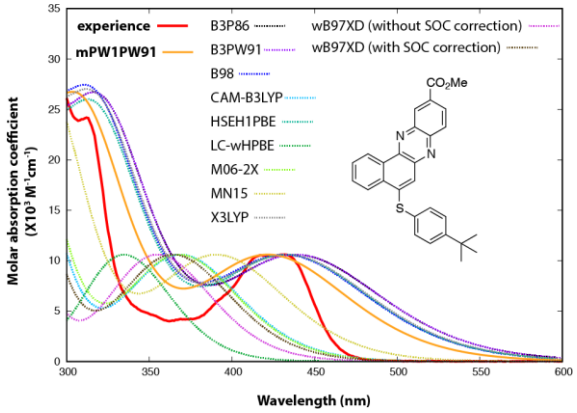
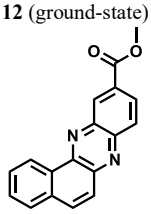


Figure B.66. Benchmark study of functionals towards the prediction of the UV-visible spectrum of the north-ester and south-aromatic sulfur **10f-1** (SOC = spin-orbit coupling, 100 first singlet excited-states). The theoretical spectra have been normalized against the experimental one at 432 nm.

- Cartesian coordinates and thermochemical data

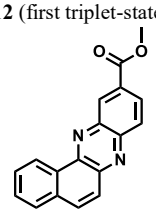
12 (ground-state) 	*E* = -953.271537253 Hartree DFT(mPW1PW91/Def2-TZVP) Zero-point correction = 0.261424 (Hartree/Particle) Thermal correction to Energy = 0.277825 Thermal correction to Enthalpy = 0.278769 Thermal correction to Gibbs Free Energy = 0.216439 Sum of electronic and zero-point Energies = -953.010114 Sum of electronic and thermal Energies = -952.993713 Sum of electronic and thermal Enthalpies = -952.992768 Sum of electronic and thermal Free Energies = -953.055098

Charge = 0, Multiplicity = 1

C	3.96492963	1.67109968	0.00007169
C	4.06389766	0.23824888	0.00010545
C	2.89266679	-0.54770360	0.00007346
C	1.60289451	0.11859942	-0.00000236
C	1.55334541	1.55599677	-0.00004852
C	2.77368657	2.30325188	-0.00000189
C	3.00195843	-1.94246341	0.00010752
C	4.24081448	-2.54627186	0.00016567
C	5.40272540	-1.77054195	0.00019505
C	5.31396936	-0.39611911	0.00016757
N	0.40144528	2.20657807	-0.00013645
C	-0.72406802	1.48007387	-0.00017571
C	-0.67469664	0.05597247	-0.00012234
N	0.49727121	-0.59656256	-0.00003520
C	-1.98336135	2.12580605	-0.00027145
C	-3.13157692	1.39307370	-0.00026575
C	-3.08444653	-0.02584634	-0.00021949
C	-1.88021261	-0.67692780	-0.00017129
C	-4.32280763	-0.85007170	-0.00026695
H	2.10050705	-2.54009555	0.00008420
H	4.31356480	-3.62662181	0.00018768
H	6.37318578	-2.25086089	0.00023838
H	6.20998090	0.21289183	0.00019077
H	2.70216817	3.38344104	-0.00003014
H	-1.83640378	-1.75795909	-0.00015904
H	-4.09071168	1.89091371	-0.00033543

H	-2.00609481	3.20820693	-0.00035097
H	4.88605324	2.24190258	0.00010306
O	-4.33216768	-2.05737202	-0.00143405
O	-5.42561105	-0.10661710	0.00114947
C	-6.66623287	-0.81710160	0.00085163
H	-6.75033025	-1.43898114	-0.88956777
H	-7.44137303	-0.05564262	0.00128038
H	-6.75024563	-1.43984271	0.89068334

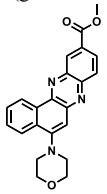
12 (first triplet-state)



E = -953.195723057 Hartree DFT(mPW1PW91/Def2-TZVP)
Zero-point correction = 0.256914 (Hartree/Particle)
Thermal correction to Energy = 0.273798
Thermal correction to Enthalpy = 0.274742
Thermal correction to Gibbs Free Energy = 0.210498
Sum of electronic and zero-point Energies = -952.938809
Sum of electronic and thermal Energies = -952.921925
Sum of electronic and thermal Enthalpies = -952.920981
Sum of electronic and thermal Free Energies = -952.985225

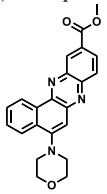
Charge = 0, Multiplicity = 3

C	3.99857379	1.64722426	-0.00005427
C	4.09531228	0.25807059	-0.00002910
C	2.90358083	-0.53419935	0.00001843
C	1.61143180	0.11460134	0.00001931
C	1.56614901	1.54106610	-0.00000404
C	2.73974607	2.27316075	-0.00003817
C	3.02398968	-1.92796589	0.00006365
C	4.26391955	-2.52729724	0.00005092
C	5.44133375	-1.75401998	-0.00000660
C	5.35903240	-0.39150434	-0.00004420
N	0.37118450	2.22819018	-0.00000951
C	-0.73732278	1.48290279	-0.00000212
C	-0.68830478	0.04948798	0.00002827
N	0.51196387	-0.62312401	0.00003464
C	-1.99604861	2.12046368	-0.00002085
C	-3.17048523	1.38581903	0.00000114
C	-3.11986255	-0.00105887	0.00004416
C	-1.86824320	-0.65934212	0.00005465
C	-4.34006109	-0.83671216	0.00002685
H	2.12599255	-2.53022783	0.00010714
H	4.33577366	-3.60776839	0.00008598
H	6.40623047	-2.24448959	-0.00002032
H	6.25262380	0.22072181	-0.00008534
H	2.67135173	3.35409481	-0.00005826
H	-1.83688637	-1.74081794	0.00007869
H	-4.12334180	1.89539102	-0.00001418
H	-2.01862713	3.20300538	-0.00006246
H	4.89882064	2.24795110	-0.00008649
O	-4.32779525	-2.04650560	-0.00023044
O	-5.46015230	-0.11545064	0.00034975
C	-6.68341896	-0.85294330	-0.00015247
H	-6.75395331	-1.47912708	-0.88896470
H	-7.47580569	-0.10928444	-0.00267226
H	-6.75656877	-1.47578173	0.89082847

10b (ground-state) 	*E* = -1239.91389224 Hartree DFT(mPW1PW91/Def2-TZVP) Zero-point correction = 0.377109 (Hartree/Particle) Thermal correction to Energy = 0.399022 Thermal correction to Enthalpy = 0.399966 Thermal correction to Gibbs Free Energy = 0.325363 Sum of electronic and zero-point Energies = -1239.536783 Sum of electronic and thermal Energies = -1239.514870 Sum of electronic and thermal Enthalpies = -1239.513926 Sum of electronic and thermal Free Energies = -1239.588529

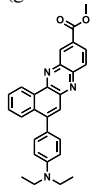
Charge = 0, Multiplicity = 1

C	-0.85407610	3.10780793	0.07809758
C	-1.85062658	4.05449255	0.00088546
C	-3.16105665	3.65514312	-0.25597077
C	-3.46677286	2.31676954	-0.37922951
C	-2.47927547	1.33059507	-0.24451170
C	-1.14398488	1.74640978	-0.06437216
H	0.17542813	3.40406607	0.22560984
H	-1.61166068	5.10502421	0.10837415
H	-3.94295027	4.39563654	-0.36920436
H	-4.48194196	2.02964484	-0.61033692
C	-0.06967612	0.76918925	-0.11450831
C	-0.40165778	-0.59885623	-0.41522856
C	-1.75826046	-0.98577172	-0.52716888
C	-2.78949664	-0.09566215	-0.37992298
H	-1.94738728	-2.04240314	-0.65049934
N	-4.10630449	-0.48287906	-0.43992661
C	-5.05904387	-0.08668676	0.59626474
C	-5.26665047	-1.21775636	1.58910669
H	-6.01242009	0.16747237	0.12379647
H	-4.69742569	0.78390206	1.13617726
O	-5.68105866	-2.41042190	0.95598614
H	-6.04931359	-0.94295536	2.29770240
H	-4.33722641	-1.39504289	2.14748291
C	-4.71696165	-2.83287354	0.01000694
C	-4.48628023	-1.75547944	-1.03245411
H	-5.10634441	-3.73513103	-0.46289104
H	-3.77937431	-3.08333699	0.52240166
H	-5.42671697	-1.59098589	-1.56858988
H	-3.74058207	-2.06920225	-1.76012111
N	1.17057184	1.14713150	0.07686040
C	2.13800098	0.21504875	-0.02643542
C	1.81702042	-1.13655215	-0.33832084
N	0.54702054	-1.52236003	-0.52568105
C	3.48115177	0.58255869	0.17142184
C	4.48136523	-0.35042950	0.05983471
C	4.16275344	-1.69541740	-0.25452922
C	2.86790172	-2.07802227	-0.44682064
H	3.71309680	1.61239663	0.40937722
H	4.95836969	-2.42198992	-0.34007582
H	2.61621027	-3.10391639	-0.68493278
C	5.88017346	0.09540172	0.27462328
O	6.19698574	1.22497322	0.56423256
O	6.75972298	-0.89168189	0.11230916
C	8.13385819	-0.54849157	0.30029177
H	8.43923135	0.21544733	-0.41391912
H	8.69240752	-1.46492465	0.12993447
H	8.30395147	-0.18840749	1.31436233

10b (first triplet-state) 	*E* = -1239.85507898 Hartree DFT(mPW1PW91/Def2-TZVP) Zero-point correction = 0.374353 (Hartree/Particle) Thermal correction to Energy = 0.396597 Thermal correction to Enthalpy = 0.397541 Thermal correction to Gibbs Free Energy = 0.320919 Sum of electronic and zero-point Energies = -1239.480726 Sum of electronic and thermal Energies = -1239.458482 Sum of electronic and thermal Enthalpies = -1239.457538 Sum of electronic and thermal Free Energies = -1239.534159

Charge = 0, Multiplicity = 3

C	-0.84749302	3.11202523	0.05384243
C	-1.83888148	4.05917402	-0.01288189
C	-3.16304343	3.66613448	-0.24814583
C	-3.47561623	2.33517824	-0.36207874
C	-2.48640216	1.33558297	-0.24407558
C	-1.13227762	1.74247479	-0.08160034
H	0.18397915	3.40557246	0.19221849
H	-1.59434869	5.10928033	0.08784992
H	-3.94120066	4.41142886	-0.35438186
H	-4.49603409	2.05734046	-0.58295246
C	-0.05116953	0.78438711	-0.11005754
C	-0.37020865	-0.57431310	-0.37508953
C	-1.70033823	-0.96436401	-0.51946287
C	-2.77700316	-0.06048545	-0.38369624
H	-1.88766884	-2.02110436	-0.64985799
N	-4.03954768	-0.56878177	-0.32398769
C	-5.07053831	-0.07259302	0.57395645
C	-5.48217015	-1.19535924	1.52174371
H	-5.93492801	0.25558313	-0.00891473
H	-4.69091761	0.75929475	1.15815324
O	-5.91706568	-2.33987243	0.82869492
H	-6.31277454	-0.84786394	2.13600309
H	-4.63709080	-1.44407083	2.17591898
C	-4.89036915	-2.84254847	0.00411922
C	-4.43941076	-1.79197429	-0.99715851
H	-5.29070048	-3.70387609	-0.52955924
H	-4.03724502	-3.16640214	0.61320469
H	-5.28381098	-1.53315870	-1.64400076
H	-3.63906235	-2.16660920	-1.62726938
N	1.20479640	1.18547608	0.07637125
C	2.17484852	0.22859586	-0.02104492
C	1.85325988	-1.13922376	-0.31032492
N	0.58299160	-1.54294468	-0.47440260
C	3.51075876	0.57356186	0.15982505
C	4.52775965	-0.37611880	0.05790448
C	4.21018490	-1.71015312	-0.23147180
C	2.89873987	-2.08129157	-0.41158310
H	3.75984162	1.60312682	0.38159611
H	4.99713768	-2.44664557	-0.31139913
H	2.63695269	-3.10888698	-0.63283806
C	5.92064562	0.07040795	0.26169051
O	6.24228580	1.20750839	0.52565460
O	6.80788013	-0.91932757	0.12371457
C	8.17764813	-0.56415311	0.30580964
H	8.48301066	0.18349121	-0.42590440
H	8.74267068	-1.48113821	0.15970761
H	8.34616452	-0.17774394	1.31072832

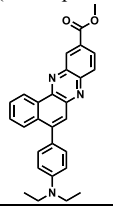
10c (ground-state) 	*E* = -1396.98565006 Hartree DFT(mPW1PW91/Def2-TZVP) Zero-point correction = 0.472459 (Hartree/Particle) Thermal correction to Energy = 0.500627 Thermal correction to Enthalpy = 0.501571 Thermal correction to Gibbs Free Energy = 0.411210 Sum of electronic and zero-point Energies = -1396.513191 Sum of electronic and thermal Energies = -1396.485023 Sum of electronic and thermal Enthalpies = -1396.484079 Sum of electronic and thermal Free Energies = -1396.574440

Charge = 0, Multiplicity = 1

C	1.10217773	3.34273054	-0.22369726
C	0.21928517	4.39183124	-0.34775434
C	-1.14902741	4.13660254	-0.42963262
C	-1.61918720	2.84315865	-0.35910931
C	-0.74493897	1.75714544	-0.19949156
C	0.64301507	2.02255454	-0.15998504
H	2.16769038	3.52351001	-0.18554849
H	0.58803231	5.40859345	-0.39826927
H	-1.84726729	4.95472531	-0.55549412
H	-2.68076958	2.66185218	-0.44323850
C	1.58421931	0.91980427	-0.09183237
C	1.07666154	-0.42290959	-0.09901552
C	-0.32906508	-0.63844129	-0.10893280
C	-1.22813412	0.38338878	-0.12689416
H	-0.66714116	-1.66529892	-0.05149221
C	-2.66546564	0.06778361	-0.08100021
N	2.87619840	1.15872302	-0.04038641
C	3.70918873	0.10563214	0.00115618
C	3.20760446	-1.22819771	-0.01271651
N	1.89078609	-1.46864438	-0.06047955
C	5.10076346	0.32103133	0.05824288
C	5.96515927	-0.74129368	0.09807777
C	5.46484028	-2.06917938	0.08097257
C	4.12407892	-2.30608128	0.02749060
H	5.47356239	1.33671684	0.07010564
H	6.15874750	-2.89721898	0.11147011
H	3.73169983	-3.31508094	0.01525680
C	7.42183490	-0.45317520	0.16087992
O	7.89258543	0.65887566	0.17917672
O	8.15743303	-1.56160245	0.19641947
C	9.57319210	-1.37731027	0.26432466
H	9.93162835	-0.83751991	-0.61143639
H	9.99920820	-2.37649903	0.28881204
H	9.84493017	-0.83086933	1.16677311
C	-3.54323336	0.68034171	0.81794355
C	-4.87321003	0.32343038	0.90172329
C	-5.42166619	-0.67614673	0.06967419
C	-4.53282613	-1.29485601	-0.83513582
C	-3.20254376	-0.93326010	-0.89432888
H	-2.56106667	-1.43767469	-1.60762743
H	-3.17481024	1.44235068	1.49381633
H	-5.49498656	0.83675190	1.62053208
H	-4.88065735	-2.07656109	-1.49471175
N	-6.73767815	-1.02485439	0.13762195
C	-7.63125071	-0.45846891	1.13078764
C	-8.28670685	0.84199227	0.69454017
H	-7.09327753	-0.31706692	2.06930131
H	-8.40113402	-1.20482280	1.33436846
H	-7.54391938	1.61922187	0.50815813
H	-8.96605307	1.20074334	1.47081048
H	-8.86529470	0.69765948	-0.22004533

C	-7.32589078	-1.98076721	-0.78188164
C	-7.21940444	-3.42419222	-0.31680712
H	-6.87337613	-1.86478855	-1.76770861
H	-8.37713816	-1.71120789	-0.89892747
H	-6.17800902	-3.73303926	-0.21364492
H	-7.70104205	-4.08887841	-1.03724995
H	-7.71166946	-3.55924085	0.64833879

10c (first triplet-state)



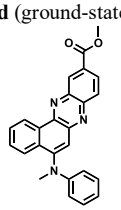
E = -1396.93148132 Hartree DFT(mPW1PW91/Def2-TZVP)
Zero-point correction = 0.471220 (Hartree/Particle)
Thermal correction to Energy = 0.499248
Thermal correction to Enthalpy = 0.500192
Thermal correction to Gibbs Free Energy = 0.410536
Sum of electronic and zero-point Energies = -1396.460262
Sum of electronic and thermal Energies = -1396.432233
Sum of electronic and thermal Enthalpies = -1396.431289
Sum of electronic and thermal Free Energies = -1396.520945

Charge = 0, Multiplicity = 3

C	1.08630438	3.37393735	-0.14376654
C	0.22398157	4.43749262	-0.23771533
C	-1.15129507	4.20469654	-0.37282452
C	-1.63599568	2.92051865	-0.37732583
C	-0.78120024	1.80547324	-0.23906377
C	0.61855481	2.04753598	-0.15708904
H	2.15310980	3.53635994	-0.07122326
H	0.60569716	5.45100695	-0.23012815
H	-1.83443166	5.03731124	-0.48789855
H	-2.69592310	2.76275151	-0.52005210
C	1.55952463	0.95135070	-0.11985833
C	1.05484760	-0.37269427	-0.22602453
C	-0.33042668	-0.57934084	-0.30727724
C	-1.26152481	0.45246516	-0.26101033
H	-0.66627851	-1.60877719	-0.33741577
C	-2.66347742	0.08732007	-0.15392110
N	2.86381952	1.19895632	-0.00692595
C	3.69777970	0.12102125	-0.00772441
C	3.18777315	-1.21405245	-0.12770866
N	1.87258403	-1.45752925	-0.23070950
C	5.07445424	0.30754569	0.10988557
C	5.95860467	-0.76979964	0.10997931
C	5.45555126	-2.07528086	-0.01178411
C	4.10397327	-2.28972807	-0.12841600
H	5.45725886	1.31591514	0.20273215
H	6.13679722	-2.91485624	-0.01308130
H	3.70786626	-3.29401604	-0.22129210
C	7.39872547	-0.49334822	0.23912321
O	7.88135724	0.61386091	0.34293243
O	8.14568757	-1.60518238	0.23188460
C	9.55292424	-1.41516888	0.35637834
H	9.93894671	-0.82112069	-0.47191720
H	9.98927814	-2.41060067	0.33454320
H	9.79582633	-0.92268084	1.29787192
C	-3.55647356	0.76207857	0.70834661
C	-4.86260748	0.38610800	0.83753116
C	-5.38969499	-0.69735136	0.08188011
C	-4.49139994	-1.38979975	-0.77721094
C	-3.18200138	-1.01594540	-0.86918477
H	-2.53406448	-1.56341116	-1.54085534
H	-3.19180795	1.57646523	1.31846191
H	-5.49108292	0.92997583	1.52603229
H	-4.83397230	-2.22838647	-1.36411914

N	-6.67922851	-1.05956196	0.18304489
C	-7.60015335	-0.43092768	1.12545136
C	-8.29017593	0.78734422	0.53668566
H	-7.06610259	-0.17914873	2.03856801
H	-8.33786263	-1.18933596	1.38610399
H	-7.57199170	1.57157533	0.29600540
H	-9.00065502	1.18134376	1.26449613
H	-8.83870170	0.52685206	-0.36942721
C	-7.26486712	-2.11176380	-0.64181608
C	-7.15100993	-3.48298161	0.00144899
H	-6.80229265	-2.09888249	-1.62570883
H	-8.31332156	-1.84757058	-0.77739183
H	-6.10811264	-3.77741352	0.12145636
H	-7.64670475	-4.21775900	-0.63425067
H	-7.63223107	-3.49831273	0.98015512

10d (ground-state)



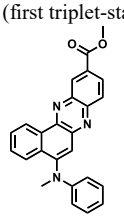
E = -1279.02311426 Hartree DFT(mPW1PW91/Def2-TZVP)
Zero-point correction = 0.387618 (Hartree/Particle)
Thermal correction to Energy = 0.411301
Thermal correction to Enthalpy = 0.412245
Thermal correction to Gibbs Free Energy = 0.333241
Sum of electronic and zero-point Energies = -1278.635497
Sum of electronic and thermal Energies = -1278.611813
Sum of electronic and thermal Enthalpies = -1278.610869
Sum of electronic and thermal Free Energies = -1278.689874

Charge = 0, Multiplicity = 1

C	-0.67245788	2.74188271	-0.41201197
C	-1.74525441	3.58280581	-0.60203601
C	-3.00931856	3.04408982	-0.83735590
C	-3.19290615	1.67838531	-0.84008318
C	-2.12398145	0.80210876	-0.60631436
C	-0.83757233	1.35227455	-0.42750953
H	0.32122042	3.14246460	-0.26560238
H	-1.60295554	4.65605681	-0.59068426
H	-3.85225401	3.69749533	-1.02442810
H	-4.17733103	1.28243695	-1.03902180
C	0.31739044	0.47726367	-0.32420521
C	0.12007480	-0.93988720	-0.45712723
C	-1.19396988	-1.45754912	-0.59444672
C	-2.29491943	-0.65110859	-0.61714402
H	-1.28860222	-2.53337806	-0.62689410
N	1.51264371	0.98606897	-0.13950111
C	2.55662047	0.13865975	-0.08203259
C	2.36609922	-1.26553098	-0.22072854
N	1.14303165	-1.78250580	-0.40632802
C	3.85453413	0.64626262	0.11660310
C	4.93023873	-0.20239893	0.17443281
C	4.74044838	-1.60062277	0.03429972
C	3.49362816	-2.11787499	-0.15770029
H	3.98939791	1.71478881	0.22168183
H	5.59656266	-2.25863296	0.08145090
H	3.33850452	-3.18411522	-0.26486961
C	6.27608620	0.38917041	0.38488983
O	6.48566606	1.57228914	0.50960034
O	7.23613973	-0.53246550	0.42202727
C	8.56630702	-0.04977220	0.62171862
H	8.85816187	0.61555876	-0.19014024
H	9.20134776	-0.93147514	0.62967372
H	8.64394298	0.47771938	1.57176439
N	-3.56885473	-1.18448188	-0.74374296
C	-3.68633000	-2.53390049	-1.27528530

H	-3.05932148	-2.63535273	-2.15964666
H	-4.71828189	-2.71544476	-1.56321346
H	-3.39680933	-3.29545149	-0.54270751
C	-4.59359755	-0.79419527	0.15592219
C	-4.29528567	-0.40846904	1.46100119
C	-5.30911395	-0.02844843	2.32828447
C	-6.63254471	-0.04752574	1.91479548
C	-6.93372514	-0.44714514	0.61862994
C	-5.92592184	-0.81345689	-0.25732558
H	-6.17120480	-1.09746643	-1.27280861
H	-3.26729024	-0.41005032	1.80028994
H	-5.05870145	0.27122176	3.33868758
H	-7.42318716	0.24392398	2.59457759
H	-7.96256139	-0.46256305	0.28024897

10d (first triplet-state)



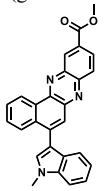
E = -1278.95993022 Hartree DFT(mPW1PW91/Def2-TZVP)
Zero-point correction = 0.384595 (Hartree/Particle)
Thermal correction to Energy = 0.408744
Thermal correction to Enthalpy = 0.409689
Thermal correction to Gibbs Free Energy = 0.328603
Sum of electronic and zero-point Energies -1278.575335
Sum of electronic and thermal Energies = -1278.551186
Sum of electronic and thermal Enthalpies = -1278.550242
Sum of electronic and thermal Free Energies = -1278.631327

Charge = 0, Multiplicity = 3

C	-0.68413740	2.72490181	-0.41712247
C	-1.75142033	3.56598358	-0.60952954
C	-3.02804561	3.02934662	-0.82190459
C	-3.21909100	1.67148971	-0.79618335
C	-2.14836453	0.78268879	-0.56174566
C	-0.84410934	1.32911406	-0.40624269
H	0.31268674	3.12233384	-0.28454258
H	-1.60433187	4.63875348	-0.61705280
H	-3.86826033	3.68494132	-1.01328896
H	-4.21014698	1.28274479	-0.97765914
C	0.32099635	0.47947999	-0.28523556
C	0.13507690	-0.92723052	-0.37707881
C	-1.14369627	-1.45081284	-0.52522872
C	-2.30086325	-0.64272839	-0.56134483
H	-1.23588084	-2.52804964	-0.53928065
N	1.52395138	1.01669809	-0.12032212
C	2.58166450	0.15130365	-0.05925894
C	2.39542019	-1.26737793	-0.16489833
N	1.17698993	-1.80732649	-0.31183301
C	3.87058542	0.64361305	0.10655581
C	4.97337481	-0.21060135	0.16677842
C	4.78920868	-1.59585003	0.05993605
C	3.52561510	-2.11155435	-0.10283496
H	4.01664419	1.71280270	0.18846833
H	5.64213471	-2.25804290	0.10581607
H	3.36650477	-3.17979566	-0.18570463
C	6.31102698	0.39019016	0.34216540
O	6.51810801	1.57884799	0.44319540
O	7.28743410	-0.52110344	0.37886222
C	8.61149362	-0.01643858	0.54637058
H	8.88120733	0.64130347	-0.27959732
H	9.26072770	-0.88811729	0.55570003
H	8.70153948	0.52673193	1.48680192
N	-3.51713022	-1.27746375	-0.58124982
C	-3.63144625	-2.59914515	-1.18283694
H	-2.93278974	-2.69514706	-2.00819010

H	-4.64035390	-2.72973314	-1.56372702
H	-3.44572453	-3.37812400	-0.43933946
C	-4.61838807	-0.82235630	0.17420505
C	-4.40871055	-0.30602191	1.45419618
C	-5.48553206	0.11334982	2.21229126
C	-6.77752869	0.02710228	1.70762639
C	-6.98487753	-0.48938006	0.43601466
C	-5.91541412	-0.91768034	-0.33128967
H	-6.08659794	-1.29136867	-1.33178564
H	-3.40469891	-0.25676594	1.85413163
H	-5.31560859	0.49861021	3.20975445
H	-7.61798810	0.35719648	2.30465309
H	-7.98710336	-0.55389984	0.03178808

10e (ground-state)



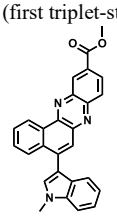
E = -1355.26902521 Hartree DFT(mPW1PW91/Def2-TZVP)
Zero-point correction = 0.400273 (Hartree/Particle)
Thermal correction to Energy = 0.425119
Thermal correction to Enthalpy = 0.426063
Thermal correction to Gibbs Free Energy = 0.344071
Sum of electronic and zero-point Energies = -1354.868752
Sum of electronic and thermal Energies = -1354.843906
Sum of electronic and thermal Enthalpies = -1354.842962
Sum of electronic and thermal Free Energies = -1354.924954

Charge = 0, Multiplicity = 1

C	0.24564565	3.35022013	-0.47109971
C	-0.66758606	4.35925376	-0.67936573
C	-2.03090859	4.06915557	-0.66378959
C	-2.46435391	2.78471609	-0.41527114
C	-1.55789603	1.74345791	-0.16701166
C	-0.17645056	2.03923157	-0.22475927
H	1.30689317	3.55518002	-0.50445575
H	-0.32692890	5.36919636	-0.86993026
H	-2.75480490	4.85180292	-0.85378236
H	-3.52332384	2.57334193	-0.42938772
C	0.79644567	0.97474446	-0.06004388
C	0.32438919	-0.36530034	0.14185755
C	-1.07300605	-0.60965176	0.22487207
C	-2.00194504	0.37990263	0.10624389
H	-1.37723385	-1.62608961	0.43604751
C	-3.41540179	0.04258599	0.25201946
N	2.08242295	1.24342535	-0.10975683
C	2.94406393	0.22217035	0.03009844
C	2.47741469	-1.10963277	0.22903150
N	1.16676263	-1.37967610	0.28350481
C	4.33044672	0.46917224	-0.02223176
C	5.22340560	-0.56103029	0.11479764
C	4.75788066	-1.88683830	0.31313690
C	3.42283601	-2.15364261	0.36937919
H	4.67646385	1.48309721	-0.17392900
H	5.47420926	-2.68898439	0.42035204
H	3.05688498	-3.16141736	0.52010316
C	6.67313789	-0.24140054	0.04650988
O	7.11512483	0.87089862	-0.11503661
O	7.43812764	-1.32180568	0.18247645
C	8.84987638	-1.10597113	0.12533897
H	9.13281031	-0.67810813	-0.83573585
H	9.30273463	-2.08607488	0.24729964
H	9.16859238	-0.44246763	0.92850225
C	-4.36623327	0.72782602	0.97658551
N	-5.55387276	0.06889267	0.96218773
C	-5.41750299	-1.06975093	0.21137326

C	-4.08186700	-1.13185528	-0.24921937
H	-4.26948843	1.63943574	1.54405326
C	-6.76189780	0.49470611	1.62537934
H	-7.09020884	-0.25687204	2.34445343
H	-7.55957307	0.66249738	0.90021220
H	-6.56389422	1.42462155	2.15246504
C	-6.36495919	-2.03830389	-0.10679139
C	-5.95806570	-3.08861652	-0.90738551
C	-4.64250914	-3.16579408	-1.38619440
C	-3.70527718	-2.20143078	-1.06827970
H	-2.69632920	-2.27721689	-1.45321378
H	-6.66785168	-3.86229999	-1.17292344
H	-4.35762282	-3.99797866	-2.01828928
H	-7.38263081	-1.97044228	0.25600712

10e (first triplet-state)



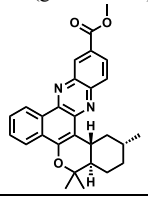
E = -1355.20774614Hartree DFT(mPW1PW91/Def2-TZVP)
Zero-point correction = 0.397535 (Hartree/Particle)
Thermal correction to Energy = 0.422591
Thermal correction to Enthalpy = 0.423535
Thermal correction to Gibbs Free Energy = 0.340428
Sum of electronic and zero-point Energies -1354.810211
Sum of electronic and thermal Energies = -1354.785156
Sum of electronic and thermal Enthalpies = -1354.784211
Sum of electronic and thermal Free Energies = -1354.867319

Charge = 0, Multiplicity = 3

C	0.23131552	3.39007107	-0.39499557
C	-0.66617324	4.41652114	-0.57052923
C	-2.03643034	4.13741175	-0.63627831
C	-2.48346005	2.84745969	-0.49218227
C	-1.59176594	1.77835716	-0.25932289
C	-0.19782473	2.06217512	-0.25063163
H	1.29422029	3.58838999	-0.37617893
H	-0.31269102	5.43384457	-0.68333679
H	-2.74526268	4.93530442	-0.81948888
H	-3.54019517	2.64280547	-0.59503035
C	0.77871037	0.99892922	-0.12279853
C	0.30443884	-0.34331977	-0.04892592
C	-1.06384284	-0.59388219	-0.05093057
C	-2.03974766	0.42737994	-0.10000882
H	-1.37349610	-1.62277884	0.07275065
C	-3.39851033	0.05250718	0.12651080
N	2.07081928	1.28605801	-0.09208109
C	2.93749612	0.23109373	0.00050549
C	2.46281938	-1.11993961	0.06266825
N	1.15298057	-1.40626910	0.04676197
C	4.30736311	0.46289268	0.03538205
C	5.21979784	-0.58882940	0.12529413
C	4.75382420	-1.91039622	0.18236344
C	3.40470482	-2.16863430	0.15124802
H	4.66710931	1.48267797	-0.00913390
H	5.45852714	-2.72717707	0.25128269
H	3.03154221	-3.18456782	0.19617756
C	6.65882153	-0.26218231	0.15658149
O	7.10613442	0.86216553	0.10813625
O	7.43503428	-1.34659816	0.24505100
C	8.84152909	-1.11036349	0.28184950
H	9.17207416	-0.60399588	-0.62474635
H	9.30419045	-2.09149100	0.35052946
H	9.10958091	-0.50963496	1.15073809
C	-4.34990227	0.78666802	0.86163696
N	-5.49286799	0.10922423	0.96703990

C	-5.37226305	-1.10080341	0.29523449
C	-4.07171788	-1.17589364	-0.23787915
H	-4.23049730	1.73117724	1.36642446
C	-6.66980609	0.54124165	1.68364732
H	-6.90898854	-0.17310870	2.47125384
H	-7.51524003	0.61490472	0.99933598
H	-6.47513686	1.51526620	2.12383226
C	-6.31969310	-2.09050005	0.11652764
C	-5.94370875	-3.19579582	-0.63548244
C	-4.67057862	-3.28534255	-1.19791766
C	-3.73151367	-2.28153161	-1.01620238
H	-2.76057724	-2.35919243	-1.48628813
H	-6.65694353	-3.99383859	-0.79758345
H	-4.41323649	-4.15122736	-1.79448228
H	-7.31414553	-2.00675264	0.53421513

10a (ground-state)



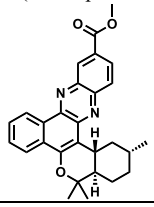
E = -1419.29645220Hartree DFT(mPW1PW91/Def2-TZVP)
Zero-point correction = 0.507326 (Hartree/Particle)
Thermal correction to Energy = 0.534992
Thermal correction to Enthalpy = 0.535936
Thermal correction to Gibbs Free Energy = 0.450264
Sum of electronic and zero-point Energies = -1418.789126
Sum of electronic and thermal Energies = -1418.761460
Sum of electronic and thermal Enthalpies = -1418.760516
Sum of electronic and thermal Free Energies = -1418.846188

Charge = 0, Multiplicity = 1

C	0.12237883	3.93675806	-0.66141109
C	-0.70982757	5.02853346	-0.78155858
C	-2.08659373	4.87725511	-0.61413967
C	-2.62009257	3.63728705	-0.33358639
C	-1.78833032	2.51618186	-0.22221661
C	-0.40185515	2.67125722	-0.38097457
H	1.19198482	4.04426844	-0.77901945
H	-0.29407239	6.00383636	-1.00144776
H	-2.74040182	5.73585301	-0.70365146
H	-3.68633772	3.52084135	-0.20282993
C	0.45424227	1.51279708	-0.21039660
C	-2.33754458	1.19766711	0.03683523
C	-1.57129043	0.06504591	0.04689641
C	-0.14382217	0.22012561	0.02774005
N	1.75599896	1.66942893	-0.25218525
N	0.62466036	-0.83120206	0.27231953
C	2.53520147	0.59461877	-0.03736294
C	1.95544369	-0.67018777	0.25027954
O	-3.65535975	1.20201287	0.25188992
C	-4.26932050	0.01813214	0.84154353
C	-3.74028334	-1.17959826	0.05987370
C	-5.75326829	0.23799163	0.63190609
C	-3.93281544	-0.00510418	2.32316283
C	-2.21627272	-1.29230038	0.15537253
H	-2.85793305	-0.04985802	2.49821641
H	-4.39067063	-0.87471904	2.79537055
H	-4.32403240	0.89033424	2.80825566
H	-6.00509829	0.21678875	-0.42970586
H	-6.04613868	1.20617595	1.04072629
H	-6.33052843	-0.53154005	1.14258750
C	-4.37695509	-2.52276809	0.39271510
H	-3.98067381	-0.95707422	-0.98781406
C	-3.89867093	-3.58935453	-0.58533979
H	-5.46556785	-2.45292916	0.35109937
H	-4.11393511	-2.81139205	1.41539677

C	-2.37795562	-3.67526264	-0.66689179
H	-4.29070513	-3.35689676	-1.58275534
H	-4.31053179	-4.56392751	-0.30775139
C	-1.76452293	-2.29797297	-0.91234936
H	-2.01081708	-4.02475890	0.30676497
C	-1.93433126	-4.67289071	-1.72487538
H	-2.07227316	-1.93071936	-1.89859300
H	-0.67936546	-2.38074083	-0.92152769
H	-1.95575829	-1.71984524	1.13207777
H	-2.26905619	-4.36193755	-2.71870910
H	-0.84587651	-4.76416712	-1.75407311
H	-2.34762310	-5.66589731	-1.53144971
C	3.93613370	0.72618738	-0.07730483
C	2.80734392	-1.76914154	0.51165571
C	4.16193191	-1.61626778	0.47203181
C	4.73994414	-0.35705102	0.17059313
H	2.35757110	-2.72784674	0.73747717
H	4.80661027	-2.46089027	0.66968812
H	4.36733712	1.69302807	-0.30176686
C	6.21101290	-0.16239676	0.11467440
O	6.74732764	0.88707688	-0.15049311
O	6.88268118	-1.27859810	0.39017252
C	8.30792189	-1.18097809	0.35580027
H	8.66011993	-0.45551789	1.08830608
H	8.64804490	-0.89087850	-0.63774876
H	8.67710885	-2.17249300	0.60334571

10a (first triplet-state)

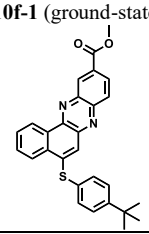


E = -1419.22698295 Hartree DFT(mPW1PW91/Def2-TZVP)
Zero-point correction = 0.504093 (Hartree/Particle)
Thermal correction to Energy = 0.532148
Thermal correction to Enthalpy = 0.533092
Thermal correction to Gibbs Free Energy = 0.445470
Sum of electronic and zero-point Energies -1418.722890
Sum of electronic and thermal Energies = -1418.694835
Sum of electronic and thermal Enthalpies = -1418.693891
Sum of electronic and thermal Free Energies = -1418.781512

Charge = 0, Multiplicity = 3

C	0.04116726	3.92022832	-0.69706158
C	-0.79541245	5.00184488	-0.85067021
C	-2.18240323	4.85742064	-0.68940572
C	-2.71097339	3.63098777	-0.38424791
C	-1.87130159	2.50400248	-0.24107681
C	-0.46843456	2.65134547	-0.39096721
H	1.11077602	4.03329127	-0.80706511
H	-0.38072828	5.97206461	-1.09450050
H	-2.83326595	5.71418087	-0.80840807
H	-3.77850476	3.51090881	-0.26158595
C	0.41362762	1.52606746	-0.17523625
C	-2.39526655	1.22822818	0.06619708
C	-1.55158782	0.06646171	0.08977413
C	-0.15616631	0.24714203	0.09540880
N	1.72574119	1.71142002	-0.24439814
N	0.62768999	-0.83716482	0.35433056
C	2.52295710	0.62304646	-0.01227902
C	1.95656804	-0.65353871	0.29784059
O	-3.68145592	1.15842572	0.34470250
C	-4.25690434	-0.06931306	0.91396765
C	-3.70982111	-1.21642388	0.07740589
C	-5.74752560	0.12333575	0.73645487
C	-3.88623864	-0.11505494	2.38524442

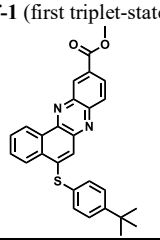
C	-2.18278373	-1.28857093	0.13219631
H	-2.80755863	-0.14652117	2.53942861
H	-4.32242190	-1.00184527	2.84539621
H	-4.28159437	0.76326060	2.89668917
H	-6.01805408	0.13235570	-0.32030226
H	-6.05700999	1.06701991	1.18715235
H	-6.29227659	-0.68036298	1.22948540
C	-4.29037823	-2.59181216	0.38144607
H	-3.98539685	-0.96834464	-0.95545440
C	-3.80345620	-3.60475416	-0.64800486
H	-5.38100019	-2.55689845	0.37119097
H	-3.98797639	-2.90447178	1.38582169
C	-2.28323229	-3.63896278	-0.77372318
H	-4.23097408	-3.35008879	-1.62492037
H	-4.17452149	-4.60156440	-0.39442399
C	-1.71787562	-2.23686697	-0.98656397
H	-1.87749306	-4.00994487	0.17607709
C	-1.83870890	-4.58091447	-1.88095515
H	-2.05968890	-1.84183613	-1.94958804
H	-0.63075854	-2.27664910	-1.01229380
H	-1.87624382	-1.74731182	1.08173050
H	-2.21212305	-4.24485499	-2.85238548
H	-0.74935451	-4.63534673	-1.94319741
H	-2.21509016	-5.59275549	-1.71235063
C	3.90344566	0.74801366	-0.06054088
C	2.81644305	-1.74085915	0.55411675
C	4.18461049	-1.59076766	0.50099535
C	4.73948168	-0.34539938	0.19075601
H	2.37074721	-2.69936977	0.79001792
H	4.82942452	-2.43518629	0.69851825
H	4.33760636	1.71132062	-0.29424605
C	6.20044672	-0.13402076	0.11796589
O	6.72229735	0.92392376	-0.15326021
O	6.89815819	-1.24084189	0.38414705
C	8.31885178	-1.11476853	0.33193997
H	8.66805913	-0.38436705	1.06135559
H	8.64285685	-0.81598525	-0.66467727
H	8.71177732	-2.09912817	0.57243181

10f-1 (ground-state) 	*E* = -1739.85339143 Hartree DFT(mPW1PW91/Def2-TZVP) Zero-point correction = 0.455554 (Hartree/Particle) Thermal correction to Energy = 0.484075 Thermal correction to Enthalpy = 0.485019 Thermal correction to Gibbs Free Energy = 0.393271 Sum of electronic and zero-point Energies = -1739.397837 Sum of electronic and thermal Energies = -1739.369316 Sum of electronic and thermal Enthalpies = -1739.368372 Sum of electronic and thermal Free Energies = -1739.460121

Charge = 0, Multiplicity = 1

C	-1.97983652	4.01539931	-0.02210058
C	-1.51772186	5.31249332	-0.03225905
C	-0.14580277	5.56030941	-0.02765320
C	0.74695346	4.51095981	-0.01303132
C	0.30060466	3.18244012	-0.00230428
C	-1.08918517	2.93716304	-0.00691727
H	-3.04152707	3.81013820	-0.02566721
H	-2.21861150	6.13758221	-0.04378604
H	0.22285298	6.57815925	-0.03556426
H	1.80744463	4.72702716	-0.00979829
C	-1.57942567	1.57057786	0.00357217

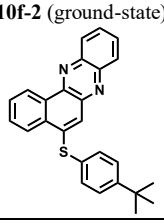
C	-0.62966480	0.49415731	0.02140248
C	0.76449192	0.78185241	0.02726088
C	1.22289716	2.05762597	0.01405388
H	1.44041079	-0.06192345	0.04109323
N	-2.87230322	1.33734335	-0.00346477
C	-3.28095830	0.05721673	0.00597916
C	-2.34019376	-1.01249242	0.02402691
N	-1.02201539	-0.77110744	0.03176335
C	-4.65969512	-0.23311852	-0.00267658
C	-5.09330244	-1.53284472	0.00578824
C	-4.15575684	-2.59753813	0.02400474
C	-2.81662118	-2.34482764	0.03306738
H	-5.36763195	0.58512497	-0.01656568
H	-4.51308099	-3.61745266	0.03065394
H	-2.09289089	-3.14995863	0.04691809
C	-6.55898187	-1.77915889	-0.00513172
O	-7.39265655	-0.90553543	-0.02015926
O	-6.85589857	-3.07629236	0.00328694
C	-8.24708703	-3.40435505	-0.00671412
H	-8.74168371	-3.00088052	0.87610890
H	-8.29368083	-4.48980648	0.00082934
H	-8.72596313	-3.01391796	-0.90394583
S	2.93495817	2.45873356	0.01601320
C	3.74380097	0.88579995	0.01864235
C	4.14860250	0.31202955	1.21549526
C	4.84015555	-0.89177936	1.21179667
C	5.14634953	-1.55073413	0.02354638
C	4.73454112	-0.95153002	-1.17065697
C	4.04801323	0.24889070	-1.18130093
H	3.74614842	0.69239439	-2.12186579
H	3.92551914	0.80276089	2.15459520
H	5.14070909	-1.31115336	2.16174060
H	4.95533327	-1.42743900	-2.11771927
C	5.90168113	-2.87585713	-0.01363542
C	6.27784423	-3.36767639	1.38131851
C	7.18878508	-2.70391286	-0.82987298
C	5.02012406	-3.93879694	-0.68105546
H	6.93243353	-2.66350917	1.89885466
H	6.81241761	-4.31562670	1.29652722
H	5.39767573	-3.53857780	2.00434924
H	4.09545536	-4.09006095	-0.11985117
H	5.55247007	-4.89189955	-0.72042114
H	4.75541191	-3.66078354	-1.70220877
H	7.83936512	-1.94947268	-0.38215589
H	6.97994983	-2.40508281	-1.85812252
H	7.73714559	-3.64816721	-0.86119188

10f-1 (first triplet-state) 	*E* = -1739.78509641 Hartree DFT(mPW1PW91/Def2-TZVP) Zero-point correction = 0.452594 (Hartree/Particle) Thermal correction to Energy = 0.481403 Thermal correction to Enthalpy = 0.482347 Thermal correction to Gibbs Free Energy = 0.389679 Sum of electronic and zero-point Energies -1739.332503 Sum of electronic and thermal Energies = -1739.303693 Sum of electronic and thermal Enthalpies = -1739.302749 Sum of electronic and thermal Free Energies = -1739.395417

Charge = 0, Multiplicity = 3

C	1.77908030	3.91441003	0.59279678
C	1.24717785	5.16667467	0.80438284
C	-0.12716724	5.38048757	0.63919126

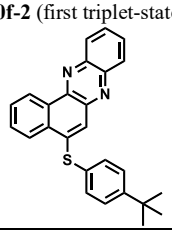
C	-0.94327361	4.34654411	0.25943610
C	-0.42152471	3.05615835	0.01303603
C	0.97361179	2.84093562	0.19780028
H	2.83716210	3.73816211	0.73011758
H	1.88924249	5.98309880	1.10974270
H	-0.54972913	6.35993423	0.82406943
H	-2.00842937	4.51593129	0.16512640
C	1.56021145	1.52769505	-0.01258137
C	0.69897709	0.45532635	-0.42042216
C	-0.65181509	0.68601013	-0.60229389
C	-1.23362736	1.97021359	-0.40286289
H	-1.26436978	-0.13823843	-0.94282337
N	2.84854693	1.34873656	0.17068221
C	3.34141883	0.08363090	-0.03553465
C	2.48552124	-0.98894531	-0.44215358
N	1.17374823	-0.80420672	-0.64355183
C	4.69195796	-0.16588743	0.14940908
C	5.22484190	-1.44075619	-0.05233899
C	4.38802150	-2.49172556	-0.45022195
C	3.04518433	-2.27001041	-0.64129824
H	5.33994207	0.64486720	0.45568882
H	4.80040962	-3.47840320	-0.60654156
H	2.38576838	-3.07198796	-0.94917627
C	6.67478369	-1.63157952	0.16675088
O	7.43241284	-0.75223302	0.50864114
O	7.06858178	-2.88734297	-0.05269689
C	8.45779790	-3.15324345	0.14120487
H	9.06331336	-2.54924493	-0.53394282
H	8.59003628	-4.20868942	-0.08153446
H	8.74849962	-2.94883391	1.17131527
S	-2.86537592	2.24454770	-0.88391142
C	-3.71215828	0.75987967	-0.48642750
C	-4.68587732	0.30857917	-1.37066585
C	-5.43062834	-0.81747355	-1.05990436
C	-5.22538499	-1.52491683	0.12417897
C	-4.24369675	-1.04712621	0.99904191
C	-3.49983697	0.08019747	0.71392571
H	-2.76594676	0.43953833	1.42367528
H	-4.85796451	0.82770045	-2.30558282
H	-6.17717287	-1.14576023	-1.76909636
H	-4.06007208	-1.55910809	1.93506054
C	-6.02272381	-2.77215127	0.48776670
C	-7.04453502	-3.13973736	-0.58456432
C	-6.76871180	-2.52890241	1.80603278
C	-5.05843800	-3.95200629	0.66466784
H	-7.77950713	-2.34661481	-0.73596768
H	-7.58406334	-4.03644043	-0.27447923
H	-6.56911747	-3.35411451	-1.54383104
H	-4.51191995	-4.15372460	-0.25909696
H	-5.61895553	-4.85117503	0.93019150
H	-4.33115729	-3.76533934	1.45599100
H	-7.46580239	-1.69326312	1.71389591
H	-6.08253163	-2.31064216	2.62550676
H	-7.34076209	-3.41920204	2.07669377

10f-2 (ground-state) 	*E* = -1511.93779309 Hartree DFT(mPW1PW91/Def2-TZVP) Zero-point correction = 0.412823 (Hartree/Particle) Thermal correction to Energy = 0.436655 Thermal correction to Enthalpy = 0.437600 Thermal correction to Gibbs Free Energy = 0.35764 Sum of electronic and zero-point Energies = -1511.524970 Sum of electronic and thermal Energies = -1511.501138 Sum of electronic and thermal Enthalpies = -1511.500193 Sum of electronic and thermal Free Energies = -1511.580152

Charge = 0, Multiplicity = 1

C	1.83716002	-3.74955315	-0.01669474
C	1.76166505	-2.34973644	0.00327005
C	2.96283564	-1.60850172	-0.02423564
C	4.18772383	-2.28318749	-0.06889141
C	4.23671864	-3.65897886	-0.08594093
C	3.05301706	-4.39570114	-0.05983548
C	0.49023502	-1.64577572	0.05087177
C	0.44677139	-0.29194674	0.07214812
C	1.63822894	0.49046947	0.04529811
C	2.91491262	-0.15772100	-0.00591258
N	4.03191652	0.53721479	-0.03530289
C	3.94333736	1.87643174	-0.01397482
C	2.67306089	2.52329609	0.04065419
N	1.53754059	1.81094605	0.06872800
C	5.12000791	2.66019039	-0.04496507
C	5.03449323	4.02251053	-0.02170966
C	3.77529392	4.66478961	0.03323728
C	2.62067349	3.93729863	0.06375850
S	-0.95371297	-2.65339955	0.08268876
C	-2.28656996	-1.49114513	0.05905963
C	-2.87953283	-1.08167300	1.24483773
C	-3.96777159	-0.21955372	1.21839377
C	-4.49181188	0.25279293	0.01754357
C	-3.88326481	-0.17777752	-1.16533201
C	-2.80090400	-1.03816609	-1.15287238
C	-5.68430670	1.20233600	-0.04688020
C	-5.25848487	2.49827088	-0.74818462
H	3.73344043	5.74669659	0.05078946
H	5.93517942	4.62291336	-0.04506216
C	-6.21896644	1.55660501	1.33796876
C	-6.81354867	0.54318014	-0.84846634
H	5.09841585	-1.70047785	-0.08949374
H	5.19210099	-4.16712987	-0.12006480
H	3.08549529	-5.47779083	-0.07397153
H	0.93083307	-4.34091327	0.00038547
H	-0.49172746	0.24377628	0.11013983
H	6.07519734	2.15160222	-0.08674545
H	1.64964725	4.41493952	0.10547597
H	-2.35283225	-1.35982018	-2.08469487
H	-2.49375442	-1.43433571	2.19315329
H	-4.40547669	0.07988252	2.16044772
H	-4.26227610	0.16088230	-2.12132579
H	-6.56610714	0.67385900	1.87872865
H	-7.06705680	2.23588022	1.23352063
H	-5.46615830	2.05839384	1.94923201
H	-4.45567881	2.99549856	-0.19941535
H	-6.10566292	3.18555019	-0.80566767
H	-4.90923144	2.31171147	-1.76472312
H	-7.14246980	-0.38345943	-0.37299528
H	-6.50330110	0.30973368	-1.86794180
H	-7.67120825	1.21735222	-0.90564129

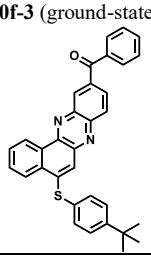
10f-2 (first triplet-state)	*E* = -1511.86731299 Hartree DFT(mPW1PW91/Def2-TZVP) Zero-point correction = 0.409536 (Hartree/Particle) Thermal correction to Energy = 0.433737 Thermal correction to Enthalpy = 0.434681 Thermal correction to Gibbs Free Energy = 0.353283 Sum of electronic and zero-point Energies -1511.457777 Sum of electronic and thermal Energies = -1511.433576 Sum of electronic and thermal Enthalpies = -1511.432632 Sum of electronic and thermal Free Energies = -1511.514030



Charge = 0, Multiplicity = 3

C	1.44872779	-3.77393488	-0.21560150
C	1.52176687	-2.37750871	-0.00130157
C	2.76553240	-1.72009111	-0.22728607
C	3.87027629	-2.47944233	-0.62842363
C	3.77529837	-3.84102493	-0.80818872
C	2.55045430	-4.49056153	-0.60323590
C	0.40908770	-1.60970181	0.42032909
C	0.54281204	-0.19836330	0.58819523
C	1.73667190	0.45869569	0.36871555
C	2.89360583	-0.28247832	-0.05211556
N	4.04598993	0.30371160	-0.27773552
C	4.10343383	1.66686121	-0.10411748
C	2.95850988	2.40998013	0.31652239
N	1.77919020	1.80892416	0.56411531
C	5.29643396	2.33983598	-0.33782752
C	5.38321337	3.71807374	-0.16810780
C	4.27002649	4.44891373	0.24198836
C	3.07269601	3.80488070	0.48170578
S	-1.03822854	-2.39011930	0.93950549
C	-2.32598187	-1.26534114	0.53173424
C	-3.36820968	-1.10549523	1.43708544
C	-4.44059609	-0.28707084	1.11840048
C	-4.50209051	0.39629288	-0.09503677
C	-3.44256257	0.21568340	-0.99039052
C	-2.37211834	-0.60548483	-0.69658309
C	-5.66363820	1.31046603	-0.46837443
C	-5.13066324	2.72707973	-0.71837694
H	4.34376932	5.52112241	0.37298073
H	6.32253706	4.22280278	-0.35625754
C	-6.72168705	1.37947134	0.62926834
C	-6.32699665	0.78819319	-1.74913789
H	4.80893337	-1.96921708	-0.79615854
H	4.64367986	-4.40810154	-1.11874926
H	2.46945667	-5.55815804	-0.76391421
H	0.50061685	-4.28109753	-0.08922946
H	-0.30116491	0.38422940	0.93286486
H	6.15953063	1.76689882	-0.65501876
H	2.19453253	4.35291180	0.80150071
H	-1.57962140	-0.74295487	-1.42086713
H	-3.34197769	-1.61117076	2.39438253
H	-5.23368784	-0.18060111	1.84505146
H	-3.45406138	0.71868301	-1.94884995
H	-7.16104117	0.40105304	0.83361883
H	-7.52691035	2.04410715	0.31103889
H	-6.31551911	1.77455728	1.56255705
H	-4.65148035	3.12935576	0.17677287
H	-5.95533536	3.39054211	-0.98853601
H	-4.40386014	2.74896446	-1.53160380
H	-6.71911990	-0.22077078	-1.60422166
H	-5.62833340	0.76411659	-2.58656005
H	-7.15956455	1.43861279	-2.02658510

10f-3 (ground-state)	*E* = -1856.36928013 Hartree DFT(mPW1PW91/Def2-TZVP) Zero-point correction = 0.503650 (Hartree/Particle) Thermal correction to Energy = 0.534211 Thermal correction to Enthalpy = 0.535156 Thermal correction to Gibbs Free Energy = 0.438265 Sum of electronic and zero-point Energies = -1855.865630 Sum of electronic and thermal Energies = -1855.835069 Sum of electronic and thermal Enthalpies = -1855.834124 Sum of electronic and thermal Free Energies = -1855.931015

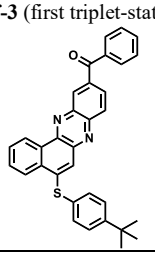


Charge = 0, Multiplicity = 1

C	4.79370441	-0.37736854	-1.27222830
C	4.63800205	0.38775874	-0.11993264
C	4.93364412	-0.17283942	1.11470812
C	5.36706272	-1.48902423	1.19572709
C	5.52184849	-2.27512954	0.05613593
C	5.22696706	-1.68751387	-1.17750361
S	4.15978894	2.08662130	-0.23533432
C	2.40507849	2.04360588	-0.12322591
C	1.72678525	3.32936679	-0.17959124
C	0.31886862	3.37327273	-0.09256115
C	-0.43302810	2.13953142	0.05128946
C	0.28145240	0.89531644	0.09923993
C	1.70238657	0.89195763	0.00896014
C	-0.33731609	4.60725631	-0.14502063
C	0.37275683	5.77924068	-0.28054646
C	1.76367396	5.74149071	-0.36702102
C	2.42762882	4.53519578	-0.31711510
N	-0.35437110	-0.25953421	0.22709245
C	-1.69161038	-0.22600611	0.31260660
C	-2.39879304	1.01047713	0.26957125
N	-1.74345060	2.17638125	0.13616944
C	-2.42265837	-1.42868452	0.45112083
C	-3.78404311	-1.40176063	0.52478336
C	-4.49209279	-0.17220670	0.48926898
C	-3.80364873	1.00866732	0.37428487
C	-5.97656997	-0.11370253	0.63412926
C	-6.81756873	-1.19366238	0.05122055
C	5.99631130	-3.72412753	0.11174797
C	4.91821437	-4.63156803	-0.49394804
O	-6.49191061	0.81822979	1.22278777
C	6.27213531	-4.18952960	1.53885663
C	7.28835121	-3.86473125	-0.70249741
H	-1.41642391	4.62298221	-0.07666250
H	-0.14863699	6.72721245	-0.31968967
H	2.32701722	6.65982474	-0.47349973
H	3.50766177	4.52967624	-0.38555863
H	2.19499459	-0.06948040	0.05178793
H	-4.32882187	1.95496535	0.35414095
H	-4.33179929	-2.32770569	0.63886913
H	-1.87513388	-2.36156001	0.49757301
H	4.57540801	0.05317637	-2.24149578
H	4.82552924	0.41614564	2.01686784
H	5.58693819	-1.89533211	2.17305602
H	5.33904035	-2.26075169	-2.08911230
H	7.05531870	-3.59739689	2.01654219
H	6.60731697	-5.22819594	1.52011474
H	5.37762488	-4.14133078	2.16314373
H	3.98280033	-4.55602639	0.06477154
H	5.24832612	-5.67242053	-0.46254487
H	4.71318786	-4.37713959	-1.53480044

H	8.07926249	-3.23080911	-0.29567633
H	7.13872809	-3.59184332	-1.74800471
H	7.63536607	-4.90011908	-0.67294315
C	-8.05171644	-1.46856653	0.64105536
C	-8.88462275	-2.43226810	0.10147131
C	-8.50382066	-3.11430745	-1.04822637
C	-7.28580201	-2.83451319	-1.65080737
C	-6.43918842	-1.88569338	-1.09816551
H	-8.34409523	-0.92388031	1.52953571
H	-9.83394530	-2.65204677	0.57379892
H	-9.15926886	-3.86348822	-1.47504730
H	-6.99299252	-3.35663011	-2.55302790
H	-5.49434376	-1.66713870	-1.57864574

10f-3 (first triplet-state)



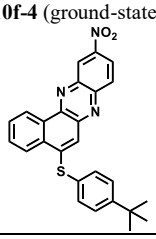
E = -1856.30174671 Hartree DFT(mPW1PW91/Def2-TZVP)
Zero-point correction = 0.500654 (Hartree/Particle)
Thermal correction to Energy = 0.531515
Thermal correction to Enthalpy = 0.532459
Thermal correction to Gibbs Free Energy = 0.434539
Sum of electronic and zero-point Energies -1855.80109
Sum of electronic and thermal Energies = -1855.770232
Sum of electronic and thermal Enthalpies = -1855.769288
Sum of electronic and thermal Free Energies = -1855.867208

Charge = 0, Multiplicity = 3

C	4.21501068	-0.36275735	-0.72673391
C	4.59932774	0.32456369	0.42562038
C	5.48919074	-0.26661570	1.31545804
C	5.98115842	-1.53597595	1.05784302
C	5.60089752	-2.24970806	-0.07807744
C	4.70731254	-1.63117893	-0.95924906
S	4.09106317	1.97407984	0.74492277
C	2.41833273	2.01422459	0.33042120
C	1.82982952	3.21707396	-0.13983350
C	0.41543323	3.27916972	-0.28658522
C	-0.41653986	2.12698767	0.01709986
C	0.22288824	0.93113648	0.48303027
C	1.59690017	0.89262731	0.62694281
C	-0.16831962	4.46899571	-0.73508849
C	0.59904354	5.57215822	-1.03427912
C	1.99249606	5.51162648	-0.90659506
C	2.59399109	4.35731329	-0.47636806
N	-0.48991538	-0.18982067	0.79907326
C	-1.81436366	-0.11899175	0.62811025
C	-2.45110085	1.07794898	0.16165099
N	-1.71951634	2.20123124	-0.13499678
C	-2.61457862	-1.24532404	0.92152812
C	-3.97769811	-1.20780812	0.74641520
C	-4.60369476	-0.03889242	0.28937480
C	-3.82680279	1.09413805	0.01590783
C	-6.07506759	0.07232261	0.16427944
C	-6.90134193	-1.14709382	-0.06389731
C	6.12398537	-3.64769208	-0.38673458
C	4.94096149	-4.61886015	-0.48965841
O	-6.61879493	1.16269982	0.24966590
C	7.07745302	-4.16017163	0.68900457
C	6.87209531	-3.62024706	-1.72587126
H	-1.24370413	4.50417307	-0.84273298
H	0.12613933	6.48274436	-1.37956632
H	2.59816201	6.37238260	-1.16010718
H	3.67372368	4.31228037	-0.41076619

H	2.04102274	-0.01548012	1.01247682
H	-4.30803974	2.00192094	-0.32439126
H	-4.56990888	-2.07870076	0.99167954
H	-2.12351510	-2.13756178	1.28967789
H	3.54584485	0.09822846	-1.44170448
H	5.79311909	0.25765883	2.21303658
H	6.66846721	-1.96968431	1.77031004
H	4.39502214	-2.14494445	-1.85945370
H	7.95908719	-3.52396695	0.78867030
H	7.42001665	-5.16058897	0.41850531
H	6.59167285	-4.22872350	1.66439033
H	4.38575211	-4.66167260	0.44980934
H	5.30592835	-5.62369802	-0.71376305
H	4.24756453	-4.33105879	-1.28112494
H	7.72530070	-2.93979352	-1.68434734
H	6.22461302	-3.30351284	-2.54472351
H	7.24612610	-4.61913582	-1.96134703
C	-8.17738010	-1.19915670	0.49731520
C	-8.99962831	-2.28841561	0.26808694
C	-8.56620939	-3.32645003	-0.54807076
C	-7.30661793	-3.27276716	-1.12717253
C	-6.47186776	-2.19332853	-0.87877070
H	-8.51235507	-0.37996819	1.12070037
H	-9.98208926	-2.32861084	0.72187683
H	-9.21280091	-4.17499457	-0.73501116
H	-6.97166207	-4.07319250	-1.77504756
H	-5.49469302	-2.15396007	-1.34229441

10f-4 (ground-state)

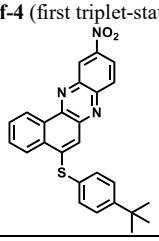


E = -1716.47761177 Hartree DFT(mPW1PW91/Def2-TZVP)
Zero-point correction = 0.415206 (Hartree/Particle)
Thermal correction to Energy = 0.441706
Thermal correction to Enthalpy = 0.442650
Thermal correction to Gibbs Free Energy = 0.355499
Sum of electronic and zero-point Energies = -1716.062405
Sum of electronic and thermal Energies = -1716.035906
Sum of electronic and thermal Enthalpies = -1716.034961
Sum of electronic and thermal Free Energies = -1716.122113

Charge = 0, Multiplicity = 1

C	3.77711818	0.56156355	1.22041362
C	3.33065946	1.10123164	0.02244561
C	3.72569885	0.51951847	-1.17901295
C	4.54751353	-0.59268430	-1.16915788
C	5.00604030	-1.15547766	0.02566631
C	4.60274766	-0.55444978	1.21570218
S	2.35751208	2.57793475	0.02060914
C	0.69903630	2.00224669	0.01463415
C	0.37501053	0.68477061	0.02448351
C	-0.98036180	0.25610366	0.01761117
C	-2.03753886	1.23070627	0.00082308
C	-1.69120571	2.64042839	-0.00755120
C	-0.33435429	3.02674464	-0.00090349
N	-1.24127572	-1.04292612	0.02656897
C	-2.52676542	-1.41795584	0.01888293
C	-3.57142912	-0.44942258	0.00170641
N	-3.29815887	0.86650319	-0.00674217
C	-2.85929410	-2.79435159	0.02736856
C	-4.16208069	-3.19060876	0.01920401
C	-5.17746361	-2.21287706	0.00228221
C	-4.91365881	-0.87342043	-0.00644642
C	-2.68853479	3.62028743	-0.02240392
C	-2.36206279	4.95815206	-0.03034151

C	-1.02313952	5.34545922	-0.02362575
C	-0.02680817	4.39359336	-0.00923095
N	-6.56852119	-2.65126352	-0.00604886
C	5.91810721	-2.37786452	-0.01344133
C	6.30883301	-2.85436214	1.38284934
C	7.19835086	-2.02728647	-0.78194438
C	5.19610989	-3.52404144	-0.73269392
H	-3.72340994	3.30682604	-0.02753278
H	-3.14418411	5.70662888	-0.04185622
H	-0.76107586	6.39579842	-0.02975016
H	1.00563243	4.71770918	-0.00447279
H	1.13468351	-0.08441973	0.03754708
H	-5.70662544	-0.13981178	-0.01954506
H	-4.42933625	-4.23666683	0.02544771
H	-2.05519622	-3.51854257	0.04036821
H	3.39076816	0.93791748	-2.11984407
H	3.48320120	1.01113666	2.16059485
H	4.93279170	-0.95002832	2.16604632
H	4.84013600	-1.02608529	-2.11717408
H	6.85722950	-2.08920844	1.93599993
H	6.95679933	-3.72855185	1.29661473
H	5.43721956	-3.14485840	1.97286960
H	4.27859378	-3.79979593	-0.20827558
H	5.84209773	-4.40414222	-0.77067819
H	4.93414733	-3.25709759	-1.75750731
H	7.73893638	-1.21417023	-0.29256307
H	6.98384082	-1.72316616	-1.80742505
H	7.85802428	-2.89713017	-0.82131074
O	-6.78581936	-3.84748917	0.00102738
O	-7.43942380	-1.80394988	-0.01948507

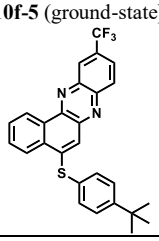
10f-4 (first triplet-state) 	*E* = -1716.41245504Hartree DFT(mPW1PW91/Def2-TZVP) Zero-point correction = 0.412413 (Hartree/Particle) Thermal correction to Energy = 0.439129 Thermal correction to Enthalpy = 0.440073 Thermal correction to Gibbs Free Energy = 0.352290 Sum of electronic and zero-point Energies -1716.000042 Sum of electronic and thermal Energies = -1715.973326 Sum of electronic and thermal Enthalpies = -1715.972382 Sum of electronic and thermal Free Energies = -1716.060165

Charge = 0, Multiplicity = 3

C	-4.35673762	0.60275713	-1.36157147
C	-3.31860399	0.93578958	-0.49626055
C	-3.14649438	0.21818546	0.68983596
C	-3.99551975	-0.83000691	0.97833400
C	-5.04143821	-1.19098580	0.12136823
C	-5.20260781	-0.44695643	-1.04818970
S	-2.34138162	2.33042236	-0.89819096
C	-0.74165132	1.91439117	-0.41517358
C	-0.27701377	0.59249992	-0.61668700
C	1.05167790	0.24557829	-0.42224493
C	1.99691606	1.23443204	-0.00528467
C	1.52949933	2.59416772	0.19923039
C	0.16137284	2.92940396	0.00587573
N	1.41523965	-1.04780661	-0.64415709
C	2.69462285	-1.35094401	-0.43445042
C	3.64355493	-0.35787359	-0.01174020
N	3.26492019	0.93928334	0.19168563
C	3.13561607	-2.68244768	-0.63786850
C	4.44358649	-3.02846284	-0.43587835
C	5.35131213	-2.04667111	-0.02254915

C	4.96538612	-0.72645214	0.18808600
C	2.42343205	3.59322938	0.59834036
C	2.00000473	4.88723581	0.80463922
C	0.65159279	5.21888663	0.63074903
C	-0.24948927	4.25788991	0.24800179
N	6.72220866	-2.41616326	0.18915223
C	-5.95403919	-2.35365291	0.49046642
C	-7.02622660	-2.60822069	-0.56528310
C	-6.64753069	-2.04484672	1.82386847
C	-5.11060784	-3.62610980	0.64367347
H	3.46125799	3.32640902	0.74276300
H	2.70829565	5.64544408	1.11338109
H	0.31436802	6.23159875	0.81107327
H	-1.29546092	4.51926147	0.14852040
H	-0.95232581	-0.17498952	-0.97067883
H	5.68515825	0.01364337	0.50528015
H	4.78431834	-4.04154937	-0.58923690
H	2.40854550	-3.41746446	-0.95808009
H	-2.36413973	0.49028070	1.38621152
H	-4.49808003	1.15388668	-2.28313885
H	-5.99567830	-0.68621532	-1.74211485
H	-3.84530912	-1.37102247	1.90361930
H	-7.68228949	-1.74544028	-0.69640239
H	-7.64554390	-3.45045689	-0.25186154
H	-6.59138641	-2.85935007	-1.53485963
H	-4.60172710	-3.87420301	-0.29019310
H	-5.75558651	-4.46578915	0.91187024
H	-4.35621186	-3.52104553	1.42455970
H	-7.25818927	-1.14261403	1.74871685
H	-5.92789456	-1.90240236	2.63123458
H	-7.30131949	-2.87498491	2.10032695
O	7.05001581	-3.58163707	0.00198650
O	7.50886445	-1.54984378	0.54896030

10f-5 (ground-state)



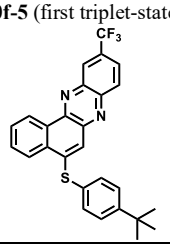
E = -1849.05394327 Hartree DFT(mPW1PW91/Def2-TZVP)
Zero-point correction = 0.417077 (Hartree/Particle)
Thermal correction to Energy = 0.444696
Thermal correction to Enthalpy = 0.445640
Thermal correction to Gibbs Free Energy = 0.355305
Sum of electronic and zero-point Energies = -1848.636866
Sum of electronic and thermal Energies = -1848.609247
Sum of electronic and thermal Enthalpies = -1848.608303
Sum of electronic and thermal Free Energies = -1848.698638

Charge = 0, Multiplicity = 1

C	4.13876511	0.41736111	1.22243833
C	3.71145541	0.98096651	0.02859128
C	4.03748530	0.36079503	-1.17445033
C	4.76867706	-0.81293182	-1.16990393
C	5.20491261	-1.40107957	0.02114256
C	4.87506050	-0.75964053	1.21259864
S	2.84669090	2.52385242	0.03280626
C	1.14984776	2.06191248	0.02431313
C	0.73695441	0.77097924	0.04122355
C	-0.64654587	0.43473544	0.03054162
C	-1.63316711	1.47628200	0.00267044
C	-1.19208485	2.85885157	-0.01108940
C	0.18828599	3.15307388	-0.00097017
N	-0.99481662	-0.84326808	0.04589235
C	-2.30349615	-1.13049017	0.03315206
C	-3.27988354	-0.09525064	0.00371171
N	-2.91776227	1.19692770	-0.01038373

C	-2.73079521	-2.48008878	0.04807817
C	-4.05919935	-2.77921728	0.03383994
C	-5.02478033	-1.74296148	0.00396188
C	-4.65235081	-0.43073063	-0.01068743
C	-2.12041047	3.90489015	-0.03480990
C	-1.70445225	5.21732350	-0.04808851
C	-0.34208082	5.51345690	-0.03835953
C	0.58721660	4.49657055	-0.01542210
C	-6.47108405	-2.13175100	-0.00830213
C	6.01384337	-2.69393548	-0.02313020
C	6.39406098	-3.18767964	1.37008390
C	7.30200526	-2.45731673	-0.82153513
C	5.18589778	-3.78428169	-0.71444018
H	-3.17417243	3.66240963	-0.04243601
H	-2.43396093	6.01708971	-0.06625979
H	-0.00955695	6.54364076	-0.04894003
H	1.63935342	4.75007283	-0.00902021
H	1.44193931	-0.04852020	0.06220787
H	-5.37806892	0.37088519	-0.03347722
H	-4.38484374	-3.81152005	0.04474132
H	-1.97961100	-3.25915103	0.07060125
H	3.71797521	0.79672249	-2.11272729
H	3.89866444	0.89525344	2.16395024
H	5.19220900	-1.17175356	2.16031938
H	5.00617544	-1.27580539	-2.11937650
H	7.01604147	-2.46562440	1.90292776
H	6.96525178	-4.11352991	1.28017809
H	5.51452219	-3.39923255	1.98148205
H	4.26032532	-3.97942556	-0.16844810
H	5.75728633	-4.71439800	-0.75574641
H	4.92476645	-3.50682148	-1.73664031
H	7.91605073	-1.68397382	-0.35487235
H	7.09204243	-2.15091906	-1.84734160
H	7.88887997	-3.37785955	-0.86072060
F	-7.29541816	-1.08141397	-0.06203826
F	-6.76758444	-2.91537642	-1.06140227
F	-6.80756357	-2.83585995	1.08846145

10f-5 (first triplet-state)



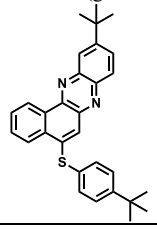
E = -1848.98449877 Hartree DFT(mPW1PW91/Def2-TZVP)
Zero-point correction = 0.414204 (Hartree/Particle)
Thermal correction to Energy = 0.442062
Thermal correction to Enthalpy = 0.443006 Thermal correction to Gibbs Free Energy = 0.352018
Sum of electronic and zero-point Energies -1848.570295
Sum of electronic and thermal Energies = -1848.542437
Sum of electronic and thermal Enthalpies = -1848.541493
Sum of electronic and thermal Free Energies = -1848.632481

Charge = 0, Multiplicity = 3

C	-4.69077589	0.43514836	-1.36922004
C	-3.68944687	0.84240955	-0.49401036
C	-3.48997235	0.14793151	0.70021955
C	-4.27408397	-0.95104999	0.98768440
C	-5.28336499	-1.38516157	0.12154667
C	-5.47499747	-0.66276117	-1.05605427
S	-2.78955871	2.29336708	-0.89521976
C	-1.17176062	1.96543465	-0.40550242
C	-0.62866007	0.66445490	-0.61921618
C	0.71612492	0.39078703	-0.44190526
C	1.60740483	1.43440630	-0.02271405
C	1.06051831	2.76189137	0.20177166

C	-0.32813159	3.02110688	0.02105242
N	1.15285077	-0.87765492	-0.67764793
C	2.46297365	-1.10319990	-0.47427762
C	3.34405544	-0.06045828	-0.05718002
N	2.89054514	1.21559314	0.15936184
C	2.98484428	-2.39604455	-0.68371474
C	4.32148190	-2.65747161	-0.49100006
C	5.17554880	-1.62943786	-0.08412996
C	4.69234307	-0.34583570	0.13165339
C	1.89803853	3.80667318	0.60728191
C	1.40419744	5.07197042	0.83297208
C	0.03640858	5.32862482	0.67247237
C	-0.81081314	4.32401061	0.28299016
C	6.61719084	-1.94622243	0.15636498
C	-6.12359944	-2.60295985	0.48775806
C	-7.17060726	-2.92578016	-0.57462990
C	-6.84462048	-2.33855840	1.81581586
C	-5.20300116	-3.81967187	0.64761634
H	2.95050405	3.59783508	0.74158055
H	2.07074307	5.86533956	1.14643087
H	-0.35629741	6.31811319	0.86925580
H	-1.87081860	4.52561735	0.19357968
H	-1.26633024	-0.13657355	-0.96874612
H	5.34994764	0.45300801	0.44728154
H	4.70915121	-3.65461141	-0.65458859
H	2.30581903	-3.17731455	-1.00134252
H	-2.73517324	0.47484935	1.40362358
H	-4.85356122	0.96674058	-2.29880174
H	-6.24230781	-0.95715853	-1.75789965
H	-4.10053610	-1.47494207	1.91895931
H	-7.87710207	-2.10497717	-0.71341821
H	-7.73969908	-3.80347817	-0.26308614
H	-6.71438694	-3.15243224	-1.54038809
H	-4.67426373	-4.03630593	-0.28307715
H	-5.79457909	-4.69848624	0.91386426
H	-4.46088622	-3.66583328	1.43220495
H	-7.51077013	-1.47685753	1.73583476
H	-6.14122411	-2.15049770	2.62815985
H	-7.44659019	-3.20811579	2.08897400
F	7.37993692	-0.85249335	0.27431891
F	6.79568259	-2.66019530	1.28781211
F	7.14702014	-2.68561993	-0.83421457

Adapted 10f-6 (ground-state)

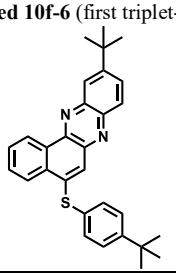


E = -1551.26180368 Hartree DFT(mPW1PW91/Def2-TZVP)
Zero-point correction = 0.440354 (Hartree/Particle)
Thermal correction to Energy = 0.465937
Thermal correction to Enthalpy = 0.466881
Thermal correction to Gibbs Free Energy = 0.383421
Sum of electronic and zero-point Energies = -1550.821449
Sum of electronic and thermal Energies = -1550.795867
Sum of electronic and thermal Enthalpies = -1550.794923
Sum of electronic and thermal Free Energies = -1550.878383

Charge = 0, Multiplicity = 1

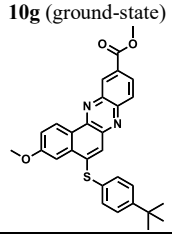
C	-5.16372826	-1.83599862	-0.00595898
C	-3.89577352	-1.20956723	-0.00145072
C	-2.71651496	-2.01092386	0.00897881
C	-2.85333598	-3.42022074	0.01449412
C	-4.09193109	-3.98698817	0.01001903
C	-5.27778128	-3.19953013	-0.00032194
N	-3.81286047	0.12941440	-0.00679330

C	-2.61401302	0.67598753	-0.00197078
C	-1.43106541	-0.12832536	0.00845221
N	-1.50005671	-1.45254039	0.01368554
C	-0.14869177	0.49474674	0.01393250
C	-0.01840058	1.84313494	0.00915529
C	-1.19010525	2.70315202	-0.00153962
C	-2.47660142	2.12073708	-0.00688220
C	-3.60644135	2.94645698	-0.01662938
C	-3.48068708	4.31721972	-0.02113560
C	-2.21237099	4.89741474	-0.01596818
C	-1.08798389	4.10193945	-0.00634193
S	1.54357375	2.65868094	0.01700018
C	2.71857662	1.33679928	0.02106378
C	3.20913511	0.82946939	-1.17888482
C	4.17811995	-0.15743829	-1.16728789
C	4.69279218	-0.66605216	0.02888136
C	4.19270272	-0.14053642	1.21811188
C	3.21998511	0.84998589	1.22009387
C	5.76438979	-1.75158210	-0.00770068
C	6.99325547	-1.22309341	-0.75807018
C	-6.60838231	-3.88034603	-0.00466409
C	5.21449428	-2.97934359	-0.74420260
C	6.20104739	-2.18282656	1.38956993
H	-4.58399240	2.48407921	-0.02044816
H	-4.36433639	4.94280909	-0.02858556
H	-2.10716361	5.97495027	-0.01948590
H	-0.11409507	4.57414258	-0.00249321
H	0.71378329	-0.15754440	0.02246368
H	-6.04351624	-1.20323266	-0.01378351
H	-4.18772547	-5.06672613	0.01438062
H	-1.95474425	-4.02478417	0.02229224
H	2.83213814	1.20825403	-2.12063616
H	2.85254964	1.24308511	2.15976970
H	4.56049872	-0.49692087	2.17016639
H	4.54177956	-0.53411311	-2.11498167
H	6.63301112	-1.35480616	1.95519080
H	6.96368816	-2.95921342	1.30471695
H	5.37095889	-2.59538318	1.96653821
H	4.33707141	-3.38241471	-0.23376812
H	5.97506272	-3.76263061	-0.78019784
H	4.93062416	-2.74144555	-1.77030856
H	7.41163898	-0.34709446	-0.25756851
H	6.75063908	-0.94390961	-1.78437612
H	7.76652440	-1.99384202	-0.79448657
H	-7.42511813	-3.15979058	-0.01323963
H	-6.70989862	-4.52763953	-0.87939860
H	-6.72028071	-4.51846867	0.87553170

Adapted 10f-6 (first triplet-state) 	*E* = -1551.19122640 Hartree DFT(mPW1PW91/Def2-TZVP) Zero-point correction = 0.436891 (Hartree/Particle) Thermal correction to Energy = 0.462930 Thermal correction to Enthalpy = 0.463874 Thermal correction to Gibbs Free Energy = 0.378190 Sum of electronic and zero-point Energies -1550.754335 Sum of electronic and thermal Energies = -1550.728296 Sum of electronic and thermal Enthalpies = -1550.727352 Sum of electronic and thermal Free Energies = -1550.813036

Charge = 0, Multiplicity = 3			
C	0.79870317	4.06244852	0.21966658

C	1.00609679	2.67987178	0.00616456
C	2.31459447	2.15128345	0.19956888
C	3.34807994	3.02002677	0.57163249
C	3.12087835	4.36465230	0.75316880
C	1.83178356	4.88744127	0.57912178
C	-0.03512393	1.80165581	-0.38718430
C	0.23622030	0.41617734	-0.56020923
C	1.49256893	-0.11646869	-0.36958551
C	2.58061411	0.73482789	0.02139607
N	3.79341776	0.26783840	0.21636274
C	3.98170307	-1.08452484	0.03732931
C	2.90230045	-1.93738334	-0.35610185
N	1.66508776	-1.46160453	-0.56988966
C	5.23609458	-1.63217917	0.23641419
C	5.48328211	-3.00349237	0.06434809
C	4.42605658	-3.82882384	-0.31968248
C	3.16160238	-3.31167147	-0.52625582
S	-1.57680549	2.44179561	-0.83255057
C	-2.72638143	1.15944955	-0.46900790
C	-3.72653016	0.89298502	-1.39507045
C	-4.70364835	-0.04828814	-1.10696166
C	-4.70714576	-0.75118662	0.09598742
C	-3.68962531	-0.46380553	1.01233601
C	-2.71696059	0.48041026	0.74913994
C	-5.76325518	-1.79648468	0.43867795
C	-5.07646295	-3.14592898	0.68430648
C	6.85397395	-3.55129490	0.29127574
C	-6.78848186	-1.97268353	-0.67806417
C	-6.50299809	-1.36847517	1.71255988
H	4.33737565	2.60735321	0.71447941
H	3.93541845	5.01746139	1.04053868
H	1.64825333	5.94228939	0.73961614
H	-0.19749105	4.47268989	0.11348769
H	-0.55280183	-0.25021543	-0.88226033
H	6.04348618	-0.97157871	0.53258254
H	4.60255970	-4.88891404	-0.45684463
H	2.33995675	-3.95184459	-0.82470135
H	-1.95652046	0.69521839	1.48888068
H	-3.74255342	1.41286224	-2.34492220
H	-5.46659593	-0.23310804	-1.84995844
H	-3.65865870	-0.98008312	1.96340530
H	-7.33378378	-1.04859483	-0.88035723
H	-7.51745644	-2.72875551	-0.38073845
H	-6.32467150	-2.30759939	-1.60805811
H	-4.54173136	-3.48159173	-0.20685112
H	-5.82352371	-3.90203823	0.93621031
H	-4.36330566	-3.09272312	1.50813935
H	-7.00551407	-0.40922291	1.57068970
H	-5.82498937	-1.27437744	2.56195372
H	-7.26009219	-2.11287323	1.96932268
H	7.58185059	-3.06833418	-0.36621680
H	7.18445890	-3.36461792	1.31668562
H	6.88804434	-4.62500114	0.11058969

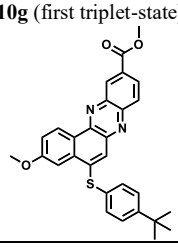
10g (ground-state) 	*E* = -1854.39740599 Hartree DFT(mPW1PW91/Def2-TZVP) Zero-point correction = 0.488324 (Hartree/Particle) Thermal correction to Energy = 0.519449 Thermal correction to Enthalpy = 0.520393 Thermal correction to Gibbs Free Energy = 0.423164 Sum of electronic and zero-point Energies = -1853.909082 Sum of electronic and thermal Energies = -1853.877957 Sum of electronic and thermal Enthalpies = -1853.877013 Sum of electronic and thermal Free Energies = -1853.974242

Charge = 0, Multiplicity = 1

C	3.97851906	-0.39393731	-1.17849952
C	3.69426491	0.24958430	0.02278312
C	4.05389061	-0.35335218	1.21977392
C	4.68035924	-1.59231306	1.21470065
C	4.96535627	-2.25797207	0.02482606
C	4.60075470	-1.62892719	-1.16932523
S	2.96838343	1.86239757	0.02192862
C	1.23716306	1.55203330	0.01668760
C	0.37383033	2.72388193	0.00300825
C	-1.02329740	2.54446361	-0.00217494
C	-1.58550027	1.21231786	0.00502053
C	-0.69383481	0.08540573	0.01959532
C	0.71285002	0.30151182	0.02587836
C	-1.85008533	3.67708787	-0.01443966
C	-1.32608531	4.94190716	-0.02085795
C	0.06525657	5.12324441	-0.01554237
C	0.90284248	4.02153207	-0.00417343
N	-1.15088797	-1.15721500	0.02718437
C	-2.48027617	-1.32992397	0.02003404
C	-3.36356439	-0.21239728	0.00520822
N	-2.89046356	1.04525697	-0.00172646
C	-3.02437638	-2.63596233	0.02681698
C	-4.37470232	-2.82056159	0.01872808
C	-5.25564671	-1.70865682	0.00360276
C	-4.75548788	-0.43272828	-0.00273993
C	-6.73204940	-1.87942598	-0.00632135
O	-7.09484131	-3.15988376	0.00051253
C	-8.50071709	-3.41715465	-0.00902541
C	5.64800075	-3.62191104	-0.01479242
C	4.71491652	-4.63103609	-0.69568110
O	-7.52065484	-0.96476591	-0.01936375
C	5.98549719	-4.14191717	1.37978995
C	6.94894544	-3.51564546	-0.82005914
H	-2.92224341	3.53618994	-0.01853546
H	-1.96776168	5.81370176	-0.02984782
O	0.48941945	6.39645905	-0.02201098
H	1.97307627	4.16532284	-0.00073524
H	1.34487948	-0.57571141	0.03749980
H	-5.42065414	0.42068395	-0.01418058
H	-4.78371476	-3.82085807	0.02371922
H	-2.34234325	-3.47683089	0.03816490
H	-8.97414160	-2.98972825	0.87415181
H	-8.60202474	-4.49890536	-0.00206219
H	-8.95978216	-3.00256121	-0.90580589
H	3.71169039	0.07176407	-2.11891936
H	3.84598091	0.14189750	2.16000062
H	4.94653897	-2.03402867	2.16481405
H	4.80769623	-2.10915627	-2.11735913
H	6.67147051	-3.47640031	1.90772112
H	6.47026631	-5.11610968	1.29291362
H	5.09211133	-4.27043122	1.99412804

H	3.77947325	-4.73550206	-0.14169037
H	5.19500457	-5.61136798	-0.73814441
H	4.47267698	-4.33218943	-1.71654912
H	7.63685089	-2.80180335	-0.36168128
H	6.76500015	-3.19790817	-1.84734831
H	7.44436198	-4.48858032	-0.85492287
C	1.88634680	6.64333442	-0.01646838
H	1.99858234	7.72479608	-0.02234147
H	2.35649634	6.23514646	0.88114018
H	2.36542518	6.22454836	-0.90441341

10g (first triplet-state)



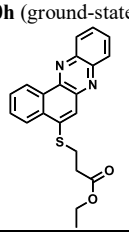
E = -1854.32869742 Hartree DFT(mPW1PW91/Def2-TZVP)
Zero-point correction = 0.485251 (Hartree/Particle)
Thermal correction to Energy = 0.516646
Thermal correction to Enthalpy = 0.517590 Thermal correction to Gibbs Free Energy = 0.419543
Sum of electronic and zero-point Energies -1853.843447
Sum of electronic and thermal Energies = -1853.812051
Sum of electronic and thermal Enthalpies = -1853.811107
Sum of electronic and thermal Free Energies = -1853.909154

Charge = 0, Multiplicity = 3

C	3.37854602	-0.51768058	-0.67020119
C	3.63305192	0.10468642	0.55292254
C	4.57763204	-0.43720295	1.41753987
C	5.25136402	-1.59536592	1.06501264
C	5.00259794	-2.24581896	-0.14304635
C	4.05197446	-1.67735793	-0.99764822
S	2.87748065	1.62338518	1.00483020
C	1.23181901	1.46213867	0.52154900
C	0.48485281	2.60617105	0.13878492
C	-0.91458470	2.46710742	-0.06273532
C	-1.57628114	1.18731031	0.10074571
C	-0.78203057	0.05519850	0.48954123
C	0.57658909	0.20543822	0.68462591
C	-1.65080246	3.60211801	-0.42964352
C	-1.05491403	4.82475517	-0.59147141
C	0.33359015	4.96469117	-0.40012600
C	1.09061016	3.86973115	-0.04902838
N	-1.33103705	-1.17940439	0.67711252
C	-2.64851204	-1.28405456	0.45669655
C	-3.43588828	-0.15515893	0.06442605
N	-2.87014960	1.08467460	-0.10317673
C	-3.28295536	-2.53509590	0.61962200
C	-4.63325092	-2.67606144	0.40573545
C	-5.40279107	-1.57053486	0.01982597
C	-4.79537324	-0.32397408	-0.14539983
C	-6.85763432	-1.67253673	-0.22412854
O	-7.32828833	-2.90607438	-0.03106794
C	-8.72766951	-3.08603848	-0.24910629
C	5.72248864	-3.52485836	-0.55413814
C	4.68777932	-4.63348670	-0.78546379
O	-7.55695037	-0.74488833	-0.56283265
C	6.71100042	-4.00017908	0.50690616
C	6.49203571	-3.27381754	-1.85739099
H	-2.71570355	3.49648468	-0.58534159
H	-1.63305884	5.69450098	-0.87630946
O	0.82268125	6.20087583	-0.59593375
H	2.16055511	3.96237669	0.06774048
H	1.14227364	-0.65917868	1.00542719
H	-5.39220795	0.52868258	-0.44168368

H	-5.10285217	-3.64083987	0.53458290
H	-2.67440233	-3.37994783	0.91759629
H	-9.30655386	-2.45670853	0.42629436
H	-8.92572124	-4.13484892	-0.04425159
H	-8.98994563	-2.84989301	-1.28004614
H	2.66759971	-0.08962902	-1.36503110
H	4.78202643	0.03655704	2.36976163
H	5.97636074	-1.99438041	1.76025619
H	3.83734951	-2.14298532	-1.95112220
H	7.49574996	-3.26391123	0.69192109
H	7.19235952	-4.91783253	0.16409635
H	6.21617042	-4.21959843	1.45514638
H	4.12399918	-4.84035557	0.12672342
H	5.19292267	-5.55359219	-1.08777087
H	3.97834798	-4.36779650	-1.57035611
H	7.23831650	-2.48719738	-1.72694181
H	5.82648774	-2.97958312	-2.67013370
H	7.01044568	-4.18560987	-2.16242376
C	2.21401168	6.40802782	-0.41814459
H	2.38692534	7.46430715	-0.61020173
H	2.52160455	6.16995796	0.60295479
H	2.79649199	5.81175677	-1.12461508

10h (ground-state)



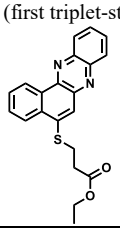
E = -1469.46046164 Hartree DFT(mPW1PW91/Def2-TZVP)
Zero-point correction = 0.347672 (Hartree/Particle)
Thermal correction to Energy = 0.369880
Thermal correction to Enthalpy = 0.370824
Thermal correction to Gibbs Free Energy = 0.292772
Sum of electronic and zero-point Energies = -1469.112790
Sum of electronic and thermal Energies = -1469.090581
Sum of electronic and thermal Enthalpies = -1469.089637
Sum of electronic and thermal Free Energies = -1469.167690

Charge = 0, Multiplicity = 1

C	-3.69495461	-3.52093704	0.00011166
C	-3.30173401	-2.16166873	0.00008106
C	-4.30580258	-1.14867262	0.00009452
C	-5.66923743	-1.52333029	0.00013193
C	-6.01508635	-2.84409207	0.00015850
C	-5.01999161	-3.84939142	0.00014989
N	-1.99960918	-1.84136961	0.00003848
C	-1.68138492	-0.55569297	0.00001432
C	-2.69118210	0.46025357	0.00003890
N	-3.97004010	0.15115790	0.00007545
C	-0.30359386	-0.18804300	-0.00003430
C	0.08303865	1.11298135	-0.00005161
C	-0.90873098	2.17944469	-0.00000734
C	-2.28152922	1.85286620	0.00003208
C	-3.23443109	2.87759147	0.00006648
C	-2.85080540	4.19965230	0.00006314
C	-1.49555084	4.52792764	0.00002532
C	-0.54305886	3.53277230	-0.00000932
S	1.75855267	1.61484732	-0.00010481
C	2.66728592	0.05626919	-0.00045704
C	4.14900243	0.37755461	-0.00006158
C	4.98952065	-0.87078587	-0.00048788
O	4.55930235	-1.99727330	-0.00151637
H	-7.05897309	-3.13133749	0.00018732
O	6.28527383	-0.57196044	0.00038818
C	7.20603483	-1.68031605	0.00001120
C	8.60163230	-1.12217113	0.00124382
H	-4.28199323	2.60942242	0.00009593

H	-3.59949781	4.98179603	0.00008939
H	-1.18718060	5.56572115	0.00002288
H	0.50298187	3.81026450	-0.00004053
H	0.40885500	-1.00022668	-0.00004411
H	-6.41722613	-0.74008992	0.00013905
H	-5.31920234	-4.89003968	0.00017373
H	-2.92182318	-4.27933901	0.00010431
H	2.39921176	-0.51685955	-0.88723749
H	2.39886524	-0.51747446	0.88582431
H	4.42892416	0.96816841	0.87580261
H	4.42920705	0.96887328	-0.87536853
H	7.01651085	-2.29032873	-0.88423951
H	7.01551859	-2.29175915	0.88305841
H	8.78353502	-0.51240888	-0.88497745
H	9.31717890	-1.94598050	0.00095653
H	8.78255530	-0.51387977	0.88867578

10h (first triplet-state)



E = -1469.38859277 Hartree DFT(mPW1PW91/Def2-TZVP)
Zero-point correction = 0.344232 (Hartree/Particle)
Thermal correction to Energy = 0.366922
Thermal correction to Enthalpy = 0.367867
Thermal correction to Gibbs Free Energy = 0.287253
Sum of electronic and zero-point Energies -1469.044361
Sum of electronic and thermal Energies = -1469.021670
Sum of electronic and thermal Enthalpies = -1469.020726
Sum of electronic and thermal Free Energies = -1469.101339

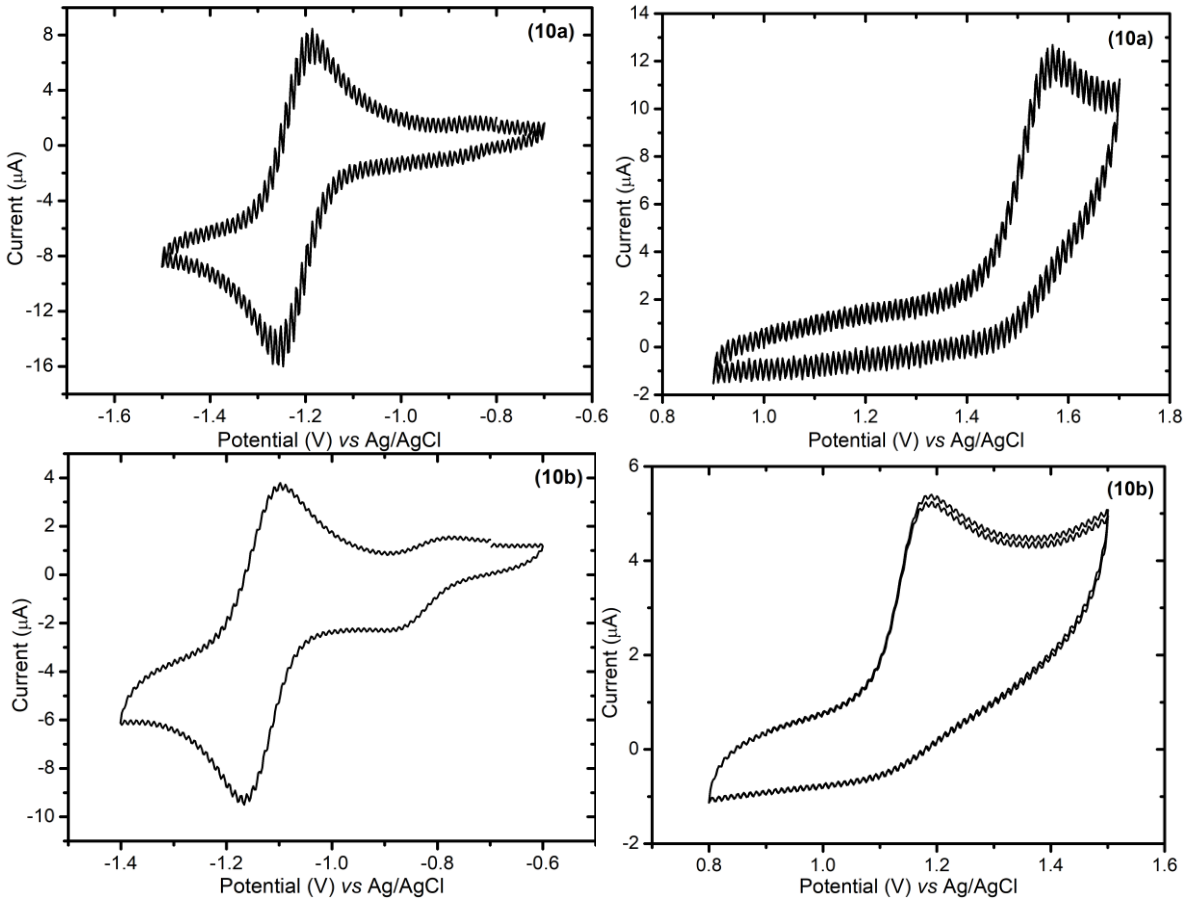
Charge = 0, Multiplicity = 3

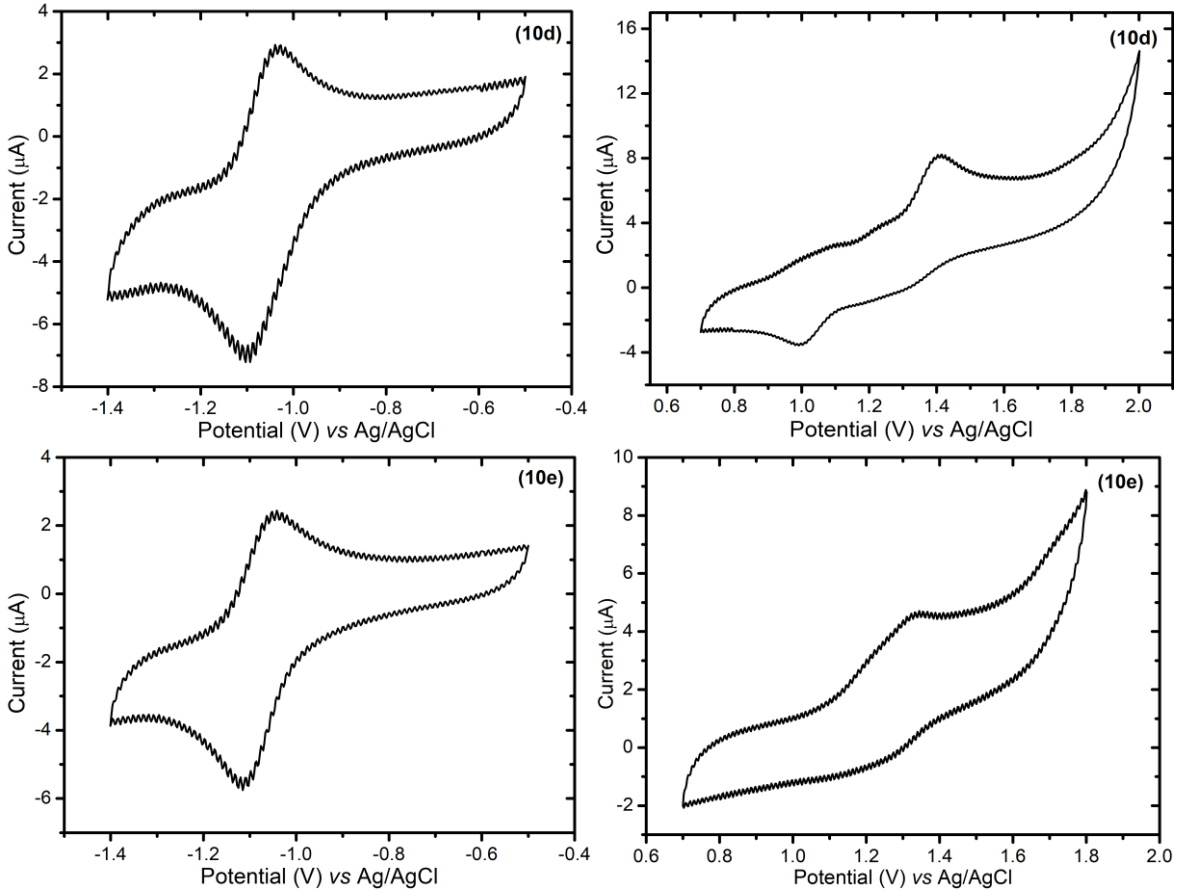
C	3.67560697	-3.53457755	0.00105194
C	3.28505266	-2.17964801	0.00070383
C	4.29565006	-1.16588326	-0.00028640
C	5.62714111	-1.54877993	-0.00095805
C	5.98807582	-2.89879041	-0.00063438
C	5.01269142	-3.88851788	0.00039269
N	1.97653212	-1.87338449	0.00129512
C	1.67233096	-0.53223764	0.00086520
C	2.68779768	0.47472146	0.00001251
N	3.97048044	0.17254826	-0.00056427
C	0.34041848	-0.17670166	0.00126593
C	-0.08447480	1.17910110	0.00093140
C	0.89165351	2.21437249	0.00019222
C	2.27031806	1.86370365	-0.00022695
C	3.22968295	2.88566844	-0.00091902
C	2.86196376	4.21026785	-0.00120179
C	1.50467576	4.56083524	-0.00084618
C	0.54399169	3.58397266	-0.00018073
S	-1.75060508	1.60438161	0.00178208
C	-2.65641029	0.04137878	0.00063976
C	-4.13642634	0.37335270	0.00039659
C	-4.97708002	-0.87559092	-0.00152019
O	-4.54373957	-2.00071881	-0.00483850
H	7.03628948	-3.17013583	-0.00117794
O	-6.27149776	-0.57679077	0.00068431
C	-7.19277307	-1.68568786	-0.00131010
C	-8.58810775	-1.12731384	0.00151101
H	4.27429175	2.60637519	-0.00123036
H	3.62022216	4.98320302	-0.00173455
H	1.21329613	5.60342968	-0.00112384
H	-0.49930010	3.87381802	0.00000613
H	-0.38326130	-0.97954678	0.00193235
H	6.38770572	-0.77721378	-0.00174173
H	5.29697065	-4.93302795	0.00066212

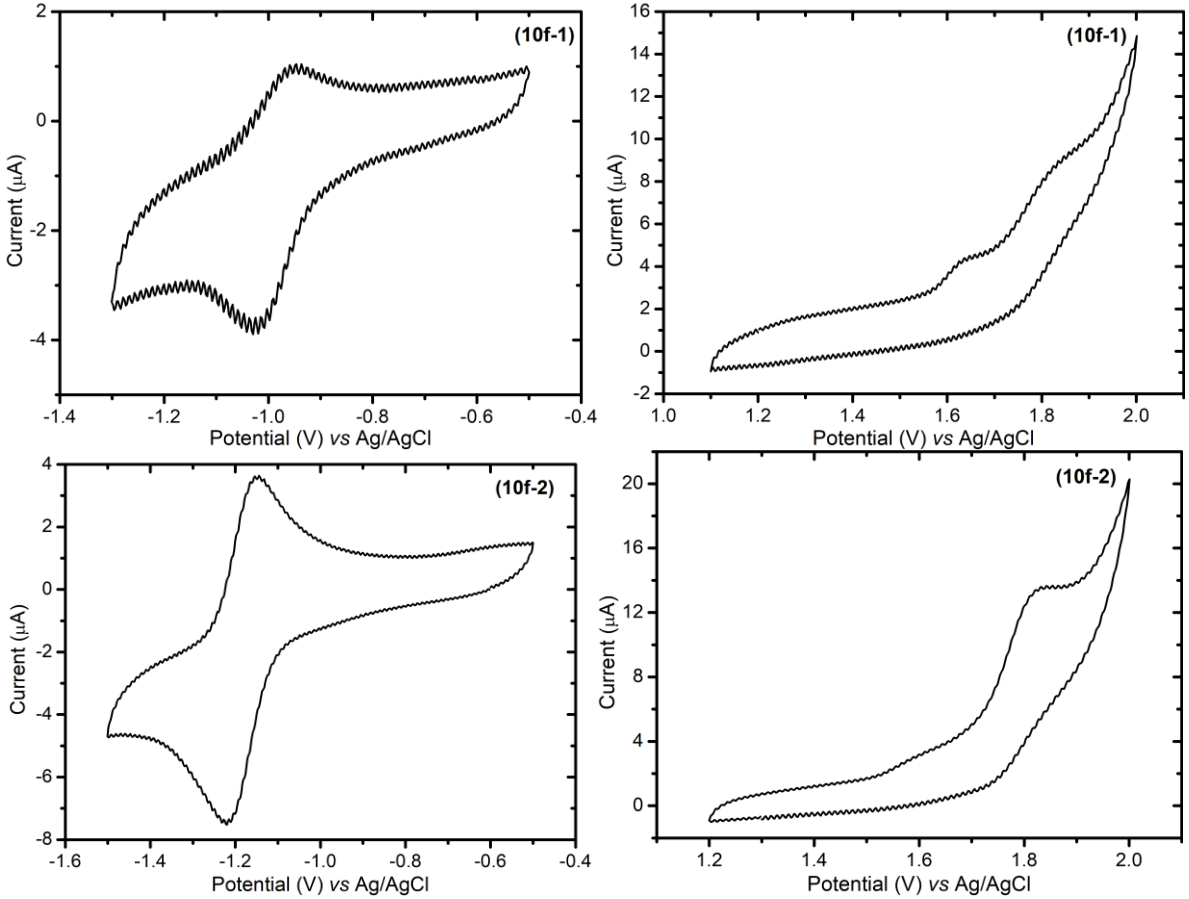
H	2.89610260	-4.28702315	0.00184108
H	-2.38867347	-0.52780139	0.88893986
H	-2.38808141	-0.52669859	-0.88817857
H	-4.41302456	0.96516319	-0.87555336
H	-4.41381767	0.96341466	0.87723508
H	-7.00134272	-2.29821609	0.88069777
H	-7.00306710	-2.29361269	-0.88686672
H	-8.76869001	-0.52080796	0.89020278
H	-9.30341759	-1.95130454	-0.00000532
H	-8.77038264	-0.51606294	-0.88357619

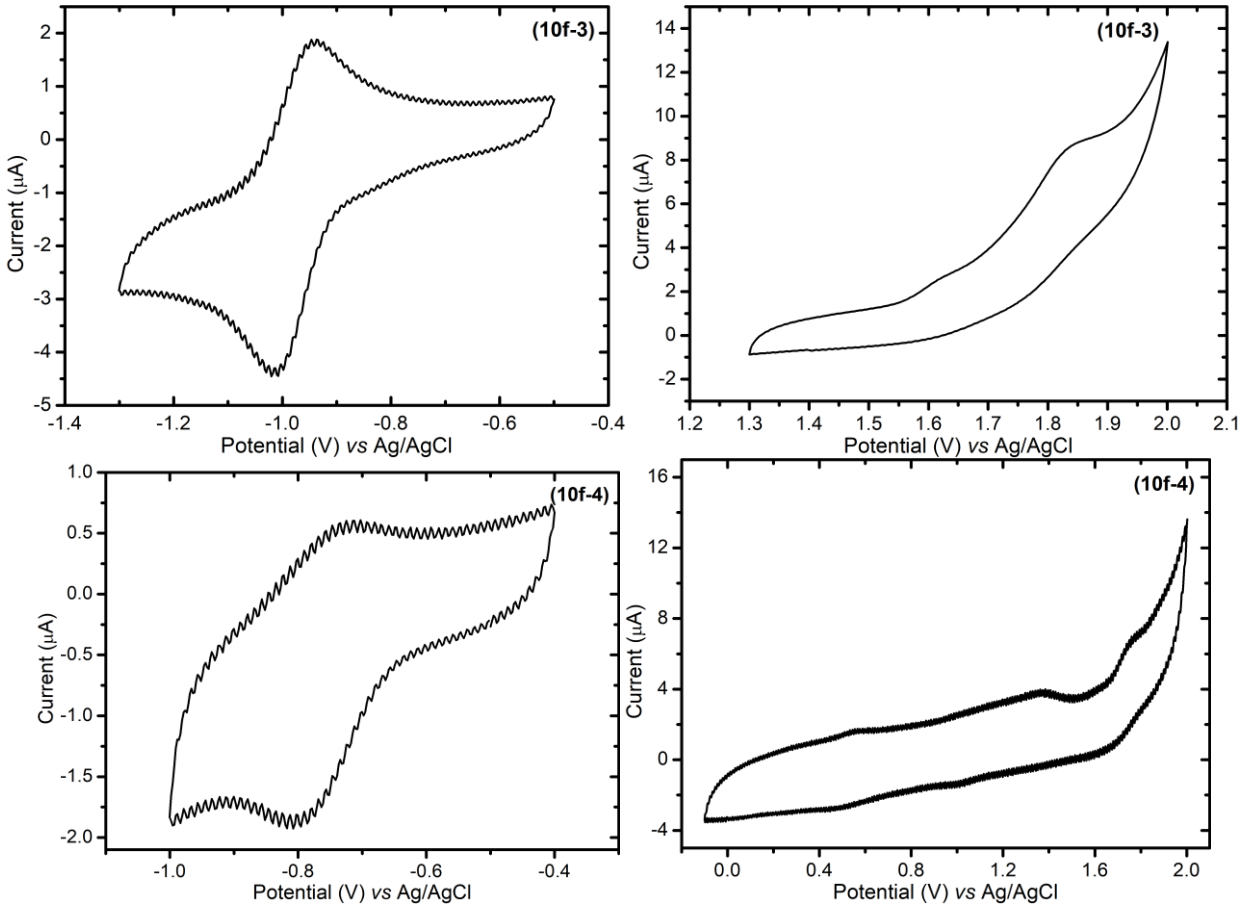
Annex C

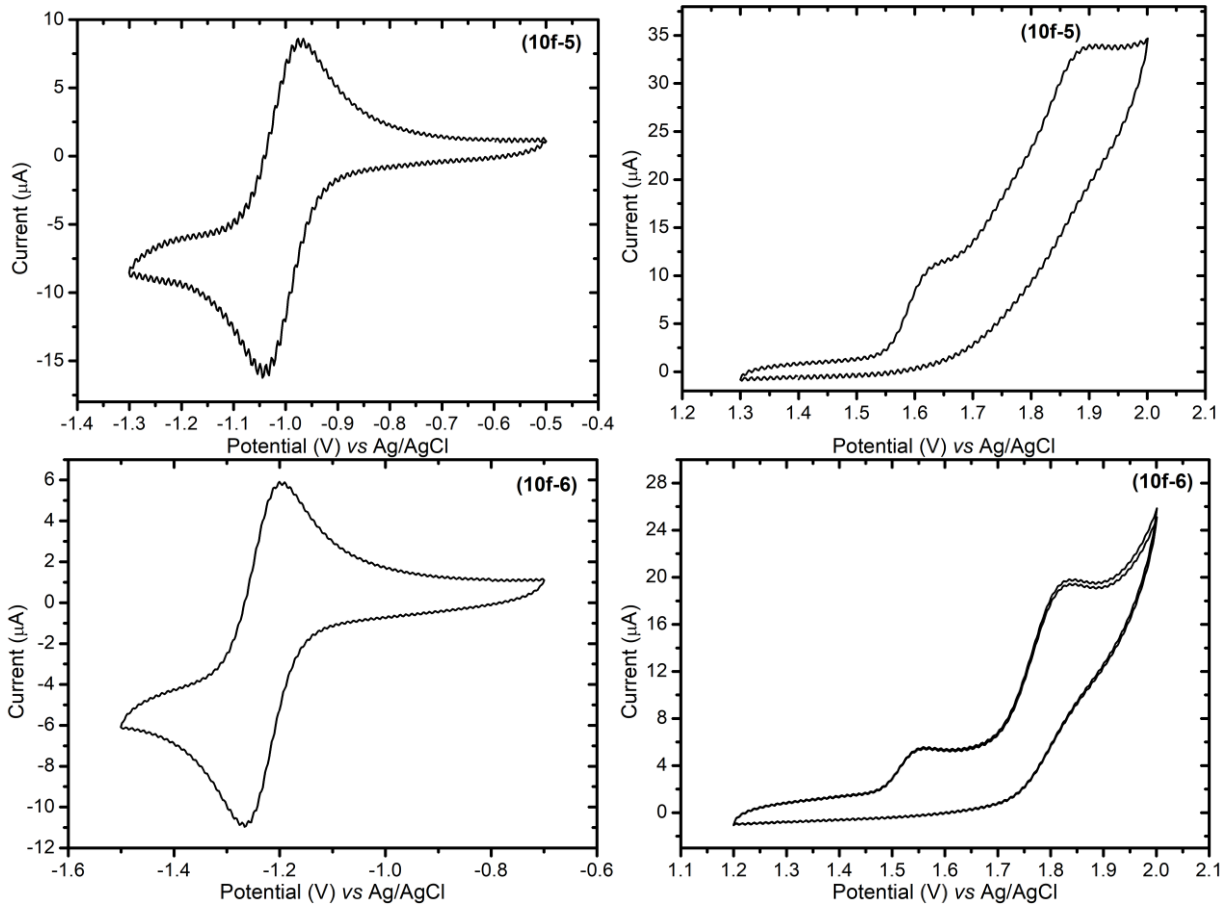
Supporting information – Chapter 5


(10a)
Current (μA)
Potential (V) vs Ag/AgCl
(10a)
Current (μA)
Potential (V) vs Ag/AgCl
(10b)
Current (μA)
Potential (V) vs Ag/AgCl
(10b)
Current (μA)
Potential (V) vs Ag/AgCl


(10d)
Current (μA)
Potential (V) vs Ag/AgCl
(10d)
Current (μA)
Potential (V) vs Ag/AgCl
(10e)
Current (μA)
Potential (V) vs Ag/AgCl
(10e)
Current (μA)
Potential (V) vs Ag/AgCl


(10f-1)
Current (μA)
Potential (V) vs Ag/AgCl
(10f-1)
Current (μA)
Potential (V) vs Ag/AgCl
(10f-2)
Current (μA)
Potential (V) vs Ag/AgCl
(10f-2)
Current (μA)
Potential (V) vs Ag/AgCl


(10f-3)
Current (μA)
Potential (V) vs Ag/AgCl
(10f-3)
Current (μA)
Potential (V) vs Ag/AgCl
(10f-4)
Current (μA)
Potential (V) vs Ag/AgCl
(10f-4)
Current (μA)
Potential (V) vs Ag/AgCl


(10f-5)
Current (μA)
Potential (V) vs Ag/AgCl
(10f-5)
Current (μA)
Potential (V) vs Ag/AgCl
(10f-6)
Current (μA)
Potential (V) vs Ag/AgCl
(10f-6)
Current (μA)
Potential (V) vs Ag/AgCl

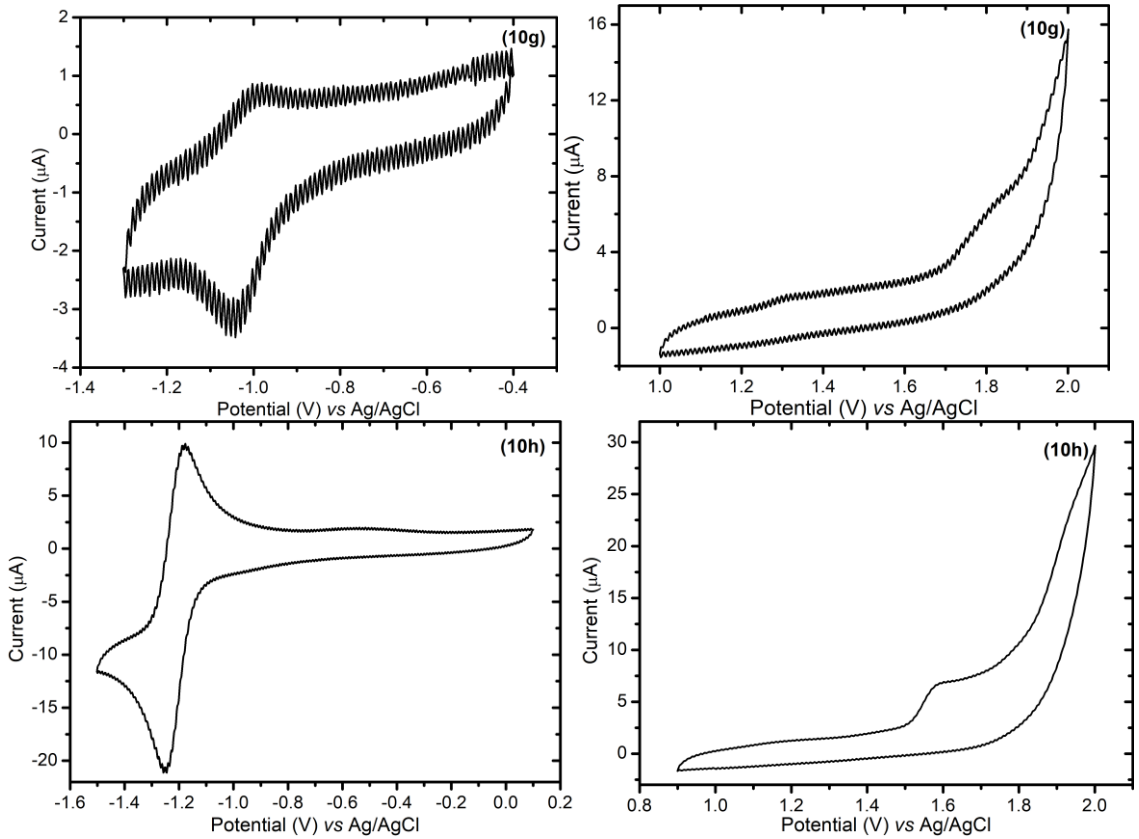


Figure C.1. Cyclic voltammetry (CV) of benzophenazine derivatives.

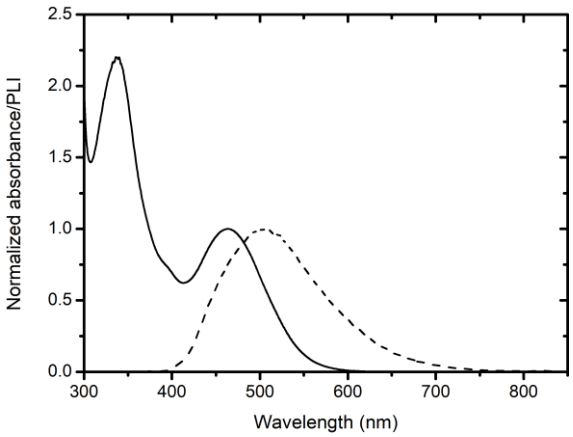
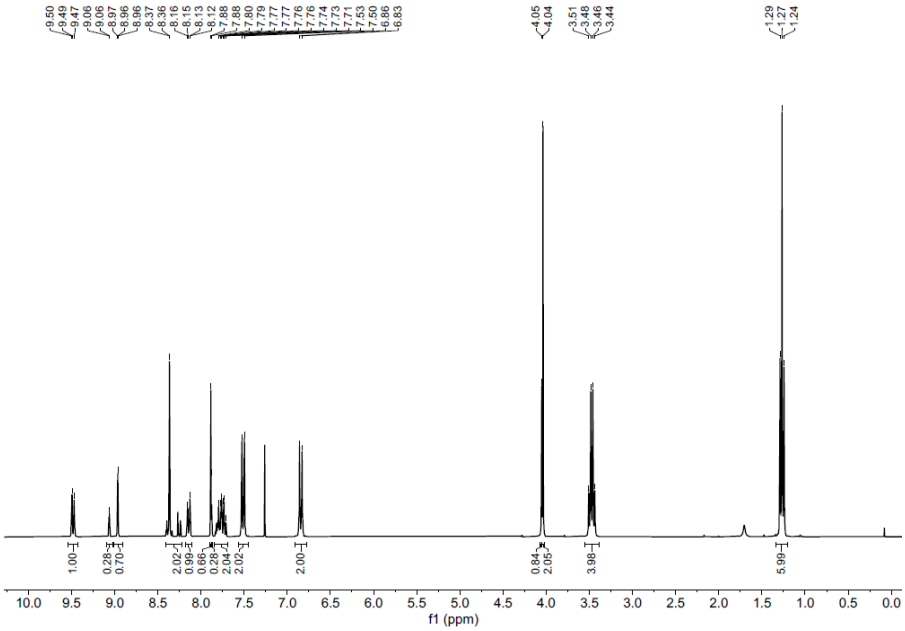


Figure C.2. Normalized absorbance (solid) and photoluminescence (dashed) of diethylaniline **10c** in acetonitrile. The intersection between the two spectra was used to determine the $E_{0,0}$.



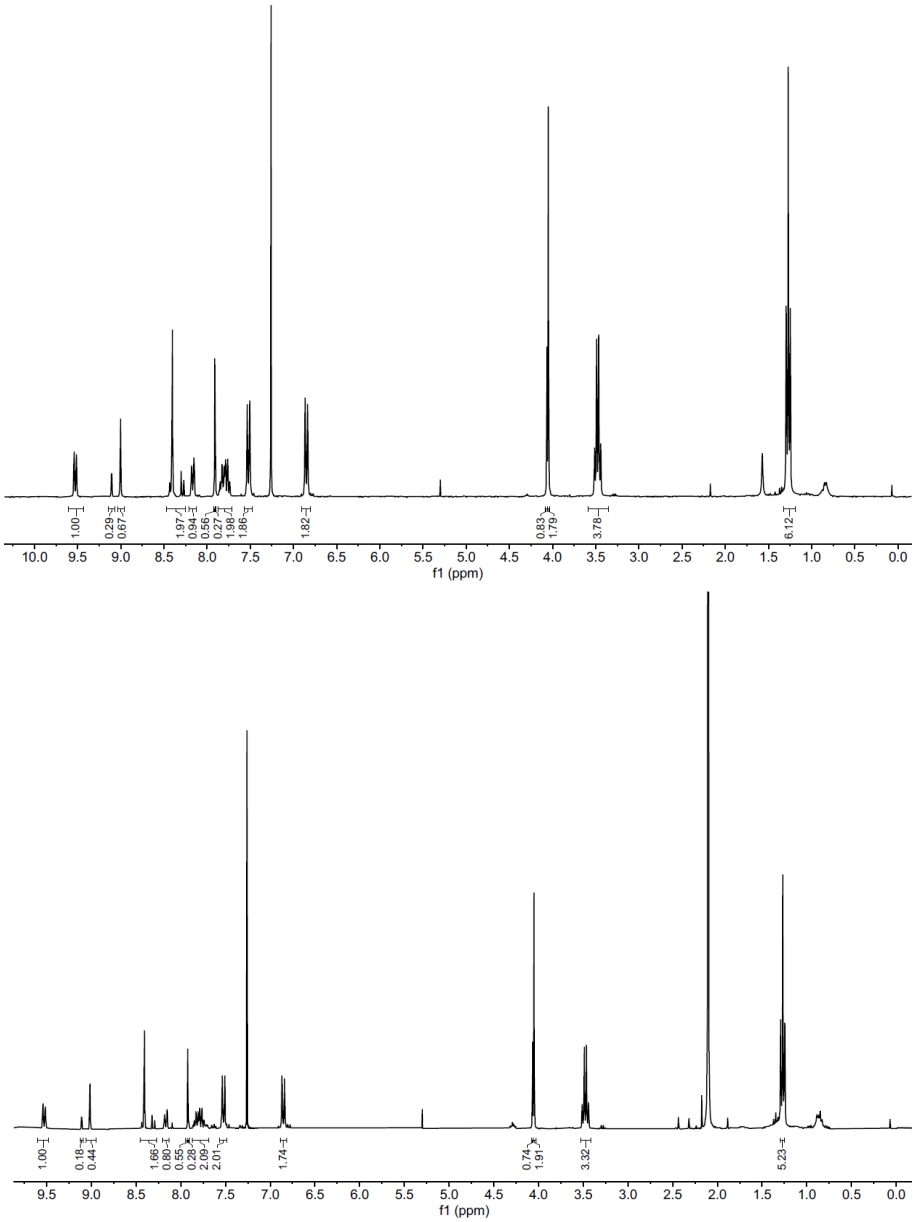


Figure C.3. NMR spectra of diethylaniline **10c** without irradiation (top), after 24 h of irradiation with two blue Thorlabs lamps (middle) and after 24 h of irradiation in acidic conditions (bottom) recorded in $CDCl_3$ at 300 MHz and 298 K.

Annex D

Supporting information – Chapter 6

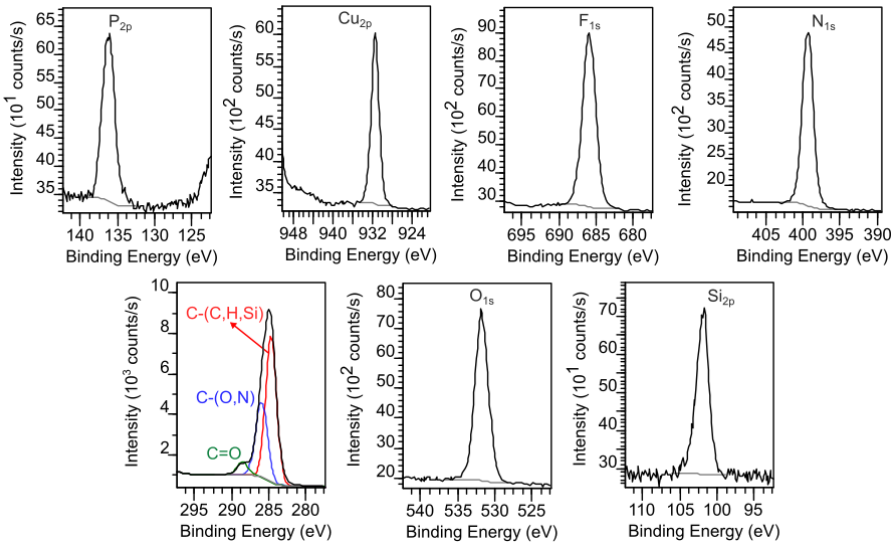
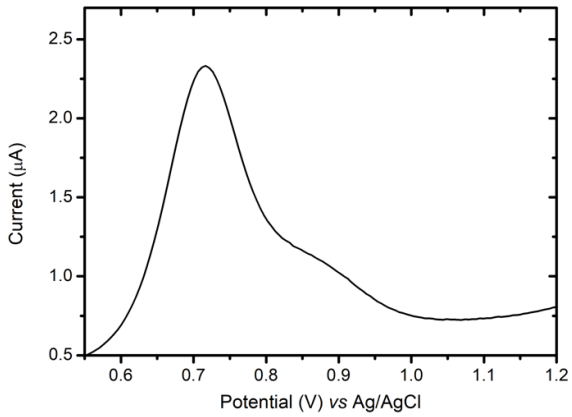


Figure D.1. P_{2p}, Cu_{2p}, F_{1s}, N_{1s}, C_{1s}, O_{1s} and Si_{2p} XPS spectra of complex **Cu-1**.



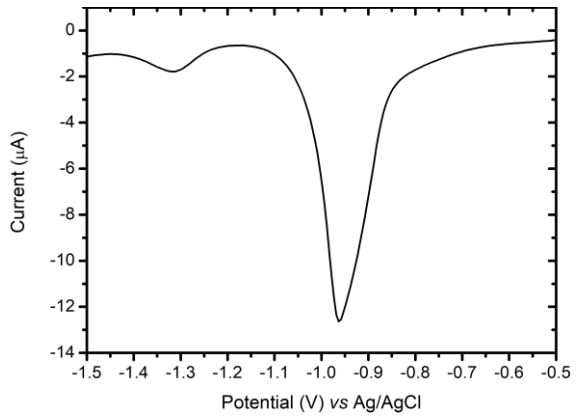


Figure D.2. Differential pulse voltammetry (DPV) of **Cu-1**.

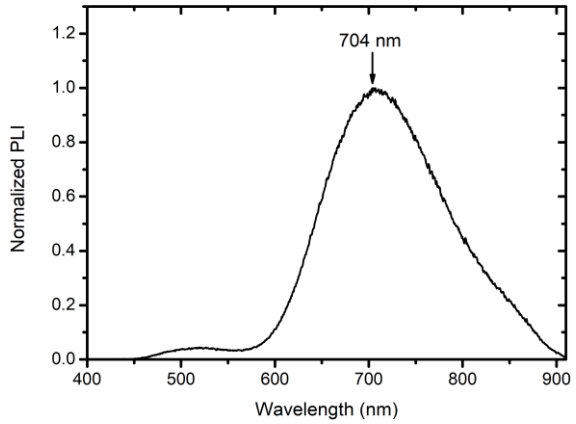


Figure D.3. Normalized emission spectra of **Cu-1** recorded at ambient temperature in DCM.

$E_{0,0}$[a] (eV)	$E(Cu^{I}/Cu^{0})$ (V *vs* NHE)	$E(Cu^{II}/Cu^{I})$ (V *vs* NHE)	$E(Cu^{I*}/Cu^{0})$[b] (V *vs* NHE)	$E(Cu^{II}/Cu^{I*})$[c] (V *vs* NHE)
1.76	–1.12	0.91	0.64	–0.85

[a] Estimated from the maximum of the emission band of **Cu-1**.
[b]Excited-state reduction potential determined according to the Rehm-Weller equation[387]: $E(Cu^{I*}/Cu^{0}) = E(Cu^{I}/Cu^{0}) + E_{0-0}$
[c]Excited-state oxidation potential determined according to the Rehm-Weller equation[387]: $E(Cu^{II}/Cu^{I*}) = E(Cu^{II}/Cu^{I}) - E_{0-0}$

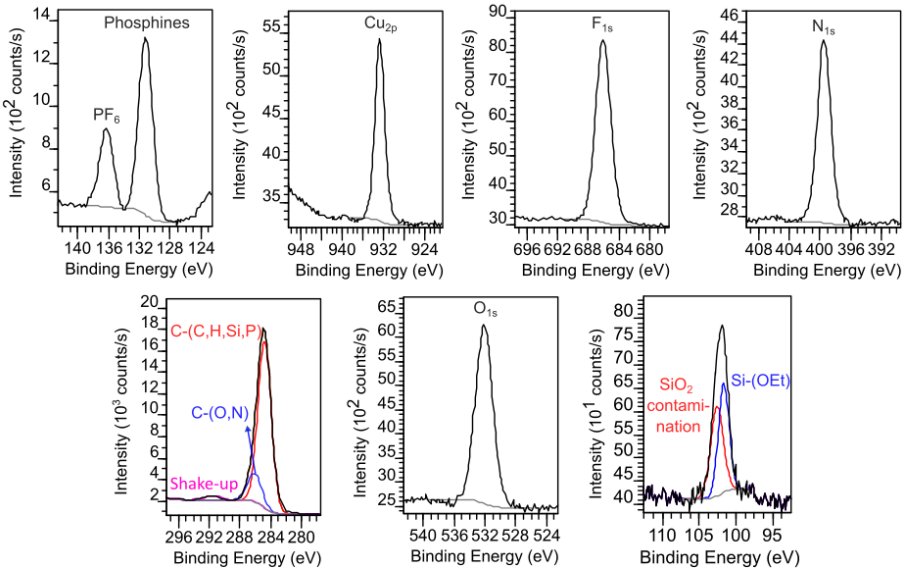
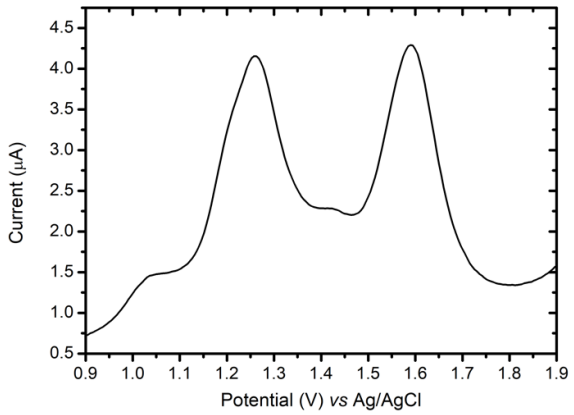


Figure D.4. P_{2p}, Cu_{2p}, F_{1s}, N_{1s}, C_{1s}, O_{1s} and Si_{2p} XPS spectra of **Cu-2**. The SiO_2 contamination was not considered in atomic percentage ratios calculation.



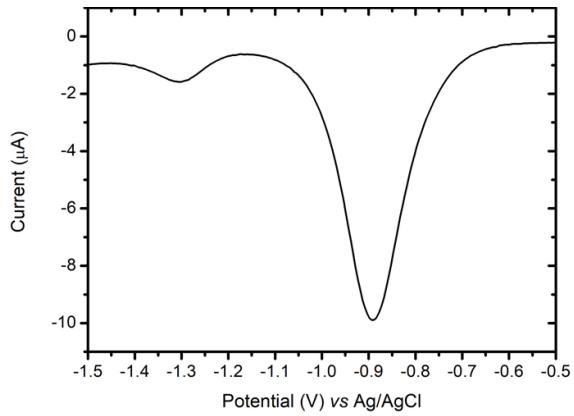


Figure D.5. Differential pulse voltammetry (DPV) of **Cu-2**.

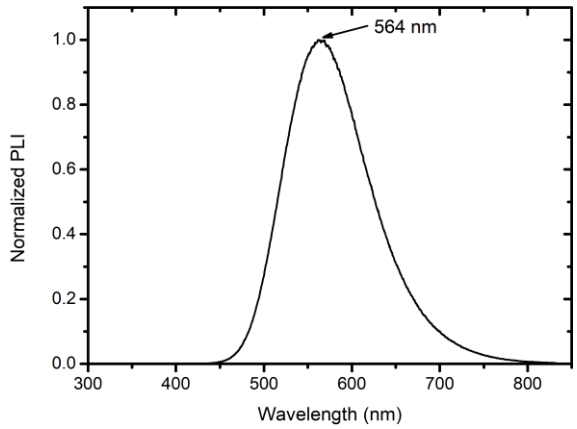


Figure D.6. Normalized emission spectra of **Cu-2** recorded at ambient temperature in MeCN.

$E_{0,0}$[a] (eV)	$E(Cu^{I}/Cu^{0})$ (V *vs* NHE)	$E(Cu^{II}/Cu^{I})$ (V *vs* NHE)	$E(Cu^{I*}/Cu^{0})$[b] (V *vs* NHE)	$E(Cu^{II}/Cu^{I*})$[c] (V *vs* NHE)
2.20	–1.11	1.46	1.09	–0.74

[a] Estimated from the maximum of the emission band of **Cu-2**.
[b]Excited-state reduction potential determined according to the Rehm-Weller equation[1]: $E(Cu^{I*}/Cu^{0}) = E(Cu^{I}/Cu^{0}) + E_{0\text{-}0}$
[c]Excited-state oxidation potential determined according to the Rehm-Weller equation[1]: $E(Cu^{II}/Cu^{I*}) = E(Cu^{II}/Cu^{I}) - E_{0\text{-}0}$

Photostability of Cu-2 in the dark

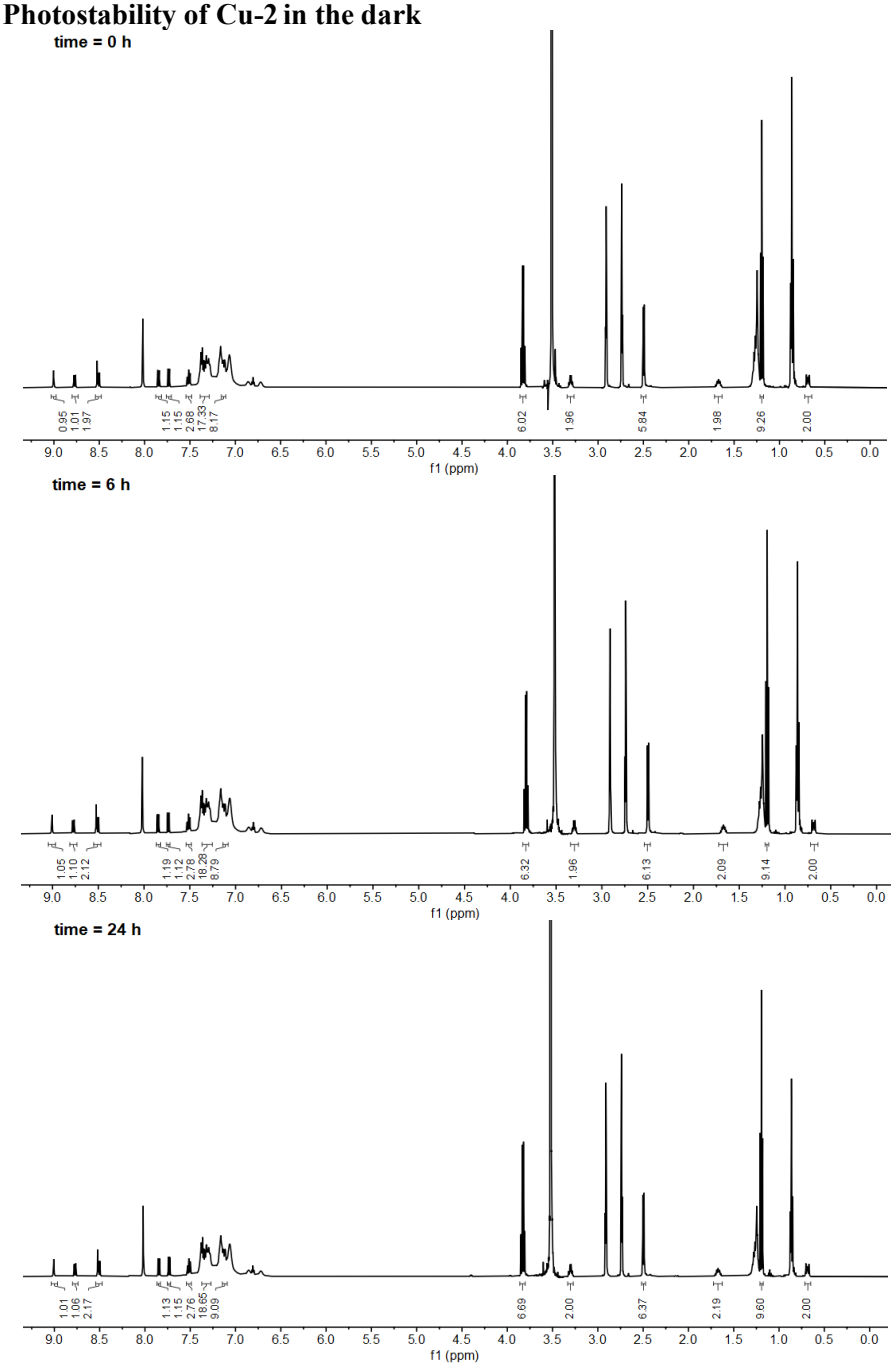


Figure D.7. Monitoring of the stability of **Cu-2** by ^{1}H-NMR in DMF-d_7 at ambient temperature in the dark.

Photostability of Cu-2 under irradiation of two blue Thorlabs LEDs

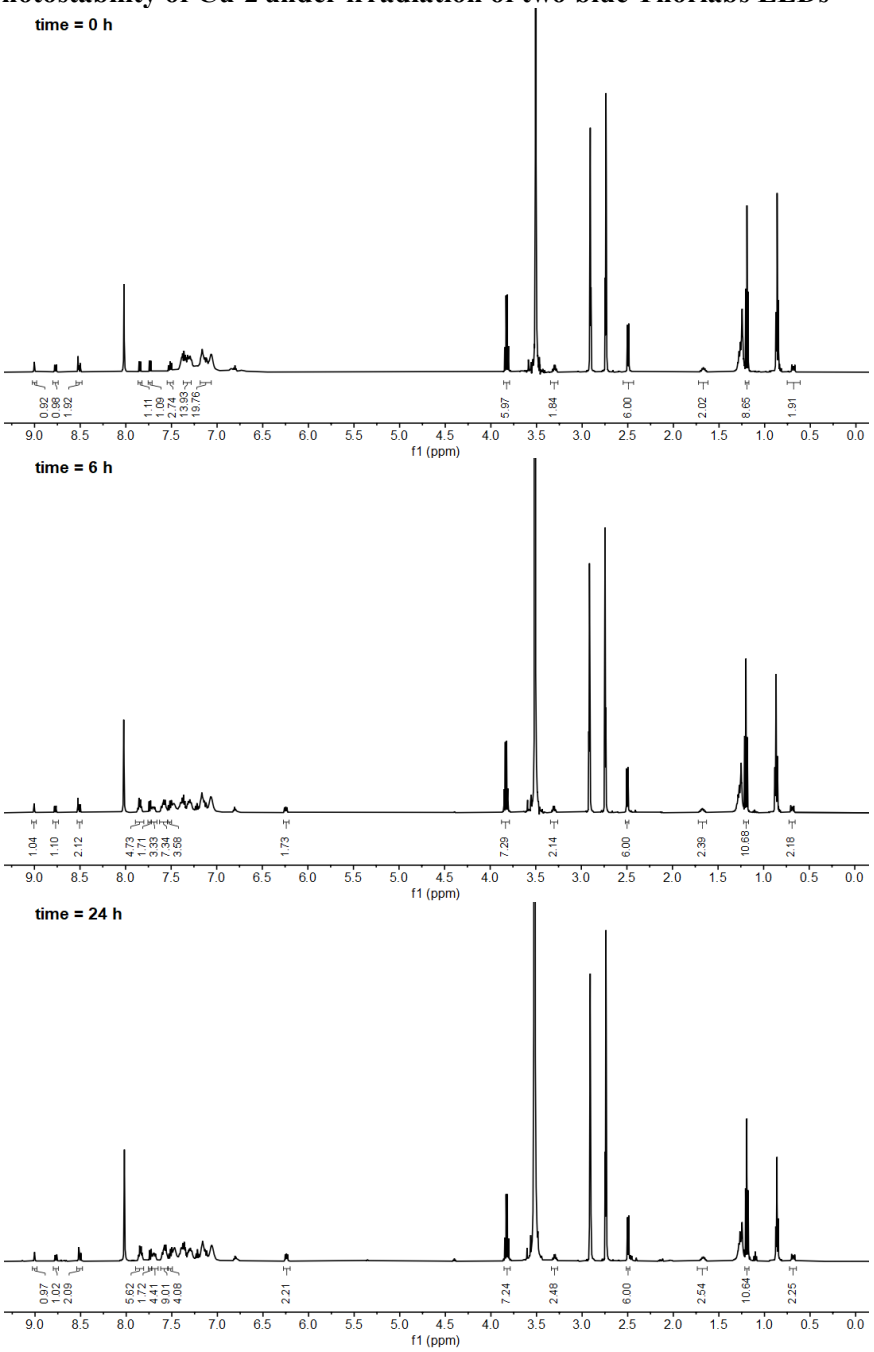


Figure D.8. Monitoring of the photostability of **Cu-2** by ^{1}H-NMR in DMF-d_7 at ambient temperature under irradiation with two Thorlabs blue LEDs.

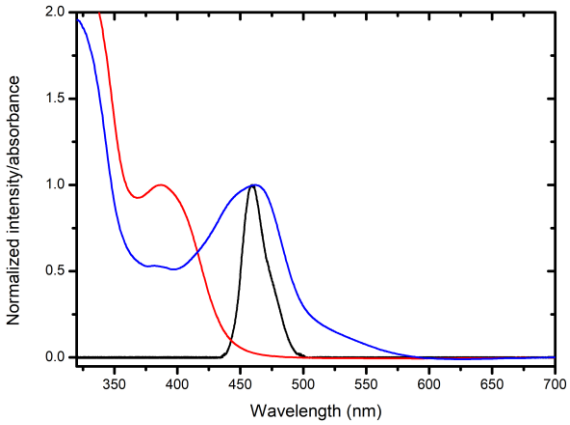


Figure D.9. Normalized Blue Thorlabs LED emission (black) and normalized absorbance of **Cu-1** (blue) and **Cu-2** (red) complexes.

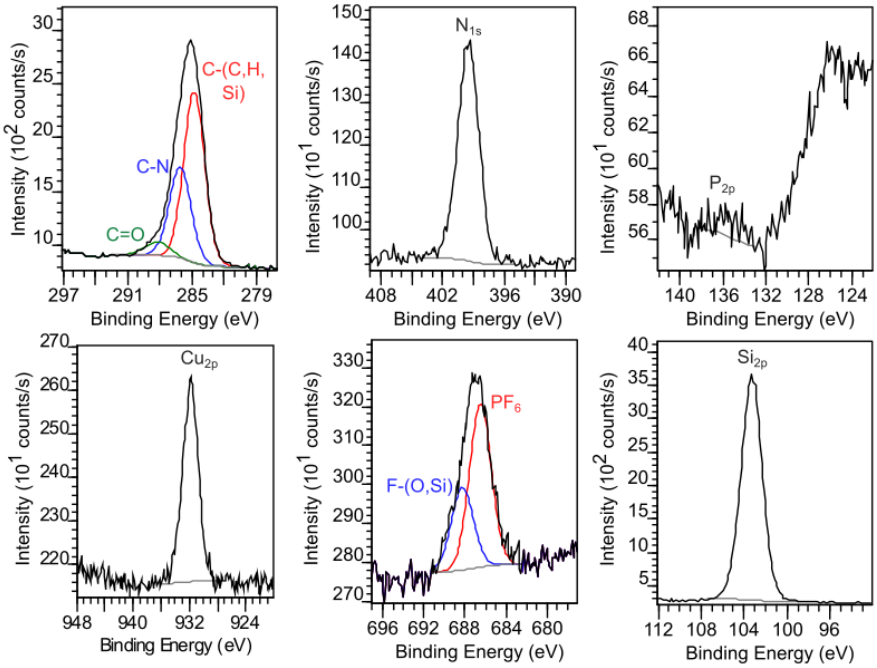


Figure D.10. C_{1s}, N_{1s}, P_{2p}, Cu_{2p}, F_{1s} and Si_{2p} XPS spectra of **NS-Cu-1**.

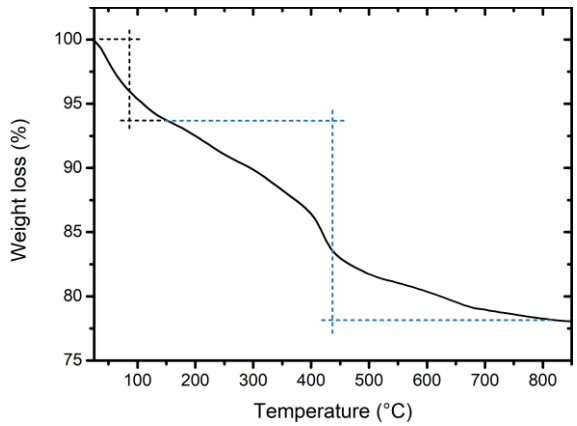


Figure D.11. TGA thermogram of **NS-Cu-1**. The TGA thermogram was measured by applying a temperature of 25°C for 5 minutes under an air flow rate of 100 mL min^{-1} followed by an increase of temperature at a rate of 10 °C min^{-1}, under an air flow rate of 100 mL min^{-1}. The first step (black) corresponds to solvents loss (6.3 wt.%) and the second step (blue) corresponds to organic components loss (15.6 wt.%).

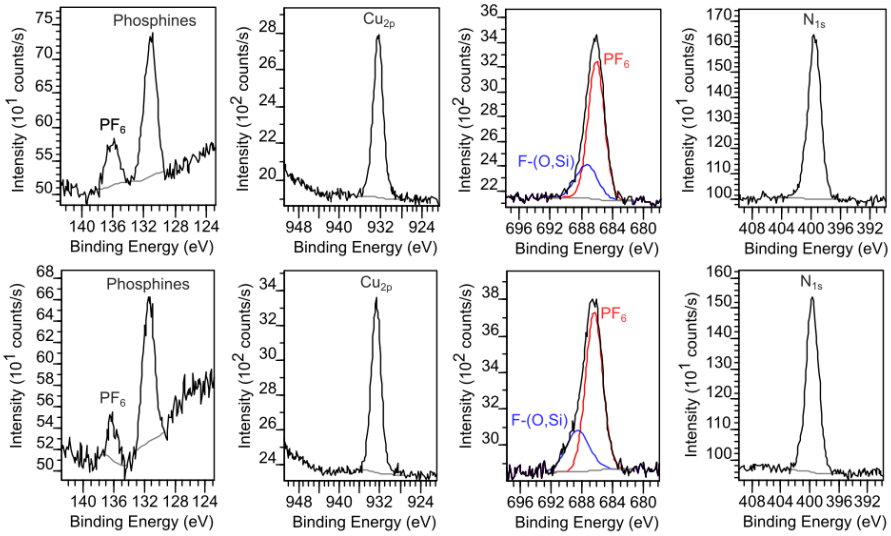


Figure D.12. P_{2p}, Cu_{2p}, F_{1s} and N_{1s} XPS spectra of **CS-Cu-2** (top) and **NS-Cu-2** (bottom).

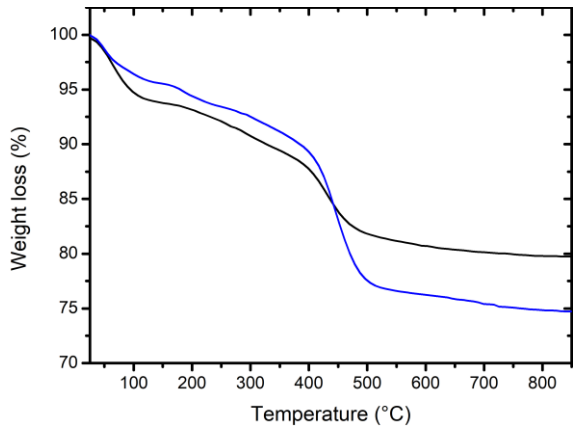


Figure D.13. TGA thermograms of **NS-Cu-2** (black line; 14.0 wt.%) and **CS-Cu-2** (blue line; 20.8 wt.%). The TGA thermogram was measured by applying a temperature of 25°C for 5 minutes under an air flow rate of 100 mL min^{-1} followed by an increase of temperature at a rate of 10 °C min^{-1}, under an air flow rate of 100 mL min^{-1}.

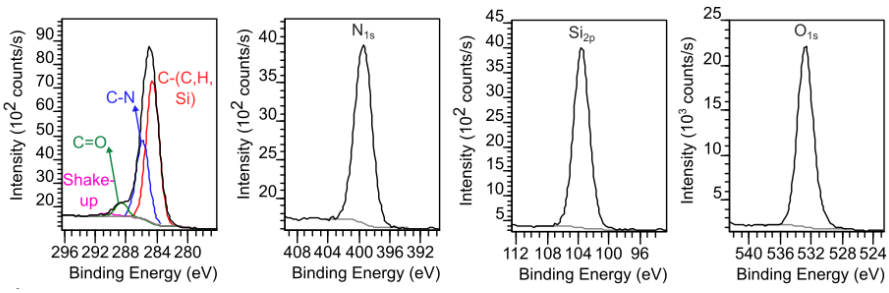


Figure D.14. C_{1s}, N_{1s}, Si_{2p} and O_{1s} XPS spectra of DMP-Si ligand anchored onto CS silica nanoparticles.

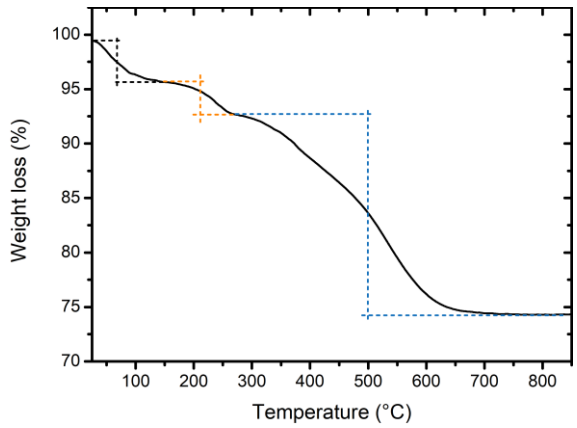


Figure D.15. TGA thermogram of heterogenized DMP-Si ligand The TGA thermogram was measured by applying a temperature of 25°C for 5 minutes under an air flow rate of 100 mL min^{-1} followed by an increase of temperature at a rate of 10 °C min^{-1}, under an air flow rate of 100 mL min^{-1}. The first step (black) corresponds to solvents loss (4.4 wt.%) the second (orange) and third steps (blue) corresponds to ligand loss (18.1 wt.%).

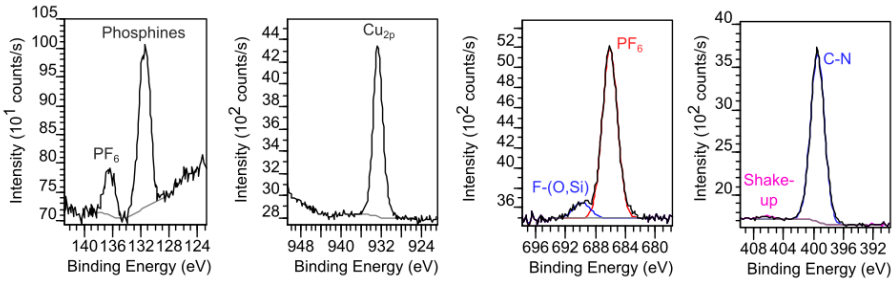


Figure D.16. P_{2p}, Cu_{2p}, F_{1s} and N_{1s} XPS spectra of **CS-Cu-2** obtained with the two-step methodology.

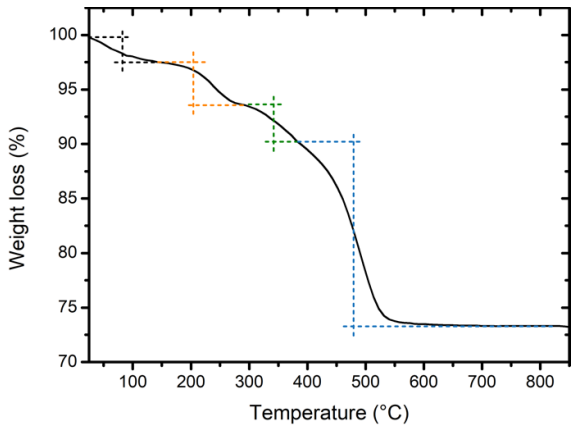


Figure D.17. TGA thermogram of **CS-Cu-2** obtained with the two-step methodology. The TGA thermogram was measured by applying a temperature of 25°C for 5 minutes under an air flow rate of 100 mL min^{-1} followed by an increase of temperature at a rate of 10 °C min^{-1}, under an air flow rate of 100 mL min^{-1}. The first step (black) corresponds to solvents loss (2.5 wt.%), the second (orange; 3.8 wt.%), third (green; 4.0 wt.%) and fourth steps (blue; 16.4 wt.%) correspond to calcination of organic parts.

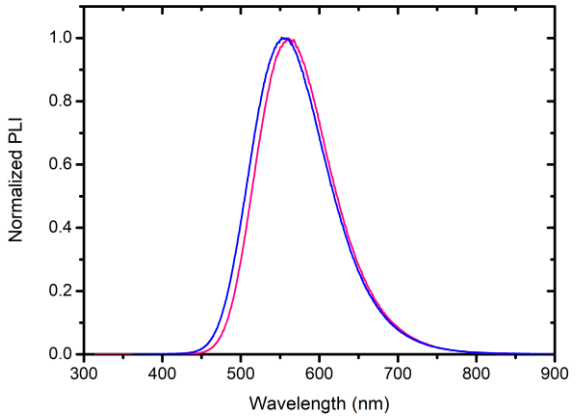


Figure D.18. Steady-state photoluminescence spectra of **Cu-2** in DCM (pink) and of **NS-Cu-2** obtained with the one-step procedure in DCM (blue).

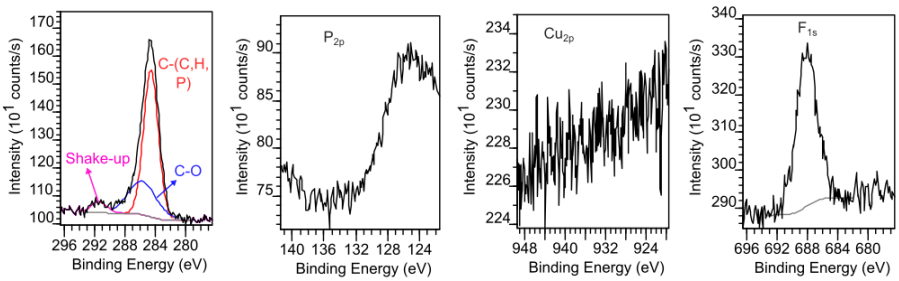
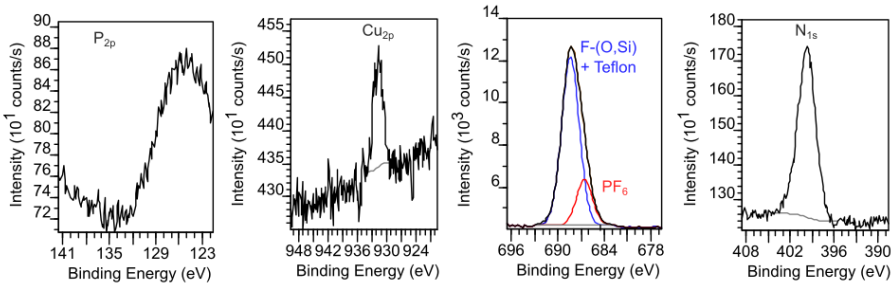


Figure D.19. C_{1s}, P_{2p}, Cu_{2p} and F_{1s} XPS spectra of $[Cu(DPEPhos)_2]PF_6$ that was put in contact with pristine NS silica nanoparticles.



	NS-Cu-1	NS-Cu-1 after 5 runs
Atomic percentage (%)		
C_{1s}	16.3	11.1
O_{1s}	56.6	53.6
Si_{2p}	23.4	20.1
N_{1s}	2.1	1.4
F_{1s}	1.3	13.7 (Teflon impurity)
Cu_{2p}	0.3	0.06
Ratios		
N/Si	0.09	0.07
N/C	0.13	0.13
Cu/C	0.018	0.006
Cu/N	0.14	0.05

Figure D.20. P_{2p}, Cu_{2p}, F_{1s} and N_{1s} XPS spectra of recycled **NS-Cu-1** during 5 runs and the corresponding table with atomic percentages and atomic ratios.

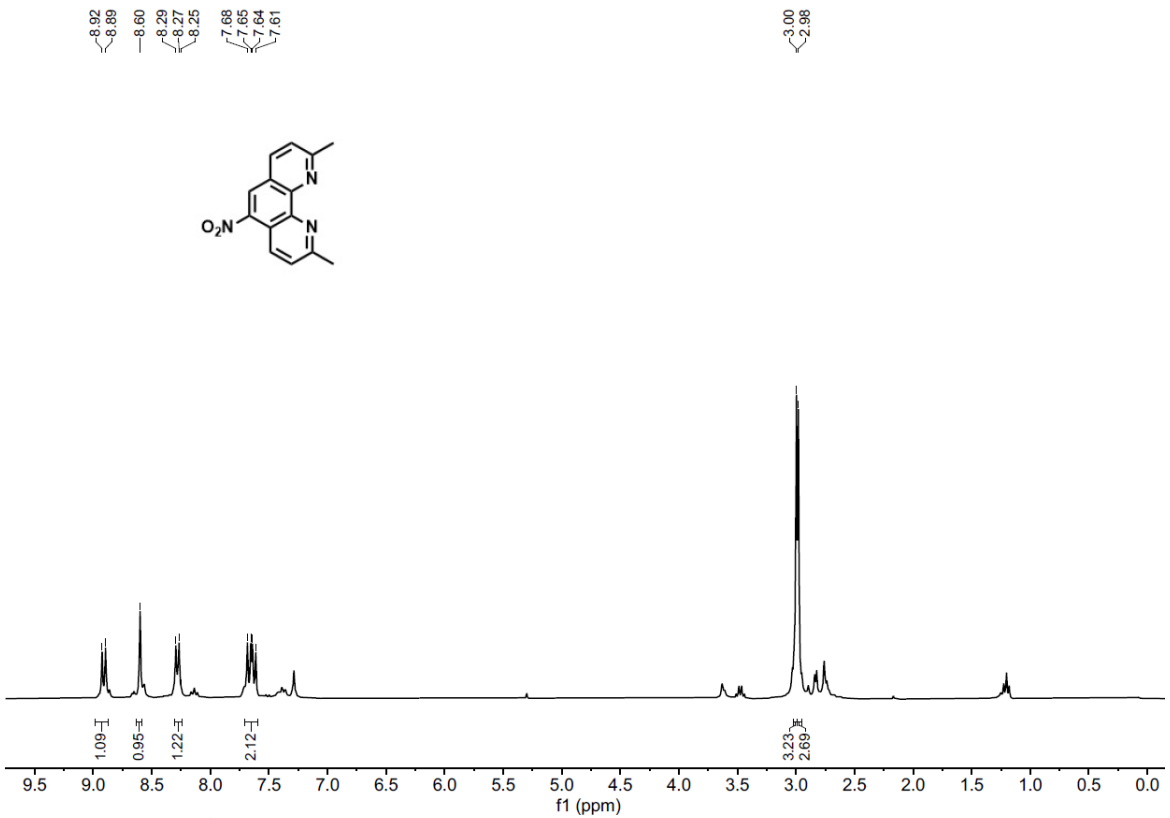


Figure D.21. ^{1}H NMR of NO_2-dimethylphenanthroline recorded in $CDCl_3$ at 300 MHz and 298 K.

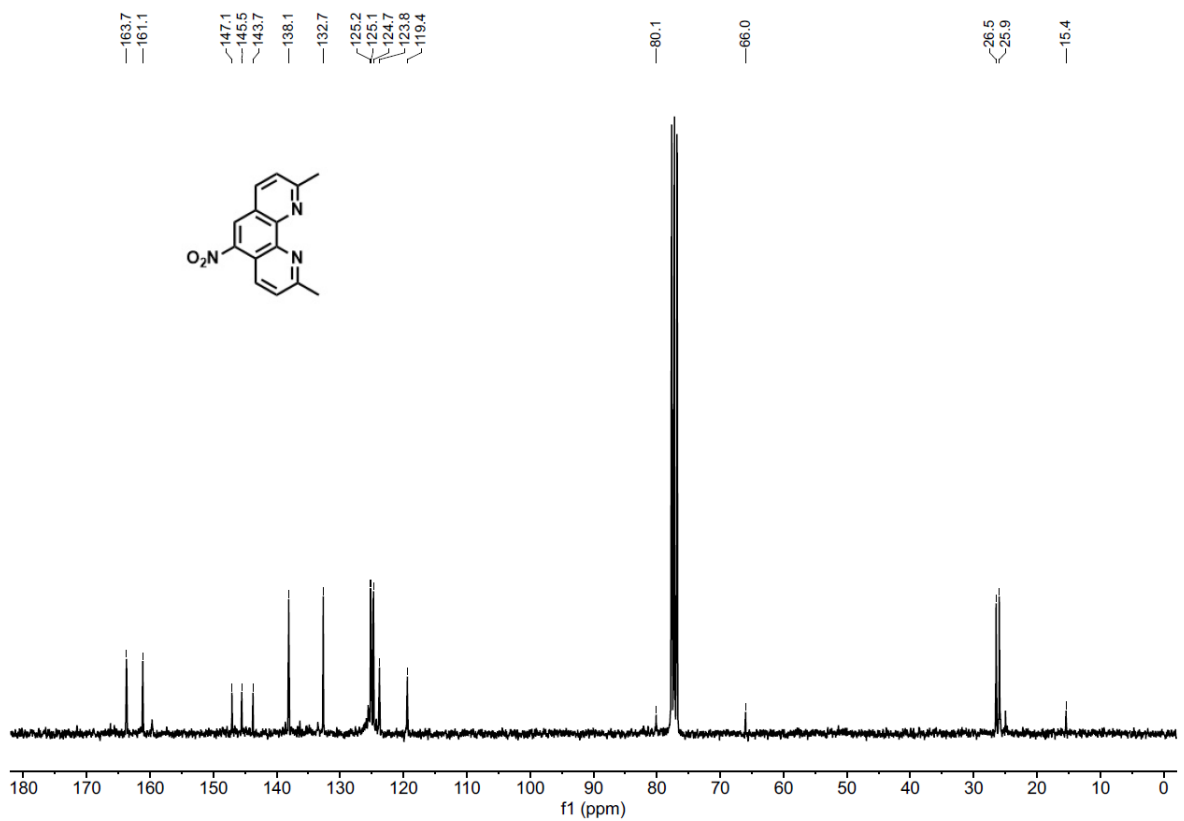


Figure D.22. ^{13}C NMR of NO_2-dimethylphenanthroline recorded in $CDCl_3$ at 75 MHz and 298 K.

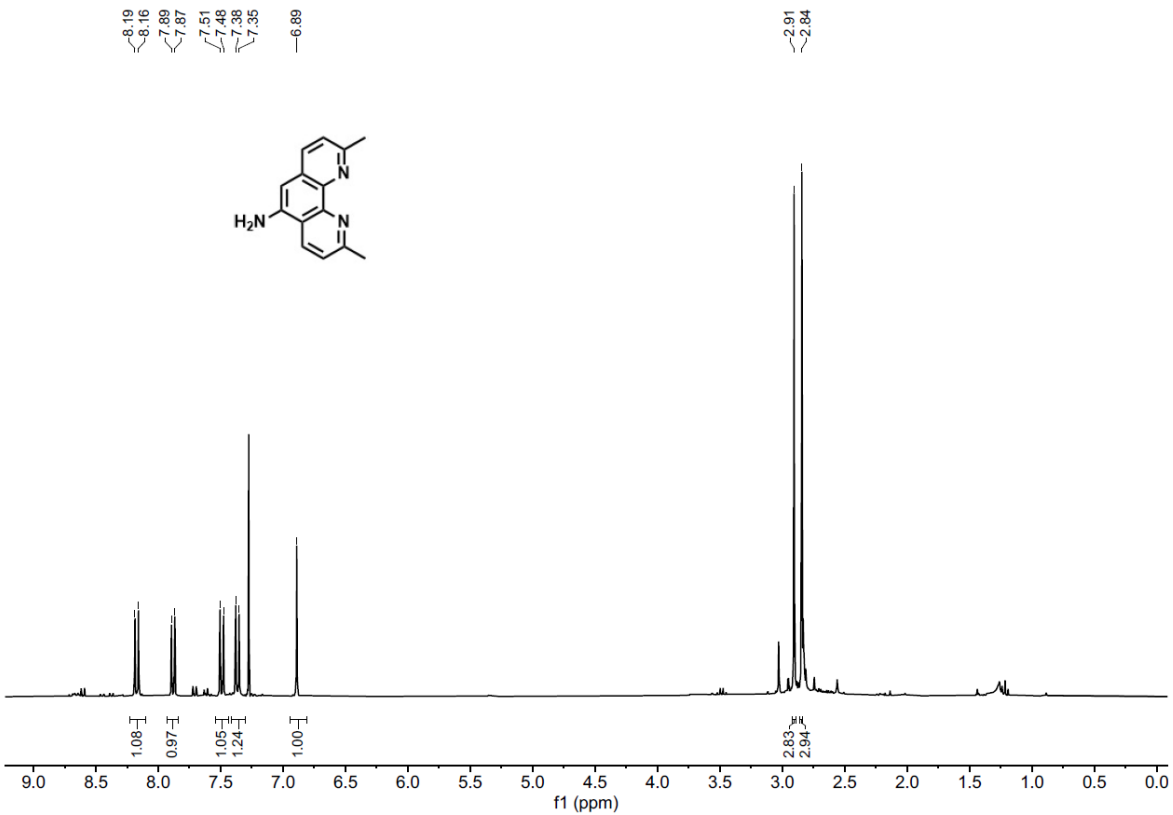


Figure D.23. ^{1}H NMR of NH_2-dimethylphenanthroline recorded in $CDCl_3$ at 300 MHz and 298 K.

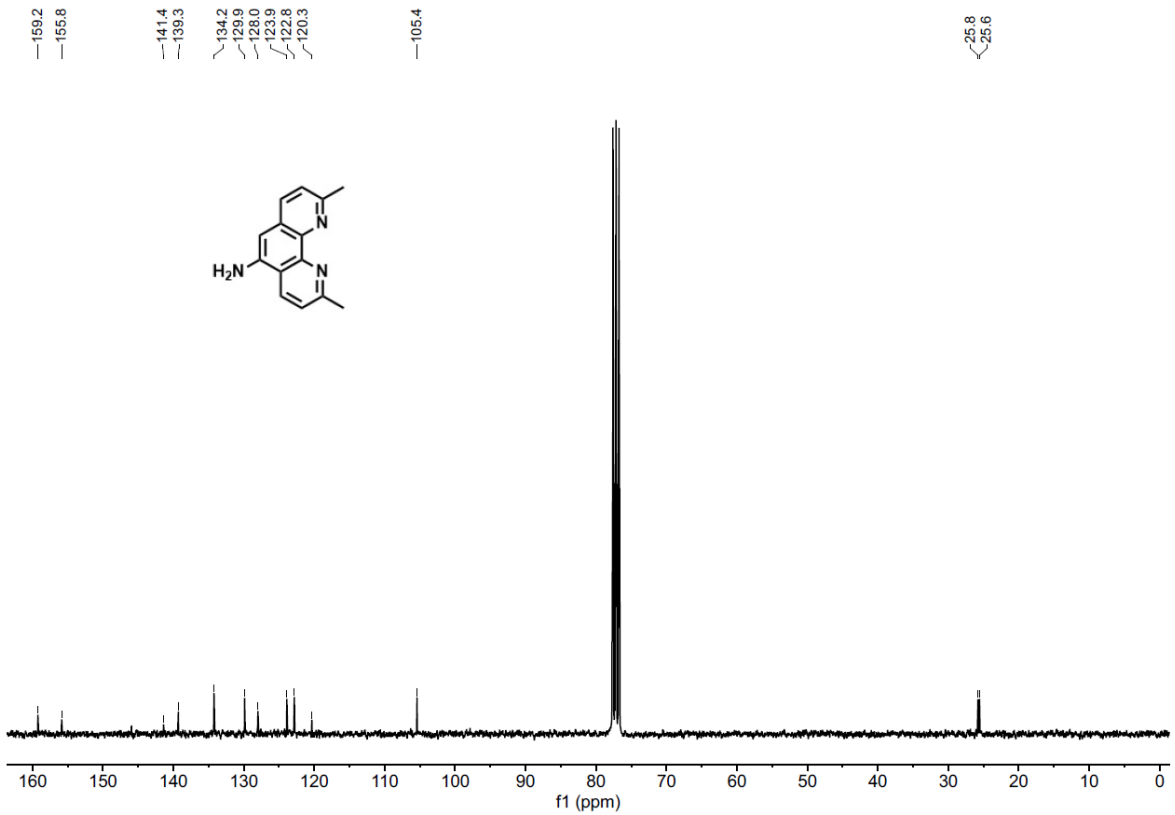


Figure D.24. ^{13}C NMR of NH_2-dimethylphenanthroline recorded in $CDCl_3$ at 75 MHz and 298 K.

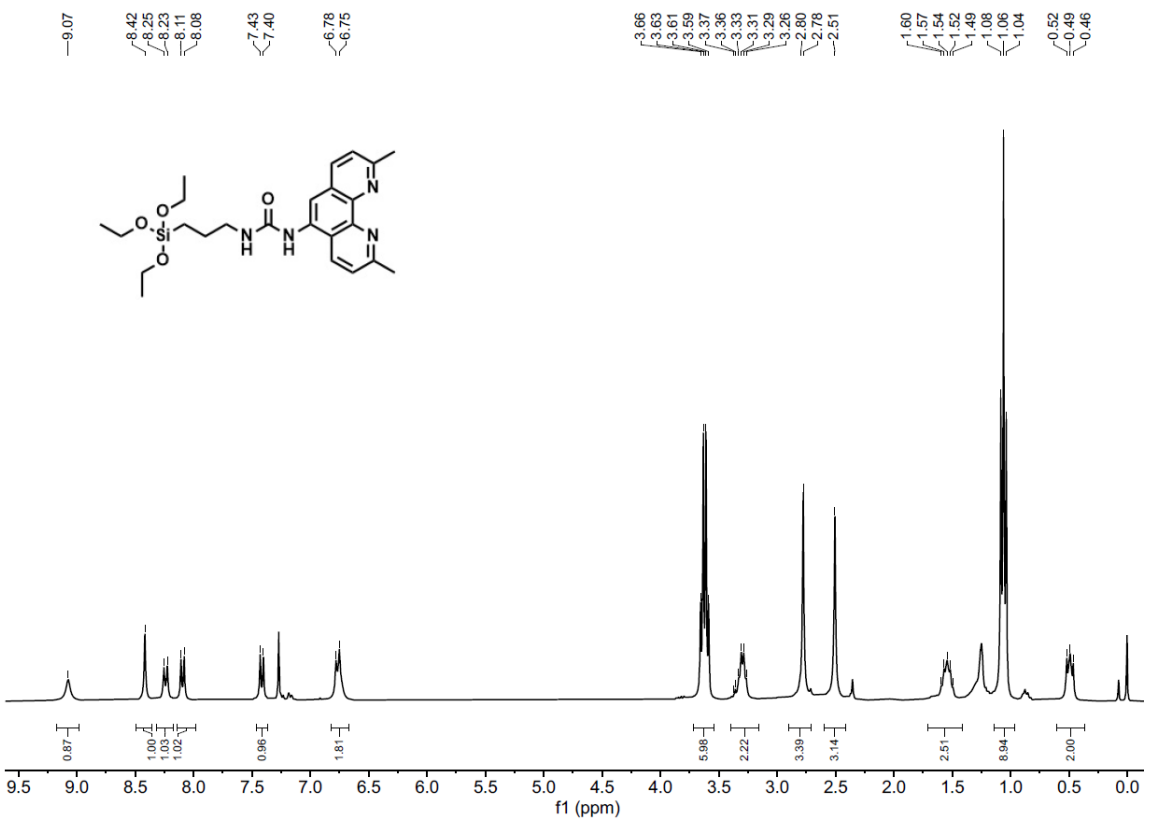


Figure D.25. ^{1}H NMR of dimethylphenanthroline-siloxane ligand (DMP-Si) recorded in $CDCl_3$ at 300 MHz and 298 K.

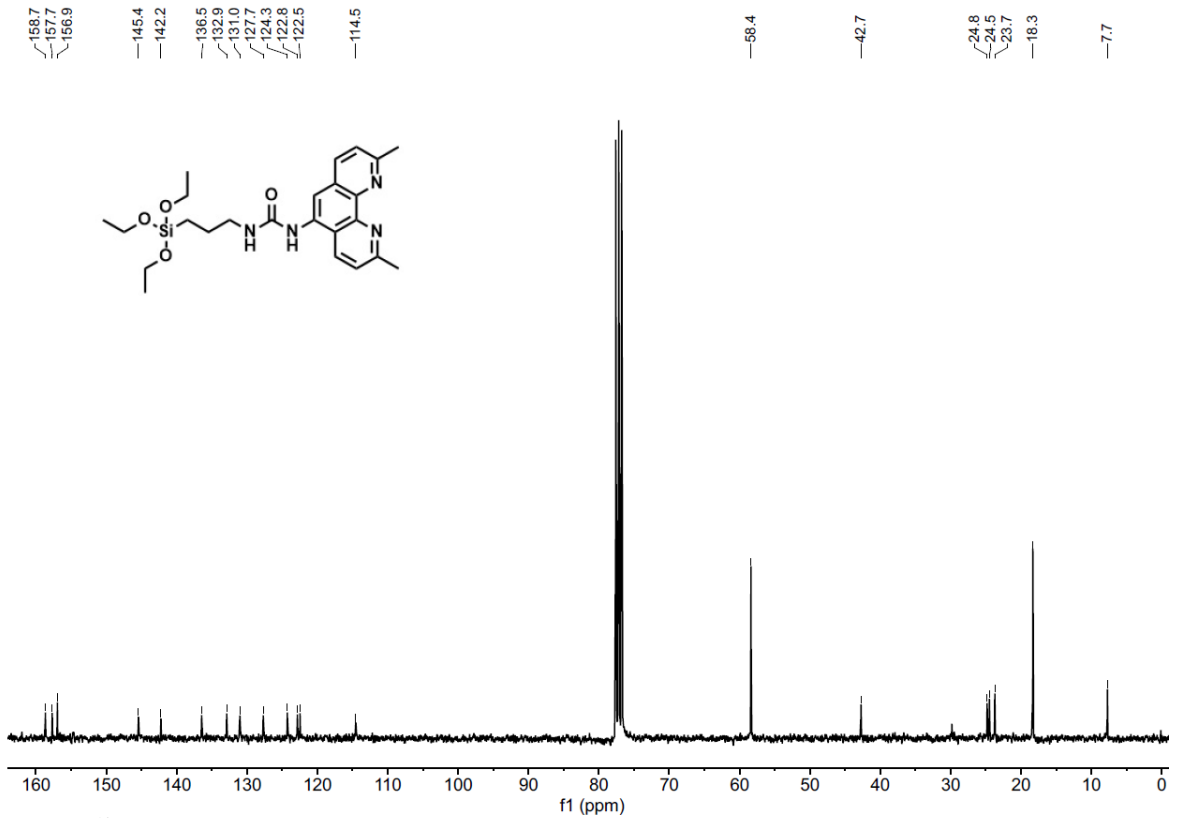


Figure D.26. ^{13}C NMR of dimethylphenanthroline-siloxane ligand (DMP-Si) recorded in $CDCl_3$ at 75 MHz and 298 K.

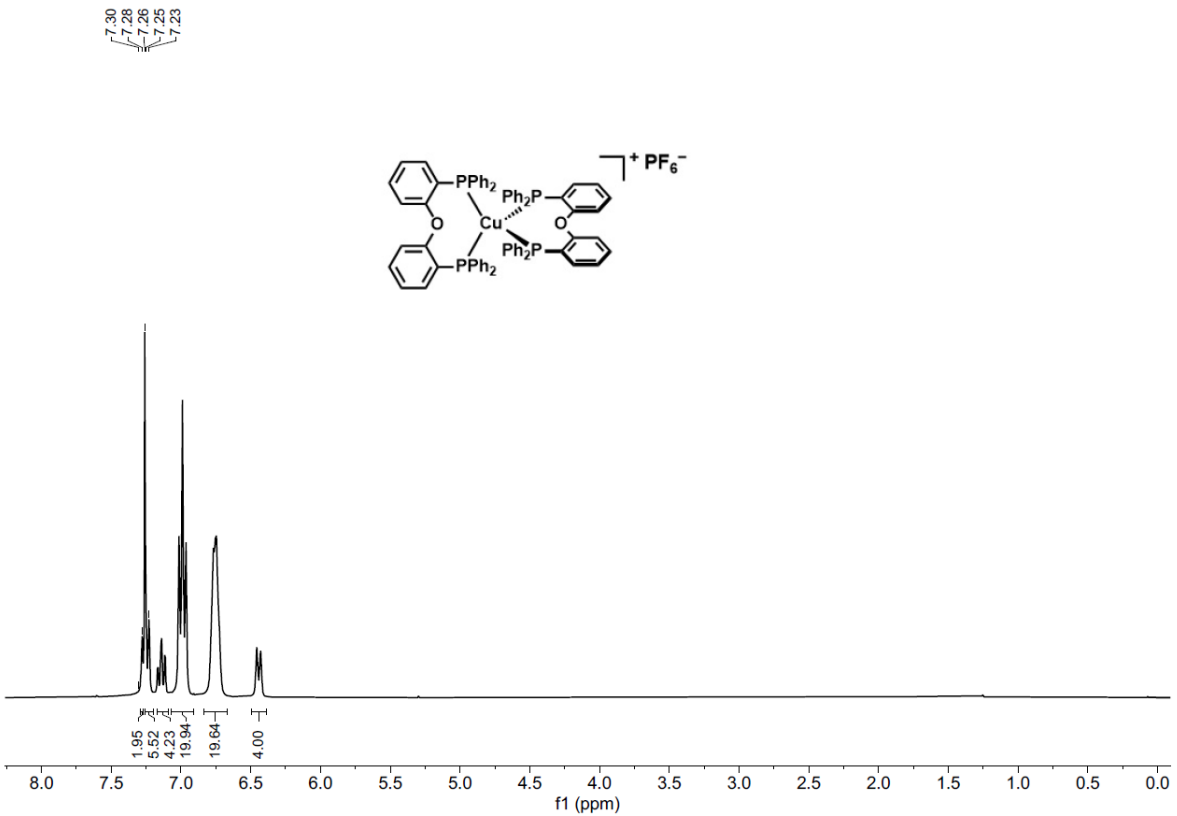


Figure D.27. ^{1}H NMR of $[Cu(DPEPhos)_2]PF_6$ recorded in $CDCl_3$ at 300 MHz and 298 K.

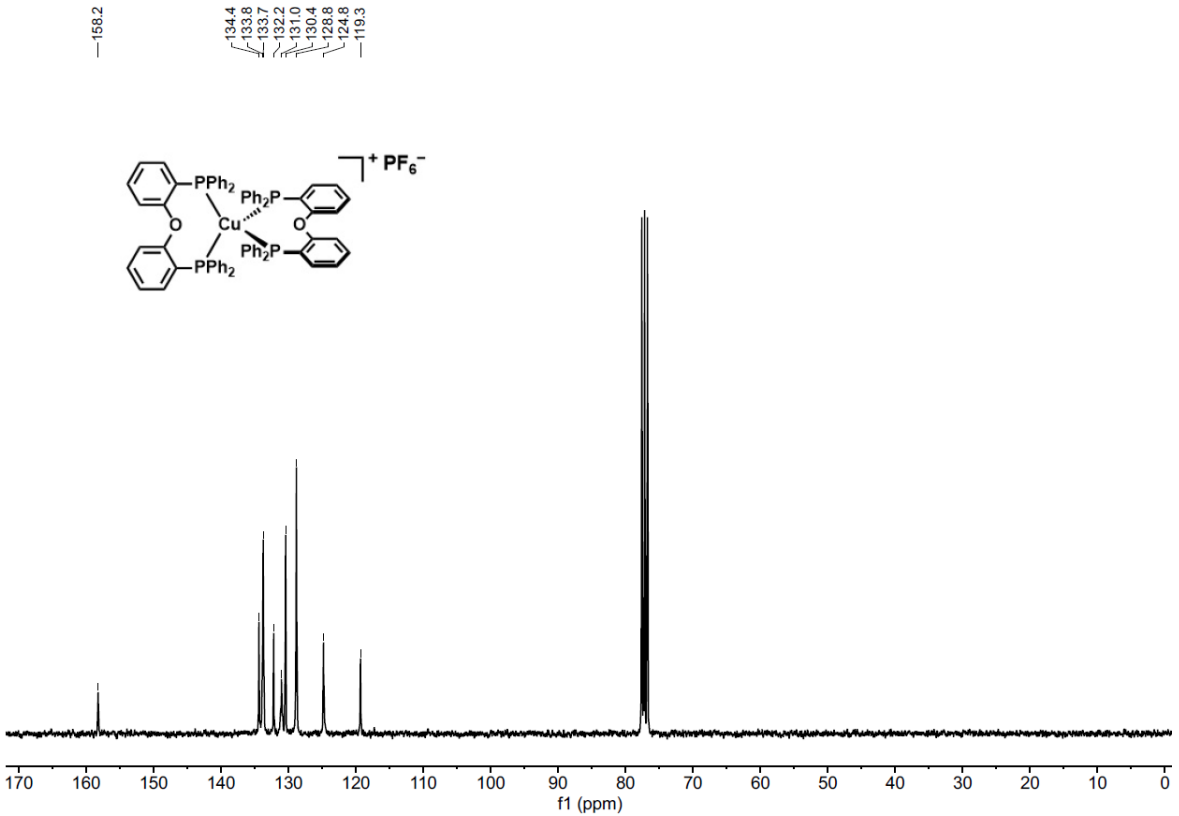


Figure D.28. ^{13}C NMR of $[Cu(DPEPhos)_2]PF_6$ recorded in $CDCl_3$ at 75 MHz and 298 K.

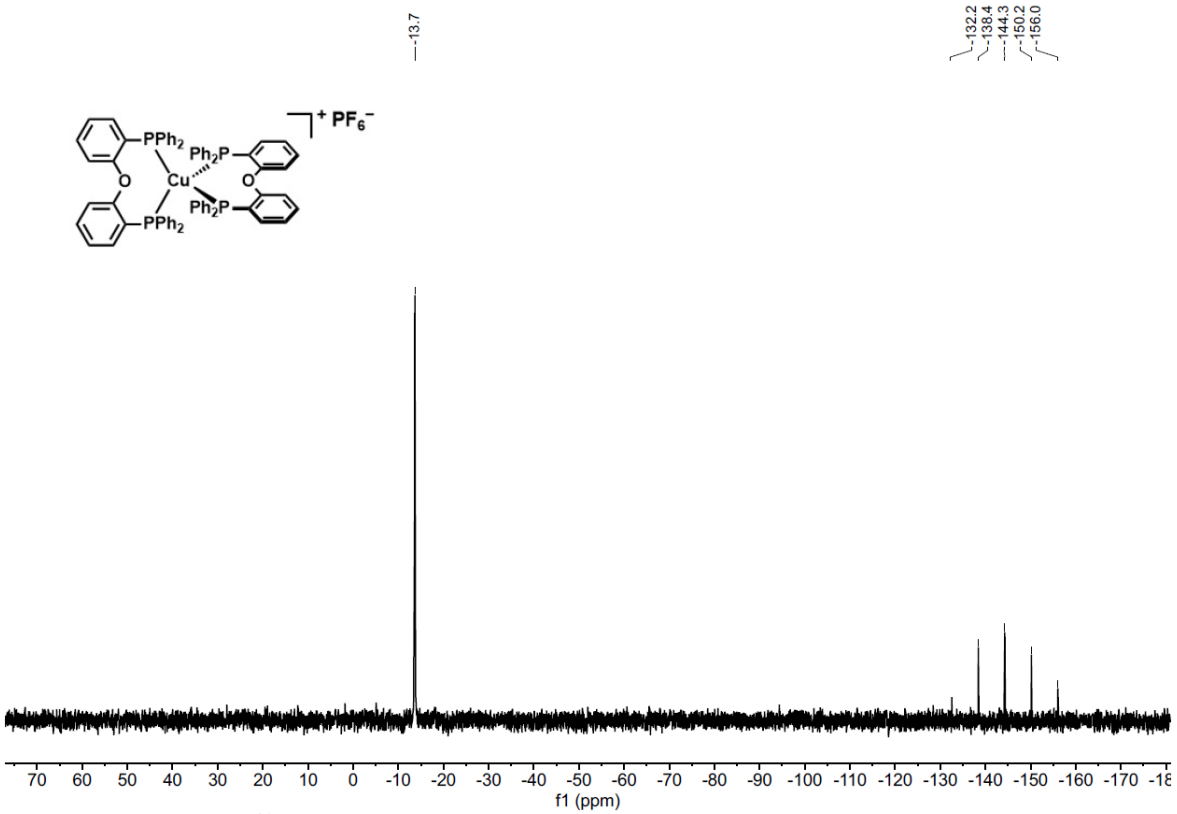


Figure D.29. ^{31}P NMR of [Cu(DPEPhos)$_2$]PF$_6$ recorded in CDCl$_3$ at 121 MHz and 298 K.

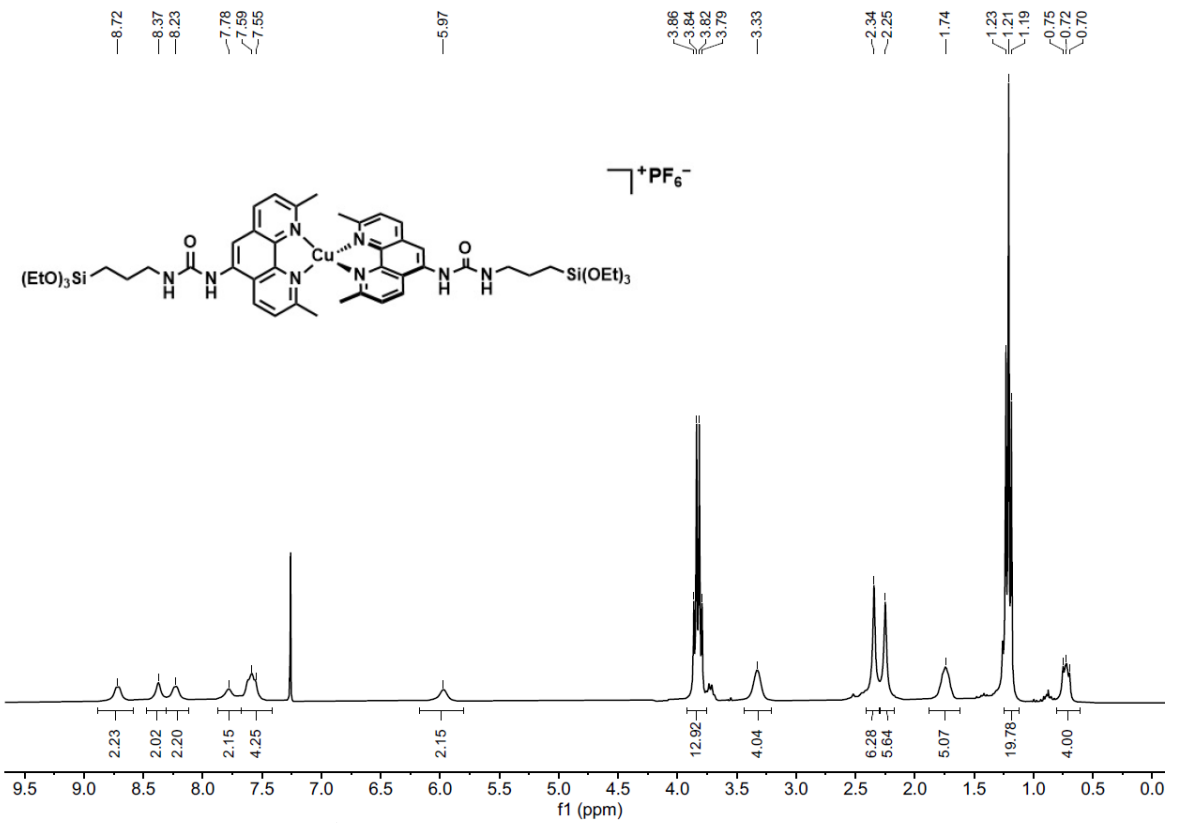


Figure D.30.. ^{1}H NMR of **Cu-1** recorded in $CDCl_3$ at 300 MHz and 298 K.

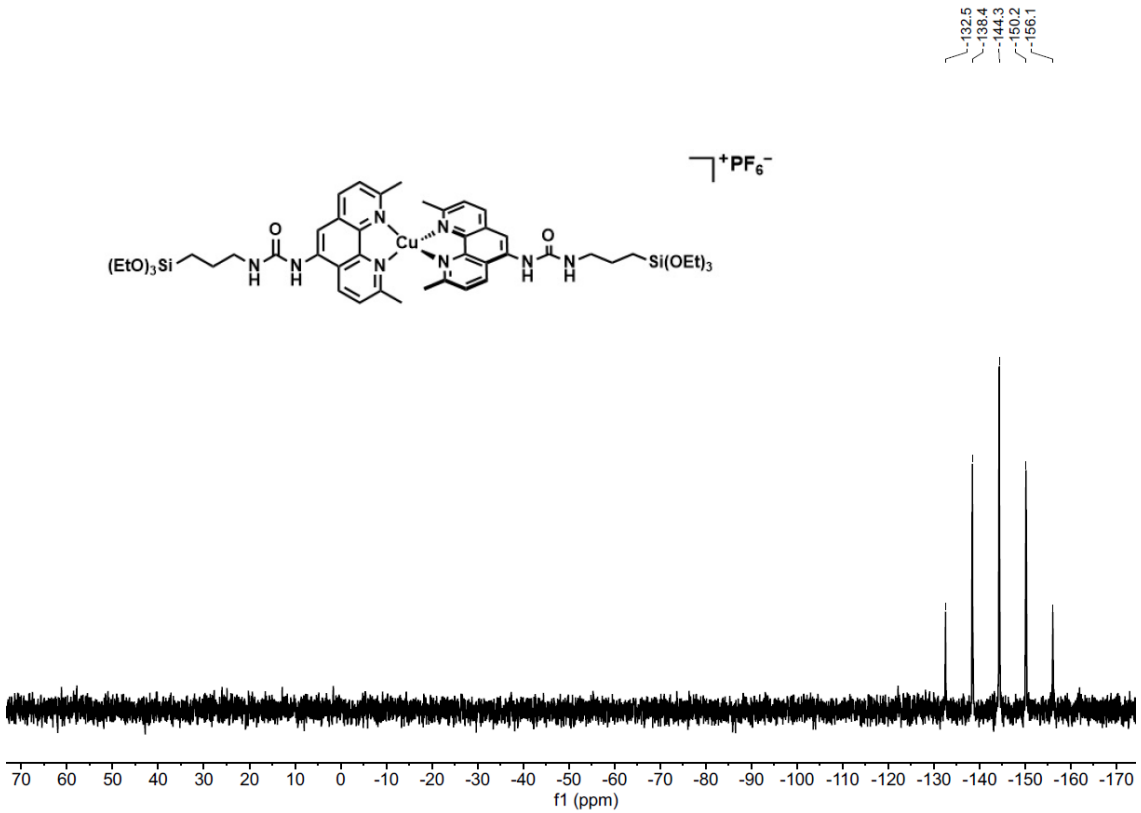


Figure D.31. ^{31}P NMR of **Cu-1** recorded in $CDCl_3$ at 121 MHz and 298 K.

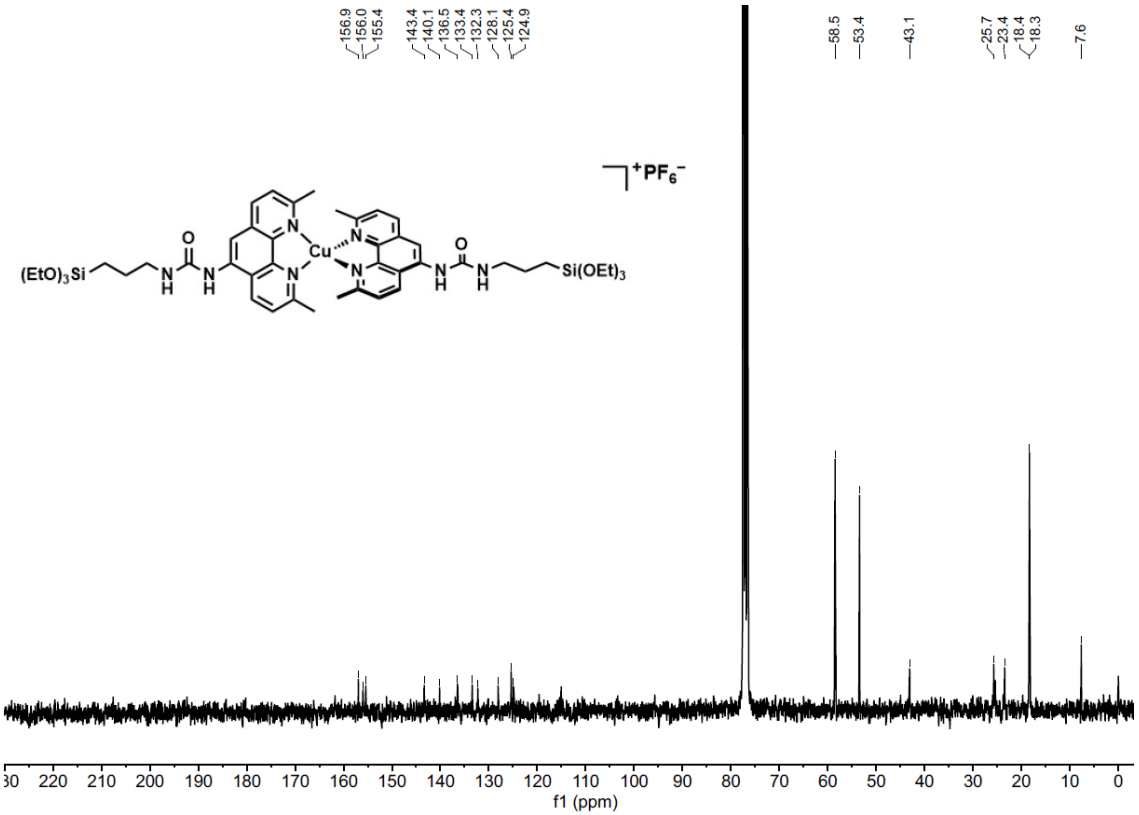


Figure D.32. ^{13}C NMR of **Cu-1** recorded in $CDCl_3$ at 75 MHz and 298 K.

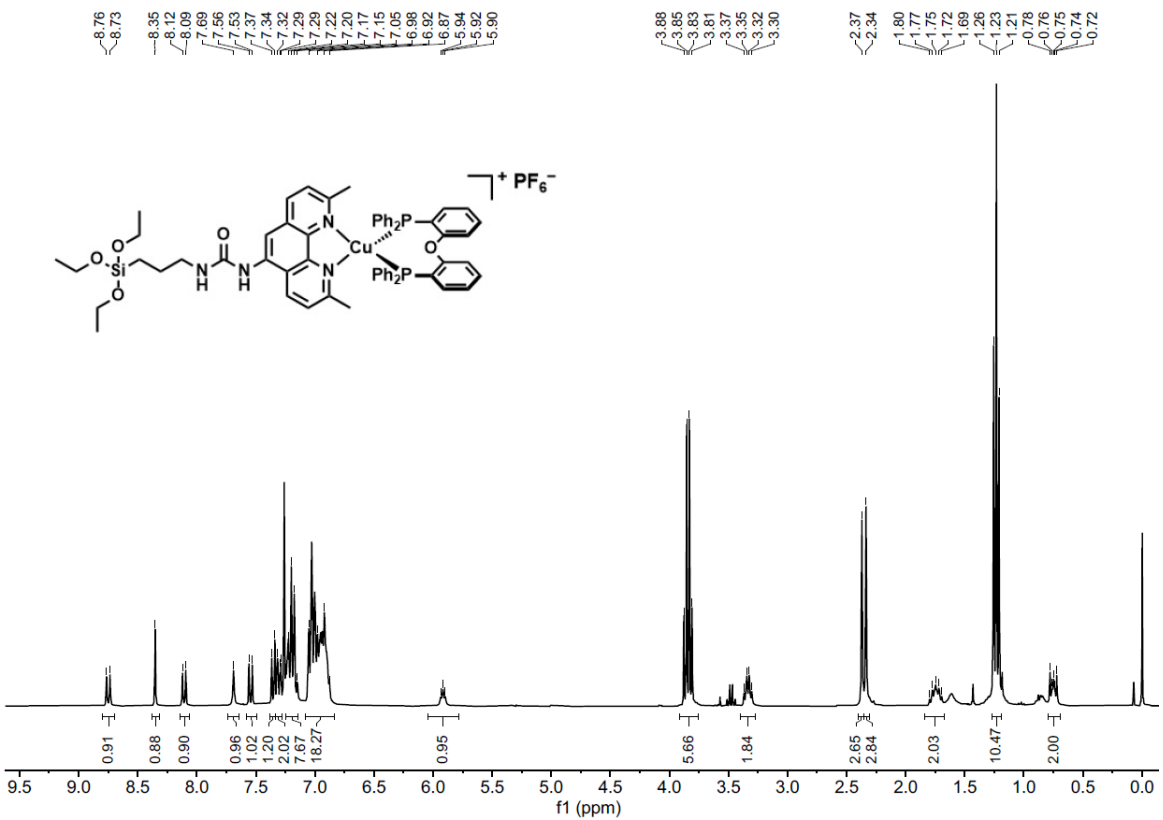


Figure D.33. ^{1}H NMR of **Cu-2** recorded in $CDCl_3$ at 300 MHz and 298 K.

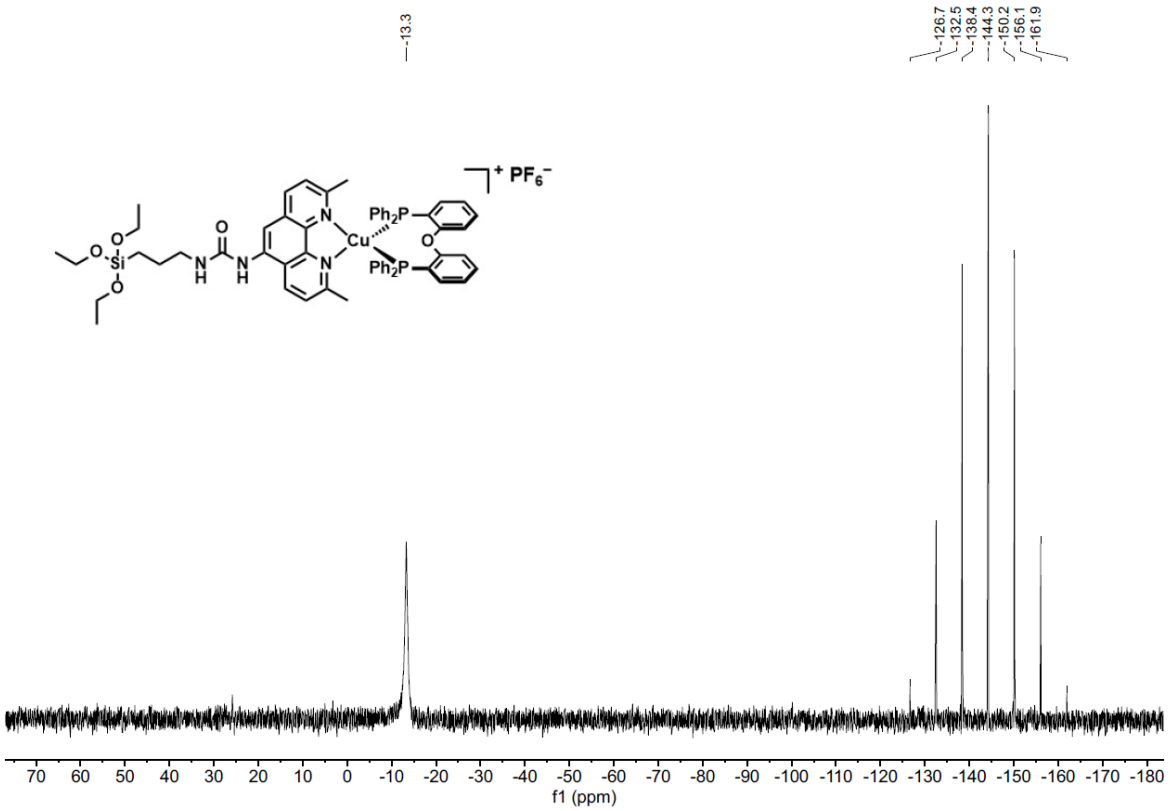


Figure D.34. ^{31}P NMR of **Cu-2** recorded in $CDCl_3$ at 121 MHz and 298 K.

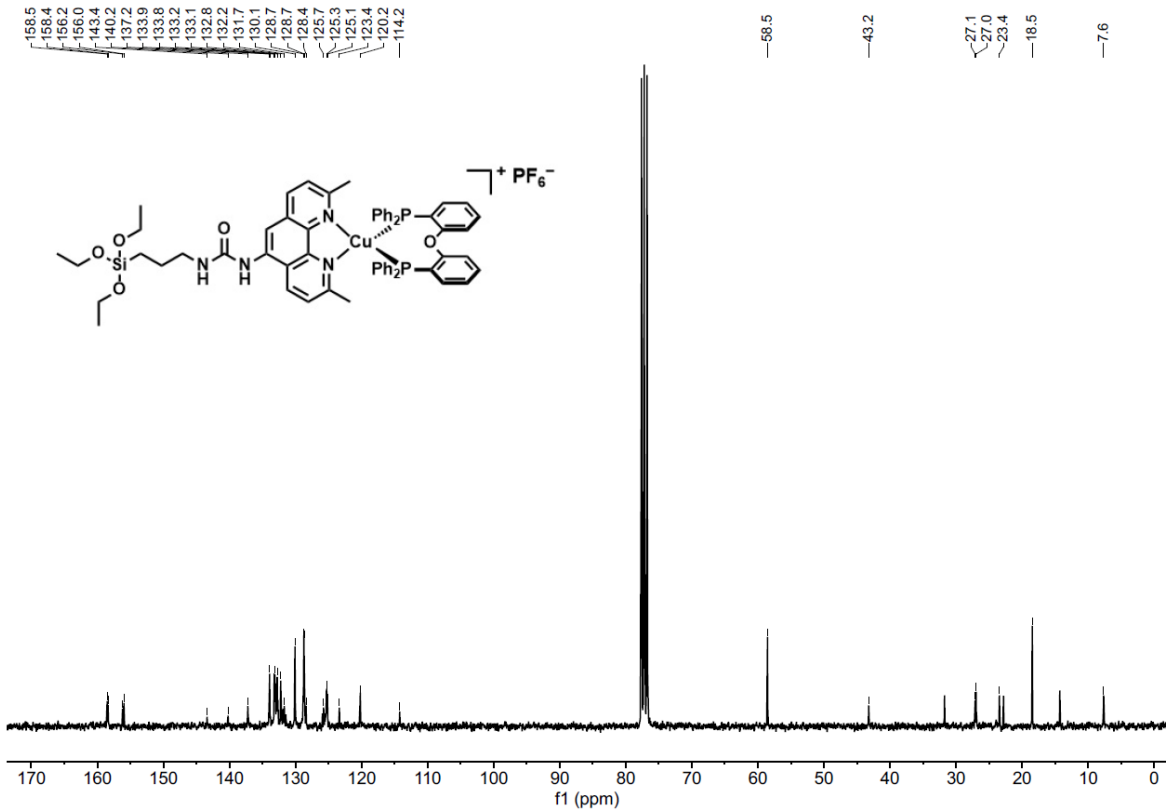


Figure D.35. ^{13}C NMR of **Cu-2** recorded in $CDCl_3$ at 75 MHz and 298 K.

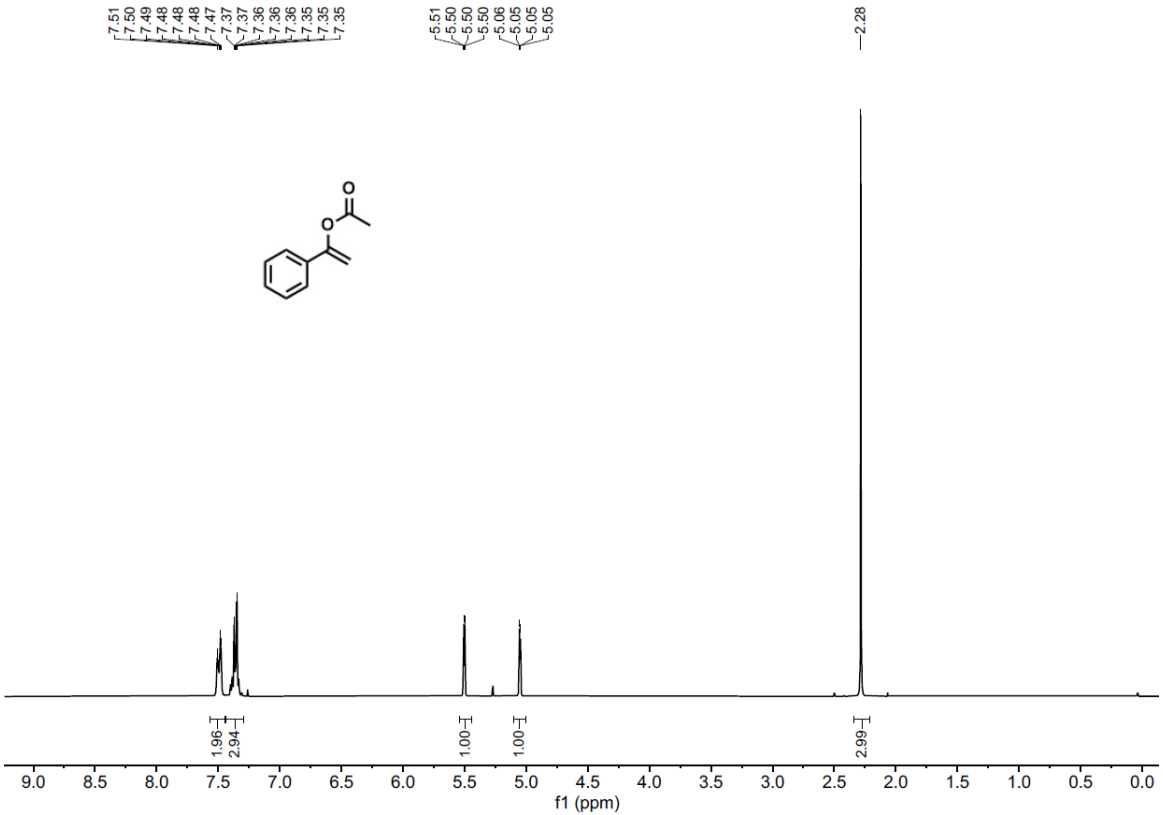


Figure D.36. ^{1}H NMR of 1-phenylvinyl acetate recorded in $CDCl_3$ at 300 MHz and 298 K.

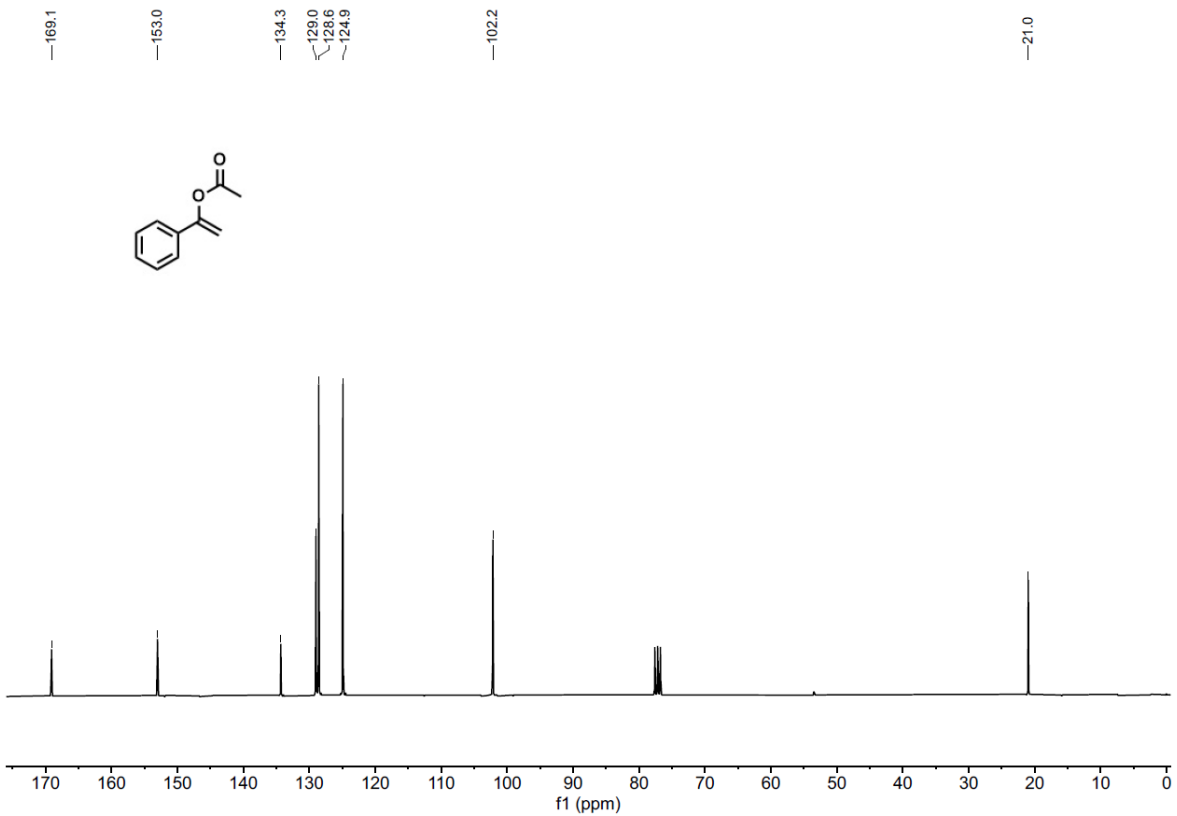


Figure D.37. ^{13}C NMR of 1-phenylvinyl acetate recorded in $CDCl_3$ at 75 MHz and 298 K.

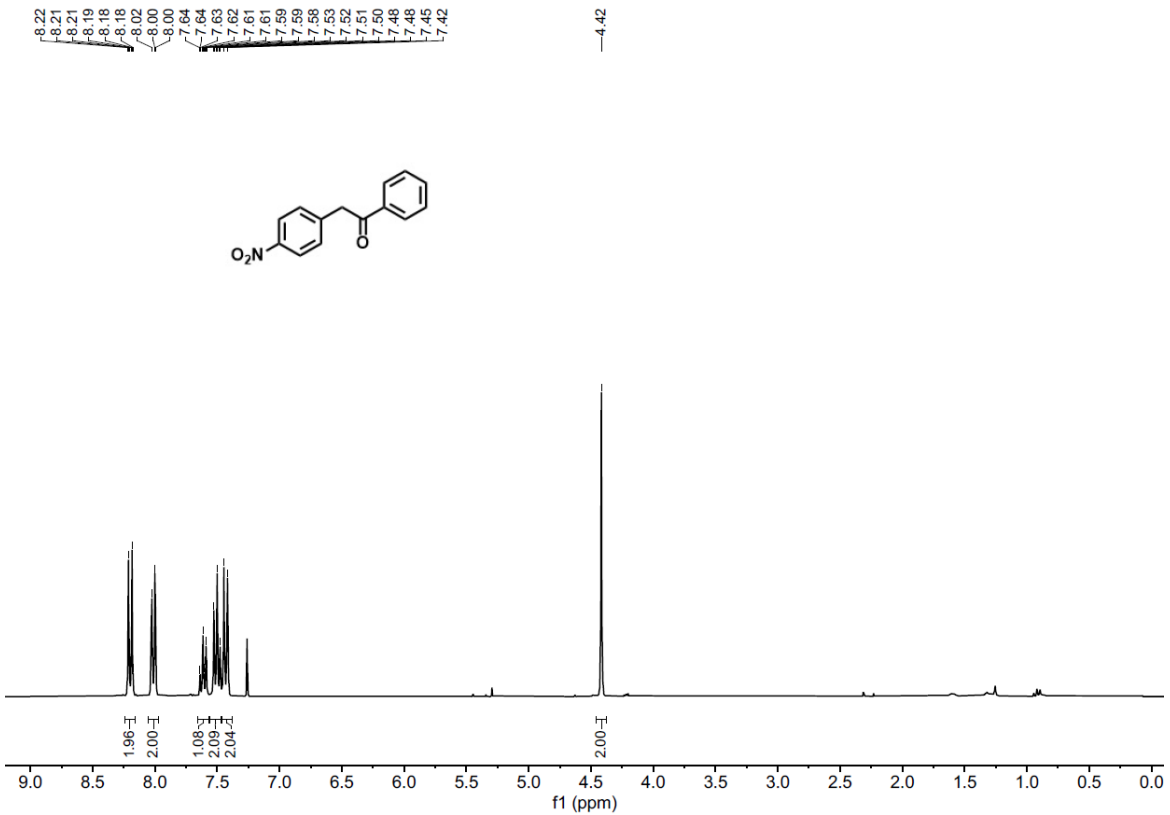


Figure D.38. ^{1}H NMR of 2-(4-nitrophenyl)-1-phenylethan-1-one recorded in $CDCl_3$ at 300 MHz and 298 K.

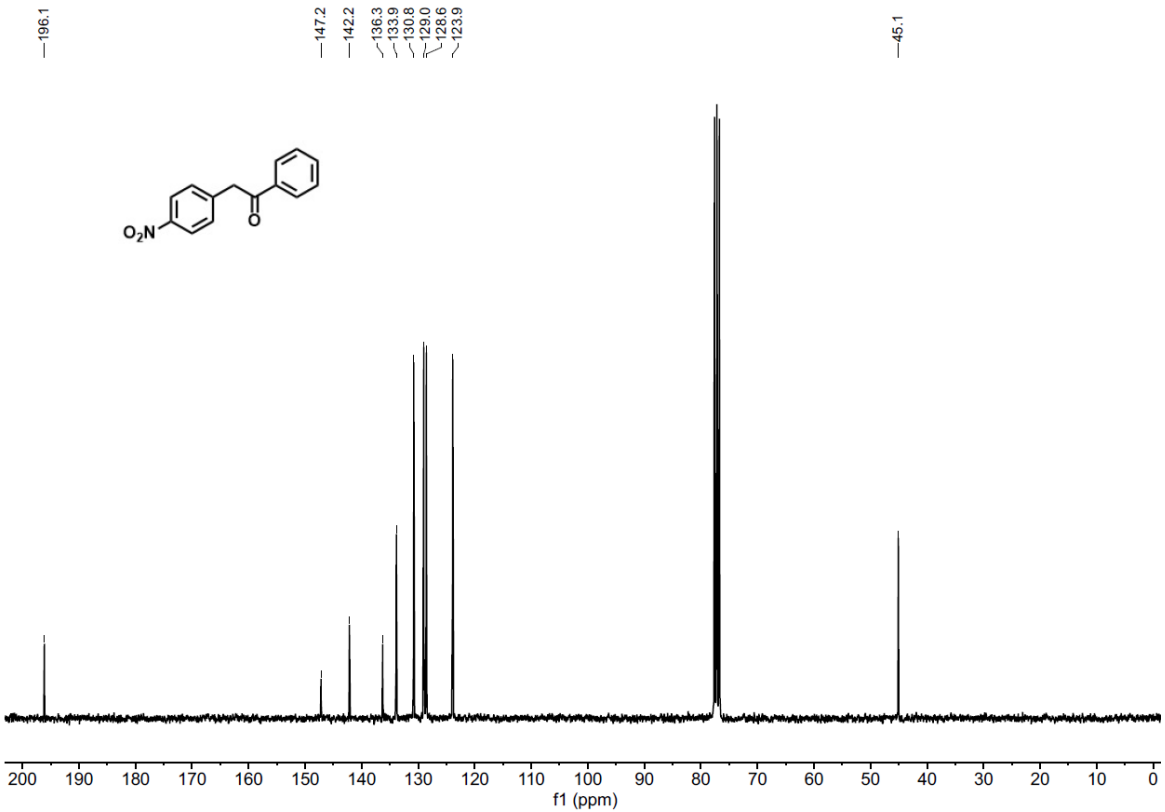


Figure D.39. ^{13}C NMR of 2-(4-nitrophenyl)-1-phenylethan-1-one recorded in $CDCl_3$ at 75 MHz and 298 K.

Bibliography

[1] V. Balzani, P. Ceroni, A. Juris, *Photochemistry and Photophysics - Concepts, Research, Applications*, Wiley-VCH, Weinheim, **2014**.

[2] P. Klán, J. Wirz, *Photochemistry of Organic Compounds - From Concepts to Practice*, John Wiley & Sons Ltd, Chichester, **2009**.

[3] J. Delaire, J. Piard, R. Méallet-Renault, G. Clavier, *Photophysique et Photochimie - Des Fondements Aux Applications*, EDP Sciences, **2016**.

[4] N. Armaroli, V. Balzani, N. Serpone, *Powering Planet Earth - Energy Solutions for the Future*, Wiley-VCH, Weinheim, **2013**.

[5] S. Cerfontaine, Tuning the Excited State Deactivation Pathways of Multinuclear Ruthenium(II) Polypyridyl Complexes: From Synthesis to Photochemistry, UCLouvain, **2020**.

[6] N. S. Lewis, D. G. Nocera, *Proc. Natl. Acad. Sci.* **2006**, *103*, 15729–15735.

[7] G. Ciamician, *Science* **1912**, *36*, 385–394.

[8] Our World in Data, "Global primary energy consumption source," can be found under https://ourworldindata.org/search?q=energy+consumption., **2023**.

[9] A. Aydogan, Towards the Usage of Iron(II/III) Complexes as Potent Photosensitizers in Organic Photoredox Catalysis, UCLouvain, **2022**.

[10] D. M. Schultz, T. P. Yoon, *Science* **2014**, *343*, 1239176.

[11] N. Holonyak Jr, S. F. Bevacqua, *Appl. Phys. Lett.* **1962**, *1*, 82–83.

[12] W.-K. Jo, R. J. Tayade, *Ind. Eng. Chem. Res.* **2014**, *53*, 2073–2084.

[13] R. D. Costa, E. Ortí, H. J. Bolink, F. Monti, G. Accorsi, N. Armaroli, *Angew. Chem. Int. Ed.* **2012**, *51*, 8178–8211.

[14] C. J. Humphreys, *MRS Bull.* **2008**, *33*, 459–470.

[15] S. Nakamura, T. Mukai, M. Senoh, *Appl. Phys. Lett.* **1994**, *64*, 1687–1689.

[16] S. Fujita, S. Yoshihara, A. Sakamoto, S. Yamamoto, S. Tanabe, *Proc SPIE 5941* **2005**, *Fifth International Conference on Solid State Lighting*, 594111.

[17] G. Zissis, S. Kitsinelis, *J. Phys. Appl. Phys.* **2009**, *42*, 173001.

[18] C. W. Tang, S. A. VanSlyke, *Appl. Phys. Lett.* **1987**, *51*, 913–915.

[19] B. Geffroy, P. Le Roy, C. Prat, *Polym. Int.* **2006**, *55*, 572–582.

[20] Q. Wei, N. Fei, A. Islam, T. Lei, L. Hong, R. Peng, X. Fan, L. Chen, P. Gao, Z. Ge, *Adv. Opt. Mater.* **2018**, *6*, 1800512.

[21] S. Sudheendran Swayamprabha, D. K. Dubey, Shahnawaz, R. A. K. Yadav, M. R. Nagar, A. Sharma, F.-C. Tung, J.-H. Jou, *Adv. Sci.* **2021**, *8*, 2002254.

[22] C. Pac, M. Ihama, M. Yasuda, Y. Miyauchi, H. Sakurai, *J. Am. Chem. Soc.* **1981**, *103*, 6495–6497.

[23] D. M. Hedstrand, W. H. Kruizinga, R. M. Kellogg, *Tetrahedron Lett.* **1978**, *19*, 1255–1258.
[24] H. Cano-Yelo, A. Deronzier, *J Chem Soc Perkin Trans II* **1984**, 1093–1098.
[25] J.-M. Kern, J.-P. Sauvage, *J. Chem. Soc. Chem. Commun.* **1987**, 546–548.
[26] M. A. Ischay, M. E. Anzovino, J. Du, T. P. Yoon, *J. Am. Chem. Soc.* **2008**, *130*, 12886–12887.
[27] D. A. Nicewicz, D. W. MacMillan, *Science* **2008**, *322*, 77–80.
[28] J. M. R. Narayanam, J. W. Tucker, C. R. J. Stephenson, *J. Am. Chem. Soc.* **2009**, *131*, 8756–8757.
[29] K. Kalyanasundaram, M. Grätzel, *Coord. Chem. Rev.* **1998**, *177*, 347–414.
[30] M. Grätzel, *Acc. Chem. Res.* **1981**, *14*, 376–384.
[31] T. J. Meyer, *Acc. Chem. Res.* **1989**, *22*, 163–170.
[32] K. Kalyanasundaram, *Coord. Chem. Rev.* **1982**, *46*, 159–244.
[33] V. Balzani, A. Credi, M. Venturi, *ChemSusChem Chem. Sustain. Energy Mater.* **2008**, *1*, 26–58.
[34] C. Ulbricht, B. Beyer, C. Friebe, A. Winter, U. S. Schubert, *Adv. Mater.* **2009**, *21*, 4418–4441.
[35] M. S. Lowry, S. Bernhard, *Chem. Eur. J.* **2006**, *12*, 7970–7977.
[36] L. Marzo, S. K. Pagire, O. Reiser, B. König, *Angew. Chem. Int. Ed.* **2018**, *57*, 10034–10072.
[37] S. G. Kumar, L. G. Devi, *J. Phys. Chem. A* **2011**, *115*, 13211–13241.
[38] A. N. Banerjee, *Nanotechnol. Sci. Appl.* **2011**, *4*, 35–65.
[39] A. Fujishima, X. Zhang, D. A. Tryk, *Surf. Sci. Rep.* **2008**, *63*, 515–582.
[40] M. A. Henderson, *Surf. Sci. Rep.* **2011**, *66*, 185–297.
[41] Y. Yu, P. Zhang, L. Guo, Z. Chen, Q. Wu, Y. Ding, W. Zheng, Y. Cao, *J. Phys. Chem. C* **2014**, *118*, 12727–12733.
[42] K. Wetchakun, N. Wetchakun, S. Sakulsermsuk, *J. Ind. Eng. Chem.* **2019**, *71*, 19–49.
[43] J. G. Mahy, L. Lejeune, T. Haynes, N. Body, S. De Kreijger, B. Elias, R. H. M. Marcilli, C.-A. Fustin, S. Hermans, *Catalysts* **2021**, *11*, 1182.
[44] A. Mclaren, T. Valdes-Solis, G. Li, S. C. Tsang, *J. Am. Chem. Soc.* **2009**, *131*, 12540–12541.
[45] J. Li, Y. Yu, L. Zhang, *Nanoscale* **2014**, *6*, 8473–8488.
[46] K. Sharma, V. Dutta, S. Sharma, P. Raizada, A. Hosseini-Bandegharaei, P. Thakur, P. Singh, *J. Ind. Eng. Chem.* **2019**, *78*, 1–20.
[47] O. O. Fadeyi, J. J. Mousseau, Y. Feng, C. Allais, P. Nuhant, M. Z. Chen, B. Pierce, R. Robinson, *Org. Lett.* **2015**, *17*, 5756–5759.
[48] L. Buglioni, P. Riente, E. Palomares, M. A. Pericàs, *Eur. J. Org. Chem.* **2017**, *2017*, 6986–6990.
[49] M. J. Enright, K. Gilbert-Bass, H. Sarsito, B. M. Cossairt, *Chem. Mater.* **2019**, *31*, 2677–2682.
[50] S. Meng, X. Ning, S. Chang, X. Fu, X. Ye, S. Chen, *J. Catal.* **2018**, *357*, 247–256.

[51] V. C. Gerken, E. M. Carreira, *ACS Catal.* **2022**, *12*, 10787–10792.
[52] A. Hayat, A. G. Al-Sehemi, K. S. El-Nasser, T. Taha, A. A. Al-Ghamdi, J. A. S. Syed, M. A. Amin, T. Ali, T. Bashir, A. Palamanit, J. Khan, W. I. Nawawi, *Int. J. Hydrog. Energy* **2022**, *47*, 5142–5191.
[53] J. Wang, L. Xue, M. Hong, B. Ni, T. Niu, *Green Chem.* **2020**, *22*, 411–416.
[54] I. Ghosh, J. Khamrai, A. Savateev, N. Shlapakov, M. Antonietti, B. König, *Science* **2019**, *365*, 360–366.
[55] X. Wang, S. Blechert, M. Antonietti, *ACS Catal.* **2012**, *2*, 1596–1606.
[56] J. C. Colmenares, Y.-J. Xu, *Heterogeneous Photocatalysis - From Fundamentals to Green Applications*, Springer, **2016**.
[57] C. G. Thomson, A.-L. Lee, F. Vilela, *Beilstein J. Org. Chem.* **2020**, *16*, 1495–1549.
[58] S. Gisbertz, B. Pieber, *ChemPhotoChem* **2020**, *4*, 456–475.
[59] A. Y. Shan, T. I. M. Ghazi, S. A. Rashid, *Appl. Catal. Gen.* **2010**, *389*, 1–8.
[60] Y. Lin, J. Guo, J. San Martin, C. Han, R. Martinez, Y. Yan, *Chem. Eur. J.* **2020**, *26*, 13118–13136.
[61] H. M. Southam, J. A. Butler, J. A. Chapman, R. K. Poole, *Adv. Microb. Physiol.* **2017**, *71*, 1–96.
[62] M. Zhong, X. Pannecoucke, P. Jubault, T. Poisson, *Beilstein J. Org. Chem.* **2020**, *16*, 451–481.
[63] C. K. Prier, D. A. Rankic, D. W. MacMillan, *Chem. Rev.* **2013**, *113*, 5322–5363.
[64] C. Förster, K. Heinze, *Chem. Soc. Rev.* **2020**, *49*, 1057–1070.
[65] A. Vega-Peñaloza, J. Mateos, X. Companyó, M. Escudero-Casao, L. Dell'Amico, *Angew. Chem. Int. Ed.* **2021**, *60*, 1082–1097.
[66] D. Ravelli, M. Fagnoni, *ChemCatChem* **2012**, *4*, 169–171.
[67] Y. Lee, M. S. Kwon, *Eur. J. Org. Chem.* **2020**, *2020*, 6028–6043.
[68] N. A. Romero, D. A. Nicewicz, *Chem. Rev.* **2016**, *116*, 10075–10166.
[69] M. V. Bobo, J. J. Kuchta, A. K. Vannucci, *Org. Biomol. Chem.* **2021**, *19*, 4816–4834.
[70] D. A. Nicewicz, T. M. Nguyen, *ACS Catal.* **2014**, *4*, 355–360.
[71] Y. Du, R. M. Pearson, C. Lim, S. M. Sartor, M. D. Ryan, H. Yang, N. H. Damrauer, G. M. Miyake, *Chem. Eur. J.* **2017**, *23*, 10962–10968.
[72] M. A. Bryden, E. Zysman-Colman, *Chem. Soc. Rev.* **2021**, *50*, 7587–7680.
[73] Y. Zhang, J. L. Petersen, C. Milsmann, *J. Am. Chem. Soc.* **2016**, *138*, 13115–13118.
[74] J. A. Kübler, B. Pfund, O. S. Wenger, *JACS Au* **2022**, *2*, 2367–2380.
[75] D. B. Bagal, G. Kachkovskyi, M. Knorn, T. Rawner, B. M. Bhanage, O. Reiser, *Angew. Chem. Int. Ed.* **2015**, *54*, 6999–7002.
[76] T. Rawner, E. Lutsker, C. A. Kaiser, O. Reiser, *ACS Catal.* **2018**, *8*, 3950–3956.
[77] F. Glaser, O. S. Wenger, *JACS Au* **2022**, *2*, 1488–1503.

[78] W. Leis, M. A. Argüello Cordero, S. Lochbrunner, H. Schubert, A. Berkefeld, *J. Am. Chem. Soc.* **2022**, *144*, 1169–1173.
[79] A. Aydogan, R. E. Bangle, A. Cadranel, M. D. Turlington, D. T. Conroy, E. Cauët, M. L. Singleton, G. J. Meyer, R. N. Sampaio, B. Elias, L. Troian-Gautier, *J. Am. Chem. Soc.* **2021**, *143*, 15661–15673.
[80] A. Ilic, J. Schwarz, C. Johnson, L. H. de Groot, S. Kaufhold, R. Lomoth, K. Wärnmark, *Chem. Sci.* **2022**, *13*, 9165–9175.
[81] A. Ripak, S. De Kreijger, R. N. Sampaio, C. A. Vincent, É. Cauët, I. Jabin, U. K. Tambar, B. Elias, L. Troian-Gautier, *Chem Catal.* **2023**, *3*, 100490.
[82] O. S. Wenger, *J. Am. Chem. Soc.* **2018**, *140*, 13522–13533.
[83] J. Beaudelot, S. Oger, S. Peruško, T.-A. Phan, T. Teunens, C. Moucheron, G. Evano, *Chem. Rev.* **2022**, *122*, 16365–16609.
[84] C. B. Larsen, O. S. Wenger, *Chem. Eur. J.* **2018**, *24*, 2039–2058.
[85] S. Das, C. Zhu, D. Demirbas, E. Bill, C. K. De, B. List, *Science* **2023**, *379*, 494–499.
[86] C. Jacob, H. Baguia, A. Dubart, S. Oger, P. Thilmany, J. Beaudelot, C. Deldaele, S. Peruško, Y. Landrain, B. Michelet, S. Neale, E. Romero, C. Moucheron, V. Van Speybroeck, C. Theunissen, G. Evano, *Nat. Commun.* **2022**, *13*, 560.
[87] B. Michelet, C. Deldaele, S. Kajouj, C. Moucheron, G. Evano, *Org. Lett.* **2017**, *19*, 3576–3579.
[88] M. Rentschler, P. J. Boden, M. A. Argüello Cordero, S. T. Steiger, M.-A. Schmid, Y. Yang, G. Niedner-Schatteburg, M. Karnahl, S. Lochbrunner, S. Tschierlei, *Inorg. Chem.* **2022**, *61*, 12249–12261.
[89] Y. Yang, F. Doettinger, C. Kleeberg, W. Frey, M. Karnahl, S. Tschierlei, *Front. Chem.* **2022**, *10*, 936863.
[90] N. Hoffmann, *ChemSusChem* **2012**, *5*, 352–371.
[91] M. Pirtsch, S. Paria, T. Matsuno, H. Isobe, O. Reiser, *Chem. Eur. J.* **2012**, *18*, 7336–7340.
[92] X.-J. Tang, W. R. Dolbier Jr, *Angew. Chem. Int. Ed.* **2015**, *54*, 4246–4249.
[93] Z. Zhang, X. Tang, C. S. Thomoson, W. R. Dolbier Jr, *Org. Lett.* **2015**, *17*, 3528–3531.
[94] G. Fumagalli, P. T. Rabet, S. Boyd, M. F. Greaney, *Angew. Chem. Int. Ed.* **2015**, *54*, 11481–11484.
[95] M. S. Lazorski, F. N. Castellano, *Polyhedron* **2014**, *82*, 57–70.
[96] M. C. Rosko, K. A. Wells, C. E. Hauke, F. N. Castellano, *Inorg. Chem.* **2021**, *60*, 8394–8403.
[97] R. Fayad, A. T. Bui, S. G. Shepard, F. N. Castellano, *ACS Appl. Energy Mater.* **2020**, *3*, 12557–12564.
[98] R. S. Khnayzer, C. E. McCusker, B. S. Olaiya, F. N. Castellano, *J. Am. Chem. Soc.* **2013**, *135*, 14068–14070.
[99] S. Paria, O. Reiser, *ChemCatChem* **2014**, *6*, 2477–2483.
[100] Y. Zhang, M. Schulz, M. Wächtler, M. Karnahl, B. Dietzek, *Coord. Chem. Rev.* **2018**, *356*, 127–146.

[101] D. G. Cuttell, S.-M. Kuang, P. E. Fanwick, D. R. McMillin, R. A. Walton, *J. Am. Chem. Soc.* **2002**, *124*, 6–7.
[102] M. Zhong, Y. Gagné, T. O. Hope, X. Pannecoucke, M. Frenette, P. Jubault, T. Poisson, *Angew. Chem.* **2021**, *133*, 14619–14624.
[103] C. Cruche, W. Neiderer, S. K. Collins, *ACS Catal.* **2021**, *11*, 8829–8836.
[104] A. C. Hernandez-Perez, S. K. Collins, *Angew. Chem. Int. Ed.* **2013**, *52*, 12696–12700.
[105] T. P. Nicholls, J. C. Robertson, M. G. Gardiner, A. C. Bissember, *Chem. Commun.* **2018**, *54*, 4589–4592.
[106] H. Baguia, J. Beaudelot, C. Moucheron, G. Evano, *Chem. Commun.* **2022**, *58*, 9080–9083.
[107] J. E. Huheey, E. A. Keiter, R. L. Keiter, *Inorganic Chemistry - Principles of Structure and Reactivity*, HarperCollins College, **1993**.
[108] D. M. Arias-Rotondo, J. K. McCusker, *Chem. Soc. Rev.* **2016**, *45*, 5803–5820.
[109] J. Franck, E. G. Dymond, *Trans. Faraday Soc.* **1926**, *21*, 536–542.
[110] E. Condon, *Phys. Rev.* **1926**, *28*, 1182–1201.
[111] B. Valeur, *Molecular Fluorescence: Principles and Applications*, Wiley-VCH, **2001**.
[112] A. Jablonski, *Nature* **1933**, *131*, 839–840.
[113] G. G. Stokes, *Philos. Trans. R. Soc. Lond.* **1852**, 463–562.
[114] M. Kasha, *Discuss. Faraday Soc.* **1950**, *9*, 14–19.
[115] V. Gray, K. Moth-Poulsen, B. Albinsson, M. Abrahamsson, *Coord. Chem. Rev.* **2018**, *362*, 54–71.
[116] T. N. Singh-Rachford, F. N. Castellano, *Coord. Chem. Rev.* **2010**, *254*, 2560–2573.
[117] L. Troian-Gautier, M. D. Turlington, S. A. Wehlin, A. B. Maurer, M. D. Brady, W. B. Swords, G. J. Meyer, *Chem. Rev.* **2019**, *119*, 4628–4683.
[118] J. R. Lakowicz, *Principles of Fluorescence Spectroscopy*, Springer, **2006**.
[119] O. Stern, M. Volmer, *Phys. Z* **1919**, *20*, 183–188.
[120] M. V. Smoluchowski, *Z Phys Chem* **n.d.**, *92*, 129.
[121] F. C. Collins, G. E. Kimball, *J. Colloid Sci.* **1949**, *4*, 425–437.
[122] G. Wilemski, M. Fixman, *J. Chem. Phys.* **1973**, *58*, 4009–4019.
[123] S. G. Amos, M. Garreau, L. Buzzetti, J. Waser, *Beilstein J. Org. Chem.* **2020**, *16*, 1163–1187.
[124] S. Sharma, A. Sharma, *Org. Biomol. Chem.* **2019**, *17*, 4384–4405.
[125] K. Fidaly, C. Ceballos, A. Falguières, M. S.-I. Veitia, A. Guy, C. Ferroud, *Green Chem.* **2012**, *14*, 1293–1297.
[126] J. Zhou, W. Li, H. Zheng, Y. Pei, X. Liu, H. Cao, *Org. Lett.* **2021**, *23*, 2754–2759.
[127] Y. Lv, P. Bao, H. Yue, J.-S. Li, W. Wei, *Green Chem.* **2019**, *21*, 6051–6055.

[128] Y. Pan, C. W. Kee, L. Chen, C.-H. Tan, *Green Chem.* **2011**, *13*, 2682–2685.
[129] H. Liu, W. Feng, C. W. Kee, Y. Zhao, D. Leow, Y. Pan, C.-H. Tan, *Green Chem.* **2010**, *12*, 953–956.
[130] A. Tlahuext-Aca, L. Candish, R. A. Garza-Sanchez, F. Glorius, *ACS Catal.* **2018**, *8*, 1715–1719.
[131] J. C. Theriot, C.-H. Lim, H. Yang, M. D. Ryan, C. B. Musgrave, G. M. Miyake, *Science* **2016**, *352*, 1082–1086.
[132] C. Wu, N. Corrigan, C.-H. Lim, W. Liu, G. Miyake, C. Boyer, *Chem. Rev.* **2022**, *122*, 5476–5518.
[133] D. Koyama, H. J. Dale, A. J. Orr-Ewing, *J. Am. Chem. Soc.* **2018**, *140*, 1285–1293.
[134] J. P. Cole, C. R. Federico, C.-H. Lim, G. M. Miyake, *Macromolecules* **2019**, *52*, 747–754.
[135] S. Paria, M. Pirtsch, V. Kais, O. Reiser, *Synthesis* **2013**, *45*, 2689–2698.
[136] T. P. Nicholls, G. E. Constable, J. C. Robertson, M. G. Gardiner, A. C. Bissember, *ACS Catal.* **2016**, *6*, 451–457.
[137] A. Baralle, L. Fensterbank, J. Goddard, C. Ollivier, *Chem. Eur. J.* **2013**, *19*, 10809–10813.
[138] A. Nitelet, D. Thevenet, B. Schiavi, C. Hardouin, J. Fournier, R. Tamion, X. Pannecoucke, P. Jubault, T. Poisson, *Chem. Eur. J.* **2019**, *25*, 3262–3266.
[139] W. Zhao, R. P. Wurz, J. C. Peters, G. C. Fu, *J. Am. Chem. Soc.* **2017**, *139*, 12153–12156.
[140] M. S. Lazorski, R. H. Gest, C. M. Elliott, *J. Am. Chem. Soc.* **2012**, *134*, 17466–17469.
[141] R. Stuhr, P. Bayer, A. J. von Wangelin, *ChemSusChem* **2022**, *15*, e202201323.
[142] M. C. DeRosa, R. J. Crutchley, *Coord. Chem. Rev.* **2002**, *233*, 351–371.
[143] T. Entradas, S. Waldron, M. Volk, *J. Photochem. Photobiol. B* **2020**, *204*, 111787.
[144] E. Clennan, A. Pace, *Tetrahedron* **2005**, *61*, 6665–6691.
[145] K. Behm, R. D. McIntosh, *ChemPlusChem* **2020**, *85*, 2611–2618.
[146] S. Lacombe, T. Pigot, *Catal. Sci. Technol.* **2016**, *6*, 1571–1592.
[147] C. Michelin, C. Lefebvre, N. Hoffmann, *L'actualité chimique* **2019**, 19–27.
[148] M. Lancel, C. Gomez, M. Port, Z. Amara, *Front. Chem. Eng.* **2021**, *3*, 752364.
[149] J. Turconi, F. Griolet, R. Guevel, G. Oddon, R. Villa, A. Geatti, M. Hvala, K. Rossen, R. Göller, A. Burgard, *Org. Process Res. Dev.* **2014**, *18*, 417–422.
[150] W. Schilling, Y. Zhang, D. Riemer, S. Das, *Chem. Eur. J.* **2020**, *26*, 390–395.

[151] A. A. Ghogare, A. Greer, *Chem. Rev.* **2016**, *116*, 9994–10034.
[152] L. Marin, G. Force, R. Guillot, V. Gandon, E. Schulz, D. Lebœuf, *Chem. Commun.* **2019**, *55*, 5443–5446.
[153] T. Montagnon, M. Tofi, G. Vassilikogiannakis, *Acc. Chem. Res.* **2008**, *41*, 1001–1011.
[154] T. Montagnon, D. Kalaitzakis, M. Triantafyllakis, M. Stratakis, G. Vassilikogiannakis, *Chem. Commun.* **2014**, *50*, 15480–15498.
[155] D. Kalaitzakis, A. Bosveli, K. Sfakianaki, T. Montagnon, G. Vassilikogiannakis, *Angew. Chem.* **2021**, *133*, 4381–4387.
[156] S. P. Foxon, M. A. Alamiry, M. G. Walker, A. J. Meijer, I. V. Sazanovich, J. A. Weinstein, J. A. Thomas, *J. Phys. Chem. A* **2009**, *113*, 12754–12762.
[157] A. A. Abdel-Shafi, D. R. Worrall, A. Y. Ershov, *Dalton Trans.* **2004**, 30–36.
[158] Q. Zhou, W. Lei, J. Chen, C. Li, Y. Hou, X. Wang, B. Zhang, *Chem. Eur. J.* **2010**, *16*, 3157–3165.
[159] P. I. Djurovich, D. Murphy, M. E. Thompson, B. Hernandez, R. Gao, P. L. Hunt, M. Selke, *Dalton Trans.* **2007**, 3763–3770.
[160] S. Takizawa, R. Aboshi, S. Murata, *Photochem. Photobiol. Sci.* **2011**, *10*, 895–903.
[161] D. Ashen-Garry, M. Selke, *Photochem. Photobiol.* **2014**, *90*, 257–274.
[162] J. Sun, J. Zhao, H. Guo, W. Wu, *Chem. Commun.* **2012**, *48*, 4169–4171.
[163] M. G. Kallitsakis, D. K. Gioftsidou, M. A. Tzani, P. A. Angaridis, M. A. Terzidis, I. N. Lykakis, *J. Org. Chem.* **2021**, *86*, 13503–13513.
[164] P. Rana, B. Kaushik, K. Solanki, K. M. Saini, R. Sharma, *Chem. Commun.* **2022**, *58*, 11354–11377.
[165] A. Kaeser, M. Mohankumar, J. Mohanraj, F. Monti, M. Holler, J.-J. Cid, O. Moudam, I. Nierengarten, L. Karmazin-Brelot, C. Duhayon, B. Delavaux-Nicot, N. Armaroli, J.-F. Nierengarten, *Inorg. Chem.* **2013**, *52*, 12140–12151.
[166] D. V. Scaltrito, D. W. Thompson, J. A. O'Callaghan, G. J. Meyer, *Coord. Chem. Rev.* **2000**, *208*, 243–266.
[167] S.-M. Kuang, D. G. Cuttell, D. R. McMillin, P. E. Fanwick, R. A. Walton, *Inorg. Chem.* **2002**, *41*, 3313–3322.
[168] J. Wahlen, D. E. De Vos, P. A. Jacobs, P. L. Alsters, *Adv. Synth. Catal.* **2004**, *346*, 152–164.
[169] A. A. Yakushev, A. S. Abel, A. D. Averin, I. P. Beletskaya, A. V. Cheprakov, I. S. Ziankou, L. Bonneviot, A. Bessmertnykh-Lemeune, *Coord. Chem. Rev.* **2022**, 214331.
[170] B. M. Estevão, F. Cucinotta, N. Hioka, M. Cossi, M. Argeri, G. Paul, L. Marchese, E. Gianotti, *Phys. Chem. Chem. Phys.* **2015**, *17*, 26804–26812.

[171] C. Mendoza, N. Emmanuel, C. A. Páez, L. Dreesen, J. M. Monbaliu, B. Heinrichs, *ChemPhotoChem* **2018**, *2*, 890–897.
[172] C. Mendoza, N. Emmanuel, C. A. Paez, L. Dreesen, J.-C. Monbaliu, B. Heinrichs, *J. Photochem. Photobiol. Chem.* **2018**, *356*, 193–200.
[173] J. C. Terra, A. Desgranges, Z. Amara, A. Moores, *Catal. Today* **2023**, *407*, 52–58.
[174] S. M. Soria-Castro, B. Lebeau, M. Cormier, S. Neunlist, T. J. Daou, J. Goddard, *Eur. J. Org. Chem.* **2020**, *2020*, 1572–1578.
[175] Y. Guo, S. Rogelj, P. Zhang, *Nanotechnology* **2010**, *21*, 065102.
[176] J. Flores, P. Moya, F. Bosca, M. L. Marin, *Catal. Today* **2023**, *413–415*, 113994.
[177] P. Paramanantham, A. P. Antony, S. B. S. Lal, A. Sharan, A. Syed, M. Ahmed, A. A. Alarfaj, S. Busi, M. Maaza, K. Kaviyarasu, *Sci. Afr.* **2018**, *1*, e00007.
[178] F. Ronzani, N. Costarramone, S. Blanc, A. K. Benabbou, M. Le Bechec, T. Pigot, M. Oelgemoeller, S. Lacombe, *J. Catal.* **2013**, *303*, 164–174.
[179] P. Li, G.-W. Wang, X. Zhu, L. Wang, *Tetrahedron* **2019**, *75*, 3448–3455.
[180] P. Rana, R. Gaur, B. Kaushik, S. Yadav, P. Yadav, P. Sharma, M. B. Gawande, R. K. Sharma, *J. Catal.* **2021**, *401*, 297–308.
[181] K. Mori, M. Tottori, K. Watanabe, M. Che, H. Yamashita, *J. Phys. Chem. C* **2011**, *115*, 21358–21362.
[182] H. He, W. Li, Z. Xie, X. Jing, Y. Huang, *Chem. Res. Chin. Univ.* **2014**, *30*, 310–314.
[183] G. J. Barbante, T. D. Ashton, E. H. Doeven, F. M. Pfeffer, D. J. Wilson, L. C. Henderson, P. S. Francis, *ChemCatChem* **2015**, *7*, 1655–1658.
[184] B. Tambosco, K. Segura, C. Seyrig, D. Cabrera, M. Port, C. Ferroud, Z. Amara, *ACS Catal.* **2018**, *8*, 4383–4389.
[185] K. Mori, M. Kawashima, M. Che, H. Yamashita, *Angew. Chem.* **2010**, *49*, 8598–8601.
[186] C. E. Housecroft, E. C. Constable, *Chem. Sci.* **2022**, *13*, 1225–1262.
[187] C. E. Housecroft, E. C. Constable, *Chem. Soc. Rev.* **2015**, *44*, 8386–8398.
[188] A. B. Muñoz-García, I. Benesperi, G. Boschloo, J. J. Concepcion, J. H. Delcamp, E. A. Gibson, G. J. Meyer, M. Pavone, H. Pettersson, A. Hagfeldt, M. Freitag, *Chem. Soc. Rev.* **2021**, *50*, 12450–12550.
[189] M. Karnahl, E. Mejía, N. Rockstroh, S. Tschierlei, S. Luo, K. Grabow, A. Kruth, V. Brüser, H. Junge, S. Lochbrunner, M. Beller, *ChemCatChem* **2014**, *6*, 82–86.
[190] I. Choi, V. Müller, G. Lole, R. Köhler, V. Karius, W. Viöl, C. Jooss, L. Ackermann, *Chem. Eur. J.* **2020**, *26*, 3509–3514.
[191] P. Yadav, M. Yadav, R. Gaur, R. Gupta, G. Arora, P. Rana, A. Srivastava, R. K. Sharma, *ChemCatChem* **2020**, *12*, 2488–2496.

[192] Y. Lin, M. Cai, Z. Fang, H. Zhao, *RSC Adv.* **2016**, *6*, 85186–85193.
[193] Y. Lin, M. Cai, Z. Fang, H. Zhao, *RSC Adv.* **2017**, *7*, 34722–34729.
[194] M. V. Appleby, P. G. Walker, D. Pritchard, S. van Meurs, C. M. Booth, C. Robertson, M. D. Ward, D. J. Kelly, J. A. Weinstein, *Mater. Adv.* **2020**, *1*, 3417–3427.
[195] A. Corma, V. Fornés, H. García, M. A. Miranda, J. Primo, M.-J. Sabater, *J. Am. Chem. Soc.* **1994**, *116*, 2276–2280.
[196] A. M. Amat, A. Arques, S. H. Bossman, A. M. Braun, S. Göb, M. A. Miranda, *Angew. Chem. Int. Ed.* **2003**, *42*, 1653–1655.
[197] C. H. Mak, X. Han, M. Du, J.-J. Kai, K. F. Tsang, G. Jia, K.-C. Cheng, H.-H. Shen, H.-Y. Hsu, *J. Mater. Chem. A* **2021**, *9*, 4454–4504.
[198] A. P. Schaap, A. L. Thayer, E. C. Blossey, D. C. Neckers, *J. Am. Chem. Soc.* **1973**, *95*, 5820–5822.
[199] M. I. Burguete, R. Gavara, F. Galindo, S. V. Luis, *Catal. Commun.* **2010**, *11*, 1081–1084.
[200] P. Li, G.-W. Wang, *Org. Biomol. Chem.* **2019**, *17*, 5578–5585.
[201] J.-X. Jiang, Y. Li, X. Wu, J. Xiao, D. J. Adams, A. I. Cooper, *Macromolecules* **2013**, *46*, 8779–8783.
[202] X. Li, Y. C. Zhang, Y. Zhao, H. P. Zhao, B. Zhang, T. Cai, *Macromolecules* **2020**, *53*, 1550–1556.
[203] X. Yu, Z. Yang, B. Qiu, S. Guo, P. Yang, B. Yu, H. Zhang, Y. Zhao, X. Yang, B. Han, Z. Liu, *Angew. Chem. Int. Ed.* **2019**, *58*, 632–636.
[204] C. Wang, Z. Xie, K. E. deKrafft, W. Lin, *ACS Appl. Mater. Interfaces* **2012**, *4*, 2288–2294.
[205] Z. Mou, Y. Dong, S. Li, Y. Du, X. Wang, P. Yang, S. Wang, *Int. J. Hydrog. Energy* **2011**, *36*, 8885–8893.
[206] A. Kumar, P. Kumar, S. Paul, S. L. Jain, *Appl. Surf. Sci.* **2016**, *386*, 103–114.
[207] X. Li, Z. Hao, F. Zhang, H. Li, *ACS Appl. Mater. Interfaces* **2016**, *8*, 12141–12148.
[208] A. Jacques, A. Devaux, C. Rubay, F. Pennetreau, A. Desmecht, K. Robeyns, S. Hermans, B. Elias, *ChemCatChem* **2023**, *15*, e202201672.
[209] Y. Chu, Z. Huang, R. Liu, C. Boyer, J. Xu, *ChemPhotoChem* **2020**, *4*, 5201–5208.
[210] M. C. Nongbe, A. Abollé, V. Coeffard, F. Felpin, *ChemPlusChem* **2022**, *87*, e202200242.
[211] Y. Zhang, W. Wang, S. Li, *Asian J. Chem.* **2015**, *27*, 111–116.
[212] Y. Liu, B. Li, H.-S. Li, P. Wu, J. Wang, *Dalton Trans.* **2020**, *49*, 17520–17526.
[213] H. Wang, Q. Tang, Z. Chen, T. Li, J. Wang, *Sci. China Mater.* **2020**, *63*, 2189–2205.
[214] A. Vinu, K. Z. Hossain, K. Ariga, *J. Nanosci. Nanotechnol.* **2005**, *5*, 347–371.
[215] F. Hoffmann, M. Cornelius, J. Morell, M. Fröba, *Angew. Chem. Int. Ed.* **2006**, *45*, 3216–3251.

[216] J. A. S. Costa, R. A. de Jesus, D. O. Santos, J. B. Neris, R. T. Figueiredo, C. M. Paranhos, *J. Environ. Chem. Eng.* **2021**, *9*, 105259.
[217] R. G. Acres, A. V. Ellis, J. Alvino, C. E. Lenahan, D. A. Khodakov, G. F. Metha, G. G. Andersson, *J. Phys. Chem. C* **2012**, *116*, 6289–6297.
[218] D. W. Kurka, M. Niehues, S. Kudruk, V. Gerke, B. J. Ravoo, *Chem. Eur. J.* **2021**, *27*, 7667–7676.
[219] I. Rahman, P. Vejayakumaran, C. Sipaut, J. Ismail, C. Chee, *Mater. Chem. Phys.* **2009**, *114*, 328–332.
[220] W. Stöber, A. Fink, E. Bohn, *J. Colloid Interface Sci.* **1968**, *26*, 62–69.
[221] S. B. Yoon, J.-Y. Kim, J. H. Kim, Y. J. Park, K. R. Yoon, S.-K. Park, J.-S. Yu, *J. Mater. Chem.* **2007**, *17*, 1758–1761.
[222] T. Haynes, O. Bougnouch, V. Dubois, S. Hermans, *Microporous Mesoporous Mater.* **2020**, *306*, 110400.
[223] A. Maity, V. Polshettiwar, *ChemSusChem* **2017**, *10*, 3866–3913.
[224] A. Maity, R. Belgamwar, V. Polshettiwar, *Nat. Protoc.* **2019**, *14*, 2177–2204.
[225] J. Ryu, J. Yun, J. Lee, K. Lee, J. Jang, *Chem. Commun.* **2016**, *52*, 2165–2168.
[226] N. Bayal, B. Singh, R. Singh, V. Polshettiwar, *Sci. Rep.* **2016**, *6*, 24888.
[227] P. P. Ghimire, M. Jaroniec, *J. Colloid Interface Sci.* **2021**, *584*, 838–865.
[228] Y. Han, Z. Lu, Z. Teng, J. Liang, Z. Guo, D. Wang, M.-Y. Han, W. Yang, *Langmuir* **2017**, *33*, 5879–5890.
[229] D. L. Green, S. Jayasundara, Y.-F. Lam, M. T. Harris, *J. Non-Cryst. Solids* **2003**, *315*, 166–179.
[230] A. H. Bari, R. B. Jundale, A. A. Kulkarni, *Chem. Eng. J.* **2020**, *398*, 125427.
[231] V. K. LaMer, *Ind. Eng. Chem.* **1952**, *44*, 1270–1277.
[232] D. Green, J. Lin, Y.-F. Lam, M.-C. Hu, D. W. Schaefer, M. Harris, *J. Colloid Interface Sci.* **2003**, *266*, 346–358.
[233] H. Giesche, *J. Eur. Ceram. Soc.* **1994**, *14*, 189–204.
[234] K. Lee, A. N. Sathyagal, A. V. McCormick, *Colloids Surf. Physicochem. Eng. Asp.* **1998**, *144*, 115–125.
[235] A. Van Blaaderen, J. Van Geest, A. Vrij, *J. Colloid Interface Sci.* **1992**, *154*, 481–501.
[236] N. Plumeré, A. Ruff, B. Speiser, V. Feldmann, H. A. Mayer, *J. Colloid Interface Sci.* **2012**, *368*, 208–219.
[237] G. Bogush, M. Tracy, C. Zukoski Iv, *J. Non-Cryst. Solids* **1988**, *104*, 95–106.
[238] S. K. Park, K. Do Kim, H. T. Kim, *Colloids Surf. Physicochem. Eng. Asp.* **2002**, *197*, 7–17.
[239] I. A. Rahman, V. Padavettan, *J. Nanomater.* **2012**, *2012*, 132424.
[240] N. Shimura, M. Ogawa, *J. Mater. Sci.* **2007**, *42*, 5299–5306.

[241] S.-Y. Sun, Y.-Y. Ge, Z.-B. Tian, J. Zhang, Z. Xie, *Adv. Powder Technol.* **2017**, *28*, 2496–2502.
[242] Z. A. ALOthman, *Materials* **2012**, *5*, 2874–2902.
[243] V. Polshettiwar, D. Cha, X. Zhang, J. M. Basset, *Angew. Chem. Int. Ed.* **2010**, *49*, 9652–9656.
[244] L. Zhuravlev, *Colloids Surf. Physicochem. Eng. Asp.* **2000**, *173*, 1–38.
[245] S. L. Burkett, S. D. Sims, S. Mann, *Chem. Commun.* **1996**, 1367–1368.
[246] S. Huh, J. W. Wiench, J.-C. Yoo, M. Pruski, V. S.-Y. Lin, *Chem. Mater.* **2003**, *15*, 4247–4256.
[247] D. J. Macquarrie, *Chem. Commun.* **1996**, 1961–1962.
[248] L.-L. Lou, S. Jiang, K. Yu, Z. Gu, R. Ji, Y. Dong, S. Liu, *Microporous Mesoporous Mater.* **2011**, *142*, 214–220.
[249] G. Castruita-de León, Y. A. Perera-Mercado, L. A. García-Cerda, J. A. Mercado-Silva, H. I. Meléndez-Ortiz, Y. Olivares-Maldonado, L. Alvarez-Contreras, *Microporous Mesoporous Mater.* **2015**, *204*, 156–162.
[250] L. Wang, U. S. Schubert, S. Hoeppener, *Chem. Soc. Rev.* **2021**, *50*, 6507–6540.
[251] S. Sheikh, M. A. Nasseri, M. Chahkandi, A. Allahresani, O. Reiser, *J. Hazard. Mater.* **2020**, *400*, 122985.
[252] O. Olkhovyk, V. Antochshuk, M. Jaroniec, *Colloids Surf. Physicochem. Eng. Asp.* **2004**, *236*, 69–72.
[253] K. Y. Ho, G. McKay, K. L. Yeung, *Langmuir* **2003**, *19*, 3019–3024.
[254] N. K. Mal, M. Fujiwara, Y. Tanaka, *Nature* **2003**, *421*, 350–353.
[255] E. Cano-Serrano, J. Campos-Martin, J. Fierro, *Chem. Commun.* **2003**, 246–247.
[256] Y. Zhang, Z. Gu, Y. Liu, W. Hu, C. Liu, W. Shu, Y. Wang, C. Yu, *Langmuir* **2021**, *37*, 2780–2786.
[257] H. Yang, X. Zhang, S. Li, X. Wang, J. Ma, *RSC Adv.* **2014**, *4*, 9292–9299.
[258] G. Armatas, C. Salmas, M. Louloudi, G. Androutsopoulos, P. Pomonis, *Langmuir* **2003**, *19*, 3128–3136.
[259] M. Manzano, V. Aina, C. Areán, F. Balas, V. Cauda, M. Colilla, M. Delgado, M. Vallet-Regí, *Chem. Eng. J.* **2008**, *137*, 30–37.
[260] N. Gartmann, C. Schütze, H. Ritter, D. Brühwiler, *J. Phys. Chem. Lett.* **2010**, *1*, 379–382.
[261] H. Nasrallah, A. Pagnoux, D. Didier, C. Magnier, L. Toupet, R. Guillot, C. Crévisy, M. Mauduit, E. Schulz, *Eur. J. Org. Chem.* **2014**, *2014*, 7781–7787.
[262] D. Didier, C. Magnier-Bouvier, E. Schulz, *Adv. Synth. Catal.* **2011**, *353*, 1087–1095.
[263] C. Chen, A. Chen, X. Huang, R. Ju, X. Li, J. Wang, A. Hao, M. Zhao, *J. Clean. Prod.* **2021**, *298*, 126837.

[264] J. Du, T. D. Waite, P. Biesheuvel, W. Tang, *J. Hazard. Mater.* **2023**, *442*, 130023.
[265] Q. Xia, Q. Song, Z. Xu, *Waste Manag.* **2023**, *158*, 146–152.
[266] L. Zhang, J. Ran, S.-Z. Qiao, M. Jaroniec, *Chem. Soc. Rev.* **2019**, *48*, 5184–5206.
[267] C. S. Foote, S. Wexler, *J. Am. Chem. Soc.* **1964**, *86*, 3879–3880.
[268] C. S. Foote, S. Wexler, *J. Am. Chem. Soc.* **1964**, *86*, 3880–3881.
[269] I. Pibiri, S. Buscemi, A. Palumbo Piccionello, A. Pace, *ChemPhotoChem* **2018**, *2*, 535–547.
[270] J. C. Terra, A. Desgranges, C. Monnereau, E. H. Sanchez, J. A. De Toro, Z. Amara, A. Moores, *ACS Appl. Mater. Interfaces* **2020**, *12*, 24895–24904.
[271] L. Liu, H. Liu, Y.-P. Zhao, Y. Wang, Y. Duan, G. Gao, M. Ge, W. Chen, *Environ. Sci. Technol.* **2008**, *42*, 2342–2348.
[272] A. Maldotti, A. Molinari, G. Varani, M. Lenarda, L. Storaro, F. Bigi, R. Maggi, A. Mazzacani, G. Sartori, *J. Catal.* **2002**, *209*, 210–216.
[273] D. González-Muñoz, A. Gómez-Avilés, C. B. Molina, J. Bedia, C. Belver, J. Alemán, S. Cabrera, *J. Mater. Sci. Technol.* **2022**, *103*, 134–143.
[274] D. González-Muñoz, A. Casado-Sánchez, I. del Hierro, S. Gómez-Ruiz, S. Cabrera, J. Alemán, *J. Catal.* **2019**, *373*, 374–383.
[275] A. Uppal, B. Jain, P. K. Gupta, K. Das, *Photochem. Photobiol.* **2011**, *87*, 1146–1151.
[276] E. Gianotti, B. Martins Estevão, F. Cucinotta, N. Hioka, M. Rizzi, F. Renò, L. Marchese, *Chem. Eur. J.* **2014**, *20*, 10921–10925.
[277] M. Gierada, F. De Proft, M. Sulpizi, F. Tielens, *J. Phys. Chem. C* **2019**, *123*, 17343–17352.
[278] X. Li, X. Du, J. He, *Langmuir* **2010**, *26*, 13528–13534.
[279] D. Sriramulu, E. L. Reed, M. Annamalai, T. V. Venkatesan, S. Valiyaveettil, *Sci. Rep.* **2016**, *6*, 35993.
[280] S. Xiao, A. Shoaib, J. Xu, D. Lin, *Sci. Total Environ.* **2022**, *831*, 154914.
[281] X. Du, Y. Xing, X. Li, H. Huang, Z. Geng, J. He, Y. Wen, X. Zhang, *RSC Adv.* **2016**, *6*, 7864–7871.
[282] C. Deng, Y. Liu, F. Zhou, M. Wu, Q. Zhang, D. Yi, W. Yuan, Y. Wang, *J. Colloid Interface Sci.* **2021**, *593*, 424–433.
[283] Y. Wang, X. Du, Z. Liu, S. Shi, H. Lv, *J. Mater. Chem. A* **2019**, *7*, 5111–5152.
[284] D. Vidick, M. Herlitschke, C. Poleunis, A. Delcorte, R. P. Hermann, M. Devillers, S. Hermans, *J. Mater. Chem. A* **2013**, *1*, 2050–2063.
[285] M. C. Biesinger, "X-ray Photoelectron Spectroscopy (XPS) Reference Pages," can be found under http://www.xpsfitting.com/, **2021**.
[286] B. Bhushan, K. J. Kwak, S. Gupta, S. C. Lee, *J. R. Soc. Interface* **2009**, *6*, 719–733.

[287] E. Prathibha, R. Rangasamy, A. Sridhar, K. Lakshmi, *J. Clust. Sci.* **2023**, *34*, 1605–1614.
[288] M. Rauf, J. P. Graham, S. B. Bukallah, M. A. Al-Saedi, *Spectrochim. Acta. A. Mol. Biomol. Spectrosc.* **2009**, *72*, 133–137.
[289] A. Torres-Martínez, B. Bedrina, E. Falomir, M. J. Marín, C. A. Angulo-Pachón, F. Galindo, J. F. Miravet, *ACS Appl. Bio Mater.* **2021**, *4*, 3658–3669.
[290] R. Singh, R. Bapat, L. Qin, H. Feng, V. Polshettiwar, *ACS Catal.* **2016**, *6*, 2770–2784.
[291] V. Polshettiwar, *Acc. Chem. Res.* **2022**, *55*, 1395–1410.
[292] J. Zhang, M. Zhang, C. Yang, X. Wang, *Adv. Mater.* **2014**, *26*, 4121–4126.
[293] K. Imato, K. Ohira, M. Yamaguchi, T. Enoki, Y. Ooyama, *Mater. Chem. Front.* **2020**, *4*, 589–596.
[294] G. Oster, G. Kallmann Oster, G. Karg, *J. Phys. Chem.* **1962**, *66*, 2514–2517.
[295] S. M. Linden, D. C. Neckers, *J. Am. Chem. Soc.* **1988**, *110*, 1257–1260.
[296] A. Zakrzewski, D. C. Neckers, *Tetrahedron* **1987**, *43*, 4507–4512.
[297] M. Hayyan, M. A. Hashim, I. M. AlNashef, *Chem. Rev.* **2016**, *116*, 3029–3085.
[298] I. Pyszka, Z. Kucybała, B. Jędrzejewska, *Materials* **2021**, *14*, 3085.
[299] J. Delaire, J. Piard, R. Méallet-Renault, G. Clavier, *Photophysique et Photochimie - Des Fondements Aux Applications*, EDP Sciences, **2016**.
[300] L. Villén, F. Manjón, D. García-Fresnadillo, G. Orellana, *Appl. Catal. B Environ.* **2006**, *69*, 1–9.
[301] M. E. Jiménez-Hernández, F. Manjón, D. García-Fresnadillo, G. Orellana, *Sol. Energy* **2006**, *80*, 1382–1387.
[302] R. Bonnett, M. A. Krysteva, I. G. Lalov, S. V. Artarsky, *Water Res.* **2006**, *40*, 1269–1275.
[303] X. Xie, Z. Zhang, Y. Hu, H. Cheng, *Chem. Eng. J.* **2018**, *334*, 1242–1251.
[304] E. Díez-Mato, F. Cortezón-Tamarit, S. Bogialli, D. García-Fresnadillo, M. Marazuela, *Appl. Catal. B Environ.* **2014**, *160–161*, 445–455.
[305] H. Kim, W. Kim, Y. Mackeyev, G.-S. Lee, H.-J. Kim, T. Tachikawa, S. Hong, S. Lee, J. Kim, L. J. Wilson, T. Majima, P. J. J. Alvarez, W. Choi, J. Lee, *Environ. Sci. Technol.* **2012**, *46*, 9606–9613.
[306] I. S. Mfouo-Tynga, L. D. Dias, N. M. Inada, C. Kurachi, *Photodiagnosis Photodyn. Ther.* **2021**, *34*, 102091.
[307] J. Sandland, R. W. Boyle, *Bioconjug. Chem.* **2019**, *30*, 975–993.
[308] V. F. Otvagin, N. S. Kuzmina, E. S. Kudriashova, A. V. Nyuchev, A. E. Gavryushin, A. Y. Fedorov, *J. Med. Chem.* **2022**, *65*, 1695–1734.
[309] J. Li, T. Chen, *Coord. Chem. Rev.* **2020**, *418*, 213355.

[310] W. Zhang, A. Ahmed, H. Cong, S. Wang, Y. Shen, B. Yu, *Dyes Pigments* **2021**, *185*, 108937.
[311] S. Moghassemi, A. Dadashzadeh, R. B. Azevedo, O. Feron, C. A. Amorim, *J. Controlled Release* **2021**, *339*, 75–90.
[312] V.-N. Nguyen, Y. Yan, J. Zhao, J. Yoon, *Acc. Chem. Res.* **2021**, *54*, 207–220.
[313] D. Chen, Z. Zhong, Q. Ma, J. Shao, W. Huang, X. Dong, *ACS Appl. Mater. Interfaces* **2020**, *12*, 26914–26925.
[314] Y. Liu, R. Qin, S. A. Zaat, E. Breukink, M. Heger, *J. Clin. Transl. Res.* **2015**, *1*, 140–167.
[315] E. Polat, K. Kang, *Biomedicines* **2021**, *9*, 584.
[316] Q. Han, J. W. Lau, T. C. Do, Z. Zhang, B. Xing, *ACS Appl. Bio Mater.* **2021**, *4*, 3937–3961.
[317] D. Kalaitzakis, M. Triantafyllakis, M. Sofiadis, D. Noutsias, G. Vassilikogiannakis, *Angew. Chem.* **2016**, *55*, 4605–4609.
[318] T. Montagnon, D. Noutsias, I. Alexopoulou, M. Tofi, G. Vassilikogiannakis, *Org. Biomol. Chem.* **2011**, *9*, 2031–2039.
[319] J. Demas, D. Diemente, E. Harris, *J. Am. Chem. Soc.* **1973**, *95*, 6864–6865.
[320] K. El-Naggar, H. S. Abdel-Samad, R. M. Ramadan, M. E. El-Khouly, A. A. Abdel-Shafi, *J. Photochem. Photobiol. Chem.* **2023**, *436*, 114405.
[321] Y. Guo, S. Rogelj, P. Zhang, *Nanotechnology* **2010**, *21*, 065102.
[322] D. Kalaitzakis, T. Montagnon, E. Antonatou, N. Bardají, G. Vassilikogiannakis, *Chem. Eur. J.* **2013**, *19*, 10119–10123.
[323] C. Mendoza, N. Emmanuel, C. A. Páez, L. Dreesen, J. M. Monbaliu, B. Heinrichs, *ChemPhotoChem* **2018**, *2*, 890–897.
[324] C. Liu, H. Liu, X. Zheng, S. Chen, Q. Lai, C. Zheng, M. Huang, K. Cai, Z. Cai, S. Cai, *ACS Catal.* **2022**, *12*, 1375–1381.
[325] R. Liu, Q. Liu, H. Meng, H. Ding, J. Hao, Z. Ji, H. Yue, W. Wei, *Org. Chem. Front.* **2021**, *8*, 1970–1975.
[326] C. Sharma, S. Kumar, N. Jain, *Org. Biomol. Chem.* **2020**, *18*, 2921–2928.
[327] D. P. Hari, B. König, *Chem. Commun.* **2014**, *50*, 6688–6699.
[328] J. Vara, M. S. Gualdesi, S. G. Bertolotti, C. S. Ortiz, *J. Mol. Struct.* **2019**, *1181*, 1–7.
[329] F. Ronzani, A. Trivella, E. Arzoumanian, S. Blanc, M. Sarakha, C. Richard, E. Oliveros, S. Lacombe, *Photochem. Photobiol. Sci.* **2013**, *12*, 2160–2169.
[330] J. Xu, T. Pelluau, C. Monnereau, Y. Guari, L. Bonneviot, M. Rodríguez-Pizarro, B. Albela, *New J. Chem.* **2023**, *47*, 1861–1871.
[331] D. B. Tada, L. L. Vono, E. L. Duarte, R. Itri, P. K. Kiyohara, M. S. Baptista, L. M. Rossi, *Langmuir* **2007**, *23*, 8194–8199.
[332] X. Wang, H. Lv, Y. Sun, G. Zu, X. Zhang, Y. Song, F. Zhao, J. Wang, *Spectrochim. Acta. A. Mol. Biomol. Spectrosc.* **2022**, *279*, 121447.

[333] P. Lo, J. Huang, D. Y. Cheng, E. Y. Chan, W. Fong, W. Ko, D. K. Ng, *Chem. Eur. J.* **2004**, *10*, 4831–4838.
[334] A. Garai, M. Villa, M. Marchini, S. K. Patra, T. Pain, S. Mondal, P. Ceroni, S. Kar, *Eur. J. Inorg. Chem.* **2021**, *2021*, 4089–4095.
[335] M. Pineiro, d'A AM, R. Gonsalves, M. M. Pereira, S. J. Formosinho, L. G. Arnaut, *J. Phys. Chem. A* **2002**, *106*, 3787–3795.
[336] L. M. Rossi, P. R. Silva, L. L. Vono, A. U. Fernandes, D. B. Tada, M. S. Baptista, *Langmuir* **2008**, *24*, 12534–12538.
[337] V. Kabanov, D. J. Press, R. P. Huynh, G. K. Shimizu, B. Heyne, *Chem. Commun.* **2018**, *54*, 6320–6323.
[338] P. Rana, N. Singh, P. Majumdar, S. P. Singh, *Coord. Chem. Rev.* **2022**, *470*, 214698.
[339] S. G. Awuah, J. Polreis, V. Biradar, Y. You, *Org. Lett.* **2011**, *13*, 3884–3887.
[340] M. J. Ortiz, A. R. Agarrabeitia, G. Duran-Sampedro, J. B. Prieto, T. A. Lopez, W. A. Massad, H. A. Montejano, N. A. García, I. L. Arbeloa, *Tetrahedron* **2012**, *68*, 1153–1162.
[341] N. Adarsh, R. R. Avirah, D. Ramaiah, *Org. Lett.* **2010**, *12*, 5720–5723.
[342] A. Pinto, Y. Mace, F. Drouet, E. Bony, R. Boidot, N. Draoui, I. Lobysheva, C. Corbet, F. Polet, R. Martherus, Q. Deraedt, J. Rodríguez, C. Lamy, O. Schicke, D. Delvaux, C. Louis, R. Kiss, A. Kriegsheim, C. Dessy, B. Elias, O. Riant, O. Feron, *Oncogene* **2016**, *35*, 3976–3985.
[343] K. Ohira, K. Imato, Y. Ooyama, *Mater. Chem. Front.* **2021**, *5*, 5298–5304.
[344] Y. Hayashi, A. Morimoto, T. Maeda, T. Enoki, Y. Ooyama, Y. Matsui, H. Ikeda, S. Yagi, *New J. Chem.* **2021**, *45*, 2264–2275.
[345] K. Ohira, M. Yamamoto, K. Imato, Y. Ooyama, *New J. Chem.* **2023**, *47*.
[346] F. Hoffmann, M. Cornelius, J. Morell, M. Fröba, *Angew. Chem. Int. Ed.* **2006**, *45*, 3216–3251.
[347] N. Body, C. Lefebvre, P. Eloy, T. Haynes, S. Hermans, O. Riant, *J. Photochem. Photobiol. Chem.* **2023**, *440*, 114648.
[348] M. Tamtaji, M. Kazemeini, *J. Nanoparticle Res.* **2022**, *24*, 174.
[349] X. Ma, S. Sreejith, Y. Zhao, *ACS Appl. Mater. Interfaces* **2013**, *5*, 12860–12868.
[350] S. Kothavale, N. Sekar, *Dyes Pigments* **2017**, *136*, 31–45.
[351] B. C. Raju, K. V. Prasad, G. Saidachary, B. Sridhar, *Org Lett* **2014**, *45*, 420–423.
[352] P. Singh, A. Baheti, K. J. Thomas, *J. Org. Chem.* **2011**, *76*, 6134–6145.
[353] A. K. Mishra, J. N. Moorthy, *J. Org. Chem.* **2016**, *81*, 6472–6480.
[354] A. B. Tathe, N. Sekar, *J. Fluoresc.* **2015**, *25*, 1403–1415.
[355] N. Trempolec, B. Doix, C. Degavre, D. Brusa, C. Bouzin, O. Riant, O. Feron, *Cancers* **2020**, *12*, 545.

[356] B. Doix, N. Trempolec, O. Riant, O. Feron, *Front. Oncol.* **2019**, *9*, 811.
[357] B. Doix, E. Bastien, A. Rambaud, A. Pinto, C. Louis, V. Grégoire, O. Riant, O. Feron, *Front. Oncol.* **2018**, *8*, 393.
[358] S. Moghassemi, A. Dadashzadeh, A. Camboni, O. Feron, R. B. Azevedo, C. A. Amorim, *Photodiagnosis Photodyn. Ther.* **2022**, *40*, 103139.
[359] S. Moghassemi, A. Dadashzadeh, A. Camboni, O. Feron, R. B. Azevedo, C. A. Amorim, *Hum. Reprod. Open* **2023**, *2023*, hoad005.
[360] S. Jiménez-Alonso, H. C. Orellana, A. Estevez-Braun, A. G. Ravelo, E. Perez-Sacau, F. Machin, *J. Med. Chem.* **2008**, *51*, 6761–6772.
[361] E. Pérez-Sacau, R. G. Díaz-Peñate, A. Estévez-Braun, A. G. Ravelo, J. M. García-Castellano, L. Pardo, M. Campillo, *J. Med. Chem.* **2007**, *50*, 696–706.
[362] V. F. de Andrade-Neto, M. O. Goulart, J. F. da Silva Filho, M. J. Da Silva, F. Maria do Carmo, A. V. Pinto, M. G. Zalis, L. H. Carvalho, A. U. Krettli, *Bioorg. Med. Chem. Lett.* **2004**, *14*, 1145–1149.
[363] D. Jacquemin, V. Wathelet, E. A. Perpete, C. Adamo, *J. Chem. Theory Comput.* **2009**, *5*, 2420–2435.
[364] F. Weigend, R. Ahlrichs, *Phys. Chem. Chem. Phys.* **2005**, *7*, 3297–3305.
[365] M. J. Frisch, G. W. Trucks, H. B. Schlegel, G. E. Scuseria, M. Robb, J. R. Cheeseman, G. Scalmani, V. Barone, G. A. Petersson, H. Nakatsuji, et al., **2016**.
[366] Z. Liu, T. Lu, Q. Chen, *Carbon* **2020**, *165*, 461–467.
[367] E. D. Glendening, C. R. Landis, F. Weinhold, *J. Comput. Chem.* **2019**, *40*, 2234–2241.
[368] M. J. Hatfield, J. Chen, E. M. Fratt, L. Chi, J. C. Bollinger, R. J. Binder, J. Bowling, J. L. Hyatt, J. Scarborough, C. Jeffries, P. M. Potter, *J. Med. Chem.* **2017**, *60*, 1568–1579.
[369] A. Rodriguez-Serrano, V. Rai-Constapel, M. C. Daza, M. Doerr, C. M. Marian, *Phys Chem Chem Phys* **2015**, *17*, 11350.
[370] P. de Silva, *J Phys Chem Lett* **2019**, *10*, 5674–5679.
[371] R. Pollice, P. Friederich, C. Lavigne, G. dos Passos Gomes, A. Aspuru-Guzik, *Matter* **2021**, *4*, 1654–1682.
[372] J. Ehrmaier, E. J. Rabe, S. R. Pristash, K. L. Corp, C. W. Schlenker, A. L. Sobolewski, W. Domcke, *J Phys Chem A* **2019**, *123*, 8099–8108.
[373] E. Pang, S. Zhao, B. Wang, G. Niu, X. Song, M. Lan, *Coord. Chem. Rev.* **2022**, *472*, 214780.
[374] C. M. Marian, *Wiley Interdiscip. Rev. Comput. Mol. Sci.* **2012**, *2*, 187–203.
[375] M. Dichiara, O. Prezzavento, A. Marrazzo, V. Pittala, L. Salerno, A. Rescifina, E. Amata, *Eur. J. Med. Chem.* **2017**, *142*, 459–485.
[376] I. K. Mbaraka, B. H. Shanks, *J. Am. Oil Chem. Soc.* **2006**, *83*, 79–91.

[377] C. G. Thomson, A.-L. Lee, F. Vilela, *Beilstein J. Org. Chem.* **2020**, *16*, 1495–1549.
[378] V. Vattipalli, X. Qi, P. J. Dauenhauer, W. Fan, *Chem. Mater.* **2016**, *28*, 7852–7863.
[379] A. A. Kiss, A. C. Dimian, G. Rothenberg, *Adv. Synth. Catal.* **2006**, *348*, 75–81.
[380] V.-T. Hoang, Q. Huang, M. Eić, T.-O. Do, S. Kaliaguine, *Langmuir* **2005**, *21*, 2051–2057.
[381] S. M. Ribeiro, A. C. Serra, A. d'A R. Gonsalves, *J. Mol. Catal. Chem.* **2010**, *326*, 121–127.
[382] L. F. Tietze, G. v. Kiedrowski, K.-G. Fahlbusch, E. Voss, *Org Synth* **1990**, *69*, 31.
[383] K. Bock, N. Jacobsen, B. Terem, *J. Chem. Soc. Perkin 1* **1986**, 659–664.
[384] I. Biggs, J. Tedder, *Tetrahedron* **1978**, *34*, 1377–1380.
[385] J.-C. Henrion, B. Jacquet, M. Hocquaux, G. Barre, M. Hedayatullah, C. Lion, *Bull. Soc. Chim. Belg.* **1996**, *105*, 415–418.
[386] D. Göbel, P. Rusch, D. Duvinage, T. Stauch, N.-C. Bigall, B. J. Nachtsheim, *J. Org. Chem.* **2021**, *86*, 14333–14355.
[387] D. Rehm, A. Weller, *Isr. J. Chem.* **1970**, *8*, 259–271.
[388] Y. Wu, D. Kim, T. S. Teets, *Synlett* **2022**, *33*, 1154–1179.
[389] J.-F. Lefebvre, J. Schindler, P. Traber, Y. Zhang, S. Kupfer, S. Gräfe, I. Baussanne, M. Demeunynck, J.-M. Mouesca, S. Gambarelli, V. Artero, B. Dietzek, M. Chavarot-Kerlidou, *Chem. Sci.* **2018**, *9*, 4152–4159.
[390] A. Aydogan, R. E. Bangle, S. De Kreijger, J. C. Dickenson, M. L. Singleton, E. Cauët, A. Cadranel, G. J. Meyer, B. Elias, R. N. Sampaio, L. Troian-Gautier, *Catal. Sci. Technol.* **2021**, *11*, 8037–8051.
[391] M. Schmallegger, G. Gescheidt, *Monatshefte Für Chem.-Chem. Mon.* **2018**, *149*, 499–504.
[392] J. Hu, J. Wang, T. H. Nguyen, N. Zheng, *Beilstein J. Org. Chem.* **2013**, *9*, 1977–2001.
[393] A. Tlili, S. Lakhdar, *Angew. Chem.* **2021**, *133*, 19678–19701.
[394] S. M. Sartor, C. H. Chrisman, R. M. Pearson, G. M. Miyake, N. H. Damrauer, *J. Phys. Chem. A* **2020**, *124*, 817–823.
[395] Y. Liu, Q. Chen, Y. Tong, Y. Ma, *Macromolecules* **2020**, *53*, 7053–7062.
[396] J. M. Narayanam, C. R. Stephenson, *Chem. Soc. Rev.* **2011**, *40*, 102–113.
[397] M. C. Rosko, E. M. Espinoza, S. Arteta, S. Kromer, J. P. Wheeler, F. N. Castellano, *Inorg. Chem.* **2023**, *62*, 3248–3259.
[398] T. P. Nicholls, A. C. Bissember, *Tetrahedron Lett.* **2019**, *60*, 150883.
[399] C. Deldaele, B. Michelet, H. Baguia, S. Kajouj, E. Romero, C. Moucheron, G. Evano, *Chimia* **2018**, *72*, 621–629.
[400] A. Hossain, A. Bhattacharyya, O. Reiser, *Science* **2019**, *364*, eaav9713.

[401] P. Xiao, F. Dumur, J. Zhang, J. P. Fouassier, D. Gigmes, J. Lalevee, *Macromolecules* **2014**, *47*, 3837–3844.
[402] Y. Zhang, M. Heberle, M. Wächtler, M. Karnahl, B. Dietzek, *RSC Adv.* **2016**, *6*, 105801–105805.
[403] M. Nishikawa, D. Kakizoe, Y. Saito, T. Ohishi, T. Tsubomura, *Bull. Chem. Soc. Jpn.* **2017**, *90*, 286–288.
[404] V. Kabanov, B. Heyne, *ACS Appl. Nano Mater.* **2020**, *3*, 8126–8137.
[405] O. Planas, N. Macia, M. Agut, S. Nonell, B. Heyne, *J. Am. Chem. Soc.* **2016**, *138*, 2762–2768.
[406] S. Shanmugam, S. Xu, N. N. M. Adnan, C. Boyer, *Macromolecules* **2018**, *51*, 779–790.
[407] V. Blanchard, Z. Asbai, K. Cottet, G. Boissonnat, M. Port, Z. Amara, *Org. Process Res. Dev.* **2020**, *24*, 822–826.
[408] K. Mori, M. Tottori, K. Watanabe, M. Che, H. Yamashita, *J. Phys. Chem. C* **2011**, *115*, 21358–21362.
[409] H. Zhao, W. He, R. Yao, M. Cai, *Adv. Synth. Catal.* **2014**, *356*, 3092–3098.
[410] F. Habeche, M. Hachemaoui, A. Mokhtar, K. Chikh, F. Benali, A. Mekki, F. Zaoui, Z. Cherifi, B. Boukoussa, *J. Inorg. Organomet. Polym. Mater.* **2020**, *30*, 4245–4268.
[411] R. Hosseinzadeh, N. Aghili, M. Mavvaji, *Polyhedron* **2022**, *213*, 115631.
[412] S. Sakaki, T. Kuroki, T. Hamada, *J. Chem. Soc. Dalton Trans.* **2002**, 840–842.
[413] F. J. Malzner, S. Y. Brauchli, E. Schönhofer, E. C. Constable, C. E. Housecroft, *Polyhedron* **2014**, *82*, 116–121.
[414] D. J. Monk, D. S. Soane, R. T. Howe, *Thin Solid Films* **1993**, *232*, 1–12.
[415] D. J. Monk, D. S. Soane, R. T. Howe, *J. Electrochem. Soc.* **1993**, *140*, 2339.
[416] X.-G. Teng, F.-Q. Li, P.-H. Ma, Q.-D. Ren, S.-Y. Li, *Thermochim. Acta* **2005**, *436*, 30–34.
[417] P. Barnes, K. Smith, R. Parrish, C. Jones, P. Skinner, E. Storch, Q. White, C. Deng, D. Karsann, M. L. Lau, J. J. Dumais, E. J. Dufek, H. Xiong, *J. Power Sources* **2020**, *447*, 227363.
[418] R. Xiao, H. Zhao, M. Cai, *Tetrahedron* **2013**, *69*, 5444–5450.
[419] C. Li, R. Dickson, N. Rockstroh, J. Rabeah, D. B. Cordes, A. M. Slawin, P. Hünemörder, A. Spannenberg, M. Bühl, E. Mejía, E. Zysman-Colman, P. C. J. Kamer, *Catal. Sci. Technol.* **2020**, *10*, 7745–7756.
[420] M. Ruthkosky, F. N. Castellano, G. J. Meyer, *Inorg. Chem.* **1996**, *35*, 6406–6412.
[421] S. Cerfontaine, S. A. Wehlin, B. Elias, L. Troian-Gautier, *J. Am. Chem. Soc.* **2020**, *142*, 5549–5555.
[422] A. Soupart, F. Alary, J.-L. Heully, P. I. P. Elliott, I. M. Dixon, *Coord. Chem. Rev.* **2020**, *408*, 213184.

[423] R. Z. Boota, S. J. O. Hardman, G. P. Ashton, C. R. Rice, P. A. Scattergood, P. I. P. Elliott, *Inorg. Chem.* **2021**, *60*, 15768–15781.
[424] K. Eastham, P. A. Scattergood, D. Chu, R. Z. Boota, A. Soupart, F. Alary, I. M. Dixon, C. R. Rice, S. J. O. Hardman, P. I. P. Elliott, *Inorg. Chem.* **2022**, *61*, 19907–19924.
[425] J. K. White, R. H. Schmehl, C. Turro, *Inorganica Chim. Acta* **2017**, *454*, 7–20.
[426] S. Cerfontaine, L. Troian-Gautier, S. A. Wehlin, F. Loiseau, E. Cauët, B. Elias, *Dalton Trans.* **2020**, *49*, 8096–8106.
[427] T. Hering, D. P. Hari, B. König, *J. Org. Chem.* **2012**, *77*, 10347–10352.
[428] S. Fischer, D. Hollmann, S. Tschierlei, M. Karnahl, N. Rockstroh, E. Barsch, P. Schwarzbach, S.-P. Luo, H. Junge, M. Beller, S. Lochbrunner, R. Ludwig, A. Brückner, *ACS Catal.* **2014**, *4*, 1845–1849.
[429] Z. Singh, P. R. Donnarumma, M. B. Majewski, *Inorg. Chem.* **2020**, *59*, 12994–12999.
[430] J. Yuasa, M. Dan, T. Kawai, *Dalton Trans.* **2013**, *42*, 16096–16101.
[431] J. Sandland, R. W. Boyle, *Bioconjug. Chem.* **2019**, *30*, 975–993.
[432] G. Van Dongen, G. Visser, M. Vrouenraets, *Adv. Drug Deliv. Rev.* **2004**, *56*, 31–52.
[433] C. C. Rennie, R. M. Edkins, *Dalton Trans.* **2022**, *51*, 13157–13175.
[434] V. F. Otvagin, N. S. Kuzmina, E. S. Kudriashova, A. V. Nyuchev, A. E. Gavryushin, A. Y. Fedorov, *J. Med. Chem.* **2022**, *65*, 1695–1734.
[435] Y. Zhai, H. J. Busscher, Y. Liu, Z. Zhang, T. G. van Kooten, L. Su, Y. Zhang, J. Liu, J. Liu, Y. An, L. Shi, *Biomacromolecules* **2018**, *19*, 2023–2033.
[436] L. Hou, X. Zhang, T. C. Pijper, W. R. Browne, B. L. Feringa, *J. Am. Chem. Soc.* **2014**, *136*, 910–913.
[437] Z. Li, S. Chen, Y. Huang, H. Zhou, S. Yang, H. Zhang, M. Wang, H. Guo, J. Yin, *Chem. Eng. J.* **2022**, *450*, 138087.
[438] J. E. Yarnell, K. A. Wells, J. R. Palmer, J. M. Breaux, F. N. Castellano, *J. Phys. Chem. B* **2019**, *123*, 7611–7627.
[439] K. Guan, P. Wang, F. Zhou, Y. Wang, H.-W. Liu, Q. Xie, G. Song, X. Yin, S. Huan, X.-B. Zhang, *Chem. Commun.* **2020**, *56*, 14007–14010.
[440] A. J. Sandee, J. N. Reek, P. C. Kamer, P. W. van Leeuwen, *J. Am. Chem. Soc.* **2001**, *123*, 8468–8476.
[441] S. Ricken, P. W. Osinski, P. Eilbracht, R. Haag, *J. Mol. Catal. Chem.* **2006**, *257*, 78–88.
[442] D. Yang, H. Liu, D.-L. Wang, Z. Luo, Y. Lu, F. Xia, Y. Liu, *Green Chem.* **2018**, *20*, 2588–2595.
[443] W. P. Mul, K. Ramkisoensing, P. C. Kamer, J. N. Reek, A. J. van der Linden, A. Marson, P. W. van Leeuwen, *Adv. Synth. Catal.* **2002**, *344*, 293–298.
[444] H.-J. Werner, P. J. Knowles, F. R. Manby, J. A. Black, K. Doll, A. Heßelmann, D. Kats, A. Köhn, T. Korona, D. A. Kreplin, Q. Ma, T. F.

Miller III, A. Mitrushchenkov, K. A. Peterson, I. Polyak, G. Rauhut, M. Sibaev, *J. Chem. Phys.* **2020**, *152*, 144107.
[445] T. Lu, F. Chen, *J. Comput. Chem.* **2012**, *33*, 580–592.
[446] E. D. Glendening, J. K. Badenhoop, A. E. Reed, J. E. Carpenter, J. A. Bohmann, C. M. Morales, P. Karafiloglou, C. R. Landis, F. Weinhold, *NBO 7.0 Program*, Theoretical Chemistry Institute, University Of Wisconsin, Madison, **2018**.
[447] A. Gilbert, "IQmol Molecular Viewer," can be found under http://iqmol.org/.

Publications and scientific communications

Accepted publications in peer-reviewed journals

- **N. Body**, C. Lefebvre, P. Eloy, T. Haynes, S. Hermans O. Riant. Impact of silica nanoparticles architectures on the photosensitization of O_2 by immobilized Rose Bengal. *Journal of Photochemistry and Photobiology A: Chemistry* **2023**, *440*, 114648. https://doi.org/10.1016/j.jphotochem.2023.114648
- J. G. Mahy, L. Lejeune, T. Haynes, **N. Body**, S. De Kreijger, B. Elias, R. H. M. Marcilli, C.-A. Fustin, S. Hermans. Crystalline ZnO Photocatalysts Prepared at Ambient Temperature: Influence of Morphology on *p*-Nitrophenol Degradation in Water. *Catalysts* **2021**, *11*, 1182. https://doi.org/10.3390/catal11101182
- J. G. Mahy, S. Douven, J. Hollevoet, **N. Body**, T. Haynes, S. Hermans, S. D. Lambert, C. A. Paez. Easy stabilization of Evonik Aeroxide P25 colloidal suspension by 4-hydroxybenzoic acid functionalization. *Surfaces and Interfaces* **2021**, *27*, 101501. https://doi.org/10.1016/j.surfin.2021.101501

Publications submitted in peer-reviewed journals

- **N. Body**, R. Bevernaegie, C. Lefebvre, I. Jabin, S. Hermans, O. Riant, L. Troian-Gautier. *Chem. Eur. J* **2023**, under revision.

Publication to be submitted soon to peer-reviewed journals

- **N. Body**, C. Lefebvre, S. Eeckhout, A.-S. Léonard, L. Troian-Gautier, S. Hermans, O. Riant. Structure-activity relationship investigation of new

benzophenazine derivatives as homogeneous and heterogenized photooxygenation catalysts, waiting for approval from co-authors.

Oral communications

- Dimethylphenanthroline, a suitable platform for the anchoring of copper photocatalysts. Presented in Louvain-la-Neuve, Belgium at the Ph.D. Students' Day 2022. Université catholique de Louvain. May, 2022.
- Impact of silica nanoparticles architectures on the photosensitization of O_2 by Rose Bengal. Presented in Liège, Belgium at the 14th One-Day Meeting of Young Chemist. Université de Liège. April, 2022.
- Photocatalysts' Heterogenization on Nanostructured Silica for Applications in Organic Synthesis. Presented online for the Athens Summer School on Organic Synthesis (ASSOS2021) and International Young Investigator Symposium. August, 2021.
- Synthesis and immobilization on carbon nanotubes of chiral catalysts used in enantioselective catalysis. Presented in Namur, Belgium at the Scientific Day of Société Royale de Chimie. Université de Namur. October, 2019.

Posters

- Photo-Catalyzed α-Arylation of Enol Acetate Using Recyclable Silica-Supported Heteroleptic and Homoleptic Copper(I) Photosensitizers. Presented in Louvain-la-Neuve, Belgium at the Ph.D. Students' Day 2023. Université catholique de Louvain. May, 2023.
- One-step immobilization of copper photocatalysts by using urea bond as photostable linker. Presented in Namur, Belgium at the 17th Belgian Organic Synthesis Symposium BOSS 2022. Université de Namur. July, 2022.
- Synthesis and immobilization on carbon nanotubes of chiral catalysts used in enantioselective catalysis. Presented in Namur, Belgium at Journées-rencontres des Jeunes Chimistes. Université de Namur. March, 2020.